

THE UNIVERSITY *of* EDINBURGH

The role of transcription factor Pax6 in the development of the ventral lateral geniculate nucleus

Ziwen Li

A Thesis Submitted for the Degree of Doctor of Philosophy

School of Biomedical Sciences

University of Edinburgh

January 2018

Disclaimer

I (Ziwen Li) declare that this thesis has been composed solely by myself and that it has not been submitted, in whole or in part, in any previous application for a degree. Except where states otherwise by reference or acknowledgment, the work presented is entirely my own.

Signed:

Date:

“莫听穿林打叶声，

何妨吟啸且徐行。

竹杖芒鞋轻胜马，谁怕？

一蓑烟雨任平生。

料峭春风吹酒醒，微冷，

山头斜照却相迎。

回首向来萧瑟处，

归去，也无风雨也无晴。”

— 【宋】苏轼

“Listen not to the rain beating against the trees.

Why don’t you slowly walk and chant at ease?

Better than saddled horse I like sandals and cane.

O I would fain

Spend a straw-cloaked life in mist and rain.

Drunken, I’m sobered by vernal wind shrill

And rather chill.

In front I see the slanting sun atop the hill;

Turning my head, I see the dreary beaten track.

Let me go back!

Impervious to wind, rain or shine, I’ll have my will.”

- Shi Su (Song Dynasty)

Acknowledgements

I would like to take this great opportunity to thank:

my supervisor Professor David Price, for guiding me

Dr Tom Pratt and Dr Martine Manuel, for advising

Dr Anisha Kubasik-Thayil, for helping with confocal microscopy

Vivian Alison and Louis Dunn, for helping with histology

Mike Molinek, for supervising the lab work

Zrinko Kozic, for consulting on the RNA-seq experiment

Mi Da, Gosia, Nikky, Elena, Hannah, Calvin, Alex, Tian
Jim, Idoia, Vassiliki, Kerstin, Thomas
Rebecca, Innes, Hannah, Anne, Chrissy

DBUG group, for hosting my PhD

My boyfriend, fiance and husband Ben, for always being there for me

Mum and dad, for being patient

My in-laws, for looking after me

Abstract

The development of the diencephalon can be summarised as a process in which cells that initially appear similar give rise to a complex structure that contains a variety of cell groups called nuclei. It involves two stages: the early patterning of the diencephalic prosomeres and the later formation of the individual nuclei. It has been shown that transcription factors and morphogens regulate the first stage but their further effects on the second stage remain unclear. The ventral lateral geniculate nucleus (vLGN) is involved in the visual system and is shown to have complex origins from the thalamus, the zona limitans intrathalamica (ZLI) and the prethalamus.

The transcription factor Pax6 is involved in the development of brain structures including the cortex, the diencephalon and the major axonal tracts in the forebrain by playing a multifaceted role in patterning, proliferation, differentiation, migration and axon guidance. It is known that Pax6 is essential in setting up the prosomeric boundaries in the developing diencephalon but its role in the formation of individual nuclei has not yet been explored. By using a conditional Pax6 knock-out mouse driven by *Zic4Cre* with a green fluorescent protein (GFP) reporter showing the Cre activity, the formation of the thalamic nuclei vLGN, dorsal lateral geniculate nucleus (dLGN) and VP (ventral posterior nuclei) was examined in postnatal day 0 (P0) $Pax6^{+/+}$, $Pax6^{fl/+}$ and $Pax6^{fl/fl}$ pups.

Using this mouse model, I found an increase in nuclear volume at the rostral level and a global decrease in cell density in the P0 $Pax6^{fl/fl}$ vLGN, whereas in the dLGN an increase of GFP+ve cell proportion was observed. In $Pax6^{fl/+}$, I found an increase in GFP+ve cell proportion in the caudal part of the vLGN and across the dLGN. No significant change was observed in the VP in either the $Pax6^{fl/+}$ or the $Pax6^{fl/fl}$. The defects in the vLGN and dLGN could be caused by: 1. disruption of the expression of patterning factors such as Shh and Nkx2.2; 2. cell proliferation defcts and abnormal apoptosis; 3. ocular developmental defects; 4. failure in cell sorting/migration; 5. cell fate change. During my PhD, I tested the first three theories and explored the fourth but was not able to pursue the last due to the time limit of the project.

To test the hypothesized mechanisms underlying those defects seen in the vLGN and dLGN, I performed BrdU labelling to study the time origin of cells that contribute to these two nuclei and discovered that E11.5 and E12.5 are the main ages when these cells and the GFP+ve subpopulation are born. Then I carried out experiments to examine the cell proliferation and cell apoptosis in the thalamus (pTH-R, rostral part of the progenitor zone of the thalamus, and pTH-C, caudal part of the progenitor zone of the thalamus) and the prethalamus (Pth) from E11.5 to E13.5 and found: 1. the proliferation rate decreased in the pTH-R in $Pax6^{fl/+}$ at E11.5; 2. the growth fraction decreased in both pTH-C and pTH-R in E12.5 $Pax6^{fl/fl}$; 3. there is no change in cell proliferation in the GFP+ve subpopulation; 4. no abnormal apoptosis is observed in either the whole cell population or the GFP+ve subpopulation. Judging by the amplitude of the change in proliferation in the pTH-R and pTH-C at E11.5 and E12.5, it is unlikely that these changes alone are responsible for the phenotypes seen in P0 vLGN and dLGN.

Then I examined the expression patterns of *Shh* and *Nkx2.2* and the expansion of both was observed in $Pax6^{fl/fl}$ at both E12.5 and E13.5, which could explain the volume change of the vLGN but not the change in the proportion of GFP+ve subpopulation in both the vLGN and dLGN. Then I continued to examine if the ocular input from the retinal ganglionic cells are severely affected by the deletion of *Pax6* and found no gross change in the conditional mutants, which rejected the ocular developmental defects theory.

At the end of my PhD, I performed a BrdU short-term survival experiment and a brain slice culture combined with live imaging experiment to explore the possibility of abnormal cell migration causing the vLGN and dLGN phenotypes and found that the cells moving along the border of the thalamus and prethalamus move faster in the $Pax6^{fl/fl}$ than in the $Pax6^{fl/+}$, but rather than moving directly toward the lateral surface of the diencephalon, they take a detour.

These findings indicate that the deletion of Pax6 causes minor changes in the proliferation of E11.5 to E13.5 diencephalon and expansion of regional marker expression such as *Shh* and *Nkx2.2*, which could potenially affect the volume and change the proportion of GFP+ve cells in P0 vLGN and dLGN. Migration defects caused by Pax6 could also contribute to the phenotype observed in those two nuclei. Potential cell fate change caused by Pax6 deletion could be another factor that contributes to the defects in the conditional mutants. More work needs to be done to test the migration defect and cell fate change hypotheses in future.

Lay summary

The thalamus is a structure in the middle of the brain containing many cell groups that send information around the brain. In embryos, the growth of the thalamus starts from a mass of cells. These cells look like each other but gradually they produce new cells that move to different places and form groups with different functions. I study how these cell groups are formed.

Like all biological events, the formation of these cell groups requires specific proteins and my study is focused on one of these proteins called Pax6. To study the function of this protein in the formation of the cell groups, I used a genetically modified mouse lacking the protein. I found one cell group became bigger but with no change in cell number. I also found a type of cells becoming more dominant within the cell group.

There are several possibilities where those changes in the cell group could come from. The cells may have been produced more slowly. The cells could have died before they formed the group. The cells could travel faster, forming an abnormally big group. Some cells could even switch group identity to make some groups bigger and leave others smaller. My study of the mouse lacking the Pax6 protein suggests that cell production drops, some cells changed their identity and some cells travel faster than normal, which all contribute to the changes I saw in the cell group.

Contents

1 Introduction **2**

1.1 Development of the diencephalon . . . 3

1.1.1 Development of the mouse brain . . . 3

1.1.2 Prosomeric model of the neural tube development . . . 4

1.1.3 Development of the diencephalon . . . 5

1.1.4 Neuroanatomy of the thalamus . . . 5

1.2 Signalling molecules and transcription factors and their roles in controlling the subdividing of diencephalon . . . 6

1.3 Pax6's role in the development of the diencephalon . . . 7

1.4 Nuclei formation in the diencephalon . . . 10

1.4.1 Development of the ventral lateral geniculate nucleus . . . 10

1.4.1.1 What is ventral lateral geniculate nucleus? . . . 10

1.4.1.2 Neurogenesis in developing ventral lateral geniculate nucleus 11

1.4.1.3 Marker gene expression in developing ventral lateral geniculate nucleus . . . 12

1.4.2 Neurogenesis in developing dorsal lateral geniculate nucleus . . . 13

1.4.3 Neurogenesis in developing ventral posterior nuclei . . . 13

1.5 Cell proliferation, cell cycle and cell apoptosis in developing thalamus . . . 15

1.6 Zic4 and its role in the development of the central nervous system . . . 22

1.6.1 Discovery of the *Zic4* gene . . . 22

1.6.2 *Zic4* gene and Dandy-Walker malformation . . . 23

1.6.3 Expression of the *Zic4* gene in the developing mouse nervous system . . . 28

1.6.4 *Zic4* gene is involved in neural tube development . . . 28

1.6.5 The role of *Zic4* gene in the visual pathway development . . . 29

1.7 Lineage tracing and fate mapping in developing diencephalon . . . 30

1.7.1 Lineage tracing and fate mapping techniques in developmental biology 30

1.7.2 Lineage tracing and fate mapping studies in diencephalic development 31

1.8 Aim of the study and hypotheses . . . 35

2 Materials and methods **36**

2.1 Animal . . . 36

2.1.1 Animal husbandary . . . 36

2.1.2 Genotyping . . . 36

2.1.3 Embryo/pups Collection . . . 39

2.2 Histological protocols . . . 40

2.2.1 Cresyl violet staining on paraffin embedded sections . . . 40

2.2.2 Immunohistochemistry on paraffin embedded sections . . . 40

2.2.3 Colourimetric *In situ* hybridisation on sucrose/OCT(1:1) embedded tissue 40

2.2.4 Fluorescent *In situ* hybridisation on sucrose/OCT(1:1) embedded tissue 42

2.3 Solutions, antibodies and RNA probes . . . 44

2.4 Quantitative analysis of fluorescence microscopy images . . . 47

2.4.1 Image aquisition . . . 47

2.4.2 Image processing . . . 48

2.5 Statistical analysis and plotting methodology . . . 48

2.6 Ocular NeuroVue Red injection . . . 48

3 Dynamic expression of *Zic4* and *Zic4* lineage cell fate mapping in the developing diencephalon **50**

3.1 Introduction . . . 50

3.2 Aim of the project . . . 51

3.3 Results . . . 53

3.3.1 Expression of *Zic4* transcripts and GFP in the E11.5 $Zic4Cre^{+/-};RCE^{+/-}$ mouse diencephalon . . . 53

3.3.2 Expression of *Zic4* transcripts and GFP in the E12.5 $Zic4Cre^{+/-};RCE^{+/-}$ mouse diencephalon . . . 59

3.3.3 Expression of *Zic4* transcripts and GFP in the E13.5 $Zic4Cre^{+/-};RCE^{+/-}$ mouse diencephalon . . . 64

3.3.4 Expression of *Zic4* transcripts and GFP in the E14.5 $Zic4Cre^{+/-};RCE^{+/-}$ mouse diencephalon . . . 69

3.3.5 Expression of *Zic4* transcripts and GFP in the E15.5 $Zic4Cre^{+/-};RCE^{+/-}$ mouse diencephalon . . . 74

3.3.6 Expression of *Zic4* transcripts and GFP in the E16.5 $Zic4Cre^{+/-};RCE^{+/-}$ mouse diencephalon . . . 78

3.3.7 Expression of *Zic4* transcripts and GFP in E17.5 $Zic4Cre^{+/-};RCE^{+/-}$ mouse diencephalon . . . 82

3.3.8 Expression of *Zic4* transcripts and GFP in the E18.5 and P0 $Zic4Cre^{+/-};RCE^{+/-}$ mouse diencephalon . . . 85

3.4 Synopsis . . . 89
3.5 Discussion . . . 91

4 Quantitative analysis of *Zic4* transcripts and GFP reporter at cellular levels in the developing diencephalon in *Zic4Cre*$^{+/-}$;*RCE*$^{+/-}$ mice 97
4.1 Introduction . . . 97
4.1.1 Visualisation and quantification of mRNA molecules . . . 97
4.1.2 Computational image analysis and cell segmentation . . . 98
4.1.3 Distribution of mRNA molecules across a single cell . . . 102
4.2 Aim of the project . . . 102
4.3 Results . . . 103
4.3.1 Quantitative analysis of *Zic4* transcript signals in *Zic4Cre*$^{+/-}$;*RCE*$^{+/-}$ mouse diencephalic cells at E11.5 . . . 110
4.3.2 Quantitative analysis of *Zic4* transcript signal in *Zic4Cre*$^{+/-}$;*RCE*$^{+/-}$ mouse diencephalic cells at E12.5 . . . 113
4.3.3 Quantitative analysis of *Zic4* transcript signal in *Zic4Cre*$^{+/-}$;*RCE*$^{+/-}$ mouse diencephalic cells at E13.5 . . . 117
4.3.4 Quantitative analysis of *Zic4* transcript signal in *Zic4Cre*$^{+/-}$;*RCE*$^{+/-}$ mouse diencephalic cells at E14.5 . . . 126
4.3.5 Quantitative analysis of *Zic4* transcript signal in *Zic4Cre*$^{+/-}$;*RCE*$^{+/-}$ mouse diencephalic cells at E15.5 . . . 133
4.4 Synopsis . . . 138
4.5 Discussion . . . 141
4.5.1 Other available FISH techniques . . . 141
4.5.2 Pros and cons in using computational image analysis for this project . . . 141
4.5.3 A speculated lifetime of a *Zic4* lineage cell . . . 142
4.5.4 The emergence and growth of *Zic4* cell lineage in the diencephalon . . . 144

5 Deletion of Pax6 driven by *Zic4Cre* in the developing diencephalon in *Zic4Cre*$^{+/-}$;*RCE*$^{+/-}$;*Pax6*$^{fl/+}$ and *Zic4Cre*$^{+/-}$;*RCE*$^{+/-}$;*Pax6*$^{fl/fl}$ mice 145
5.1 Introduction . . . 145
5.2 Aim of the project . . . 146
5.3 Results . . . 146
5.3.1 Deletion of Pax6 in the E12.5 *Zic4Cre*$^{+/-}$;*RCE*$^{+/-}$;*Pax6*$^{fl/+}$ and *Zic4Cre*$^{+/-}$;*RCE*$^{+/-}$;*Pax6*$^{fl/fl}$ diencephalon . . . 147
5.3.2 Deletion of Pax6 in the E13.5 *Zic4Cre*$^{+/-}$;*RCE*$^{+/-}$;*Pax6*$^{fl/+}$ and *Zic4Cre*$^{+/-}$;*RCE*$^{+/-}$;*Pax6*$^{fl/fl}$ diencephalon . . . 150

5.3.3 Deletion of Pax6 in the E14.5 *Zic4Cre*$^{+/-}$;*RCE*$^{+/-}$;*Pax6*$^{fl/+}$ and *Zic4Cre*$^{+/-}$;*RCE*$^{+/-}$;*Pax6*$^{fl/fl}$ diencephalon . . . 153
5.3.4 Deletion of Pax6 in the E16.5 *Zic4Cre*$^{+/-}$;*RCE*$^{+/-}$;*Pax6*$^{fl/+}$ and *Zic4Cre*$^{+/-}$;*RCE*$^{+/-}$;*Pax6*$^{fl/fl}$ diencephalon . . . 156
5.4 Synopsis . . . 158
5.5 Discussion . . . 158
5.5.1 Pax6 deletion is well related to the Cre activation pattern in the hom diencephalon . . . 158
5.5.2 Up-regulation of Pax6 in the het diencephalon and potential mechanisms 159

6 *Zic4Cre* mediated deletion of *Pax6* causes developmental defects in vLGN, dLGN and VP 162
6.1 Introduction . . . 162
6.2 Aim of the project . . . 162
6.3 Results . . . 163
6.3.1 Delineation of diencephalic nuclei vLGN, dLGN and VP . . . 163
6.3.1.1 Image alignment and reference atlas . . . 163
6.3.1.2 Boundary determination for vLGN, dLGN and VP . . . 175
6.3.2 Estimated volume change in vLGN, dLGN and VP in conditional *Pax6* mutants . . . 179
6.3.3 Cell composition change in vLGN, dLGN and VP in conditional *Pax6* mutants . . . 185
6.3.3.1 Cell density change in vLGN, dLGN and VP in conditional *Pax6* mutants . . . 187
6.3.3.2 GFP+ve cell proportion change in vLGN, dLGN and VP in conditional *Pax6* mutants . . . 192
6.3.3.3 Altered expression of Nkx2.2 and Lim1/2 in the vLGN in conditional *Pax6* mutants . . . 194
6.4 Synopsis . . . 196
6.5 Discussion . . . 196

7 BrdU labelling identifies the birth dates of the GFP+ve cells in P0 vLGN, dLGN and VP in *Zic4Cre*$^{+/-}$;*RCE*$^{+/-}$;*Pax6*$^{+/+}$ mice 200
7.1 Introduction . . . 200
7.2 Aim of the project . . . 201
7.3 Results . . . 201
7.4 Synopsis . . . 211

8 *Zic4Cre* mediated deletion of *Pax6* causes cell proliferation defects and abnormal apoptosis at E11.5, E12.5 and E13.5 **213**
8.1 Introduction . . . 213
8.2 Aim of the project . . . 214
8.3 Results . . . 214
8.3.1 Cell Proliferation . . . 214
8.3.2 Cell proliferation change in conditional *Pax6* mutants at E11.5, E12.5 and E13.5 . . . 219
8.3.2.1 Growth fraction . . . 219
8.3.2.2 Proliferation rate . . . 221
8.3.2.3 Cycling speed . . . 223
8.3.2.4 Basal dividing population . . . 224
8.3.3 Cell apoptosis in conditional *Pax6* mutants induced by *Zic4Cre* at E11.5, E12.5, E13.5 and E14.5 . . . 228
8.4 Synopsis . . . 234
8.5 Discussion . . . 236
8.6 Future work . . . 238

9 *Zic4Cre* mediated deletion of *Pax6* causes early diencephalic patterning defects at E12.5 and E13.5 **239**
9.1 Introduction . . . 239
9.2 Aim of the project . . . 240
9.3 Results . . . 240
9.4 Synopsis . . . 243
9.5 Discussion . . . 244

10 *Zic4Cre* mediated deletion of Pax6 causes eye malformation but has no effects on the innervation of retinal ganglionic processes into vLGN or dLGN **246**
10.1 Introduction . . . 246
10.2 Aim of the project . . . 247
10.3 Result . . . 248
10.4 Synopsis . . . 249

11 Discussion **250**
11.1 Diencephalic developmental defects observed in $Pax6^{fl/+}$: haploinsufficiency or dominant negative effects? . . . 251
11.2 Developmental defects observed in non-GFP+ve diencephalic cells suggests Pax6 plays a non-cell autonomous role in the developing diencephalon . . . 253
11.3 Pax6 plays different roles in the development of the thalamus and the prethalamus 254

11.4 Pax6's role in vLGN formation - the big picture 255

12 Future directions **257**

13 Conclusion **259**

List of Figures

1.1 Schematics of E8.5 (horizontal view) and E10.5 (sagittal view) neural tube . . . 3
1.2 Schematics of prosomeric model . . . 4
1.3 Diagrams of coronal sections of the rostral, middle and caudal parts of the vLGN 11
1.4 Schematic of neuronal time origin in the vLGN . . . 12
1.5 Schematic of neuronal time origin in the dLGN . . . 13
1.6 Positioning of VP in the diagrams of coronal sections of the rostral, middle and caudal parts of the vLGN . . . 14
1.7 Schematic of neuronal time origin in the VP . . . 15
1.8 Regulatory mechinary of cell cycle progression . . . 16
1.9 Schematic overview of neurogenesis in the embryonic vertebrate CNS . . . 18
1.10 Schematic of the MADM Strategy . . . 21
1.11 Whole mount dorsal view of an adult mouse cerebellum(left) and schematic midsagittal section of the cerebellar vermis. . . . 25
1.12 Dorsal views of whole mount cerebellum and staining of midsagittal sections through the vermis from wild type and different Zic1, Zic4 and Shh single or compound mutant mice at P20 and P22. . . . 26
1.13 Summary of lineage fate-mapping studies . . . 34

3.1 Schematic of the strategy for Zic4 genomic BAC modification . . . 51
3.2 Schematic of Cre-loxP system driven by Zic4 in this project . . . 52
3.3 E11.5 mouse brain sagittal and coronal view schematic . . . 54
3.4 GFP immunohistochemistry and Zic4 fluorescent in situ hybridisation on E11.5 Zic4Cre$^{+/-}$;RCE$^{+/-}$mouse brain coronal sections . . . 57
3.5 High power images for GFP immunohistochemistry (green) and Zic4 fluorescent in situ hybridisation (red) on E11.5 Zic4Cre$^{+/-}$;RCE$^{+/-}$mouse brain coronal sections 58
3.6 E12.5 mouse brain sagittal and coronal view schematic . . . 59
3.7 GFP immunohistochemistry and Zic4 fluorescent in situ hybridisation on E12.5 Zic4Cre$^{+/-}$;RCE$^{+/-}$mouse brain coronal sections . . . 62

3.8 High power images for GFP immunohistochemistry and Zic4 fluorescent in situ hybridisation on E12.5 Zic4Cre$^{+/-}$;RCE$^{+/-}$mouse brain coronal sections 63
3.9 E13.5 mouse brain sagittal and coronal view schematic 64
3.10 GFP immunohistochemistry and Zic4 fluorescent in situ hybridisation on E13.5 Zic4Cre$^{+/-}$;RCE$^{+/-}$mouse brain coronal sections 67
3.11 High power images for GFP immunohistochemistry and Zic4 fluorescent in situ hybridisation on E13.5 Zic4Cre$^{+/-}$;RCE$^{+/-}$mouse brain coronal sections 68
3.12 E14.5 mouse brain sagittal and coronal view schematic 69
3.13 GFP immunohistochemistry and Zic4 fluorescent in situ hybridisation on E14.5 Zic4Cre$^{+/-}$;RCE$^{+/-}$mouse brain coronal sections 72
3.14 High power images for GFP immunohistochemistry and Zic4 fluorescent in situ hybridisation on E14.5 Zic4Cre$^{+/-}$;RCE$^{+/-}$mouse brain coronal sections 73
3.15 E15.5 mouse brain sagittal and coronal view schematic 74
3.16 GFP immunohistochemistry and Zic4 fluorescent in situ hybridisation on E15.5 Zic4Cre$^{+/-}$;RCE$^{+/-}$mouse brain coronal sections 76
3.17 High power images for GFP immunohistochemistry and Zic4 fluorescent in situ hybridisation on E15.5 Zic4Cre$^{+/-}$;RCE$^{+/-}$mouse brain coronal sections 77
3.18 E16.5 mouse brain sagittal and coronal view schematic 78
3.19 GFP immunohistochemistry and Zic4 fluorescent in situ hybridisation on E16.5 Zic4Cre$^{+/-}$;RCE$^{+/-}$mouse brain coronal sections 80
3.20 High power images for GFP immunohistochemistry and Zic4 fluorescent in situ hybridisation on E16.5 Zic4Cre$^{+/-}$;RCE$^{+/-}$mouse brain coronal sections 81
3.21 E17.5 mouse brain sagittal and coronal view schematic 82
3.22 GFP immunohistochemistry and Zic4 fluorescent in situ hybridisation on E17.5 Zic4Cre$^{+/-}$;RCE$^{+/-}$mouse brain coronal sections 84
3.23 High power images for GFP immunohistochemistry and Zic4 fluorescent in situ hybridisation on E17.5 Zic4Cre$^{+/-}$;RCE$^{+/-}$mouse brain coronal sections 85
3.24 E18.5 mouse brain sagittal and coronal view schematic 86
3.25 GFP immunohistochemistry and Zic4 fluorescent in situ hybridisation on E18.5 Zic4Cre$^{+/-}$;RCE$^{+/-}$mouse brain coronal sections 87
3.26 High power images for GFP immunohistochemistry and Zic4 fluorescent in situ hybridisation on E18.5 Zic4Cre$^{+/-}$;RCE$^{+/-}$mouse brain coronal sections 88
3.27 GFP immunohistochemistry on P0 Zic4Cre$^{+/-}$;RCE$^{+/-}$mouse brain coronal sections with annotation 89
3.28 Schematic of featured Zic4 expression pattern in E12.5 thalamus and prethalamus 92
3.29 Genes with similar expression pattern to Zic4 gene in E12.5 thalamus and prethalamus 94
3.30 Genes with similar expression pattern to Zic4 gene in E13.5 prethalamus 95

3.31 Schematic of featured Zic4 expression pattern in the subventricular zone of E13.5 prethalamus . . . 95

4.1 Examples of cell segmentation approaches . . . 100
4.2 Examples of morphological processing using operators . . . 101
4.3 Sample Image used for the analysis . . . 104
4.4 Schematic of section and position number on a typical slide . . . 104
4.5 Channel split step to obtain monochrome images for further processing . . . 105
4.6 Background noise is removed for each channel by thresholding . . . 106
4.7 Mast cells, blood cells and cells from other structures are excluded from further analysis . . . 107
4.8 Schematic of four different types of cells defined by GFP and Zic4 intensities . 109
4.9 Zic4 fluorescence in situ hybridization (red) and GFP immunohistochemistry (green) on coronal sections of E11.5 mouse brain . . . 111
4.10 Quantification of GFP and Zic4 intensity at cellular levels in E11.5 cortex, epithalamus, prethalamus and thalamus . . . 112
4.11 Mean proportion ($\pm$ sem) of each cell type in E11.5 cortex, epithalamus, prethalamus and thalamus . . . 113
4.12 Zic4 fluorescence in situ hybridization (red) and GFP immunohistochemistry (green) on coronal sections of E12.5 mouse brain . . . 115
4.13 Quantification of GFP and Zic4 intensity at cellular levels in E12.5 cortex, epithalamus, prethalamus and thalamus . . . 116
4.14 Comparison of cell proportion in each type in E12.5 cortex, epithalamus, prethalamus and thalamus . . . 117
4.15 Schematic of subregions in the thalamus and the prethalamus . . . 118
4.16 Zic4 fluorescence in situ hybridization (red) and GFP immunohistochemistry (green) on coronal sections of E13.5 mouse brain (cortex and epithalamus) . . . 118
4.17 Zic4 fluorescence in situ hybridization (red) and GFP immunohistochemistry (green) on coronal sections of E13.5 mouse brain (prethalamus) . . . 120
4.18 Zic4 fluorescence in situ hybridization (red) and GFP immunohistochemistry (green) on coronal sections of E13.5 mouse brain (thalamus part 1) . . . 122
4.19 Zic4 fluorescence in situ hybridization (red) and GFP immunohistochemistry (green) on coronal sections of E13.5 mouse brain (thalamus part 2) . . . 124
4.20 Comparison of cell number and proportion in each type in E13.5 cortex, epithalamus, prethalamus and thalamus. . . . 125
4.21 Comparison of cell proportion in each type in E13.5 cortex, epithalamus, prethalamus and thalamus . . . 126

4.22 Zic4 fluorescence in situ hybridization (red) and GFP immunohistochemistry (green) on coronal sections of E14.5 mouse brain (cortex and epithalamus) . . . 127
4.23 Zic4 fluorescence in situ hybridization (red) and GFP immunohistochemistry (green) on coronal sections of E14.5 mouse brain (prethalamus) 128
4.24 Zic4 fluorescence in situ hybridization (red) and GFP immunohistochemistry (green) on coronal sections of E14.5 mouse brain (thalamus part 2) 130
4.25 Zic4 fluorescence in situ hybridization (red) and GFP immunohistochemistry (green) on coronal sections of E14.5 mouse brain (thalamus part 2) 131
4.26 Comparison of cell number and proportion in each type in E14.5 cortex, epithalamus, prethalamus and thalamus. 132
4.27 Comparison of cell proportion in each type in E14.5 cortex, epithalamus, prethalamus and thalamus 133
4.28 Zic4 fluorescence in situ hybridization (red) and GFP immunohistochemistry (green) on coronal sections of E15.5 mouse brain (cortex and epithalamus) . . . 134
4.29 Zic4 fluorescence in situ hybridization (red) and GFP immunohistochemistry (green) on coronal sections of E15.5 mouse brain (pethalamus and thalamus) . 135
4.30 Comparison of cell number and proportion in each type in E15.5 cortex, epithalamus, prethalamus and thalamus. 137
4.31 Comparison of cell proportion in each type in E15.5 cortex, epithalamus, prethalamus and thalamus 138
4.32 Proportion change of each cell type in all the structures from E11.5 to E14.5 . . 140
4.33 Speculated Zic4 and GFP expression during the lifetime of individual Zic4 lineage cells 143

5.1 Pax6 immunohistochemistry on E12.5 diencephalon coronal sections from *Zic4Cre*$^{+/-}$;*RCE*$^{+/-}$;*Pax6*$^{+/+}$, *Zic4Cre*$^{+/-}$;*RCE*$^{+/-}$;*Pax6*$^{fl/+}$ and *Zic4Cre*$^{+/-}$;*RCE*$^{+/-}$;*Pax6*$^{fl/fl}$ mice 148
5.2 High Power images of Pax6 immunohistochemistry on E12.5 diencephalon coronal sections from *Zic4Cre*$^{+/-}$;*RCE*$^{+/-}$;*Pax6*$^{+/+}$, *Zic4Cre*$^{+/-}$;*RCE*$^{+/-}$;*Pax6*$^{fl/+}$ and *Zic4Cre*$^{+/-}$;*RCE*$^{+/-}$;*Pax6*$^{fl/fl}$ mice 149
5.3 Pax6 immunohistochemistry on E13.5 diencephalon coronal sections from *Zic4Cre*$^{+/-}$;*RCE*$^{+/-}$;*Pax6*$^{+/+}$, *Zic4Cre*$^{+/-}$;*RCE*$^{+/-}$;*Pax6*$^{fl/+}$ and *Zic4Cre*$^{+/-}$;*RCE*$^{+/-}$;*Pax6*$^{fl/fl}$ mice 151
5.4 High Power images of Pax6 immunohistochemistry on E13.5 diencephalon coronal sections from *Zic4Cre*$^{+/-}$;*RCE*$^{+/-}$;*Pax6*$^{+/+}$, *Zic4Cre*$^{+/-}$;*RCE*$^{+/-}$;*Pax6*$^{fl/+}$ and *Zic4Cre*$^{+/-}$;*RCE*$^{+/-}$;*Pax6*$^{fl/fl}$ mice 152
5.5 Pax6 immunohistochemistry on E14.5 diencephalon coronal sections from *Zic4Cre*$^{+/-}$;*RCE*$^{+/-}$;*Pax6*$^{+/+}$, *Zic4Cre*$^{+/-}$;*RCE*$^{+/-}$;*Pax6*$^{fl/+}$ and *Zic4Cre*$^{+/-}$;*RCE*$^{+/-}$;*Pax6*$^{fl/fl}$ mice 154

5.6 High Power images of Pax6 immunohistochemistry on E14.5 diencephalon coronal sections from *Zic4Cre*$^{+/-}$;*RCE*$^{+/-}$;*Pax6*$^{+/+}$, *Zic4Cre*$^{+/-}$;*RCE*$^{+/-}$;*Pax6*$^{fl/+}$ and *Zic4Cre*$^{+/-}$;*RCE*$^{+/-}$;*Pax6*$^{fl/fl}$ mice 155
5.7 Pax6 immunohistochemistry on E16.5 diencephalon coronal sections from *Zic4Cre*$^{+/-}$;*RCE*$^{+/-}$;*Pax6*$^{+/+}$, *Zic4Cre*$^{+/-}$;*RCE*$^{+/-}$;*Pax6*$^{fl/+}$ and *Zic4Cre*$^{+/-}$;*RCE*$^{+/-}$;*Pax6*$^{fl/fl}$ mice 157
5.8 Diagram of Pax6 deletion on E12.5 to E14.5 diencephalon coronal sections from *Zic4Cre*$^{+/-}$;*RCE*$^{+/-}$;*Pax6*$^{+/+}$, *Zic4Cre*$^{+/-}$;*RCE*$^{+/-}$;*Pax6*$^{fl/+}$ and *Zic4Cre*$^{+/-}$;*RCE*$^{+/-}$;*Pax6*$^{fl/fl}$ mice 161

6.1 Coronal mouse brain atlas by Paxinos and Franklin for anatomical registration 164
6.2 Coronal mouse brain atlas by Allen Brain Institute for anatomical registration . 165
6.3 Standard coronal series of P0 Pax6$^{+/+}$ mouse brain for position registration of all the Pax6$^{+/+}$ sections from rostral to medial levels (COUP-TFI) 167
6.4 Standard coronal series of P0 Pax6$^{+/+}$ mouse brain for position registration of all the Pax6$^{+/+}$ sections from middle to caudal levels (COUP-TFI) 168
6.5 Standard coronal series of P0 Pax6$^{+/+}$ mouse brain for position registration of all the Pax6$^{+/+}$ sections from rostral to middle levels (COUP-TFII) 169
6.6 Standard coronal series of P0 Pax6$^{+/+}$ mouse brain for position registration of all the Pax6$^{+/+}$ sections from middle to caudal levels (COUP-TFII) 170
6.7 Standard coronal series of P0 Pax6$^{+/+}$ mouse brain for position registration of all the Pax6$^{+/+}$ sections from rostral to middle levels (Lim1/2) 171
6.8 Standard coronal series of P0 Pax6$^{+/+}$ mouse brain for position registration of all the Pax6$^{+/+}$ sections from middle to caudal levels (Lim1/2) 172
6.9 Standard coronal series of P0 Pax6$^{+/+}$ mouse brain for position registration of all the Pax6$^{+/+}$ sections from rostral to middle levels (Nkx2.2) 173
6.10 Standard coronal series of P0 Pax6$^{+/+}$ mouse brain for position registration of all the Pax6$^{+/+}$ sections from middle to caudal levels (Nkx2.2) 174
6.11 High power images of COUP-TFI staining for vLGN in P0 Pax6$^{+/+}$ mouse brain 175
6.12 High power images of COUP-TFII staining for vLGN in P0 Pax6$^{+/+}$ mouse brain 176
6.13 High power images of COUP-TFI staining for dLGN in P0 Pax6$^{+/+}$ mouse brain 177
6.14 High power images of cresyl violet staining for VP in P0 Pax6$^{+/+}$ mouse brain . 178
6.15 High power images of COUP-TFII staining for VP in P0 Pax6$^{+/+}$ mouse brain . 178
6.16 COUP-TFII ISH and reference atlas at P56 for VP from Allen Mouse Brain Atlas 179
6.17 Nuclei volume estimation with Volumest and parameter optimisation 180
6.18 Estimated volume change in vLGN in conditional Pax6 mutants 181
6.19 Estimated volume change in dLGN in conditional Pax6 mutants 182
6.20 Estimated volume change in VP in conditional Pax6 mutants 182
6.21 Area of vLGN on observed sections in conditional Pax6 mutants 183

6.22 Area of dLGN on observed sections in conditional Pax6 mutants 184
6.23 Area of VP on observed sections in conditional Pax6 mutants 184
6.24 Example sectioning and numbering of coronal brain sections for cell counting in vLGN, dLGN and VP 185
6.25 SD and SEM plots against sampling percentage for cell counting 186
6.26 Cell density change in vLGN in conditional Pax6 mutants 187
6.27 Total cell number in vLGN 188
6.28 vLGN cell number on observed sections in conditional Pax6 mutants 188
6.29 Cell density change in dLGN in conditional Pax6 mutants 189
6.30 Total cell number in dLGN 189
6.31 dLGN cell number on observed sections in conditional Pax6 mutants 190
6.32 Cell density change in VP in conditional Pax6 mutants 191
6.33 Total cell number in VP 191
6.34 VP cell number on observed sections in conditional Pax6 mutants 192
6.35 GFP staining of coronal brain sections from $Pax6^{+/+}$, the $Pax6^{fl/+}$ and the $Pax6^{fl/fl}$ brains 192
6.36 GFP+ve cell proportion change in vLGN in conditional Pax6 mutants 193
6.37 GFP+ve cell proportion change in dLGN in conditional Pax6 mutants 193
6.38 GFP+ve cell proportion change in VP in conditional Pax6 mutants 194
6.39 Expressions of Lim1/2 and Nkx2.2 are altered in vLGN in conditional Pax6 mutants 195
6.40 Pax6 immunohistochemistry of P0 $Pax6^{+/+}$ vLGN 198

7.1 Preprocessed vLGN image series for CellProfiler analysis 201
7.2 Thresholding three single-channel grayscale images of the vLGN 202
7.3 Cell nuclei identification in the vLGN based on DAPI staining 203
7.4 Cell categorisation based on GFP and BrdU staining 203
7.5 Proportion of vLGN cells born at E10.5, E11.5, E12.5 and E13.5 205
7.6 Proportion of vLGN cells born at each position at different ages 206
7.7 Proportion of GFP+ve vLGN cells born at E10.5, E11.5, E12.5 and E13.5 206
7.8 Proportion of GFP+ve vLGN cells born at each position at different ages 207
7.9 Proportion of dLGN cells born at E10.5, E11.5, E12.5 and E13.5 208
7.10 Proportion of dLGN cells born at each position at different ages 208
7.11 Proportion of GFP+ve dLGN cells born at E10.5, E11.5, E12.5 and E13.5 209
7.12 Proportion of GFP+ve dLGN cells born at each position at different ages 209
7.13 Proportion of VP cells born at E10.5, E11.5, E12.5 and E13.5 210
7.14 Proportion of VP cells born at each position at different ages 210
7.15 Proportion of GFP+ve VP cells born at E10.5, E11.5, E12.5 and E13.5 211

7.16 Proportion of GFP+ve VP cells born at each position at different ages 211

8.1 ROI selection for BrdU/pHH3/GFP/DAPI and Ki67/Tuj1/GFP/DAPI immunostainings 215
8.2 Schematic of cell cycling speed calculation 218
8.3 Growth fraction in pTH-C, pTH-R and Pth in E11.5, E12.5 and E13.5 $Pax6^{+/+}$, $Pax6^{fl/+}$ and $Pax6^{fl/fl}$ mice 220
8.4 GFP+ve cell growth fraction in pTH-C, pTH-R and Pth in E11.5, E12.5 and E13.5 $Pax6^{+/+}$, $Pax6^{fl/+}$ and $Pax6^{fl/fl}$ mice 221
8.5 Proliferation rate in pTH-C, pTH-R and Pth in E11.5, E12.5 and E13.5 $Pax6^{+/+}$, $Pax6^{fl/+}$ and $Pax6^{fl/fl}$ mice 222
8.6 GFP+ve cell proliferation rate in pTH-C, pTH-R and Pth in E11.5, E12.5 and E13.5 $Pax6^{+/+}$, $Pax6^{fl/+}$ and $Pax6^{fl/fl}$ mice 223
8.7 Cell cycling speed in pTH-C, pTH-R and Pth in E11.5, E12.5 and E13.5 $Pax6^{+/+}$, $Pax6^{fl/+}$ and $Pax6^{fl/fl}$ mice 224
8.8 pHH3+ve cell number in pTH-C, pTH-R and Pth in E11.5, E12.5 and E13.5 $Pax6^{+/+}$, $Pax6^{fl/+}$ and $Pax6^{fl/fl}$ mice 225
8.9 Basal pHH3+ve cell proportion in pTH-C, pTH-R and Pth in E11.5, E12.5 and E13.5 $Pax6^{+/+}$, $Pax6^{fl/+}$ and $Pax6^{fl/fl}$ mice 227
8.10 Cleaved caspase 3 immunohistochemistry on E13.5 coronal paw sections of $Pax6^{+/+}$ mice 228
8.11 Cleaved caspase 3 immunohistochemistry on E11.5 coronal brain sections of $Pax6^{+/+}$, $Pax6^{fl/+}$ and $Pax6^{fl/fl}$ mice 230
8.12 Cleaved caspase 3 immunohistochemistry on E12.5 coronal brain sections of $Pax6^{+/+}$, $Pax6^{fl/+}$ and $Pax6^{fl/fl}$ mice 231
8.13 Cleaved caspase 3 immunohistochemistry on E13.5 coronal brain sections of $Pax6^{+/+}$, $Pax6^{fl/+}$ and $Pax6^{fl/fl}$ mice 232
8.14 Cleaved caspase 3 immunohistochemistry on E14.5 coronal brain sections of $Pax6^{+/+}$, $Pax6^{fl/+}$ and $Pax6^{fl/fl}$ mice 233
8.15 Cell apoptotic rate in E11.5 to E13.5 thalamus of $Pax6^{+/+}$, $Pax6^{fl/+}$ and $Pax6^{fl/fl}$ mice 234

9.1 Shh in situ hybridisation in E12.5 and E13.5 $Pax6^{+/+}$, $Pax6^{fl/+}$ and $Pax6^{fl/fl}$ diencephalon 241
9.2 Nkx2.2 in situ hybridisation in E12.5 and E13.5 $Pax6^{+/+}$, $Pax6^{fl/+}$ and $Pax6^{fl/fl}$ diencephalon 242
9.3 Nkx2.2 and GFP immunohistochemistry of coronal sections of vLGN at the rostral most postion in $Pax6^{+/+}$, $Pax6^{fl/+}$, and $Pax6^{fl/fl}$ at P0 244
9.4 A model showing how the changes in the expression of Shh and Nkx2.2 at E12.5 and E13.5 can contribute to the volume change of vLGN 245

10.1 Zic4 in situ and GFP immunohistochemistry of E11.5 $Pax6^{+/+}$ eyes 247
10.2 DAB-Pax6 and cresyl violet stainings of E13.5, E14.5 and P0 $Pax6^{+/+}$, $Pax6^{fl/+}$ and $Pax6^{fl/fl}$ eyes 248
10.3 Axon tracing using lipophilic dye in the P0 $Pax6^{+/+}$ brain reveals the ascending visual pathway 249
10.4 Axon tracing using lipophilic dye in the P0 $Pax6^{+/+}$, $Pax6^{fl/+}$ and $Pax6^{fl/fl}$ brains reveals no difference among different genotypes 249

13.1 Migration progress of cells born from E13.5 to E14.5 in the pTH-C, pTH-R and Pth in $Pax6^{+/+}$, $Pax6^{fl/+}$ and $Pax6^{fl/fl}$ 290
13.2 GFP+ve cell movement speed comparison in E13.5 Pth 291

List of Tables

1.1 Cerebellar phenotypes of various single, double and triple Zic1, Zic4 and Shh mutant mice 27

3.1 Summary of *Zic4* transcripts and GFP expression pattern in the E11.5 diencephalon 56
3.2 Summary of *Zic4* transcripts and GFP expression pattern in the E12.5 diencephalon 61
3.3 Summary of *Zic4* transcripts and GFP expression pattern in the E13.5 diencephalon 66
3.4 Summary of *Zic4* transcripts and GFP expression pattern in the E14.5 diencephalon 71
3.5 Summary of *Zic4* transcripts and GFP expression pattern in the E15.5 diencephalon 75
3.6 Summary of *Zic4* transcripts and GFP expression pattern in the E16.5 diencephalon 79
3.7 Summary of *Zic4* transcripts and GFP expression pattern in the E17.5 diencephalon 83
3.8 Summary of *Zic4* transcripts and GFP expression pattern in the E18.5 diencephalon 86

4.1 Parameters used for DAPI based nuclei segmentation using CellProfiler 108

6.1 Volume and cell composition change in the vLGN, dLGN and VP in$Pax6^{fl/+}$ and the $Pax6^{fl/fl}$ mutants 196

7.1 Parameters used for DAPI based nuclei segmentation in vLGN using CellProfiler 204

8.1 Parameters used for DAPI based nuclei segmentation in cell cycle analysis using CellProfiler 216
8.2 Cell proliferation related change in the pTH-C, pTH-R and Pth in $Pax6^{fl/+}$ and the $Pax6^{fl/fl}$ mutants at E11.5, E12.5 and E13.5 235

9.1 Early patterning change in the pTH-R and ZLI in $Pax6^{fl/+}$ and the $Pax6^{fl/fl}$ mutants at E12.5 and E13.5 243

Chapter 1

Introduction

The aim of this study is to determine the role of the transcription factor Pax6 in the development of the diencephalon, especially the formation of specific diencephalic nuclei such as the ventral lateral geniculate nucleus (vLGN), using conditional *Pax6* mutant mice driven by the diencephalon specific *Zic4Cre* with a EGFP reporter showing the Cre activity. In order to dissect Pax6's role in the diencephalic development, I first monitored *Zic4* lineage dynamics within the developing diencephalon from E11.5 to P0 and studied the associated Pax6 deletion pattern; then I identified gross morphological changes in the diencephalic nuclei at P0 in the conditional *Pax6* mutants and formed hypotheses about the mechanisms underlying the defects; in the last part of this project, I explored through four factors that could potentially cause the observed defects - 1) disruption of the expression of patterning factors such as *Shh* and *Nkx2.2*; 2) proliferation defects and abnormal apoptosis; 3) ocular developmental defects; 4) failure in cell sorting/migration.

A general review of the background of this study is given here. It consists of the following major components: (1) the development of the diencephalon, from the formation of the neural tube to the subdivisioning of the diencephalon into epithalamus, thalamus, prethalamus, and hypothalamus, to the development of individual diencephalic nuclei including the vLGN, dLGN and VP, and the signalling molecules and transcription factors involved at different stages; (2) Pax6 and its role in the development of the diencephalon; (3) Zic4 and its function in the development of the central nervous system; (4) lineage tracing and fate mapping in developing diencephalon.

1.1 Development of the diencephalon

1.1.1 Development of the mouse brain

The brain is the core of the central nervous system and the most sophisticated organ in vertebrates. It regulates and coordinates the functioning of other organs and exerts the higher functions such as learning, memory, perception and motivation. The multifaceted functions of the brain are determined by its intricate structure and the study of brain development is of great interest in neurobiology.

The development of the brain initiates from a fundamental event of embryogenesis, called neurulation, during which the neural tube is formed by the folding of the neural plate [1, 2]. As the closure of the neural tube progresses, its shape changes dramatically Figure 1.1, when the anterior part bends and forms into the forebrain (or prosencephalon), the midbrain (or mesencephalon) and the hindbrain (or rhombencephalon) and the posterior part gives rise to the spinal cord [2]. The forebrain vesicle then expands to form two bilateral telencephalic vesicles with one diencephalic vesicle engulfed underneath. The telencephalon is divided into dorsal and the ventral parts, the former forming the future cerebral cortex and the hippocampus and the latter becoming the basal ganglia [2]. The rostroventral diencephalon generates the hypothalamus, regulating homeostasis and reproduction [3], and the caudodorsal part mainly gives rise to the thalamus, which relays the information from peripheral sensors to the cerebral cortex [2].

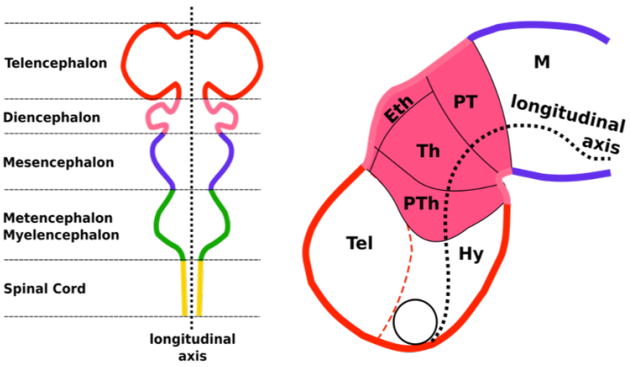


Figure 1.1: ***Schematics of E8.5 (horizontal view) and E10.5 (sagittal view) neural tube.*** *Tel, telencephalon; Eth, epithalamus; PT, pretectum; PTh, prethalamus; Th, thalamus; Hy, hypothalamus; M, messencephalon.*

1.1.2 Prosomeric model of the neural tube development

The widely used prosomeric model is a segmental structural model of vertebrate brain that consists a continuous series of transverse subunits of the neural tube, called neuromeres [4, 5]. A large rostral forebrain unit, the secondary prosencephalon, encompasses hypothalamus, eyes and telencephalon; the following three caudal forebrain or diencephalic neuromeres are considered as serially homologous with more caudal neuromeres - a single midbrain mesomere, 11 hindbrain rhombomeres and the spinal myelomeres. In the prosomeric model, the diencephalon is divided into four domains from ventral to dorsal, the floor plate, basal plate, alar plate and roof plate. The alar plate is rostrocaudally divided into three transverse prosomeres, prethalamus or p3, thalamus together with epithalamus as p2, and pretectum or p1; and the boundary which separates p3 and p2 is called the zona limitans intrathalamica (ZLI) [4, 5]. The prosomeric model is based on evolutionarily conserved topological relationships and molecular expression data in the neural tube. It can serve as a guide for our interpretation of data using established spatial dimensions and provide a common background for meaningful comparisions between different regions or the same region across different species.

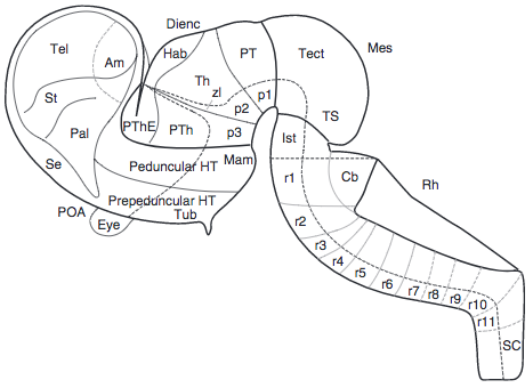


Figure 1.2: ***Schematics of prosomeric model.*** *[6] A sagittal view of the prosomeric model with the forebrain lying to the left. The longitudinal alarbasal boundary is present throughout the the neural tube. A unique structure called zona limitans is a transversal spike shaped deviation of the alarbasal boundary. The secondary prosencehpalon is the rostralmost unit, consisting of telencephalon (Tel), eye and hypothalamus. Within the telencephalon, several structures can be recognised, including septum (Se), striatum (St), pallidum (Pal), preoptic area (POA) and amygdala (Am). In the hypothalamus, tuberal (Tub) and mammillary (Mam) subregions can be appreciated. The diencaphalon consists of three prosomeres, p1 - p3, whose alar regions include the pretectum (PT), the thalamus and habenula (Th and Hab), and the prethalamus (PTh). The large mesencephalic alar plate (Mes) divides into superior colliculus or tectum (Tect) and inferior colliculus or torus semicircularis (TS). The hindbrain or rhombencephalon (Rh) consists of 12 neuromeric units, from the isthmus (Ist) and ehombomere 1 (rl) down to rhombomere 11 (r11), which limits with the spinal cord (SC).*

1.1.3 Development of the diencephalon

After neurulation, a combinatorial expression of signalling molecules and transcription factors delineates the further compartmentation of the diencephalon, which initiates at embryonic day (E) 9.5 and continues for 2 to 3 days [4, 7]. During early development, the progenitor cells in the ventricular zone of the diencephalon undergo several rounds of proliferation and differentiation to generate numerous postmitotic neurons, which immediately migrate to the mantle zone and aggregate to form distinct nuclei [4, 8, 9]. Cells of different nuclei gain diverse morphological properties, form connections with various brain regions and exert specific functions [8, 9].

Being the major derivative of the diencephalon, the thalamus contains a variety of nuclei which relay sensory information from the peripheral nervous system to the corresponding areas of cerebral cortex [9, 10]. Understanding the generation of the thalamic progenitors and their progeny, the postmitotic neurons, is critical for studying the parcellation of the thalamic nuclei and further assessing the formation of the connections between different regions of the cerebral cortex and specific thalamic nuclei.

1.1.4 Neuroanatomy of the thalamus

The thalamus is a symmetrical structure situated in the central part of the brain of vertebrate including humans and rodents. It plays a key role in information distribution of the nervous system, relaying almost all the sensory except olfactory inputs from perippheral sensors to the cerebral cortex for further processing.

From early developmental and comparative studies, the thalamus is divided into three parts: the epithalamus, thalamus (or dorsal thalamus) and prethalamus (or ventral thalamus). During brain development, the thalamic neurons group into distinct complexes called nuclei, which connect with specific or a broader range of regions in the nervous system.

In the early 19^{th} century, Karl Friedrich Burdach recognised the masses of the thalamic nuclei, the external and internla medullary laminae and the reticular nucleus in the thalamus of fixed human brain slices [11]. Luys made the first delineations of the human thalamic nulcei in 1865. He emphasized the subdivision of the thalamus into four isolated centres, made up of neurons communicating with specific groups of afferent fibres. He also stressed the function of the thalamus as a sensory relay station [11]. Using his newly developed cell stain, Franz Nissl published the study on rabbits in 1889, in which he identified most of the thalamic nuclei that we know today [11].

Later, using lesion-induced retrograde degeneration method, COnstantin Von Monakow found that the disruption of cortex at different regions caused the degeneration of certain thalamic nuclei and his work contributed to the anatomy of several projection connections [11].

In early studies, it's quite difficult to define the borders of specific nuclei based on Nissl staining. However, it is found that some thalamic neurons obey the rules of the nucleus-to-field principle and their axon terminals seem to stop abruptly at cytoarchitectonic borders in the cortex, which provided a way of looking for different types of thalamic nuclei. Several interesting points were made based on the studies performed by Macchi and Jones: (1) every dorsal thalamic nucleus projects to the cerebral cortex; (2) the whole cortex receives a projection from the dorsal thalamus; (3) the nature of the projection upon the neocortex can vary from nucleus from nucleus and even amound different cell groups in the same nucleus; (4) some dorsal nuclei only project to the cerebral cortex while others project to both the cerebral cortex and striatum; (5) the epithalamus and the ventral thalamus do not project to the cortex.

1.2 Signalling molecules and transcription factors and their roles in controlling the subdividing of diencephalon

A great number of studies have unravelled the secreted signalling molecules, such as sonic hedgehog (Shh) [12], fibroblast growth factor (Fgfs) [13, 14] and Wnts [15], act in concert in the diencephalic patterning. Transcription factors such as Pax6, Otx2, Emx2, Fezf2 and Irx3 play important roles in controlling the fate of progenitors in different diencephalic prosomeres [7, 16, 17, 18, 19].

Shh was reported to be expressed in the ZLI around E10.5 [12, 13]. Shh signalling from the ZLI at the rostral border of the thalamic primordium is responsible for inducing the GABAergic rostral thalamus and glutamatergic caudal thalamus. A conditional increase or decrease of the Shh signal in the thalamus caused a regional identity shift in the affected areas: a high Shh activity positively regulated the identity of the pTH-R and induced an increase in the postmitotic derivatives, whereas down regulation of Shh signal reduced the expression of the pTH-R markers in both the progenitor cells and the corresponding postmitotic cells [12]. Fibroblast growth factor 8 (Fgf8), which is expressed in the dorsal diencephalon, was found to play a role in dorsal diencephalic patterning, especially the habenular region and the pineal gland, and a decrease of the Fgf8 signalling caused a size reduction of the thalamus [13, 14]. The restricted over-expression and inhibition of Fgf8 demonstrated that Fgf8 specifically regulates the patterning of p2 of the developing diencephalon, independently from the Shh

and Wnt signalling [13]. A study showed that the impaired Wnts signalling resulted in a reduced and disorganised thalamus and the lack of thalamocorical projections [15]. Moreover, the development of the mid-diencephalic organizer (MDO) ZLI was abnormally formed in the absence of Wnt signalling, which indicates a critical role of Wnt signalling in the thalamic patterning [15].

The cooperation between *Otx2* and *Emx2* is required during the development of the prethalamus, thalamus and anterior pretectum [7]. Transcriptional repressors encoded by zinc-finger genes *Fez* and *Fezl* are expressed in the region rostral to the *Irx1* expression, which marks the position of the ZLI. Misexpression of *Fez* or *Fezl* caudal to the ZLI affects the formation of the ZLI and represses the caudal diencephalon fate [16]. The homeodomain transcription factor Irx3 has been suggested to limit the thalamic fate to the neuroepithelium caudal to the ZLI as ectopic Irx3 expression rostral to the ZLI results in a mirrored duplication of the pTH-R and pTH-C markers Sox14 and Gbx2 [19]. Expression of both Irx3 and Pax6 and Shh signalling from ZLI are required for thalamus induction and patterining [17]. The partition of prosomere 2 domain into epithalamus and thalamus requires the function of Pax6 mediated by Shh [18].

The mosaic composition of the thalamic progenitor population [8] is supported by the short-term lineage tracing analyses combined with the study of region-specific markers [20]. It was demonstrated that the transcription factors Ngn2, Mash1 and Nkx2.2 are expressed in positionally distinct progenitor patches in the thalamic ventricular zone which give rise to different postmitotic cell populations later on [20]. A further division of the thalamus into the pTH-R (R stands for rostral) and pTH-C (C stands for caudal), was subsequently proposed based on the analyses of the expression pattern of these transcription factors [20]. Ngn2 is expressed in both the pTH-C and ZLI and *Ngn2* lineage cells contribute to all the thalamic nuclei that project to the cortex; Mash1 is expressed complementarily in the pTH-R progenitor cells and the prethalamus, which generate non-cerebral projecting nuclei such as the reticular nuclei, intergeniculate leaflet (IGL, a region between vLGN an dLGN) and lateral vLGN [20]. Nkx2.2 is expressed in a small strip of progenitor cells positioned caudally to the ZLI, corresponding to the pTH-R and the prethalamus [20].

1.3 Pax6's role in the development of the diencephalon

Pax6, a transcription factor first defined in *Drosophila* segmentation genes, contains two DNA binding motifs, a paired domain and a homeodomain [21, 22]. The *Pax6* mutation in human is reported to underlie the severe defects such as aniridia, anophthalmia and Peters anomaly [23,

24, 25]. The conservation of *Pax6* between the humans and rodents grants us the opportunity to investigate the role of Pax6 in mouse models, which will assist the studies of Pax6-related human diseases. The *small eye* (*sey*) mouse, with a naturally occurring mutation in *Pax6* [26], has severely reduced eyes and was first used as the model for aniridia patients [27]. Since then, a great number of studies have been performed to investigate the role of Pax6 and showed that Pax6 not only plays a pivotal role in the development of the eye, but is also essential to the formation of other parts of the brain, including the cortex, the thalamus and the cerebellar system. Studies performed via mouse model manipulation, such as the conditional knock-in and knock-out, and the chimera development, demonstrated that both the lack of and over-expression of Pax6 can cause severe defects in the central nervous system.

It was found that a specific *Pax6* deletion in cortical progenitors at the mid stage of corticogenesis caused defects in both the number and specification of late-born neurons [28]. The study performed on *Pax6* null mutant mice showed a pronouced pallial defect near the pallial-subpallial boundary (PSPB) around E11.5, suggesting the functional Pax6 is required in the formation of PSPB [29]. Another study showed the restricted deletion of *Pax6* in a subgroup of progenitors caused specific defects related to the progenitors, indicating that *Pax6* plays a role in the generation of subtype neurons [30]. Previous studies also demonstrated that the Pax6 over-expression specifically increases the cell cycle length of the apical progenitors and drives the progress of neurogenesis at the late stage of corticogenesis, while the progenitors at an early stages are not affected [31, 28]. The study of Pax6 over-expression on eye formation demonstrated the over-expression of Pax6 causes severely affected retina and abnormal development of retinal axons [32].

Early studies of Pax6's role in the diencephalic development were carried out in the *Pax6* null mutants such as the *Sey/Sey* mice, in which *Small eye* (*Sey*) is a spontaneous mutation in the *Pax6* gene, resulting from a single base pair GGA $\rightarrow$ TGA substitution [33]. One of these early studies was accomplished in this lab and it was found that proliferative rates in the E10.5 *Sey/Sey* diencephalon are significantly reduced in the alar region where *Pax6* is normally expressed. This leads to a depletion of the proliferating precursor pool at E12.5 and a further reduction of the total cell number in the E14.5 diencephalon[34]. In the same year, another study was published using the homozygous $Pax6^{Sey\text{-}1Neu}$ mice, in which the Sey^{Neu} allele was created in an ethylnitrosourea (ENU)-induced mutation screen. A point mutation G $\rightarrow$ T within a *Pax6* splice acceptor sequence caused a splicing error, in which a 116 bp sequence from intron 10 fails to be spliced out. This splicing error subsequently introduced a premature STOP codon and resulted in a C-terminal truncated transcript [33]. The protein produced by this mutated allele showed a significantly reduced ability to transactivate target

gene expression [35]. It is found that in the diencephalon of $Pax6^{Sey\text{-}1Neu}/Pax6^{Sey\text{-}1Neu}$ embryos, the interprosomeric boundaries between p1 and p2, and p2 and p3 are blurred, possibly due to an increased cell mixing. The Shh expressing ZLI is expanded in this mutant as well [35]. A detailed analysis of the thalamic markers such as *VMAT2*, *Hbnf*, *Lim1/Lhx1* and *Nkx2.2* in the $Pax6^{Sey/Sey}$ embryos carried out previously in the lab revealed that the thalamus fails to differentiate correctly in the absence of functional Pax6 protein despite the fact that it is recognisable in the mutants [36].

Pax6's role in diencephalic progenitor specification was also studied using the *Sey/Sey* mutants. The loss of Pax6 altered the fate of the progenitors and the expression of the neuronal marker *Lhx1* in the thalamus was lost, suggesting that Pax6 could be involved in the determination of diencephalic neuron identities [37]. A later study focused on a group of basally dividing progenitor cells in the mouse embryonic thalamus called basal progenitors, whose counterparts have been thoroughly studied in the cerebral cortex. It was found that the thalamus contains a large number of basal progenitor cells, some of which form the subventricular zone, similar to what was seen in the neocortex [38]. A reduction of basal PH3-positive progenitors accompanied by an increase in the number of apical PH3-positive progenitors was observed in the *Pax6* mutants [38] generated by replacing the start codon and the entire paired domain of Pax6 with a β-galactosidase gene [39]. The total number of basal and apical PH3-positive progenitors did not change in the mutants, suggesting that Pax6 is involved in generating basal progenitor cells from apical progenitor cells [38].

A study of the habenula, a specific diencephalic nucleus, in the $Pax6^{Sey/Sey}$ mutants revealed that *Pax6* deletion causes expanded expression of *Shh* in the ZLI, the dorsal shift of the thalamic domain and the absence of the epithalamus [18]. These defects are largely rescued by attenuating Shh signaling in the $Pax6^{Sey/Sey}$ mutants, suggesting that *Shh* acts downstream of *Pax6* in controlling the formation of the habenula [18]. The relationship between *Pax6* and *Shh* during diencephalic development was further studied in the $Pax6^{+/+};Pax6^{-/-}$ chimeras in this lab. It was found that Pax6 acts cell-autonomously to block *Shh* expression around the ZLI whereas the defects observed in regional gene expression in the $Pax6^{-/-}$ thalamic cells are resulted from a non-cell-autonomous defect rooted in intercellular signaling [40]. The findings indicate that the mutual repression between Pax6 and Shh is crucial for cell specification in diencephalic formation [40]. It was also found that the $Pax6^{-/-}$ thalamic neurons express an abnormal combination of transcription factors compared to their wild type neighbours using the same model [41].

1.4 Nuclei formation in the diencephalon

The subdivision of diencephalon into the prethalamus, thalamus and epithalamus and pretectum requires a combinatorial expression of different signalling molecules and transcription factors to act harmoniously. However, little is known about the process in which individual diencephalic nuclei are derived from these subdivisions. There have been some speculations on the potential mechanisms underlying the development of the diencephalic nuclei. According to early birth-dating experiment [42], cells born at certain stage tend to aggregate in certain position within the develping diencephalon, which goes on to form certain nuclei. Studies on cadherin expression in the post natal mouse brain showed that three type-II cadherins, cadherin-6, cadherin-8 and cadherin-11 are differentially expression in subregions within the diencephalon - the medial geniculate body expressing only cad6; the ventral posterior nuclei expressing cad6 and cad11; and the anteroventral thalamic nucleus, cad6 and cad8 [43]. Since adhesion property can affect the migration and sorting of cells, it is likely the expression of these adhesion molecules is required during nuclei formation in the diencephalon.

1.4.1 Development of the ventral lateral geniculate nucleus

1.4.1.1 What is ventral lateral geniculate nucleus?

In mice, the LGN are a pair of structures situated at the ventral lateral part of the thalamus. They are essential parts of the visual system, receiving inputs from the retina and projecting to the primary visual cortex. The mouse LGN can be divided into the dLGN, vLGN and the region in between which is called the intergeniculate leaflet (IGL), among which the vLGN and the IGL are closely related in terms of neurochemicals, projections and physiological properties [44]. The earliest description of the morphology of the mouse vLGN is given by R. L. Holmes in the *Nuclear studies on the thalamus of the mouse* [45], in which he pointed out that the vLGN is situated in the caudal third of the thalamus. The vLGN first appears as a tiny group of small neurons located dorsally to the reticular nucleus and at the anteror tip of the dLGN Figure 1.3 [11]. The reticular nucleus is situated rostrally and ventrally to the vLGN; the zona incerta (ZI) is situated medially and ventrally; the medial geniculate body is situated caudally Figure 1.3 [44, 11]. No clear border is observed between the ventral part of the vLGN and the ZI.

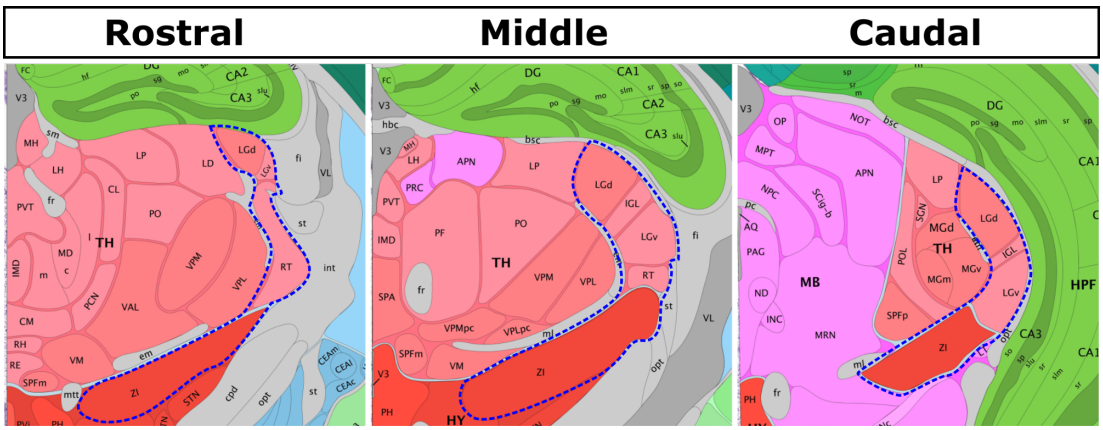


Figure 1.3: ***Diagrams of coronal sections of the rostral, middle and caudal parts of the vLGN.*** *Dashed blue contours are used to outline the regions of interest including the vLGN, dLGN, RT and ZI. Regions colour-coded generally in the diagram include thalamus (pink), hypothalamus (red), midbrain (magenta) and hippocampus (green).* ***LGd, dorsal lateral geniculate nucleus or dLGN; IGL, intergeniculate leaflet; LGv, ventral lateral geniculate nucleus or vLGN; RT, reticular nucleus; ZI, zona incerta****.*

1.4.1.2 Neurogenesis in developing ventral lateral geniculate nucleus

It is widely accepted that the progenitors in the ventricular zone of the thalamus, including the thalamus and the prethalamus, produce neurons after several rounds of division and differentiation. Once born, these neurons start to migrate toward the final location at which they group with other neurons to form the future diencephalic nuclei. The time origin of the thalamic neurons in mice are first described in 1970 in the *Time of Neuron Origin in the Diencephalon of the Mouse. An Autoradiographic Study* by Jay B. Angevine [42]. Thymidine - H^3 autoradiography was used in the study to determine the times of neuron origin for the thalamus. The incorporation of the tritiated thymidine into the DNA of the mitotically active progenitor cells during S-phase allowed the study of the time origins of the thalamic neurons and determination of the path of migration. A single dose of thymidine - H^3 was administered by intraperitoneal injection to pregnant mice at different stages of gestation, from E10 to E16 and the offsprings were all adults when harvested [42]. Two types of labelled cells were observed in this autoradiographic studies: heavily labelled neurons and lightly labelled neurons. The former represents the definitive neuron population as end products of the division of their progenitors at the time of injection and the latter includes those neurons whose label was diluted by subsequent divisions and those that were engaged in final DNA replication and exposed to the label during only part of the S-phase. The vLGN neurons are mainly born from E10 to E13 (Figure 1.4). The oldest neurons were observed in the ventrolateral quarter of the nucleus and incorparated thymidine - H^3 on E10. The injection on E11 heavily

labelled a larger population of cells occupying the dorsal region within the nucleus. The E12 injection revealed labelled cells throughout the nucleus except the most medial part. The neuron origin ends around E13 and the youngest neurons of this nucleus were observed in the dorsomedial quarter of the nucleus. This study revealed a general lateromedial neurogenesis gradient or an **outside-in** sequence of neuronal time origin in the thalamus, which is contrary to the inside-out sequence described in the cortical development in mice [42].

1.4.1.3 Marker gene expression in developing ventral lateral geniculate nucleus

Several lineage studies have shown that the vLGN has multiple embryonic origins: the pTH-R [20, 46], ZLI [47, 48] and prethalamus [46] and they also revealed dynamic marker gene expression at different stages of vLGN formation. The embryonic vLGN can be appreciated close to the lateral surface of the diencephalic wall as early as E14.5 [49, 50, 48]. At this stage, cells expressing *Brx1*, *Nkx2.2*, *Dlx1*, *Arx* are found in the vLGN and their expression subdivides the vLGN into four domains: *Nkx2.2*, *Dlx1* and *Arx* are expressed complementarily in three of them whereas in the domain situated at the dorsal edge of the vLGN all four genes are expressed [50]. At E18.5, *Dlx1* and *Nkx2.2* are exclusively expressed in the rostral and the caudal vLGN respectively whereas in the middle vLGN, *Dlx1* and *Nkx2.2* are expressed complimentarily in the medial and the lateral half of the vLGN. The expression of *Arx* and *Brx1* partially overlaps with the *Dlx1* expression in the region close to the medial boundary of the vLGN [50].

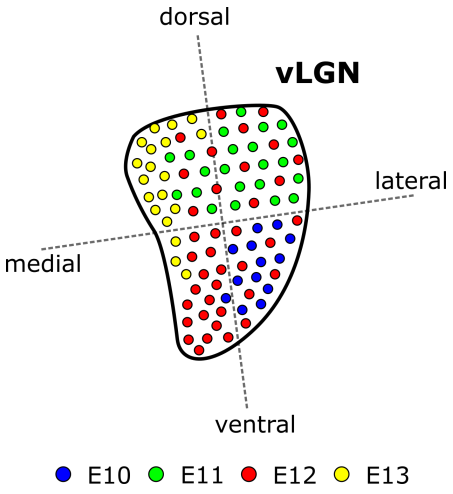


Figure 1.4: ***Schematic of neuronal time origin in the vLGN.*** *Neurons of difference time origins are colour-coded in the schematic vLGN. Dashed grey lines indicate the dorsal-ventral and the medial-lateral axes.*

1.4.2 Neurogenesis in developing dorsal lateral geniculate nucleus

In mice, 90% of the primary visual projections target the dLGN, which is reciprocally connected with the primary visual cortex. The dLGN is situated dorsolaterally on the surface of the thalamus, dorsomedially to the vLGN and IGL. Angevine's autoradiographic study showed that a significant number of dLGN neurons arise on early E11 and are positioned externally. Afterwards, the labelled neurons shift their positions inward and the E12 injection labelled neurons throughout the dLGN. The most medially positioned neurons are born on E13 [42].

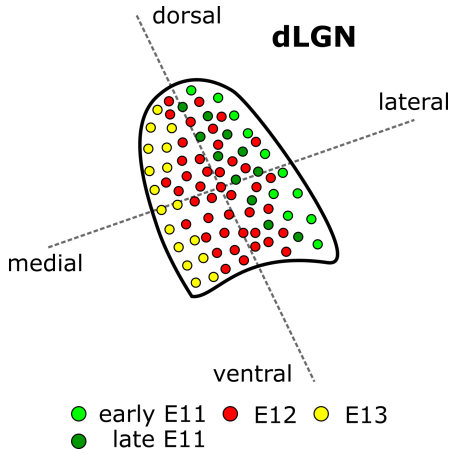


Figure 1.5: ***Schematic of neuronal time origin in the dLGN.***

1.4.3 Neurogenesis in developing ventral posterior nuclei

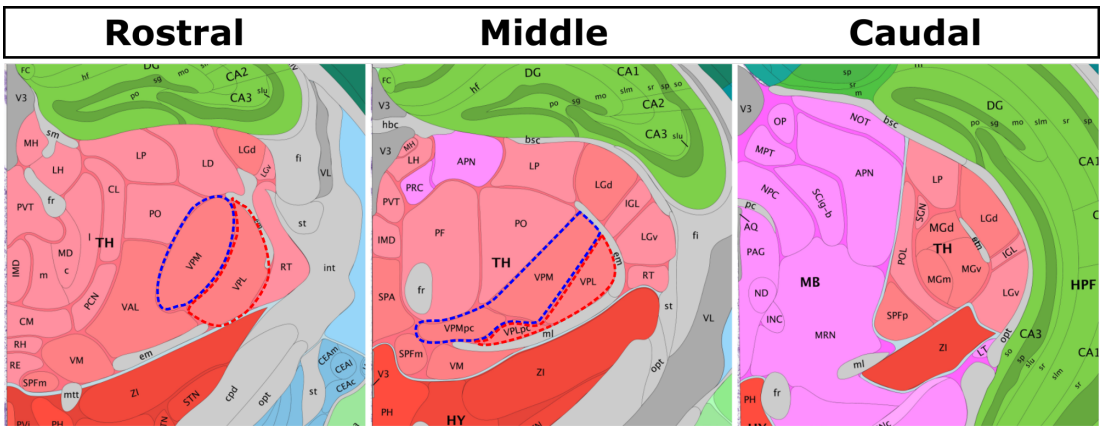


Figure 1.6: ***Positioning of VP in the diagrams of coronal sections of the rostral, middle and caudal parts of the vLGN.*** *Dashed blue contour outlines the ventral posterior nuclei medial part (VPM); Dashed red contour outlines the ventral posterior nuclei lateral part (VPL).*

The ventral posterior nuclei (VP), including the ventral posterior nuclei medial part (VPM, Figure 1.6 dashed blue contour) and the ventral posterior nuclei lateral part (VPL, Figure 1.6 dashed red contour), are the somato-sensory relay thalamic nuclei in mice. At the rostral level, the VP is situated medially to the RT and ventromedially to the vLGN and dLGN at the rostral level and at the middle level it is positioned medially to the IGL, vLGN and RT (Figure 1.6 rostral). The VP is positioned rostrally to the MGN and at the caudal most level where the vLGN and dLGN are still visible, the MGN instead of the VP is observed immediately medial to the dLGN, IGL and vLGN (Figure 1.6 middle and caudal). The neurogenesis pattern of the VP revealed in Angevine's study is complex: the earliest neurons, born on E10, are positioned most medially; the cell labelling patterns then spread progressively laterally throughout the nucleus on E11 and E12; the latest born neurons arise early on E13, then the pattern shifts medially again [42]. According to Angevine's description, the neurogenesis gradient in VP is **inside-out** before E13 but changes to **outside-in** afterwards (Figure 1.7).

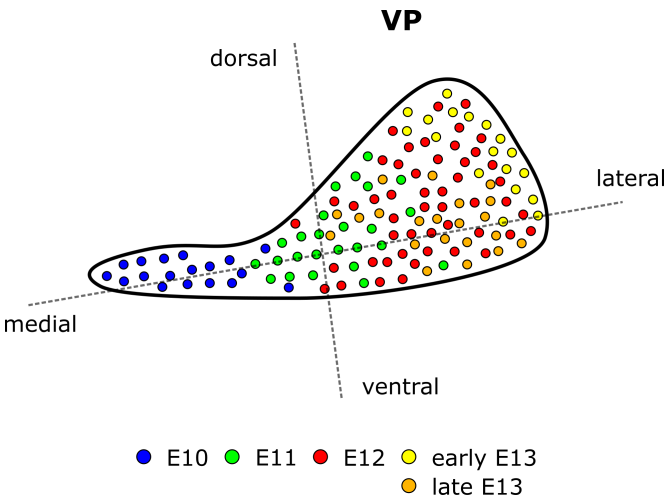


Figure 1.7: ***Schematic of neuronal time origin in the VP.***

1.5 Cell proliferation, cell cycle and cell apoptosis in developing thalamus

The cell cycle is a series of biological events through which a cell reproduces itself by duplicating its contents and undergoing division to produced two daughter cells [57]. The cell cycle of eukaryotic cells contains four successive phases: M phase (mitosis), in which the nucleus and the cytoplasm divide; S phase (DNA synthesis), in which the DNA in the nucleus is replicated, and two gap phases, G1 (critical stage of determining whether to re-entre or withdraw from the cell cycle) and G2 (DNA replication and genome integrity check). The cell cycle is closely linked with neurogenesis - proliferation and differentiation means cell cycle re-entry and exit respectively in cell cycle terms. The size of the cortex largely depends on the number of times the cortical progenitor cells re-entre the cell cycle and the fraction of progenitor cells that exit at each cycle [58]. The progression of the cell cycle is controlled by complex regulatory networks and signalling pathways and is highly conserved (Figure 1.8). The mechanism underlying the determination of proliferative versus differentiative division remains unclear however evidence has showed that the mode of cell division largely depends on the cell cycle components associated with G1-phase regulation. The lengthening of the G1-phase and the accompanied slowing-down of cell cycle progression is observed during corticogenesis, as the neuron production and the frequency of differentiative divisions increase [59].

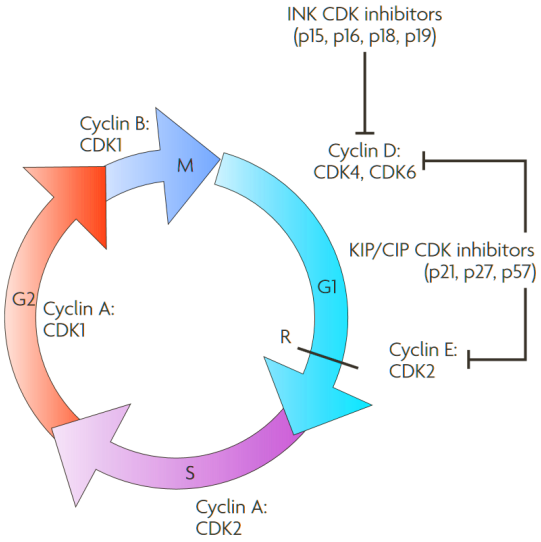


Figure 1.8: ***Regulatory mechinary of cell cycle progression.*** *Adapted from* [59].

Neurogenesis and cell cycle have been extensively studied in the developing cortex for decades whereas in the thalamus there is still much to learn. Considering both the cortex and the thalamus are derivatives of the forebrain, it is likely they share some characteristics in neurogenesis and cell cycle while maintaining their own specificities. In this section, I review the critical events during corticogenesis and the involvement of some major regulators, to assist the understanding of the thalamic neurogenesis and the roles of the corresponding regulators especially the transcription factor Pax6.

During the early development of the vertebrate embryo, the neural tube wall contains a single layer of neural epithelial cells (NECs), which translocate their nuclei during the cell cycle from a basal position in S phase to an apical position during M phase with the daughter cell nuclei moving back to the basal side of the ventricular zone to enter S phase. The symmetric proliferative division of NECs increases the size of the NECs pool. The expression of an anti-proliferative gene *Tis21* in the NECs leads to their identity transition into radial glial cells (RGCs) [51, 52]. Both NECs and RGCs show apical-basal polarity with apical and basal processes spanning through the whole cortical neuroepithelium (Figure 1.9). The RGCs undergo asymmetric division to give rise to a daughter RGC cell and a differentiating cell, either a neuron or a more fate restricted progenitor cell called intermediate progenitor (IP), which usually divides symmetrically to generate two neurons. During mammalian corticogenesis, there is also a group of non-IPs basal progenitors with glial characteristics called basal radial glial cells (bRGs), which derive from RGCs and divide asymmetrically to give rise to a daughter bRG and an IP. These bRGs are believed to associate with cortical expansion in some mammals [51, 52].

Neocortex expansion is a hallmark of primate evolution especially in human. A recent comparative study of the neural stem and progenitor cell subpopulations in human and mouse neocortex revealed that in mice bRGs are very similar to IPs and neurons but distinct from RGCs, whereas in human fewer genes were differentially expressed in bRGs and RGCs [53], which makes it interesting to study the significance of bRGs population in both mice and humans. The gene ontology (GO) term analysis of the differentially expressed genes supports the importance of the endogenous extracellular matrix production (ECM) and the expression of ECM receptors by human RGCs and bRGs which supposedly contribute to their greater proliferative potential compared to their counterparts in mice [53]. Human-specific ARHGAP11B gene, which encodes a Rho guanosine triphosphatase-activating protein, was found to induce RGCs to switch from symmetric-proliferative and asymmetric differentiative to symmetric differentiative divisions when expressed in the E14.5 mouse cortex. Another four Rho signalling pathway related genes ARHGAP24, ARHGAP28, ARHGEF28 and RHOH, show similarly distinct expression in bRGs/RGCs compared to neurons, suggesting Rho proteins play a role in human RGCs [53]. A Rho family GTP-binding protein Rnd3 is shown to regulate the interkinetic nuclear migration of the RGCs and maintain the adherens junctions among these cells. It was also found that Rnd3 limits the proliferative division of the bRGs by suppressing the expression of cyclinD1 (Ccnd1). Further, Rnd3 expression is transcriptionally controlled by Ascl1 [54], a transcription factor highly expressed in the developing thalamus, however Ascl1 itself is only required for proper orientation of cell division in the RGCs. During cortical development, Pax6 not only regulates regional patterning, it also promotes radial glial cell proliferation and spindle orientation, and boosts neurogenesis through the induction of basic-helix-loop-helix proneural genes such as the Neurogenins - the seemingly opposing effects of Pax6 was shown mediated by alternative splicing of *Pax6* [55]. It was also shown that Pax6 interacts with BAF155 and BAF170, components of ATP-dependent multi-subunit mSWI/SNF nucleosome remodelling complexes. These two subunits compete with each other to modify euchromatin structure during early neurogenesis, which leads to the recruitment of Pax6/REST-corepressor complex to repress the expression of Pax6 target genes that are involved in IPs production, such as *Tbr2*, *Cux2* and *Tle2* [56].

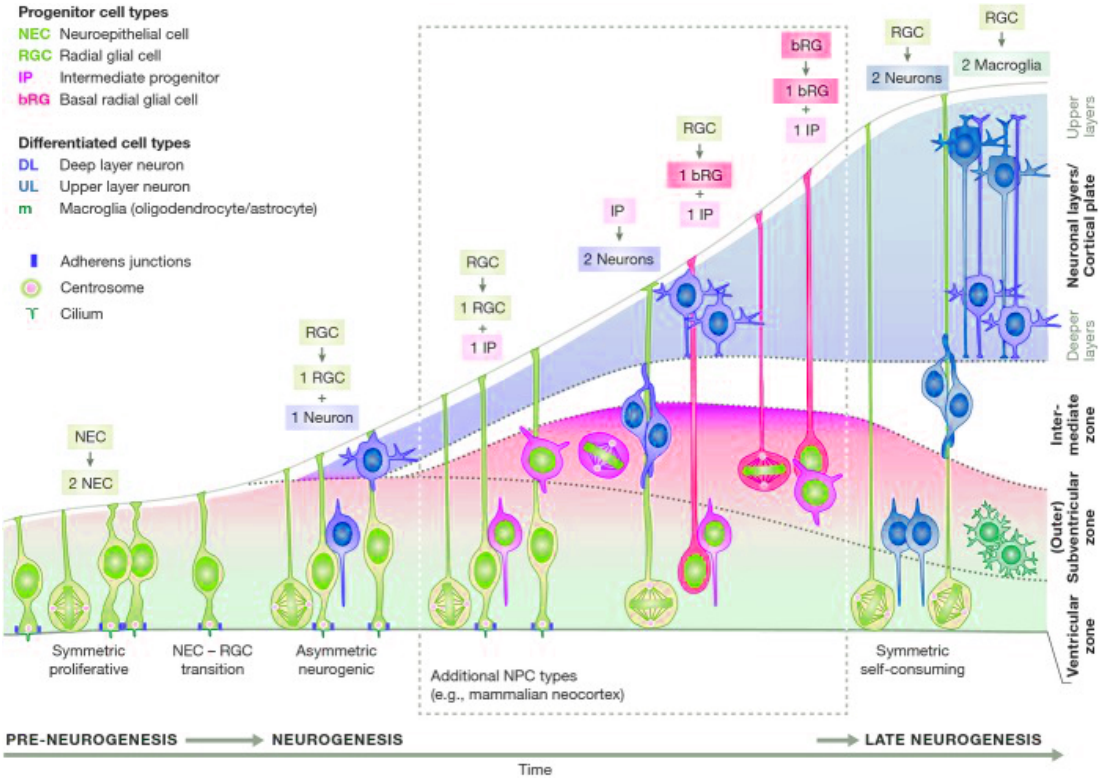


Figure 1.9: ***Schematic overview of neurogenesis in the embryonic vertebrate CNS.*** *Adapted from* [52].

It was shown that the lengthening of the G1-phase is associated with the transition of stem cell-like apical progenitors to more fate-restricted intermediate progenitors [60]. It was also found in the same study that proliferative progenitors invest more time controlling the DNA replication quality during the S-phase than those committed to neuron production [60]. A high throughput RNAi study using hESCs revealed that the S and G2 phases promote the pluripotent state of these cells and the regulation is independent from the G1 phase [61]. In E12.5 mouse cortical progenitor cells, high levels of *Pax6* expression are associated with long cell cycles and the loss of Pax6 in *Pax6 null* mutants causes significant shortening of the total cell cycle without affecting the length of the S phase in the regions where its expression level is high or medium. The shortening of the total cell cycle subsequently leads to an increase in M phase cells with abnormal positioning through the depth of the ventricular zone rather than at the ventricular surface where these cells normally reside [62]. These M-phase cells could be bRGs and/or IPs which suggests the loss of *Pax6* could potentially causes an increase in the basal progenitor population in the developing cortex. *Pax6* directly represses the expression of *Cdk6*, one of the critical cell cycle regulators that facilitate the progression of progenitors through the G1 phase, and subsequently inhibits the phosphorylation of *pRb*, limiting the transcription of genes involved in the cell cycle progression [62].

Compared to the abundant research on corticogenesis, studies of thalamic neurogenesis are much more limited. Many studies of the thalamic progenitor cells, focused more on their positional identities like the pTH-R and pTH-C revealed by differential expression of transcription factors such as Olig3, Nkx2.2, Ascl1, Ngn2, Olig2, Pax6 and Gsx2 [63, 9, 5], and other involved regulators among which the morphogen Shh is extensively studied [46, 63, 17, 18, 40]. However, only a very few papers looked at finer categorisation of the thalamic progenitors and asked questions such as: Does the developing thalamus have a subventricular zone like the cortex? Does the developing thalamus also have IPs and bRGs that reside in the subventricular zone? How do different types of thalamic progenitors divide and in which way (asymmetric or symmetric) to produce how many daughter progenitors and/or neurons? One of the early studies on the thalamic RGCs was carried out in rats and the staining of vimentin, the primary structural protein of RGCs, revealed that at E14 (equivalent to E12.5 in mice) the glial fibers extend radially from the ventricular zone to the pial surface of the diencephlic vesicle. The staining for calretinin showed that the migration of newly born neurons is tightly associated with the radial glial fibres. When the migration is complete at E19 (equivalent to E17.5 in mice) and the radial glial fibres are no longer required for guiding the neurons, the expression of vimentin is replaced by GFAP and the RGCs transform into astrocytes [64]. A much later project carried out by Nakagawa's group demonstrated the existence of a unique and significant basal progenitor population in the developing thalamus, studied their molecular identities and explored the roles of Ngns and Pax6 in the maintenance of this cell population [38]. The intracellular domain of Notch1 (NICD) and Pax6 were both used as markers for the RGCs and their expression patterns showed that Pax6 is expressed in a conspicuously broader region than NICD along the third ventricle. The dividing basal progenitor cells were defined as pHH3 positive cells that reside away from the surface of the third ventricle. By analysing EdU and pHH3 staining after a series of EdU labelling at 0.5 hr, 2hr, 4hr and 8hr, they found: 1. at E11.5, the cells start to enter the M phase about 2 hours after the S phase; 2. the thalamic basal progenitor cells stay in the basal location from the S phase to the M phase whereas the nuclei of the RGCs migrate medially from the S phase to the M phase by interkinetic nuclear migration [38]. The analysis of *Pax6* mutants suggests that Pax6 plays a role in generating basal progenitors from apical progenitors in the ventral part of the thalamus[38]. Though the paper nicely demonstrated the existence of the basal progenitor population in the thalamus, it did not answer whether they are bRGs or IPs and the division behavior and typical processes of the aRGs couldn't be studied using live imaging since the NICD staining only visualises the cell nuclei. Recently, a US group published a thorough lineage study of individual RGCs dividing and producing a cohort of progeny neurons using a method called MADM (mosaic analysis with double markers Figure 1.10) [65], which utilised tamoxifen inducible interchromosomal Cre recombination driven by *NestinCre*

in mice [66]. Stainings for the GFP and tdTomato revealed the bipolar aRGs with their nuclei in the ventricular zone and long fine radial glial fibres extending toward the pial surface and several daughter cells with short processes positioned along the radial glial fibres. The intermediate progenitor cells are identified by double labelling with Ki67. They also found Shh signalling promotes gliogenesis and suppresses tangential distribution of clonally related neurons in the anterior but not the posterior region of the thalamus [66]. Since *Pax6* and *Shh* mutually repress each other's expression around the Shh-secreting ZLI, the deletion of Pax6 could potentially change the level of Shh signalling and indirectly affect the gliogenesis and clonally related neuronal migration.

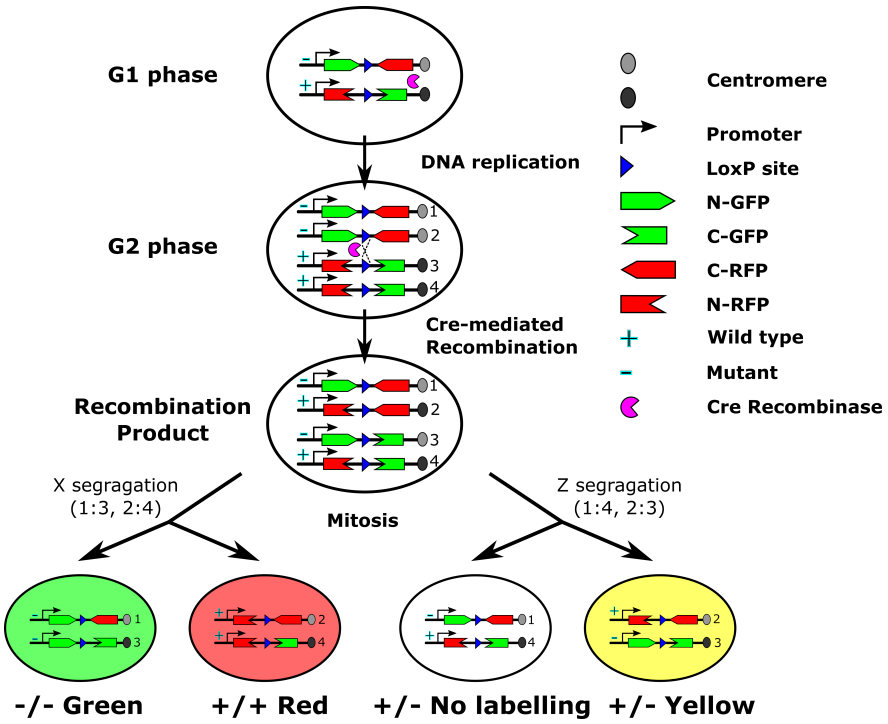


Figure 1.10: ***Schematic of the MADM Strategy.*** *MADM makes use of Cre-loxP-dependent interchromosomal mitotic recombination to generate uniquely labelled homozygous mutant cells. Two reciprocally chimeric marker genes are separately targeted by homologous recombination to identical loci on homologous chromosomes; the resulted mice are crossed to each other to make transheterozygotes. Each chimeric gene consists of part of the coding sequences of the GFP and RFP. The N- and C- terminals of each chimeric gene are separated by an intron containing a single loxP site. While the pair of the loxP sites serve as the targets for Cre-mediated interchromosomal recombination, protein expression is unaffected since the loxP sites are removded by RNA splicing. In the absence of recombination, these chimeric genes do not produce function proteins because their coding sequences are interrupted by the intron in different reading frames. After DNA replication in dividing cells (G2 phase), Cre recombinase introduced as a separate transgene can induce recombination between the loxP sites, restoring functional GFP and RFP cassettes. During the subsequent mitosis, two types of chromosomal segregations are possible. X segragation (two recombinant sister chromatids segragate into different daughter cells) produces two daughter cells, each expresses one of the two fluorescent proteins, appearing red or green. Z segregation (two recombinant sister chromatids segragate into the same daughter cell), generates one daughter cell that resembles the parental cell (colourless) and the other daughter cell expressing both fluorescent proteins, appearing yellow. Recombination can also occur in the G1 phase of the cell cycle or in postmitotic cells (G0 phase), in which cases functional GFP and RFP are restored simultaneously, resulting in double-coloured cells. Reproduced according to* [65].

Programmed cell death is a process in which the cells activate an intracellular death program and kill themselves in a controlled way [57]. Programmed cell death usually but not exclusively occurs by apoptosis, during which cells undergo a series of characteristic morphological change - nuclear shrinkage, chromatin condensation, DNA fragmentation, and membrane blebbing accompanied by extensive neurite degeneration for neurons [57, 67]. Large cells often break up into membrane-enclosed apoptotic bodies with chemically altered surfaces, which enables macrophages to recognise and quickly engulf them before the enclosed contents are released to the neighbouring environment, which could potentially causes damaging inflammatory responses [57]. Cell death not only has an important role in adjusting the initial progenitor pool needed for proper morphogenesis of the central nervous system but functions as a mechanism to match the neuron population to the target fields as well [68]. Soon after exitting the cell cycle, the newly born neurons start to elongate their axons to innervate the targets, during which they are highly susceptible to undergo programmed cell death - as much as 50% of the cells in several ganglia in the peripheral nervous system and regions in the central nervous system are eliminated around the time they make connections with other cells [69]. Caspase-3 is a predominant caspase executioner in the nervous system and is essential for normal brain development [68, 70]. The inactivation of caspase-3 reduces normal apoptosis in the developing mouse brain, which results in the subsequent death of the mice around birth with deformed brain that contains excessive numbers of cells [57]. Cell death can be detected using an antibody that recognises the cleaved fragement of caspase-3 but not the inactive proenzyme form of it [68]. The cleaved caspase-3 staining showed that the over-expression of transgenic *Pax6* in the cortex leads to massive apoptosis of the cortical progenitor cells at E11.5 with the level attenuated toward E14.5 and no longer detectable from E18.5 onwards. The cortical progenitors undergone apoptosis were observed to express a higher than normal level of ephrinA5, which leads to the possibility that Pax6 regulate apoptosis in an ephrinA5-dependent way [71].

1.6 Zic4 and its role in the development of the central nervous system

1.6.1 Discovery of the *Zic4* gene

The *Zic4* gene was first identified in the mouse nervous system in 1996 by Mikoshiba's lab [72] as a new member of the mouse *Zic* (Zinc finger protein of the cerebellum) gene family after the discovery of *Zic1*, *Zic2* and *Zic3* [73]. This family of genes are homologues to the *Drosophila* gene *odd-paired (opa)*, which is involved in the formation of the characteristic midgut

constrictions in *Drosophila* [72, 74]. Increasing evidence has shown that this gene family encodes proteins that can regulate the transcription of other genes in either a DNA-binding dependent (as transcription factors) or a DNA-binding independent (as transcription co-factors) way [75]. A RNase protection study in adult mouse carried out by Mickshiba's lab showed that *Zic4* transcripts are strongly expressed in cerebellum and weakly in the diencephalon, mesencephalon and metencephalon [72]. In embryonic mouse nervous system (E12 to E18), *Zic4* transcripts are detected as early as E12 in brain tissues (mixtures of forebrain, midbrain and hindbrain tissues) and the expression levels are relatively consistent until birth [72]. In postnatal mouse nervous system (P0 to P28), the expression of *Zic4* transcripts reaches a peak at P5 in cerebellum [72].

1.6.2 *Zic4* gene and Dandy-Walker malformation

The high expression levels of *Zic* family genes including *Zic4* in the cerebellum indicate their potential roles in the development of the cerebellum [72] but no further functional studies were carried out in the first eight years after the discovery of the *Zic4* gene. In 2004, Millen's group identified that a deletion encompassing both *ZIC1* and *ZIC4* on human chromosome 3q2 is involved in a heterogeneous disorder (medical conditions which have several etiologies) called Dandy-Walker malformation (DWM), a congenital cerebellar malformation in human [76]. The key features of DWM include hypoplasia, upward rotation of the cerebellar vermis and cystic dilation of the fourth ventricle [76]. Seven out of the eight patients with isolated DWM examined in the study have a hemizygous deletion in both *ZIC1* and *ZIC4* and in the other individual, the expression of both genes was altered by a deletion in the adjacent region [76]. The group generated a targeted heterozygous deletion in mouse embryonic stem cells, which spans both *Zic1* and *Zic4* genes to model these patients. They also carried out studies of *Zic1* and *Zic4* single mutants respectively. The *Zic1* mutants they used had been studied in Mitsushiba's group during which they found that $Zic1^{+/-}$ mutants had significantly smaller cerebelli than $Zic1^{+/+}$ but the extent of reduction was not as severe as is observed in $Zic1^{-/-}$ [77]. Millen's group generated *Zic4* mutants to explore the potential role of *Zic4* itself in the development of the cerebellum and to compare with the *Zic1* single mutant and the $Zic1^{+/-}$;$Zic4^{+/-}$ compound mutants [76]. The $Zic1^{+/-}$ $Zic4^{+/-}$ compound mice fell into two distinct phenotypic catogories: about 85% of these mice showed a mild cerebellar phenotype, similar to that of $Zic1^{+/-}$ mutants, showing a disruption of anterior folia; and around 15% of the mice were severely affected, with marked foliar defects and disproportionate hypoplasia of the vermis compared to the hemispheres, mimicking the cerebellar morphology of individuals with DWM and deletions of 3q [76]. In $Zic4^{+/-}$ mutants they found that the cerebellum is hypoplastic with a distinct foliation abnormality in the posterior part of the cerebellum [76]. The phenotypes observed in $Zic1^{+/-}$ and $Zic4^{+/-}$ mutants indicated that both *Zic1* and *Zic4* are

haploinsufficient in mice and the heterozygous loss of both *Zic1* and *Zic4* is sufficient to cause DWM-like cerebellar vermis hypoplasia in mice. The phenotype of the double-heterozygous compound mutants is not a simple addition of the phenotypes of the two single heterozygous mutants or the phenotypes of either of them, which indicates that the *Zic1* and *Zic4* gene are both required for the development of the cerebellum and there might be some redundancy and compensation between the two in regulating this biological process. It was also suggested that the variance of the cerebellar phenotype in double-heterozygous mice is likely to be caused by modifier loci (the genetic factors that distinct from the disease-causing genes), which is supported by the low empiric recurrence risk (the chance that a trait will occur or recur in a family) in human [76] as the modifier loci and the ZIC mutations may not be co-inherited.

Later on, Millen's group generated single $Zic1^{-/-}$ and $Zic4^{-/-}$ null mutants by mating $Zic1^{+/-}$ $Zic4^{+/-}$ heterozygotes [78]. The analysis of the whole mount cerebella and the sections through the vermis showed that the cerebellar size is slightly reduced in the $Zic4^{-/-}$ mutants without any conspicuous change in the foliation and in the $Zic1^{-/-}$ mutants the cerebella are smaller compared to that in the wild type with the loss of a folium anterior to the primary fissure [78]. In the $Zic1^{-/-}$;$Zic4^{-/-}$ compound null mutants, the cerebella are smaller than in the wild type and the two single null mutants and one anterior folium is missing [78]. In order to understand the underlying mechanisms, they further assessed the early postnatal external granular layer (EGL), whose rapid proliferation is essential for the expansion of cerebellum. As the postnatal EGL expansion is primarily driven by Shh signalling from the underlying Purkinje cells [79, 80], they examined the expression of *Shh* in the Purkinje cells and its target genes *Gli1* and *Ptch1* and found the expression of these two genes are significantly reduced in the $Zic1^{-/-}$ null mutants and $Zic1^{-/-}$;$Zic4^{-/-}$ compound mutants whereas the expression of *Shh* appeared to be normal [78]. It suggests that there is a specific defect in the reception/processing of the Shh signalling but not the expression of the *Shh* itself. Since Zic proteins have long been hypothesized to regulate Gli-mediated Shh signalling, they went on to generate $Zic1^{+/-}$;$Zic4^{+/-}$;$Shh^{+/-}$ compound heterozygous mutants to see if the reduction in Shh expression could cause a similar cerebellar phenotype to that of the $Zic1^{-/-}$;$Zic4^{-/-}$ ($Shh^{+/+}$) compound null mutants. The reduction of cerebellar size seen in the $Zic1^{-/-}$;$Zic4^{-/-}$ mutants is reproduced in the triple heterozygous mutants but no folia patterning defects are observed, which suggests that *Zic1* and *Zic4* regulate cerebellar size in a Shh-dependent way but regulate Purkinje cell parcellation in the cerebellum in a Shh-independent way [78].

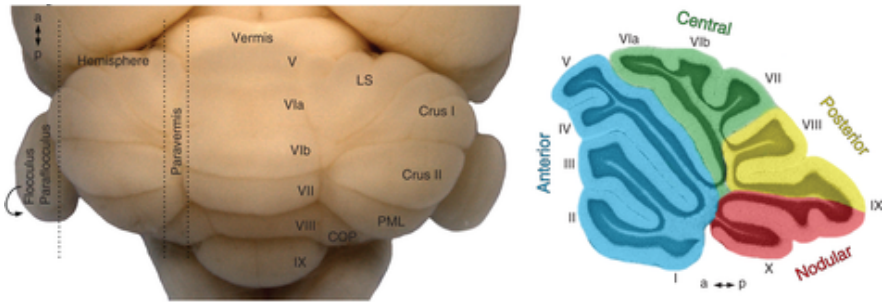


Figure 1.11: ***Whole mount dorsal view of an adult mouse cerebellum (left) and schematic midsagittal section of the cerebellar vermis (right).*** *Along the anterior-posterior axis, there are ten folds called lobules that are identified with Roman numbers. Along the medial-lateral axis, the cerebellum can be divided into four parts, a vermis in the middle, the two lateral hemispheres, the flocculi/paraflocculi under the two hemispheres. The lobules in the hemisphere are unique to the ones in the vermis (lobules I-V), including the lobulus simplex (LS), crus I, crus II, paramedian lobule (PML) and the copula pyramidis (COP). [78, 81].*

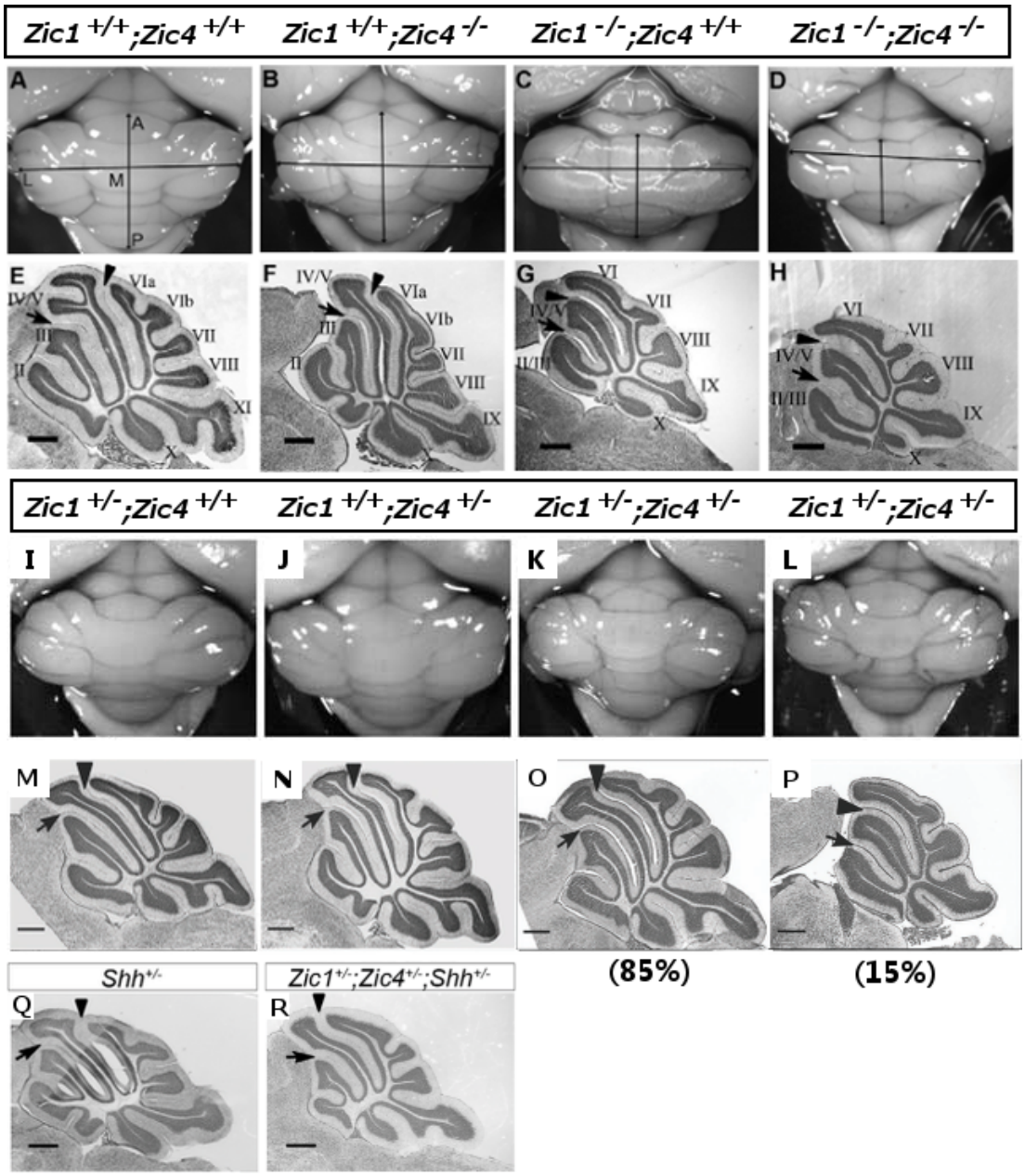


Figure 1.12: ***Dorsal views of whole mount cerebellum and staining of midsagittal sections through the vermis from wild type and different Zic1, Zic4 and Shh single or compound mutant mice at P20 (A-H, Q and R) and P22 (I-P).*** *Black arrowheads and arrows indicate the primary and preculminate fissures respectively [76, 78].*

Genotype	Phenotype
Zic1$^{+/-}$;*Zic4*$^{+/+}$	Slightly hypoplastic cerebellum with smaller anterior lobes (Figure 1.12 I, M)
Zic1$^{-/-}$;*Zic4*$^{+/+}$	Slightly smaller cerebellum along the anterior-posterior axis and the loss of one folium anterior to the primary fissure (Figure 1.12 C, G)
Zic1$^{+/+}$;*Zic4*$^{+/-}$	Hypoplastic cerebellum with a distinct foliation abnormality in the posterior cerebellum especially visible as an invagination at the secondary fissure (Figure 1.12 J, N)
Zic1$^{+/+}$;*Zic4*$^{-/-}$	Slightly smaller cerebellum with no gross change in foliation (Figure 1.12 B, F)
Zic1$^{+/-}$;*Zic4*$^{+/-}$	85% of the mice showing similar phenotype to *Zic1*$^{+/-}$;*Zic4*$^{+/+}$ mice (Figure 1.12 K, O) and 15% of them showing severe cerebellar hypoplasia: reduced width of vermis, simplified foliation pattern and lack of one entire anterior lobe (Figure 1.12 L, P)
Zic1$^{-/-}$;*Zic4*$^{-/-}$	Smaller cerebellum and loss of one anterior folium (Figure 1.12 D, H)
Shh$^{+/-}$	Cerebellar vermis section shows normal foliation and size (Figure 1.12 Q)
Zic1$^{+/-}$;*Zic4*$^{+/-}$;*Shh*$^{+/-}$	Cerebellum has the correct number of folia but vermis area was reduced, similar to what have seen in the *Zic1*$^{-/-}$;*Zic4*$^{-/-}$ mutants (Figure 1.12 R)

Table 1.1: ***Cerebellar phenotypes of various single, double and triple Zic1, Zic4 and Shh mutant mice.*** *It can be seen from the table that the severity of the phenotypes increases with decreasing gene does.* Zic1$^{+/-}$;Zic4$^{+/+}$, Zic1$^{+/+}$;Zic4$^{+/-}$, Zic1$^{+/+}$;Zic4$^{-/-}$ *and* Shh$^{+/-}$ *mutant cerebella show normal foliation and size. 85% of* Zic1$^{+/-}$;Zic4$^{+/-}$ *mutants show normal foliation whereas the other 15% of them show hypoplasia and the loss of one folium anterior to the preculminate fissue.* Zic1$^{-/-}$;Zic4$^{+/+}$, Zic1$^{-/-}$;Zic4$^{-/-}$ *and* Zic1$^{+/-}$;Zic4$^{+/-}$;Shh$^{+/-}$ *muants are indistinguishable and resembles the severe phenotype seen in the 15%* Zic1$^{+/-}$;Zic4$^{+/-}$, *with hypoplasia and anterior foliation defects. [76, 78]*

.

1.6.3 Expression of the *Zic4* gene in the developing mouse nervous system

Copp's team carried out detailed characterization of *Zic4*'s expression pattern in the developing mouse nervous system [82]. They looked at different embryonic stages as early as E8 and found that *Zic4* transcripts are first detected at E9 at low intensity in the dorsal midline of the forebrain neural tube [82]. The expression level increases at E9.5 and is further upregulated at E10.5 with the expression expanded to the boundary between the diencephalon and telencephalon [82]. At E10.5, the choroid plexus of the third ventricle, lamina terminalis and septal area also show high levels of *Zic4* expression [82]. At E12.5, the expression of *Zic4* is restricted to the midline of the forebrain, including the septum and the cortical hem, and its expression in the choroid plexus and the lamina terminalis is maintained [82]. At P2, the expression is specifically high in the external granular layer of the cerebellum which is occupied by granule cells [82].

1.6.4 *Zic4* gene is involved in neural tube development

Zic4 functional studies were also performed in zebrafish and *Xenopus* by Prince's [83] and Aruga's group [84] respectively. Prince's team knocked down *Zic1* and *Zic4* in zebrafish using morpholinos to investigate the roles of these Zic family genes in dorsal neural tube development [83]. The dorsal neural tube is the origin of three types of cells: neural crest cells, dorsal hindbrain progenitors and roof plate cells. Using a variety of molecular markers, they showed that the dorsal progenitors are reduced and the roof plate is disrupted or absent in the hind brains of the morphants whereas the neural crest induction and migration are unaffected. They also observed that the fourth ventricle (hindbrain ventricle) in *Zic1* and *Zic4* morphants do not open properly but remain completely or partially fused [83]. The alteration of the expression of roof plate markers, the LIM-homeobox gene *lmx1b.1* and *lmx1b.2* in the morphants, attracted their attention. Studies in mouse hindbrain and chick spinal cord had shown that *Lmx* gene function is required for the roof plate induction and growth. Thus they went on to knockdown *lmx1b.2* using morpholinos and observed similar phenotypes to those seen in the *Zic* morphants, such as alteration of roof plate marker expression and fusion of the hindbrain ventricle, which suggests the loss of *lmx1b* underlies the morphological defects observed in *Zic* morphants [83]. Aruga's team investigated *Zic4*'s potential role in neural crest induction by introducing Myc-epitope-tagged (MT) wild-type *Zic4* (MT-Z4) or N-terminal truncated (MT-Z4ΔN) or C-terminal truncated (MT-Z4ΔC) mutant *Zic4* RNAs into one blastomere of two-cell-stage embryos [84]. *Zic4* over-expression using MT-Z4 and MT-Z4ΔC significantly increased *Slug* (a neural crest specifier gene) expressing areas at the neurula stage, whereas MT-Z4ΔN inhibited its expression. These results indicated that *Zic4*, especially its N-terminal region, can induce neural crest tissue whereas the C-terminal region

supress the normal *Zic4* function. MT-Z4 injected embryos also showed a hypoplastic, distorted or shifted (anteriorly or dorsally) eye, which was observed in MT-Z4ΔN injected embryos but not the MT-Z4ΔC injected ones [84]. These results indicated that *Zic4*, especially the C-terminal region, is involved in eye formation and over-expression of *Zic4* or the C-terminal region of the *Zic4* gene can cause eye hypoplasia in *Xenopus* [84].

1.6.5 The role of *Zic4* gene in the visual pathway development

Zic4's function in visual pathway development was further investigated by Sur's group in the study of differential gene expression in the developing principal visual relay nucleus, the lateral geniculate nucleus (LGN, including ventral lateral geniculate nucleus, vLGN and the dorsal lateral geniculate nucleus, dLGN) and principal auditory relay nucleus medial geniculate nucleus (MGN) in mice [85]. They performed a microarray screen using the MGN and the LGN dissected from P0 and P5 wild type mice of 129/SvEv background to compare perinatal gene expression and found groups of genes enriched (Significance Analysis of Microarrays, fold change ≥ 2 and false discovery rate $< 0.01\%$) in different nuclei at P0 and P5 respectively [85]. A majority of genes enriched in LGN are transcription factors, including members of the *Zic* family like *Zic1*, *Zic3*, *Zic4* and *Zic5*; those genes that are involved in neuronal migration like *Arx*, *Dlx1* and *Zic2*; and those playing roles in patterning such as *Pax6* [85]. The enrichment of all *Zic* family members in the LGN suggested a potential role of this family in the formation of the LGN in mice. A recent study of *Zic2* mutant mice confirmed its role in the migration of the interneurons that travel from prethalamic neuroepithelium to the vLGN [86]. In this study, they also investigated *Zic4*'s function in visual pathway development using the $Zic4^{-/-}$ mutants generated by Millen's group [76, 85]. *Zic4* is strongly expressed in the LGN, which receives visual afferents from the retina, which also expresses *Zic4*; thus *Zic4* mutants are used for studying the patterning of retinogeniculate projections [85]. In $Zic4^{-/-}$ mutants, increased clustering and disorganization of the ipsilateral terminals are observed but whether that is caused by the loss of *Zic4* in the LGN or the retina or both remains unclear [85]. *Zic4* gene function has also been studied in the development of the inner ear structure in mice by Millen's group [87]. They found no distinguishable defects in inner ear development from E11.5 to E15.5 in either $Zic1^{+/-}$;$Zic4^{+/-}$ or $Zic1^{-/-}$;$Zic4^{-/-}$ compound mutants, which indicates that *Zic1* and *Zic4* are not required for inner ear development [87]. Their results fit very well with the microarray data obtained by Sur's group, in which they found that *Zic1* and *Zic4* are specifically enriched in the visual principle nucleus - LGN and not in the auditory principle nucleus - MGN [85, 87].

1.7 Lineage tracing and fate mapping in developing diencephalon

1.7.1 Lineage tracing and fate mapping techniques in developmental biology

The emergence of developmental biology especially the research in invertebrate embryos in the late 19th century led to the establishment of the important concepts of cell lineage analysis [88]. The word *lineage* literally means 'direct descent from an ancestor' and a cell's lineage can be defined as the developmental history of a cell from birth until its final division and differentiation into a particular cell type, also known as cell fate. Cell lineage can be studied by marking a single cell in such a way that the mark is transmitted to all the cell's progeny without changing the properties of the founder cell, its progeny or their neighbours [89]. Lineage tracing studies aim to establish which cells and how many of cells in the early embryo give rise to a structure and from which part of a structure a substructure derives [89]. A variety of lineage tracing techniques that have been summarised in a couple of reviews include direct observation, cell labelling with dyes and radioactive tracers, introduction of genetic markers by transfection, cells and tissue transplantation, genetic mosaic and cell marking by genetic recombination [88, 89].

Genetic markers such as GFP and β-galactosidase (encoded by the bacteria *LacZ* gene) can be knocked into the gene of interest or placed under the control of regulatory elements corresponding to the gene of interest by gene trapping [89, 90]. The gene trap vector usually contains a promoterless reporter gene, a splice acceptor (SA) immediately upstream of the reporter gene and a downstream polyA transcriptional termination sequence. When inserted into an intron of the gene of interest, the gene trap vector is transcribed from the endogenous promoter of that gene in the form of a fusion transcript in which the exon(s) upstream of insertion site is sliced in frame to the reporter gene. The fusion transcript then encodes a truncated non-functional polypeptide/protein of the gene of interest and the reporter. Gene trap simultaneously inactivates and reports the expression of the trapped gene thus can be used for lineage cell labelling as well as rescue experiments [90].

Cell marking by genetic recombination in mice is usually performed by using the *Cre-loxP* system: Cre recombinase is expressed under the control of a cell or tissue specific promoter in one mouse line and this line is then crossed with another mouse line in which a reporter such as GFP is downstream of a *loxP-STOP-loxP* sequence. Ubiquitously expressed reporter constructs are usually expressed from the *Rosa26* locus. The *loxP-STOP-loxP* sequence prevents the expression of the reporter even though the promoter activity is ubiquitous. The reporter will only be expressed when the Cre recombinase removes the *loxP-STOP-loxP* sequence. Using *Cre-loxP* system for lineage tracing, all the cells that had expressed the specific promoter

driving *Cre* are labelled, from which we can interpret the structure of interest arises from a specific gene expression region [88, 89]. However, it is impossible to distinguish cells descended from different subpopulations of progenitors in the lineage thus detailed correlation between the progenitor subgroups and the subareas in the region of interest can not be established [88, 89]. Other than expressing in the progenitors, the *Cre* is also found expressed in differentiated cells in the tissue of interest sometimes, which makes it essential to interpret the results of this kind of fate mapping study more carefully [88, 89].

A more widely used system utilises the fusion protein between Cre and a mutated form of the estrogen receptor (ER^{TM}) that makes Cre activity tamoxifen inducible, which is called the tamoxifen inducible Cre (Cre-ER^{TM}). The mutated estrogen receptor prevents the binding of its normal ligand (17β - estrodial) but makes the ER^{TM} domain sensitive to 4-hydroxy-tamoxifen. The fusion of Cre with ER^{TM} leads to ER^{TM}-dependent cytoplasmic sequestration of Cre by Hsp90 which prevents Cre-mediated recombination, a nuclear event. However, the binding of 4-hydroxy-tamoxifen causes the disruption of the interaction between Hsp90 and the fusion protein, which allows the Cre to access the nuclear and further initiate the recombination [91]. The reduction in nuclear localised Cre-ER protein was observed 48 hrs after the injection of 3 mg of tamoxifen, which suggests that further recombination is less likely beyond this time point [91]. This system provides a tighter temporal control of the Cre activity as the Cre is only activated transiently.

1.7.2 Lineage tracing and fate mapping studies in diencephalic development

The progenitors, which give rise to postmitotic neurons, are situated in the ventricular zone of the diencephalon [50, 20]. It has been widely accepted that these progenitors produce neurons after several rounds of division and differentiation, and once these neurons are born they start to migrate toward the final locations and form the future diencephalic nuclei [9]. In order to find the link between the early gene expression pattern in the embryos and the mature diencephalic nuclei after birth, several lineage tracing and fate mapping studies have been performed [20, 47, 48, 46, 18, 86].

Nakagawa's group performed detailed characterization studies of the progenitors within the developing mouse thalamus and defined two distinct progenitor domains called the pTH-R and the pTH-C, both located caudally to the ZLI (Figure 1.13 A) [20]. The pTH-R is immediately caudal to ZLI and expresses markers such as *Nkx2.2*, *Mash1* and *Olig3*. The pTH-C is positioned caudal to the pTH-R and expresses Ngn1, Ngn2 and Olig3 (Figure 1.13 A) [20]. Using $Olig3^{GFP\text{-}IRESnlslacZ/+}$ knock-in mouse line, they found that at E16.5 all thalamic nuclei that project to the cortex

express β-gal, which suggests that Olig3 expressing progenitors contribute to all the cortex projecting thalamic nuclei (Figure 1.13 B red dots) [20]. Double immunostaining of β-gal and neuropeptide Y at this stage reveals that the intergeniculate leaflet (IGL), the structure between the vLGN and the dLGN, is derived from Olig3 expressing cells (Figure 1.13 B red dots) [20]. Double immunostaining of β-gal and Nkx2.2 also indicates that the Olig3 expressing cells contribute to the lateral part of the vLGN (Figure 1.13 B red dots) [20]. By analysing the $Ngn1^{EGFP/+}$ BAC transgenic mice, they found that Ngn1-expressing cells in the ZLI contribute to the medial part of the vLGN and the transverse cell migratory stream between the thalamus and the prethalamus at E16.5 (Figure 1.13 B green dots) [20]. The study of $Ngn2^{KIEGFP/+}$ knock-in mice shows that Ngn2 expressing cells contribute to only the rostral group of thalamic nuclei at P0 [20]. They also crossed $Pitx2^{cre/+}$ with a *N-lacZ* transgenic mice (containing a conditional Cre reporter allele that expresses nuclear-localized lacZ under the control of the chicken *β-actin* promoter) to map the fate of the ZLI cells and found that ZLI cells contribute to the medial part of the vLGN and cells along the border between the thalamus and prethalamus (Figure 1.13 B blue dots) [20]. Using $Mash1^{EGFP/+}$ mice, they found that the lateral part of the vLGN and IGL are derived from Mash1 expressing pTH-R (Figure 1.13 B cyan dots) [20]. The homeodomain transcription factor Dbx1 is expressed in the cells in the pTH-C at a high-caudodorsal to low-rostroventral gradient and the analysis of $Dbx1^{nlsLacZ}$ mice shows that Dbx1 expressing progenitors mainly contribute to the caudal-dorsal part of the thalamus, including the central lateral (CL), mediodorsal (MD), and central medial (CM) nuclei, and not the more rostrally positioned nuclei such as dLGN and VP that express high levels of Sox2 [20]. The study from Nakagawa's group explored a great number of cell lineages in developing thalamus especially the forming vLGN, but the chosen lineage markers are not exclusively expressed in each of the potential orgins of vLGN cells such as the pTH-R, the ZLI and the prethalamus. The proteolipid protein (PLP) is the major protein of myelin and oligodendrocytes and has been found to be expressed in the diecephalic progenitors that are committed to different fates at different time points: the *plp* progenitors exhibit a restricted neuronal fate of differentiation at E9.5 whereas at E13.5 they show a restricted glial cell fate [47]. Using *plp-Cre* mice, Zalc's group discovered that diencephalic *plp* positive ventricular cells are neuroepithelial cells located in the ZLI and the derived neurons are found in the ZI, the subgeniculate nucleus, the vLGN and the IGL [47]. Shimogori's group crossed the Shh-IRES-Cre mouse line with the R26R reporter mouse line in which cells express β-gal following Cre-mediated recombination, to permanently label both Shh-expressing ZLI cells and their progenies [48]. At E12.5, LacZ positive cells were restricted to the ventricular zone of the ZLI, closely resembling the endogenous *Shh* mRNA expression pattern. However, by E15.5 the LacZ positive cells were observed migrating toward the pial surface along the external medullary laminae and reached the lateral most edge of the vLGN [48]. These LacZ positive cells are seen distributed mainly to the

anterior but not the posterior part of the vLGN [48]. In a study of Shh's role in thalamic interneuron fate determination, Epstein's group performed more specific lineage analyses in the pTH-R and prethalamic progenitors using the *Tal1(Scl)-creER* and the *Dlx5/6-cre;ccEGFP* mouse lines respectively [46]. They found that the *Tal1* expressing pTH-R cells contribute to vLGN and IGL at E16.5 (Figure 1.13 B magenta dots) and the *Dlx5/6* expressing prethalamic progenitors mainly contribute to the reticular nucleus, the zona incerta and also the vLGN (Figure 1.13 B yellow dots) [46]. During the study of *Zic2*'s role in controlling neuronal migration in the developing mouse brain, Herrera's group found that *Zic2* expressing cells in the developing diencephalon form a narrow migration stream from the prethalamic neuroepithelim to the vLGN and become a subpopulation of vLGN interneurons, using Tg(Zic2^{eGFP}) BAC transgenic mouse line [86]. Combining the results from Nakagawa's, Epstein's and Herrera's group, we can conclude that the vLGN is composed of a heterogeneous group of neurons originating from the pTH-R, the ZLI and the prethalamic progenitors. *Etv1*, which encodes a ETS family transcription factor, is expressed in the embryonic habenula and the *Etv1*^{creER} knock-in mouse strain was crossed with a cre-reporter line *R26R*^{RFP} to fate map these *Etv1* expressing cells. The results showed that the descendants of these cells that are labelled at E12.5 mainly contribute to the medial habenula nuclei, which indicates that the *Etv1* expressing region at E12.5 gives rise to the medial habenular nuclei [18].

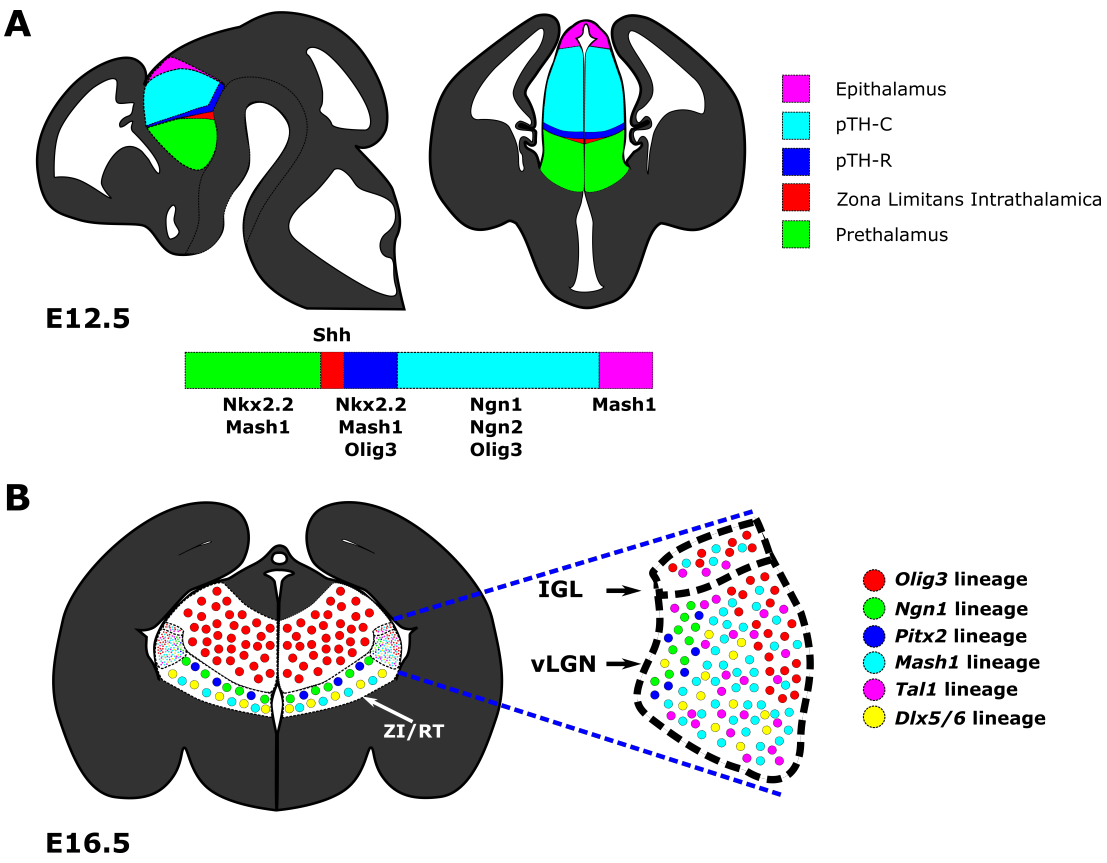


Figure 1.13: ***Summary of lineage fate-mapping studies.*** *A. At the early stage of development such as E12.5, the progenitor zone of the thalamus can be divided into the pTH-R (rostral) and pTH-C (caudal) based on the differential expression of some commonly used markers. The Shh positive zona limitans intrathalamica is positioned between the pTH-R and the prethalamus. Different subregions are colour coded. B. Lineage tracing studies reveals a heterogeneous origins of the prethalamic nuclei vLGN and IGL. Different cell lineages are colour coded and their positions in the vLGN and IGL are indicated in the enlarged vLGN and IGL schematic. [20, 47, 48, 46, 18, 86]*

The number of lineage tracing and fate mapping studies revealed heterogeneity and complexity of the constitution of diencephalic nuclei. Diffferent lineages can contribute to different nuclei; different lineages can contribute to the same nuclei in the case of the vLGN and IGL; one lineage can contribute to a number of different nuclei in the case of the *Olig3* lineage. With these information, we will be able to study how these lineage emerge, grow and distribute among different nuclei and the regulatory elements involved in this process. In the mean time, it is obvious that studying individual lineages alone is not enough to reveal the mechanisms underlying the formation of specific nuclei unless the lineage has a high coverage in a single nucleus.

In my project, I studied the *Zic4* lineage in the developing diencephalon, which constitutes the majority of the cells in vLGN. I used the *Zic4Cre* to conditionally knock out the master transcription factor Pax6 in the hope of gaining useful insights into how and to what extent the transcirption factor Pax6 regulates the formation of individual nucleus during diencephalic development.

1.8 Aim of the study and hypotheses

The aim of the study is to determine the role of the transcription factor Pax6 in the development of the diencephalon, especially the formation of specific diencephalic nuclei such as the ventral lateral geniculate nucleus (vLGN), using conditional *Pax6* mutant mice driven by the diencephalon specific *Zic4Cre* with a EGFP reporter showing the Cre activity; and to further investigate the mechanisms underlying Pax6's role in the process of thalamic nuclei formation.

I hypothesize that:

1. The conditional deletion of *Pax6* driven by the *Zic4Cre* causes defects in the formation of thalamic nuclei, especially the ones where high levels of *Pax6* and *Zic4* co-exist.

2. It is likely the observed defects are associated with cell number and volume of the given nuclei, since *Pax6* is highly involved in cell proliferation, differentiation and apoptosis.

3. *Pax6* deletion in the diencephalon causes the expression of morphogens and transcription factors such as Shh and Nkx2.2, which can potentially result in the morphological changes in diencephalic nuclei.

Chapter 2

Materials and methods

2.1 Animal

2.1.1 Animal husbandary

Conditional *Pax6* knockout embryos were generated by crossing the floxed *Pax6* mutant mice $Pax6^{fl/fl}$ [92] with *Zic4Cre* mice, which express *Cre* recombinase under the control of the Zic4 regulatory elements. In order to detect the Cre activity, these mice were then crossed with *RCE:loxP* reporter mice, in which a floxed neo cassette is upstream of an EGFP coding sequence within the Rosa26 locus [93]. The triple transgenic mice were maintained on a C57BL/6 background.

To obtain $Zic4Cre^{+/-}$;$Pax6^{fl/fl}$;$RCE^{+/-}$, $Zic4Cre^{+/-}$;$Pax6^{fl/+}$;$RCE^{+/-}$ and $Zic4Cre^{+/-}$;$Pax6^{+/+}$;$RCE^{+/-}$ embryos, $Pax6^{fl/+}$;$RCE^{+/-}$ females were crossed with $Pax6^{fl/+}$;$Zic4Cre^{+/-}$ males.

To obtain $Zic4Cre^{+/-}$;$RCE^{+/-}$ embryos, $RCE^{+/-}$ females were crossed with $Pax6^{+/+}$;$Zic4Cre^{+/-}$ males.

All the mice used in this study were maintained in accordance with Home Office and University of Edinburgh animal welfare guidelines.

2.1.2 Genotyping

Genomic DNA was extracted from ear notches of mice or tail snips of embryos or pups by applying 75 μl lysis buffer (25 mM NaOH, 0.2 mM EDTA) and heating to 90 °C for 30 min followed by a cooling step for 4 °C, after which the solution was neutralised by an addition of 75 μl 40 mM Tris HCl. PCR was then used to amplify DNA fragments from the genomic DNA

samples. The primers, the components of the reaction mixture, the PCR program and the gel electrophoresis conditions for each genotyping were listed as follows.

Pax6^{fl}

Primers	Band sizes
AAATGGGGGTGAAGTGTGAG	Wild type band: 156 bp
TGCATGTTGCCTGAAAGAAG	Mutant type band: 195 bp

PCR Program: FCRE

Step	Temperature	Duration
Denature	94 °C	4 min
Amplification (33 cycles)	94 °C	30 sec
	62 °C	45 sec
	72 °C	1 min
Elongation	72 °C	10 min
	10 °C	10 min

Reaction mixture:

Components	Quantity(μl)
ddH2O	16.3
dNTPs(10 mM; Promega)	2.5
FP6 Primer Mix (10 μM; eurofins MWG Operon)	0.5
GoTaq reaction buffer (Promega)	5
GoTaq DNA polymerase (Promega)	0.2
DNA template	1.5

Electrophresis condition
2% agarose gel
TBE buffer
60 min

RCE

Primers	Band sizes
Rosa1: CCCAAAGTCGCTCTGAGTTGTTATC	Wild type band: 550 bp
Rosa2: GAAGGAGCGGGAGAAATGGATATG	Mutant type band: 350 bp
Cag3: CCAGGCGGGCCATTTACCGTAAG	

PCR Program: RCE

Step	Temperature	Duration
Denature	94 °C	1 min
Amplification (33 cycles)	94 °C	45 sec
	59 °C	45 sec
	72 °C	1 min
Elongation	72 °C	5 min
	4 °C	20 min

Reaction mixture:

Components	Quantity(μl)
ddH2O	12.4
dNTPs(10 mM; Promega)	0.4
RCE Primer Mix (10 μM; eurofins MWG Operon)	0.8
GoTaq reaction buffer (Promega)	4
GoTaq DNA polymerase (Promega)	0.4
DNA template	2

Electrophresis condition
2% agarose gel
TBE buffer
60 min

Zic4Cre(iCre)

Primers	Band sizes
iCre250s: GAGGGACTACCTCCTGTACC	Band sizes: 630 bp
iCre880as: TGCCCAGAGTCATCCTTGGC	

PCR Program: ZIC4

Step	Temperature	Duration
Denature	95 °C	1 min
Amplification (33 cycles)	94 °C	30 sec
	60 °C	30 sec
	72 °C	30 sec
Elongation	72 °C	10 min
	4 °C	20 min

Reaction mixture:

Components	Quantity
ddH2O	17.5
dNTPs(10 mM; Promega)	0.5
iCre Primer Mix (10 μM; eurofins MWG Operon)	1
GoTaq reaction buffer (Promega)	5
GoTaq DNA polymerase (Promega)	0.1
DNA template	1

Electrophresis condition
1% agarose gel
TBE buffer
30 min

2.1.3 Embryo/pups Collection

The day that vaginal plug was found was considered as embryonic day 0.5 (E0.5). Pregnant females were culled by an overdose of isoflurane. Embryos were then extracted by caesarean section and moved into ice cold phosphate buffered saline (PBS) and tail snips were sampled for genotyping analysis by genomic PCR. For embryos aged from E11.5 to E14.5, heads were removed and fixed in 4% paraformaldehyde (PFA) in PBS overnight at 4 °C with rocking. For embryos aged from E15.5 to E18.5 the whole brain was removed from the skull and then fixed as above.

P0 pups were collected once they were littered and culled by overdose of sodium pentobarbitone followed by decapitation. The heads were then harvested into ice cold PBS and tail snips were sampled for genotyping analysis by genomic PCR. The brains were dissected from the skull and fixed in 4% PFA in PBS for 48 hours at 4 °C with rocking.

Following fixation, the heads/brains were washed with PBS and either dehydrated in 70% EtOH and embedded in paraffin wax or cryo-protected in 30% sucrose in PBS and embedded in 30% sucrose: OCT (1:1). Brains embedded in paraffin wax were sectioned coronally at 10 μm using a microtome. Sections were then mounted on Superfrost Plus slides (Thermo) and stored until use at room temperature. Brains embedded in 30% sucrose: OCT (1:1) were sectioned coronally at 10 μm using a cryostat. Sections were also mounted on Superfrost Plus slides and stored until use at -20 °C.

2.2 Histological protocols

2.2.1 Cresyl violet staining on paraffin embedded sections

Sections were dewaxed in xylene and rehydrated in 100% alcohol. Then sections were stained in 0.1% Cresyl Violet solution for 15 min at room temperature and quickly rinsed in tap water to remove excess stain. Sections were dehydrated through an alcohol series (50%, 70%, 90%, 95% and 100%), 1 min for each step, and in xylene 2 x 5 min. Sections were finally mounted in LAMB/DPX (Raymond A Lamb-laboratory Supplies), covered with coverslips and dried at room temperature overnight. The prepared slides were stored at room temperature.

2.2.2 Immunohistochemistry on paraffin embedded sections

Sections were dewaxed in xylene and rehydrated through an alcohol series (100%, 95%, 90%, 70% and 50%), 1 min for each step. For DAB (3,3' – Diaminobenzidine) immunohistochemistry, there is a 30 min incubation step in 3% hydrogen peroxide/90% methanol between the 90% and 70% rehydration steps, in order to inactivate endogenous peroxidase activity. Sections were then washed in PBS and microwaved for 20 min in 10 mM sodium citrate (pH 6.0) buffer using a microwave to aid antigen retrieval. Sections were left to cool down to room temperature and then washed in 0.1% Triton X-100/PBS (PBS-Tx) to permeablise cells. Then the sections were blocked using 10% serum from specific species (sigma) in PBS-Tx for 30 min. After blocking, sections were incubated with the primary antibody diluted to certain working concentration in blocking solution over night at 4 °C (or 30 min at 37 °C). Sections were then washed with PBS-Tx and incubated with a secondary antibody conjugated with an Alexa Fluor fluorescent dye. Sections were washed with PBS-Tx and counterstained with DAPI (4',6-Diamidino-2-Phenylindole, Dihydrochloride).

2.2.3 Colourimetric *In situ* hybridisation on sucrose/OCT(1:1) embedded tissue

Three groups of litter-matched $Zic4Cre^{+/-};Pax6^{fl/fl};RCE^{+/-}$ (hom), $Zic4Cre^{+/-};Pax6^{fl/+};RCE^{+/-}$ (het) and $Zic4Cre^{+/-};Pax6^{+/+};RCE^{+/-}$ (wt) embryos from 3 different mothers were used for performing the experiment for each probe at specific stages. The tissue was processed in triple to minimise the risk of variation between different *in situ* experiments caused by the temperature fluctuations or the nuances of the probe concentrations. The expression pattern of each probe was compared with the existing literature and the widely used resource, the Allen Developing Mouse Brain Atlas, which is based on the high-throughput RNA *in situ* hybridisation.

Day1

Hybridisation

A humidified box was made at the beginning of the experiment using 2 sheets of 3 mm Whatman papers wet with 50% formamide/1X salt and incubated at 70 °C for 4 - 6 hours.

The slides stored at -20 °C were warmed up to room temperature for 30 min. The probe was diluted in hybridisation solution to the target concentration. The diluted probe was then denatured at 85 °C for at least 10 min and well votexed before using. 150-200 μl diluted probe was added to each slide and then the slides were covered with coverslips and put in the prepared box incubated at 70 °C overnight. The wash buffer for Day 2 was prepared and pre-warmed at 65 °C overnight.

Day2

Post-hybridisation

The slides were transferred from the box to a Coplin jar and covered by the prepared wash buffer. The jar with the slides was incubated at 70 °C for 30 min. The slides were washed with fresh wash buffer for another two times, 20 min each and transferred to a new box with 1X MABT and incubated at room temperature with shaking for 30 min. Another wash with 1X MABT was performed to the slides for 2 - 4 hours.

Blocking and antibody staining

A humidified box was made by lining 2 sheets of 3 mm Whatman papers at the bottom of a Tupperware container wet with ddH_2O and incubated at room temperature for at least 1 hour in the prepared humidified box without the coverslips. Then the blocking solution was removed and the diluted Anti-Digoxigenin-AP (Roche) was added to the slides. The slides were incubated in the humidified box at 4 °C overnight.

Day3

Post-antibody staining wash

The slides were transferred to a slide box and washed with 1X MABT 5 times for 20 min each at room temperature with rocking. Then the slides were equilibrated in the pre-staining buffer

twice for 10 min each at room temperature with rocking.

Colour reaction

The slides were transferred to a new box containing the staining buffer with NBT/BCIP (Roche) and the reaction was incubated in dark at room temperature for 3 - 4 hours. The reaction was stopped by washing the slides in 1X PBS overnight after the colour was well developed.

Mounting

The slides were mounted in LAMB/DPX (Raymond A Lamb-laboratory Supplies) and covered with coverslips and dried at room temperature overnight. The prepared slides were stored at 4 °C.

2.2.4 Fluorescent *In situ* hybridisation on sucrose/OCT(1:1) embedded tissue

Day1

Hybridisation

A humidified box was made at the beginning of the experiment using 2 sheets of 3 mm Whatman papers wet with 50% formamide/1X salt and incubated at 70 °C for 4 - 6 hours.

The slides stored at -20 °C were warmed up to room temperature for 30 min. The probe was diluted in hybridisation solution to the target concentration. The diluted probe was then denatured at 85 °C for at least 10 min and well votexed before using. 150 - 200 μl diluted probe was added to each slide and then the slides were covered with coverslips and put in the prepared box incubated at 70 °C overnight. The wash buffer for Day 2 was prepared and pre-warmed at 65 °C overnight.

Day2

Post-hybridisation

The slides were transferred from the box to a Coplin jar and covered by the prepared wash buffer. The jar with the slides was incubated at 65 °C for 15 min. The slides were washed with fresh wash buffer for another two times, 30 min each and transferred to a new box with TNT

buffer and washed at room temperature with shaking twice, each for 30 min.

Blocking and antibody staining

The slides were blocked with TNB blocking buffer and then incubated with sheep anti DIG POD (1:500) at 4 °C overnight.

Detection

The slides were washed 3 times using TNT buffer, 5 min each. The cyanine3 tyramide (1:50) (PerkinElmer) was prepared in the amplification diluent 30 min before use and the slides were incubated in cy3 working solution for 5 - 10 min at room temperature. The slides were then wahsed well with TNT buffer and counterstained with DAPI.

Mounting

The slides were mounted using Vectashield (H-1400) hard set.

2.3 Solutions, antibodies and RNA probes

Solutions

Hybridisation buffer (10 ml)	1x salt	1 ml of 10x salt
	Deionised Formamide	5 ml
	10% dextran sulfate	2 ml of 50% dextran sulfate
	rRNA (1 mg/ml)	200 μl of 50 mg/ml
	1x Denhardt's	100 μl of 100x
	H_2O (Baxter)	1.7 ml
10x salt (100 ml)	NaCl	11.4 g
	Tris HCl (pH 7.5)	1.4 g
	Tris base	0.134
	$NaH_2PO_4 \bullet 2H_2O$	0.78 g
	Na_2HPO_4	0.71 g
	0.5 M EDTA (DEPC)	10 ml
	dH_2O (DEPC)	Up to 100 ml
100 x Denhardt's (100 ml)	2% w/v BSA	2 g
	2% w/v Ficoll^{TM}	2 g
	2% w/v polyvinyl pyrolidone	2 g
	H_2O (Baxter)	100 ml
Wash buffer (500 ml)	1xSSC	25 ml of 20x SSC
	50% Formamide	250 ml
	0.1% Tween-20	500 μl
	ddH_2O	225 ml

1x MABT (1L)	1 M Maleic acid	100 ml
	5 M NaCl	30 ml
	NaOH	6.4 g
	ddH_2O	870 ml
	Triton-X	1 ml
Blocking solution (5 ml)	20% sheep serum	1 ml of 100%
	2% blocking reagent	100 mg
	1x MABT	4 ml
Pre-staining buffer (300 ml)	5M NaCl	6 ml
	1M $MgCl_2$	15 ml
	1M Tris (pH 9.5)	30 ml
	Tween-20	300 μl
	ddH_2O	250 ml
Staining buffer (110 ml)	5M NaCl	2 ml
	1M Tris (pH 9.5)	10 ml
	ddH_2O	83 ml
	Polyvinyl alcohol (PVA)	9 g
	1M $MgCl_2$	4.5 ml
	Tween-20	90 μl
	NBT/BCIP	1.8 ml
4% PFA in 0.1 M Phosphate Buffer (pH 7.4)	20% PFA	10 ml
	0.2 M NaH_2PO_4	4.75 ml
	0.2 M Na_2HPO_4	20.25 g
	H_2O (Baxter)	15 ml

20% PFA paraformaldehyde (PFA) stock solution	Dissolve 100 g paraformaldehyde in 400 ml water with 1 ml 10 M NaOH in dried glassware. Stir and heat this solution no higher than 55 °C. Adjust volume to 500 ml, allow it to cool. Filter into RNase-free container. Aliquot into Falcon tubes and store at -20°C.
30% sucrose/PBS	Dissolve 15 g of sucrose in 1x Dulbecco's PBS to 50 ml. Add 0.4 ml of a 10% azide solution (0.02% final azide). Store at 4 °C.
EDTA	Dissolve EDTA in DEPC-treated water in tissue culture flask or bottle used for DEPC water. Adjust pH with NaOH. Autoclave before use.
rRNA	Dissolve yeast rRNA in DEPC water at 10 mg/ml. Heat at 65°C to help dissolve.

Antibody

Antibody	Origin	Antigen	Dilution	Company
BrdU	Mouse	IgG_1	1: 150	BD Biosciences
Ki67	Rabbit	IgG	1: 500	abcam
pHH3 (Ser10)	Rabbit		1:100	Millipore
Tuj1	Mouse		1:400	abcam
Caspase3 (cleaved)	Rabbit		1:1000	Cell Signaling Technology
GFP	Goat	IgG fraction	1:150	abcam
COUP-TFI	Mouse		1:500	Kindly provided by Dr Vassiliki Fotaki
COUP-TFII	Mouse	IgG_{2A}	1:1000	R&D system
Lim1/2	Mouse		1:50	DSHB
Nkx2.2	Mouse		1:200	DSHB
Pax6 (AD2.38)	Mouse		1:50	Kindly provided by Professor V van Heyningen

RNA probes

Probe	Dilution	Section property	Source
Shh	1: 1000	Cryo	
Nkx2.2	1: 2000	Cryo	
Zic4	1: 2000	Cryo	Kindly provided by Professor Nicoletta Kessaris

2.4 Quantitative analysis of fluorescence microscopy images

2.4.1 Image aquisition

A Nikon A1R confocal microscope equipped with the following objectives was used: 10X Plan Fluor/NA 0.3, 20X Plan Apo VC/NA 0.8 and 40X Plan Flour/ NA 1.3 OIL objective. Epi-Filter cubes DAPI, GFP and Cherry were used for visualization of different stainings. Single slices of the still images were acquired at 0.2 μm Z-step.

2.4.2 Image processing

The images were processed and analysed using a custom image analysis pipeline. The raw image .nd2 files were first converted to .tif files and then read into MATLAB with all the metadata extracted from the file names. Then the images were split into R, G and B channels and thresholded using the background fluorescence intensity. The selection of the region of interest was used to exclude mast cells, blood vessel endothelial cells and etc. The post processed images were analysed using CellProfiler.

2.5 Statistical analysis and plotting methodology

Univariate statistics (means ± SEM) were performed for all studied variables. One-way ANOVA was performed to study the effect of genotype and two-way ANOVA was performed to examine the main effects of genotype and rostral-caudal position. The Tukey post hoc test was performed for all pair-wise comparisons subsequent to the ANOVAs. n.s., not significant; *, $p< 0.05$; **, $p< 0.01$; ***, $p< 0.001$; ****, $p< 0.0001$. For two-way ANOVAs, the Tukey post hoc test results were only reported for the main effects of genotype. All experiments were repeated in four embryos for each genotype. Proportion data was transformed using either logistic or arcsine square root transformation ahead of the statistical tests.

2.6 Ocular NeuroVue Red injection

The heads of the P0 pups were obtained by decapitation. The skins and the skull that cover the cortex were removed carefully without damaging the regions around the eyes. The processed brains were kept in 4% PFA for a week in the 37 °C incubator. On the eighth day, the brains were taken out and the eyes were cut open to remove the lens (absent in the $Pax6^{fl/fl}$ eyes). The optic cup was exposed and the bright dot at the bottom of the optic cup is the injection site, where the optic nerve is visible. A small piece of the carbocyanine lipophilic dye NeuroVue Red was inserted into the optic nerve until the piece was completely in the nerve. The same protocol was carried out for both eyes. Afterwards, the brains were transferred back into 4% PFA and kept at 37 °C for another 5 weeks to allow the dye to diffuse along the axons.

When the diffusion completed, the brains were rinsed in 1x PBS and embedded in 4% agarose gel. Then the tissue blocks were sectioned coronally and the tissue sections were collected in 1x PBS and stained with DAPI.

The labelling experiment was repeated in at least 4 pups for each genotype.

Chapter 3

Dynamic expression of *Zic4* and *Zic4* lineage cell fate mapping in the developing diencephalon

3.1 Introduction

The *Zic4* gene expression pattern is described in detail by Kessaris' group during their investigation of the origins of the cortical GABAergic interneurons in the mouse forebrain [98]. They characterised *Zic4* expression in the mouse forebrain and generated bacterial artificial chromosome (BAC) transgenic mice (Figure 3.1) which express codon-improved Cre recombinase (iCre) under the control of *Zic4* transcriptional regulatory elements [98]. The endogenous *Zic4* gene is highly expressed in the septal area as early as E10.5, which makes it a good candidate gene for fate-mapping a specific subgroup of progenitors in the septal area, the *Zic4* lineage septal progenitors, and identifying their progeny in the cortex. In order to fate map this lineage, the BAC transgenic mice were crossed with a *Cre* reporter mouse line, the *Rosa26-lox-STOP-lox-YFP* mouse line, in which a floxed STOP cassette followed by a YFP coding sequence is inserted into the ubiquitously expressed *Rosa26* locus [99]. Theoretically, the *Zic4* regulatory elements carried by the BAC transgene drives the expression of the *Cre* in cells that express endogenous *Zic4* gene. The presence of Cre recombinase will then mediate Cre recombination and excise the floxed STOP cassette, which activates the YFP reporter. Ideally, the YFP reporter will permanently label most if not all of the *Zic4* expressing cells and their descendants and these cells become the so called *Zic4* lineage cells. However, the YFP reporter doesn't necessarily express in coincidence with the endogenous *Zic4* gene in all cells. Whether the expression of the YFP reporter can accurately reflect the expression pattern of the endogenous chromosomal *Zic4* gene depends on the intactness of the regulatory elements included in the transgene and

the susceptability of the *loxP* sites to the Cre recombinase. To determine whether the BAC transgene could recapitulate the specific expression pattern observed with the endogenous *Zic4* gene, they analysed the expression of endogenous *Zic4* and the YFP reporter by *in situ* hybridisation and immunohistochemistry respectively [98]. Staining for YFP showed that *Cre* has been activated at E10.5 in the midline regions of the telencephalon, especially the septal area, and the diencephalon especially the epithalamus, thalamus, prethalamus and eminentia thalami [98]. Expression of endogenous *Zic4* in the diencephalon is maintained at E12.5 . Interestingly, YFP is not expressed in the cortical hem where the *Zic4* expression is observed [98], which suggests possiblities of mis-expression of the Cre, or the threshold effect of the Cre activity. Since this study focused on the thalamus, this issue will not have critical influence on the current project. Using this model, Kessaris' group excluded the possibility of the septal area being the origin of GABAergic neurons for the cortex, and by combining the results obtained from studying other BAC transgenic mouse models such as *Nkx2.1-Cre^{Tg}/R26R-GFP$^{+/-}$* and *Nkx2.1-Cre^{Tg}/Dlx1-Venus^{fl}* they identified that these interneurons actually originate from the germinal zone of the basal ganglia [98].

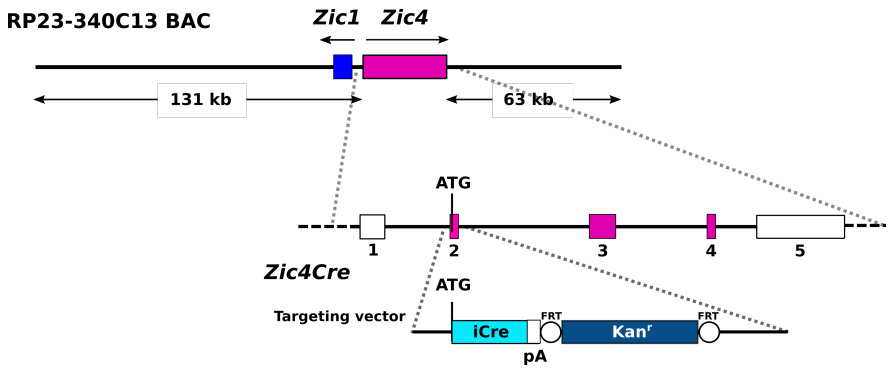


Figure 3.1: ***Schematic of the unmodifed BAC containing Zic4 and the strategy of the Zic4 genomic BAC modification by insertion of iCre and polyA into the Zic4 gene.*** *Adapted from the supplement material provided in [85].*

3.2 Aim of the project

The *in situ* hybridisation of the endogenous *Zic4* gene at E12.5 performed by Kessaris' group showed that *Zic4* is highly expressed in the thalamus (especially at the rostral to middle levels) and the prethalamus [98], which makes it a very good candidate for fate mapping subgroups of thalamic and prethalamic progenitors and monitoring the formation of thalamic nuclei. For the first part of this study, I crossed the *Zic4Cre* mouse line generated by Kessaris'

group with an *RCE* reporter mouse line that has an *EGFP* tag inserted at the ubiquitously expressed *ROSA26* locus [93] to perform a *Zic4* lineage fate mapping study in the developing diencephalon (Figure 3.2). *In situ* hybridisation for the endogenous *Zic4* gene was performed to look at the dynamic expression pattern of *Zic4* in the diencephalon especially the thalamus and prethalamus across different developmental stages. Staining for the EGFP reporter was carried out to trace the *Zic4* lineage cells during the formation of the thalamus, especially the parcellation of the thalamic nuclei. We hypothesize that: 1. the expression pattern of EGFP reporter generally resembles that of the endogenous *Zic4* gene; 2. the *Zic4* lineage cells mainly populate the thalamic nuclei positioned at the rostral to middle levels, and the prethalamic nuclei including the zona incerta (ZI) and the vLGN.

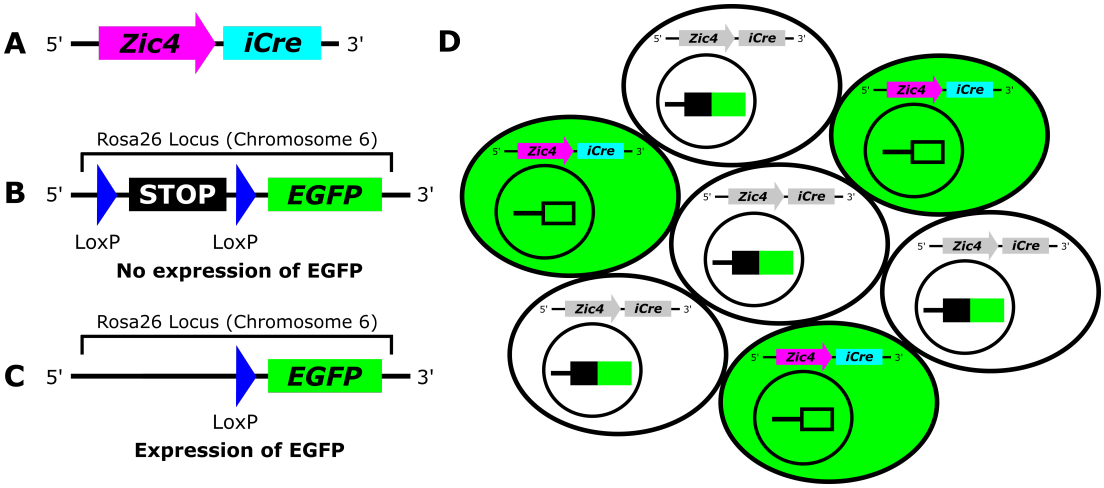


Figure 3.2: ***Schematic of Cre-loxP system driven by Zic4 in this project.*** *A. Zic4 BAC transgene with iCre inserted. B. Floxed STOP cassette in front of the EGFP sequence in Rosa26 locus leads to no EGFP expession. C. Floxed STOP is excised after the activation of the Cre-recombinase and the EGFP starts to express. D. In cells that express endogenous Zic4, the transcriptional regulatory elements bind to the Zic4 BAC transgene and activate the EGFP reporter.*

3.3 Results

Fluorescent *in situ hybridization* (FISH) for the endogenous *Zic4* gene and immunohistochemistry for the EGFP reporter were performed to visualise *Zic4* transcripts and GFP respectively at daily intervals from E11.5 to E18.5, which spans neurogenesis and early nuclei formation in the diencephalon. The mouse brains used for this experiment were embedded face up in the embedding block with the cerebellum at the bottom and were sectioned coronally. The sections that include diencephalic structures, mainly the thalamus and the prethalamus, were collected and used for the staining. The approximate cutting planes were determined by looking at landmarks and comparing with the available mouse brain atlas [100], and labelled using dashed blue lines in the sagittal schematics corresponding to each developmental stage.

The expression patterns of *Zic4* transcripts and GFP in the *Zic4Cre*$^{+/-}$;*RCE*$^{+/-}$ mouse diencephalon at each developmental stage from E11.5 to E18.5 are documented in this section, beginning with a description of the brain sectioning planes and followed by images showing the expression patterns at organ and tissue levels. The expression patterns of both molecules at the cellular level within the thalamus and prethalamus are also shown for E11.5 to E13.5 images to monitor the emergence of early *Zic4* lineage cells within the diencephalon. From E14.5 on, as the nuclei start to form, I focused more on the expression of both molecules in the forming diencephalic nuclei such as the vLGN, dLGN, ZI and VP.

3.3.1 Expression of *Zic4* transcripts and GFP in the E11.5 *Zic4Cre*$^{+/-}$;*RCE*$^{+/-}$ mouse diencephalon

This experiment aims to study the expression of *Zic4* transcripts and GFP in the *Zic4Cre*$^{+/-}$;*RCE*$^{+/-}$ mouse diencephalon at E11.5 is to find out whether the endogenous *Zic4* has started to express in the developing diencephalon and if so where and to what extent this gene is expressed, and whether the GFP reporter has a similar expression pattern. A schematic of E11.5 mouse brain from both sagittal and coronal views is given here to assist readers to understand the anatomical structure of the E11.5 diencephalon.

At E11.5, the neural tube bends at the part where the diencephalon is (Figure 3.3 left), thus it is difficult to describe the relative anatomical position of the sectioning planes using conventional terms such as *rostral*, *caudal*, *ventral* and *dorsal*. Here I use the terms *anterior* (the anterior of the head) and *posterior* (the posterior of the head) (Figure 3.3 left and middle) to describe the relative position of the sectioning planes. Within each plane, the terms *ventral* and *dorsal* are used to describe the relative position of the diencephalic structures. The main

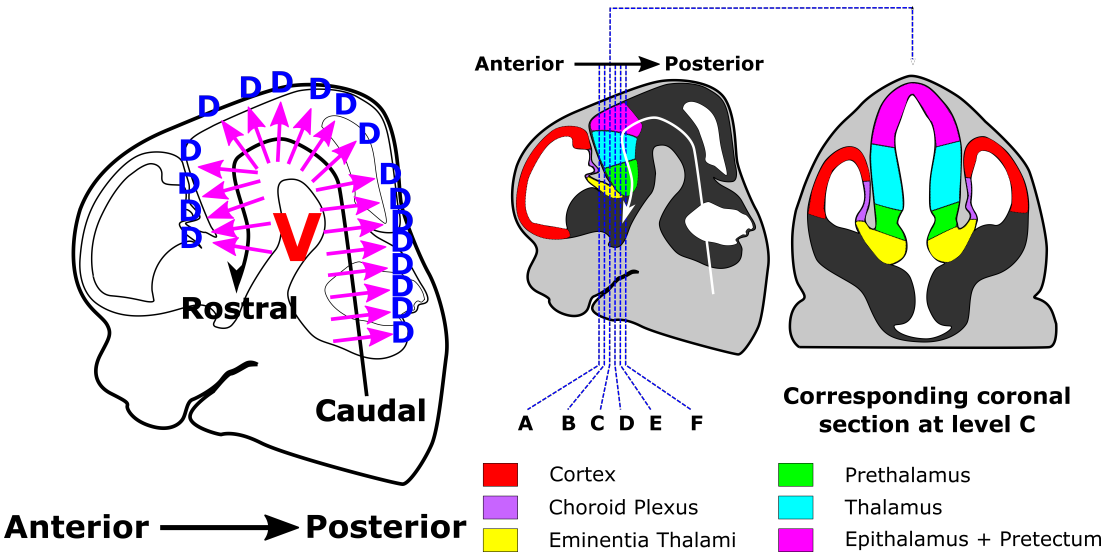


Figure 3.3: ***E11.5 mouse brain sagittal and coronal view schematic.*** *The schematic on the left shows the bending rostral-caudal axis (black curve with arrow head) and the change of dorsal-ventral axis at different points along the rostral-caudal axis (magenta arrows). The schematic in the middle demarcates the subdivisions of the diencephalon, the prethalamus (in green), the thalamus (in cyan) and the epithalamus and pretectum (in magenta) and other structures such as the eminentia thalami (in yellow), the choroid plexus of the third ventricle (in purple) and the cortex (in red) are labelled as well. Dashed blue lines show the sectioning planes, from A to F, corresponding to the images shown in the following staining results. The schematic on the right shows the coronal section corresponding to the sectioning plane C showing in the sagittal schematic.* ***D****, dorsal;* ***V****, ventral.*

anatomical structures in the diencephalon are colour coded and shown in the sagittal schematic (Figure 3.3 middle). The sectioning planes corresponding to the subsequent staining images (Figure 3.4) are indicated with dashed blue lines. In the schematic, the coronal section (Figure 3.3 right) corresponds to the sectioning plane C. The coronal schematic shows that the choroid plexus is lateral to the eminentia thalami, the eminentia thalami is ventral to the prethalamus, the thalamus is dorsal to the prethalamus, the epithalamus is dorsal to the thalamus, and the pretectum is not shown because it is positioned further posterior.

In the E11.5 diencephalon, *Zic4* transcripts are detected in the epithalamus (Figure 3.4 A1 - F1), the thalamus (Figure 3.4 A1 - C1), the prethalamus (Figure 3.4 C1 - F1) and the eminenitia thalami (Figure 3.4 A1 - C1). It also expresses in the choroid plexus of the lateral ventricle (Figure 3.4 A1 - C1), which flanks the eminentia thalami laterally.

In the thalamus, the *Zic4* transcripts are mainly detected at the anterior to middle planes in

a high-anterior low-posterior gradient (Figure 3.4 A1 - C1), and at cellular level these transcripts are observed in most of the thalamic cells in the anterior planes (Figure 3.5 G and G2).

In the prethalamus, the *Zic4* transcripts are distributed evenly traversing the diencephalic wall in the middle plane (Figure 3.4 C1) while noticeably more transcripts are found in the more lateral regions compared to the ventricular area when moving further posterior (Figure 3.4 D1 - F1). The higher power images show that in the posterior planes, the *Zic4* transcripts are highly expressed in the region close to the pial surface of the diencephalic wall (Figure 3.5 I and I1), and significantly lower levels of *Zic4* transcripts are observed in the corresponding ventricular region (Figure 3.5 I and I2).

High levels of *Zic4* expression at cellular levels can also be seen in the choroid plexus (Figure 3.5 G and G1) and the eminentia thalami (Figure 3.5 H and H1).

GFP shows a similar expression pattern to the *Zic4* transcripts and is detected in the epithalamus (Figure 3.4 A2 - F2), the thalamus (Figure 3.4 A2 - C2), the prethalamus (Figure 3.4 C2 - F2), the eminenitia thalami (Figure 3.4 A2 - C2) and the choroid plexus (Figure 3.4 A2 - C2). The GFP expressing cells are mainly seen in the prethalamus (Figure 3.5 H and H2), the eminentia thalami (Figure 3.5 H and H1) and the anterior part of the thalamus (Figure 3.5 G and G2). In the posterior planes, GFP positive cells are mainly seen in the prethalamus (Figure 3.5 I, I1 and I2).

The GFP reporter is quite often used to indicate *Cre* activity, and in this case it does not perfectly correspond to the expression of the endogenous *Zic4* transcripts as quite a few cells that express high levels of *Zic4* transcripts appear to be GFP negative (Figure 3.5 G1, H1 and I1). One possible explaination is that the GFP reporters take time to synthesize after the activation of the *Cre*.

The main findings at E11.5 are summarised in the Table 3.1.

	Zic4 **transcripts**		**GFP**
E11.5	**Structure**	Expression Note	Expression Note
	Epithalamus	Yes	Yes
	Thalamus	Anterior to middle planes, high-anterior low-posterior	Yes, anterior part
	Prethalamus	Middle to posterior planes, high-lateral low-medial	Yes
	Eminentia thalami	High	Yes
	Choroid plexus	High	Yes

Table 3.1: ***Summary of* Zic4 *transcripts and GFP expression pattern in the E11.5 diencephalon.***

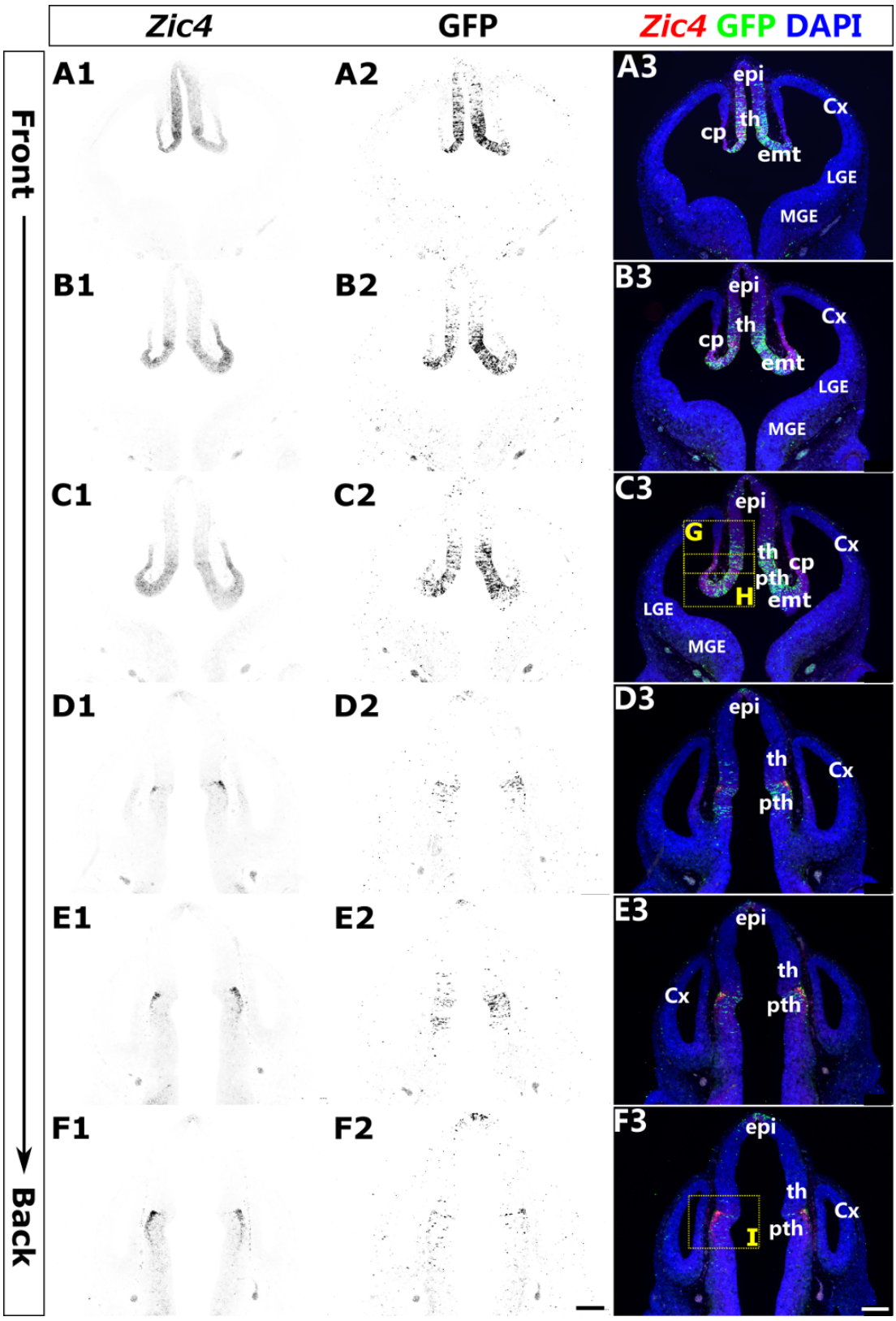


Figure 3.4: ***GFP immunohistochemistry (green) and Zic4 fluorescent in situ hybridisation (red) with DAPI counterstaining (blue) on embryonic day (E) 11.5 Zic4Cre$^{+/-}$;RCE$^{+/-}$ mouse brain coronal sections.*** *Scale bar: 250 μm. Cx, cortex; cp, choroid plexus; MGE, medial ganglionic eminence; LGE, lateral ganglionic eminence; th, thalamus; pth, prethalamus; emt, eminentia thalami; epi, epithalamus.*

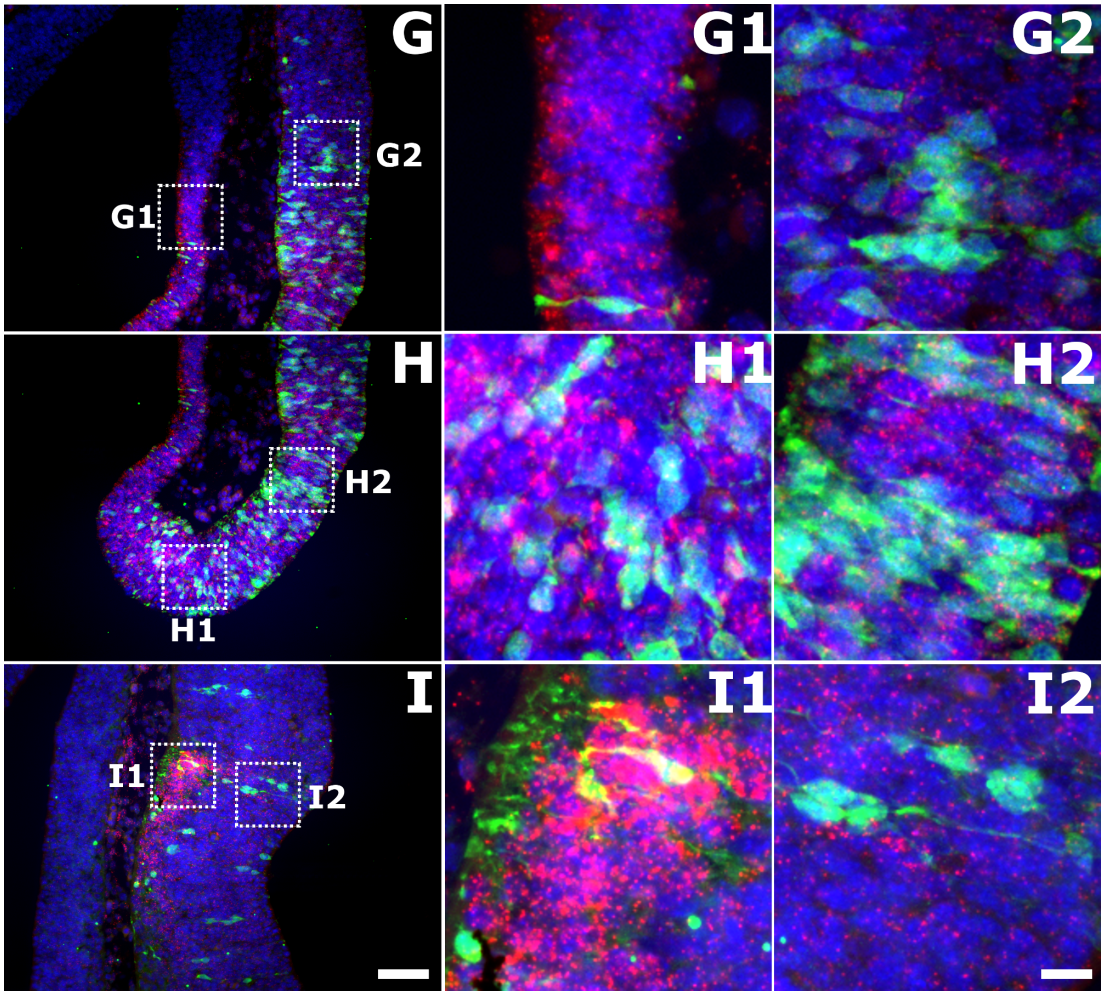


Figure 3.5: ***High power images for GFP immunohistochemistry (green) and Zic4 fluorescent in situ hybridisation (red) on E11.5 Zic4Cre$^{+/-}$;RCE$^{+/-}$mouse brain coronal sections.*** *(G, H and I) The high power images for the regions outlined by yellow dotted boxes in Figure 3.4. (G1, G2, H1, H2, I1 and I2) High power images of the regions outlined by the white dotted boxes in G, H and I. Scale bar: 75 μm and 15 μm.*

3.3.2 Expression of *Zic4* transcripts and GFP in the E12.5 *Zic4Cre*$^{+/-}$;*RCE*$^{+/-}$ mouse diencephalon

This experiment aims to study the expression of *Zic4* transcripts and GFP in the *Zic4Cre*$^{+/-}$;*RCE*$^{+/-}$ mouse diencephalon at E12.5 is to find out whether the endogenous *Zic4* has changed in terms of the expression pattern and levels compared to E11.5, and what the GFP reporter expression pattern looks like. A schematic of E12.5 mouse brain from both sagittal and coronal views is given here to assist readers to understand the anatomical structure of the E12.5 diencephalon.

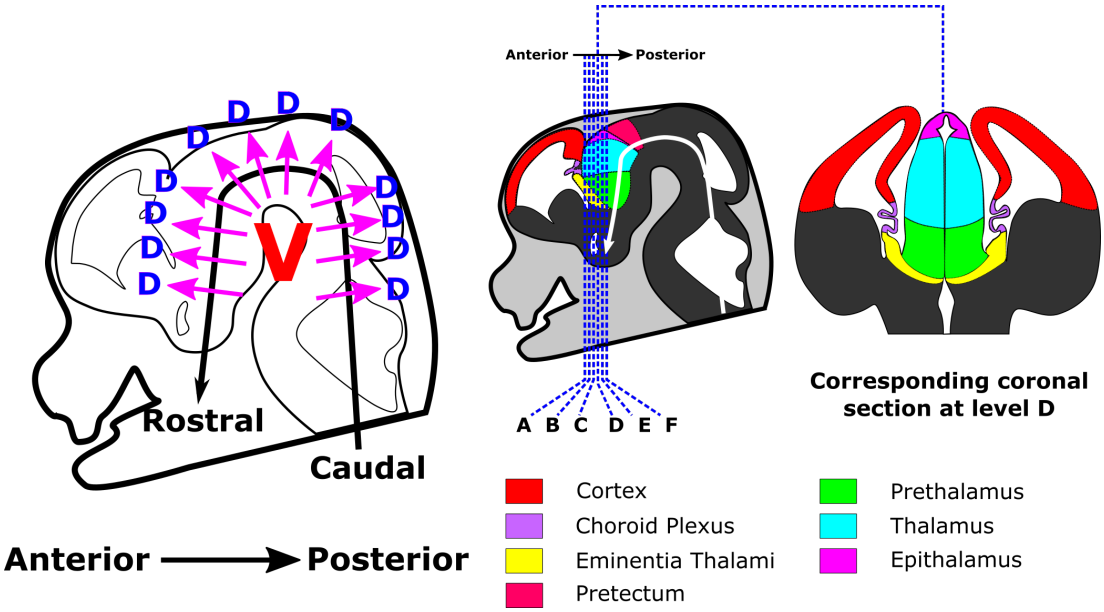


Figure 3.6: ***E12.5 mouse brain sagittal and coronal view schematic.***

In the E12.5 schematic (Figure 3.6), the coronal section corresponds to the sectioning plane D shown on the sagittal schemetic.

Similar to E11.5, *Zic4* transcripts are detected in the epithalamus (Figure 3.7 A1 - F1), the thalamus (Figure 3.7 A1 - F1), the prethalamus (Figure 3.7 A1 - F1), the eminenitia thalami (Figure 3.7 A1 - C1) and the choroid plexus (Figure 3.7 A1 - D1) in the E12.5 diencephalon.

In the thalamus, the high-anterior low-posterior *Zic4* expression gradient is maintained (Figure 3.7 A1 - F1). Within each section, the regions close to the lateral surface of the diencephalic wall show distinguishably higher levels of *Zic4* expression, especially in the anterior to middle planes (Figure 3.7 B1 - D1), which was not seen at E11.5.

The prethalamus shows higher levels of *Zic4* expression than the thalamus especially in

the middle to posterior planes (Figure 3.7 C1 - F1). In the prethalamus, the ventricular regions show relatively low levels of *Zic4* expression compared to the laterally adjacent regions (Figure 3.7 C1 - E1), similar to E11.5. *Zic4* transcripts are also highly expressed in the epithalamus, showing a high-anterior low-posterior gradient (Figure 3.7 A1 - F1).

At cellular level, various levels of *Zic4* are detected in different subregions within the same structure. In the eminentia thalami, the general level of *Zic4* expression is high (Figure 3.8 G, I and K) and the regions adjacent to the prethalamus (Figure 3.8 G3) and the chorid plexus (Figure 3.8 G1, I3 and K3) show higher expression levels compared to the regions in between those two (Figure 3.8 G2).

In the thalamus, general expession levels of *Zic4* transcripts are higher at the anterior (Figure 3.8 H, H1 and H2) and lower at the posterior (Figure 3.8 J, J1 and J2). Within each sectioning plane, the regions close to the ventricle show recognisably lower levels of *Zic4* expression (Figure 3.8 H1 and J1) compared to the regions positioned close to the pial surface (Figure 3.8 H2 and J2).

Compared to the thalamus, the ventricular regions in the prethalamus have a similar, maybe slightly higher levels of *Zic4* expression (Figure 3.8 H1, J1 in thalamus and I1, K1 in prethalamus) whereas in the lateral regions, the prethalamus shows a significantly higher expression of *Zic4* (Figure 3.8 H2, J2 in thalamus and I2, K2 in prethalamus). Moving toward the posterior (Figure 3.8 L), a region in the prethalamus (Figure 3.8 L2) shows a very high level of *Zic4* expression, as high as the lateral most region (Figure 3.8 L1), and conspicuously higher than the ventricular region at the similar ventrodorsal level (Figure 3.8 L1).

The expression level of *Zic4* in the choroid plexus is lower at the anterior (Figure 3.8 H3) and higher at the posterior (Figure 3.8 J3).

GFP shows expression patterns similar to the *Zic4* transcripts and is detected in the epithalamus (Figure 3.7 A2 - F2), the thalamus (Figure 3.7 A2 - C2), the prethalamus (Figure 3.7 C2 - F2), the eminenitia thalami (Figure 3.7 A2 - C2) and the choroid plexus (Figure 3.7 A2 - C2). However, the distribution of the GFP positive cells within each diencephalic subdivision does not match the more detailed *Zic4* expression variance within the same structure. The high-lateral low-medial gradient of *Zic4* expression (Figure 3.7 C1 - D1) is not reflected by more GFP+ve cells occupying the lateral region (Figure 3.7 C2 - D2). Although the distribution of GFP+ve cells does not reflect the change of the *Zic4* expression level, the fluorescent intensity of the GFP is higher in the cells in the lateral regions (expressing high level of *Zic4*) (Figure 3.8 H2, I2, J2, K2, L1)

and lower in the cells in the ventricular regions (expressing low level of *Zic4*) (Figure 3.8 H1, I1, J1, K1, L3) in both the thalamus (Figure 3.8 H1, H2, J1, J2) and the prethalamus (Figure 3.8 I1, I2, K1, K2, L1, L2, L3). The difference in GFP expression levels between the lateral and the ventricular regions is potentially due to the different durations of GFP accumulation in the cells born at different times. The difference in *Zic4* expression level between the lateral regions and the ventricular regions could be explained by a spike of *Zic4* transcription in the cells that start to differentiate. There is no clear correlation between the expression level of *Zic4* transcripts and the expression level of GFP within individual cells as expected.

The main findings at E12.5 are summarised in the Table 3.2.

	***Zic4* transcripts**		**GFP**
E12.5	**Structure**	Expression Note	Expression Note
	Epithalamus	high	Yes
	Thalamus	High-anterior low-posterior, high-lateral low-medial	Yes
	Prethalamus	high-lateral low-medial	Yes
	Eminentia thalami	higher in the region adjacent to the prethalamus and the choroid plexus	Yes
	Choroid plexus	low-anterior high-posterior	Yes

Table 3.2: ***Summary of* Zic4 *transcripts and GFP expression pattern in the E12.5 diencephalon.*** *Magenta coloured texts were used to show the change at E12.5 compared to E11.5.*

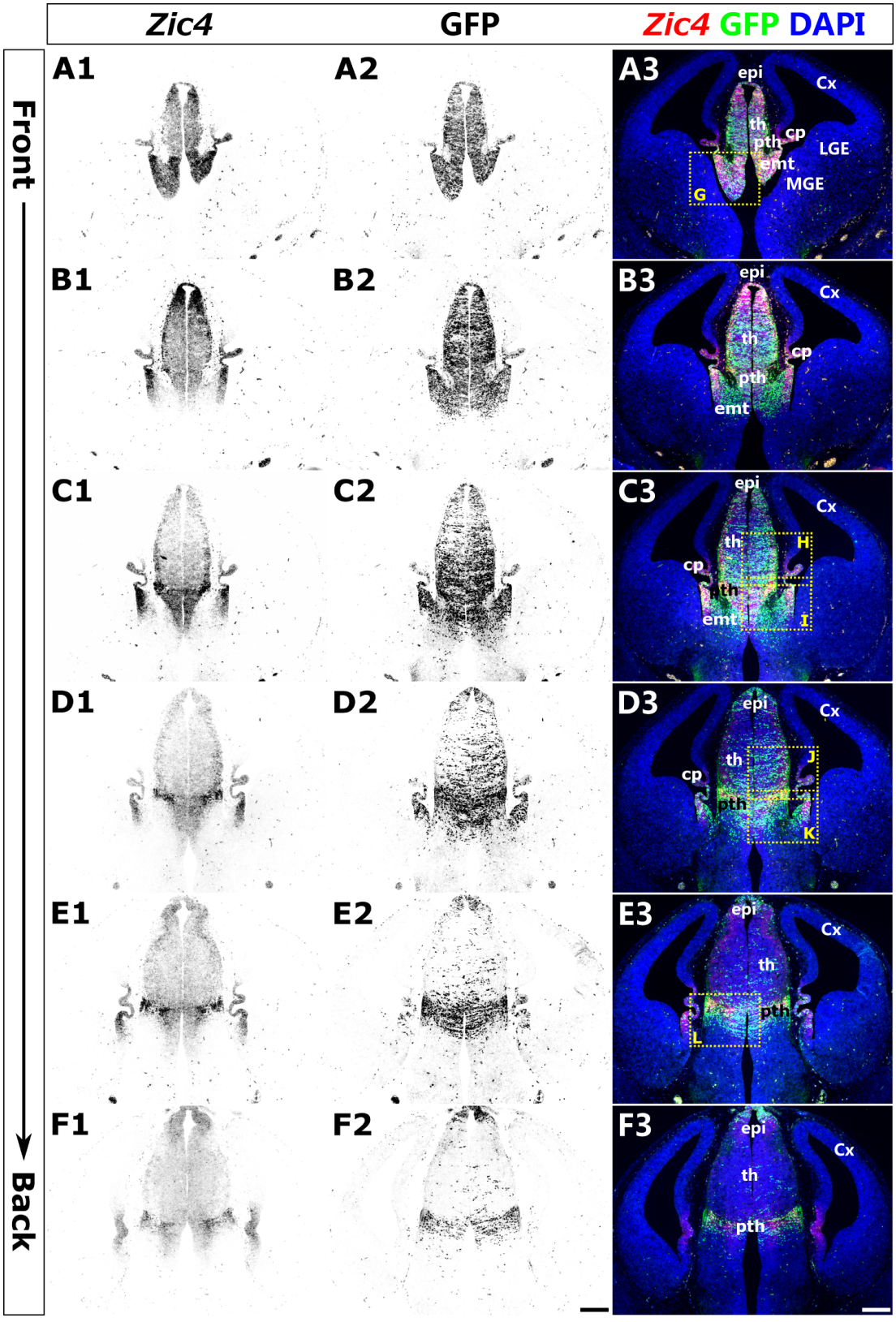


Figure 3.7: ***GFP immunohistochemistry (green) and Zic4 fluorescent in situ hybridisation (red) with DAPI counterstaining (blue) on embryonic day (E) 12.5 Zic4Cre$^{+/-}$;RCE$^{+/-}$mouse brain coronal sections.*** *Scale bar: 250 μm.*

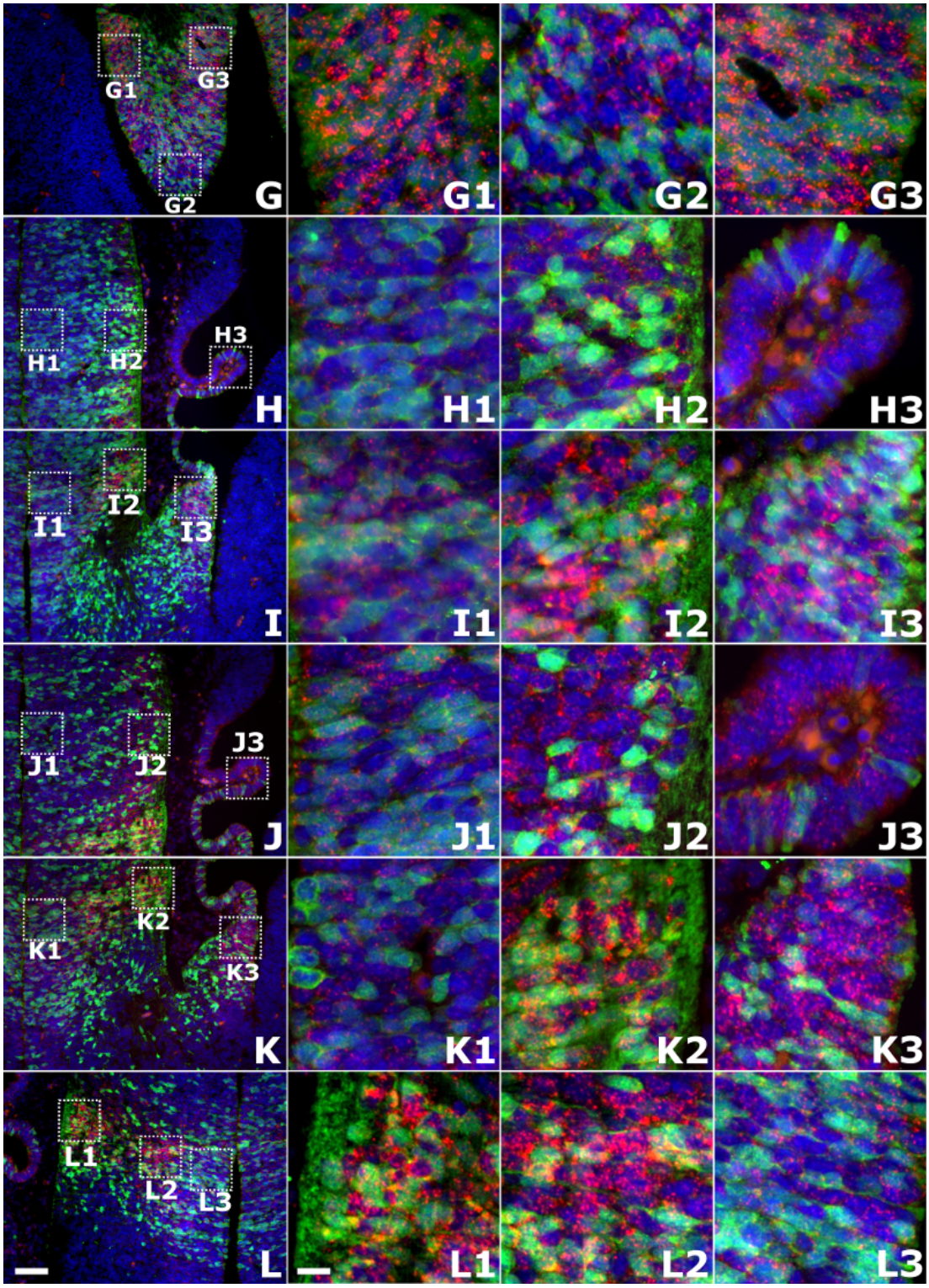


Figure 3.8: ***High power images for GFP immunohistochemistry and Zic4 fluorescent in situ hybridisation on E12.5 Zic4Cre$^{+/-}$;RCE$^{+/-}$ mouse brain coronal sections.*** *(G, H, I, J, K and L) The high power images for the regions outlined by yellow dotted boxes in Figure 3.7. (G1-G3, H1-H3, I1-I3, J1-J3, K1-K3 and L1-L3) High power images of the regions outlined by the white dotted boxes in G, H, I, J, K and L. Scale bar: 75 μm and 15 μm.*

3.3.3 Expression of *Zic4* transcripts and GFP in the E13.5 *Zic4Cre*$^{+/-}$;*RCE*$^{+/-}$ mouse diencephalon

This experiment aims to study the expression of *Zic4* transcripts and GFP in the *Zic4Cre*$^{+/-}$;*RCE*$^{+/-}$ mouse diencephalon at E13.5 is to find out whether the endogenous *Zic4* has changed in terms of the expression pattern and levels compared to E11.5 and E12.5, and what the GFP reporter expression pattern looks like at this stage. A schematic of E13.5 mouse brain from both sagittal and coronal views is given here to assist readers to understand the anatomical structure of the E13.5 diencephalon.

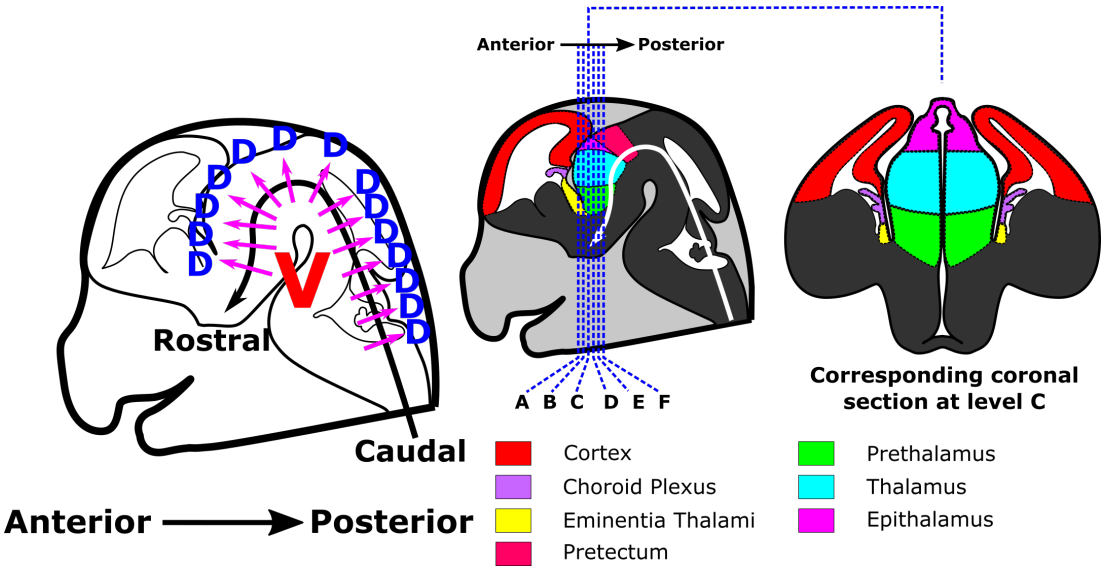


Figure 3.9: ***E13.5 mouse brain sagittal and coronal view schematic.***

In the E13.5 schematic (Figure 3.9), the coronal section is corresponding to the sectioning plane C shown on the sagittal schematic.

In the E13.5 diencephalon, high levels of *Zic4* expression are maintained in the epithalamus especially in the anterior to middle planes (Figure 3.10 A1 - D1). The presence of *Zic4* transcripts can still be seen in the choroid plexus (Figure 3.11 G3, H3) and the ventricular zone of the eminentia thalami (Figure 3.11 G3). However, as the diencephalic cells proliferate and start to differentiate, new *Zic4* expression patterns gradually emerge.

In the thalamus, the high-anterior low-posterior *Zic4* expression gradient is beginning to wane and a more compartmentalised pattern becomes evident. In the anterior most plane (Figure 3.10 A1), the staining for the *Zic4* transcripts demarcates two subregions within the

thalamus, a low-expression region close to the third ventricle (Figure 3.11 G, G1) and an adjacent high-expression region close to the pial surface of the thalamic wall (Figure 3.11 G, G2). In the plane B (Figure 3.10 B1), these two subregions are still visible with a noticeable decrease of *Zic4* in the lateral region compared to plane A (Figure 3.10 A1). In the plane C, three thalamic subregions are appreciated from the *Zic4* staining (Figure 3.10 C1). According to their positioning between the ventricular surface and the pial surface, they are named as the ventricular region (Figure 3.11 H, H1), the subventricular region and the mantle region (Figure 3.11 H, H2), from medial to lateral. The subventricular region shows the highest *Zic4* expression among the three, the ventricular region comes the second and the mantle layer shows the lowest. In the plane D, it seems that the mantle region, shown in the plane C, grows larger (Figure 3.10 D1), which is presumably the forming ventral posterior complex. In the posterior most plane (Figure 3.10 E1 and F1), *Zic4* expression is only maintained in the ventricular area whereas the rest of the thalamus does not express or expresses very little *Zic4*.

In the prethalamus, high levels of *Zic4* transcripts are mainly seen in the region imediately adjacent to the pial surface of the diencephalic wall and a subventricular region at similar ventrodorsal levels within the same plane (Figure 3.10 C1 - E1 and Figure 3.11 H, H4, H5, I, I1, I2). In the posterior planes, the cells with high levels of *Zic4* seem to form a continuous stream of cells populating the regions connecting the ventricular surface and presumably the forming vLGN, which indicates that *Zic4* lineage cells in the prethalamus contribute to the future vLGN.

The expression of GFP corresponds with the general pattern of the *Zic4* expression. In the anterior most plane (Figure 3.11 G), it seems the cells in the ventricular region of the thalamus express a lower level of GFP (Figure 3.11 G1) comparing to their counterparts in the mantle region (Figure 3.11 G2), which could be explained by dilution effects during cell division and/or a longer period of GFP accumulation in the postmitotic neurons compared to the progenitors. In the middle plane (Figure 3.11 H3), the GFP positive cells are mainly seen in the ventricular region of the thalamus, which coincide with the *Zic4* expression. Noticeably fewer GFP+ve cells are seen in the more lateral region (Figure 3.11 H2) which correspond with the emerging *Zic4* negative cell group, presumably the forming ventral posterior complex (VP). There is also a transverse stripe of cells with high level *Zic4* expression observed in the prethalamus (Figure 3.11 H4, I1).

The main findings at E13.5 are summarised in the Table 3.3.

	Zic4 **transcripts**		**GFP**
E13.5	**Structure**	Expression Note	Expression Note
	Thalamus	compartmentalised pattern	low in ventricular cells and high in mantle cells
	Prethalamus	high-lateral low-medial, high in transverse migratory cell stream	high in transverse cell strip in the subventricular zone

Table 3.3: ***Summary of* Zic4 *transcripts and GFP expression pattern in the E13.5 diencephalon.*** *Magenta coloured texts were used to show the change at E13.5 compared to E12.5.*

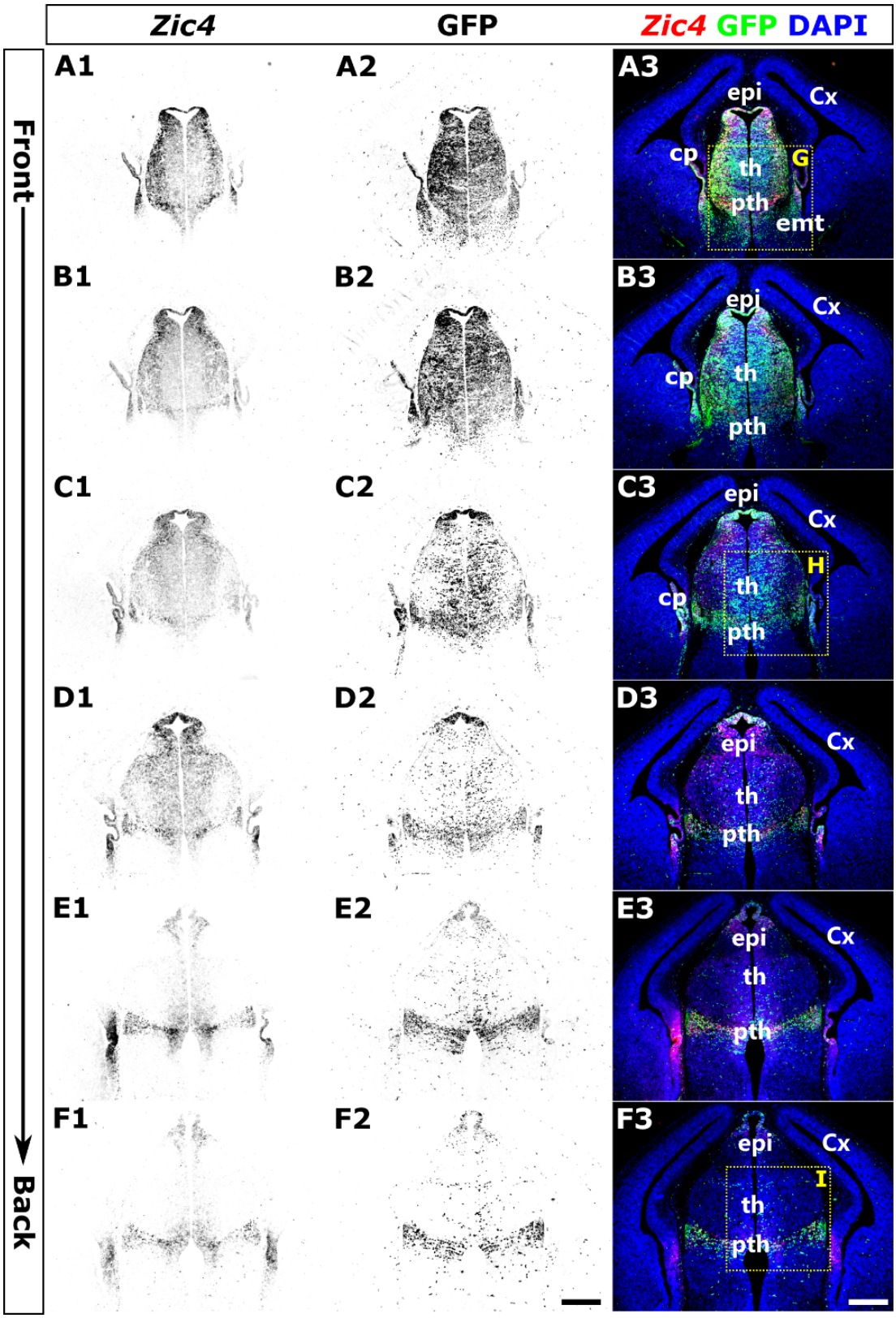


Figure 3.10: ***GFP immunohistochemistry (green) and Zic4 fluorescent in situ hybridisation (red) with DAPI counterstaining (blue) on embryonic day (E) 13.5 Zic4Cre$^{+/-}$;RCE$^{+/-}$mouse brain coronal sections.*** *Scale bar: 250 μm.*

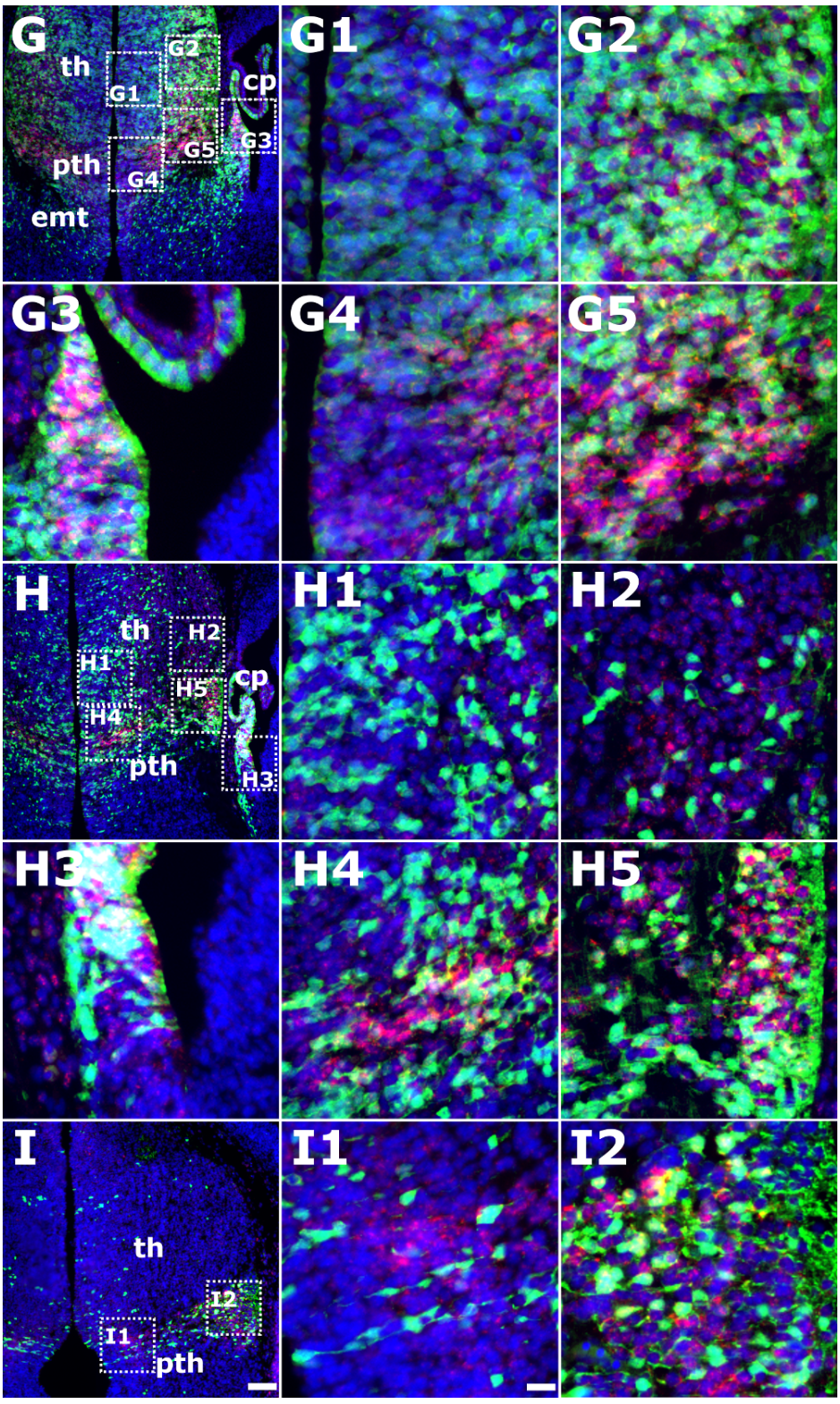


Figure 3.11: ***High power images for GFP immunohistochemistry and Zic4 fluorescent in situ hybridisation on E13.5 Zic4Cre$^{+/-}$;RCE$^{+/-}$ mouse brain coronal sections.*** *(G, H and I) The high power images for the regions outlined by yellow dotted boxes in Figure 3.10. (G1-G5, H1-H5, I1-I2) High power images of the regions outlined by the white dotted boxes in G, H and I. Scale bar: 75 μm and 15 μm.*

3.3.4 Expression of *Zic4* transcripts and GFP in the E14.5 *Zic4Cre*$^{+/-}$;*RCE*$^{+/-}$ mouse diencephalon

This experiment aims to study the expression of *Zic4* transcripts and GFP in the *Zic4Cre*$^{+/-}$;*RCE*$^{+/-}$ mouse diencephalon at E14.5 is to find out whether the endogenous *Zic4* has changed in terms of the expression pattern and levels compared to E11.5 to E13.5, and what the GFP reporter expression pattern looks like at this stage. A schematic of E14.5 mouse brain from both sagittal and coronal views is given here to assist readers to understand the anatomical structure of the E14.5 diencephalon.

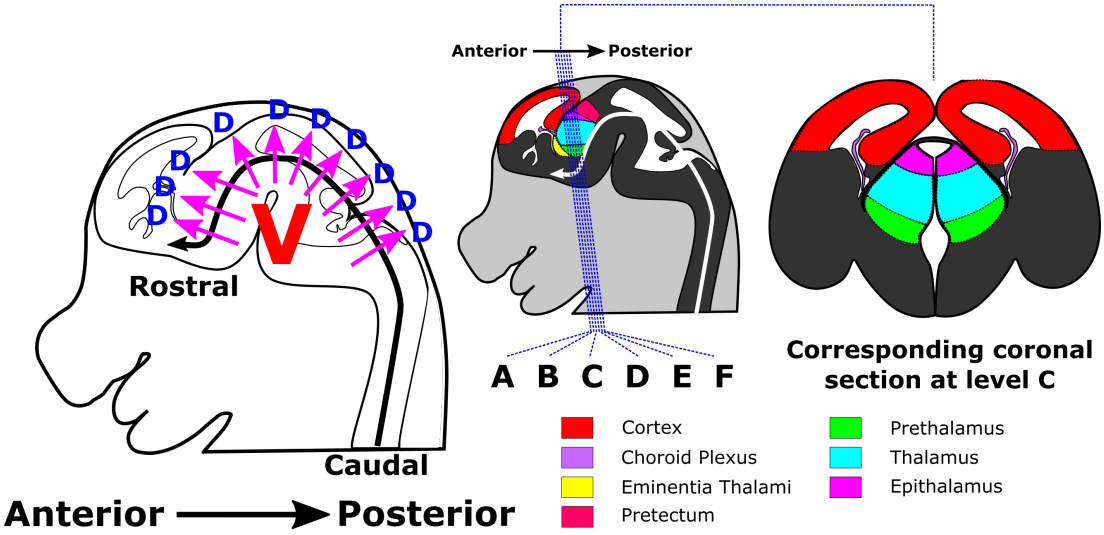


Figure 3.12: ***E14.5 mouse brain sagittal and coronal view schematic.*** *At this stage, a forming vLGN, colour coded blue, can be appreciated within the prethalamus.*

In the E14.5 schematic (Figure 3.12), a forming vLGN can be observed at lateral most region in the prethalamus and it is labelled in blue in the schematic.

As neurogenesis and parcellation continue in the diencephalon, the volumes of the thalamus and prethalamus are significantly larger at E14.5 compared to previous stages. Several new *Zic4* expression features (Figure 3.10) are appreciated: 1. the general expression level of *Zic4* is significantly higher compared to E13.5 (Figure 3.10) ; 2. the *Zic4* expression pattern demarcates a more compartmentalised diencephalon with low *Zic4* regions surrounded by high *Zic4* expressing cells; 3. the emergence of the early vLGN with distinctly high levels of *Zic4* at the lateral surface of the prethalamus (Figure 3.13 A1 - F1, Figure 3.14 G1, I1 and J1, magenta arrow).

It seems that the diencephalic cells with high levels of *Zic4* divide the diecephalon into several subdivisions, the epithalamus, thalamus, and prethalamus, and this pattern is conspicuous in the middle to posterior planes (Figure 3.13 C1 - E1). The low *Zic4* main body of the thalamus seems to be surrounded, dorsally by high *Zic4* expressing cells at the boundary between the epithalamus and the thalamaus (Figure 3.14 G1 and I1, cyan star), medially by the high *Zic4* expressing ventricular cells (Figure 3.14 G1, red arrow), ventrally by the prethalamic cells with high *Zic4*, and laterally by the thalamic cells with relatively high *Zic4* expression (Figure 3.14 H1 and J1, yellow star).

In the prethalamus, the emergence of the vLGN is revealed by the high level of *Zic4* expression (Figure 3.13 B1 - F1). A very high level of *Zic4* expression is detected in a group of cells in the presumably subventricular region (Figure 3.14 H1 and J1, red star) and they are likely to be the same high *Zic4* expressing cells I saw at E13.5 (Figure 3.10 E1). The staining pattern displayed by this cohort of cells seems elongated along the thalamus-prethalamus boundary comparing to E13.5, which indicates that this cohort of cells starts to migrate laterally toward the forming vLGN at E14.5.

The GFP expression shows a similar pattern to the *Zic4* expression but differences can be found in some regions especially in the thalamus. As mentioned above, the expression of *Zic4* in the thalamus at this stage is mainly in the ventricular zone (Figure 3.14 H1 and J1, yellow star) but instead of homogeneously expressing in all *Zic4* positive cells, the GFP is only present in a subpopulation of these cells in a mosaic manner, which suggests heterogenous characteristics of these progenitor cells. It is also noticeable that in the main body of the thalamus, presumably the forming ventral posterior complex, there are quite a few GFP positive cells with little *Zic4* presence (Figure 3.14 G1 and G2, H1 and H2, I1 and I2, J1 and J2, dashed white circle), suggesting that the *Zic4* gene has been turned down in these cells. The selective persistence of *Zic4* expression in some forming thalamic nuclei but not the others suggests that *Zic4* serves a crucial function in the formation of specific diencephalic nuclei.

The main findings at E14.5 are summarised in the Table 3.4.

	Zic4 **transcripts**		**GFP**
E14.5	**Structure**	Expression Note	Expression Note
	Thalamus	compartmentalised, low in the main body, high in the surrounding areas	expressed in a fraction of ventricular cells
	Prethalamus	high in transverse migratory cell stream, high in the forming vLGN	high in transverse cell strip in the subventricular zone, high in the forming vLGN

Table 3.4: ***Summary of* Zic4 *transcripts and GFP expression pattern in the E14.5 diencephalon.*** *Magenta coloured texts were used to show the change at E14.5 compared to E13.5.*

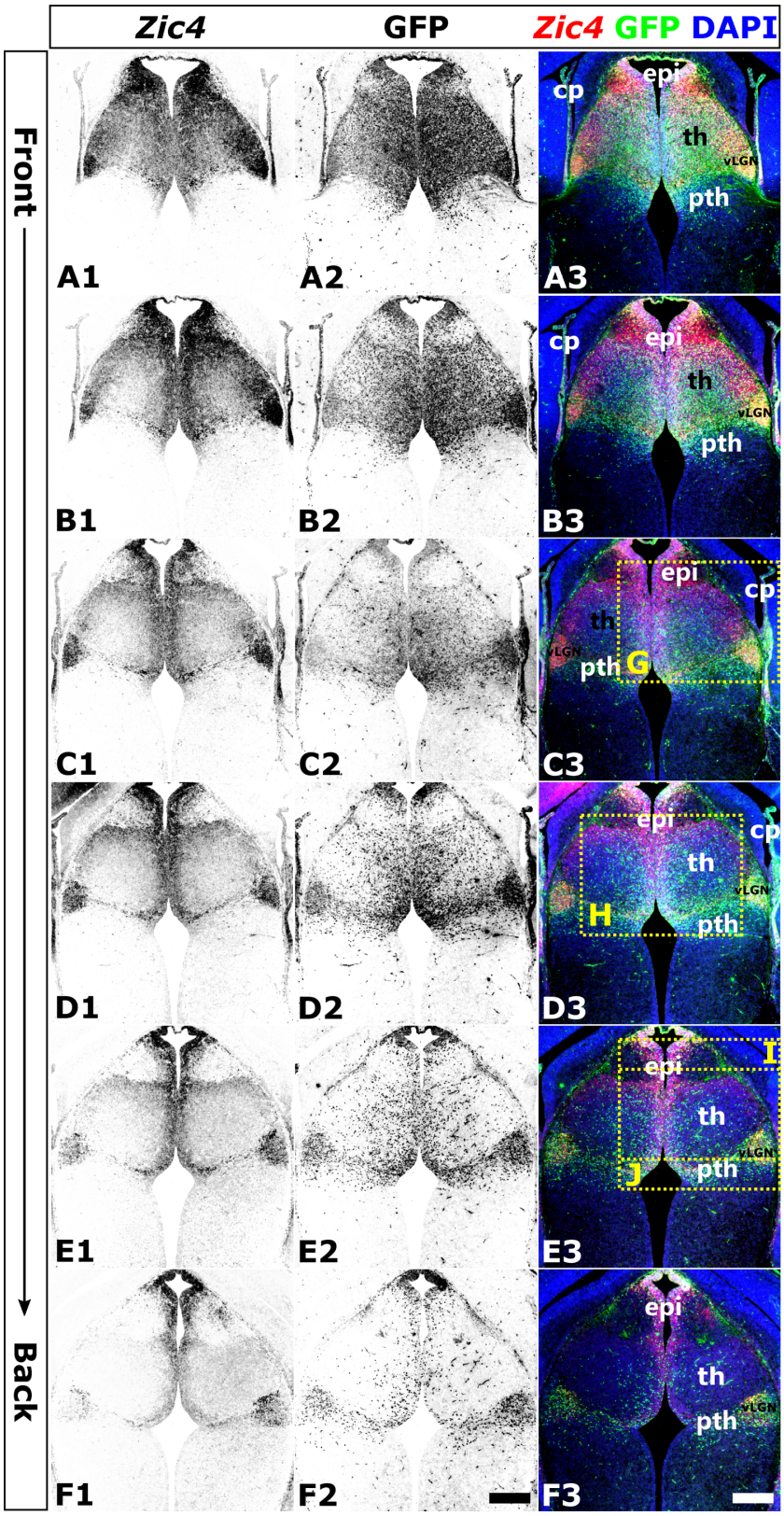


Figure 3.13: ***GFP immunohistochemistry (green) and Zic4 fluorescent in situ hybridisation (red) with DAPI counterstaining (blue) on embryonic day (E) 14.5 Zic4Cre$^{+/-}$;RCE$^{+/-}$mouse brain coronal sections.*** *Scale bar: 250 μm.*

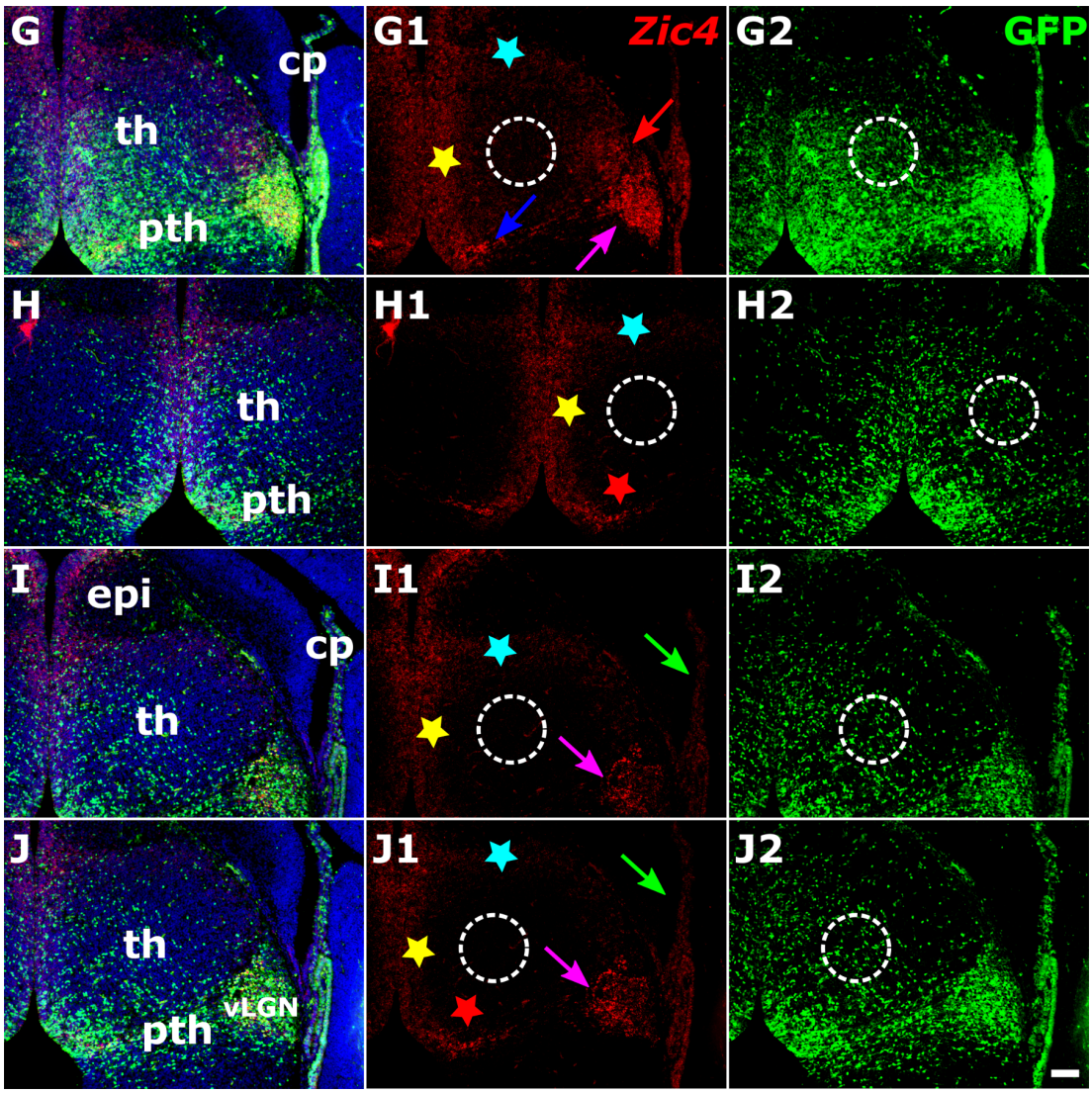


Figure 3.14: ***High power images for GFP immunohistochemistry and Zic4 fluorescent in situ hybridisation on E14.5 Zic4Cre$^{+/-}$;RCE$^{+/-}$ mouse brain coronal sections.*** *(G, H, I and J) The high power images for the regions outlined by yellow dotted boxes in Figure 3.13. (G1-G2, H1-H2, I1-I2 and J1-J2) High power images of the regions outlined by the white dotted boxes in G, H, I and J. Scale bar: 75 μm.*

3.3.5 Expression of *Zic4* transcripts and GFP in the E15.5 *Zic4Cre*$^{+/-}$;*RCE*$^{+/-}$ mouse diencephalon

This experiment aims to study the expression of *Zic4* transcripts and GFP in the *Zic4Cre*$^{+/-}$;*RCE*$^{+/-}$ mouse diencephalon at E15.5 is to find out whether the endogenous *Zic4* has changed in terms of the expression pattern and levels compared to E11.5 to E14.5, and what the GFP reporter expression pattern looks like at this stage. A schematic of E15.5 mouse brain from both sagittal and coronal views is given here to assist readers to understand the anatomical structure of the E15.5 diencephalon.

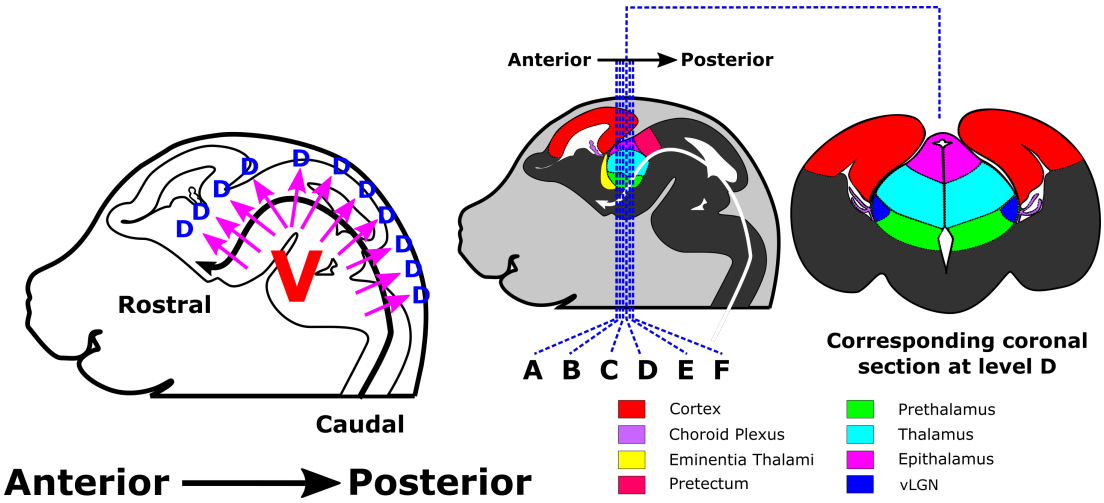


Figure 3.15: ***E15.5 mouse brain sagittal and coronal view schematic.***

In the E15.5 schematic (Figure 3.15), the coronal section on the right corresponds to the sectioning plane D.

Despite the fact that the morpholoy of the diencephalon does not change greatly from E14.5 to E15.5, there are quite a few new features in terms of the expression pattern of the *Zic4* transcripts that are observed. The parcellation demarcated by high *Zic4* expressing cells at E14.5 (Figure 3.13 C1, D1) is disappearing, which could be due to the turning down of *Zic4* transcription or a dilution effect caused by further cell movement and mixing. The ventricular region with high *Zic4* expression in the thalamus can only be recognised in the anterior planes (Figure 3.16 A1 - C1), which is much narrower than what it was at E14.5 (Figure 3.13 B1 - D1). The vLGN grows larger and maintains its high level of *Zic4* expression. A region that immediately dorsal to the vLGN with high level of *Zic4* is forming (Figure 3.16 C1 - F1, Figure 3.17 G1 and G2 dotted magenta circle) and it is potentially the developing dLGN. At the posterior most plane (Figure 3.16 F1), a group of high *Zic4* expressing cells form a wedge

like pattern at the ventricular zone of the prethalamus (Figure 3.17 G2 white star) and within the vLGN, cells that occupying the medial most postions appear to have high *Zic4* expression (Figure 3.17 G2, white arrow).

The expression of GFP generally corresponds to the expression pattern of the *Zic4* transcripts. In the main body of the thalamus (Figure 3.16 C2 - E2), quite a lot of cells are GFP positive but *Zic4* negative (Figure 3.16 C1 - E1), suggesting that these cells have turned down *zic4* expression after the activation of the GFP reporter. In the prethalamus, the forming vLGN is mainly occupied by GFP positive cells (Figure 3.16 B2 - F2). The strip of GFP positive cells extending from the ventricular surface to the forming vLGN (Figure 3.16 E2 and F2, Figure 3.17 G1 and G3) is potentially the forming zona incerta (ZI).

The main findings at E15.5 are summarised in the Table 3.5.

	***Zic4* transcripts**		**GFP**
E15.5	**Structure**	Expression Note	Expression Note
	Thalamus	high in the ventricular zone in the anterior planes and the forming dLGN	expressed in most of the cells
	Prethalamus	high in the forming vLGN	high in the forming ZI and vLGN

Table 3.5: ***Summary of* Zic4 *transcripts and GFP expression pattern in the E15.5 diencephalon.*** *Magenta coloured texts were used to show the change at E15.5 compared to E14.5.*

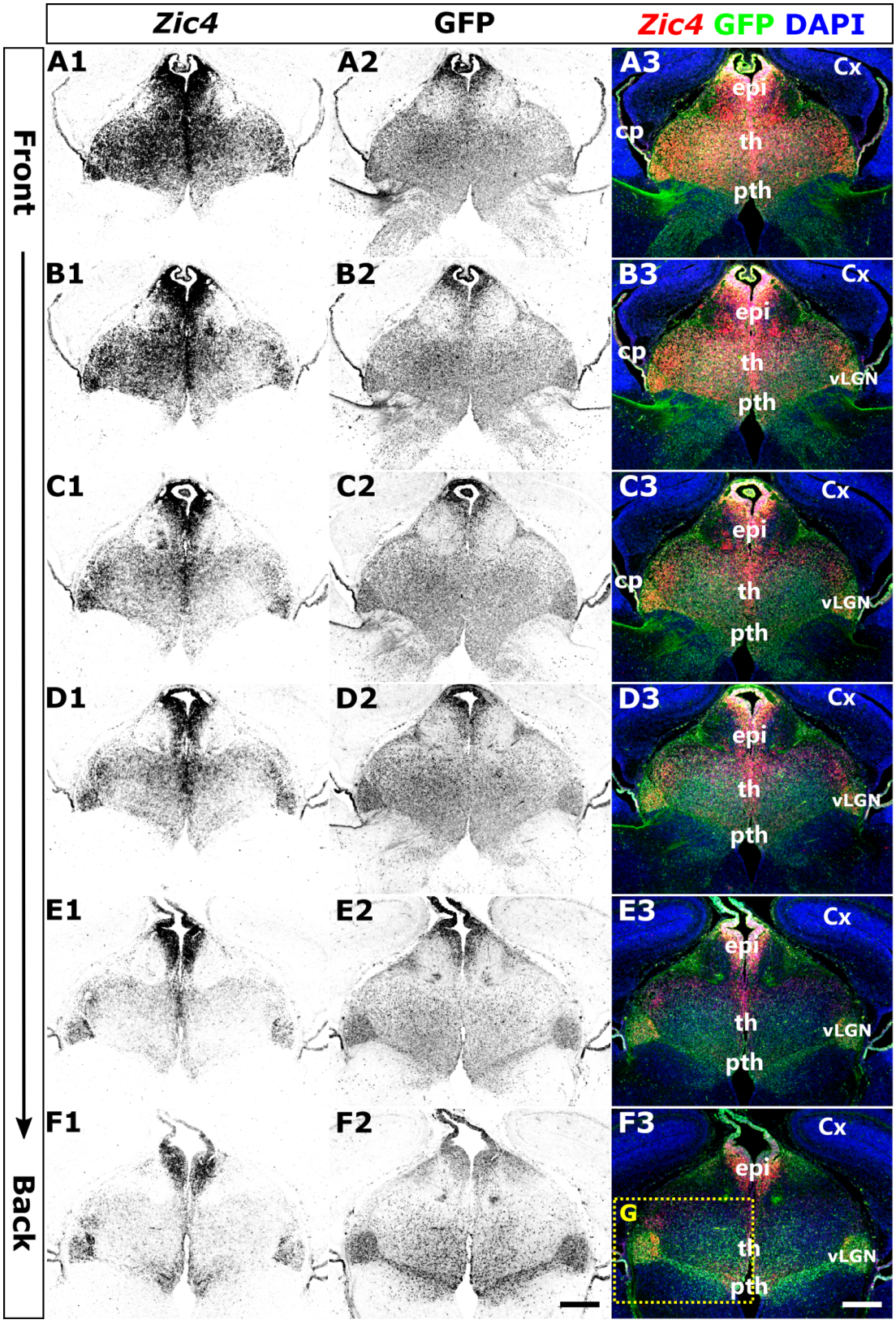


Figure 3.16: ***GFP immunohistochemistry (green) and Zic4 fluorescent in situ hybridisation (red) with DAPI counterstaining (blue) on embryonic day (E) 15.5 Zic4Cre$^{+/-}$;RCE$^{+/-}$mouse brain coronal sections.*** *Scale bar: 250 μm. Cx, cortex; vLGN, ventral lateral geniculate nucleus.*

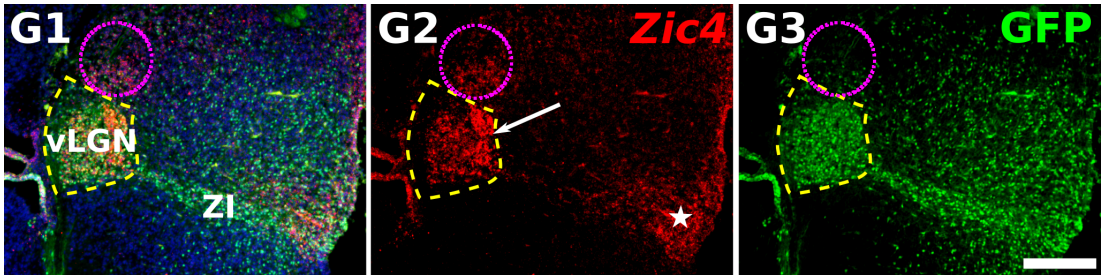


Figure 3.17: ***High power images for GFP immunohistochemistry and Zic4 fluorescent in situ hybridisation on E15.5 Zic4Cre$^{+/-}$;RCE$^{+/-}$ mouse brain coronal sections.*** *(G1, G2 and G3) The high power images for the regions outlined by yellow dotted box in Figure 3.16. The vLGN is outlined using dashed yellow line. The dotted magenta circle indicates the forming dLGN. Scale bar: 75 μm.*

3.3.6 Expression of *Zic4* transcripts and GFP in the E16.5 *Zic4Cre*$^{+/-}$;*RCE*$^{+/-}$ mouse diencephalon

This experiment aims to study the expression of *Zic4* transcripts and GFP in the *Zic4Cre*$^{+/-}$;*RCE*$^{+/-}$ mouse diencephalon at E16.5 is to find out whether the endogenous *Zic4* has changed in terms of the expression pattern and levels compared to E11.5 to E15.5, and what the GFP reporter expression pattern looks like at this stage. A schematic of E16.5 mouse brain from both sagittal and coronal views is given here to assist readers to understand the anatomical structure of the E16.5 diencephalon.

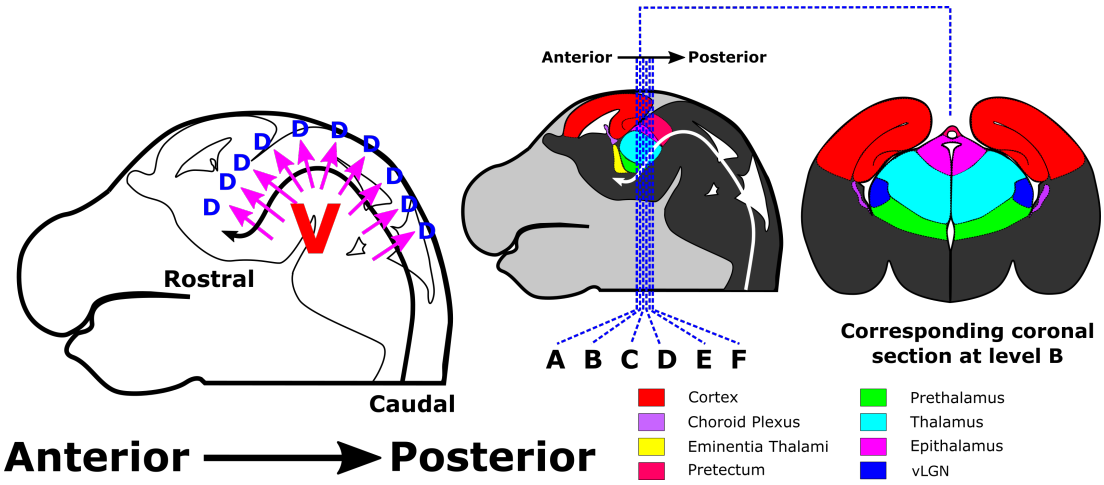


Figure 3.18: ***E16.5 mouse brain sagittal and coronal view schematic.***

The schematic used for E16.5 (Figure 3.18) is quite similar to the E15.5 one (Figure 3.18) but the sectioning planes are further posterior. The coronal section on the right corresponds to the sectioning level B in the sagittal schematic. The structure, dorsal to the epithalamus (presumably the forming habenular), is the pretectum.

At E16.5, *Zic4* transcripts are highly expressed in the more differentiated epithalamus and pretectal area (Figure 3.19 A1 - F1). In the thalamus, the expression of *Zic4* seems similar to what was seen at E15.5 (Figure 3.16) with a few noticeable changes. The high expression of *Zic4* transcripts in the thin ventricular zone at E15.5 (Figure 3.16 A1 - E1) is not visible any more at this stage (Figure 3.19 A1 - F1). In the prethalamus, the vLGN and ZI retain their high level expression of *Zic4* transcripts (Figure 3.19 A1 - F1). Within the vLGN, the presence of the *Zic4* transcripts shows a high medial and low lateral gradient whereas the GFP expression pattern in the corresponding regions does not show such a obvious gradient (Figure 3.20 G2 - H2 white arrow). It is possible that these GFP positive cells in the lateral area (Figure 3.20 H3)

are the earliest born vLGN neurons and they have turned down their expression of *Zic4*. This might also be the case with the cells in the forming ZI, which are GFP positive but expressing little or no *Zic4* transcripts.

The main findings at E16.5 are summarised in the Table 3.6.

	***Zic4* transcripts**		**GFP**
E16.5	**Structure**	Expression Note	Expression Note
	Thalamus	Yes, lower in the forming dLGN	expressed in cells at the anterior
	Prethalamus	high in the forming vLGN and ZI	high in the forming vLGN

Table 3.6: ***Summary of Zic4 transcripts and GFP expression pattern in the E16.5 diencephalon.*** *Magenta coloured texts were used to show the change at E16.5 compared to E15.5.*

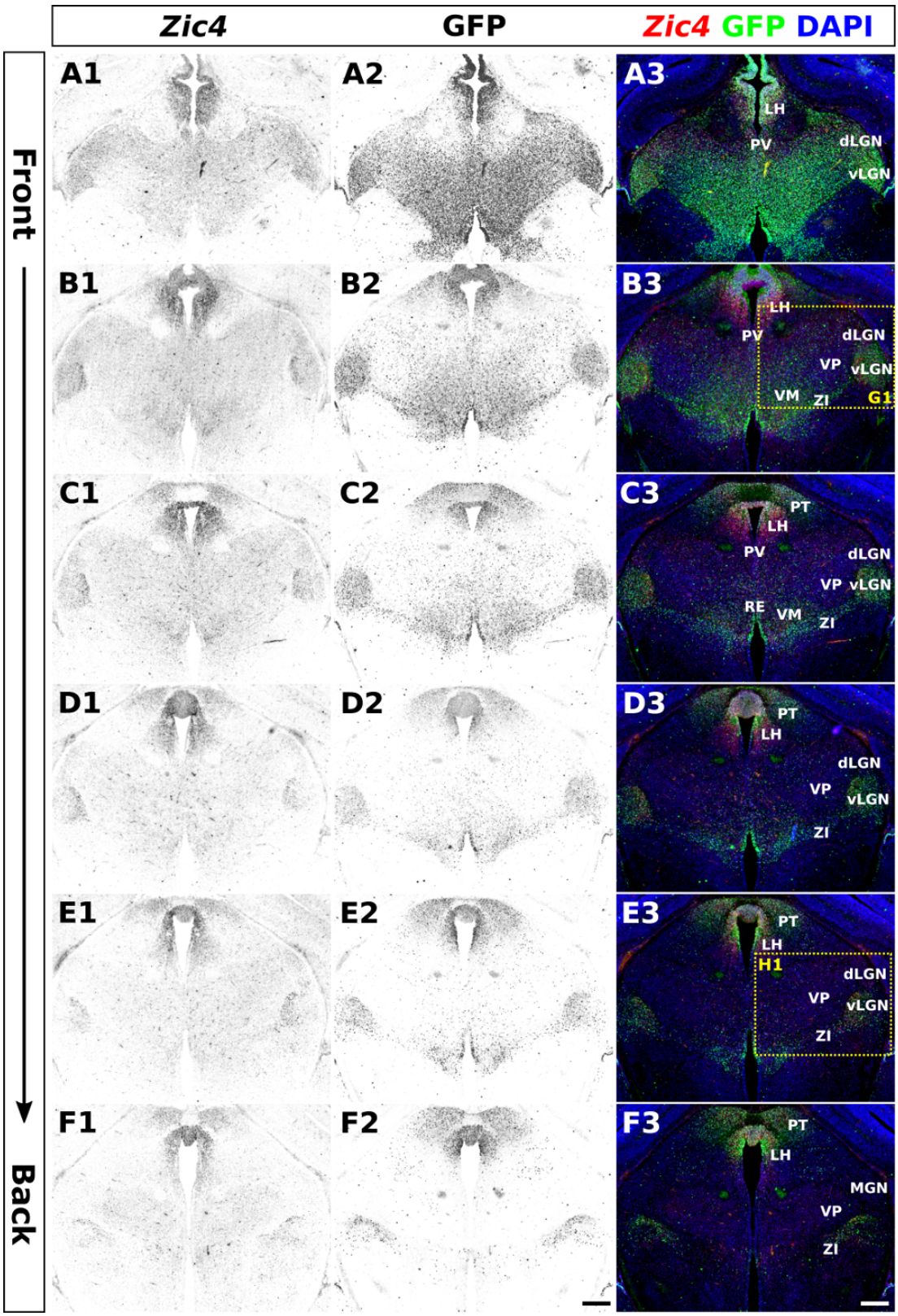


Figure 3.19: ***GFP immunohistochemistry (green) and Zic4 fluorescent in situ hybridisation (red) with DAPI counterstaining (blue) on embryonic day (E) 16.5 Zic4Cre$^{+/-}$;RCE$^{+/-}$mouse brain coronal sections.*** *Scale bar: 250 µm. PV, paraventricular nucleus; VP, ventral posterior complex; VM, ventral medial nucleus; LH, lateral habenula; PT, paratenial nucleus; RE, nucleus of reunions.*

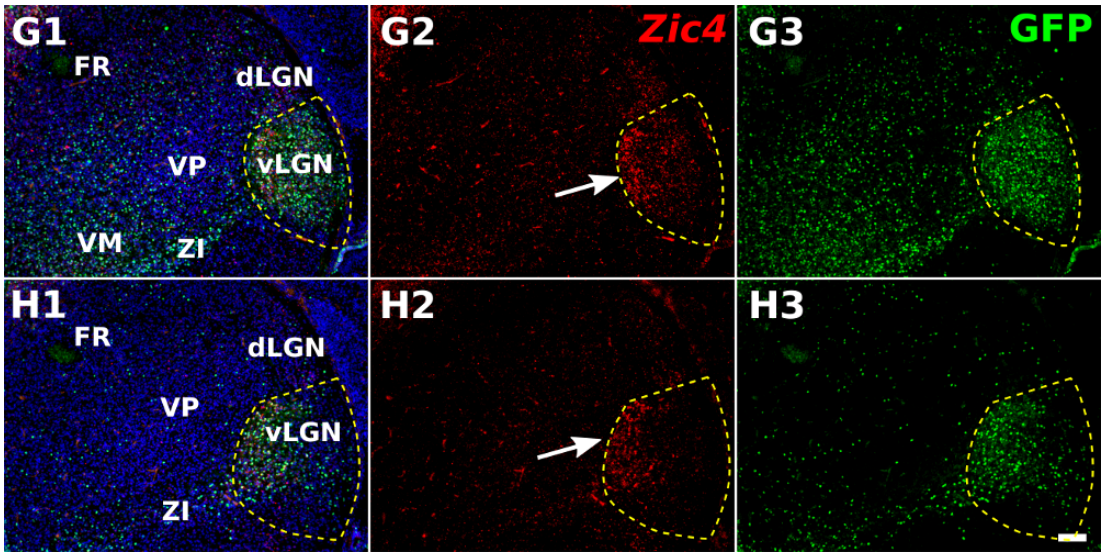


Figure 3.20: ***High power images for GFP immunohistochemistry and Zic4 fluorescent in situ hybridisation on E16.5 Zic4Cre$^{+/-}$;RCE$^{+/-}$mouse brain coronal sections.*** *(G1 and H1) The high power images for the regions outlined by yellow dotted boxes in Figure 3.19. The vLGN is outlined using dashed yellow line. Scale bar: 75 μm.*

3.3.7 Expression of *Zic4* transcripts and GFP in E17.5 *Zic4Cre*$^{+/-}$;*RCE*$^{+/-}$ mouse diencephalon

This experiment aims to study the expression of *Zic4* transcripts and GFP in the *Zic4Cre*$^{+/-}$;*RCE*$^{+/-}$ mouse diencephalon at E17.5 is to find out whether the endogenous *Zic4* has changed in terms of the expression pattern and levels compared to E11.5 to E16.5, and what the GFP reporter expression pattern looks like at this stage. A schematic of E17.5 mouse brain from both sagittal and coronal views is given here to assist readers to understand the anatomical structure of the E17.5 diencephalon.

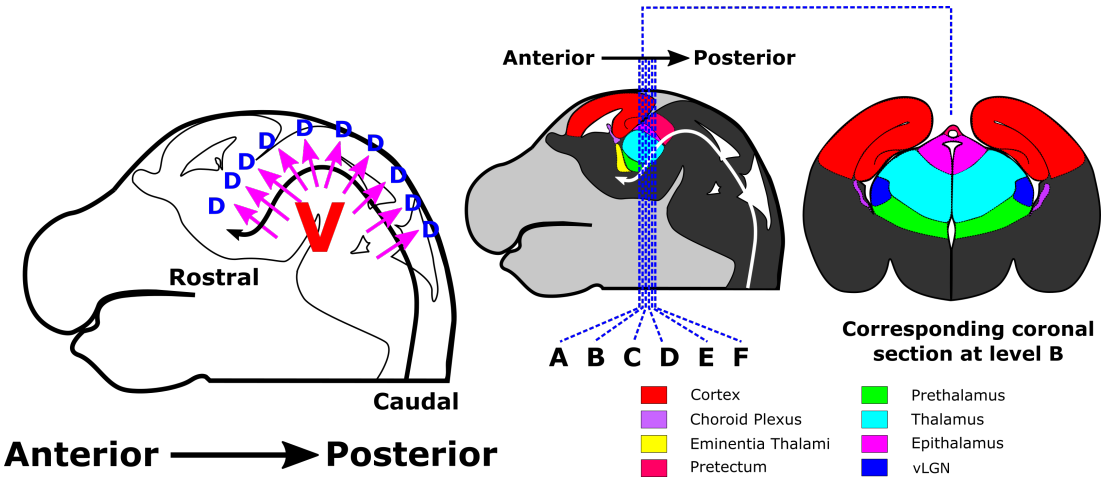


Figure 3.21: ***E17.5 mouse brain sagittal and coronal view schematic.***

The E17.5 schematic (Figure 3.21) is similar to the E16.5 one as the major subdivisions in the diencephalon only show noticeably volume change. The coronal section corresponds to the sectioning level B showing in the sagittal schematic.

The general expression pattern of *Zic4* at this stage (Figure 3.22) is similar to what I saw at E16.5 (Figure 3.19) with a further decrease of *Zic4* expression in the middle to posterior levels in the thalamus (Figure 3.22 C1 - E1). There also seems to be an increase in the *Zic4* expression in the dLGN (Figure 3.23 G1, G2). The expression within the vLGN remains similar, with a high medial and low lateral gradient shown in the middle planes (Figure 3.23 G2 yellow arrow). Moving further posterior of the vLGN, the GFP+ve cells do not seem to express much *Zic4* and they can be the earliest born cells in which the *Zic4* has been turned down (Figure 3.23 H2 - H3 white star). The strong expression of *Zic4* is observed in the ZI, which is likely to be continuous from the vLGN at the adjacent and more anterior levels (Figure 3.23 H2 cyan arrow).

The main findings at E17.5 are summarised in the Table 3.7.

	***Zic4* transcripts**		**GFP**
E17.5	**Structure**	Expression Note	Expression Note
	Thalamus	decrease at middle to posterior levels, increase in the dLGN	expressed in cells at the anterior
	Prethalamus	high in the forming vLGN and ZI	high in the forming vLGN

Table 3.7: ***Summary of* Zic4 *transcripts and GFP expression pattern in the E17.5 diencephalon.*** *Magenta coloured texts were used to show the change at E17.5 compared to E16.5.*

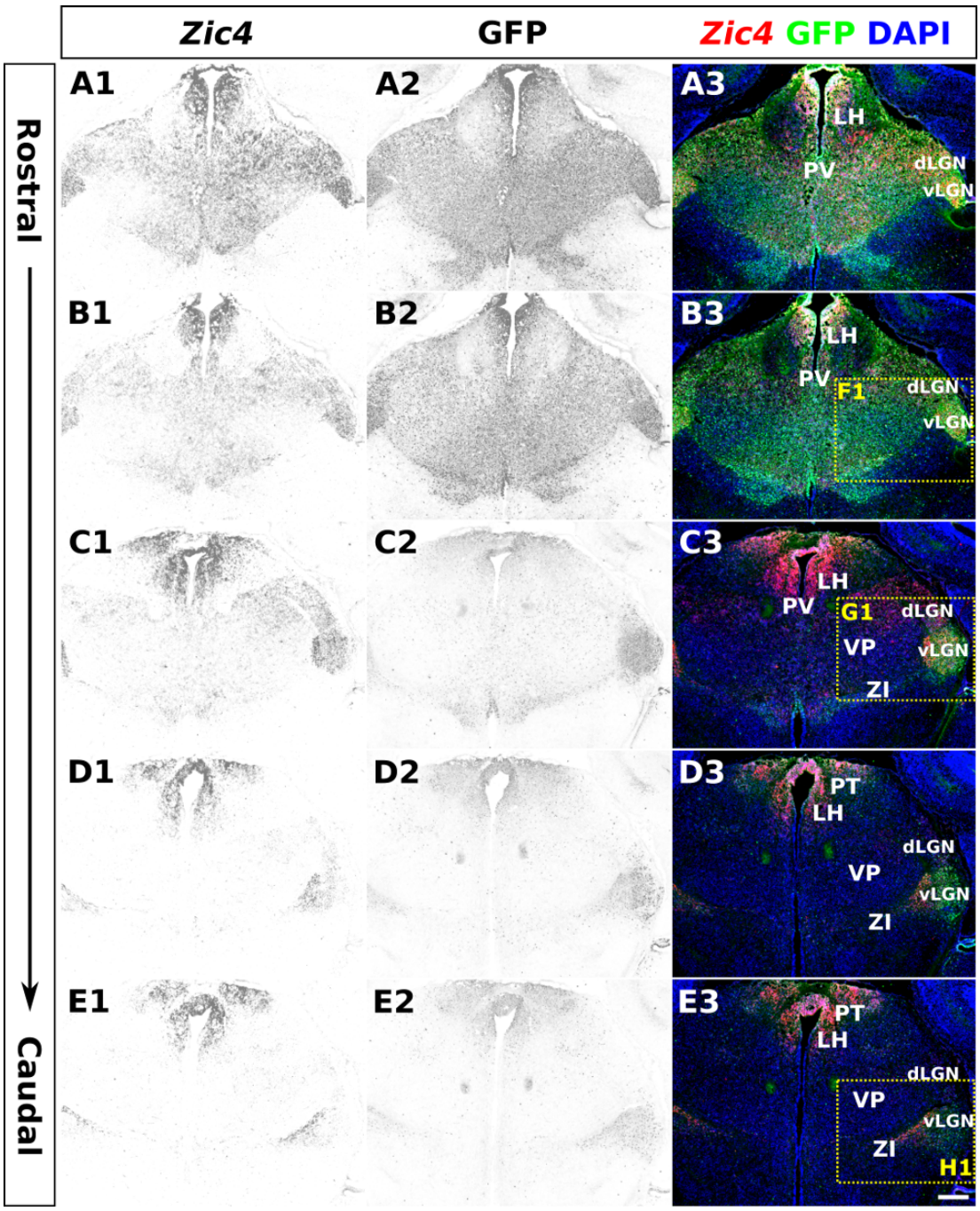


Figure 3.22: ***GFP immunohistochemistry (green) and Zic4 fluorescent in situ hybridisation (red) with DAPI counterstaining (blue) on embryonic day (E) 17.5 Zic4Cre$^{+/-}$;RCE$^{+/-}$mouse brain coronal sections.*** *Scale bar: 250 μm. LH, lateral habenula; PV, paraventricular nucleus; VP, ventral posterior complex; ZI, zona incerta.*

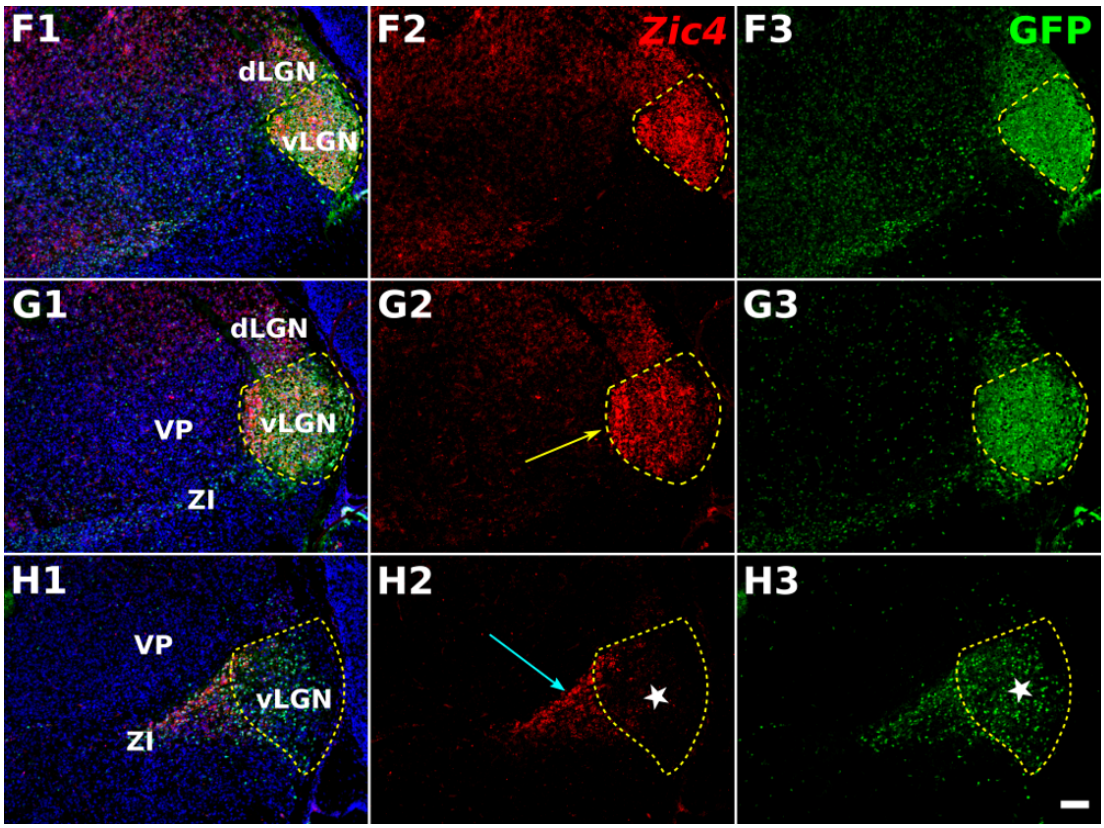


Figure 3.23: ***High power images for GFP immunohistochemistry and Zic4 fluorescent in situ hybridisation on E17.5 Zic4Cre$^{+/-}$;RCE$^{+/-}$ mouse brain coronal sections.*** *(F1, G1 and H1) The high power images for the regions outlined by yellow dotted boxes in Figure 3.22. The vLGN is outlined using dashed yellow line. Scale bar: 75 μm.*

3.3.8 Expression of *Zic4* transcripts and GFP in the E18.5 and P0 *Zic4Cre*$^{+/-}$;*RCE*$^{+/-}$ mouse diencephalon

This experiment aims to study the expression of *Zic4* transcripts and GFP in the *Zic4Cre*$^{+/-}$;*RCE*$^{+/-}$ mouse diencephalon at E18.5 is to find out whether the endogenous *Zic4* has changed in terms of the expression pattern and levels compared to E11.5 to E17.5, and what the GFP reporter expression pattern looks like at this stage. A schematic of E18.5 mouse brain from both sagittal and coronal views is given here to assist readers to understand the anatomical structure of the E18.5 diencephalon.

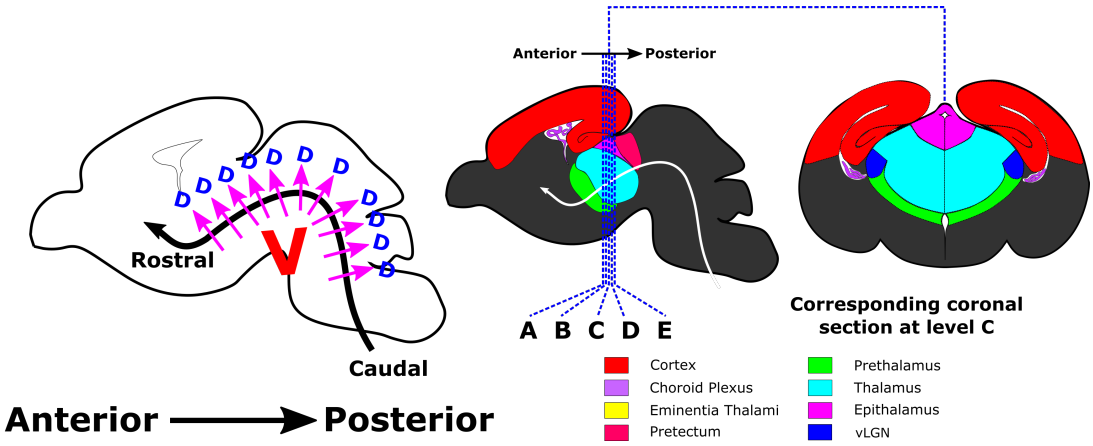


Figure 3.24: ***E18.5 mouse brain sagittal and coronal view schematic.***

The E18.5 mouse brains used for the experiment were taken out of the skull to achieve a better fixation and the schematic (Figure 3.24) shows the dissected-out brains. At E18.5, the expression pattern of *Zic4* seems quite similar to what has been seen a day ealier. The expression of *Zic4* in the dLGN increases, which makes the nucleus more recognisable from the *in situ* staining (Figure 3.25 A1 - C1). Higher power images show that within the dLGN there are a great number of cells expressing *Zic4* but not GFP positive. They might have just started expressing high levels of *Zic4* and not yet turned on the GFP reporter (Figure 3.26 H2 - H3 white arrows). Whereas in the vLGN, the medial high and lateral low gradient of *Zic4* expression is not recognisable any more and at more caudal levels the GFP positive cells no longer express *Zic4* (Figure 3.26 I2 - I3).

The main findings at E18.5 are summarised in the Table 3.8.

	***Zic4* transcripts**		**GFP**
E18.5	**Structure**	Expression Note	Expression Note
	Thalamus	increase in the dLGN	expressed in cells at the anterior
	Prethalamus	high in the forming vLGN	high in the forming vLGN

Table 3.8: ***Summary of* Zic4 *transcripts and GFP expression pattern in the E18.5 diencephalon.*** *Magenta coloured texts were used to show the change at E18.5 compared to E17.5.*

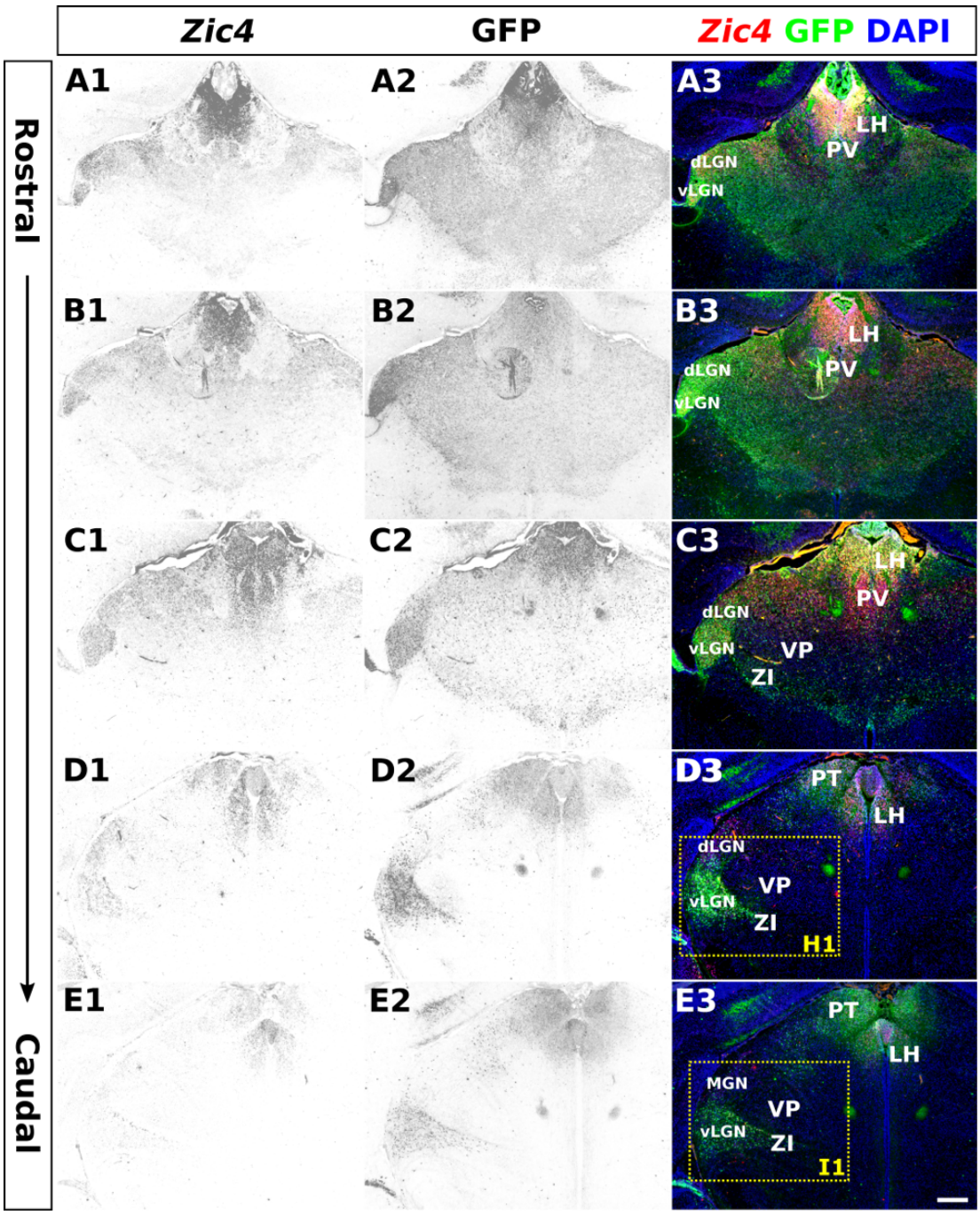


Figure 3.25: ***GFP immunohistochemistry (green) and Zic4 fluorescent in situ hybridisation (red) with DAPI counterstaining (blue) on embryonic day (E) 18.5 Zic4Cre$^{+/-}$;RCE$^{+/-}$ mouse brain coronal sections.*** *LH, lateral habenular; PV, paraventricular nucleus; MGN, medial geniculate nucleus; ZI, zona incerta; PT, paratenial nucleus. Scale bar: 250 μm.*

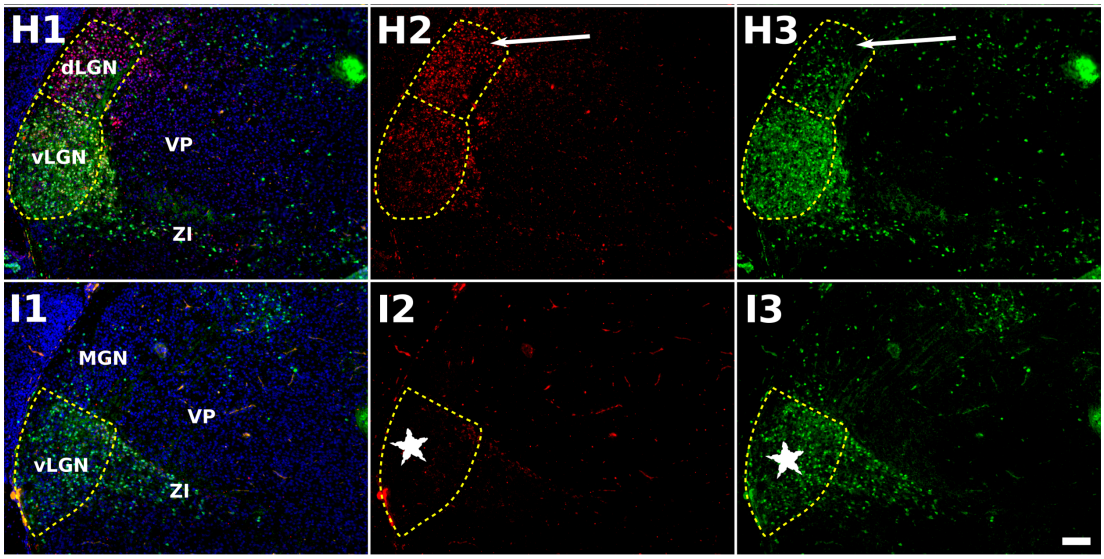


Figure 3.26: ***High power images for GFP immunohistochemistry and Zic4 fluorescent in situ hybridisation on E18.5 Zic4Cre$^{+/-}$;RCE$^{+/-}$ mouse brain coronal sections.*** *(H1 and I1) The high power images for the regions outlined by yellow dotted boxes in Figure 3.25. Scale bar: 75 μm.*

These results are in line with the characterisation study carried out by Kessaris' group in the similar compound transgenic mice *Zic4-Cre^{Tg}/R26R-YFP$^{+/-}$* at E12.5 [98]. Moreover, this experiment revealed the dynamic expression levels and patterns of *Zic4* transcripts and the emergence, growth and distribution of *Zic4* lineage cells during thalamic development especially the formation of the vLGN. The GFP immunohistochemistry on postnatal day (P) 0 Zic4Cre$^{+/-}$; RCE$^{+/-}$ mouse brain sections (Figure 3.27) shows that GFP expressing *Zic4* lineage cells aggregate in a greater density into specific thalamic nuclei such as vLGN than into the adjacent dLGN and VP including the ventral posteromedial nucleus (VPM) and the ventral posterolateral nucleus (VPL), which suggests that *Zic4* is a very good lineage marker for studying the formation of vLGN and *Zic4* itself may play a role in the process.

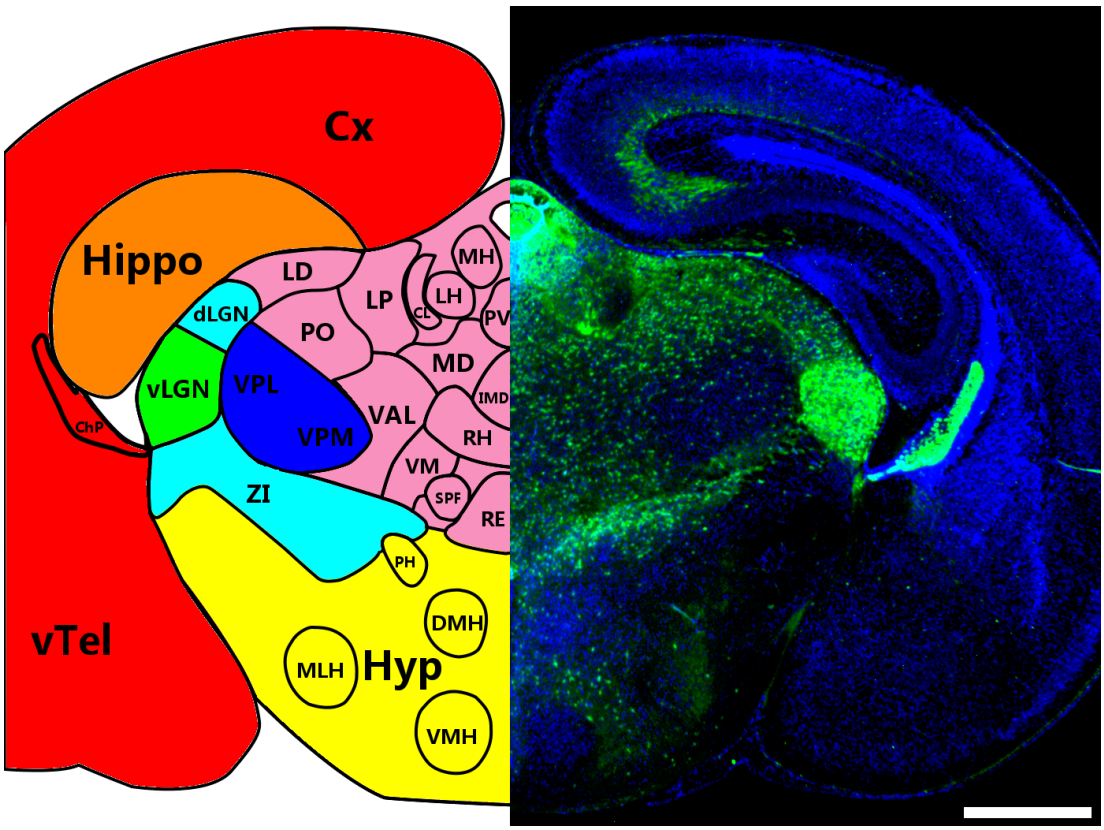


Figure 3.27: ***GFP immunohistochemistry (green) on postnatal day 0 Zic4Cre$^{+/-}$;RCE$^{+/-}$ mouse brain coronal sections counterstained with DAPI (blue) (right half) and annotated to detailed brain structures (left half).*** *Major forebrain structures are annotated and labelled in different colours. Cx, cortex(red); vTel, ventral telencephalon (red); ChP, choroid plexus (red); Hippo, hippocampus (orange); Hyp, hypothalamus (yellow). Hypothalamic nuclei are labelled in yellow and thalamic nuclei are mostly labelled in pink apart from the ones of interest in this study: dLGN, dorsal lateral geniculate nucleus (cyan); vLGN, ventral lateral geniculate nucleus (green); VPL, ventral posterolateral nucleus (blue); VPM, ventral posteromedial nucleus (blue); ZI, zona incerta (cyan). MH, medial habenula; PV, paraventricular nucleus; LH, lateral habenula; CL, central lateral nucleus; MD, medial dorsal nucleus, intermedial dorsal nucleus; LP, lateral posterior nucleus; LD, lateral dorsal nucleus; PO, posteror nucleus; VAL, ventral anterial - lateral nucleus; RH, rhomboid nucleus; VM, ventral medial nucleus; SPF, submedial nucleus; RE, nucleus of reunions; PH, posterial hypothalamic nucleus; DMH, dorsomedial nucleus of hypothalamus; VMH, ventromedial nucleus of hypothalamus; MLH, magnocellular nucleus of lateral hypothalamus. Scale bar: 75 μm.*

3.4 Synopsis

This section is a synopsis of the results from the series stainings for endogenous *Zic4* transcripts and the GFP reporter, reporting *Cre* recombinase activity, from E11.5 to E18.5, which reveals the emerging and the growing of the *Zic4* lineage population during the prenatal development

of the diencephalon.

At E11.5, high levels of *Zic4* expression are seen in most of the cells from the prethalamus and eminentia thalami but only a small fraction of them express GFP. The descrepancy between the *Zic4* and the GFP expression pattern at this stage can be explained by a possible requirement of time to synthesize the GFP after the initiation of *Zic4* transcription. It was also observed that the onset of GFP expression is independent of *Zic4* transcriptional levels, especially in the prethalamus where the GFP is turned on in the cells with low *Zic4* expression in the ventricular region but not on in the cells with high *Zic4* levels in the potentially differentiating neurons. A possible explanation could be these differentating cells are experiencing a rapid transcription of *Zic4* whereas the expression of the GFP reporter is relatively lagged behind.

At E12.5, the proportion of *Zic4* and GFP double positive cells increases in the thalamus, prethalamus and eminentia thalami, which supports the hypothesis that the GFP synthesis takes time after *Zic4* transcription initiates. In the meantime, a group of cells with high *Zic4* expression are observed in the subventricular area in the prethalamus, which could be differentiating neurons or a subgroup of progenitors with specific functions. There are still a number of *Zic4* positive cells that do not express GFP in the thalamus, prethalamus and eminentia thalami.

At E13.5, the proportions of *Zic4* and GFP double positive cells continue increasing in the thalamus, prethalamus and eminentia thalami but there are still some *Zic4* positive cells that do not express GFP. This could be explained by more cells starting to express *Zic4* as the development proceeds. Comparing to E12.5, the GFP expression level is significantly higher in all the structures of interest, which could be due to the accumulation of GFP in individual cells. It was also noticed that most GFP+ve cells in the lateral region of the thalamus are *Zic4* positive whereas in the same region most GFP negative cells are *Zic4* negative, which indicates a great number of non-*Zic4* lineage neurons are born at this stage.

At E14.5, most GFP positive cells in the thalamus no longer express *Zic4*, suggesting that in these cells *Zic4* has been turned down. In the prethalamus, most GFP+ve cells stop expressing *Zic4* and high levels of *Zic4* are only seen in a restricted group of cells residing in the ventricular and subventricular regions, which indicates the heterogeneity of prethalamic cell population.

At E15.5, the forming vLGN can be appreciated, in which the *Zic4* expression is lost in the lateral-most regions whereas its levels remain high in the medial-most areas. In the thalamus, a group of high *Zic4* expressing cells are positioned dorsal to the forming vLGN, which could

contribute to the future dLGN. Not many of these cells express GFP, which indicates that they only just started to express *Zic4*.

At E16.5, the general expression level of *Zic4* decreases further in the vLGN especially in the lateral region but the medial region maintains high levels of *Zic4*. This selective expression of high level *Zic4* in specific subregions within the vLGN suggests a heterogeneous composition of the nucleus and potential differences in function among different subregions.

At E17.5, the proportion of the GFP and *Zic4* double positive cells increases in the forming dLGN, supporting the idea that the GFP in these cells takes time to turn on. At E18.5, there are still a number of *Zic4* positive cells that do not express GFP and the proportion of double positive cells does not seem to increase. It could be that: 1.these *Zic4* positive and GFP negative cells need more time to turn on the GFP; 2.the BAC *Zic4* transgene does not possess all the elements required for a complete recapitulation of the endogenous *Zic4* expression, which causes the discrepancy between the GFP and the endogenous *Zic4* expressions; 3. epigenetic factors could well be causing the difference - densely packaged chromatin could deny access of the Cre recombinase to the floxed STOP cassette and stall the expression of GFP.

In summary, the expression of GFP reporter well respects the expression of endogenous *Zic4* gene in the *Zic4Cre* mouse line. From E11.5 to P0, the endogenous *Zic4* transcripts and the GFP reporter reporting the Cre activity show that *Zic4* lineage cells emerge in the epithalamus and the prethalamus from E11.5 with more and more lineage cells appear in the rostral thalamus as development proceeds. From E15.5 to P0, this lineage seems to be aggregating specifically in the forming vLGN, which makes this lineage a good candidate for studying the formation of this particular nucleus.

3.5 Discussion

Specific *Zic4* expression and potential biological functions

The specific expression pattern of *Zic4* transcripts at different stages suggests that this gene might have critical roles during the diencephalic development. It is ideal to look into *Zic4* mutants to study its function. However, I do not have the animal model to carry out the study and what I can do is to speculate on Zic4's function based on its expression. The specific features I would like to highlight in this section includes: 1. the strong *Zic4* expression in the region close to the pial surface of the prethalamic wall at E11.5 (Figure 3.5 I and I1); 2. the strong *Zic4* expression in the prethalamus (Figure 3.8 I1, I2, K1, K2) and the lateral most

region of the thalamic wall at E12.5 (Figure 3.8 H1, H2, J1, J2); 3. the strong *Zic4* expression in the subventricular zone of the prethalamus at E13.5 (Figure 3.11 H4, I1); 4. the strong *Zic4* expression in the subventricular zone of the prethalamus (Figure 3.14 H1 and J1, red star) and the forming vLGN (Figure 3.14 I1 and J1, magenta arrow) at E14.5. In order to make our speculation more equitable, I searched for other genes with similar expression patterns at the specific stage in published studies and extrapolated potential biological function of *Zic4* gene.

In the middle to posterior planes of the E11.5 prethalamus, a rim of high *Zic4* expressing cells are seen ocuppying the region along the lateral prethalamic surface (Figure 3.5 I and I1). I have not yet found any other genes having a similar expression pattern at this stage in mice. It is reasonable to speculate from the position of these cells that they may be the differentiating and/or the newly born neurons in the prethalamus and the high level of *Zic4* may hence be associated with cell differentiation and/or cell fate commitment.

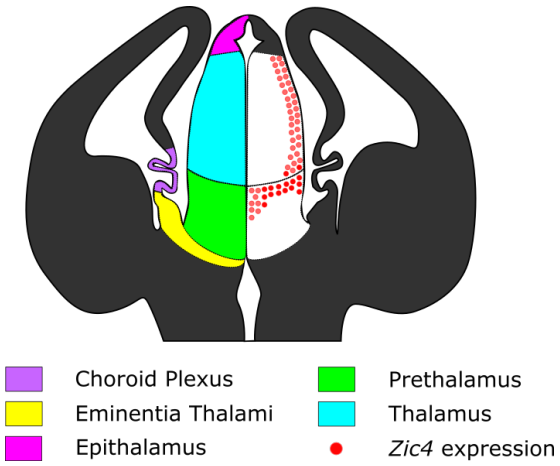
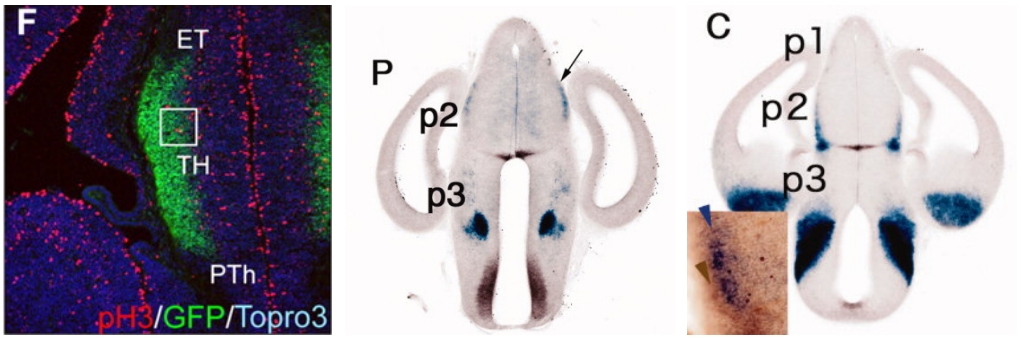


Figure 3.28: ***Schematic of featured Zic4 expression pattern in E12.5 thalamus and prethalamus***

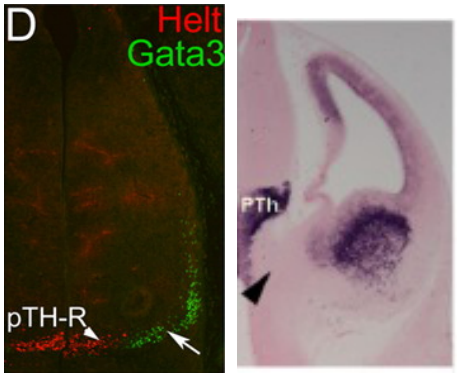
At E12.5, I focus on two features (Figure 3.28): the overall strong expression of *Zic4* in the prethalamus (Figure 3.8 I1, I2, K1, K2) and the strong expression particularly in the lateral region of the thalamic wall (Figure 3.8 H1, H2, J1, J2). The feature in the thalamus at this stage is similar to the expression pattern of several other genes, such as *Gbx2* (Figure 3.29 (a)), *D2R* (Figure 3.29 (b)) and *iGluR1* (Figure 3.29 (c)). *Gbx2* is reported to play a cell-nonautonomus role in the segregation of postmitotic thalamic nuerons from the neighbouring brain structures, such as the epithalamus and the prethalamus [101], which supports our speculation on E11.5 data that *Zic4* may be involved in cell fate commitment. It has been observed that *Zic4* plays a role in neural crest tissue induction [84], which again indicates that *Zic4* can potentially affect cell fate.

The expressions of *D2R* (Figure 3.29 (b)) and *iGluR1* (Figure 3.29 (c)) are complimentary to each other along the dorsal-ventral axis of the lateral thalamic wall, with the *iGluR1* ventral

to the *D2R* expression. The *D2R* gene encodes the D2 subtype of dopamine receptor, which has the maximum affinity for dopamine of all the five dopamine receptors. The *iGluR1* gene encodes ionotropic glutamate receptors, ligand-gated ion channels that are activated by the neurotransmitter glutamate. These data suggest that the differentiating and/or newly born neurons in E12.5 thalamus have already committed to different electrophysiological properties and high levels of *Zic4* may well be necessary for this transition. Noticeably, the *iGluR1* gene has very strong expression in the prethalamus as well, partially overlapping with *Zic4* expression in the lateral prethalamus, which makes it interesting as the early thalamic neurons at the pial surface have similar electrophysiological properties as their counterparts in the prethalamus at this stage. The gene *Gata3* (or *Slc17a8*) also shows similar expression pattern (Figure 3.29 (d)) to the *iGluR1* and the *Zic4* [63]. A study of GABAergic neuron fate in diencephalon has shown that the Gata3 is actually expressed within the Gad1$^+$ GABAergic neurons in the thalamus and its expression is detected in the vLGN and IGL at E18.5 [102]. The *Arx* gene has a similar expression pattern (Figure 3.29 (e)) to the *Zic4* gene in the prethalamus [103] and there is no overlap between *Gata3* and *Arx* observed in the prethalamus [102]. A study of *Arx*'s role in diencephalic development [104] reveals that the loss of functioning Arx results in loss of dopaminergic neurons in ZI, a prethalamic nuclei. A study in zebrafish dopaminergic neurons also showed *Arx* is required for early patterning and for the expression of Pax6a, a homolog of the mouse Pax6 [105]. With all the information above, I think *Zic4* may be required for the neuron differentiation and the establishment of their eletrophysiological identity in the early developing thalamus and prethalamus.



(a) *Gbx2* (b) *D2R* (c) *iGluR1*

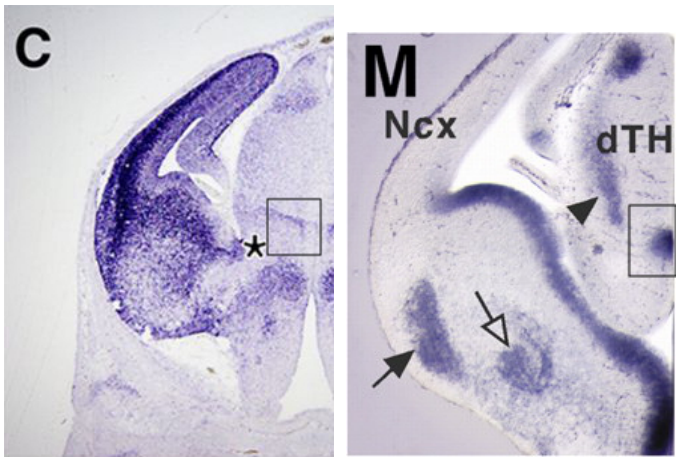


(d) *Gata3* (e) *Arx*

Figure 3.29: ***Genes with similar expression pattern to Zic4 gene in E12.5 thalamus and prethalamus*** *(a) GFP expression driven by Gbx2Cre in E12.5 Gbx2$^{CreER/+}$ mouse embryos [101]. (b) D2R (dark blue) transcripts expression in E12.5 wild type mouse brain. The black arrow points at the expression similar to Zic4 [48]. (c) iGluR (dark blue) transcripts expression in E12.5 wild type brain [48]. The brown stainings in (b) and (c) show the expression of Shh. (d) Gata 3 expression in E12.5 control brain [63]. The white arrow points at the lateral region of the prethalamus. (e) Arx expression in the prethalamus in E12.5 control brain [103].*

At E13.5, I focus on the group of cells with high *zic4* expression in the subventricular zone of the prethalamus (Figure 3.11 H4, I1). We found the axon guidance associated genes EphA5 (Figure 3.30 (a)) and Netrin1 (Figure 3.30 (b)) have similar expression pattern around the region I am interested in. The presence of these axon guidance molecules in the restricted group of cells in the subventricular zone of the prethalamus suggests that these cells might be involved in the formation of the thalamocortical tract (TCA). These cells position at the region where the TCA just start to turn laterally toward the telencaphalon-diencephalon boundary (Figure 3.31). It is possible that these cells provide extra clues for TCAs pathfinding at the very beginning of their journey. The co-existence of these axon guidance molecludes and the high level expression of *Zic4* suggests that *Zic4* could be remotely associated with the establishment of the specific environment for TCAs development in the prethalamus. The fact that in *Zic4*$^{-/-}$

mutants more clustered and disorganised ipsilateral terminals are observed in the LGN [85], supports my speculation on *Zic4*'s involvement in axon guidance.



(a) *EphA5* (b) *Netrin1*

Figure 3.30: ***Genes with similar expression pattern to Zic4 gene in E13.5 prethalamus*** *(a) EphA5 in situ in E13.5 wild type mouse brain [106]. (b) Netrin1 in situ in E13.5 wild type mouse brain [107]. Black boxes are used for labelling the region of interest.*

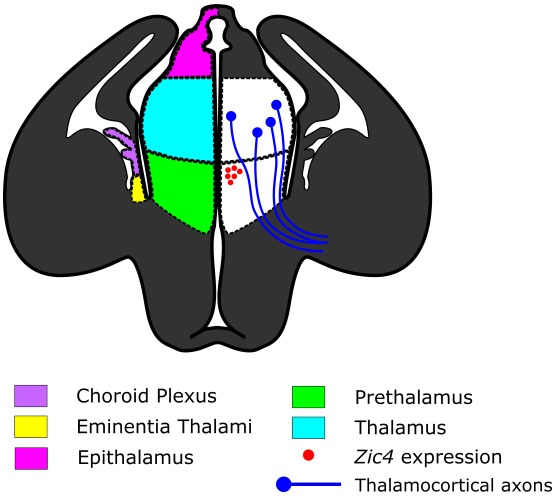


Figure 3.31: ***Schematic of featured Zic4 expression pattern in the subventricular zone of E13.5 prethalamus***

At E14.5, the strong expression of *Zic4* can still be seen in the subventricular zone of the prethalamus (Figure 3.14 H1 and J1, red star). Based on my discussion for E13.5, it is possible that the presence of high levels of *Zic4* is also required for the expression of the axon guidance molecules to maintain the regulation on the pathfinding and/or fasciculation of the TCAs. The high level *Zic4* expression in the forming vLGN (Figure 3.14 I1 and J1, magenta arrow) suggests that the *Zic4* is highly involved in the development of the prethalamic nucleus,

vLGN.

Regarding all the features I discussed before, I speculate that *Zic4* could possibly play the following roles in the development of the thalamus and the prethalamus: 1. promoting cell differentiation; 2. regulating cell fate commitment especially in gaining the electrophysiological identities; 3. contributing to the formation of the vLGN; 4. establishing the environment (axon guidance molecules) that is required for TCA navigation through the prethalamus.

Since the expression of *Zic4* transcripts are not only seen in the progenitor zone within the thalamus and the prethalamus but also in the postmitotic area and its expression pattern is not perfectly reflected by the expression of GFP, a closer observation and a quantitative and colocalisation analysis of *Zic4* transcripts and GFP at single cell level are required to monitor the *Zic4* cell lineage during the development of the diencephalon.

Chapter 4

Quantitative analysis of *Zic4* transcripts and GFP reporter at cellular levels in the developing diencephalon in *Zic4Cre*$^{+/-}$;*RCE*$^{+/-}$ mice

4.1 Introduction

The dynamic expression of endogenous *Zic4* transcripts and GFP reporter has been studied in the previous chapter from E11.5 to P0 using *in situ hybridisation* and immunohistochemistry. The emergence and growth of the *Zic4* lineage in the developing diencephalon has been described in details. However, with no quantification, it is impossible to track the change of expression level of these two molecules at cellular levels across different developmental stages. This study aims to use a quantitative approach to study the expression profiles of these two molecules in single cells within different subdivisions of the developing diencephalon.

4.1.1 Visualisation and quantification of mRNA molecules

Studying the temporal and spatial expression pattern of specific genes is an essential part of embryonic developmental biology. Colourimetric RNA *in situ* hybridisation (ISH) is normally performed to delineate the transcriptional activity of certain genes across different developmental

stages. Conventional RNA ISH involves using hapten (biotin or digoxygenin) labelled RNA probes and further antibody binding for visualisation, which tends to suffer from diffusion, non-specific binding, low sensitivity and is not ideal for double or triple labelling experiments. The fluorescence in situ hybridisation (FISH) using tyramide signal amplification (TSA) involves applying horseradish peroxidase (HRP) to catalyse the deposition of fluorophore labelled tyramine amplification reagent onto tissue sections or cells [108]. Tyramide is a compound that easily binds to peroxidase thus the sensitivity is boosted 10 to 30 folds compared to standard FISH. TSA-FISH can even detect single copy of RNA molecules [109]. TSA-FISH protocol involves several steps: 1. a peroxidase conjugated anti-hapten antibody or a compound such as streptavidin binds to the labelled probe; 2. fluorochromes or haptens like biotin are conjugated to tyramine derivatives. This process leads to a massive accumulation of fluorochromes (or moieties) that can be visualised by fluorescence microscopy, which greatly boosts the detection sensitivity and makes it possible to quantify the transcriptional activity with the help of computational image analysis.

4.1.2 Computational image analysis and cell segmentation

Computational image processing has been widely used in biological and biomedical research and it is used in this chapter to quantify the *Zic4* and GFP fluorescence intensities. A brief introduction of some essential techniques and critical issues in computational image analysis is laid out here to provide some insights into the field and the rationale for the methodology used in the analysis.

The innovations in microscopic imaging have enabled biologists to acquire a great number of images within a relatively short period of time. The abundance, heterogeneity and complexity of the data make it difficult to manage, process or analyse the images manually. As a result, computerised techniques for carrying out these tasks have become essential for further and more rapid progress in biological and biomedical research [110, 111].

Segmentation is a process of partitioning an image into multiple segments (or regions of interest) and is quite often used to identify specific features in biological images, such as cell nuclei, cell membrane and whole cell [112]. A major issue in many studies and often considered as the crux of image analysis, is image segmentation [111]. Automatic image segmentation is particularly difficult for cell analysis due to the large variability in different microscopes, cell types, stainings and cell densities. Nevertheless, the vast majority of cell segmentation methods are mainly based on a number of basic approaches (Figure 4.1), including intensity thresholding (every pixel above a defined intensity is assigned to one type of region,

whereas every pixel below that intensity is assigned to another type of region), feature detection (eg. edge detection used to identify the outer boundary of cell nuclei), morphological filtering (image processing based on the shape of the features of interest), region accumulation (a region is made up of adjacent pixels thus a specific pixel's neighbours are possibly part of the same region) [111, 112].

As one of the most predominant approaches to cell segmentation, intensity thresholding is based on the assumption that the cells have significantly and consistently different signal intensities compared to the background. However, thresholding on its own is not enough to obtain high fidelity signals/features when dealing with images with high background and thresholding is often the first step of an image analysis pipeline [111]. Rather than relying on the intensities, cells can be segmented based on the intensity derived features, like using edge detection. Morphological filtering (Figure 4.2) using operators such as erosion (shrinking an object in the image and removing isolated pixels), dilation (expanding object through its borders), opening (removing small objects) and closing (close small holes in an object) allows for examination and manipulation of the topological properties of the objects in images, which is often used together with cell segmentation [111]. Grayscale morphology is quite often used as a preprocessing step to enhance specific structure for segmentation whereas binary morphology is usually used as a postprocessing step to polish the coarse segmentations [111]. Region accumulation is an approach that starts from selected seed points and iteratively adds connected points to formed the labelled regions [111]. The watershed transformation is the most popular region accumulation approach. A grayscale image can be considered as a relief map with peaks and ridges at the high intensities (bright) and valleys at the low intensities (dark) [112]. Imagine pouring water into a region of the image so it gradually fills up the valleys, but does not spill into the next valley. The region filled with water is then defined as a specific segment object. A good example will be using watershed transformation on an image of membrane staining. Imagine water is being poured into the valley of the cell center and gradually filling up the whole cell until it reaches the membrane, thus marking an individual cell. In an image with many cells, the separate valleys for each individual cell are referred to as catchment basins and the ridges between the valleys are called watersheds. Watershed transformation is infamous for producing over-segmentation (for example a single cell is recognised as two adjacent "cells" caused by uneven illumination within the cell), and usually requires further processing [111]. None of these approaches produce satisfactory results on its own, they are all useful to some extent. Consequently, methods used in recent studies are often combinations of the approaches tailored to accommodate specific analyses.

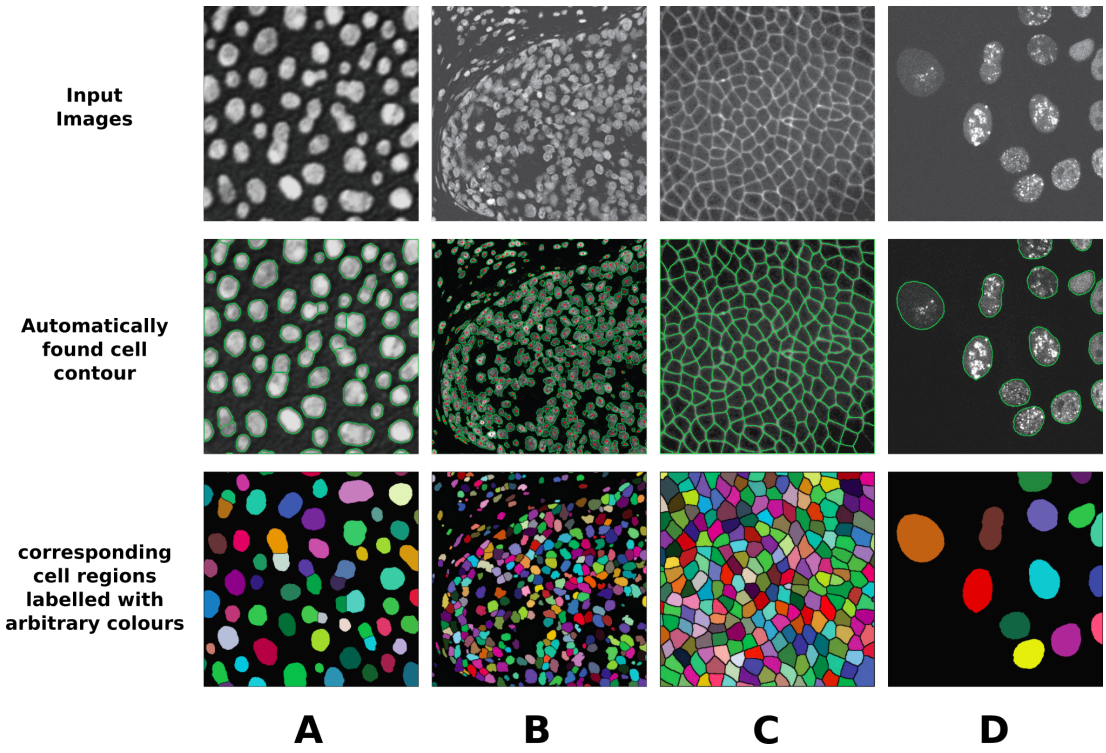


Figure 4.1: ***Examples of cell segmentation approaches*** *Three rows of images are the raw input images, automatically found cell contour and the corresponding cell regions labelled with arbitrary colours. (A-D) Examples of different kind of images that require different type of cell segmentation. (A) Most of the cell are well separated from each other and very bright compared to the background, which is easy to segment using thresholding. (B) Example of images with high cell density and intensity variation, which requires more sophiscated handling. The method involves graph-cuts based binarization, Laplacian-of-Gaussian based cell detection and marker based segmentation. The Laplacian is a specific measure of an image, which highlights regions of rapid intensity change and is often used for edge detection. The Laplacian is often applied to an image that has been preprocessed with a Gaussian smoothing filter in order to reduce its sensitivity to noise. The combination of the two is called Laplacian-of-Gaussian based cell detection. (C) Membrane staining images are ideally suited for watershed based segmentation. (D) Studies of intracellular dynamic processes often result in images with significant intensity variations and requrie robust cell segmentation and tracking methods. The image is adapted from [111].*

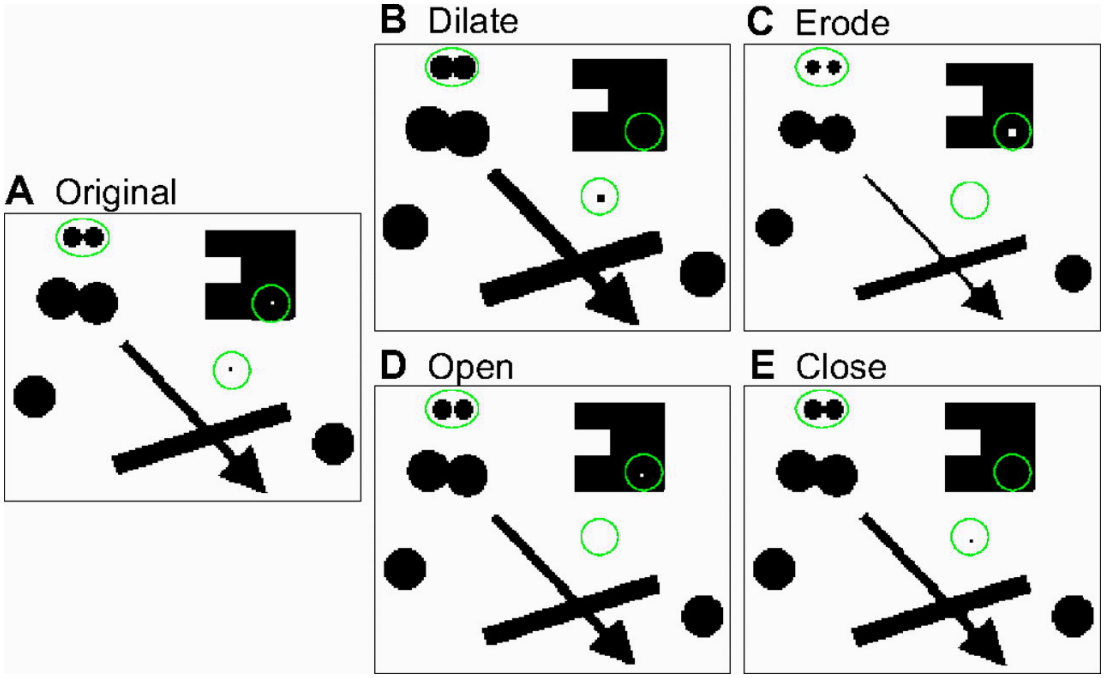


Figure 4.2: ***Examples of morphological processing using operators*** *Morphological processing using operators dilate, erode, open and close. (A) Original image. Showing an image with several black objects on a white background. The object I focuse on are outlined using green circle. They are a pair of filled black circles, a white dot in a black square object and a black dot on the white background. (B) Dilation expands object through its border. I can see the pair of circles grow bigger, the white dot in the black object disappears and the single dot on the white background grows bigger. (C) Erosion shrinks an object and removes isolated pixel. The pair of circles are smaller compared to the orginal one. The white dot in the black object becomes bigger, in other word, the hole in the object grows bigger. The isolated black dot on the white background is now gone. (D) Opening is the application of erosion followed by dilation and can be used to remove small objects. As I can see, the pair of circles stays more or less the same and the white dot in the black object still exists. However, the isolated black dot is gone. (E) Closing is the application of dilation followed by erosion and can be used to remove small holes in an object. As I can see, the pair of circles and the isolated black dot remains similar but the white dot in the black object is gone. The hole is filled. The image is adapted from [112].*

4.1.3 Distribution of mRNA molecules across a single cell

The identification of specific nucleic acid by FISH has revealed sites of mRNA processing, transportation and cytoplasmic localization [113]. The sensitivity of FISH technique allows detection of single molecules in low concentration regions whereas quantification of multiple copies of mRNA in high concentration areas such as transcription sites can be used to measure the mRNA production rate [113].

In eukaryotic cells, nascent RNAs are transcribed and processed in the nucleus to become mRNAs. Then mRNAs are transported out of the nucleus into cytoplasm, where the corresponding polypeptides are synthesized [113]. Thus, mRNAs can be detected not only in the cytoplasm but also in the nucleus [113]. In some FISH experiment, the bright spots of fluorescence were detected around the transcription sites and the dispersal of transcripts away from the transcription sites were observed to take distinct spatial patterns [113].

4.2 Aim of the project

In this project, I seek to gain insights into: **1. How the expression of GFP reporter coincides with the expression of the endogenous *Zic4* gene (the *Zic4* transcripts) at cellular levels; 2. Whether the expression of *Zic4* is persistent in the GFP tagged *Zic4* lineage cells in the developing diencephalon.** In order to answer these questions, quantitative analysis of the fluorescence signals from *Zic4 in situ* hybridisation and the GFP immunohistochemistry was performed at cellular levels in the subdivisions within the developing diencephalon.

The expression of the GFP reporter in the *Zic4* lineage cells requires a serise of events to occur, including the recruitment of the *Zic4* transcriptional regulatory elements to the *Zic4Cre* transgene, the initiation of the *Zic4Cre* transgene transcription, the synthesis and accumulation of the *Cre* recombinase, the excision of the *STOP* sequence mediated by the *Cre-loxP* system and the transcription and translation of the EGFP coding sequence. I hypothesize that: 1. four types of cells, $Zic4^{-}GFP^{-}$, $Zic4^{+}GFP^{-}$, $Zic4^{+}GFP^{+}$ and $Zic4^{-}GFP^{+}$, can be observed in the developing diencephalon based on the staining of the *Zic4* transcripts and the GFP reporter; 2. the proportions of different cell types vary in different diencephalic subdivisions as the development proceeds.

4.3 Results

To study how the *Zic4* cell lineage emerges, grows and contributes to the development of the diencephalon, a quantitative assessment of *Zic4* transcript signal units at single cell level was performed for both the GFP positive and negative cells in the diencephalon from E11.5 to E15.5.

Though the fluorescent *in situ hybridisation* (FISH) for *Zic4* was not performed using single molecule FISH probe, the quantitative analysis of the fluorescence intensity detected from the staining can still be informative, since the incorportion of DIG-labelled dUTP into the probe is at approximately every 20 to 25th nucleotide under standard conditions. In order to efficiently extract the fluorescence intensity of the *Zic4* transcripts at cellular levels, I developed a computer assisted image processing strategy.

Firstly, I used a custom MATLAB code [1] to preprocess the raw images, including background subtraction and region of interest selection (MATLAB allows great flexibility in this step). Then I used a pipeline constructed using CellProfiler [94] to extract the multiplexed information (fluorescence intensity of both the GFP and the *Zic4* transcripts) simultaneously in an efficient and unbiased way.

The .nd2 microscopic image files acquired using Nikon A1R confocal microscope were first converted and saved in .tif format to be further processed using MATLAB. The converted .tif images (Figure 4.3) were read into MATLAB. This step utilises the string handling functions to extract information such as the developmental stage (e.g. E11.5), the section number (slide number with position number for the section, e.g. 2a4 means slide 2a and position 4 (Figure 4.4)), genotype (e.g. het), the structure name (e.g. prethalamus), the magnification (e.g. 40x) and the property of the experiment (e.g. zic4gfp). This information is automatically extracted from the image file names so the amount and the content of the information completely depend on how files are named when the images are collected. For example, if an image file is named as '**`e125_zic4gfp_40x_1b2_epithalamus.tif`**', the code automatically extracts useful information such as **Stage =** '$e125$', **Experiment =** '$zic4gfp$', **Magnification =** '$40x$', **Slide =** '$2a3$', **Structure =** 'ctx' **(cortex)**. The collected information is then used for naming the image analysis output files.

[1] The code is included in Appendix III.

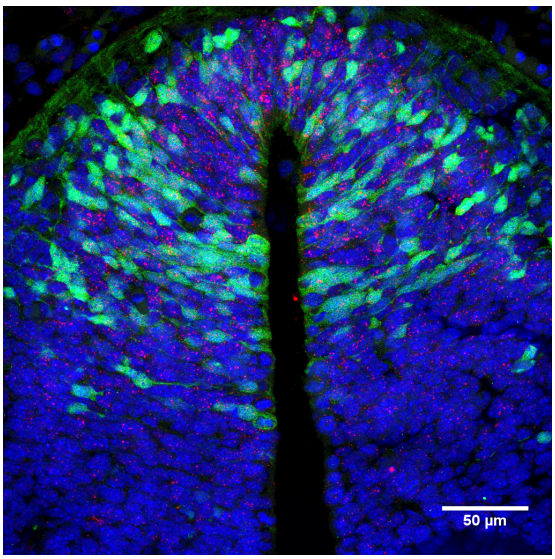


Figure 4.3: ***Sample Image used for the analysis.*** *A coronal section of epithalamus in E12.5 Zic4Cre$^{+/-}$;RCE$^{+/-}$ mice stained for Zic4 transcripts, GFP and counterstained with DAPI. Scale bar 50 μm.*

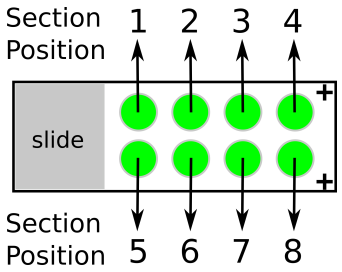


Figure 4.4: ***Schematic of section and position number on a typical slide.*** *A typical slide mounted with brain tissue sections. The brain tissue sections are presented using filled green circles. The gray area is the labelling area on the slide.*

These image files contains R, G and B three channels (Figure 4.5 A): the Red channel shows the *in situ* staining for the *Zic4* transcripts (Figure 4.5 B); the green channel shows the immunostaining for the GFP (Figure 4.5 C); the blue channel shows the DAPI counterstaining of the nuclei (Figure 4.5 D). After splitting the channels, single channelled grayscale images were saved separately and ready for further channel specific processes.

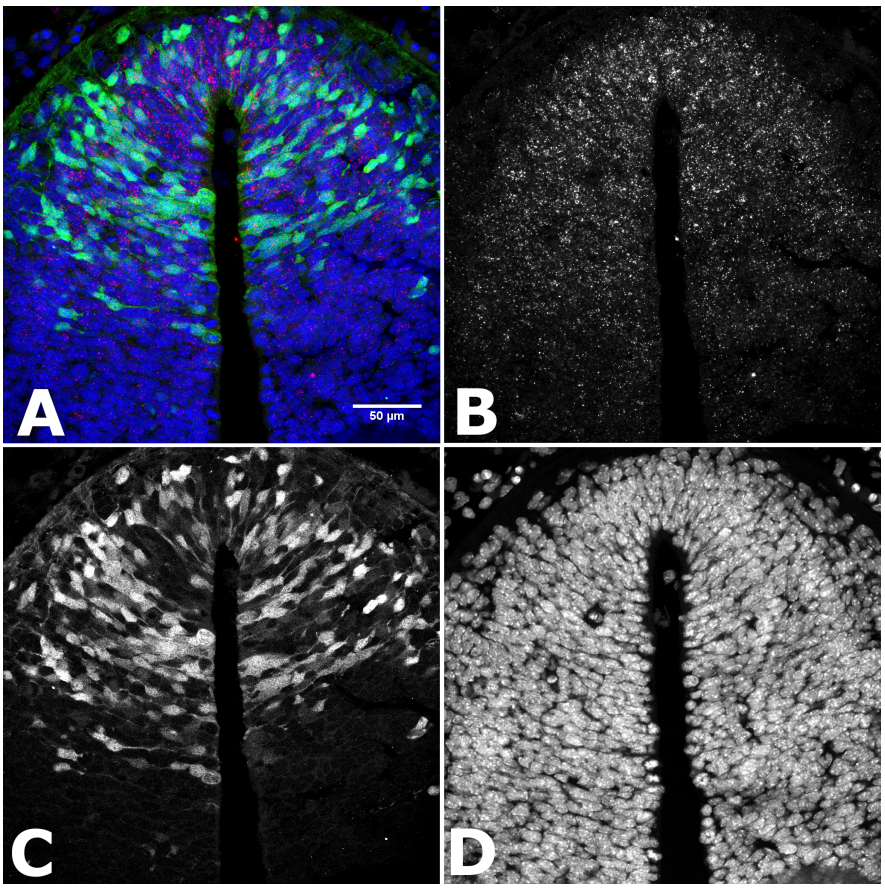


Figure 4.5: ***Channel split step to obtain monochrome images for further processing.*** *The RGB image is split into three monochrome images, representing the R(B), G(C) and B(D) channel respectively. Scale bar 50 μm.*

For images of each channel, background noise (background fluorescence intensity) was collected by cropping a small area in the image in which no tissue is present and calculating the mean signal intensity (Figure 4.6 A1, B1 and C1). Then the mean intensity value was subtracted from the raw grayscale image to gain cleaner foreground signals (Figure 4.6 A2, B2 and C2).

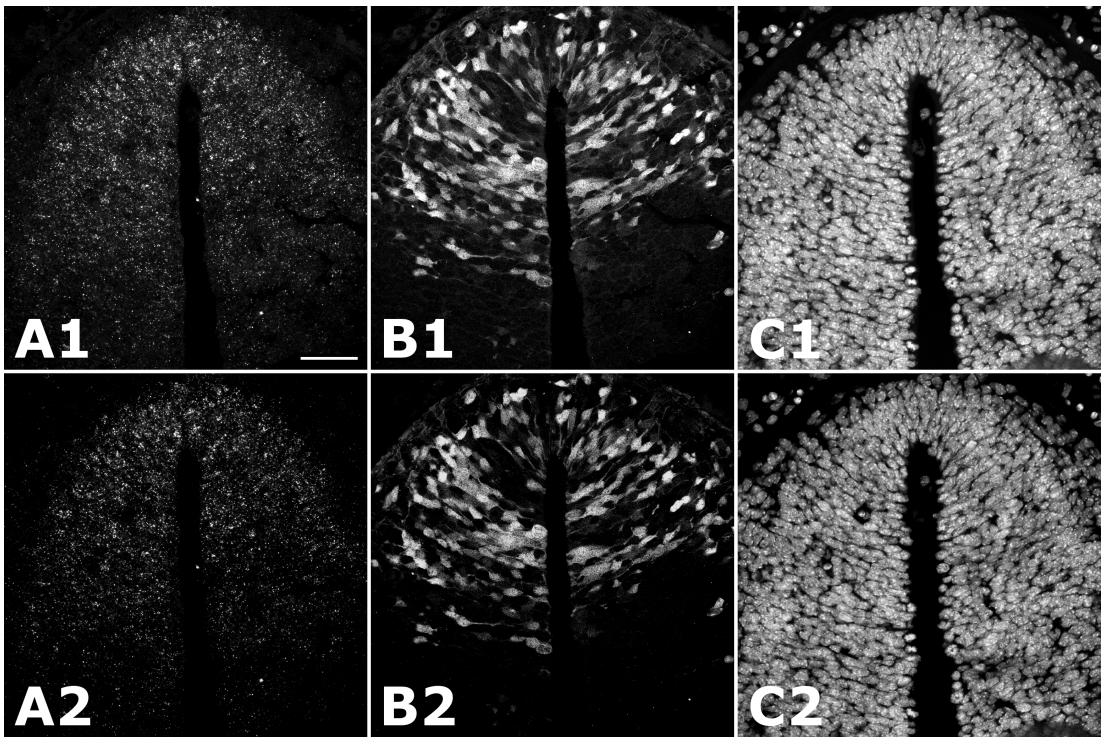


Figure 4.6: ***Background noise is removed for each channel by thresholding.*** *For each monochrome image, the background noise is collected from a small area in which no tissue is present and the mean intensity of the noise is calculated and subsequently subtracted to obtain a high signal-noise ratio image for further process. A1, B1 and C1 are raw monochrome images; A2, B2 and C2 are the result images after background subtraction. Scale bar 50 μm.*

Though the images taken were intended for specific structures, it was quite often that cells from other structures were partially included in the same image. The selection of the region of interest [2] (ROI) was used to exclude mass cells, blood vessel endothelial cells and other cells that do not belong to the structure of interest (Figure 4.7 cells outlined with dotted yellow contours).

[2]The function incorporated in my code for multiple ROI selection is created by Jonas Reber [95].

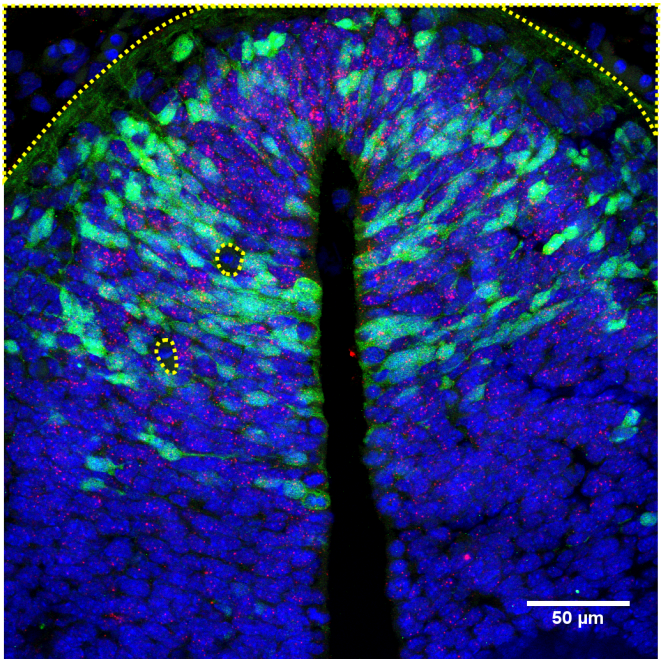


Figure 4.7: ***Mast cells, blood cells and cells from other structures are excluded from further analysis.*** *Mast cells, blood cells and other unwanted cells, outlined with yellow dotted contours, are excluded from the images in this step. Scale bar 50 µm.*

The images with background and irrelevant cells removed were then processed using CellProfiler. The advantages of using this particular software are: 1. it allows a rapid assembly of image analysis pipelines with a variety of built-in processing steps; 2. it provides a spectrum of different analysis methods and adjustment of critical parameters for each step; 3. it incorporates other software such as ImageJ; 4. it produces visualised results for each processing step and users can then adjust the parameters based on what they see to improve the result (stepwise optimisation); 5. it supports direct calculations of obtained primary data to achieve results such as the percentage of cells expressing specific markers within the whole observed population.

The pre-processed images were imported into CellProfiler and processed using a custom protocol (Table 4.1). Firstly, the cell nuclei are identified based on the DAPI staining, during which optimised thresholding strategy and declump method were used to achieve good segmentation results. Since the cell nulcei are relatively big and the cytoplasm only takes a small fraction of the cell volume, I used the segmented nuclei to approximate the whole cell in order to carry out further measurement of the GFP and *Zic4* fluorescence intensities. For each developmental stage from E11.5 to E15.5, the intensity of GFP and *Zic4* was measured at single cell levels in the cortex, prethalamus, thalamus and epithalamus. The measurements are then exported, and stored in spreadsheets. I am fully aware using this approach would lose the *Zic4* transcripts

Parameters	Values
Typical diameter of objects, in pixel units (Min, Max)	15, 40
Discard objects outside the diameter range?	Yes
Discard objects touching the border of the image?	Yes
Threshold strategy	Adaptive
Threshold method	MCT
Select the smoothing method for thresholding	Automatic
Threshold correction factor	1.0
Lower and upper bounds on the threshold	0.3, 0.9
Method to distinguish clumped objects	Shape
Method to draw dividing lines between clumped objects	Propagate
Automatically calculate size of smoothing filter for declumping?	Yes
Automatically calculate minimum allowed distance between local maxima?	Yes
Speed up by using lower-resolution image to find local maxima?	Yes
Fill holes in identified objects?	After declumping only

Table 4.1: ***Parameters used for DAPI based nuclei segmentation using CellProfiler.*** *These parameters were chosen after trying out a spectrum of combinations of settings and were used for the segmentation in this project.*

in the cytoplasm but at least the treatment was consistent between the GFP positive cells and the GFP negative cells.

The metadata obtained from MATLAB pre-processing was imported into Rstudio (RStudio, Version 1.0.136, RStudio, Inc.) and the information, such as developmental stage, section number, stack number and structure name is stored in a newly created dataframe. The data obtained from CellProfiler analysis was imported and combined into the same dataframe. The items that include any missing values were excluded from the dataframe.

In the main body the result, high power confocal images of *Zic4* FISH and GFP fluorescence immunohistochemistry are shown for each of the structures of interest, including the **cortex** (as the negative control), **epithalamus**, **prethalamus** and **thalamus** for each developmental stage I was interested in. Within each image, a fixed - size area (62 μm x 62 μm) is magnified to show more detailed staining at cellular levels. Some of the cells are randomly outlined using dashed

white contours based on the DAPI staining, which allows a closer look at the expression levels of *Zic4* transcripts and GFP.

Then the fluorescence intensities of both the *Zic4* transcripts and GFP for each cell from one sample at each stage are shown in the scatter plots. The 99th quantiles of both values obtained from the cortex were used as the cut-off lines, which divide each scatter plot into four quadrants: the bottom-left quadrant contains $Zic4^{-}GFP^{-}$ cells; the bottom-right quadrant contains $Zic4^{+}GFP^{-}$ cells; the top-right quardrant contains $Zic4^{+}GFP^{+}$ cells; the top-left quardrant contains $Zic4^{-}GFP^{+}$ cells (Figure 4.8). In order to investigate whether different structures have different cell group dynamics, I performed one-way ANOVA with post hoc Tukey tests subsequent to the logistic transformation of the proportion data using Prism 7 [3]. The arcsine square root transformation was applied instead where the data set included 0%.

The proportions of each group were calculated for each structure of interest at each studied developmental stages and a summary of the dynamic change of these populations from E11.5 to E14.5 was provided at the end of the result section. A 4 (cortex vs. epithalamus vs. prethalamus vs. thalamus) by 4 (E11.5 vs. E12.5 vs. E13.5 vs. E14.5) factorial ANOVA (two-way ANOVA) was performed to examine the main effects and interaction effects of structure and developmental stage on the proportion of each cell type using the whole data set. The summary graph in the synopsis was plotted using R and the code was included in Appendix IV. The F values and p values were recorded in the Appendix III. The p values were reported as: n.s., not significant; *, $p< 0.05$; **, $p< 0.01$; ***, $p< 0.001$; ****, $p< 0.0001$.

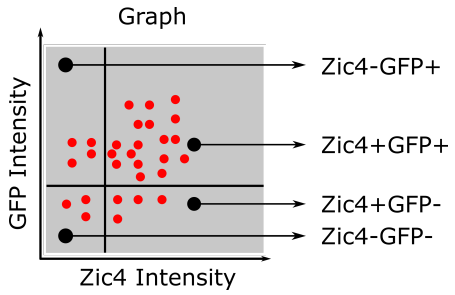


Figure 4.8: ***Schematic of four different types of cells defined by GFP and Zic4 intensities.*** *These four groups of cells are:* $Zic4^{-}GFP^{-}$, $Zic4^{+}GFP^{-}$, $Zic4^{+}GFP^{+}$ *and* $Zic4^{-}GFP^{+}$.

The terms **front** (the front of the head), **middle** (the middle of the head) and **back** (the back

[3]Since the sample size is small, I assumed that the data was not from Gaussian distributions, a prerequisite when performing the one-way ANOVA. The solution was to transform the data by arcsine square root or logistic transformation to stablise the variances and make the distributions more Gaussian. The Kruskal-Wallis nonparametric test was not chosen because it is much less powerful.

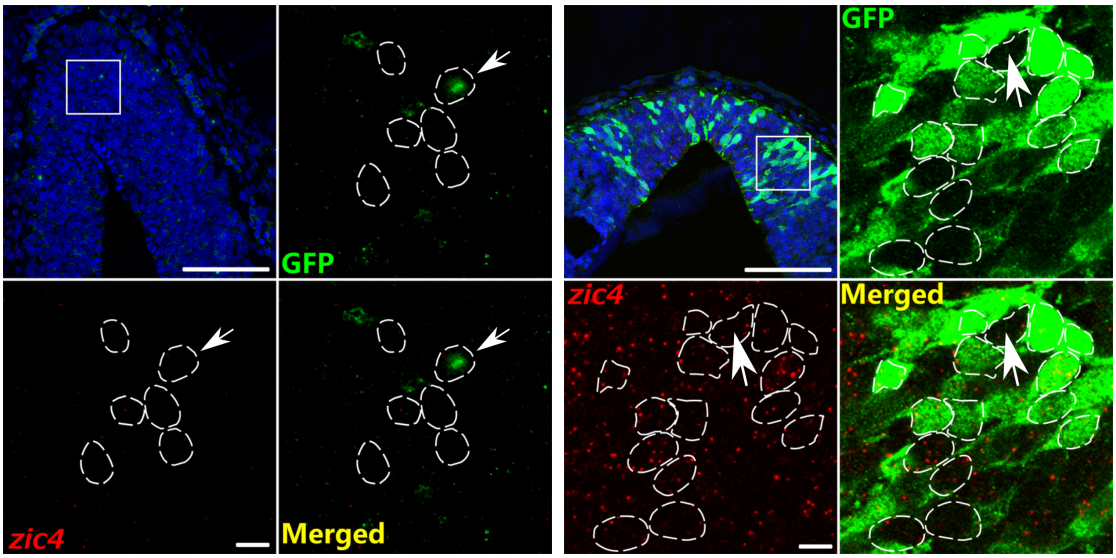
of the head) are again used to describe the relative position of the coronal sectioning planes instead of the conventional terms such as *rostral* and *caudal*. The scheme showing the defined **front-back** axis at E11.5 (Figure 3.3), E12.5 (Figure 3.6), E13.5 (Figure 3.9), E14.5 (Figure 3.12) and E15.5 (Figure 3.15) are provided in the previous chapter.

4.3.1 Quantitative analysis of *Zic4* transcript signals in *Zic4Cre*$^{+/-}$*;RCE*$^{+/-}$ mouse diencephalic cells at E11.5

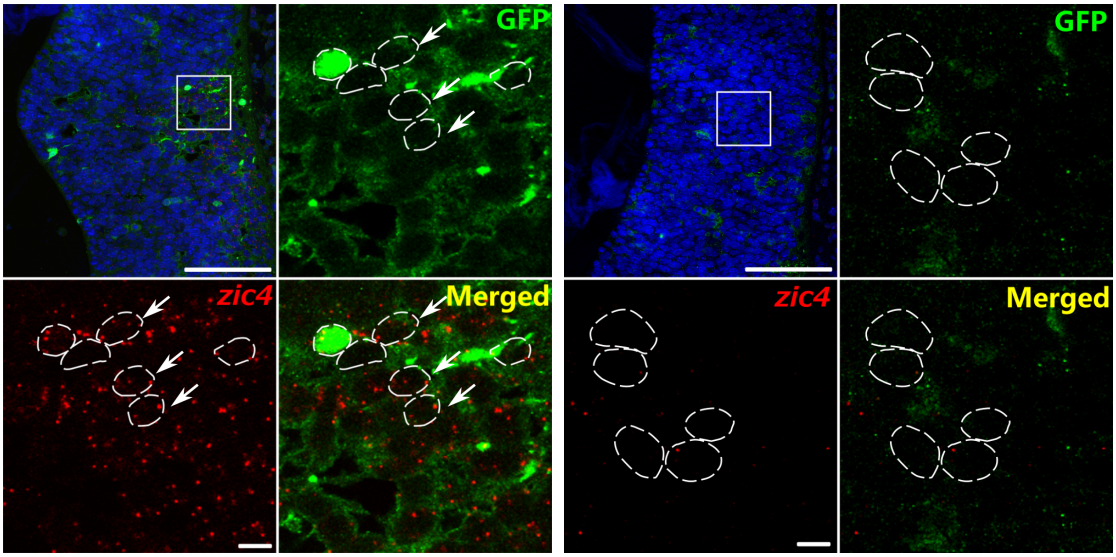
At E11.5, no *Zic4* expressing cells are seen in the cortex and only a few cortical cells show GFP signals (Figure 4.9). Almost all the cells in the epithalamus express *Zic4* and a fraction of them express GFP at various levels (Figure 4.9 (b)). Fewer GFP positive cells and noticeably higher *Zic4* expression are seen in the prethalamus (Figure 4.9 (c)) compared to the epithalamus. The expression level of GFP and *Zic4* in the thalamus (Figure 4.9 (d)) is similar to that in the cortex in the observed plane.

From the scatter plots, I can see that in the cortex (Figure 4.10 top-left) the majority of the data points are in the bottom-left quadrant. In the epithalamus and the prethalamus (Figure 4.10 bottom-left and top-right), I can see a great number of data points are in the top-right and top-left quadrants, reflecting the fact that quite a lot of cells in these two structures are Zic4^{+}GFP^{+} and Zic4^{-}GFP^{+} cells. In the thalamus, the majority of data points are in the bottom-left, which indicates there are a lot of Zic4^{-}GFP^{-} cells. A number of data points are also in the top-left quadrant, suggesting there are cells expressing GFP only at this stage.

I counted the cell number and calculated the proportion (Figure 4.11) of each cell group for all the structures of interest. It is clear that at this stage almost all the cortical cells (around 90%) are Zic4^{-}GFP^{-}. The thalamus has the second most Zic4^{-}GFP^{-} cells (around 60%). For both the epithalamus and the prethalamus, the proportions of Zic4^{-}GFP^{-} cells are under 40% and a great number of cells in the epithalamus are Zic4^{-}GFP^{+} cells (around 50%). The comparisons of proportion for each cell type between different structures showed that the proportions of Zic4^{-}GFP^{-} and Zic4^{+}GFP^{+} cells are significantly different among these structures.



(a) Cortex (b) Epithalamus



(c) Prethalamus (d) Thalamus

Figure 4.9: ***Zic4 fluorescence in situ hybridization (red) and GFP immunohistochemistry (green) on coronal sections of E11.5 mouse brain****. (a) Cortex. White arrow, positive GFP signal at cellular level resulted from staining residues. (b) Epithalamus. White arrows, GFP negative and Zic4 positive cells. (c) Prethalamus. White arrows, GFP negative and Zic4 positive cells. (d) Thalamus. High magnification images of the regions outlined by the white boxes are shown to give details at cellular level. Single channel images showing Zic4 and GFP expression respectively and merged images of both channels are provided. Scale bar: 100 μm and 10 μm.*

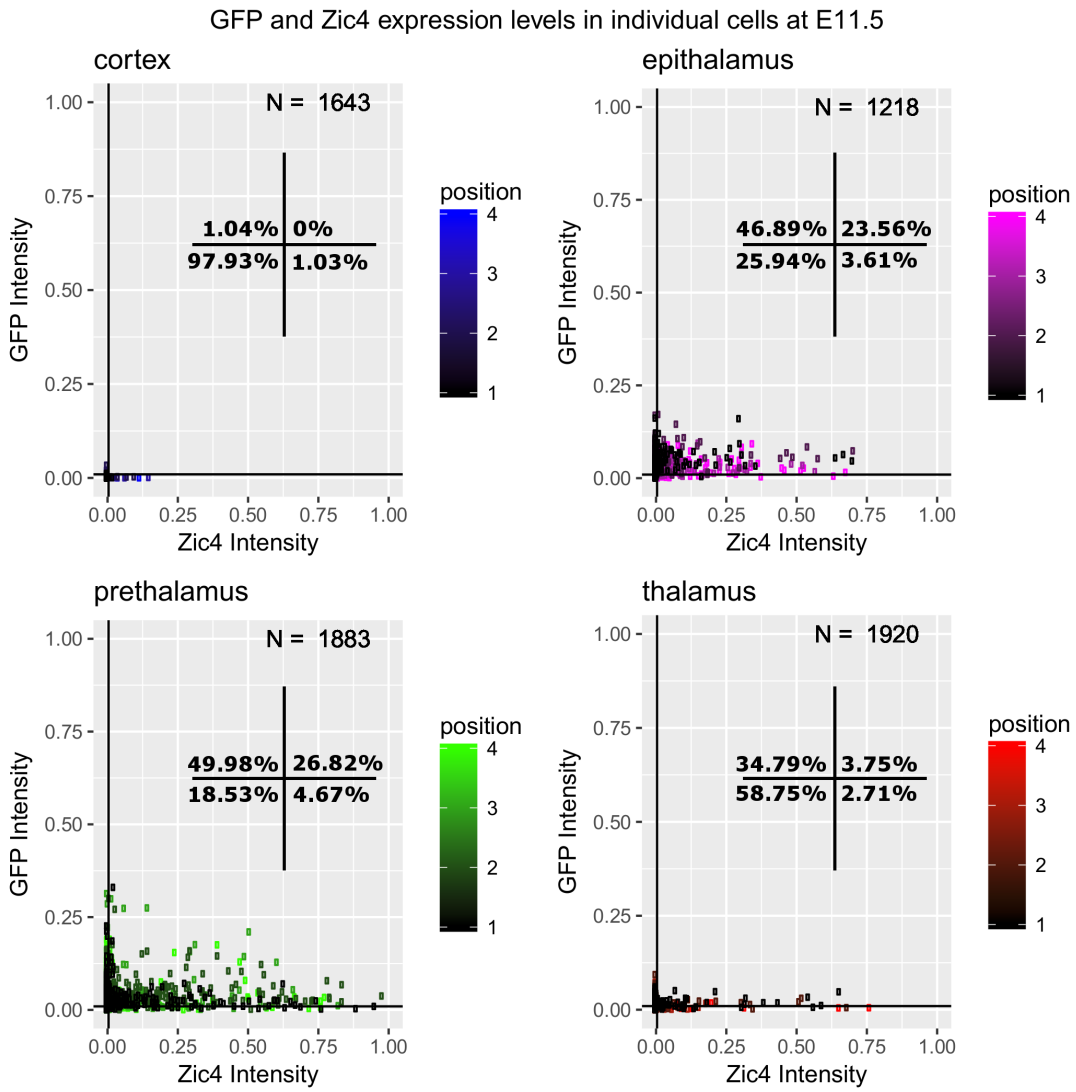


Figure 4.10: ***Quantification of GFP and Zic4 intensity at cellular levels in E11.5 cortex, epithalamus, prethalamus and thalamus.*** *The intensities of the GFP and the Zic4 stainings are measured at cellular level and plotted for each of the structure I am interested in. Each data point in the plot represents an individual cell from the specific structure and the total cell number (**N**) is also provided. The data point is colour coded according to the position of the corresponding cell along the front-back axis, with colour black to mean the very front and colours blue (for the cortex), magenta (for the epithalamus), green (for the prethalamus) and red (for the thalamus) to mean the very back. The vertical and horizontal black lines indicate the 99th quantiles of the Zic4 and GFP intensities obtained from the cortex dataset at this stage. The proportion of the data points in each quadrant is calculated and labelled for each structure.*

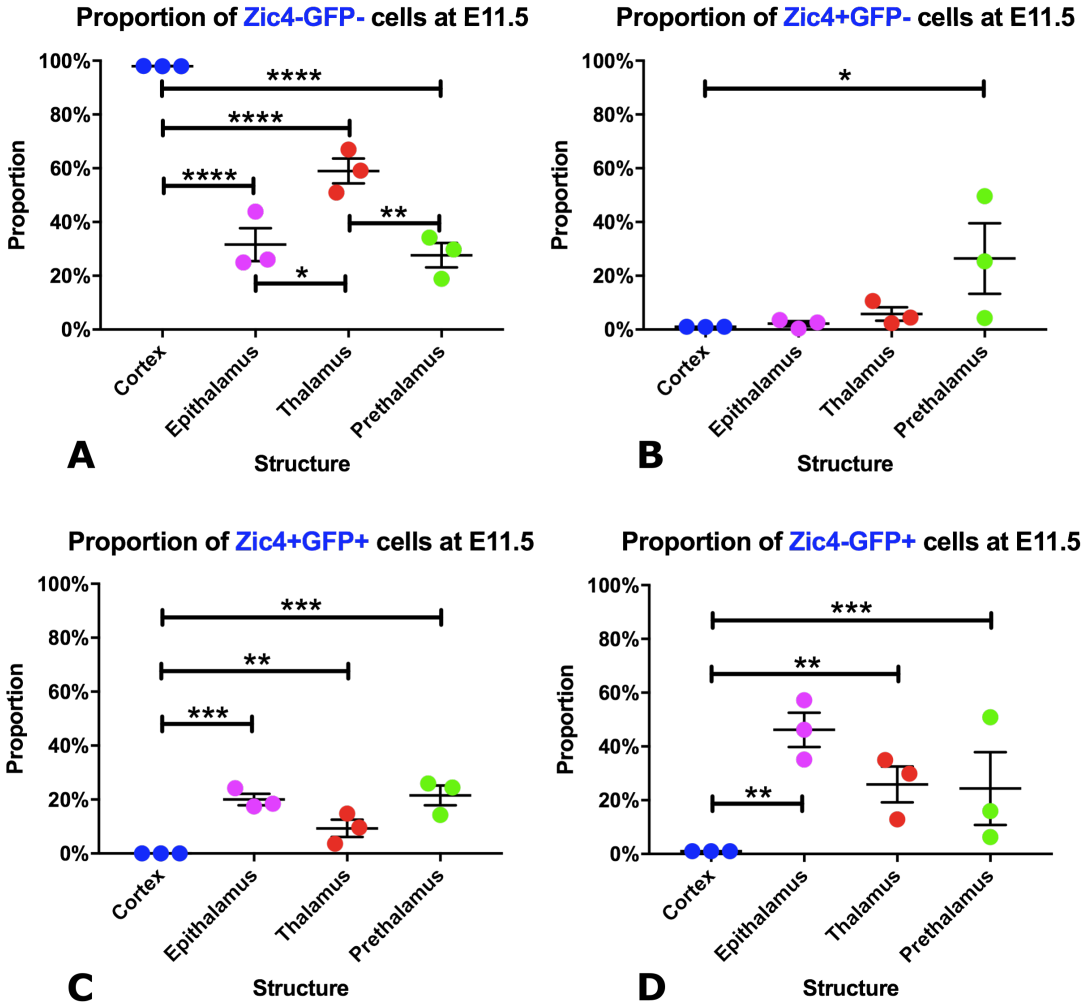


Figure 4.11: ***Mean proportion (± sem) of each cell type in E11.5 cortex, epithalamus, prethalamus and thalamus.*** *n = 3 embryos.*

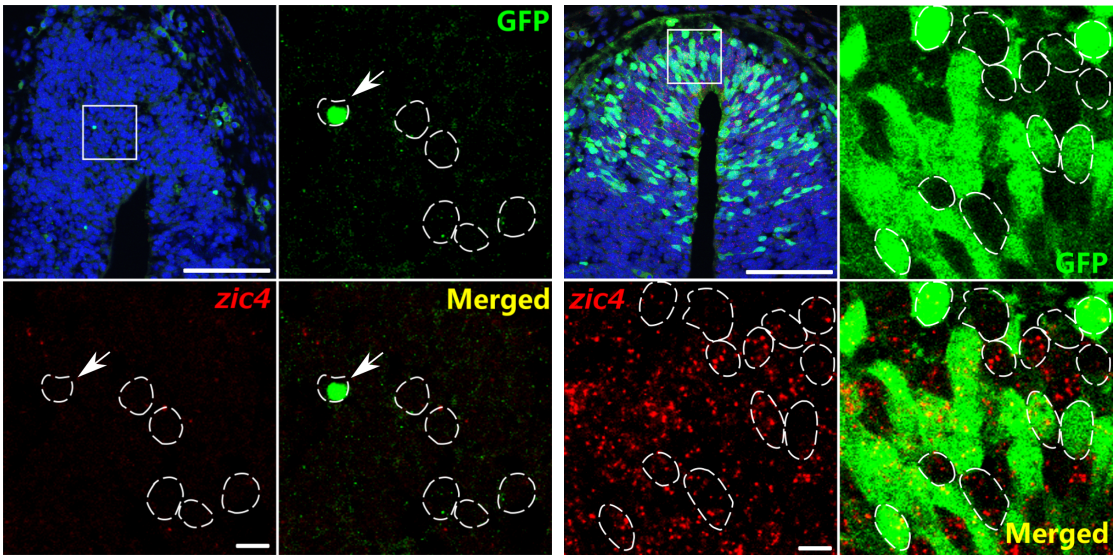
4.3.2 Quantitative analysis of *Zic4* transcript signal in *Zic4Cre*$^{+/-}$;*RCE*$^{+/-}$ mouse diencephalic cells at E12.5

The E12.5 cortex showed no expression of *Zic4* or GFP, similar to what was seen at E11.5 (Figure 4.12 (a)). In the epithalamus (Figure 4.12 (b)), the expression level of *Zic4* increased compared to E11.5 with more cells expressing GFP (Figure 4.9 (b)). More GFP positive cells are seen in the prethalamus (Figure 4.12 (c)) and not all of these cells are *Zic4* positive (Figure 4.12 (c) white arrow). The expression level of *Zic4* is lower in the thalamus (Figure 4.12 (d)) than in the prethalamus and few GFP positive cells are observed.

In the plot of the cortex, most data points occupy the bottom left quadrant (Figure 4.13 cortex). A similar trend is seen in the thalamus (Figure 4.13 thalamus) but with more data

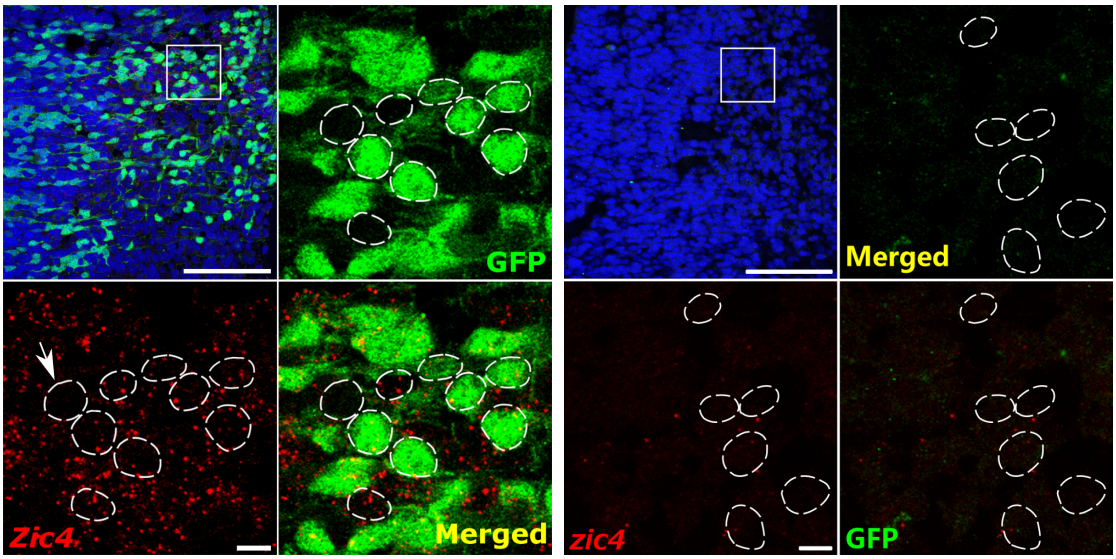
points in the top-left quadrant, representing the Zic4^{-}GFP^{+} cells. In the plots of the prethalamus and the epithalamus, a great number of points occupy the top right quadrants, indicating many cells in these two structures are Zic4^{+}GFP^{+} (Figure 4.13 prethalamus and epithalamus). It is also noticeable that cells positioned at different planes along the front-back axis in the epithalamus have distinct levels of *Zic4* and GFP expression: cells at front levels (black points) tend to have high *Zic4* and high GFP whereas cells at the back (brightly coloured points) tend to have low *Zic4* and relatively lower GFP.

Looking across different samples (Figure 4.14), I can see the general increase in Zic4^{-}GFP^{-} cell proportion in the epithalamus and the prethalamus compared to E11.5 (Figure 4.11). An increase in Zic4^{+}GFP^{-} cell proportion is seen in the epithalamus and the thalamus whereas a decrease is seen in the prethalamus. An increases in the Zic4^{+}GFP^{+} cell proportion is also observed in both the epithalamus and the thalamus.



(a) Cortex

(b) Epithalamus



(c) Prethalamus

(d) Thalamus

Figure 4.12: ***Zic4 fluorescence in situ hybridization (red) and GFP immunohistochemistry (green) on coronal sections of E12.5 mouse brain.*** *(a) Cortex. White arrows, GFP signals in cortical cells resulted from staining residue. (b) Epithalamus. (c) Prethalamus. White arrow, cell that does not express Zic4. (d) Thalamus. Scale bar: 100 μm and 10 μm.*

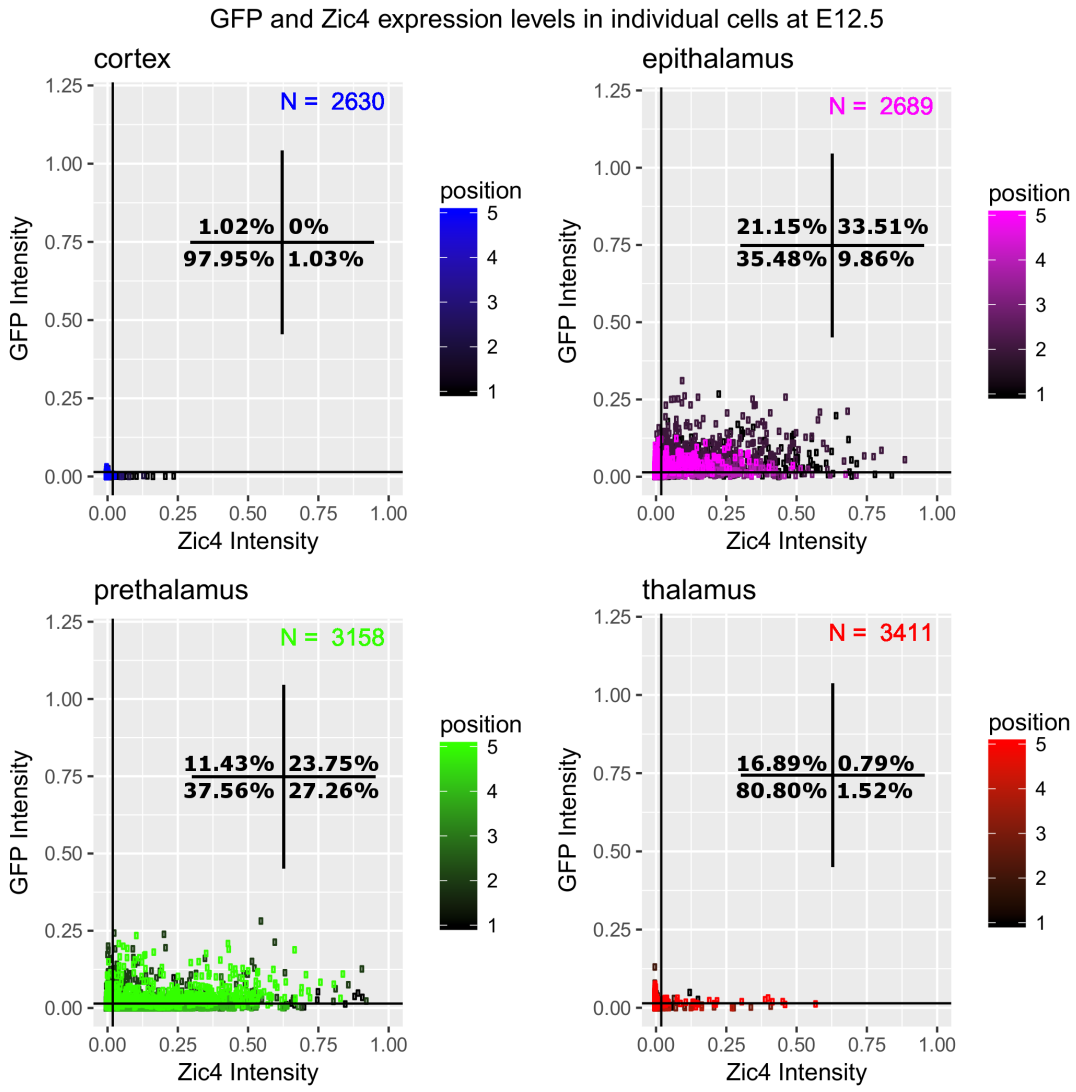


Figure 4.13: ***Quantification of GFP and Zic4 intensity at cellular levels in E12.5 cortex, epithalamus, prethalamus and thalamus.***

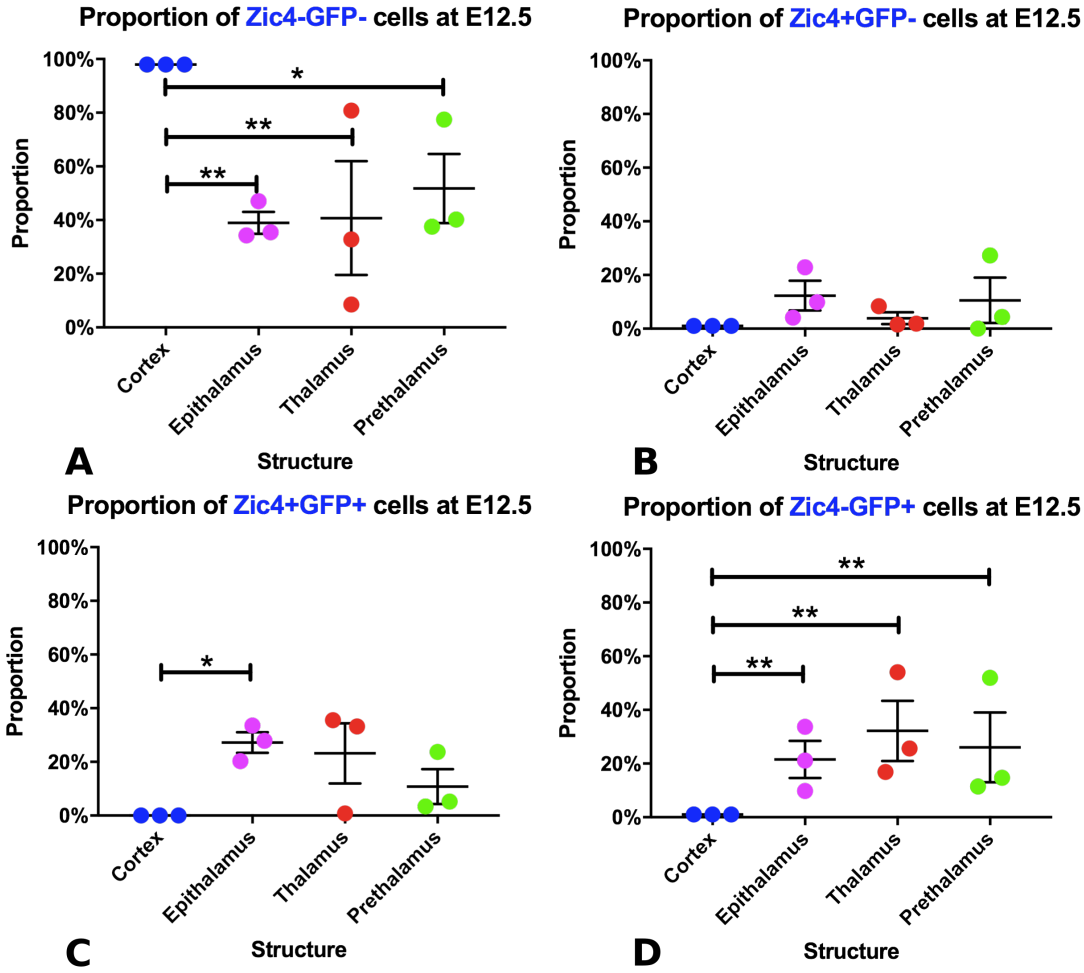


Figure 4.14: ***Comparison of cell proportion in each type in E12.5 cortex, epithalamus, prethalamus and thalamus.***

4.3.3 Quantitative analysis of *Zic4* transcript signal in *Zic4Cre*$^{+/-}$;*RCE*$^{+/-}$ mouse diencephalic cells at E13.5

At E13.5, the volume of the diencephalon significantly increases especially in the prethalamus and the thalamus. In this section, I divided the thalamus into four subregions, dorsal ventricular zone (VZ-D), ventral ventricular zone (VZ-V), dorsal mantle zone (MZ-D) and ventral mantle zone (MZ-V), and the prethalamus into two subregions, the ventricular zone (VZ) and the mantle zone (MZ) (Figure 4.15). The terms "front", "middle" and "back" are still used to depict the relative anatomical position of different sections. In this section I mainly look at images taken at the corresponding "middle" and "back" anatomical levels.

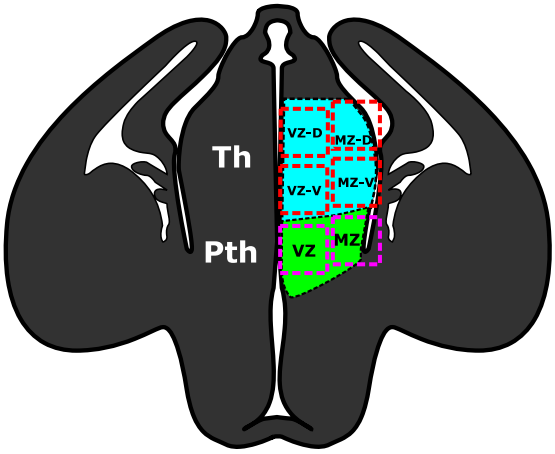
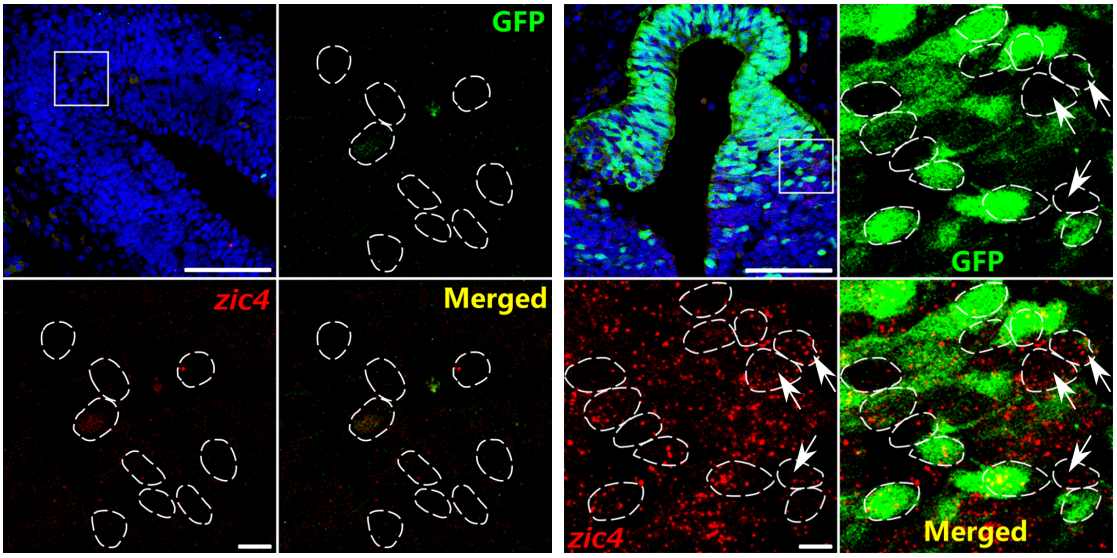


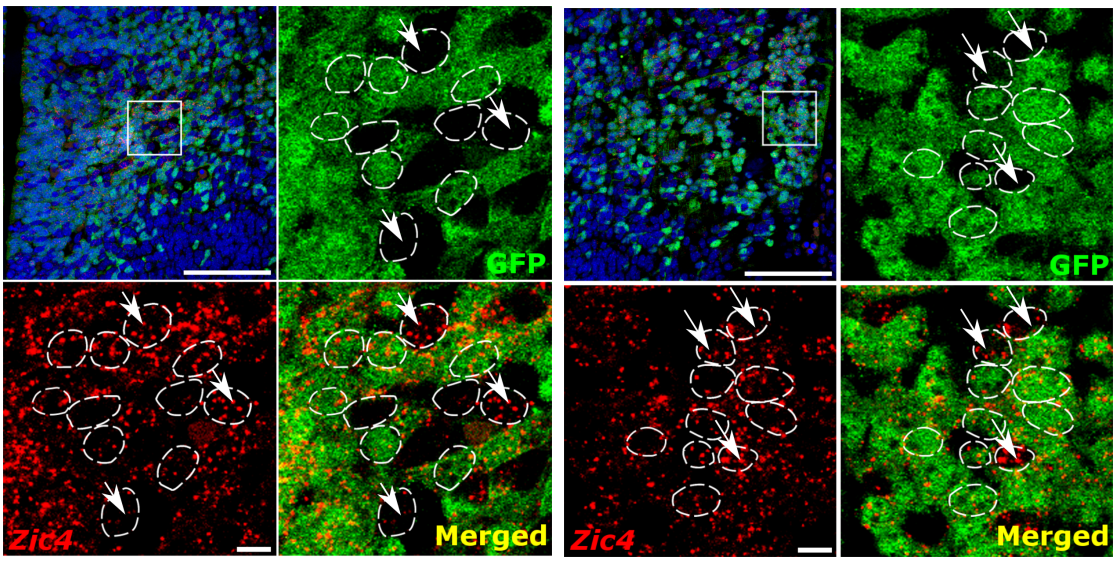
Figure 4.15: ***Schematic of subregions in the thalamus and the prethalamus.*** *Th, thalamus: VZ-D, dorsal ventricular zone; MZ-D, dorsal mantle zone; VZ-V, ventral ventricular zone; MZ-V, ventral mantle zone. Pth, prethalamus: VZ, ventricular zone; MZ, mantle zone.*



(a) Cortex (b) Epithalamus

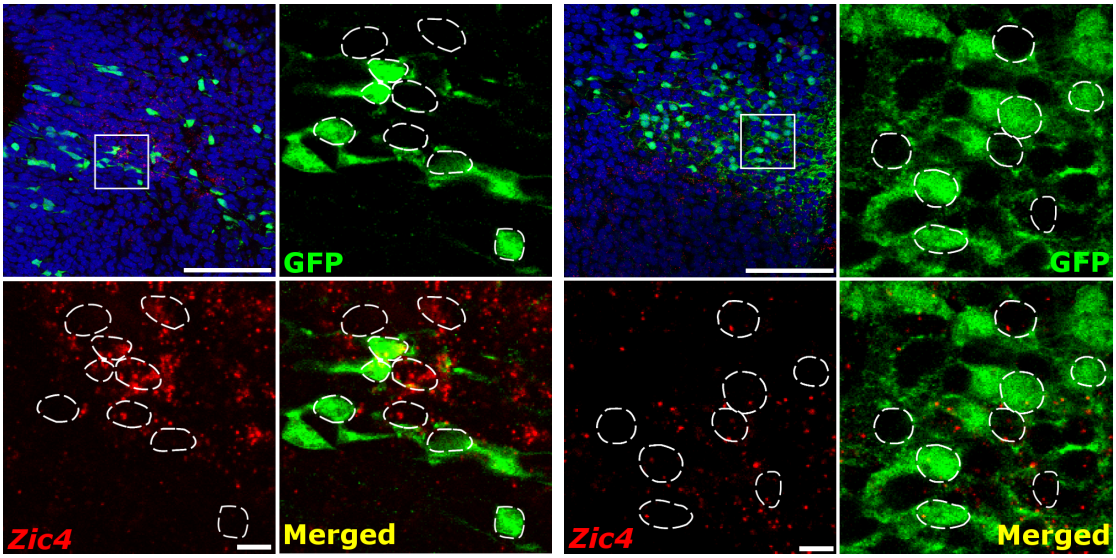
Figure 4.16: ***Zic4 fluorescence in situ hybridization (red) and GFP immunohistochemistry (green) on coronal sections of E13.5 mouse brain (cortex and epithalamus).*** *(a) Cortex. (b) Epithalamus. White arrows, Zic4^{+}GFP^{-} cells. Scale bar: 100 μm and 10 μm.*

At E13.5, the cortex (Figure 4.16 (a)) still show little expression of both the *Zic4* transcripts and the GFP. In the epithalamus, most of the cells in the loop-like developing pineal gland (Figure 4.16 (b)) are GFP positive and in the more ventral habenula area (Figure 4.16 (b) topleft, white box) more cells are $Zic4^{+}GFP^{-}$ (Figure 4.16 (b) white arrows). The *Zic4* expression level in the epithalamus is similar to what I saw at E12.5 (Figure 4.12 (b)).



(a) Prethalamus - ventricular zone - middle level

(b) Prethalamus - mantle zone - middle level

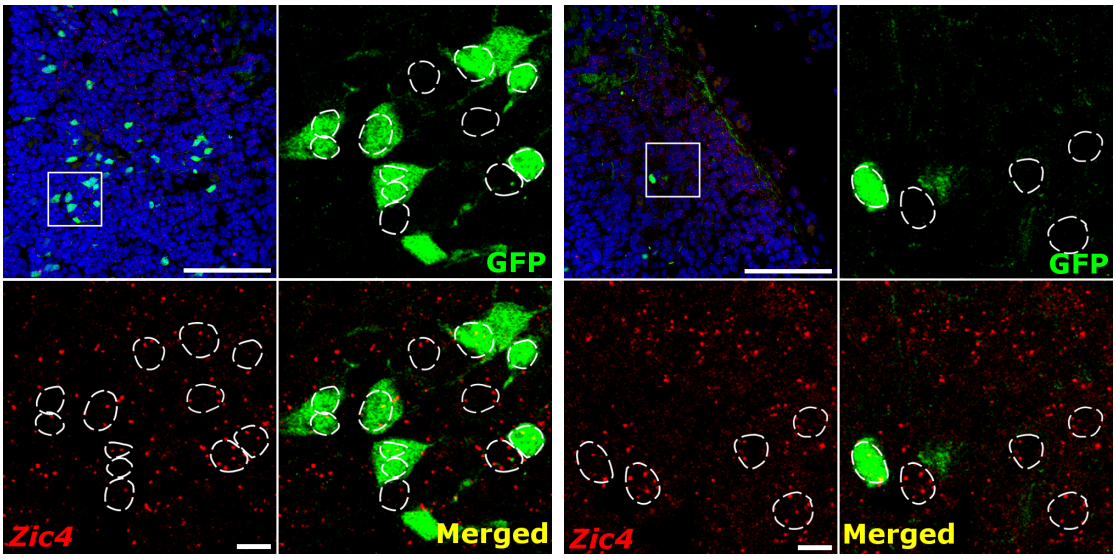


(c) Prethalamus - ventricular zone - back level

(d) Prethalamus - mantle zone - back level

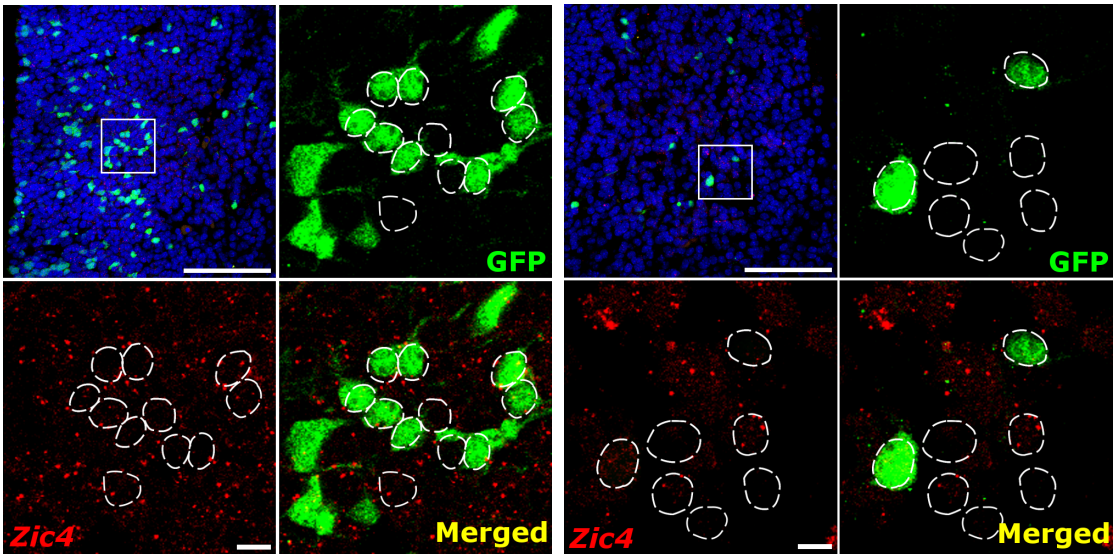
Figure 4.17: ***Zic4 fluorescence in situ hybridization (red) and GFP immunohistochemistry (green) on coronal sections of E13.5 mouse brain (prethalamus).*** *(a) Ventricular zone of the prethalamus at middle level. White arrows, Zic4^{+}GFP^{-} cells. (b) Mantle zone of the prethalamus at middle level. White arrows, Zic4^{+}GFP^{-} cells. (c) Ventricular zone of the prethalamus at back level. (d) Mantle zone of the prethalamus at back level. Scale bar: 100 μm and 10 μm.*

In E13.5 prethalamus, the expression of *Zic4* is higher at the middle level (Figure 4.17 (a) and (b)) and lower further back (Figure 4.17 (c) and (d)). At the back level, the *Zic4* expression is higher in restricted regions in the ventricular zone (Figure 4.17 (c)) and lower across the mantle zone (Figure 4.17 (d)). At the middle level, almost all GFP positive cells express *Zic4* to some extent and quite a few *Zic4* positive cells do not express GFP (Figure 4.17 (a) and (b) white arrows).



(a) Thalamus - dorsal ventricular zone - middle level

(b) Thalamus - dorsal mantle zone - middle level



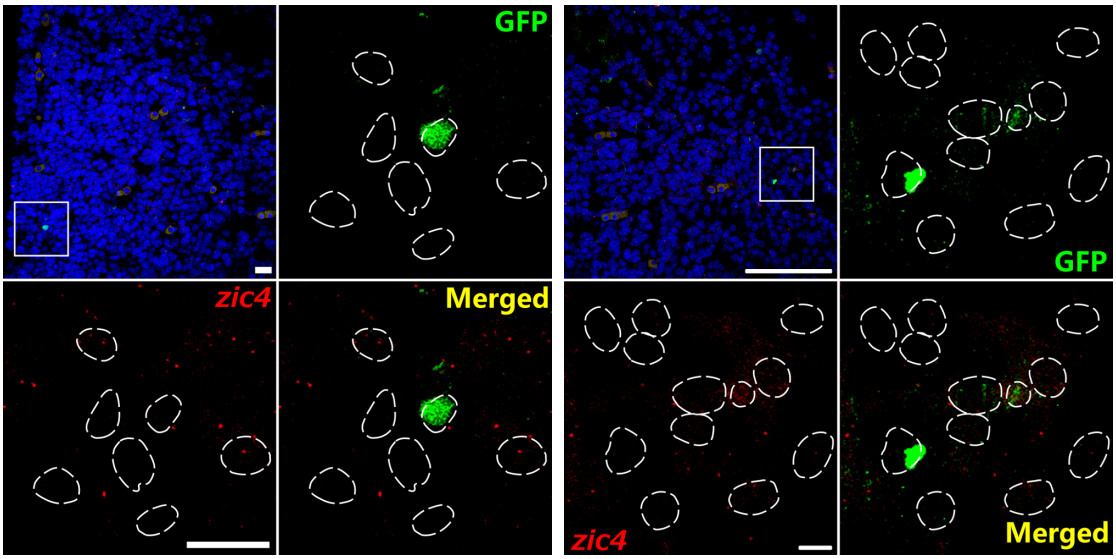
(c) Thalamus - ventral ventricular zone - middle level

(d) Thalamus - ventral mantle zone - middle level

Figure 4.18: ***Zic4 fluorescence in situ hybridization (red) and GFP immunohistochemistry (green) on coronal sections of E13.5 mouse brain (thalamus part 1).*** *(a) Thalamus - dorsal mantle zone at middle level. (b) Thalamus - ventral mantle zone at middle level. (c) Thalamus - ventral mantle zone at middle level. (d) Thalamus - ventral ventricular zone at middle level. Scale bar: 100 μm and 10 μm.*

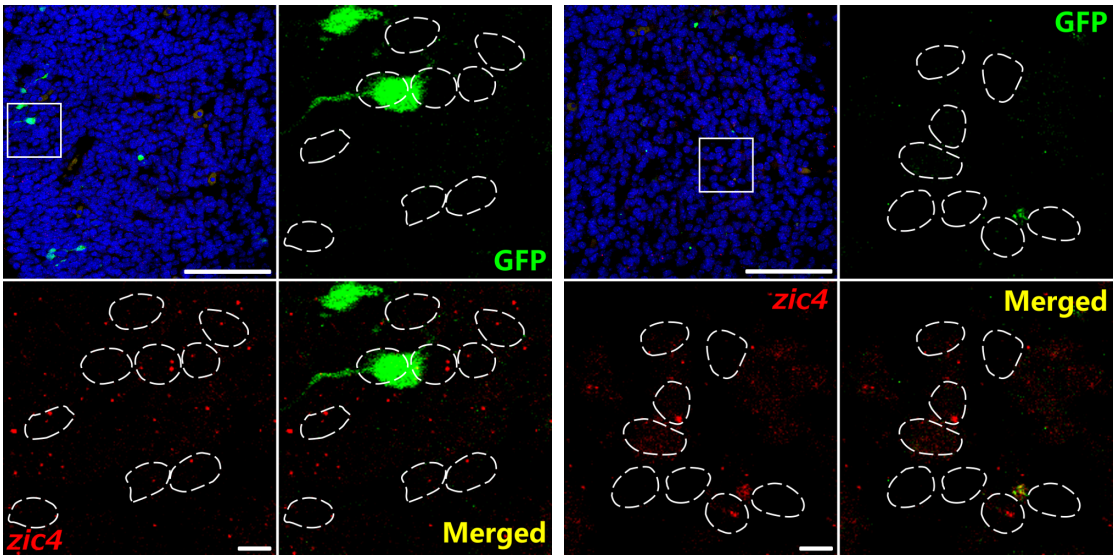
At the middle level of the E13.5 thalamus (Figure 4.18), there are much fewer GFP positive cells compared to the prethalamus at the same level and these cells are mainly in the ventricular zone (Figure 4.18 (a) and (c)). The *Zic4* expression level is much lower across the four subregions of the thalamus comparing to the prethalamus (Figure 4.17). The highest level of *Zic4* expression is seen in the ventricular zone in the ventral part of the thalamus.

At the back level, almost all the cells are GFP negative. Only a few GFP positive cells are seen in the ventricular zone (Figure 4.19 (a) and (c)). The ventral part (Figure 4.19 (c) and (d)) has a generally higher expression of *Zic4* compared to the dorsal part (Figure 4.19 (a) and (b)). A great number of $Zic4^{-}GFP^{-}$ cells are seen in the thalamus at this anatomical level.



(a) Thalamus - dorsal ventricular zone - back level

(b) Thalamus - dorsal mantle zone - back level



(c) Thalamus - ventral ventricular zone - back level

(d) Thalamus - ventral mantle zone - back level

Figure 4.19: ***Zic4 fluorescence in situ hybridization (red) and GFP immunohistochemistry (green) on coronal sections of E13.5 mouse brain (thalamus part 2).*** *(a) Thalamus - dorsal mantle zone at back level. (b) Thalamus - ventral mantle zone at back level. (c) Thalamus - ventral mantle zone at back level. (d) Thalamus - ventral ventricular zone at back level. Scale bar: 100 μm and 10 μm.*

Looking at the E13.5 scatter plots, it is clear that the cortex has little or no GFP or *Zic4* as all the data points are restricted around the origin of the plot (Figure 4.20 top-left). In the epithalamus, the thalamus and the prethalamus, most data points are in the top-right quardrant, then in the bottom-right quardrant and much fewer points are in the top-left quadrants (Figure 4.20 top-left, top-right and bottom-right).

Looking at the proportion (Figure 4.21) of different cell types, I can see: 1. In the epithalamus and the prethalamus, the proportions of $Zic4^{-}GFP^{-}$ cells decreased whereas the proportions of $Zic4^{+}GFP^{+}$ cells increased compared to E12.5 (Figure 4.14); 2. In the thalamus, the proportion of $Zic4^{+}GFP^{+}$ cells increased and the proportion of $Zic4^{+}GFP^{-}$ and $Zic4^{-}GFP^{+}$ cells decreased.

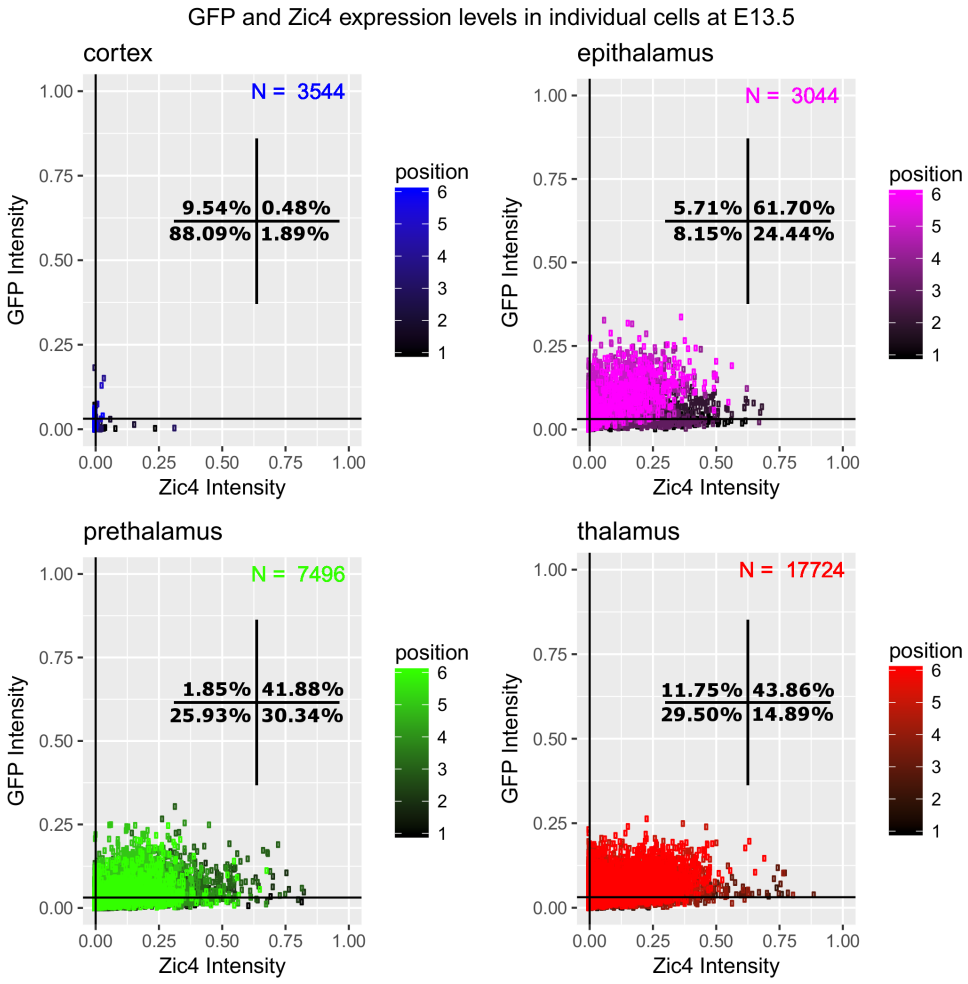


Figure 4.20: ***Comparison of cell number and proportion in each type in E13.5 cortex, epithalamus, prethalamus and thalamus.*** *(a) Cell number in each type in cortex, epithalamus, prethalamus and thalamus at E13.5. (b) Cell proportion in each type in these tissue at E13.5.*

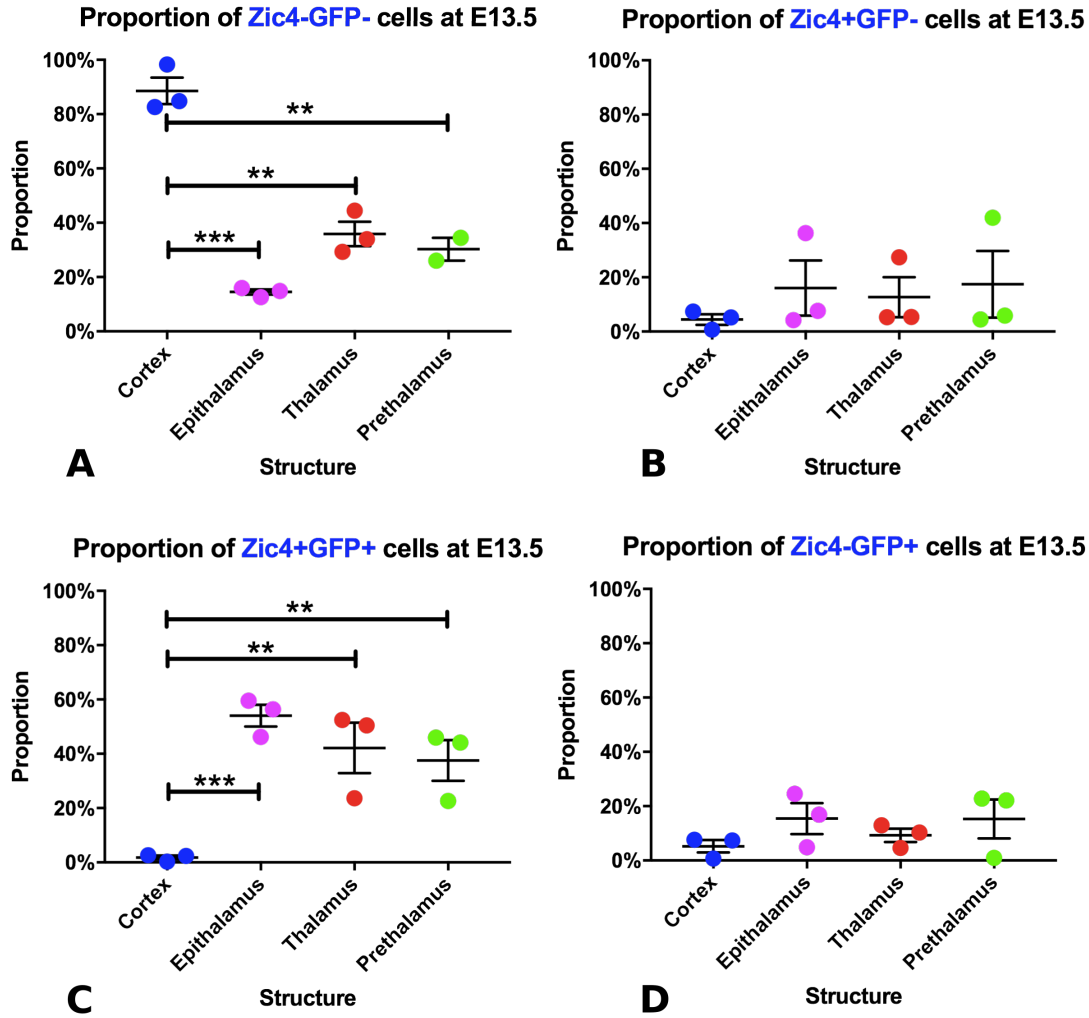
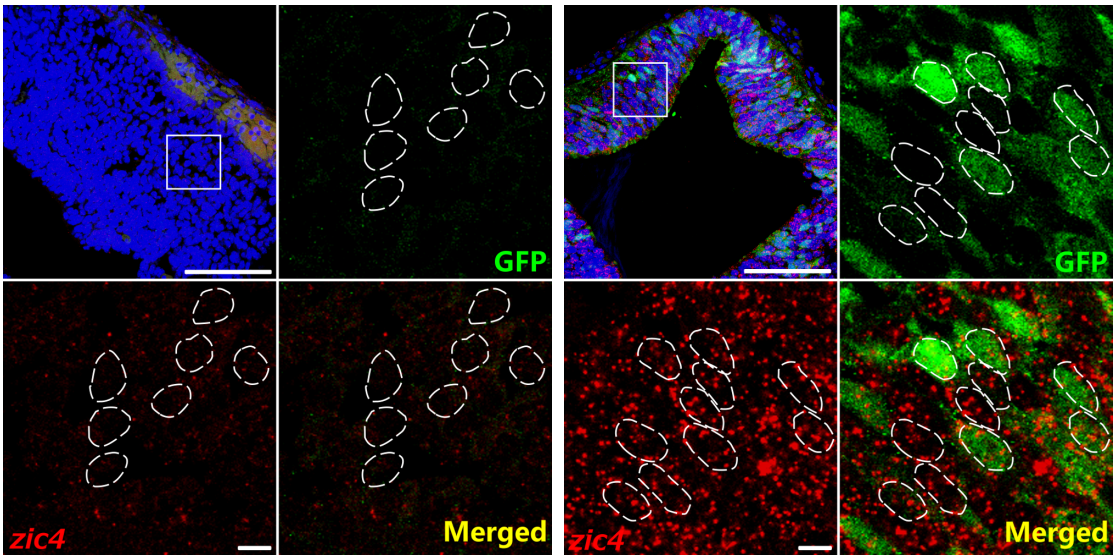


Figure 4.21: ***Comparison of cell proportion in each type in E13.5 cortex, epithalamus, prethalamus and thalamus.***

4.3.4 Quantitative analysis of *Zic4* transcript signal in *Zic4Cre*$^{+/-}$;*RCE*$^{+/-}$ mouse diencephalic cells at E14.5

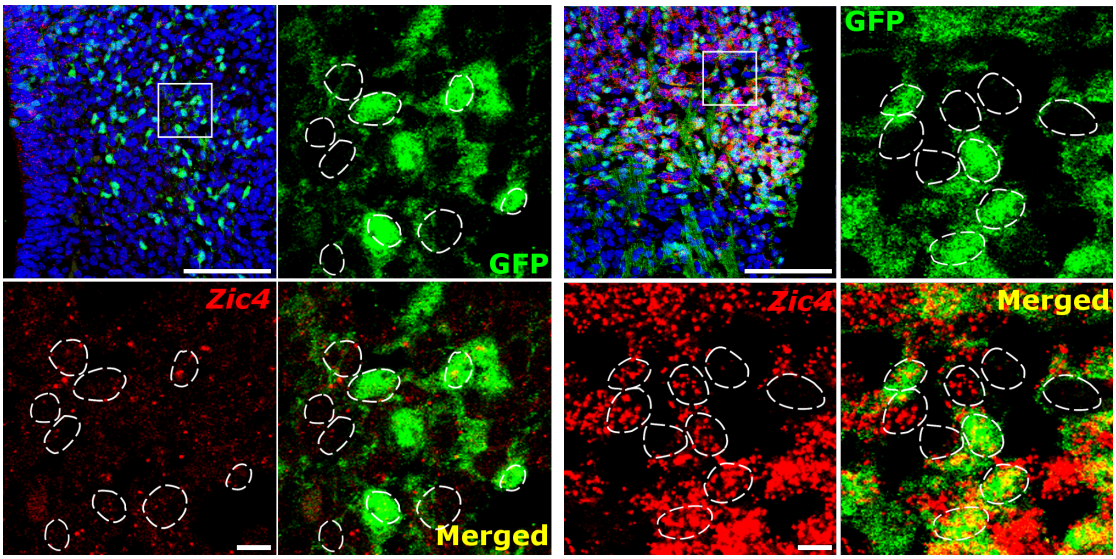
The defined regions and terminology in the E13.5 section are used for E14.5 as well. At E14.5, there is little or no expression of either *Zic4* transcripts or GFP in the cortical cells (Figure 4.22 (a)). In the epithalamus (Figure 4.22 (b)), almost all the cells are expressing *Zic4* transcripts at very high levels, some of which express various levels of GFP.



(a) Cortex (b) Epithalamus

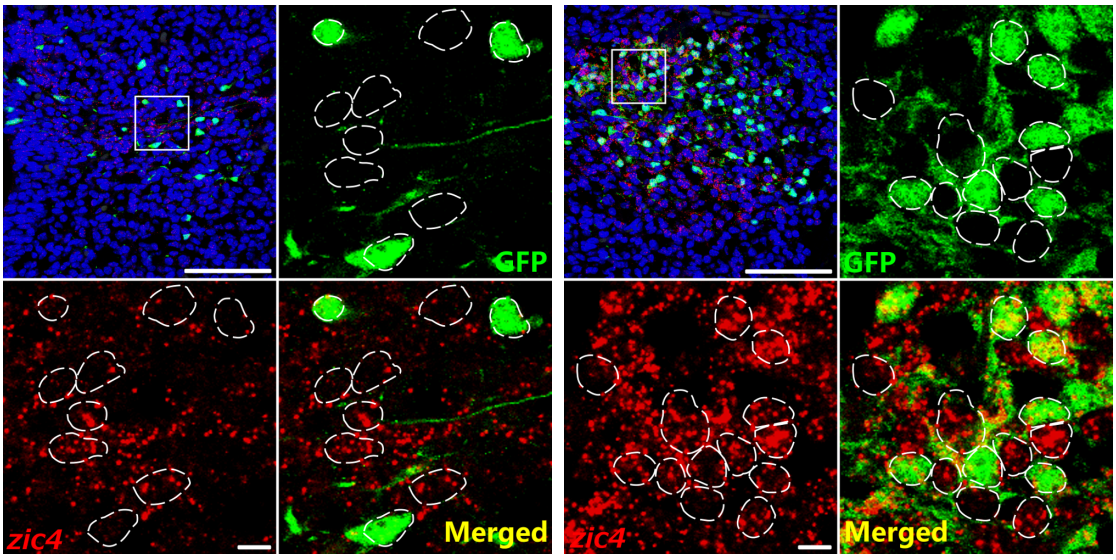
Figure 4.22: ***Zic4 fluorescence in situ hybridization (red) and GFP immunohistochemistry (green) on coronal sections of E14.5 mouse brain (cortex and epithalamus).*** *(a) Cortex. (b) Epithalamus. Scale bar: 100 μm and 10 μm.*

In E14.5 prethalamus, the mantle zones have much higher levels of *Zic4* than the ventricular zone at both the middle (Figure 4.23 (a) and (b)) and the back levels (Figure 4.23 (c) and (d)). The ventricular zone at the back level has the fewest GFP positive cells (Figure 4.23 (c)) across the two subregions at both anatomical levels. The mantle zone at both the middle and the back levels correspond to the future vLGN and ZI. Quite a lot of cells in the two regions express high levels of *Zic4* yet no GFP.



(a) Prethalamus - ventricular zone - middle level

(b) Prethalamus - mantle zone - middle level

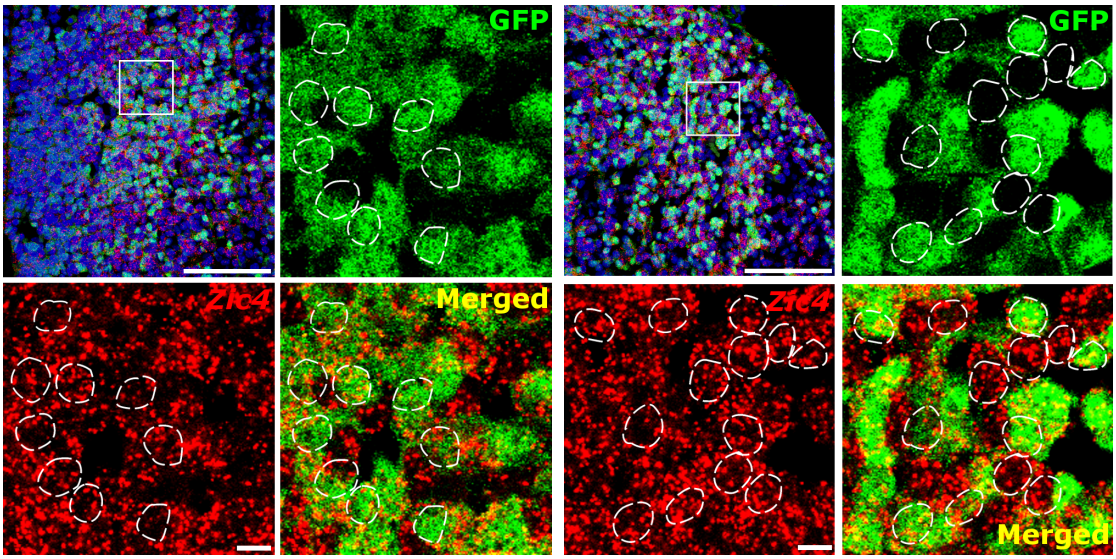


(c) Prethalamus - ventricular zone - back level

(d) Prethalamus - mantle zone - back level

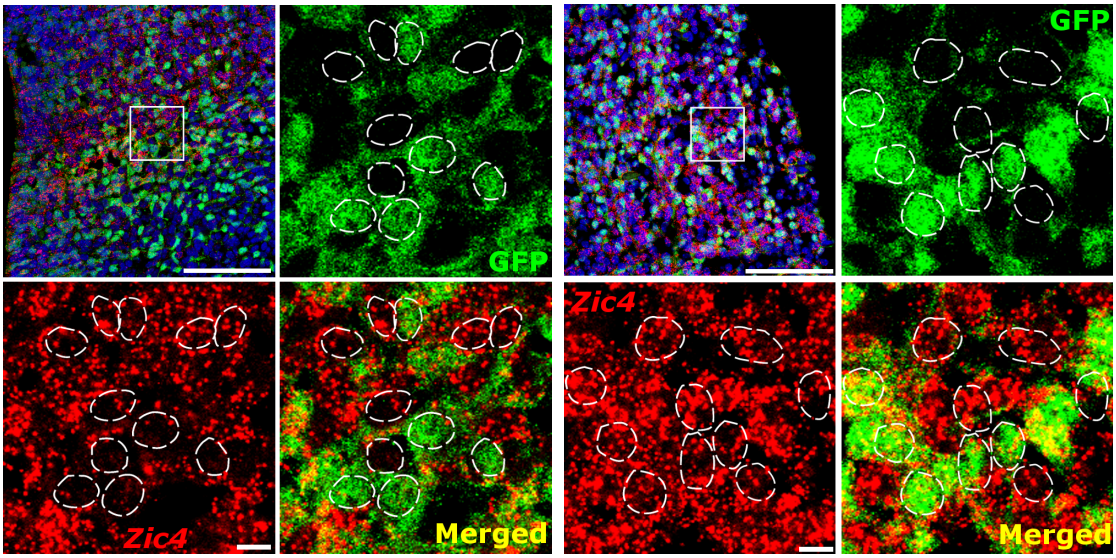
Figure 4.23: ***Zic4 fluorescence in situ hybridization (red) and GFP immunohistochemistry (green) on coronal sections of E14.5 mouse brain (prethalamus).*** *(a) Ventricular zone of the prethalamus at middle level. (b) Mantle zone of the prethalamus at middle level. (c) Ventricular zone of the prethalamus at back level. (d) Mantle zone of the prethalamus at back level. Scale bar : 100 μm and 10 μm.*

In the thalamus, higher *Zic4* expression and more GFP positive cells are seen at the middle level (Figure 4.24) than at the back level (Figure 4.25). Quite a few of cells expressing high *Zic4* and no GFP are seen in all four subregions at the middle level (Figure 4.24). At the back level (Figure 4.25), the GFP positive cells are mainly in the ventricular area. A great number of cells at this level express fair amounts of *Zic4* with little or no GFP.



(a) Thalamus - dorsal ventricular zone - middle level

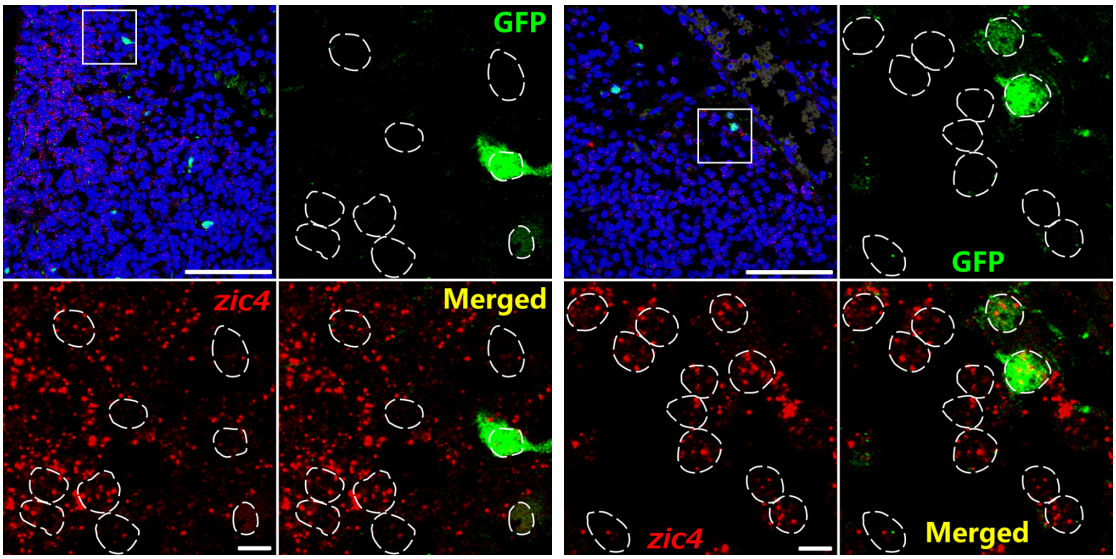
(b) Thalamus - dorsal mantle zone - middle level



(c) Thalamus - ventral ventricular zone - middle level

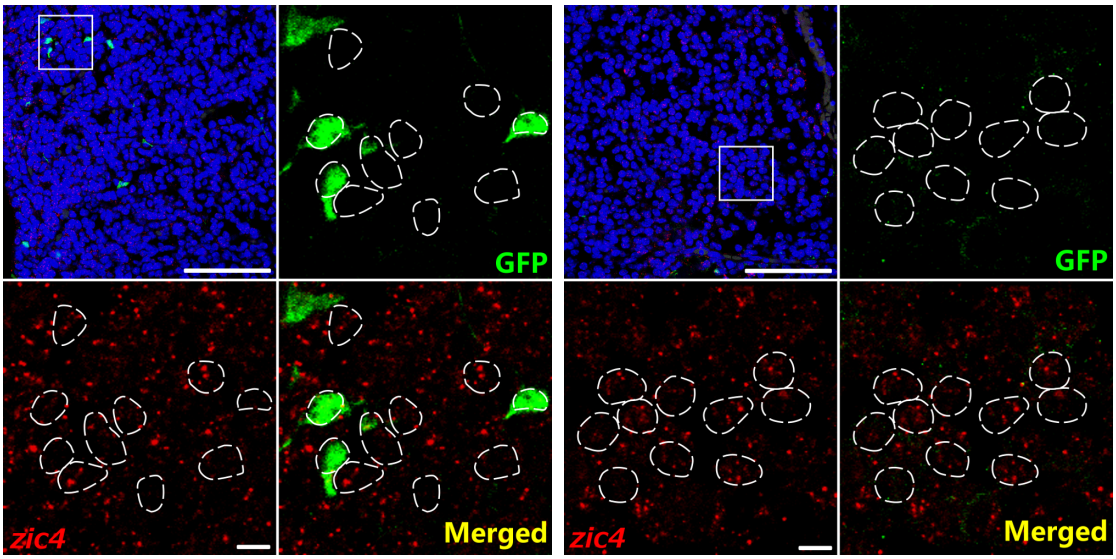
(d) Thalamus - ventral mantle zone - middle level

Figure 4.24: ***Zic4 fluorescence in situ hybridization (red) and GFP immunohistochemistry (green) on coronal sections of E14.5 mouse brain (thalamus part 2).*** *(a) Thalamus - dorsal mantle zone at middle level. (b) Thalamus - ventral mantle zone at middle level. (c) Thalamus - ventral mantle zone at middle level. (d) Thalamus - ventral ventricular zone at middle level. Scale bar: 100 μm and 10 μm.*



(a) Thalamus - dorsal ventricular zone - back level

(b) Thalamus - dorsal mantle zone - back level



(c) Thalamus - ventral ventricular zone - back level

(d) Thalamus - ventral mantle zone - back level

Figure 4.25: ***Zic4 fluorescence in situ hybridization (red) and GFP immunohistochemistry (green) on coronal sections of E14.5 mouse brain (thalamus part 2).*** *(a) Thalamus - dorsal mantle zone at back level. (b) Thalamus - ventral mantle zone at back level. (c) Thalamus - ventral mantle zone at back level. (d) Thalamus - ventral ventricular zone at back level. Scale bar: 100 μm and 10 μm.*

Looking at the summary scatter plots for the four structures of interest at E14.5 (Figure 4.26), I can see: 1. the data points in the cortex plot are crowded around the origin (Figure 4.26 top-left); 2. in the epithalamus, the data points with high GFP expression are at the back level and the ones with low GFP expression are at the front and the *Zic4* expression is similar across the front-back axis (Figure 4.26 top right); 3. in the prethalamus (Figure 4.26 bottom left), differences in GFP expression level are seen between the points representing cells at the front and the ones representing cells at the back; however, the *Zic4* expression is similar between the front and the back.

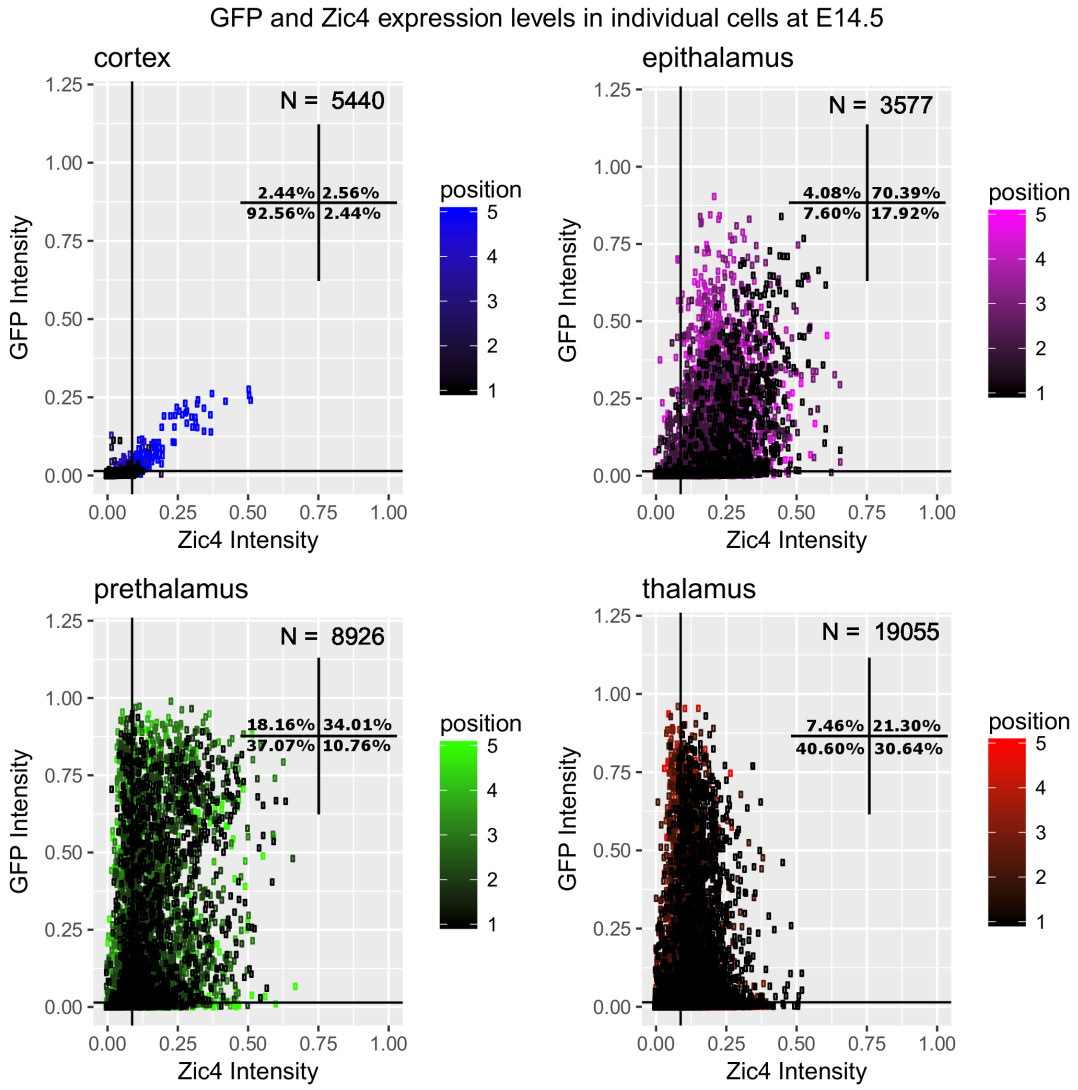


Figure 4.26: Comparison of cell number and proportion in each type in E14.5 cortex, epithalamus, prethalamus and thalamus. (a) Cell number in each type in cortex, epithalamus, prethalamus and thalamus at E14.5. (b) Cell proportion in each type in these tissue at E14.5.

Looking at the summary bar plot for cell proportion at E14.5 (Figure 4.27), I can see that:

1. decreases of Zic4^{-}GFP^{-} and Zic4^{-}GFP^{+} cell proportions and increases of Zic4^{+}GFP^{-} and Zic4^{+}GFP^{+} cell proportions in the epithalamus; 2. decreases of Zic4^{+}GFP^{+} cell proportion and increases of Zic4^{-}GFP^{-} cell proportion in the prethalamus; 3. increases of Zic4^{+}GFP^{-} and Zic4^{+}GFP^{+} cell proportions and decreases of Zic4^{-}GFP^{-} and Zic4^{+}GFP^{+} cell proportions in the thalamus. The proportions of different types of cells are significantly different amond the regions I am interested in.

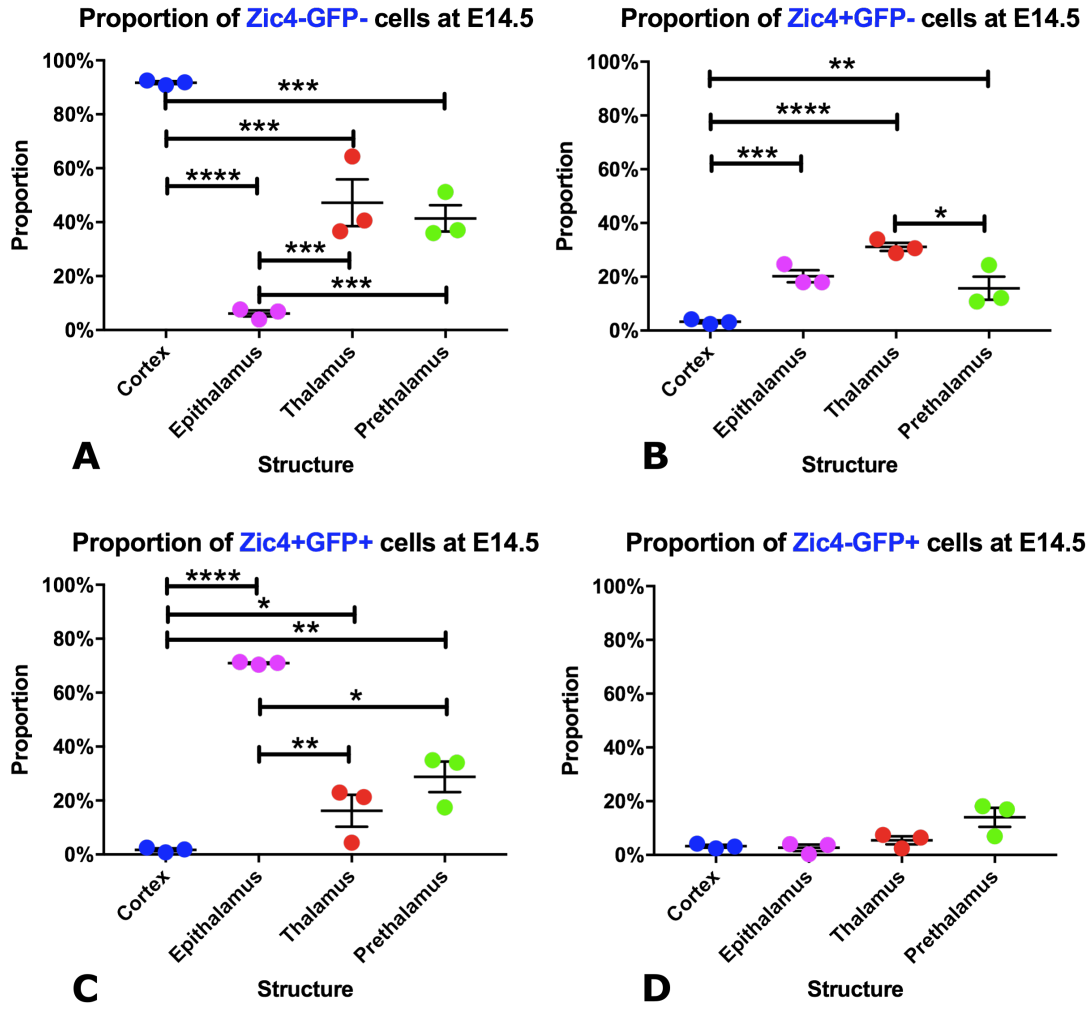


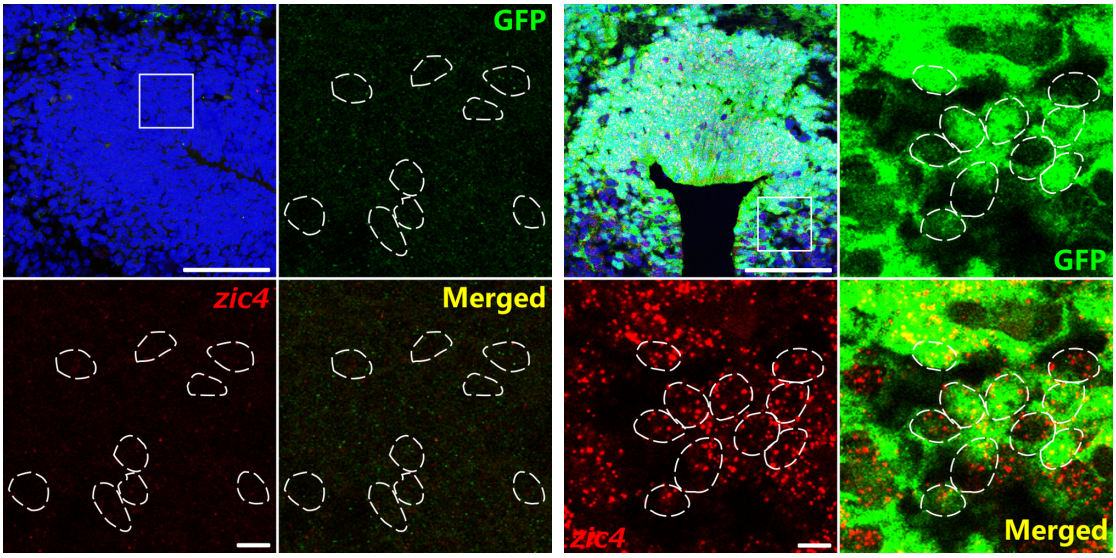
Figure 4.27: ***Comparison of cell proportion in each type in E14.5 cortex, epithalamus, prethalamus and thalamus.***

4.3.5 Quantitative analysis of *Zic4* transcript signal in *Zic4Cre*$^{+/-}$*;RCE*$^{+/-}$ mouse diencephalic cells at E15.5

At E15.5, some of the diencephalic nuclei have started to form as the volume of the diencephalon further increases. Thus, I focus on two thalamic nuclei, the VP and the dLGN, and two

prethalamic nuclei, the vLGN and the ZI/RT for our analysis.

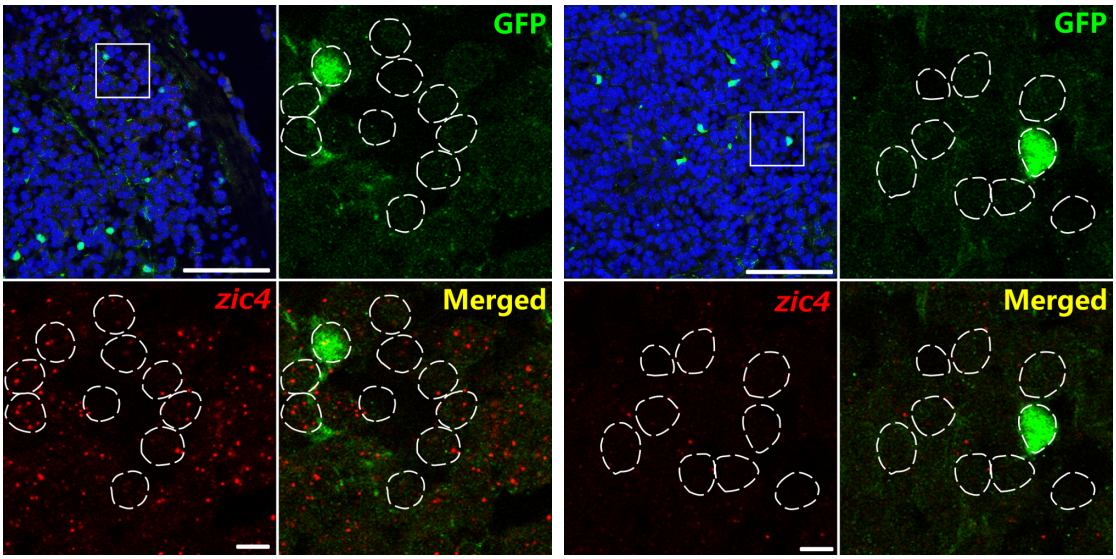
Little expression of either *Zic4* or GFP can be seen in E15.5 cortex (Figure 4.28 (a)). In the epithalamus, most cells are GFP positive and there are still a number of $Zic4^{+}GFP^{-}$ cells (Figure 4.28 (b)).



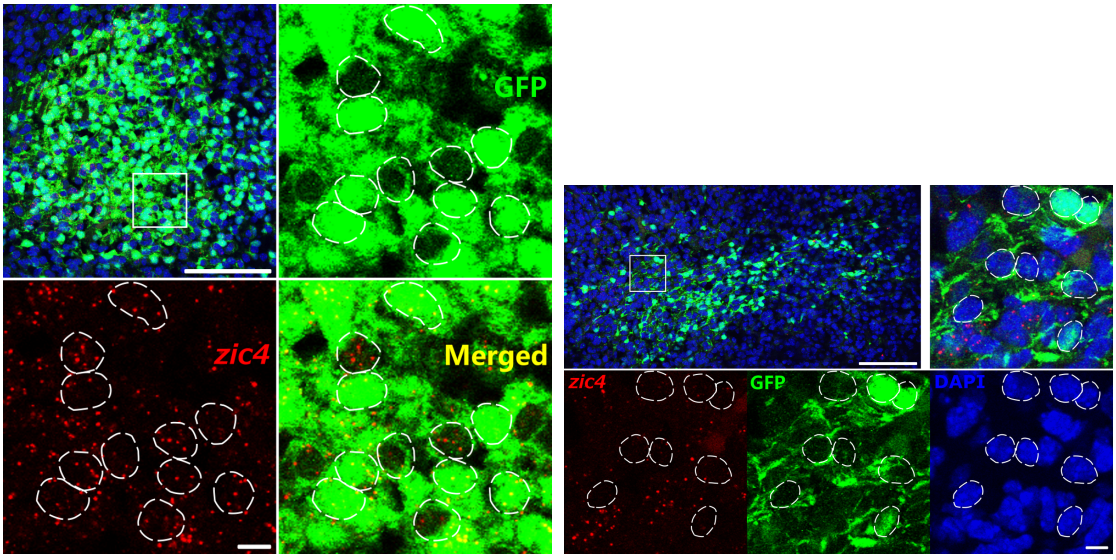
(a) Cortex (b) Epithalamus

Figure 4.28: ***Zic4 fluorescence in situ hybridization (red) and GFP immunohistochemistry (green) on coronal sections of E15.5 mouse brain (cortex and epithalamus).*** *(a) Cortex. (b) Epithalamus. Scale bar: 100 μm and 10 μm.*

A few GFP positive cells are seen in the forming dLGN (Figure 4.29 (a)) and VP (Figure 4.29 (b)). Quite a few cells in the dLGN expressing recognisable levels of *Zic4* whereas little to no *Zic4* expression is seen in the VP. On the contrary, the prethalamic nuclei vLGN (Figure 4.29 (c)) and ZI/RT (Figure 4.29 (d)) show slightly higher levels of *Zic4* and a great number of cells within these two structures are GFP positive.



(a) dLGN (b) VP



(c) vLGN (d) ZI

Figure 4.29: ***Zic4 fluorescence in situ hybridization (red) and GFP immunohistochemistry (green) on coronal sections of E15.5 mouse brain (pethalamus and thalamus).*** *(a) dLGN. (b) VP. (c) vLGN. (d) ZI. Images of higer magnification used for showing cellular level details are outlined by the white boxes. Single channel images showing* Zic4 *and GFP expression respectively and merged images of both channels are shown for the outlined area. Scale bar : 100 μm and 10 μm.*

Comparing to E14.5 (Figure 4.26), the most conspicuous change at E15.5 is that the data points representing the $Zic4^{+}GFP^{+}$ cells, which were close to the y axis at E14.5, are now close to the x axis (Figure 4.30).

Looking at the summary bar plots for all the structures at E15.5 (Figure 4.30), I can see the proportion of $Zic4^{-}GFP^{-}$ cells is increased in the epithalamus and the prethalamus and is decreased in the thalamus. I can see decreases in $Zic4^{+}GFP^{-}$ cells in all three structures. The data for the prethalamus and the thalamus are generated from specific nuclei, thus is not representative for the whole structures and I only include the plots here to keep the layout of the results consistent.

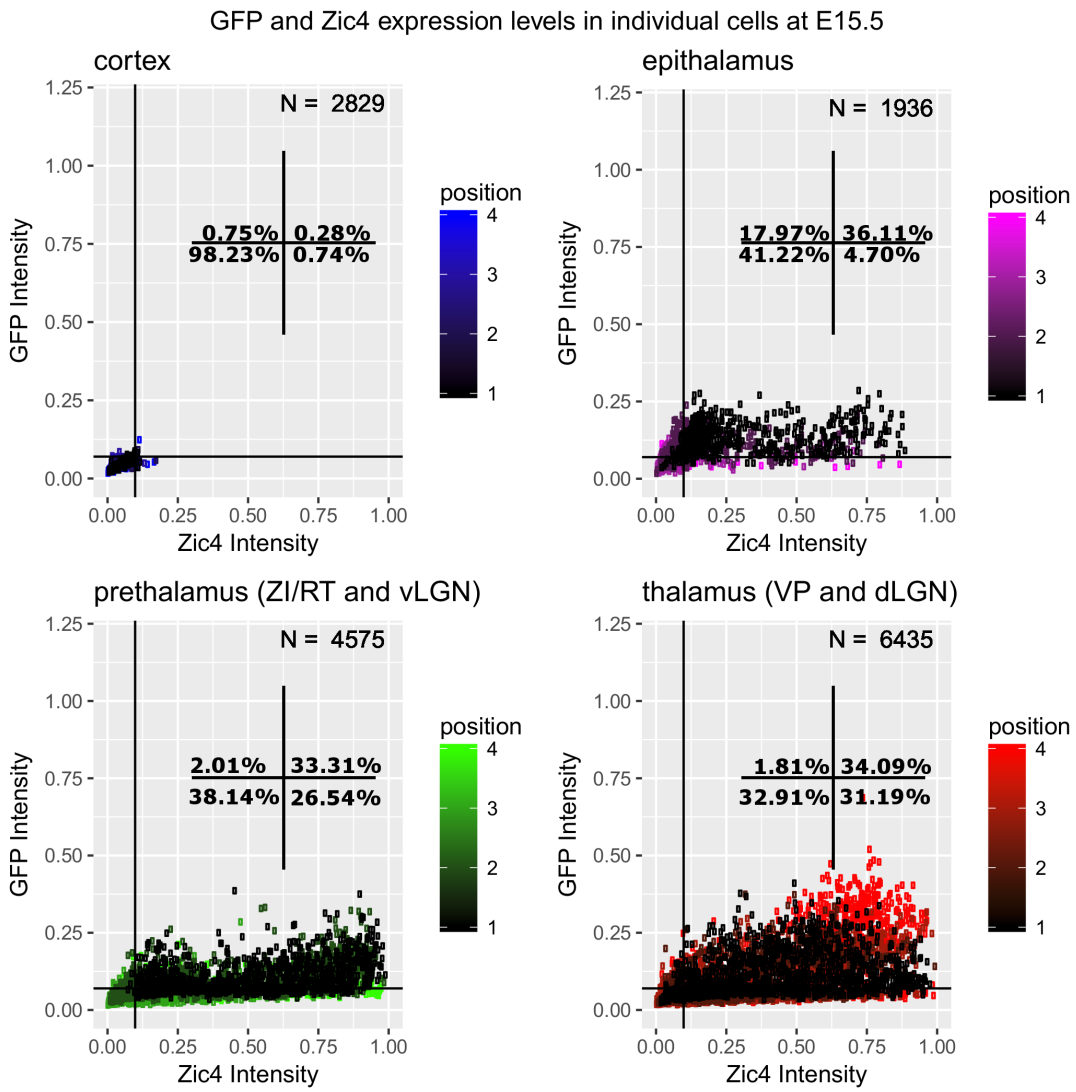


Figure 4.30: ***Comparison of cell number and proportion in each type in E15.5 cortex, epithalamus, prethalamus and thalamus.*** *(a) Cell number in each type in cortex, epithalamus, prethalamus and thalamus at E15.5. (b) Cell proportion in each type in these tissue at E15.5.*

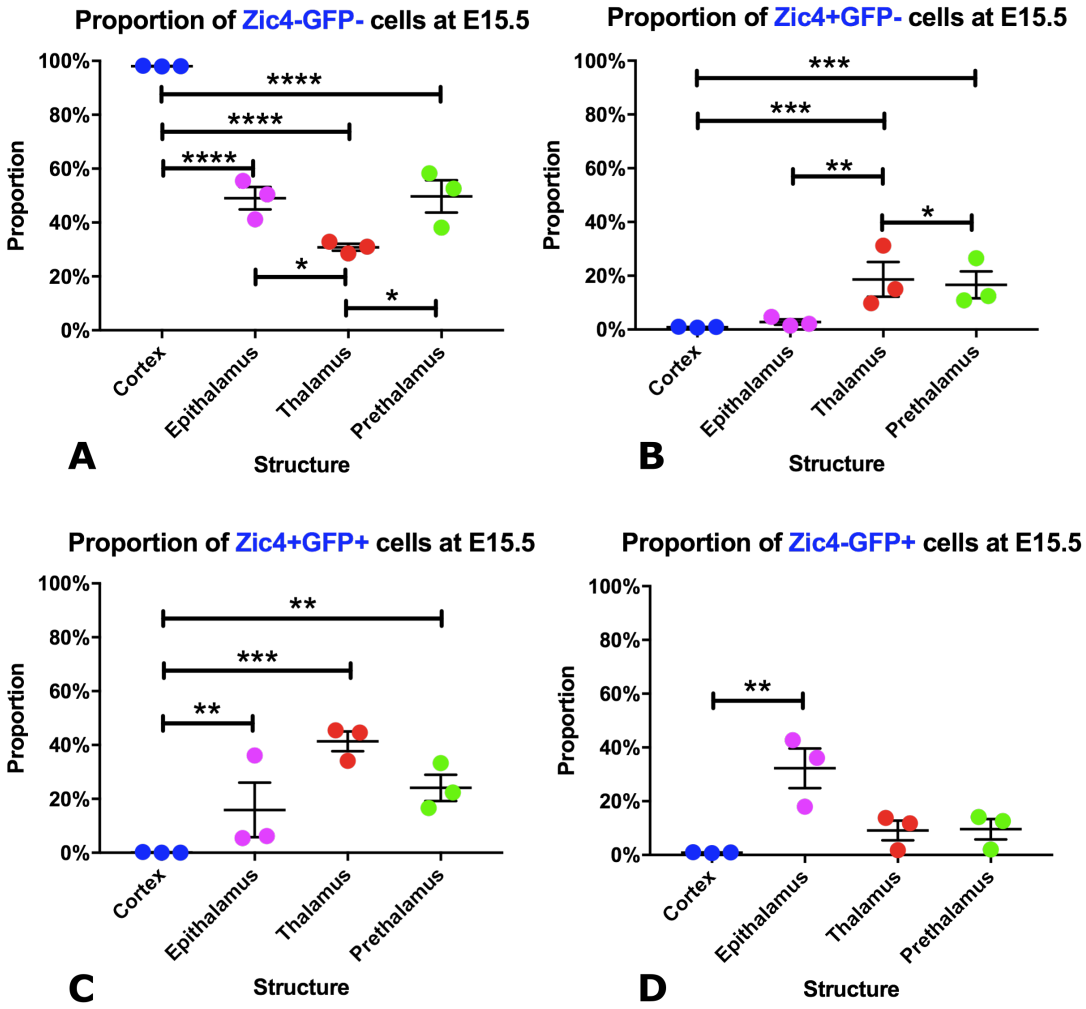


Figure 4.31: ***Comparison of cell proportion in each type in E15.5 cortex, epithalamus, prethalamus and thalamus.***

4.4 Synopsis

In this section, I provide a brief summary of the main findings from the quantitative studies of the *Zic4* transcripts and the GFP expression. The cell proportion data of each cell type from E11.5 to E14.5 are replotted (Figure 4.32) to provide a big picutre of how the *Zic4* lineage emerges and grows through time. The data obtained at E15.5 is excluded from this plot because the data is not representative for whole structures.

In the cortex, the proportion of $Zic4^{-}GFP^{-}$ cells is above 75% and the proportions of other types of cells are extremely low. In the epithalamus, the proportions of $Zic4^{-}GFP^{-}$ and $Zic4^{+}GFP^{+}$ cells decrease from E11.5 to E14.5 whereas the proportions of $Zic4^{+}GFP^{-}$ and $Zic4^{+}GFP^{+}$ cells increase. In the prethalamus, the proportions of $Zic4^{-}GFP^{-}$ and $Zic4^{+}GFP^{+}$ cells increase from

E11.5 to E12.5, decrease from E12.5 to E13.5, then increase again from E13.5 to E14.5. In the thalamus, the proportion of $Zic4^{-}GFP^{-}$ cells decrease from E11.5 to E13.5 and increases afterwards; the proportion of $Zic4^{+}GFP^{-}$ cells continuously increase from E11.5 to E14.5; the proportion of $Zic4^{+}GFP^{+}$ cells increases from E11.5 to E13.5 and then decreases from E13.5 to E14.5; the proportion of $Zic4^{-}GFP^{-}$ cells increases slightly from E11.5 to E12.5 and then decreases from E12.5 onwards.

The analysis of the whole data set revealed that both the structure and the developmental stage have significant main effects on the proportion of the four types of cells, which suggests the expression of *Zic4* and the Cre activity are structure and developmental stage specific.

As to answer the questions I asked at the beginning of this project, I think that: 1. the activation of the GFP reporter is indirectly associated with the expression level of the *Zic4* gene but the required threshold of the Cre activity regulated by the *Zic4* transcription varies among individual *Zic4* lineage cells; 2. most *Zic4* lineage cells eventually complete the transition from $Zic4^{+}GFP^{+}$ to $Zic4^{-}GFP^{+}$ and high levels of *Zic4* expression are maintained in the cells where its function is required; 3. the non-*Zic4* lineage cells born in the prethalamus and thalamus make the proportions of different types of cells oscillate.

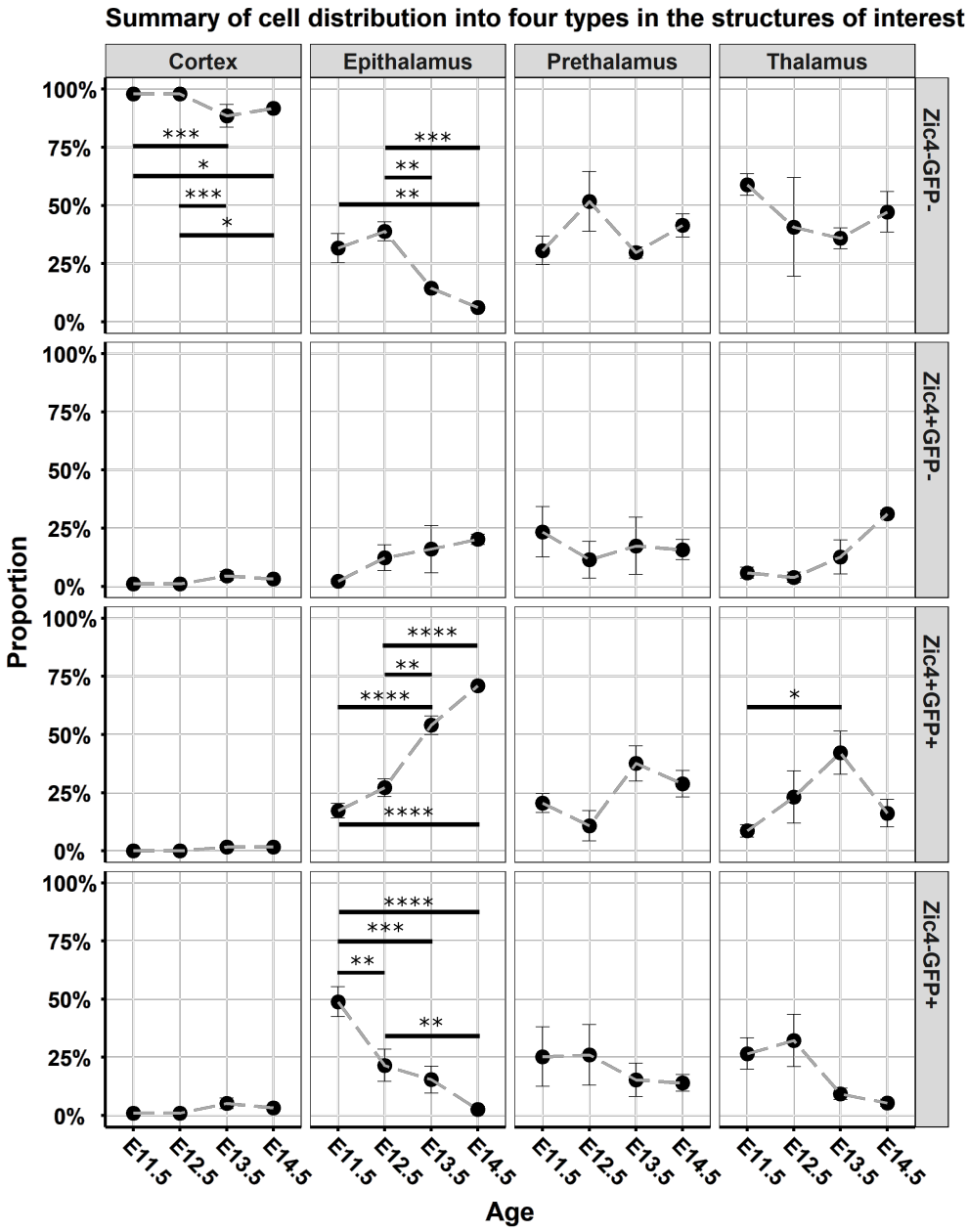


Figure 4.32: ***Proportion change of each cell type in all the structures from E11.5 to E14.5.*** *n = 3 embryos.*

4.5 Discussion

4.5.1 Other available FISH techniques

The more recent single molecule *in situ hybridisation* (smFISH) allows direct counting of mRNA molecules under a microscope. The mechanism is that individual anti-sense RNA probe is designed to bear a single fluorophore, which then binds to the mRNA of interest. When examined under the microscope, the intensity of the fluorescence of these probes can be used as a readout of the number of mRNAs.

In an earlier version of this technique, the oligodeoxynucleotide probes that recognize β-actin mRNA are synthesised with five fluorochromes for each molecule and the fluorescence emitted by a single probe is calibrated accordingly [109]. Multi-coloured smFISH allows the analysis of several different transcripts simultaneously, which is particularly useful for studying genes within the same signaling pathway. Combining smFISH with fluorescent immuno, I can investigate the association between transcription and translation levels and cellular location of mRNA and proteins in individual cells.

In this project, I do not need the exact number or the location of the *Zic4* mRNA molecules in the *Zic4* lineage cells, thus I did not use smFISH.

4.5.2 Pros and cons in using computational image analysis for this project

The aim of this project is to investigate the expression levels of the endogenous *Zic4* transcripts and the GFP reporter in the *Zic4* cell lineage in the developing diencephalon. I looked at the expression levels of these two molecules by measuring their fluorescence intensities at cellular levels in the cortex, the epithalamus, the prethalamus and the thalamus. Considering the number of cells within each structure increases as development proceeds, manually measuring the fluorescence intensity is not feasible, which is the retionale behind the computational methodology used in this project. The most powerful and undeniably advantageous feature of computational image analysis is that it is very fast, which allows high throughput analysis. It is also very consistent once the protocols are determined and it nicely avoids any bias that can be generated by human operations.

In order to perform an effcient analysis for my datasets, I tried ImageJ, MATLAB and CellProfiler and finally settled on CellProfiler. The advantage of using ImageJ is that there are a lot of plugins written for ImageJ by a lot of people for all kinds of applications and you may just find out the one that will specifically work for your project. However, things

get complicated if you cannot find one that is tailored to satisfy your need, which is exactly my case. Then I turned to MATLAB, which contains a very useful sets of functions and algorithms in the Image Processing Toolbox. It is very flexible and you can try out a spectrum of different methods to process your images and construct a sufficient protocol providing that the programmer has a very good understanding of the principles in image analysis. As a biologist, I am not confident enough to generate a good protocol that a professional image analyst can produce. Another issue is that MATLAB is not that fast and not ideal for high throughput image analysis. A common practice that professional image analysts tend to do is to build a protocol very quickly using MATLAB and then rewrite the programm in a different language such as C++, which is also beyond my reach. In the end, I searched for a software that can easily assemble analysis protocol with a fair amount of flexibility and at the same time runs very fast and I found CellProfiler. It has a spectrum of built in modules for all kinds of treatment, from general segmentation to machine learning. It accommodates my need very well except its limited choices in region of interest management. To compensate for this drawback, I decided to make a hybrid protocol combining MATLAB and CellProfiler, removing the unwanted information from the raw images in MATLAB and then processing and analysing in CellProfiler.

A major issue in computational image analysis is the segmentation step, which also turns to be difficult in this project. In my project, all the measurements are based on the segmentation of the cell nuclei, which is stained with DAPI in our case. DAPI staining is very strong, making it easy to be separated from the background. However, the staining is uneven within the nucleus and when the cell nuclei are packed very densely as what I see in the developing brain tissue, it is very difficult to achieve a good segmentation, which is exactly our situation here. There is no such thing as 'perfect segmentation' and I just have to live with the fact that there will be cells missegmented.

4.5.3 A speculated lifetime of a *Zic4* lineage cell

Since I do not possess a technique which would allow us to track the lifetime of a single *Zic4* lineage cell, it is impossible for us to know exactly how endogenous *Zic4* expression triggers the synthesis of the GFP reporters at a cellular level. All I have here are just snapshots of thousands of cells, *Zic4* lineage or not, at very specific time point of their lifetime. Needless to say, these snapshots obtained at different stages are from different embryos. This limited information cannot give us an accurate picture of how a single cell becomes a *Zic4* lineage cell but the population dynamics (the proportion change of different cell types) allows us to study how the whole *Zic4* cell lineage emerges and grows and further speculate what happens in

individual cells. From the data obtained from E11.5 and E15.5, I can see the possibility that individual *Zic4* lineage cells undergo transitions through all four types during their lifetime. I speculate the expression of *Zic4* and GFP in these cells at different stages to be similar to what is shown in the schematic below (Figure 4.33).

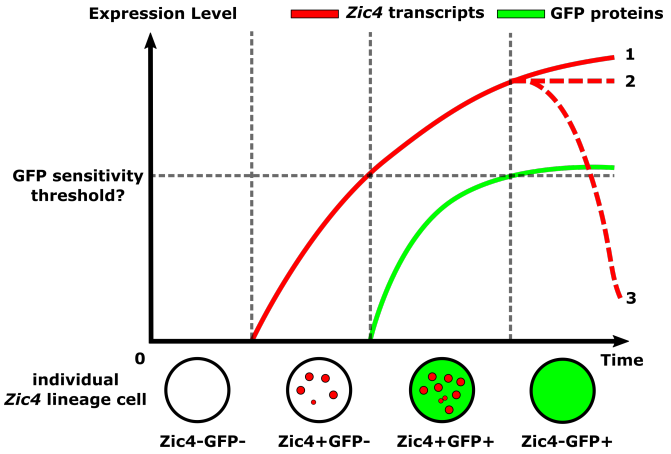


Figure 4.33: ***Speculated Zic4 and GFP expression during the lifetime of individual Zic4 lineage cells.*** *Red and green lines are used to indicate expression levels of Zic4 and GFP in individual Zic4 lineage cells. The dashed red lines are used for alternative Zic4 expression situations. The horizontal dashed gray line indicates the Cre activity threshold required for the initiation of GFP expression. The vertical dashed gray lines indicates the transitions among different types.*

In the speculated situation (Figure 4.33), an individual *Zic4* lineage cell goes through all four types in a chronological order. The $Zic4^{-}GFP^{-}$ cell does not express either *Zic4* or GFP. Once the cell starts to express the endogenous *Zic4*, it transitions to $Zic4^{+}GFP^{-}$, during which the cell does not express GFP due to the low Cre activity. As the Cre recombinase produced by the *Zic4Cre* transgene accumulates in the cell and reaches a threshold level, the STOP cassette is excised and the GFP is turned on. With the GFP turned on, the cell transitions to $Zic4^{+}GFP^{+}$, expressing both the *Zic4* and the GFP. Once the GFP is on, it is permanently on. Its expression level is independent of the endogenous *Zic4* gene and the *Zic4Cre* transgene. On the other hand, the endogenous *Zic4* expression entirely depends on the requirement of its biological function in individual cells. It may keep increasing (Figure 4.33 red line 1), or enter a stationary stage (Figure 4.33 dashed red line 2), or start to decay (Figure 4.33 dashed red line 3). When the expression of *Zic4* completely stops, the cell becomes $Zic4^{-}GFP^{+}$.

The process described above is just a speculated situation. It is possible that different cells have different requirements of Cre activity in order to turn on the GFP. It is also possible

that some *Zic4* lineage cells are born as Zic4^{+}GFP^{-}, or Zic4^{+}GFP^{+} or even Zic4^{-}GFP^{+} from progenitors of the corresponding type.

4.5.4 The emergence and growth of *Zic4* cell lineage in the diencephalon

In the previous and the current chapters, I looked at the expression of the endogenous *Zic4* transcripts and the GFP reporter for the Cre activity at different stages from tissue levels to cellular levels in the developing diencephalon. I arbitrarily categorised four types of cells within the *Zic4* lineage cells based on their expression levels of the *Zic4* and the GFP. With the discrete information obtained from E11.5 to E14.5, I constructed the map of dynamic composition of this lineage (Figure 4.32) based on the proportions of each type of the cells, including Zic4^{-}GFP^{-}, Zic4^{+}GFP^{-}, Zic4^{+}GFP^{+} and Zic4^{-}GFP^{+} for each of the structures I am interested in.

At E11.5, I can see there is already *Zic4* expression in the epithalamus, the prethalamus and the thalamus, which suggests that the *Zic4* lineage emerges earlier than E11.5. As cell proliferation and differentiation proceeds, more and more cells are born in these structures and it is likely that the step-wise transition from Zic4^{-}GFP^{-} to Zic4^{-}GFP^{+} of the *Zic4* lineage cells causes the dynamic composition of the lineage. The continuous increase of Zic4^{+}GFP^{+} cells and the first-increase-then-decrease of Zic4^{-}GFP^{+} cells indicate that after the *Zic4* lineage cells finishes the transition from Zic4^{+}GFP^{-} to Zic4^{+}GFP^{+}, some cells maintain high levels of *Zic4* expression whereas some cells start to shut down the expression of *Zic4* and transition to Zic4^{-}GFP^{+}. This divergence of the *Zic4* expression between Zic4^{+}GFP^{+} and Zic4^{-}GFP^{+} cells reflects the heterogeneity of the cell composition in the developing diencephalon. The mapping of dynamic composition of *Zic4* lineage gives us invaluable insights into the complex evolution of subgroups of cells during the development of the thalamus and makes us aware precautions should be taken when interpreting data obtained from similar animal models.

In the next few chapters, I will look at developmental defects in *Pax6* conditional knock-out mice that were generated using the *Zic4Cre* mouse line to investigate the role of Pax6 in the development of the thalamus and the prethalamus.

Chapter 5

Deletion of Pax6 driven by *Zic4Cre* in the developing diencephalon in *Zic4Cre*$^{+/-}$;*RCE*$^{+/-}$;*Pax6*$^{fl/+}$ and *Zic4Cre*$^{+/-}$;*RCE*$^{+/-}$;*Pax6*$^{fl/fl}$ mice

5.1 Introduction

In Chapter 3 and Chapter 4, the expression pattern of *Zic4* and GFP was studied in the *Zic4Cre* mouse line, which was used for generating the conditional *Pax6* mutants used for the rest of this thesis. In this chapter, the validation of Pax6 deletion in the diencephalon at E12.5, E13.5 and E14.5 is documented.

In the *Zic4Cre* mouse line, the Cre acitivity in individual cells is reported by the expression of GFP, thus theoretically, *Pax6* should be deleted in the GFP positive cells. The deletion pattern of *Pax6* can be predicted by looking at the distribution of GFP positive cells within the developing diencephalon at specific time points. At E12.5, only a fraction of cells expressing GFP can be seen in the eminentia thalami, the prethalamus and the thalamus (Figure 3.8) so the deletion of *Pax6* in these tissues is likely to be mosaic. In the E13.5 diencephalon, a number of GFP negative cells were in the thalamus, the prethalamus and the eminentia thalami (Figure 3.8) so there should still be some cells in these tissues expressing Pax6. A clear feature of the distribution of the GFP positive cells at this stage is that there are more GFP positive cells at the front than at the back along the front-back axis (as defined inFigure 3.9). Thus, I am expecting to see the deletion of *Pax6* to be more complete at the front levels than

that at back levels. At E14.5, GFP positive cells aggregate particularly in the ventricular zone of the prethalamus and the mantle area where the future vLGN is forming (Figure 3.14 J), suggesting that the deletion of *Pax6* will be significant in these two regions. In the thalamus, the GFP positive cells are mainly in the ventricular zone especially at the front level (as defined in Figure 3.12), thus I am expecting to see *Pax6* deletion to be complete in this region as *Pax6* is almost exclusively expressed in the ventricular zone in the thalamus.

5.2 Aim of the project

The mapping study of the *Zic4* cell lineage carried out in the previous two chapters allows us to track the evolving *Zic4* lineage population in the developing diencephalon across different developmental stages. The aim of the project in this chapter is to monitor the change of Pax6 expression in the developing diencephalon in the *Pax6* conditional knockout mice generated using the *Zic4Cre*, in which Pax6 is inactivated in the *Zic4* cell lineage through time.

5.3 Results

I performed DAB immunohistochemistry for Pax6 protein on paraffin embedded mouse brain sections for E12.5, E13.5 and E14.5 $Zic4Cre^{+/-};RCE^{+/-};Pax6^{+/+}$, $Zic4Cre^{+/-};RCE^{+/-};Pax6^{fl/+}$ and $Zic4Cre^{+/-};RCE^{+/-};Pax6^{fl/fl}$ embryos. I compared the expression of Pax6 among these three genotypes to investigate the deletion of *Pax6* driven by *Zic4Cre*.

The expression patterns of the Pax6 protein in the developing diencephalon of the three genotypes, $Zic4Cre^{+/-};RCE^{+/-};Pax6^{+/+}$ (wt), $Zic4Cre^{+/-};RCE^{+/-};Pax6^{fl/+}$ (het) and $Zic4Cre^{+/-};RCE^{+/-};Pax6^{fl/fl}$ (hom), at the different stages mentioned above are documented in this section. The deletion of Pax6 in the het and hom diencephalon will be described by comparing to the expression pattern in that of wt. Lower power images of the overall expression of Pax6 in the diencephalon will be summarised for each of the genotypes and high power images of the regions with differential expression patterns between the three genotypes will be presented for detailed analysis.

5.3.1 Deletion of Pax6 in the E12.5 *Zic4Cre$^{+/-}$;RCE$^{+/-}$;Pax6$^{fl/+}$* and *Zic4Cre$^{+/-}$;RCE$^{+/-}$;Pax6$^{fl/fl}$* diencephalon

In the descriptive study in chapter 3, I observed that at E11.5 the expression of *Zic4* transcripts is restricted in a small proportion of cells in the developing diencephalon thus I chose E12.5 as the starting point to study the deletion of Pax6 driven by the *Zic4Cre* in these tissues. Since most of the diencephalic nuclei are formed around E15.5 and E16.5, I chose E16.5 as the end point of my study.

At E12.5, the expression of Pax6 in the het (Figure 5.1 B1 - B6) is more-or-less the same as in the wt (Figure 5.1 A1 - A6). In the hom, the deletion of Pax6 is mainly seen in the epithalamus (Figure 5.1 C1 - C6, black star), the ventricular zone of the thalamus especially at the front levels (Figure 5.1 C1 - C3, black arrow head), and the eminentia thalami (Figure 5.1 C1 - C2, black line with diamond marker). The Pax6 expression at the middle level in the wt and the het shows a butterfly-shaped pattern and a group of cells with high levels of Pax6 are seen in the hindwing region of the butterfly (Figure 5.1 A4 and B4, black line with square marker). This group of cells is almost absent in the hom (Figure 5.1 C4, black line with square marker).

In the eminentia thalami, the deletion of Pax6 shows a mosaic-like pattern in the hom (Figure 5.2 F1), in which some of the cells maintain high levels of Pax6 whereas their neighbours do not seem to express visible Pax6 at all. In contrast, almost all the cells in the eminentia thalami in the wt (Figure 5.2 D1) and in the het (Figure 5.2 E1) are Pax6 positive. A similar deletion pattern can be seen in the ventricular zone of the thalamus in the hom (Figure 5.2 F2) especially at the front-most levels. Some cells in this region are still expressing very low levels of Pax6, indicating the deletion of Pax6 is in progress but not yet completed. In the wt (Figure 5.2 D2) and the het (Figure 5.2 E2), almost all the cells in the ventricular zone of the thalamus are Pax6 positive. The deletion of Pax6 in the ventricular zone of the prethalamus is not very obvious in the hom but I can appreciate the horizontally patchy deletion of Pax6 at the middle level (Figure 5.2 F3) compared to either the wt (Figure 5.2 D3) or the het (Figure 5.2 F3). A group of cells expressing high levels of Pax6 are observed at the boundary between the thalamus and the prethalamus close to the pial surface in the wt (Figure 5.2 D4 and D5, dashed black oval) and the het (Figure 5.2 E4 and E5, dashed black oval). This group of cells seem to be missing in the hom (Figure 5.2 F4 and F5, dashed black oval).

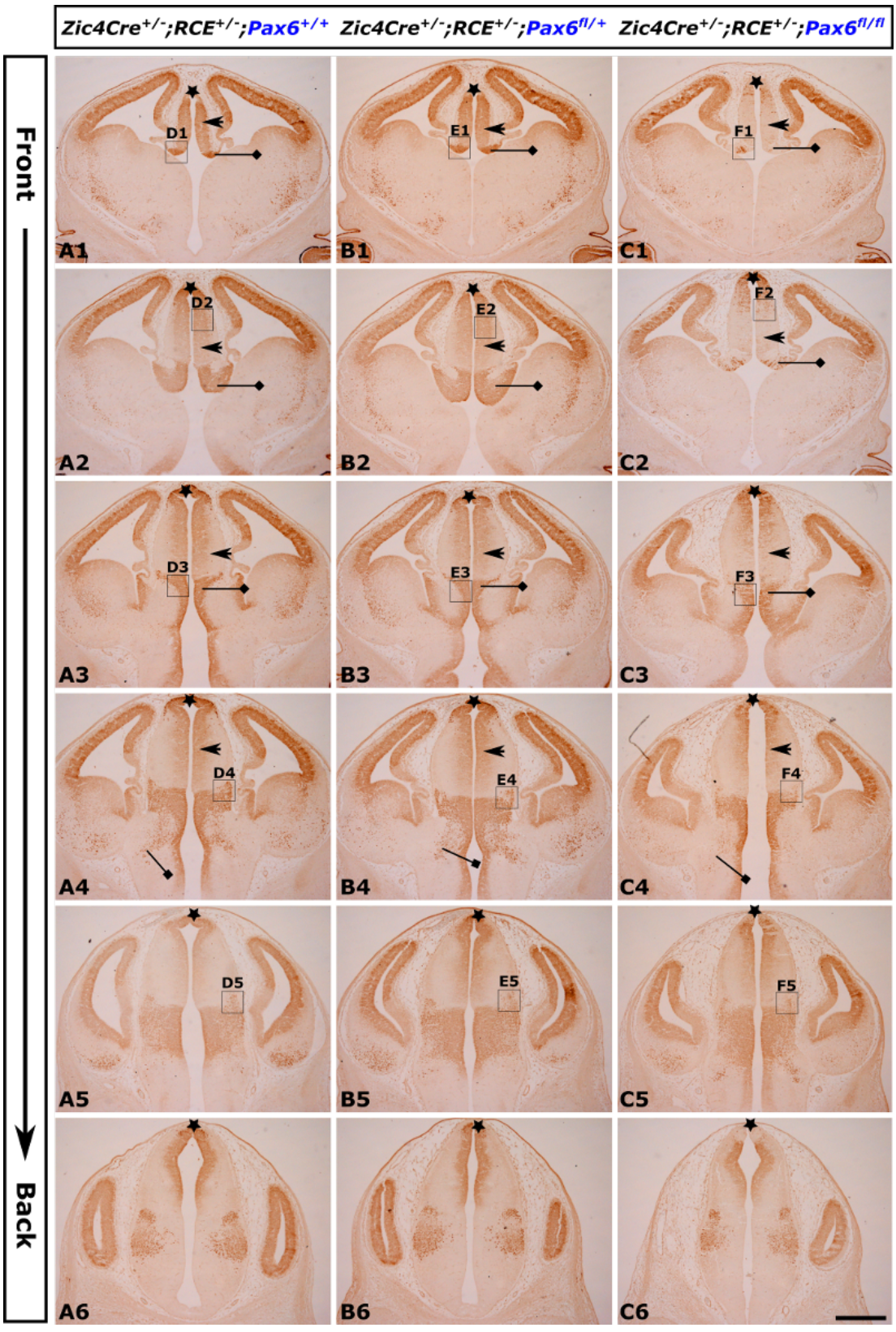


Figure 5.1: ***Pax6 immunohistochemistry on E12.5 diencephalon coronal sections from Zic4Cre$^{+/-}$;RCE$^{+/-}$;Pax6$^{+/+}$, Zic4Cre$^{+/-}$;RCE$^{+/-}$;Pax6$^{fl/+}$ and Zic4Cre$^{+/-}$;RCE$^{+/-}$;Pax6$^{fl/fl}$ mice.*** *Black star, ventricular zone of the epithalamus; black arrow head, ventricular zone of the thalamus; black line with diamond marker, ventricular zone of the prethalamus. Scale bar: 500 μm.*

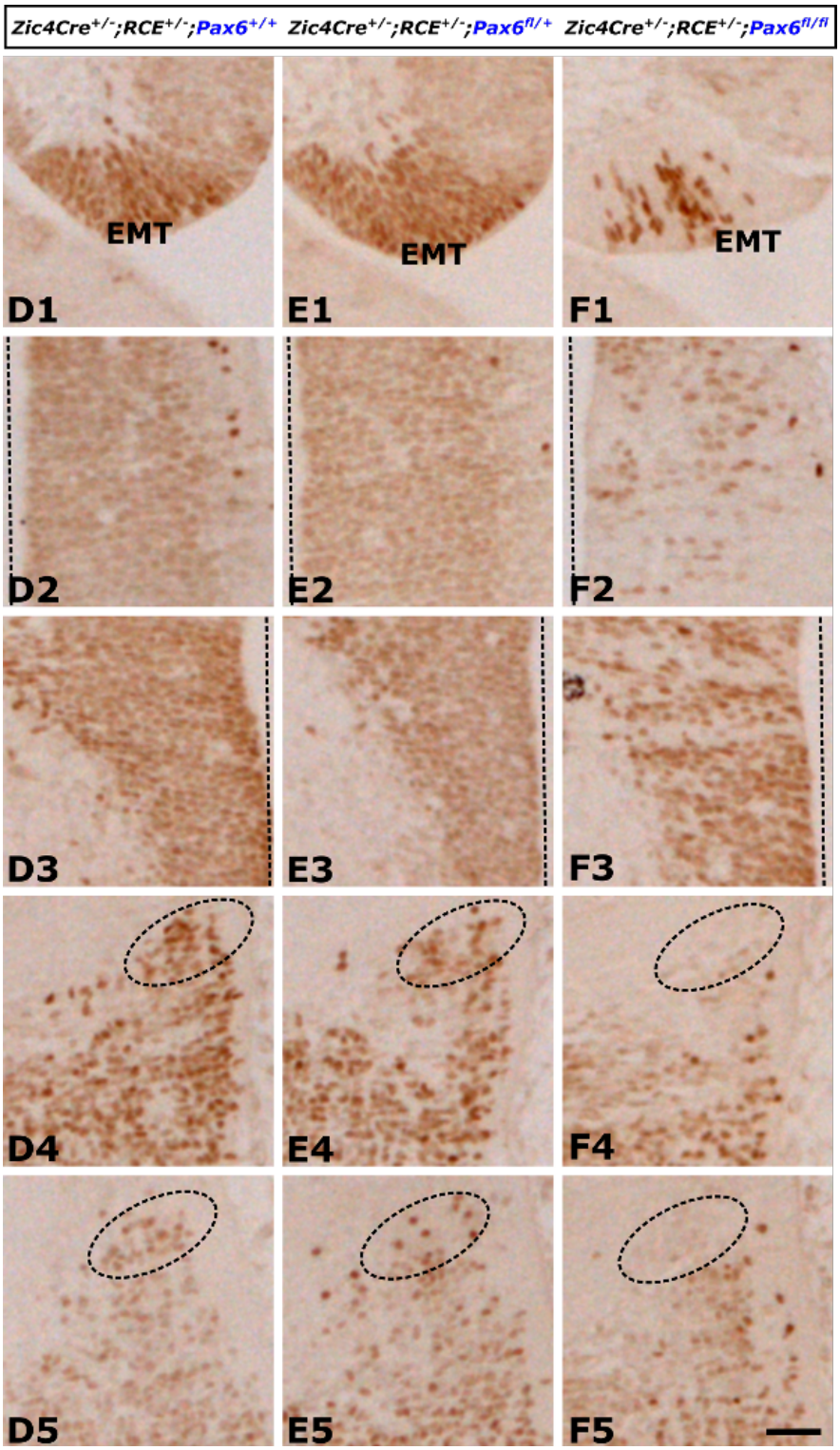


Figure 5.2: ***High Power images of Pax6 immunohistochemistry on E12.5 diencephalon coronal sections from*** **Zic4Cre$^{+/-}$;RCE$^{+/-}$;Pax6$^{+/+}$,** **Zic4Cre$^{+/-}$;RCE$^{+/-}$;Pax6$^{fl/+}$** ***and*** **Zic4Cre$^{+/-}$;RCE$^{+/-}$;Pax6$^{fl/fl}$** ***mice.*** *Dashed black line, midline; dashed black oval, outline of the cell group dorsal to the vLGN. EMT, eminentia thalami. Scale bar: 50 μm.*

5.3.2 Deletion of Pax6 in the E13.5 *Zic4Cre*$^{+/-}$;*RCE*$^{+/-}$;*Pax6*$^{fl/+}$ and *Zic4Cre*$^{+/-}$;*RCE*$^{+/-}$;*Pax6*$^{fl/fl}$ diencephalon

At E13.5, the het (Figure 5.3 B1 - B5) shows a similar Pax6 expression pattern to the wt (Figure 5.3 A1 - A5). In the hom, the deletion of Pax6 is observed across the diencephalon: 1. most cells in the epithalamus do not show expression of Pax6 in contrast to the high levels of Pax6 in the wt and the het (Figure 5.3 C1 - C5, black star); 2. the Pax6 expression in the ventricular zone of the thalamus is greatly reduced across the front-back axis (refer to Figure 3.9) especially at the front levels (Figure 5.3 C1 - C5, black arrow heads) whereas in the wt and the het a dorsal-high and ventral-low Pax6 gradient can be appreciated; 3. in the prethalamus, Pax6 expression is significantly reduced in the ventricular zone (Figure 5.3 C1 - C5, black line with dot marker) compared to either the wt (Figure 5.3 A1 - A5, black line with dot marker) or the het (Figure 5.3 B1 - B5, black line with dot marker) whereas in the mantle region where the future vLGN is going to form, its expression is almost undetectable (Figure 5.3 C1 - C5, black line with diamond marker); 4. at the middle to back levels, the expression of Pax6 is clearly reduced in the hindwing region of Pax6's butterfly-shaped expression pattern in the prethalamus (Figure 5.3 C3 - C4, black line with square marker).

A closer look at the high power images (Figure 5.4) of the regions with dramatic Pax6 expression change in the hom reveals a characteristic property of the Pax6 deletion driven by the *Zic4Cre*, which is mosaicism. At the front most level, I observed high levels of Pax6 protein expressed in the eminentia thalami in both the wt and the het (Figure 5.4 D2 and E2). In the hom eminentia thalami (Figure 5.4 F2), some cells maintained their high levels of Pax6 whereas in their neighbours it is completely absent, which makes the Pax6 expression pattern patchy. This patchy pattern of Pax6 is also seen in the ventricular zone of the prethalamus (Figure 5.4 F3) but not in the wt or in the het (Figure 5.4 D3 and E3). The patchy Pax6 deletion pattern can be explained by the unsynchronised activation of the Cre in the *Zic4* lineage cells due to the dynamic change of the lineage itself. In the thalamus, the deletion of Pax6 in the ventricular zone in the hom is more complete at the front levels (Figure 5.4 D1, E1 and F1) compared to the sections at the back levels (Figure 5.4 D5, E5 and F5). In the region where the future vLGN is going to form, I can see a clear decrease of Pax6 positive cells (Figure 5.4 D4 - F4 and D7 - F7). I also noticed that the cells in the ventricular zone of the prethalamus in the het seem to express higher levels of Pax6 compared to the wt (Figure 5.4 D3 - E3 and D6 - E7).

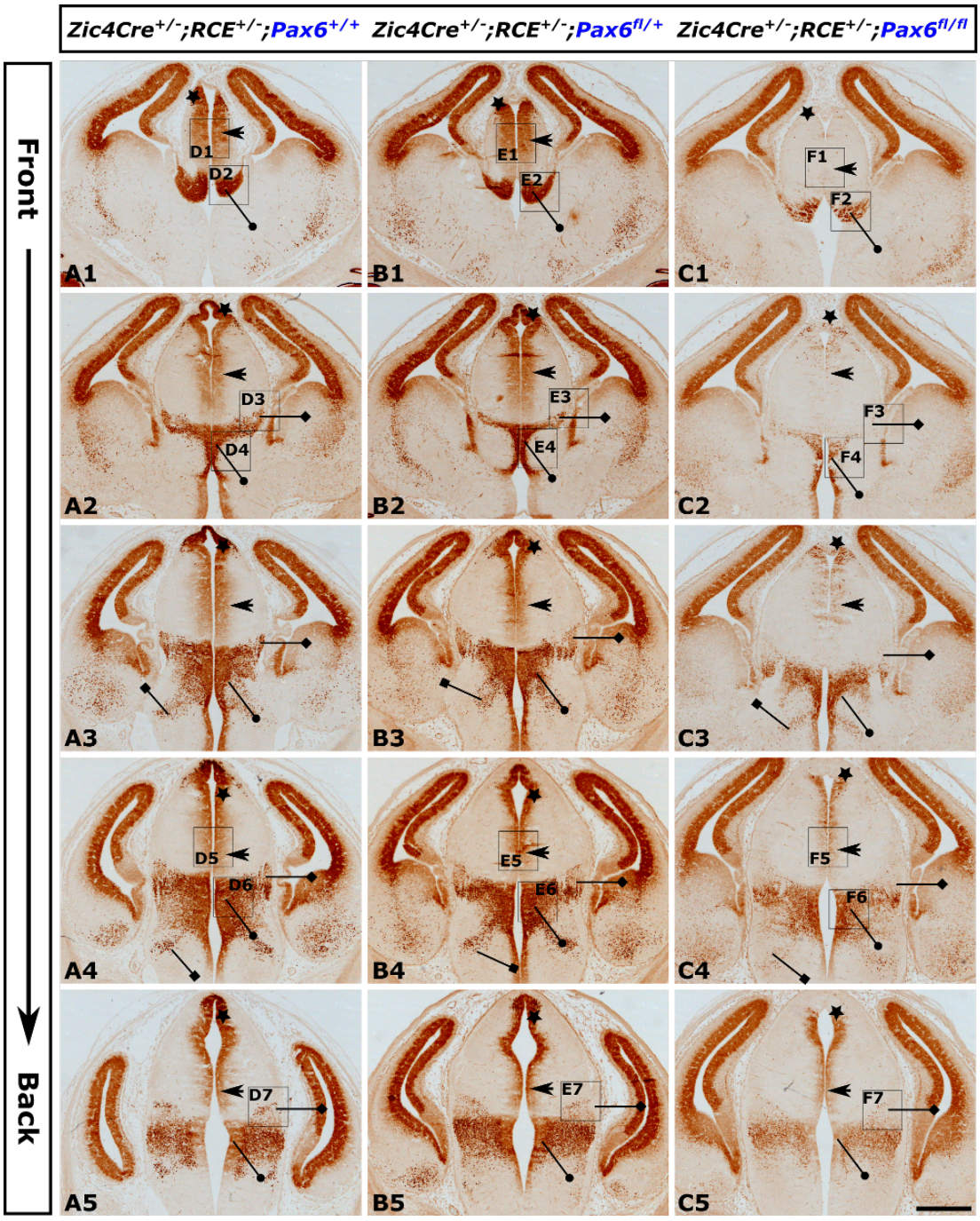


Figure 5.3: ***Pax6 immunohistochemistry on E13.5 diencephalon coronal sections from Zic4Cre$^{+/-}$;RCE$^{+/-}$;Pax6$^{+/+}$, Zic4Cre$^{+/-}$;RCE$^{+/-}$;Pax6$^{fl/+}$ and Zic4Cre$^{+/-}$;RCE$^{+/-}$;Pax6$^{fl/fl}$ mice.*** *Black star, ventricular zone of the epithalamus; black arrow head, ventricular zone of the thalamus; black line with dot marker, ventricular zone of the prethalamus; black line with diamond marker, mantle zone especially the forming vLGN in the prethalamus; black line with square marker, hindwing region of the butterfly-shaped Pax6 expression pattern. Scale bar: 500 μm.*

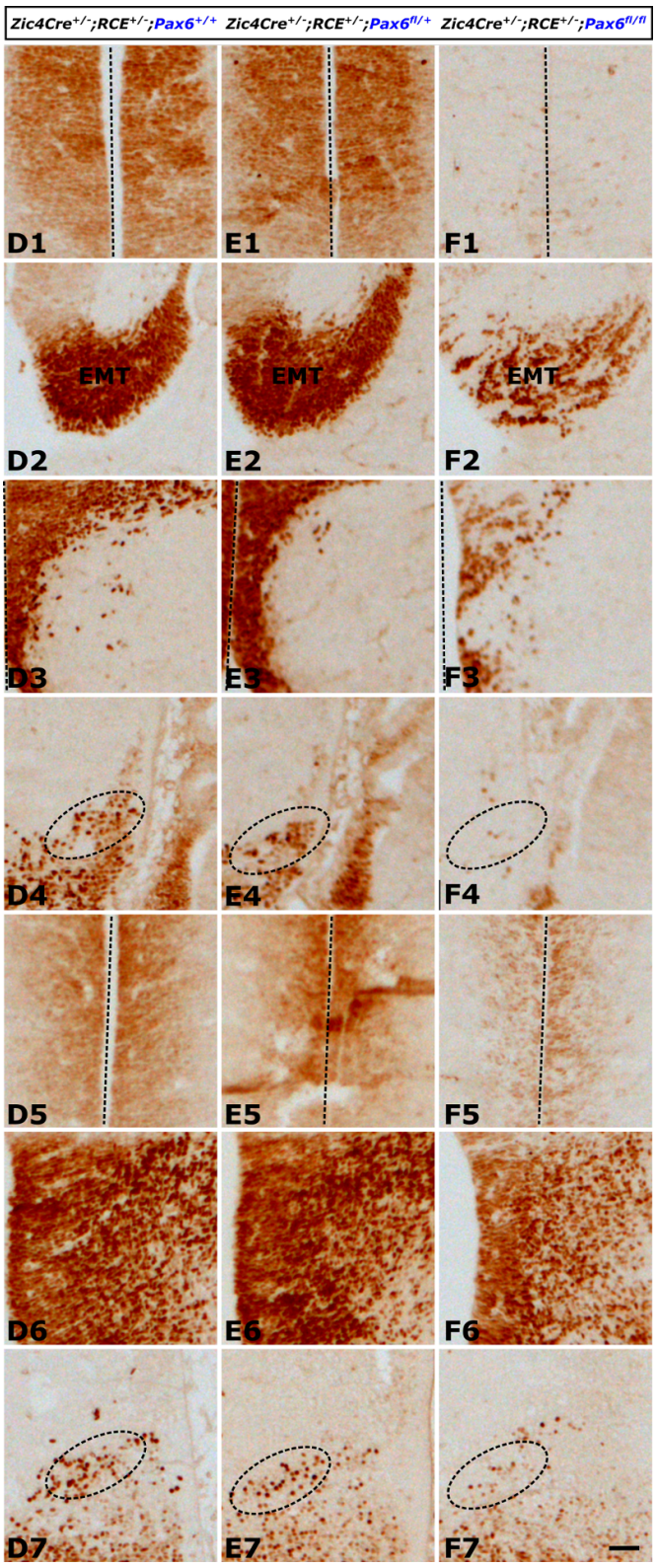


Figure 5.4: ***High Power images of Pax6 immunohistochemistry on E13.5 diencephalon coronal sections from*** **Zic4Cre$^{+/-}$;RCE$^{+/-}$;Pax6$^{+/+}$,** **Zic4Cre$^{+/-}$;RCE$^{+/-}$;Pax6$^{fl/+}$** ***and*** **Zic4Cre$^{+/-}$;RCE$^{+/-}$;Pax6$^{fl/fl}$** ***mice.*** *Dashed black line, midline; dashed oval circle, outline of a small group Pax6 positive cells along the boundary between the thalamus and the prethalamus. EMT, eminentia thalami. Scale bar: 50 μm.*

5.3.3 Deletion of Pax6 in the E14.5 *Zic4Cre$^{+/-}$;RCE$^{+/-}$;Pax6$^{fl/+}$* and *Zic4Cre$^{+/-}$;RCE$^{+/-}$;Pax6$^{fl/fl}$* diencephalon

At E14.5, the expression pattern of Pax6 in the het resembles that in the wt (Figure 5.5 A1 - A5 and B1 - B5) where as the Pax6 expression in the hom is clearly different from the previous two: 1. Pax6 expression is absent from the ventricular zone of both the epithalamus (Figure 5.5 black stars) and the thalamus (Figure 5.5 black arrow heads) in the hom; 2. in the prethalamus, the expression of Pax6 is significantly reduced in the ventricular zone (Figure 5.5 A1 - A4, B1 - B4 and C1 - C4, black lines with dot marker) at the front to middle levels and is completely abscent in the mantle zone at the front levels (Figure 5.5 A1 - C1 and A2 - C2, black lines with diamond marker) in the hom; 3. the Pax6 expressing cell stream observed at the boundary between the thalamus and the prethalamus in both the wt and the het (Figure 5.5 A3 - B3, A4 - B4 and A5 - B5, black lines with diamond marker), is not seen in the hom (Figure 5.5 C3 - C5, black lines with diamond marker); 4. in the wt and the het, Pax6 expression is absent from the ventricular zone of the prethalamus (Figure 5.5 A5 and B5, black lines with dot marker) whereas in the hom low levels of Pax6 expression can still be seen in the region at this stage (Figure 5.5 C5, black lines with dot marker); 5. the expression pattern of Pax6 in the prethalamus in the front to middle levels resembles the shape of a butterfly and the Pax6 expression in the butterfly's hindwing region is significantly reduced in the hom (Figure 5.5 A2 - C2 and A3 - C3, black lines with square marker) compared to that in the wt or the het. There is no obvious difference in Pax6 expression between the wt and the het but the Pax6-expressing region in the ventricular zone of the thalamus seems wider in the het (Figure 5.5 B1 - B3, black arrow heads) compared to the wt (Figure 5.5 A1 - A3, black arrow heads).

High power images (Figure 5.6) of the regions showing differential Pax6 expression between different genotypes are provided to show detailed changes in the het and the hom. In the ventricular zone of the thalamus, I can see that Pax6 is completed deleted (Figure 5.6 F1 and F3) in the hom whereas the het seems to have wider Pax6 positive regions compared to those in the wt (Figure 5.6 D1, D3, E1 and E3). Pax6 expression is also greatly reduced in the forming vLGN in the hom (Figure 5.6 F2 and F4) whereas the expression pattern in the het resembles the wt (Figure 5.6 D2, D4, E2 and E4). A group of Pax6 positive cells can be seen in the dorsal part of the vLGN in both the wt and the het (Figure 5.6 D4 and E4) but are absent in the hom (Figure 5.6 D4 and F4) . In the ventricular zone of the prethalamus, I can see a lot of cells expressing high levels of Pax6. There seems to be more Pax6 positive cells in this region in the het (Figure 5.6 E5) than in the wt (Figure 5.6 D5) whereas the hom has much fewer Pax6 positive cells (Figure 5.6 F5) compared to the wt or the het.

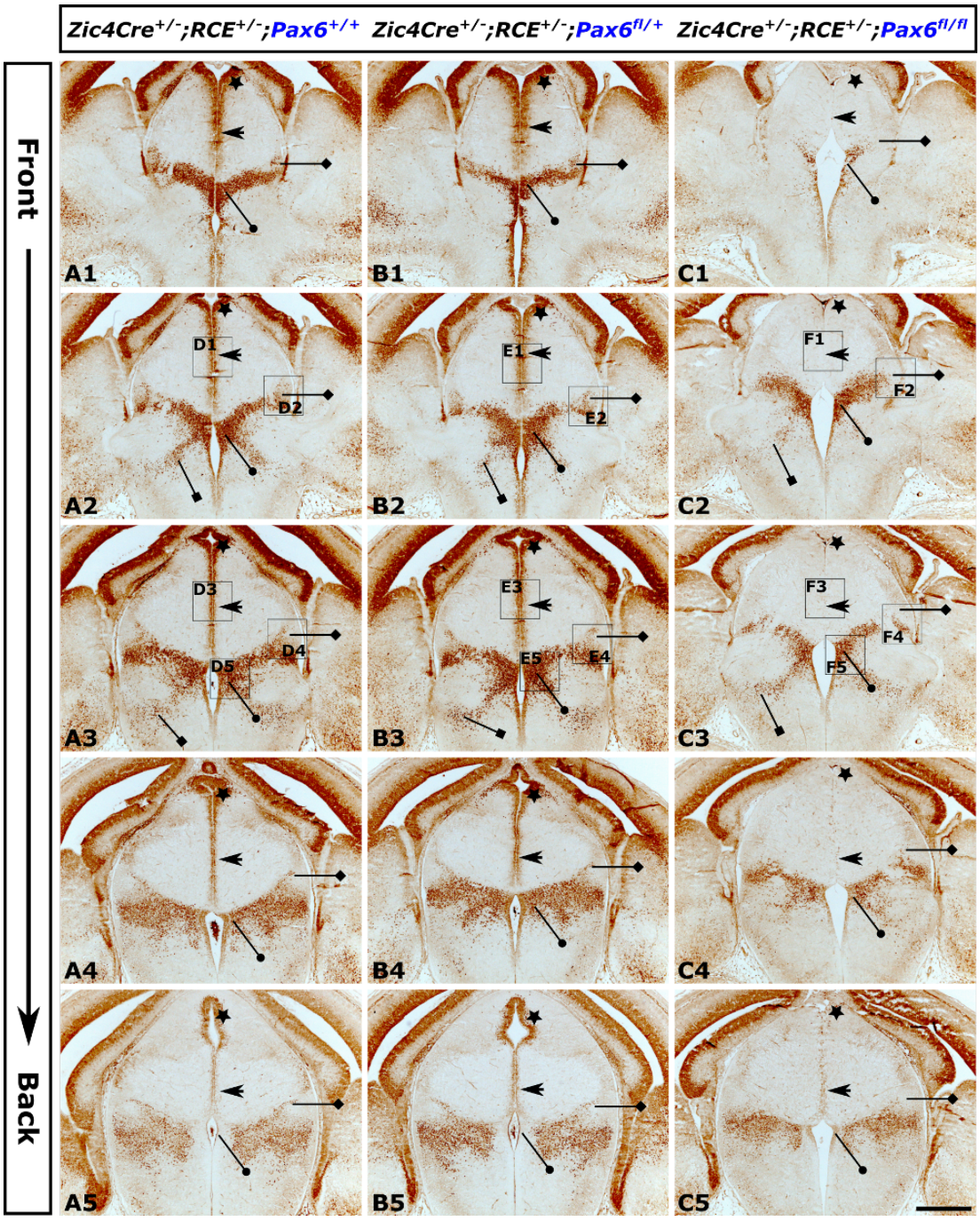


Figure 5.5: ***Pax6 immunohistochemistry on E14.5 diencephalon coronal sections from Zic4Cre$^{+/-}$;RCE$^{+/-}$;Pax6$^{+/+}$, Zic4Cre$^{+/-}$;RCE$^{+/-}$;Pax6$^{fl/+}$ and Zic4Cre$^{+/-}$;RCE$^{+/-}$;Pax6$^{fl/fl}$ mice.*** *Black star, ventricular zone of the epithalamus; black arrow head, ventricular zone of the thalamus; black line with dot marker, ventricular zone of the prethalamus; black line with diamond marker, mantle zone especially the forming vLGN in the prethalamus; black line with square marker, hindwing region of the butterfly-shaped Pax6 expression pattern. Scale bar: 500 μm.*

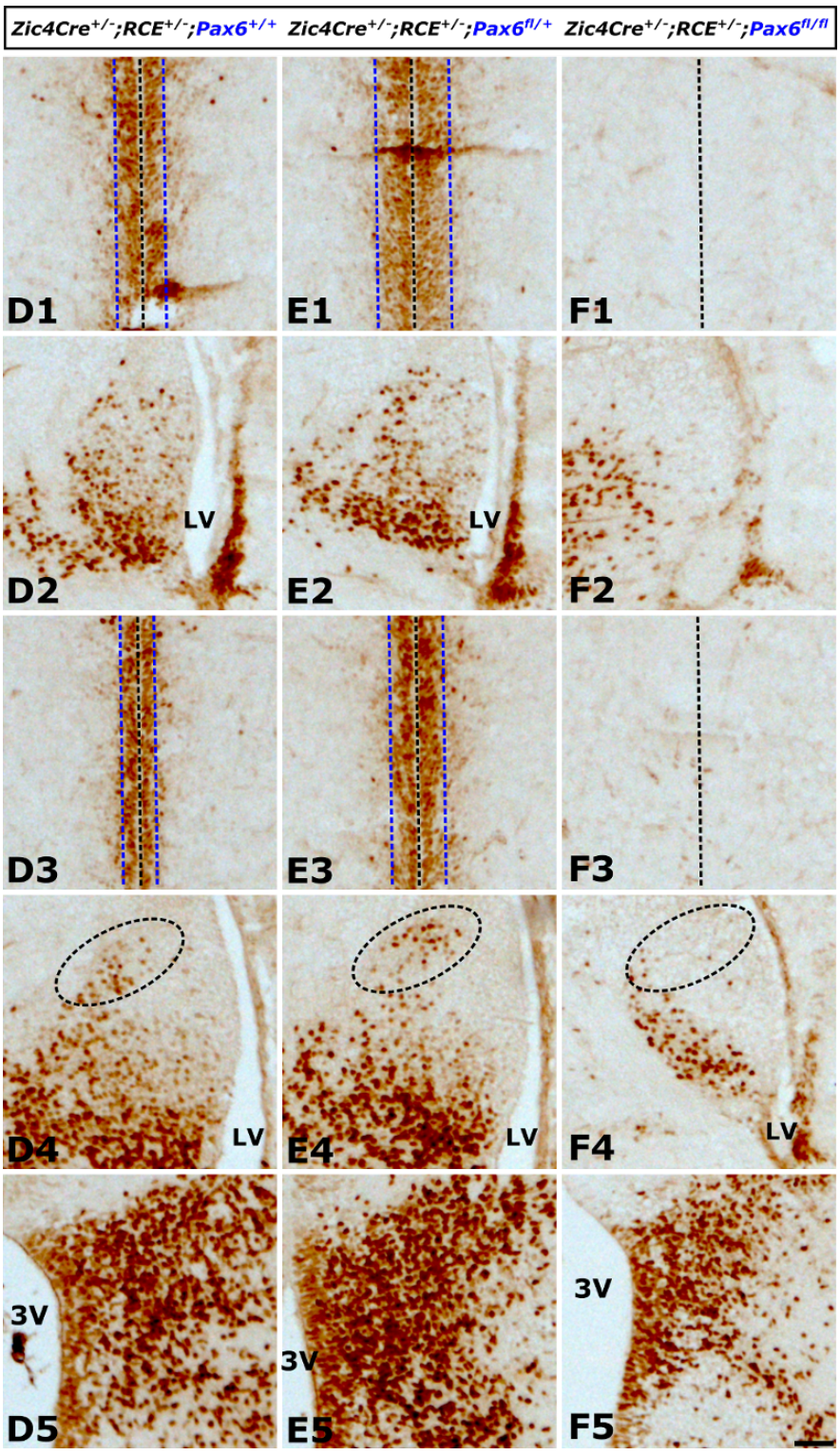


Figure 5.6: ***High Power images of Pax6 immunohistochemistry on E14.5 diencephalon coronal sections from*** **Zic4Cre$^{+/-}$;RCE$^{+/-}$;Pax6$^{+/+}$,** **Zic4Cre$^{+/-}$;RCE$^{+/-}$;Pax6$^{fl/+}$** ***and*** **Zic4Cre$^{+/-}$;RCE$^{+/-}$;Pax6$^{fl/fl}$** ***mice.*** *Dashed black line, midline; dashed blue line, boundary of Pax6 positive region in the ventricular zone of the thalamus; dashed oval circle, outline of a small group Pax6 positive cells along the boundary between the thalamus and the prethalamus. LV, lateral ventricle; 3V, third ventricle. Scale bar: 50 μm.*

5.3.4 Deletion of Pax6 in the E16.5 *Zic4Cre$^{+/-}$;RCE$^{+/-}$;Pax6$^{fl/+}$* and *Zic4Cre$^{+/-}$;RCE$^{+/-}$;Pax6$^{fl/fl}$* diencephalon

At E16.5, Pax6 is expressed in the ventricular zone of the epithalamus (black stars), the thalamus (black line with dot marker) and the prethalamus (black line with diamond marker) in the wt (Figure 5.7 A1, A3 and A5) and a similar pattern is seen in the het though at slightly lower levels especially in the prethalamus (Figure 5.7 B1, B3 and B5). The deletion of Pax6 is clearly observed in the ventricular zone of the epithalamus and the thalamus and the mantle zone of the prethalamus (Figure 5.7 C1, C3 and C5).

The forming vLGN can be appreciated at the lateral surface of the diencephalon in the all three genotypes (Figure 5.7 A2-C2, A4-C4 and A6-C6). At the front part, Pax6-expressing cells can be seen at the medial part of the vLGN in the wt (Figure 5.7 A2 black arrow) whereas in the het more Pax6-expressing cells are seen at the corresponding position (Figure 5.7 B2 black arrow). The vLGN in the hom is a conspicuously bigger than its counterparts in both the wt and the het at this level and a lot fewer Pax6 positive cells are seen in the hom vLGN (Figure 5.7 C2 black arrow). At middle level, the area of the hom vLGN (Figure 5.7 C4 black contour) is also larger than that in the wt (Figure 5.7 A4 black contour) and the het (Figure 5.7 B4 black contour). Quite a few Pax6-expressing cells are seen close to the pial surface of the vLGN in the het (Figure 5.7 B4 black arrow) whereas no Pax6-expressing cells are observed in the corresponding regions in either the wt (Figure 5.7 A4 black arrow) or the hom(Figure 5.7 C4 black arrow). At the back levels, a group of cells close to the ventrolateral surface of the vLGN in both the wt (Figure 5.7 A6 black arrow) and the het (Figure 5.7 B6 black arrow) express Pax6 whereas no such cells are seen in the similar region in the hom vLGN (Figure 5.7 C6 black arrow). A few Pax6-expressing cells are seen in the medioventral part of the hom vLGN (Figure 5.7 C6 black line with square marker) whereas a lot fewer Pax6 positive cells are seen in the corresponding region in the wt (Figure 5.7 A6 black line with square marker) and the het (Figure 5.7 B6 black line with square marker).

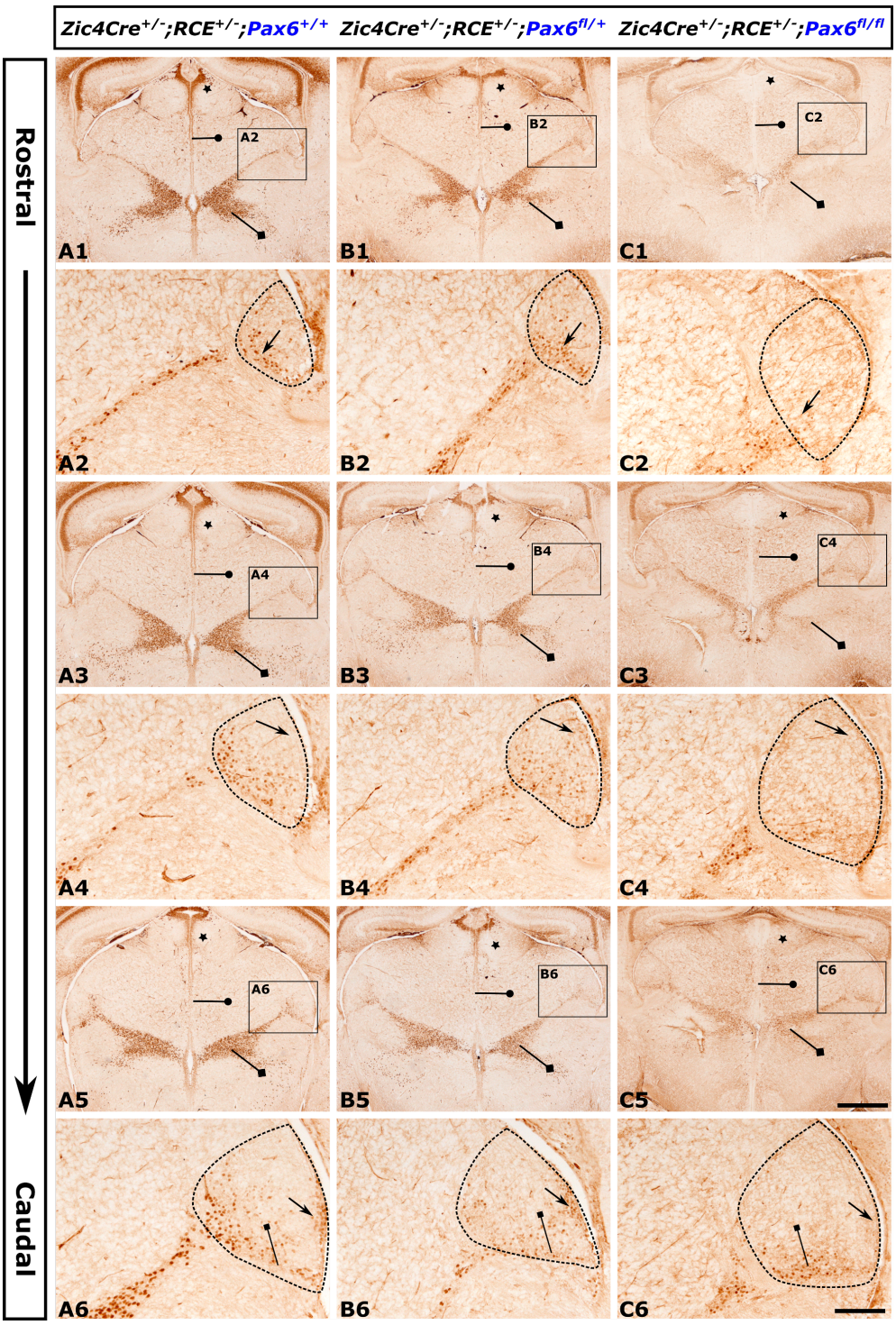


Figure 5.7: ***Pax6 immunohistochemistry on E16.5 diencephalon coronal sections from Zic4Cre$^{+/-}$;RCE$^{+/-}$;Pax6$^{+/+}$, Zic4Cre$^{+/-}$;RCE$^{+/-}$;Pax6$^{fl/+}$ and Zic4Cre$^{+/-}$;RCE$^{+/-}$;Pax6$^{fl/fl}$ mice.*** *Dashed black contour, vLGN; black star, ventricular zone of the epithalamus; black line with dot marker, ventricular zone of the thalamus; black line with diamond marker, prethalamus; black arrow and black line with square marker, differential Pax6 expression with in vLGN. Scale bar: 500 μm and 125 μm.*

5.4 Synopsis

The Pax6 immunohistochemistry from E12.5 to E16.5 enables us to see the deletion driven by the *Zic4Cre* progressing through time. At E12.5 and E13.5, I observed patchy expression of Pax6 in the hom whereas in the wt and in the het the expression is continuous in the eminitia thalami, the ventricular zone of the thalamus and the prethalamus. I also noticed the Pax6 deletion in the ventricular zone of the thalamus is more severe at the front levels than that at the back levels, which fits with the general front-high and back-low *Zic4* expressing gradient. The deletion in this region at E14.5 is almost complete at the front to middle levels whereas in the ventricular zone of the prethalamus a reduced but still considerably large numbers of cells express Pax6 at the same stage in the hom, which suggests that Pax6 plays different roles in these two subregions of the diencephalon. Pax6 deletion is observed in the region where the future vLGN is going to form through E12.5 to E14.5, which indicates that Pax6 is highly involved in the development of this specific diencephalic nucleus. At E16.5, Pax6-expressing cells are observed in the forming vLGN in all three genotypes but the number and the position of Pax6-expressing cells vary among the wt, the het and the hom. The presence of Pax6 in the vLGN cells indicates that Pax6 may play a role in the vLGN neuronal fate committement and electrophysiological identity acquirement. The change in the number and position of Pax6-expressing cells within the vLGN in the het and the hom suggests potential defects in cell fate committement and/or cell migration/sorting.

5.5 Discussion

5.5.1 Pax6 deletion is well related to the Cre activation pattern in the hom diencephalon

The staining results of Pax6 protein showed that the deletion in the E12.5, E13.5 and E14.5 *Zic4Cre*$^{+/-}$;*RCE*$^{+/-}$;*Pax6*$^{fl/fl}$ mouse diencephalon, is well related to the GFP expression that was previously studied in the *Zic4Cre* mouse line at the corresponding stages.

At E12.5, the deletion of Pax6 was seen in most of the cells in the eminentia thalami in the hom compared to the wt and het (Figure 5.2), which corresponds to the GFP expression in the same tissue at this stage (Figure 3.8 G and G2). In the ventricular zone of the thalamus and the prethalamus, Pax6 was deleted in some of the cells but maintained in the rest of the cells, which is correlated to the mosaic distribution of GFP positive cells in these two structures respectively (Figure 3.8 H, J and I, K).

At E13.5, the expression of Pax6 was maintained in a number of cells in the eminentia thalami and the prethalamus in the hom compared to the wt and the het (Figure 5.4 D2-F2, D3-F3, D4-F4), which is well reflected by the distribution of GFP positive cells at the same stage (Figure 3.11 G, G4 and G5). The deletion of Pax6 in the thalamus is almost complete at the front level (Figure 5.4 D1-F1) but not so much at the back (Figure 5.4 D5-F5). The similar pattern was seen with the GFP expression, in which more GFP positive cells were at the front than at the back (Figure 3.11 G1 and H1) in the ventricular zone of the thalamus.

At E14.5, the deletion of Pax6 in the ventricular zone of the thalamus in the hom was complete and no Pax6 staining was seen either at the front or at the back (Figure 5.6 F1-F3). This is well expected since the Pax6 deletion at the front level was completed at the previous stage and the deletion at the back is correlated with the presence of GFP positive cells at this stage (Figure 3.14 J). The deletion of Pax6 in the forming vLGN at both the front and the back levels is well related to the aggregation of GFP positive cells in the region (Figure 3.14 G and J). Pax6 deletion in the ventricular zone of the prethalamus is also reflected by the distribution of GFP positive cells in this region (Figure 3.14 I2).

At E16.5, a similar deletion pattern of Pax6 was seen in the ventricular zone of the epithalamus, the thalamus and the prethalamus in the hom compared to E14.5. Looking closely at the vLGN, I saw that a lot fewer Pax6-expressing cells in the hom vLGN at the front level (Figure 5.7 C2), which is well correlated with the GFP positive cell distribution within the vLGN at this stage (Figure 3.20 G1, G2 and G3). At the back level, I saw quite a few Pax6-expressing cells in the medioventral part of the vLGN in the hom (Figure 5.7 C6), which is well reflected by the distribution of GFP positive cells confined in the mediodorsal portion of the vLGN (Figure 3.20 H1, H2 and H3).

5.5.2 Up-regulation of Pax6 in the het diencephalon and potential mechanisms

The *Pax6* deletion driven by the *Zic4Cre* is conspicuous in the hom whereas the difference between the het and wt is more subtle. It seems there are more Pax6-expressing cells in the ventricular zone of the prethalamus (Figure 5.4 and Figure 5.6) and thalamus (Figure 5.6) at E13.5 and E14.5. In other words, the expression of Pax6 is up-regulated in the het diencephalon in which one copy of *Pax6* is inactivated.

One of the possibilities is that this up-regulation comes from one of the many Pax6 isoforms, Pax6(5a). The work carried out previously in the lab has shown that Pax6(5a) is

up-regulated in the *Sey*/+ brain whereas other Pax6 isoforms expression levels are similar to those in the wt [114]. The observation seems to fit well with the subtle phenotype in the *Sey*/+. The up-regulation of Pax6(5a) level in the *Sey*/+ heterozygous suggested the possibility that a regulatory mechanism is in place to compensate for the lower *Pax6* copy number by increasing the amount of protein produced by the remaining intact loci. Since the above result was obtained by western blot, I don't know whether the up-regulation of Pax6 protein is caused by the increase of Pax6 protein at cellular levels or the increase of the number of cells expressing Pax6. Although the *Pax6* hets I used in this study were different from the ones used in the western blot experiment, the self-regulatory *Pax6* expression could still be the mechanism behind the Pax6 up-regulation in the het brain.

The result of this chapter showed unique pattern of Pax6 deletion driven by the *Zic4Cre* especially in the hom (Figure 5.8): 1. the deletion progresses through time; 2. the deletion is more complete in the thalamus than in the prethalamus; 3. the deletion in the forming vLGN is consistent at all observed stages. Based on these characteristics, I speculate: 1. the deletion of Pax6 in the thalamic and prethalamic progenitor is likely to cause global cell number reduction in various thalamic and prethalamic nuclei in the hom; 2. the deletion in the vLGN can change the expression pattern of certain markers within the region. The het seems to have more Pax6 expressing cells than the wt, which could potentially cause an increase in the number of cells in the thalamus and prethalamus and certain patterning defects in the associated nuclei.

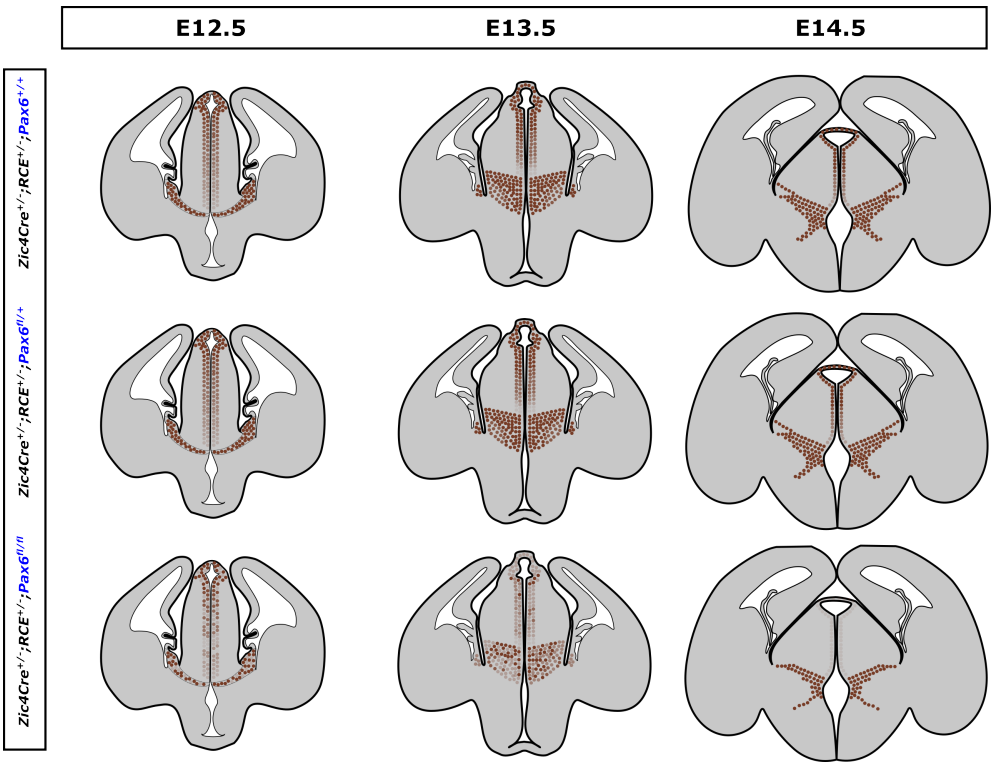


Figure 5.8: ***Diagram of Pax6 deletion on E12.5 to E14.5 diencephalon coronal sections from*** **Zic4Cre$^{+/-}$;RCE$^{+/-}$;Pax6$^{+/+}$**, **Zic4Cre$^{+/-}$;RCE$^{+/-}$;Pax6$^{fl/+}$** ***and*** **Zic4Cre$^{+/-}$;RCE$^{+/-}$;Pax6$^{fl/fl}$** ***mice.*** *Brown dots represent Pax6 positive cells.*

In the next chapter, I will look at some thalamic and prethalamic nuclei at postnatal day 0 and analyse the developmental defects caused by the *Pax6* deletion in the nuclei, especially the vLGN, dLGN and VP.

Chapter 6

Zic4Cre mediated deletion of *Pax6* causes developmental defects in vLGN, dLGN and VP

6.1 Introduction

In the previous chapter, I studied the pattern of Pax6 deletion in the diencephalon of the conditional knockouts driven by the *Zic4Cre*. The deletion of Pax6 in the ventricular zone of the thalamus and prethalamus at E12.5 to E14.5 and the change in the distribution of Pax6 positive cells in the E16.5 vLGN in the knockouts, indicates that Pax6 is involved in the development of individual nuclei such as vLGN and possibly its adjacent nuclei dLGN and VP. In this chapter, I focused on studying the morphological properties, such as volume, cell density and cell composition, of these three nuclei to see whether and how the deletion of Pax6 affects their formation.

6.2 Aim of the project

The neurogenesis in the diencephalon especially in the thalamus and prethalamus starts at around E10.5 and the first nulcei of the thalamus and prethalamus emerge at E15.5. At P0, most thalamic and prethalamic nuclei have been formed and the analysis of the formation of these newly formed nuclei at this stage in the conditional *Pax6* mutants will give us clear information about how the deletion of Pax6 could affect the development of various thalamic and prethalamic nuclei. In this project, I focused on three adjacent nuclei, the ventral lateral geniculate nuclei (vLGN), the dorsal lateral geniculate nuclei (dLGN) and the ventral

posterior nuclei (VP, including the medial ventral posterior nuclei and the lateral ventral posterior nuclei). I examined the volume of these nuclei, the total cell number, the cell density, the proportion of GFP+ve *Zic4* lineage cells respectively to further investigate the role of Pax6 in the formation of these nuclei.

6.3 Results

Immunohistochemistry of GFP, COUP-TFII, Nkx2.2 and Lim1/2 was performed on coronal sections of paraffin embedded sample brains from P0 *Zic4Cre*$^{+/-}$;*RCE*$^{+/-}$;*Pax6*$^{fl/+}$, *Zic4Cre*$^{+/-}$;*RCE*$^{+/-}$;*Pax6*$^{fl/+}$ and *Zic4Cre*$^{+/-}$;*RCE*$^{+/-}$;*Pax6*$^{fl/fl}$ mouse pups.

6.3.1 Delineation of diencephalic nuclei vLGN, dLGN and VP

6.3.1.1 Image alignment and reference atlas

Three mouse brain atlases, including the *Prenatal Mouse Brain Atlas* by Uta Schambra, *The mouse brain in stereotaxic coordinates* by George Paxinos and Keith Franklin (Figure 6.1), and the Allen Mouse Brain Atlas (Figure 6.2), have been used in this project to appreciate the anatomical levels of the acquired sections and the outlines of the nuclei of interest. Within these atlases, the Uta one provides the only reference for mouse brains at the age (gestational day 18) that is similar to the age (P0) that I am interested in. Both the Paxinos and Franklin's atlas and the Allen Mouse Brain Atlas are atlases for adult mouse brains. The former provides more detailed annotation for substructures like ventral lateral geniculate nucleus, magnocellular part (VLGMC) and ventral lateral geniculate nucleus, parvicellular part (VLGPC) within the vLGN. The latter is a full colour, high-resolution and web based reference, which supports instant interactive referencing. Though the age of the mouse brain used in the last two atlases is much older than the brains used in this project, the atlases can still provide great guidance on the recognition of the anatomical structure of P0 brains, especially in the thalamus and prethalamus, since most of the prethalamic and thalamic nuclei have been reaching their adult form at P0. The Allen Brain Atlas does also have an Allen Developing Mouse Brain Atlas providing ISH data for a great number of genes at E11.5, E13.5, E15.5, E18.5 and P4, however almost all the ISH data are from sagittal sections instead of coronal sections and the annotation of structures are only conducted to the prosomeric levels (p1, p2 and p3) with no appreciation for specific diencephalic nuclei, which is not convenient to use and thus not referred to.

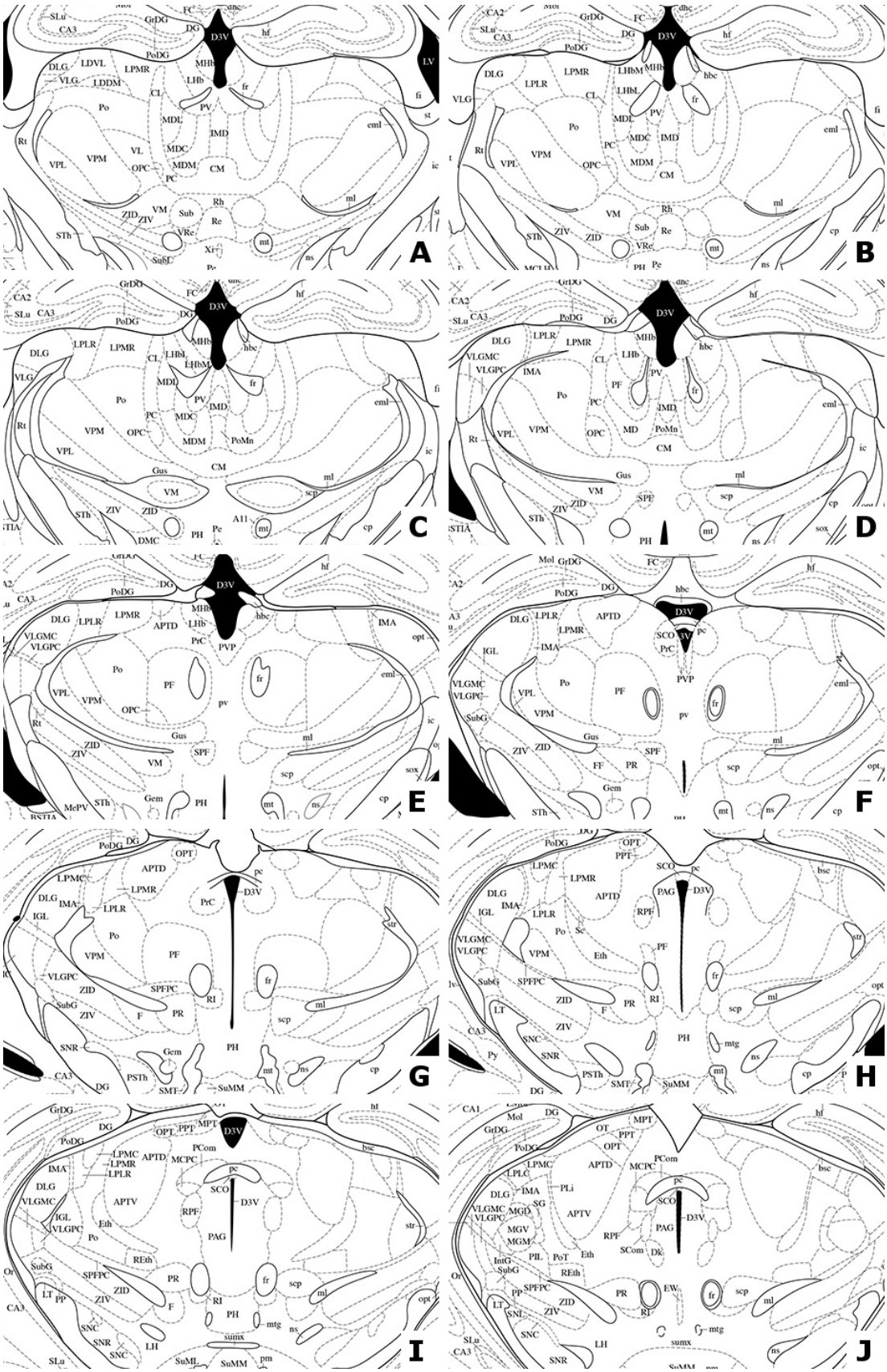


Figure 6.1: ***Coronal mouse brain atlas by Paxinos and Franklin for anatomical registration.*** *Ten adjacent coronal sections at 120 μm intervals were chosen from the atlas.*

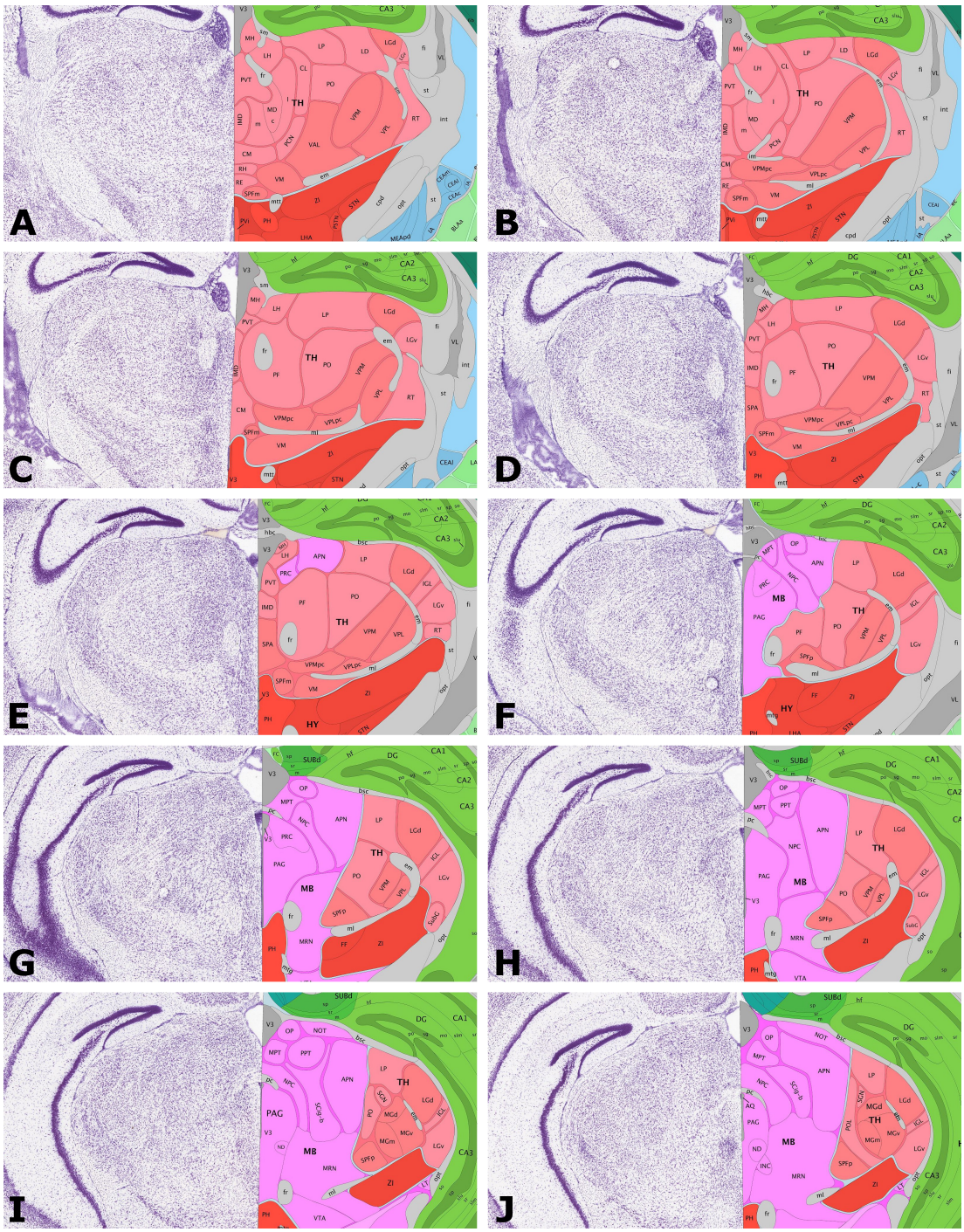


Figure 6.2: ***Coronal mouse brain atlas by Allen Brain Institute for anatomical registration.*** *Ten adjacent coronal sections at 100 µm intervals from the atlas were used to register the anatomical level of the acquired images. The images A to J were arranged from the rostral most level of the vLGN to its caudal most level.*

The low power images (10x objective) obtained via microscopy were used to confirm the anatomical level of each section in use and the higher power images (20x objective) were taken for the same sections in order to perform quantitative analyses. The acquired images were registered to the corresponding positions and the three nuclei vLGN, dLGN and VP are outlined with the help of the atlases and the staining of markers like COUP-TFI (Figure 6.3 and Figure 6.4), COUP-TFII (Figure 6.5 and Figure 6.6), Lim1/2 (Figure 6.7 and Figure 6.8), Nkx2.2 (Figure 6.9 and Figure 6.10) and Cresyl violet staining.

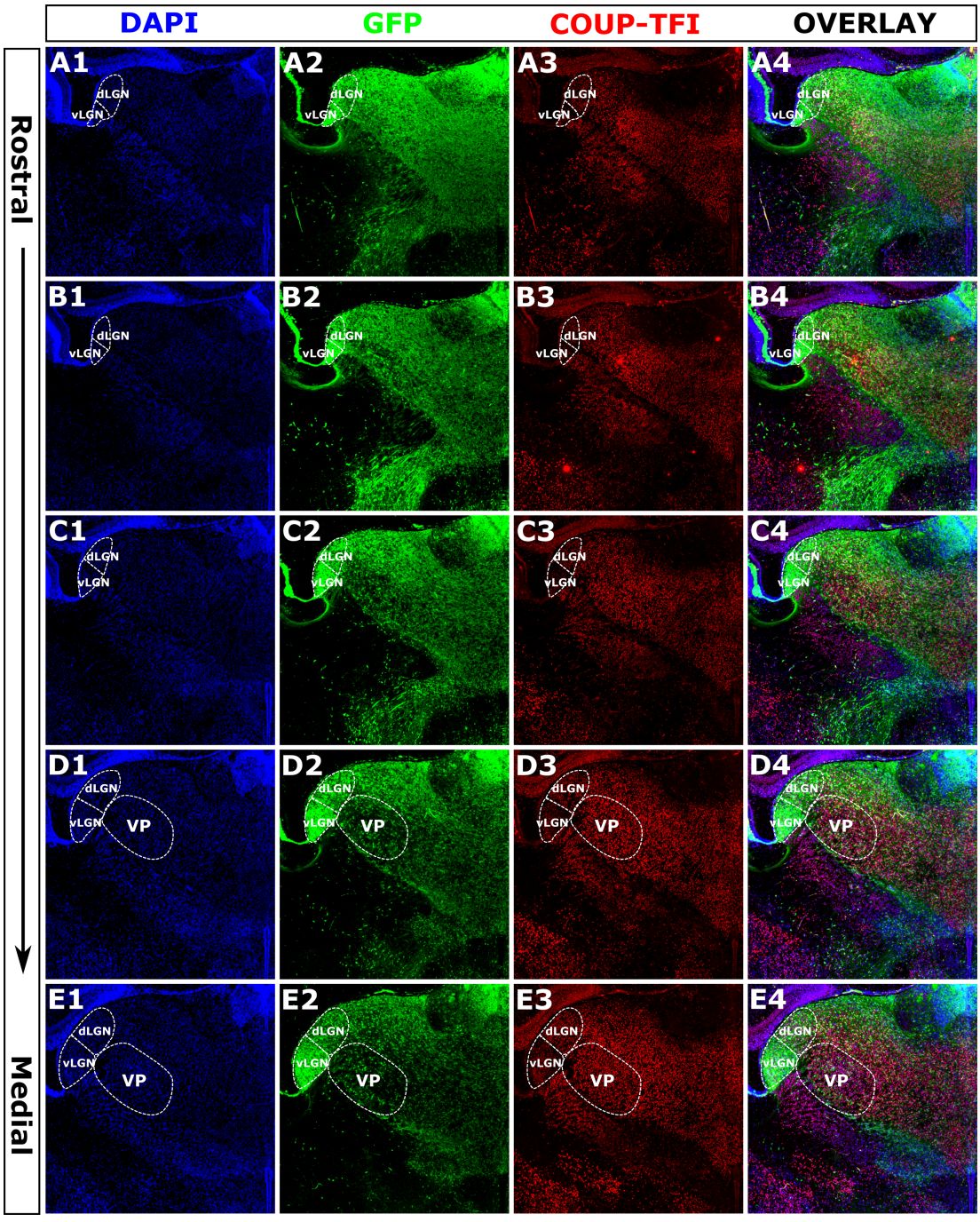


Figure 6.3: ***Standard coronal series of P0 Pax6$^{+/+}$ mouse brain for position registration of all the Pax6$^{+/+}$ sections from rostral to middle levels (COUP-TFI).*** *Scale bar: 250 μm.*

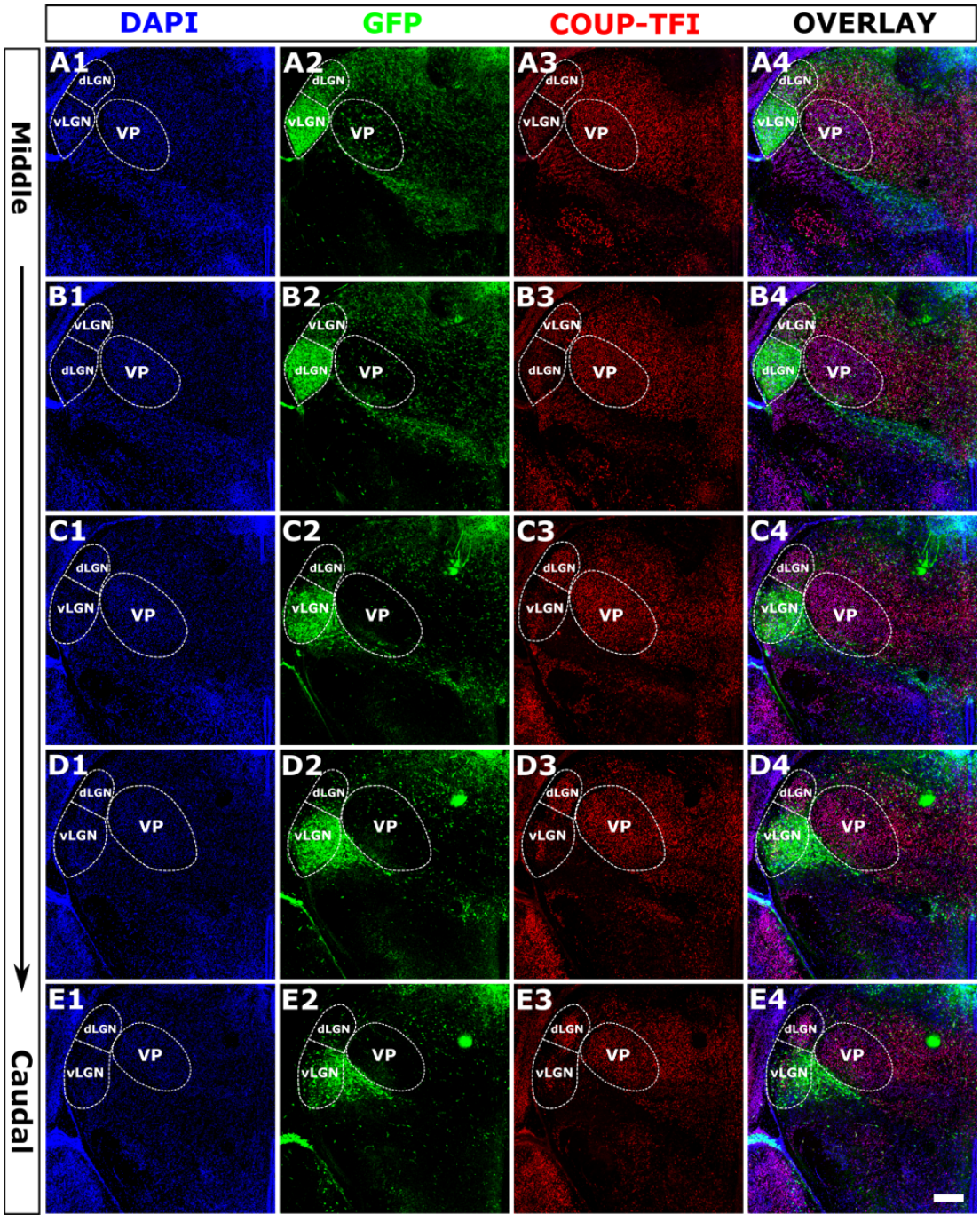


Figure 6.4: ***Standard coronal series of P0 Pax6$^{+/+}$ mouse brain for position registration of all the Pax6$^{+/+}$ sections from middle to caudal levels (COUP-TFI).*** *Scale bar: 250 μm.*

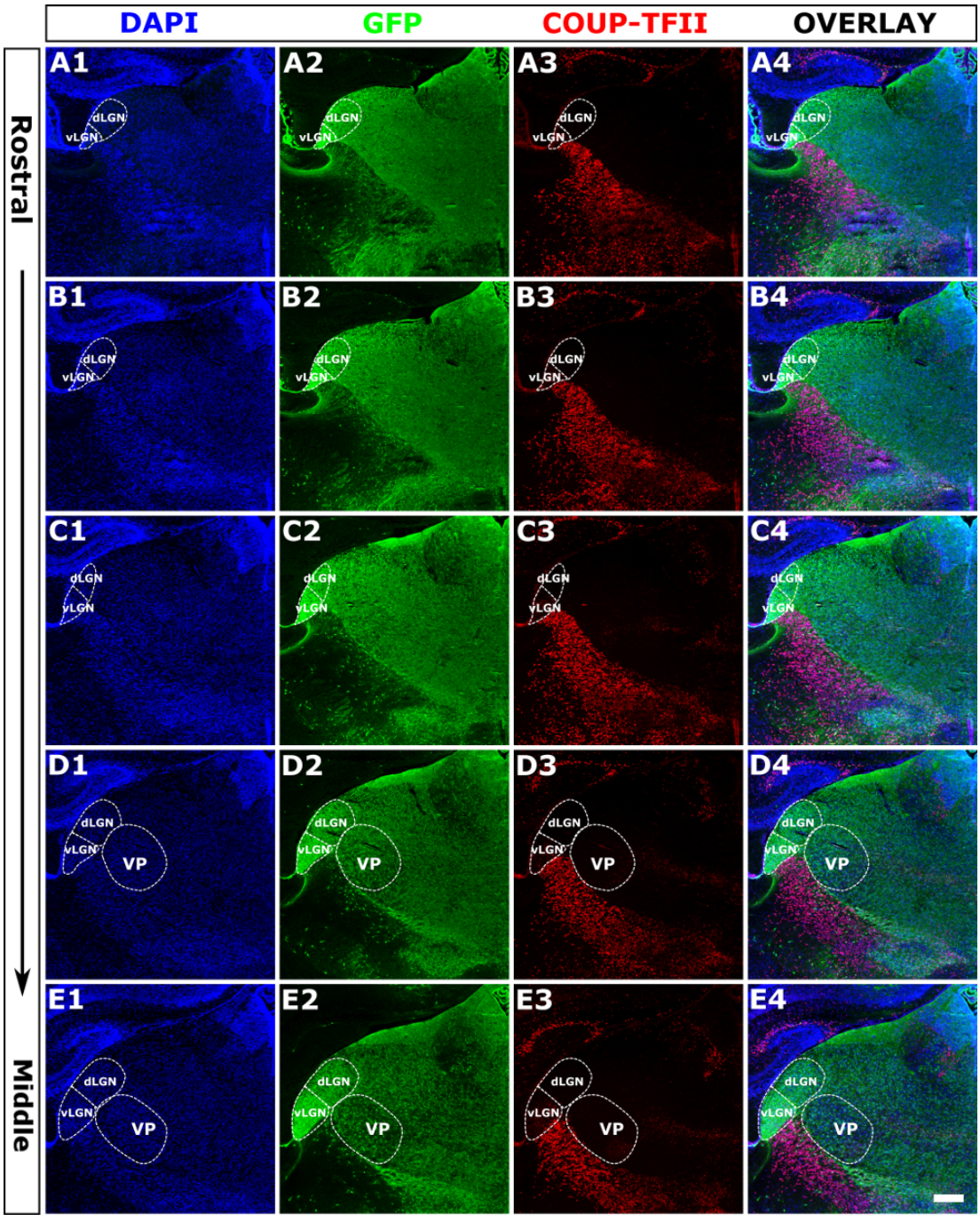


Figure 6.5: ***Standard coronal series of P0 Pax6$^{+/+}$ mouse brain for position registration of all the Pax6$^{+/+}$ sections from rostral to middle levels (COUP-TFII).*** *Scale bar: 250 μm.*

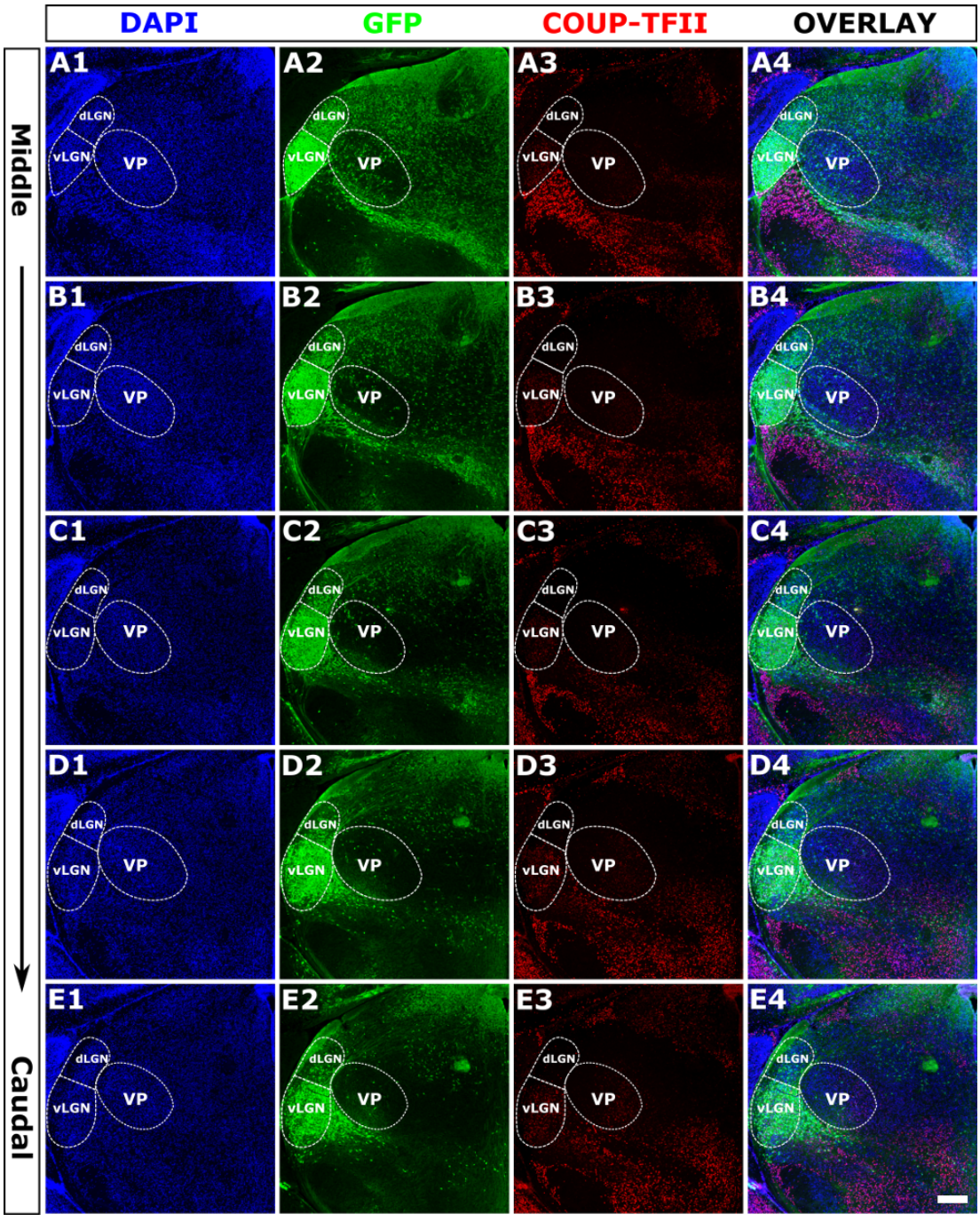


Figure 6.6: ***Standard coronal series of P0 Pax6$^{+/+}$ mouse brain for position registration of all the Pax6$^{+/+}$ sections from middle to caudal levels (COUP-TFII).*** *Scale bar: 250 μm.*

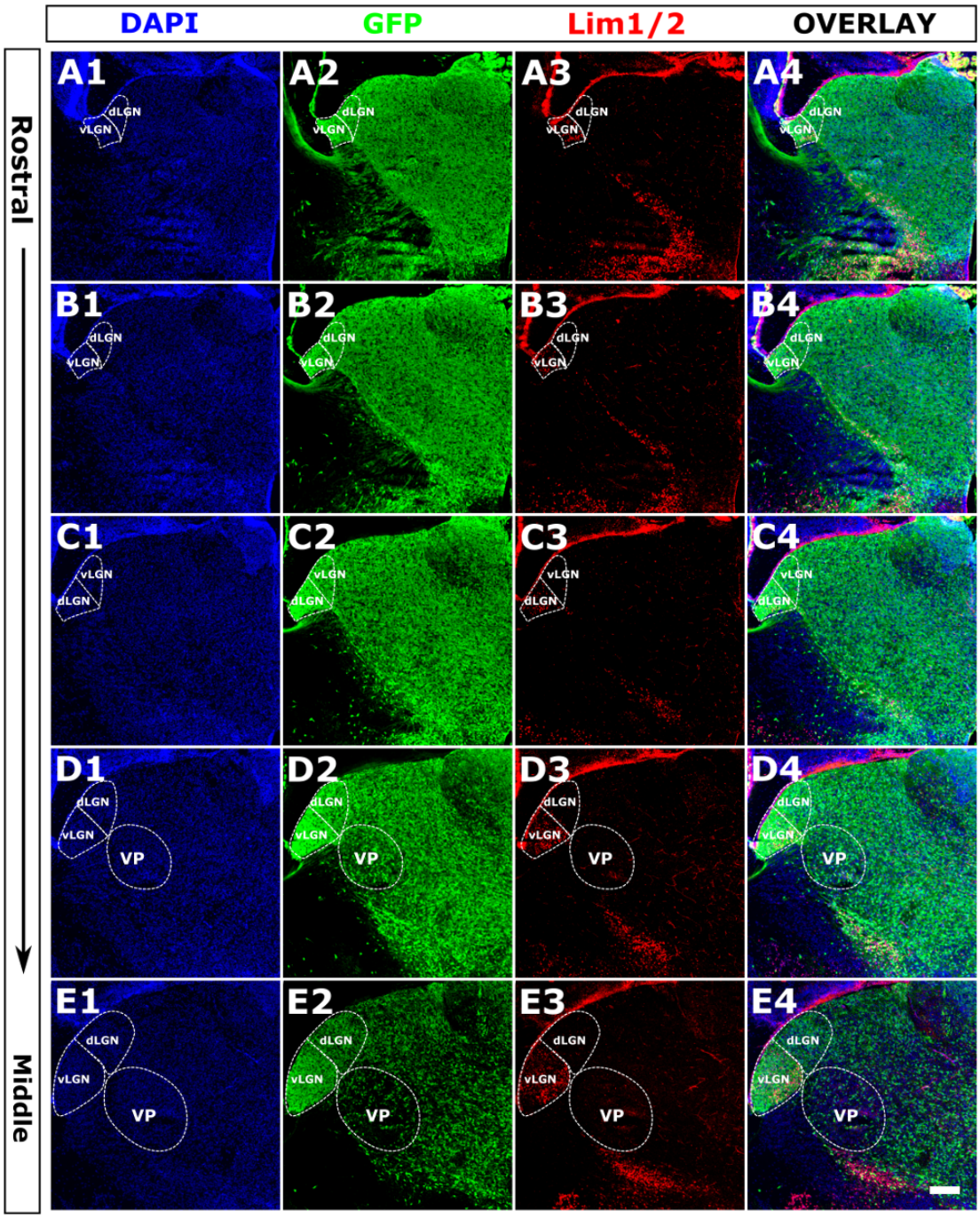


Figure 6.7: ***Standard coronal series of P0 Pax6$^{+/+}$ mouse brain for position registration of all the Pax6$^{+/+}$ sections from rostral to middle levels (Lim1/2).*** *Scale bar: 250 µm.*

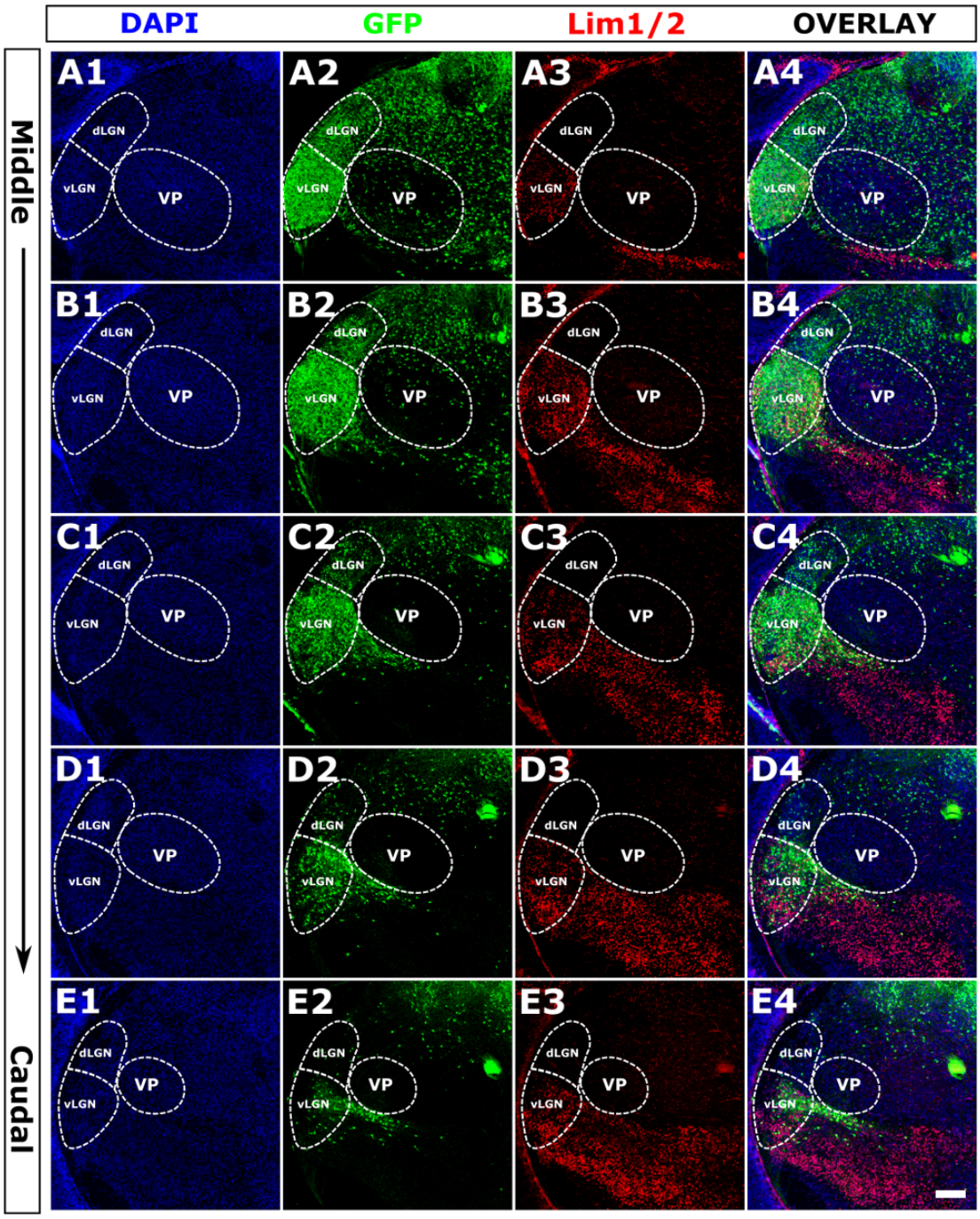


Figure 6.8: ***Standard coronal series of P0 Pax6$^{+/+}$ mouse brain for position registration of all the Pax6$^{+/+}$ sections from middle to caudal levels (Lim1/2).*** *Scale bar: 250 μm.*

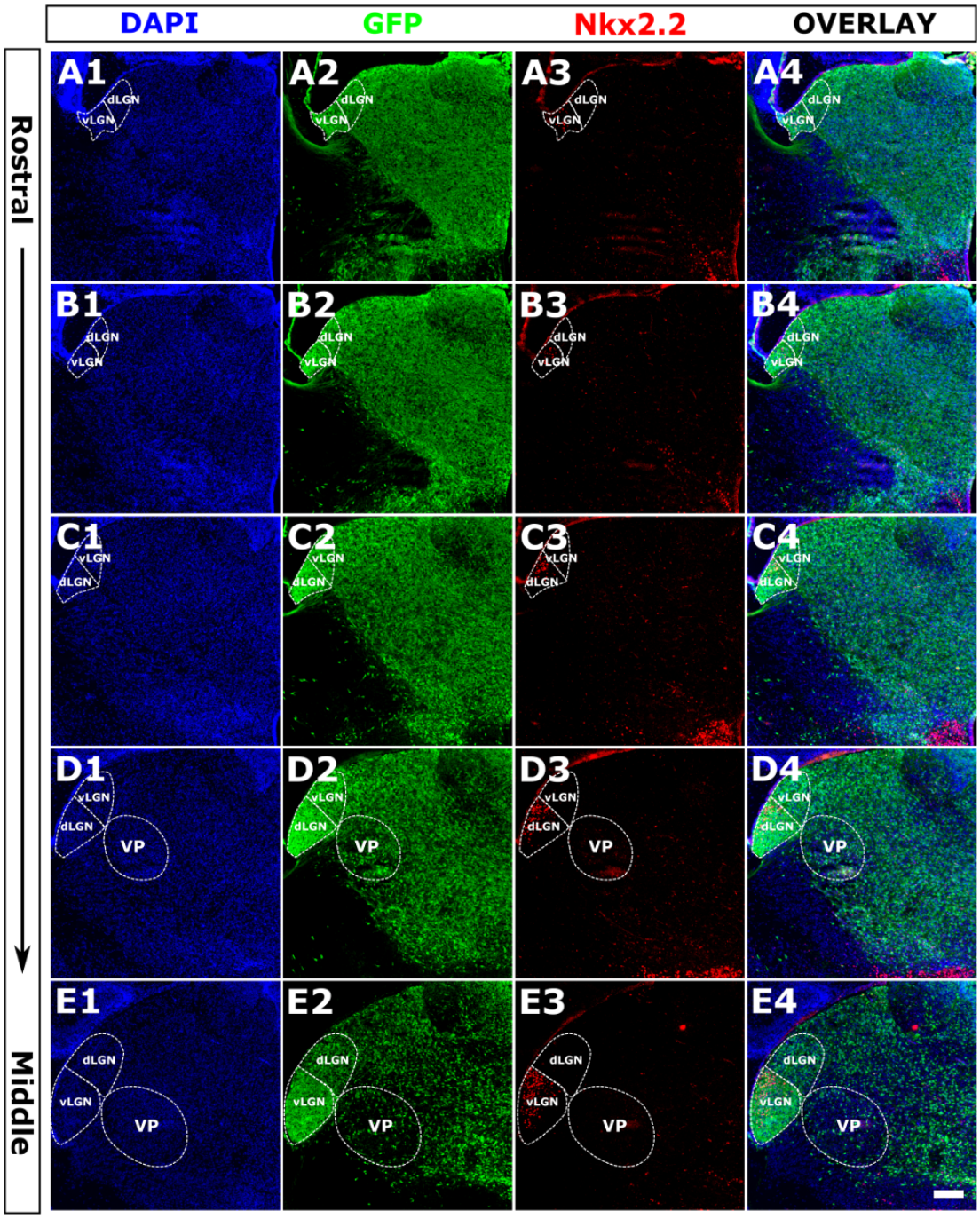


Figure 6.9: ***Standard coronal series of P0 Pax6$^{+/+}$ mouse brain for position registration of all the Pax6$^{+/+}$ sections from rostral to middle levels (Nkx2.2).*** *Scale bar: 250 µm.*

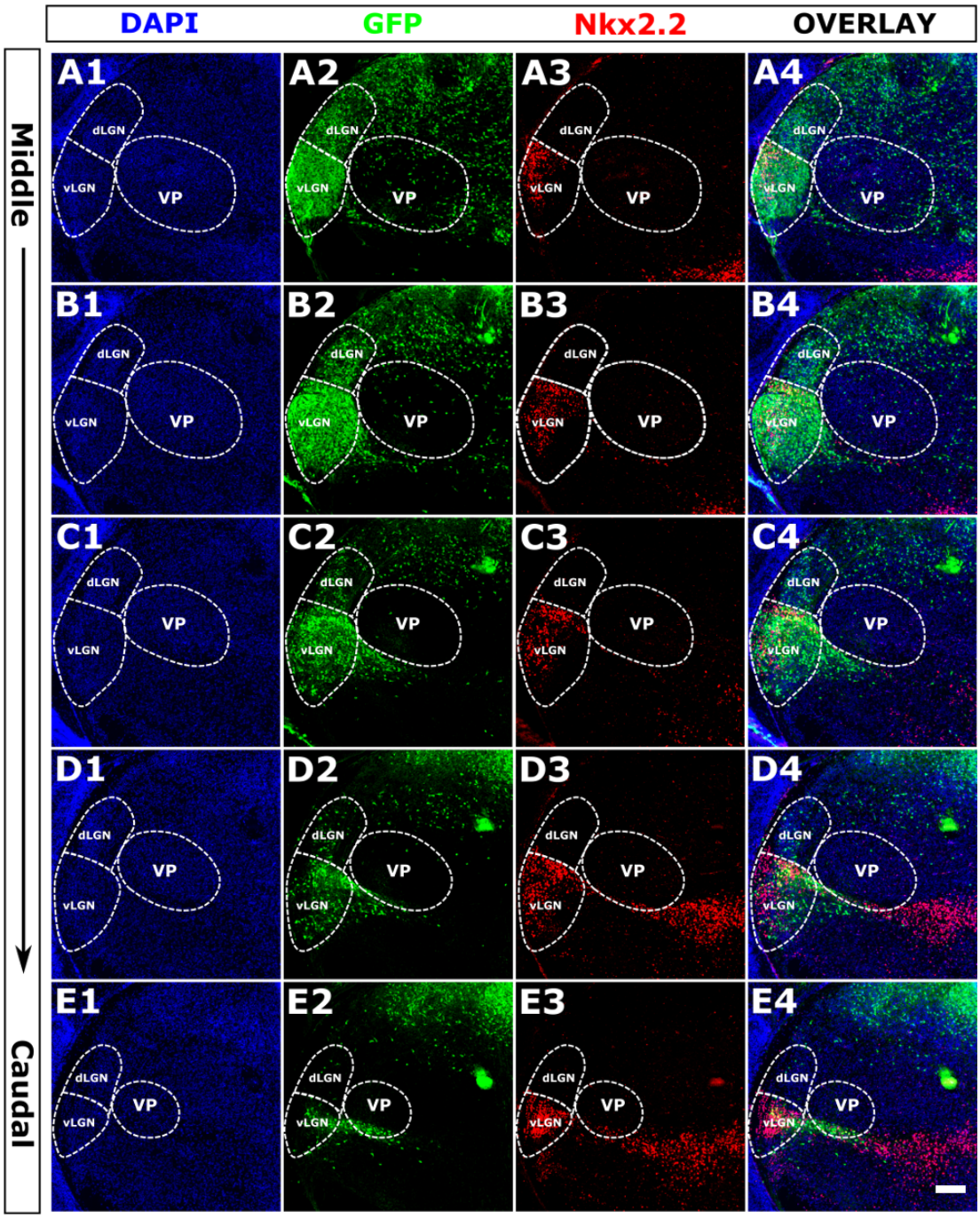


Figure 6.10: ***Standard coronal series of P0 Pax6$^{+/+}$ mouse brain for position registration of all the Pax6$^{+/+}$ sections from middle to caudal levels (Nkx2.2).*** *Scale bar : 250 µm.*

6.3.1.2 Boundary determination for vLGN, dLGN and VP

It has been montioned above that the stainings of markers like COUP-TFI (Figure 6.3 and Figure 6.4), COUP-TFII (Figure 6.5 and Figure 6.6), Nkx2.2 (Figure 6.9, Figure 6.10), Lim1/2 (Figure 6.7 and Figure 6.8) and cresyl violet staining are used to determine the boundary of the thalamic nuclei vLGN, dLGN and VP. The detailed information on how the combinatorial expression of these markers helps to determine the outlines of these nuclei is documented here.

vLGN

The staining of COUP-TFI delineates the boundary of the vLGN in most of the sections from rostral to caudal (Figure 6.11 A - H, dashed yellow contour). It is expressed across most of the thalamic nuclei including the vLGN, dLGN, RT, ZI and VP (Figure 6.11). The expression level of COUP-TFI in the vLGN is noticeably lower than the surrounding nuclei such as the dLGN, RT and VP (Figure 6.11 A - G). Within the vLGN, the cells close to the boundary express low or little COUP-TFI whereas the cells in the middle of the nucleus express a lot higher levels of COUP-TFI. At caudal levels, the vLGN becomes adjacent to the ZI which has very low to no expression of COUP-TFI (Figure 6.11 H - J). At this level, the expression of COUP-TFI in the vLGN becomes restricted in a subgroup of cells, which makes it difficult to determine the boundary between the vLGN and the ZI. Thus, the staining of COUP-TFI provides the dorsal boundary of the vLGN across all the sections and the medial boundary of the vLGN in most of the sections except the caudal-most one.

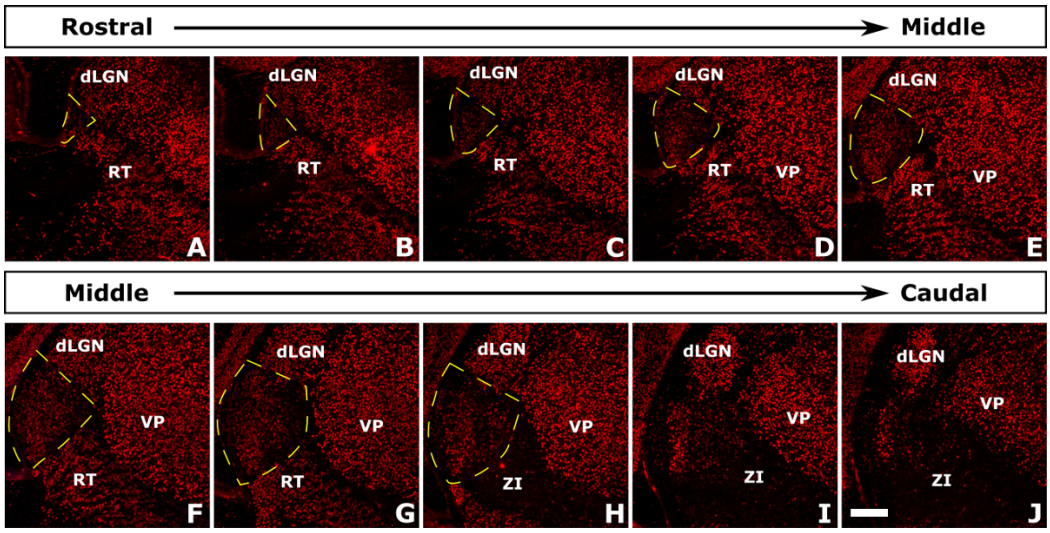


Figure 6.11: ***High power images of COUP-TFI staining for vLGN in P0 Pax6$^{+/+}$ mouse brain.*** *vLGN is outlined with dashed yellow contour. These images are corresponding to the images provided in Figure 6.3 and Figure 6.4. Scale bar: 250 μm.*

COUP-TFII is expressed in vLGN, RT, ZI and part of the VP (Figure 6.12 A - H). Among these nuclei, the RT shows the highest level of COUP-TFII expression in all cells whereas its expression in the vLGN and the ZI is conspicuously lower. The staining of COUP-TFII was used to determine the medial boundary of the vLGN at the caudal-most levels (Figure 6.12 H - J, dashed yellow contour). A great number of cells expressing high levels of COUP-TFII can be seen lateral to the boundary and only a few COUP-TFII positive cells (Figure 6.12 H and I, white arrow) are observed medial to the boundary. This difference in COUP-TFII expressing cell density between the vLGN and ZI allows me to appreciate the boundary between these two structures at the caudal-most levels.

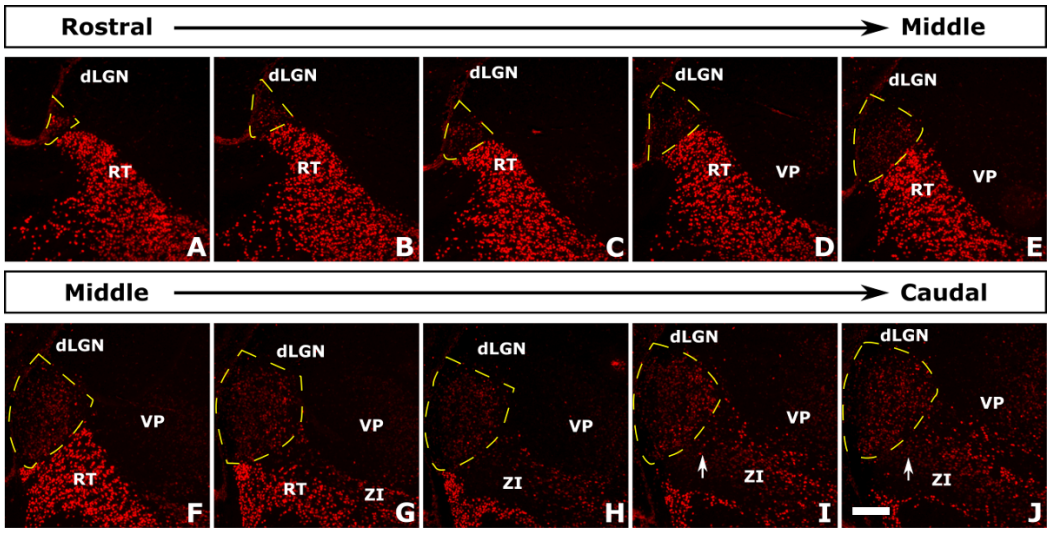


Figure 6.12: ***High power images of COUP-TFII staining for vLGN in P0 Pax6$^{+/+}$ mouse brain.*** *The vLGN is outlined with dashed yellow contour. The few COUP-TFII expressing cells in ZI are pointed at using white arrows. These images are corresponding to the images provided in Figure 6.5 and Figure 6.6. Scale bar: 250 μm.*

The boundary of vLGN is thus determined by the expression pattern of both COUP-TFI (Figure 6.11) and COUP-TFII (Figure 6.12).

dLGN

The delineation of the dLGN is performed using COUP-TFI staining and specific landmarks, such as the external medullary thalami, a layer of myelinated axon fibers. The staining of COUP-TFI is stronger in the dLGN than in the vLGN, which makes it easy to draw the boundary between the vLGN and dLGN (Figure 6.13 A - J, dashed yellow contour). The external medullary thalami (EM) in the thalamus is a fiber layer with no cells within, which leaves a gap between the dLGN and VP when the neurons are stained with markers such as

DAPI and COUP-TFI, and helps to determine the medial boundary of the dLGN. The lateral posterior nucleus (LP) is dorsomedial to the dLGN. The angle between the major axes of these two adjacent nuclei is clearly visible in all coronal sections. Also, a great more COUP-TFI expressing cells are observed in the dLGN than in the LP especially at middle to caudal levels (Figure 6.13 F - J).

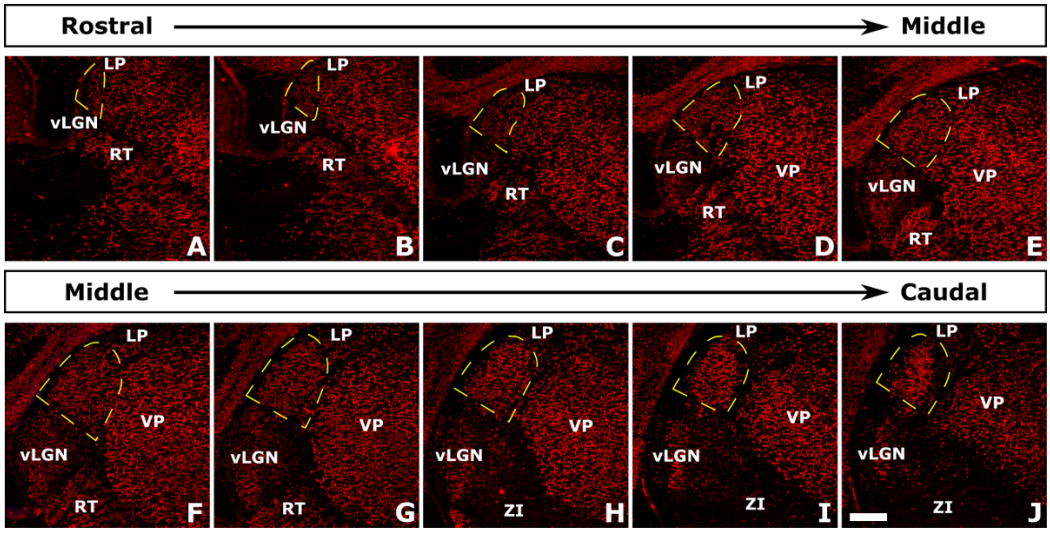


Figure 6.13: ***High power images of COUP-TFI staining for dLGN in P0 Pax6$^{+/+}$ mouse brain.*** *dLGN is outlined with dashed yellow contour. These images are corresponding to the images provided in Figure 6.3 and Figure 6.4. Scale bar : 250 μm.*

VP

The ventral posterior nuclei are ovoid with a diminishing posterior tip rostral to the medial geniculate nucleus (MGN). The vLGN and dLGN are lateral to the VP; the RT and ZI are ventral to the VP. The lateral and ventral boundary of the VP can be easily delineated as the fibre layer external medullary thalami and internal medullary thalami separate the VP from the vLGN, dLGN, RT and ZI.

The medial and the dorsal boundary of the VP is determined with the help of cresyl violet (Figure 6.14) and COUP-TFII stainings (Figure 6.15). The cresyl violet staining is helpful in depicting the VP from middle to caudal levels as the staining is stronger in the VP than in the surrounding structures (Figure 6.14 F - J). The COUP-TFII staining is used to delineate VP at rostral to middle level (Figure 6.15 C - E). The expression pattern of COUP-TFII is compared to the *COUP-TFII* (*Nr2f2*) ISH data and the corresponding reference atlas at P56 provided by the Allen Mouse Brain Atlas (Figure 6.16). The ISH data shows that the expression of *COUP-TFII* is higher in the VPM and lower in the VPL (Figure 6.16 A′ and B′) and a similar

pattern is seen in the COUP-TFII immunohistochemistry images (Figure 6.14 D - J, dashed yellow contour). The medial and the dorsal boundary of the VP is mainly determined by the relatively high expression of COUP-TFII in the VPM.

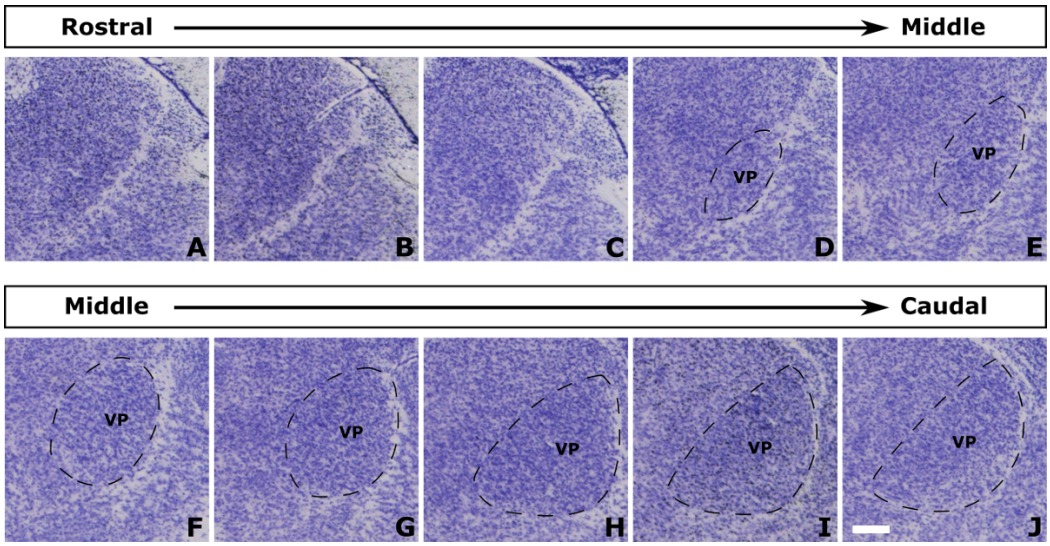


Figure 6.14: ***High power images of cresyl violet staining for VP in P0 Pax6$^{+/+}$ mouse brain.*** *VP is outlined with dashed black contour. Scale bar: 250 μm.*

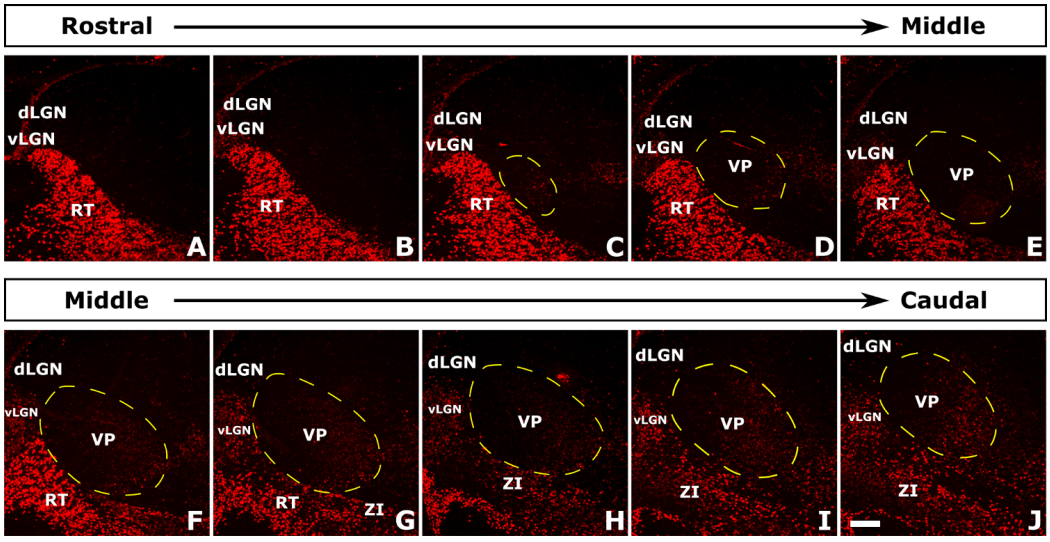


Figure 6.15: ***High power images of COUP-TFII staining for VP in P0 Pax6$^{+/+}$ mouse brain.*** *VP is outlined with dashed yellow contour. Scale bar: 250 μm.*

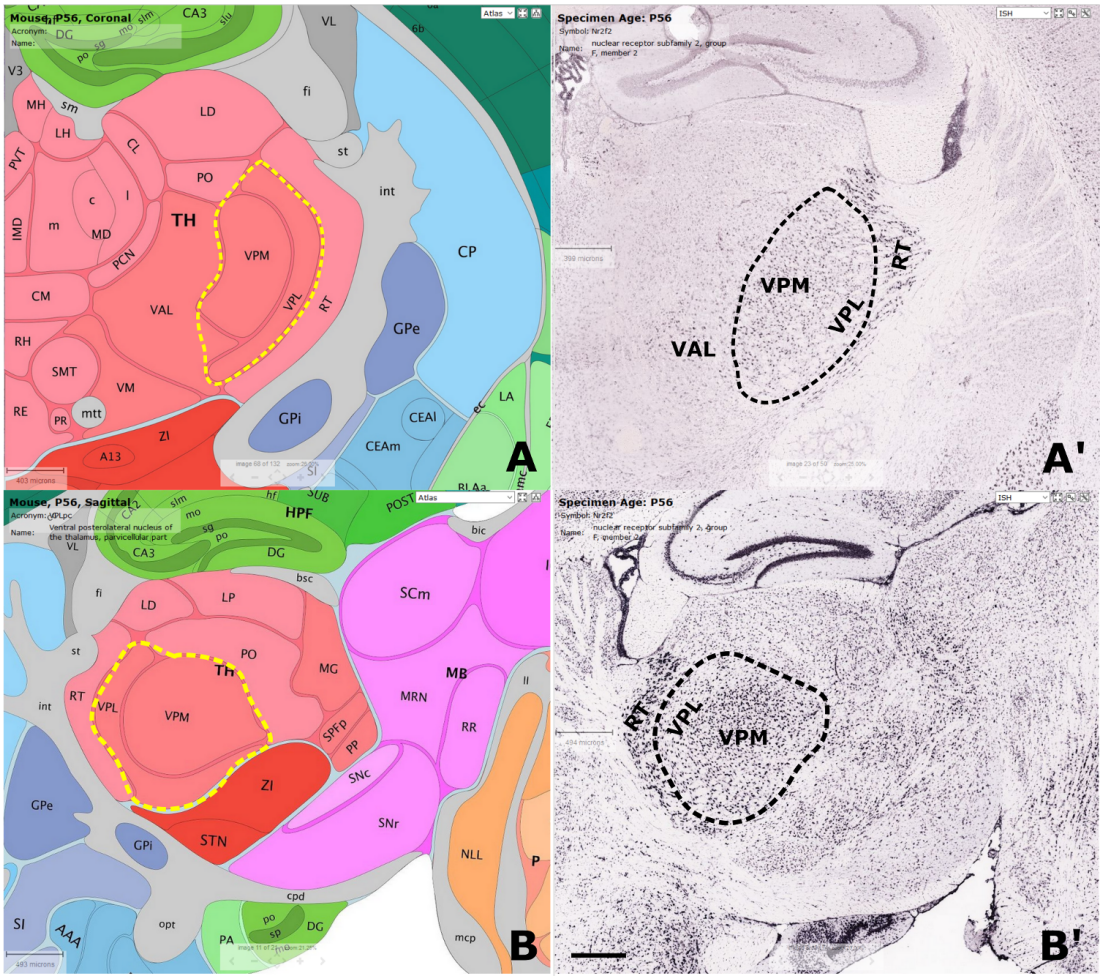


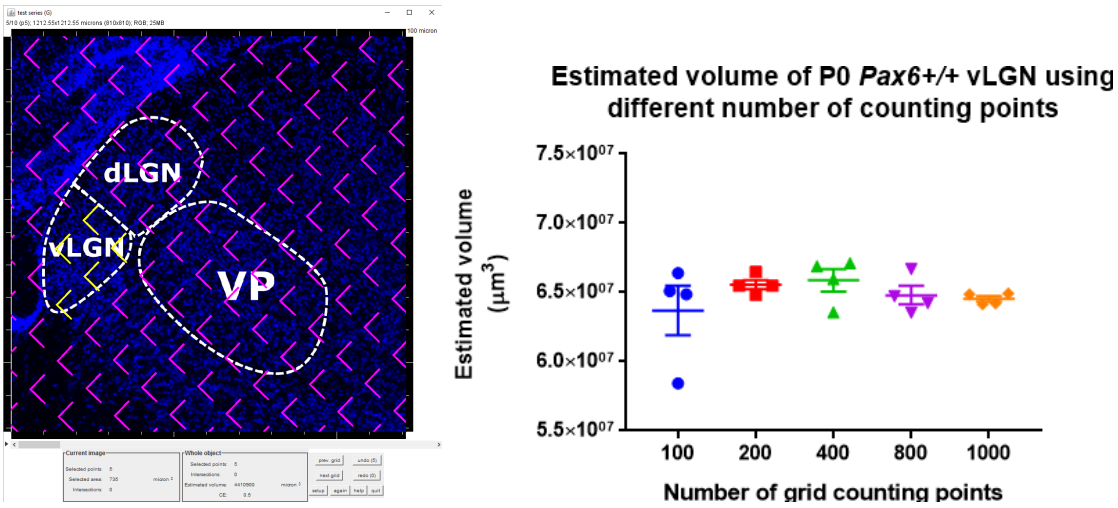
Figure 6.16: ***COUP-TFII ISH and reference atlas at P56 for VP from Allen Mouse Brain Atlas.*** *(A) Coronal reference atlas for P56 mouse brain. (A') COUP-TFII ISH on coronal mouse brain section at P56. (B) Sagittal reference atlas for P56 mouse brain. (B') COUP-TFII ISH on sagittal mouse brain section at P56. Dashed yellow contour, VP including VPM and VPL in reference atlas. Dashed black contour, VP including VPM and VPL in COUP-TFII ISH images. Scale bar: 400 μm.*

Though the marker gene expression appears to be sufficient for delineating the boundaries of the three nuclei in Pax6$^{+/+}$ diencephalon, it is possible the expression of these markers will change caused by the deletion of *Pax6* in the conditional mutants, which is a limitation of this method that I am fully aware of.

6.3.2 Estimated volume change in vLGN, dLGN and VP in conditional *Pax6* mutants

The volumes of the nuclei were estimated using the ImageJ Volumest plugin [96], a point - grid counting estimator based on Cavalieri's Principle. A series of ten coronal sections with a

regular interval of 60 μm from each brain sample were imported into ImageJ and calibrated using the straight line tool and the set scale tool. Then a pilot run of measurement of P0 *Zic4Cre*$^{+/-}$;*RCE*$^{+/-}$;*Pax6*$^{+/+}$ vLGN was performed using the recommended parameter settings based on the slice thickness (equivalent to the section interval) and image size (Figure 6.17 (a)). The pilot run reports the estimated volume and the coefficient of error (CE), usually between 0.3 to 0.5. Then the parameters used for the measurement were optimised by using different numbers of counting points (generating random grids of different sizes), to perform volume estimation for four times in order to achieve the best precision and a satisfactory CE (Figure 6.17 (b)). Usually, a total CE of less than 0.05 is considered to be adequate for most of the studies to provide accurate quantitative information. The nuclei vLGN, dLGN and VP from each selected brain section were demarcated by referencing to the standard series (Figure 6.3, Figure 6.4, Figure 6.5, Figure 6.6, Figure 6.9, Figure 6.10, Figure 6.7 and Figure 6.8) and the volumes of these nuclei were estimated using the Volumest plugin.



(a) (b)

Figure 6.17: ***Nuclei volume estimation with Volumest and parameter optimisation.*** *(a) Counting and result window of ImageJ Volumest plugin. The magenta right-angle grid is generated based on 100 points and the grid width is 104 μm. The yellow right-angle points are the ones included in the vLGN, the ones I counted. The estimated volume and the CE are reported in the gray area below the counting window. (b) Plot of estimated volumes against choosen counting point number. Four data points for each given number of counting points indicate the four repeated measurements. I can see that a point number of more than 200 gives a good precision (and a CE of 0.04) from the plot. Thus, 200 was chosen as the number of counting points for all the volume estimating measurements.*

Univariate statistics (means ± SEM) were performed for all studied variables. One-way ANOVA was performed to study the effect of genotype on the estimated volume and the total

cell number of the three nuclei. Two-way ANOVA was performed to examine the main effects of genotype and rostral-caudal position on the area, the cell density, the number of cells and the GFP+ve cell proportion of each nucleus. The Tukey post hoc test was performed for all pair-wise comparisons subsequent to the ANOVAs. For two-way ANOVAs, the Tukey post hoc test results were only reported for the main effects of genotype. All experiments were repeated in four embryos for each genotype. Proportion data was transformed using either logistic or arcsine square root transformation ahead of the statistical tests.

Since Pax6's role in neurogenesis has been studied in other parts of the brain such as the cortex, it's likely that the deletion of *Pax6* in the developing diencephalon causes cell number change in the affected nuclei, which can be reflected from the volume of the nuclei. Thus, I first studied the volume change of the diencephalic nuclei vLGN, dLGN and VP respectively.

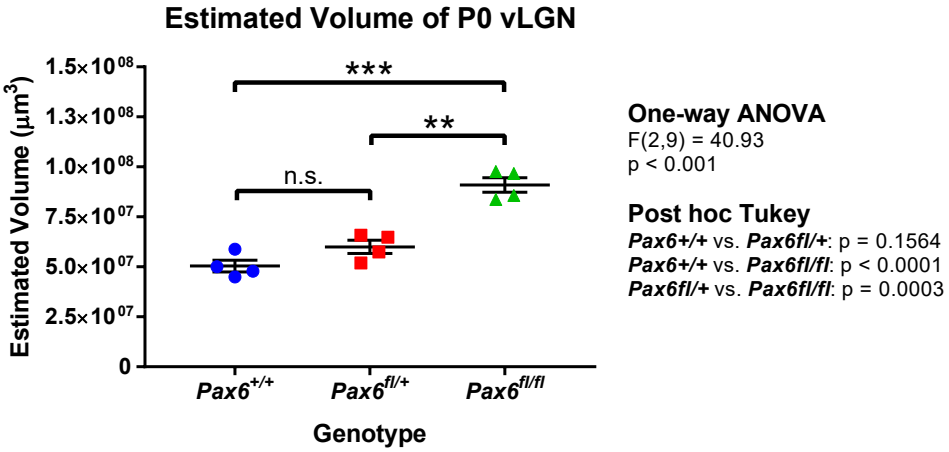


Figure 6.18: ***Estimated volume change in vLGN in conditional Pax6 mutants.***

The estimated volume of vLGN in the $Pax6^{fl/fl}$ ($9.095\times10^7 \pm 3.637192\times10^6$ μm^3) is significantly larger than that in both the $Pax6^{+/+}$ ($5.0375\times10^7 \pm 2.996213\times10^6$ μm^3) and the $Pax6^{fl/+}$ ($5.9975\times10^7 \pm 3.279323\times10^6$ μm^3) (Figure 6.18). It seems the estimated volume of vLGN in the $Pax6^{fl/+}$ is slightly larger than that in the $Pax6^{+/+}$ but the difference is not significant (Figure 6.18).

The deletion of *Pax6* caused an increase in the volume of the vLGN in the $Pax6^{fl/fl}$ compared to the $Pax6^{+/+}$ and $Pax6^{fl/+}$.

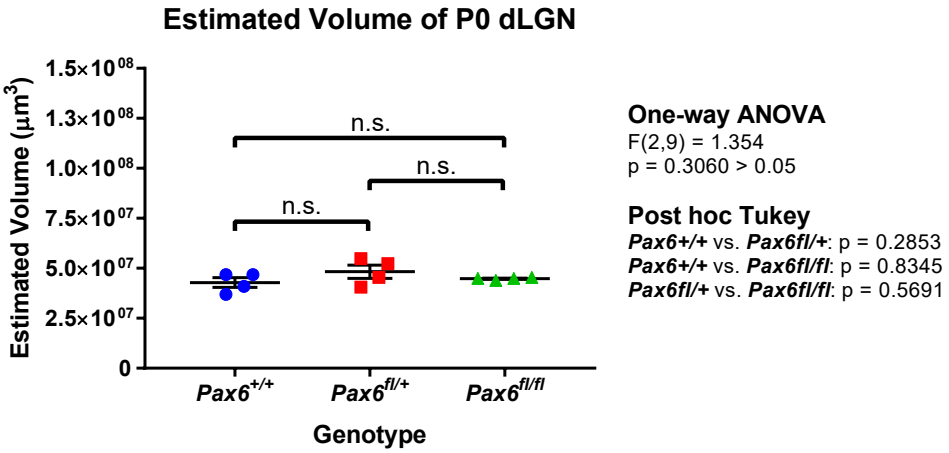


Figure 6.19: ***Estimated volume change in dLGN in conditional Pax6 mutants.***

The estimated volumes of dLGN in three different genotypes, the $Pax6^{+/+}$ ($4.285\times10^{7} \pm 2.422292\times10^{6}$ μm^3), the $Pax6^{fl/+}$ ($4.825\times10^{7} \pm 3.259473\times10^{6}$ μm^3) and the $Pax6^{fl/fl}$ ($4.4775\times10^{7} \pm 3.14576\times10^{5}$ μm^3), are more or less the same (Figure 6.19).

The deletion of *Pax6* causes no significant change in the volume of the dLGN.

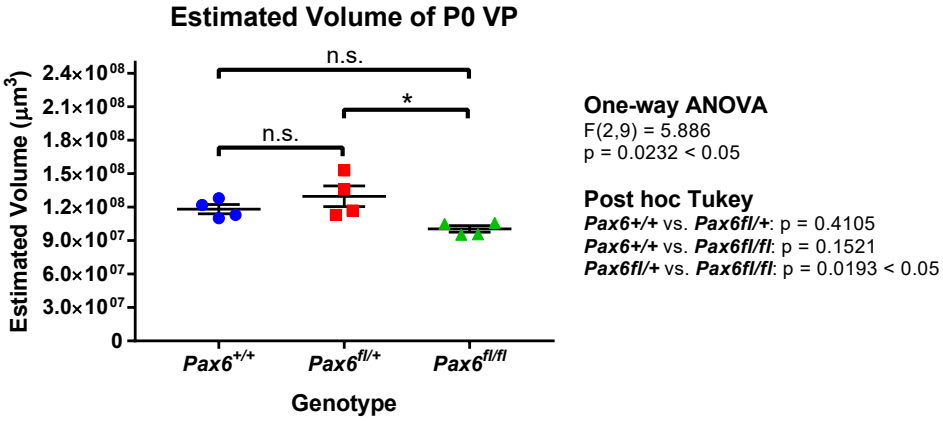


Figure 6.20: ***Estimated volume change in VP in conditional Pax6 mutants.***

The estimated volumes of VP in three different genotypes of embryos, the $Pax6^{+/+}$ ($1.1825\times10^{8} \pm 4.130678\times10^{6}$ μm^3), the $Pax6^{fl/+}$ ($1.2975\times10^{8} \pm 9.231964\times10^{6}$ μm^3) and the $Pax6^{fl/fl}$ ($1.005\times10^{8} \pm 2.895111\times10^{6}$ μm^3), are different according to the result of the one-way ANOVA (Figure 6.20). Post hoc Tukey test revealed that the only significant difference between groups was found between the $Pax6^{fl/+}$ and the $Pax6^{fl/fl}$.

The deletion of *Pax6* causes no significant change in the volume of the VP in the $Pax6^{fl/fl}$ and $Pax6^{fl/+}$ compared to the emphPax6$^{+/+}$.

In order to further assess the morphological change of each of the three nuclei, I measured the area that each nuclei occupies on observed sections at similar anatomical levels.

It is clear that at the area of vLGN in the $Pax6^{fl/fl}$ is significantly larger compared to that in both the $Pax6^{+/+}$ and the $Pax6^{fl/+}$ at the rostral to middle levels (Figure 6.21).

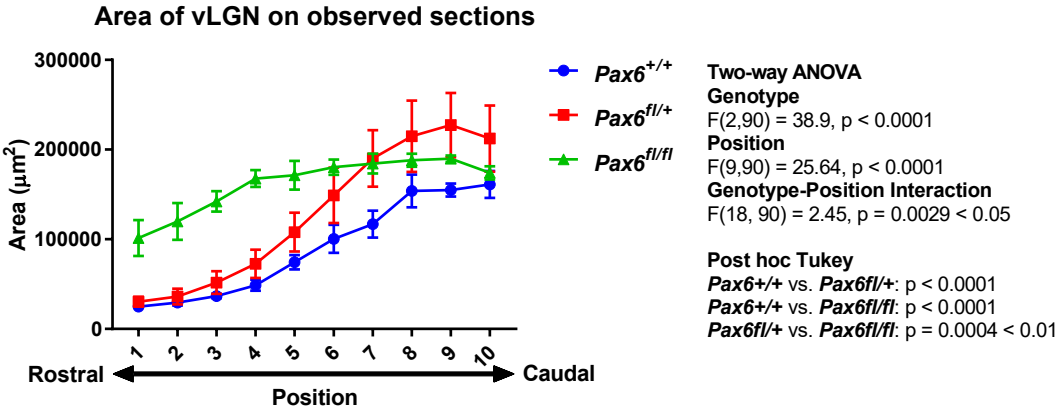


Figure 6.21: ***Area of vLGN on observed sections in conditional Pax6 mutants.***

At the caudal levels, the area of $Pax6^{fl/+}$ seems larger than that in the $Pax6^{+/+}$ and the $Pax6^{fl/fl}$ (Figure 6.21). Thus, the loss of two copies of functional *Pax6* gene leads to the significant increase of vLGN volume especially at the rostral to middle levels along the rostral-caudal axis whereas the loss of only one copy of functional *Pax6* leads to a potential increase of vLGN volume especially at the caudal levels.

Even though there is no significant change in the volume of the dLGN and VP in the conditional *Pax6* mutants, the possibility of a change in volume distribution within the nuclei along the rostral-caudal axis cannot be excluded. Thus, similar studies on each observed sections were carried out for the dLGN and VP as well.

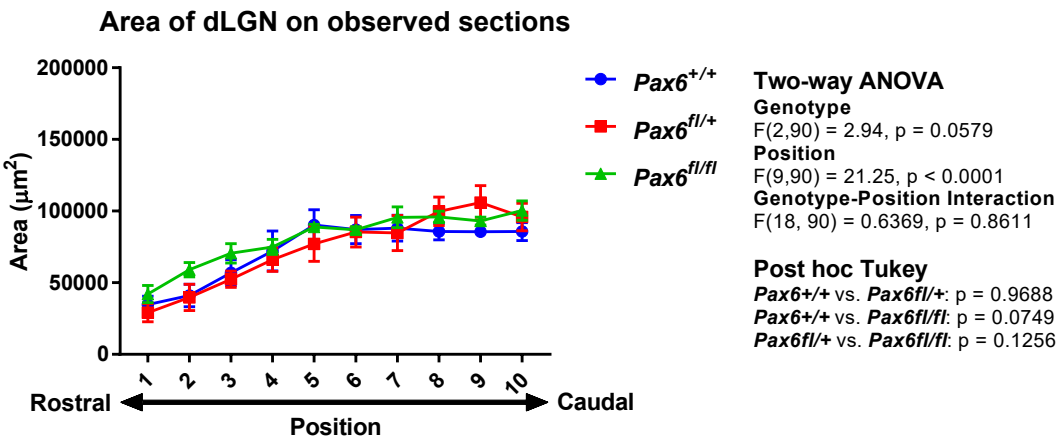


Figure 6.22: ***Area of dLGN on observed sections in conditional Pax6 mutants.***

In the dLGN, there is no significant differences in the avereage area at each position between the three genotypes (Figure 6.22).

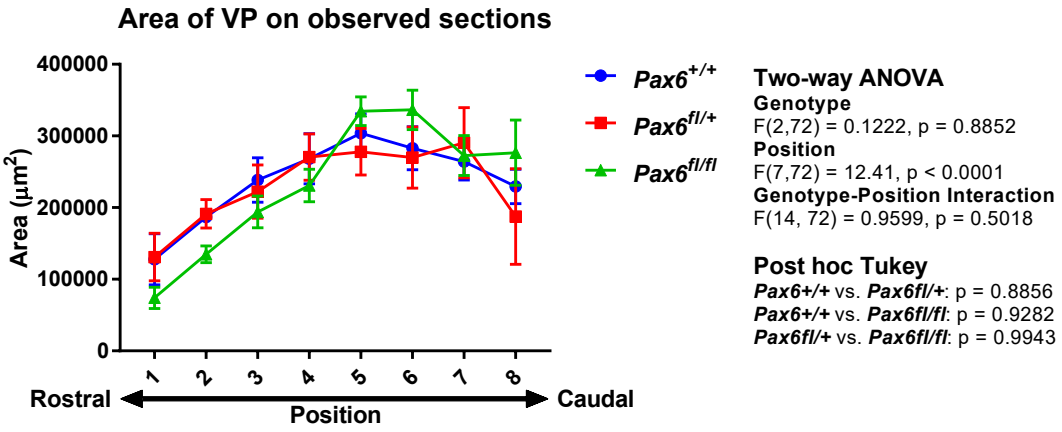


Figure 6.23: ***Area of VP on observed sections in conditional Pax6 mutants.***

In the VP, there is no significant differences in the avereage area at each position between the three genotypes (Figure 6.23).

In summary, the deletion of Pax6 causes volume change in the vLGN but not the adjacent dLGN or VP. From the study on a series of sections evenly situated from rostral to caudal of the vLGN, I can see that more volume was distributed towards the rostral part of the vLGN in the $Pax6^{fl/fl}$ and the main change in the $Pax6^{fl/+}$ is at the caudal part.

6.3.3 Cell composition change in vLGN, dLGN and VP in conditional *Pax6* mutants

The vLGN volume change observed in the *Pax6* conditional mutants opens the question whether the cell number and/or composition changes in vLGN, dLGN or VP in the conditional mutants in which one or both functional *Pax6* alleles are missing. In order to answer this question, I performed cell counting for all the cells in these nuclei with the help of DAPI staining and for the GFP+ve cells using both DAPI and GFP staining; I also calculated the proportion of GFP+ve cells in each of the three nuclei I'm interested in in all three genotypes.

In order to look at potential change in cell composition of the diencephalic nuclei vLGN, dLGN and VP, I performed cell counting for all the cells and the GFP+ve cells presented within the boundary of each nucleus in the thalamus of the $Pax6^{+/+}$, the $Pax6^{fl/+}$ and the $Pax6^{fl/fl}$ brains. Four embryos of each genotype were used for the cell counting experiment with each brain coronally sectioned at 10 μm. Each section is numbered according to its position along the rostral-caudal axis (Figure 6.24) and the sections for performing the counting were chosen with the help of the standard series provided before. For each brain section, the structure of interest from both the left and the right sides were examined and data from both sides were averaged to generate the data at each specific position.

	Series a				Series b					Series c				
Slide No.	1a	1	2	3	4	1b	1	2	3	4	1c	1	2	3	4
Section No.		50	110	170	230		70	130	190	250		90	150	210	270
Position No.		5	6	7	8		5	6	7	8		5	6	7	8
		100	120	180	240		80	140	200	260		100	160	220	280
	2a	1	2	3	4	2b	1	2	3	4	2c	1	2	3	4
		290	350	410	470		310	370	430	490		330	390	450	510
		5	6	7	8		5	6	7	8		5	6	7	8
		300	360	420	480		320	380	440	500		340	400	460	520
	3a	1	2	3	4	3b	1	2	3	4	3c	1	2	3	4
		530	590	650	710		550	650	670	730		570	630	690	750
		5	6	7	8		5	6	7	8		5	6	7	8
		540	600	660	720		560	620	680	740		580	640	700	760
	4a	1	2	3	4	4b	1	2	3	4	4c	1	2	3	4
		770	830	890	950		790	850	910	970		810	870	930	990
		5	6	7	8		5	6	7	8		5	6	7	8
		780	840	900	960		800	860	920	980		820	880	940	1000
	5a	1	2	3	4	5b	1	2	3	4	5c	1	2	3	4
		1010	1070	1130	1190		1030	1090	1150	1210		1050	1110	1170	1230
		5	6	7	8		5	6	7	8		5	6	7	8
		1020	1080	1140	1200		1040	1100	1160	1220		1060	1120	1180	1240

Figure 6.24: ***Example sectioning and numbering of coronal brain sections for cell counting in vLGN, dLGN and VP.*** *Three series of coronal sections were cut for each of the brain sample, named series a, b and c. Each section corresponds to a unique combination of slide number, section number and position number. Only one series from each brain was used for counting (example series was outlined with yellow box).*

On each section, the structure of interest was outlined and a counting grid was overlayed on top of the structure using custom ImageJ macro [1], which divides the structure of interest into a number of tiles for further counting. The size of the square tile is 30 μm x 30 μm. 30 % (Figure 6.25) of the generated counting tiles were randomly sampled for cell counting to produce data that is representative of the actual values. The number of all cells and GFP+ve cells in each chosen tile was counted manually. The cell density was calculated by dividing the total cell number (DAPI counts) by the area of each tile, which is 900 μm^2. The GFP+ve cell proportion was caculated by dividing the GFP+ve cell number by the total cell number of each tile. The calculated values from all the counting tiles of each structure on each section were averaged to get the value for a specific section.

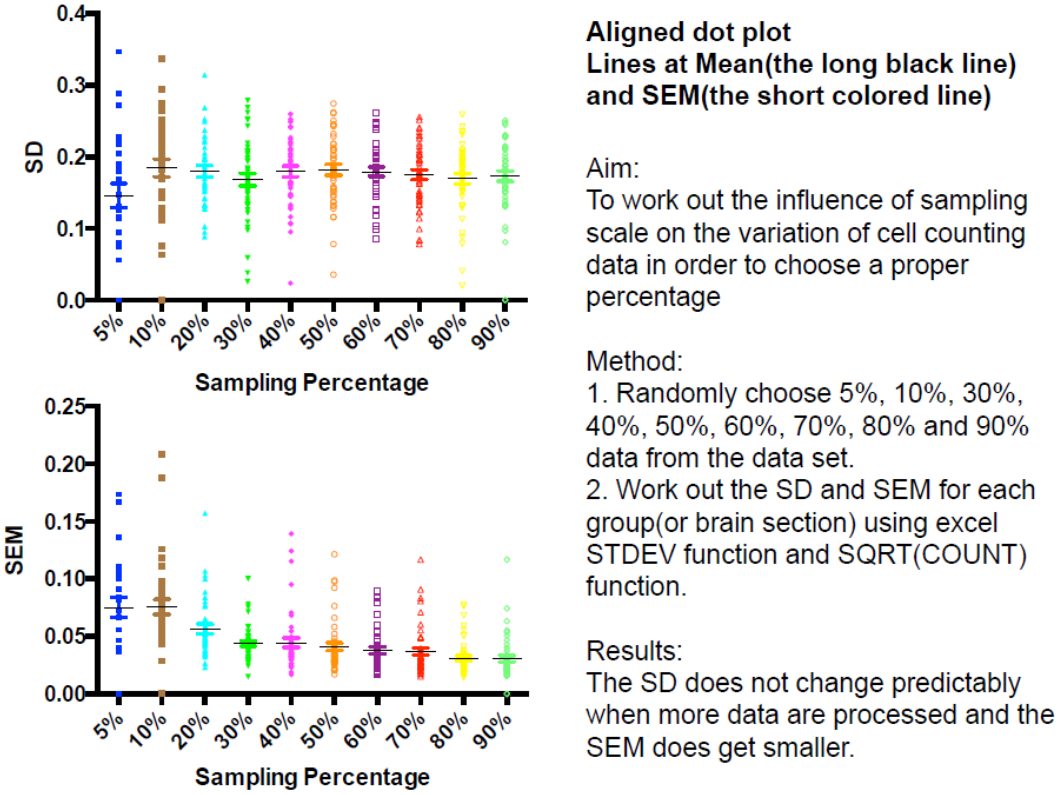


Figure 6.25: ***SD and SEM plots against sampling percentage for cell counting.*** *The SD does not change predictably when more data are processed and the SEM does get smaller. A relatively big drop of SEM can be seen from the data point corresponding to 20 % to the one corresponding to 30 % and after 30 % the SEM doesn not seem to change that much. Thus 30 % was chosen as a proper sampling percentage for my counting.*

[1] The code is included in Appendix III.

6.3.3.1 Cell density change in vLGN, dLGN and VP in conditional *Pax6* mutants

I first measured the cell density and calculated the total cell number in each observed sections and the whole nucleus body for each of the three nuclei to see if there is a change in cell density that could potentially explain the change in nuclei volumes.

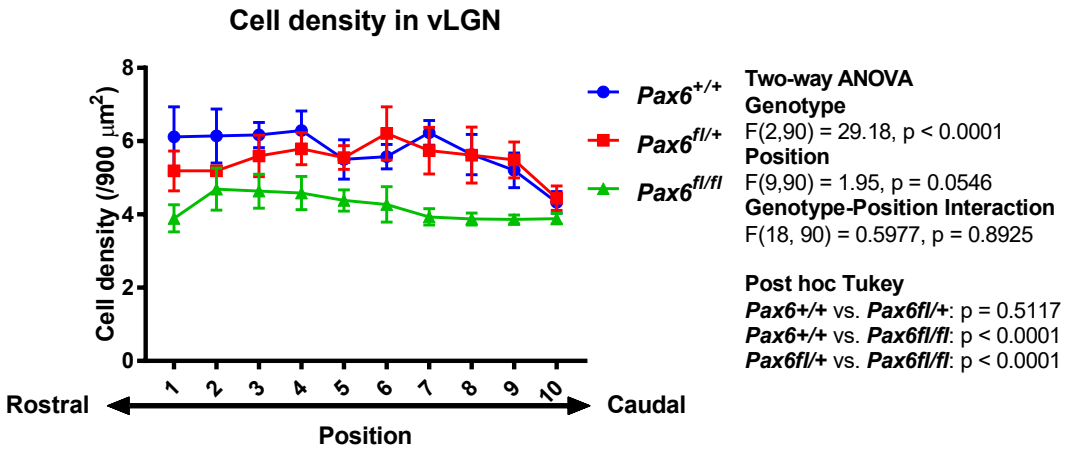


Figure 6.26: ***Cell density change in vLGN in conditional Pax6 mutants.***

The cell density in the $Pax6^{fl/fl}$ vLGN in all is lower than that in the $Pax6^{+/+}$ ($P<0.0001$) and the $Pax6^{fl/+}$ ($P<0.0001$) whereas no significant difference is observed between the $Pax6^{+/+}$ and the $Pax6^{fl/+}$. Looking at specific rostral-caudal levels (Figure 6.26), it is clear that the difference in vLGN cell density between the $Pax6^{+/+}$ and the $Pax6^{fl/fl}$ is evenly distributed along the rostral-caudal axis whereas the difference between the $Pax6^{fl/+}$ and the $Pax6^{fl/fl}$ is mainly seen in the middle to caudal part.

The volume estimation result showed that the volume of vLGN is significantly increased in the $Pax6^{fl/fl}$ compared to both the $Pax6^{+/+}$ and the $Pax6^{fl/+}$ especially at the rostral levels (Figure 6.21) and here a decrease in overall cell density in the vLGN is observed. In order to answer whether the cell number in the vLGN is changed in the $Pax6^{fl/fl}$, I combined these two sets of data and calculated the cell number by multiplying cell density and area in the vLGN at each position and add the values up to get the total cell number for all three genotypes. There is no significant difference in the total cell number in the vLGN seen between the $Pax6^{+/+}$ (5412 ± 323), the $Pax6^{fl/+}$ (7667 ± 1130) and the $Pax6^{fl/fl}$ (7442 ± 313) (Figure 6.27). A further study of the cell number at each observed position in the vLGN (Figure 6.28) shows that the overall distribution of the vLGN cells in these three types of brains is significantly different ($Pax6^{+/+}$ vs. $Pax6^{fl/+}$, $P<0.0001$; $Pax6^{+/+}$ vs. $Pax6^{fl/fl}$, $P<0.0001$; $Pax6^{fl/+}$ vs. $Pax6^{fl/fl}$, $P<0.05$). There are conspicuously more cells in the $Pax6^{fl/fl}$ vLGN at rostral to middle levels

compare to the other two whereas at middle to caudal levels more cells are seen in the *Pax6*$^{fl/+}$.

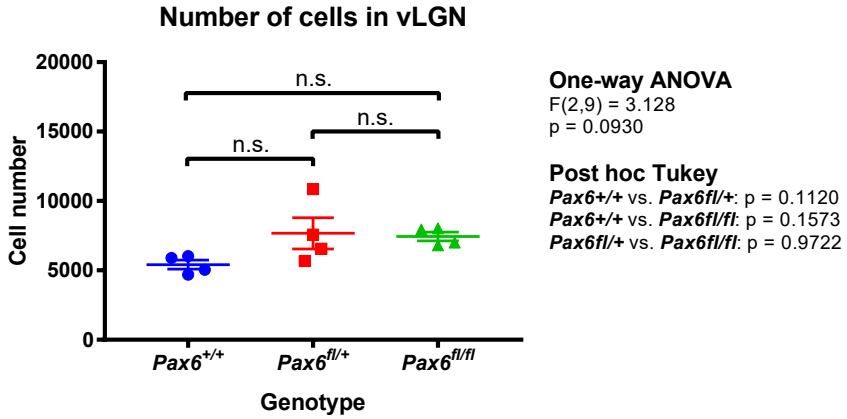


Figure 6.27: ***Total cell number in vLGN.***

There is no significant change in the number of cells in the vLGN in the conditional mutants.

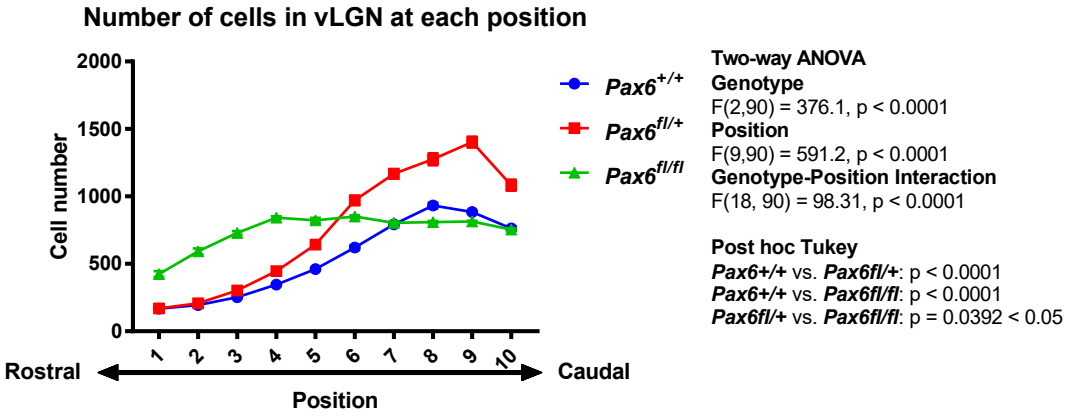


Figure 6.28: ***vLGN cell number on observed sections in conditional Pax6 mutants.***

The number of cells at the rostral to middle part of the *Pax6*$^{fl/fl}$ vLGN is larger than in the *Pax6*$^{+/+}$ and *Pax6*$^{fl/+}$. The number of cells at the middle to caudal part of the *Pax6*$^{fl/+}$ vLGN is larger than in the *Pax6*$^{+/+}$ and *Pax6*$^{fl/fl}$.

Combining these results, it is clear that the total number of cells did not change in the absence of functional *Pax6* but the distribution of cells along the rostral - caudal axis in the vLGN has altered.

In the dLGN, it was found that the cell density does not change along the rostral-caudal axis but there are significant differences between the three genotypes (Figure 6.29). Post hoc Tukey test showed significant differences between the $Pax6^{+/+}$ and the $Pax6^{fl/fl}$ ($p<0.01$) and between the $Pax6^{fl/+}$ and the $Pax6^{fl/fl}$ ($p<0.05$). No significant difference was found in the total cell number in dLGN among the three genotypes (Figure 6.30).

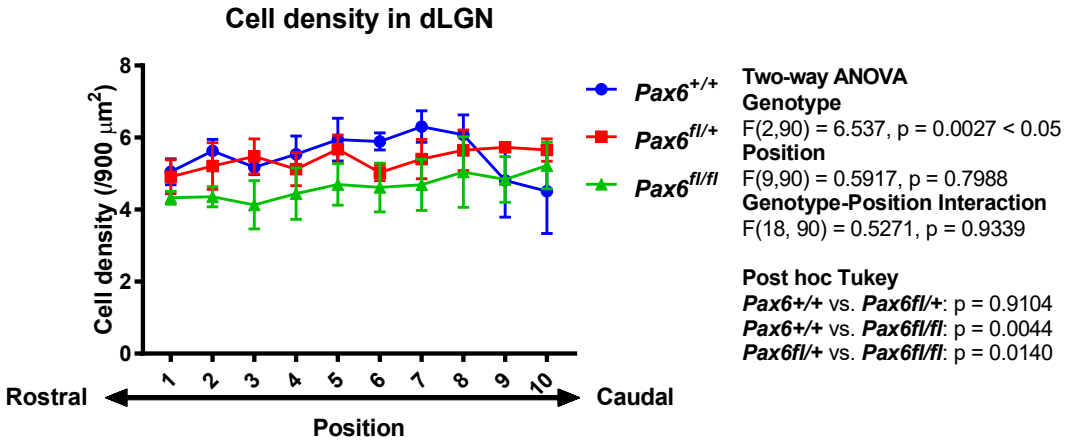


Figure 6.29: ***Cell density change in dLGN in conditional Pax6 mutants.***

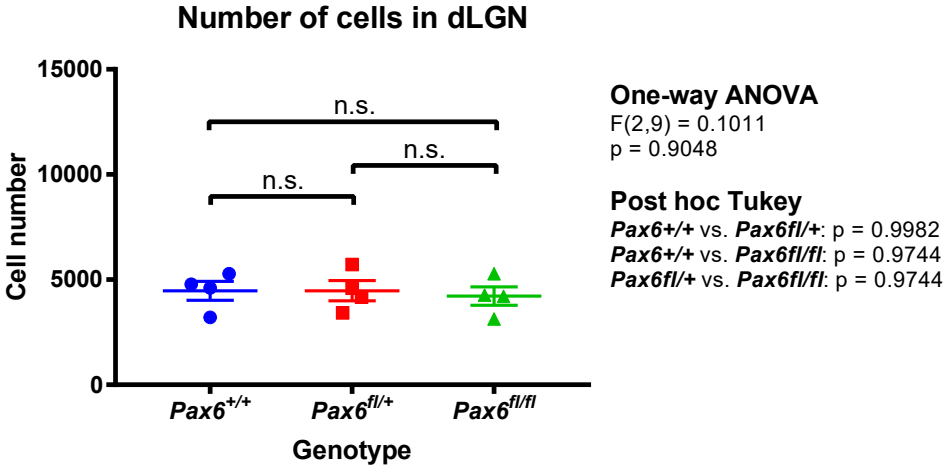


Figure 6.30: ***Total cell number in dLGN.***

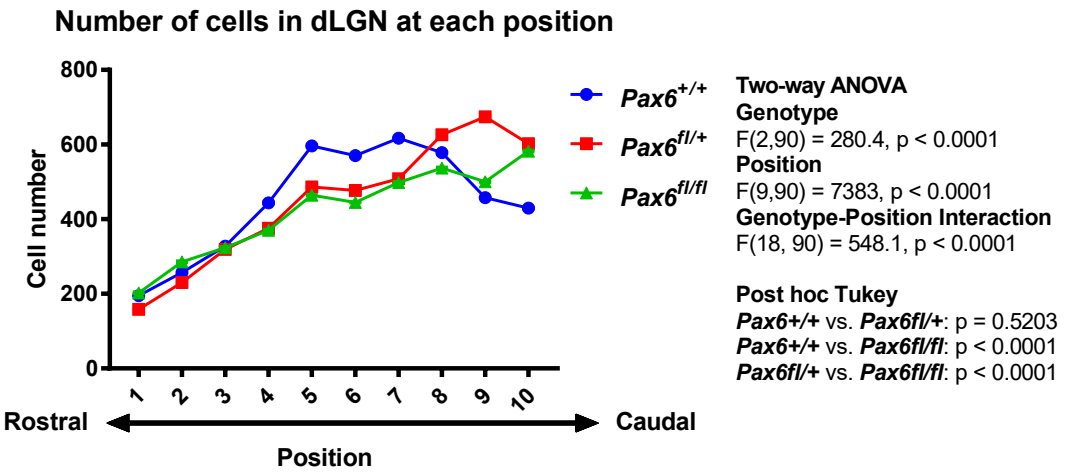


Figure 6.31: ***dLGN cell number on observed sections in conditional Pax6 mutants.***

The number of cells in dLGN at each position was found significantly different between three genotypes Figure 6.31 and post hoc Tukey test showed the significant difference between groups are between the $Pax6^{+/+}$ (4470 $\pm$ 445) and the $Pax6^{fl/fl}$ (4220 $\pm$ 438) ($p<0.0001$) and between the $Pax6^{fl/+}$ (4471 $\pm$ 480) and the $Pax6^{fl/fl}$ ($p<0.0001$).

Combining these results, it is clear that though there is no significant change in the volume of the dLGN, the distribution of cells within the nucleus along the rostral-caudal axis changed because of the deletion of *Pax6*.

Even though there is no significant change in nucleus volume in the VP, it is still possible that the distribution of cells within the nucleus is changed without functional Pax6. Thus, I looked at total cell number and the number of cells on each observed sections to see if there are any defects caused by *Pax6* deletion.

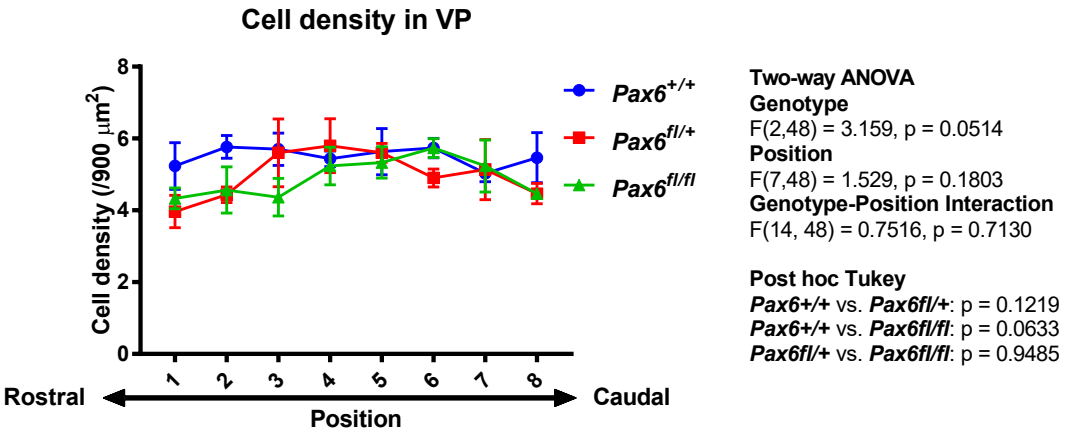


Figure 6.32: ***Cell density change in VP in conditional Pax6 mutants.***

No significant differences are seen in the cell density (Figure 6.32) or cell number (Figure 6.33) in VP between the $Pax6^{+/+}$ (11662 ± 839.8) , the $Pax6^{fl/+}$ (10295 ± 1030) and the $Pax6^{fl/fl}$ (10389 ± 440.7). The number of cells at each postion is significantly different among the three genotypes (Figure 6.34), especially between the $Pax6^{+/+}$ and the $Pax6^{fl/+}$ ($p<0.0001$) and between the $Pax6^{+/+}$ and the $Pax6^{fl/fl}$ ($p<0.0001$).

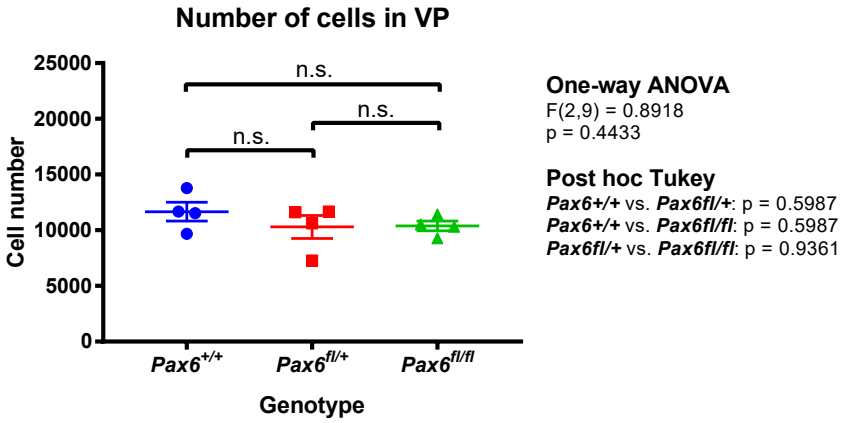


Figure 6.33: ***Total cell number in VP.***

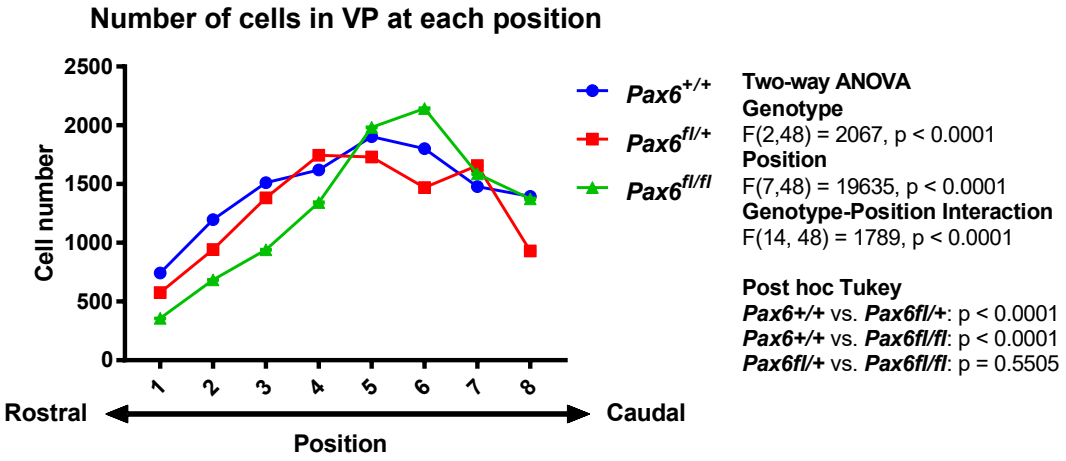


Figure 6.34: ***VP cell number on observed sections in conditional Pax6 mutants.***

Combining these results, it is clear that the cell distribution within the VP along the rostral-caudal axis was altered even though the volume of the nuclei remains the same.

6.3.3.2 GFP+ve cell proportion change in vLGN, dLGN and VP in conditional *Pax6* mutants

During the examination of morphological properties of the sections with GFP staining for the $Pax6^{+/+}$, the $Pax6^{fl/+}$ and the $Pax6^{fl/fl}$, I noticed that the vLGN and dLGN in the $Pax6^{fl/+}$ have stronger staining for the GFP compared to the $Pax6^{+/+}$ whereas the $Pax6^{fl/fl}$ vLGN and dLGN seems weaker than in the $Pax6^{+/+}$ (Figure 6.35). This suggests that the proportion of GFP+ve cells is changed when one or both copies of functional *Pax6* gene are mutated and thus I carried out cell counting experiment to verify the change and study its extent in the $Pax6^{fl/+}$ and the $Pax6^{fl/fl}$ compared to the $Pax6^{+/+}$.

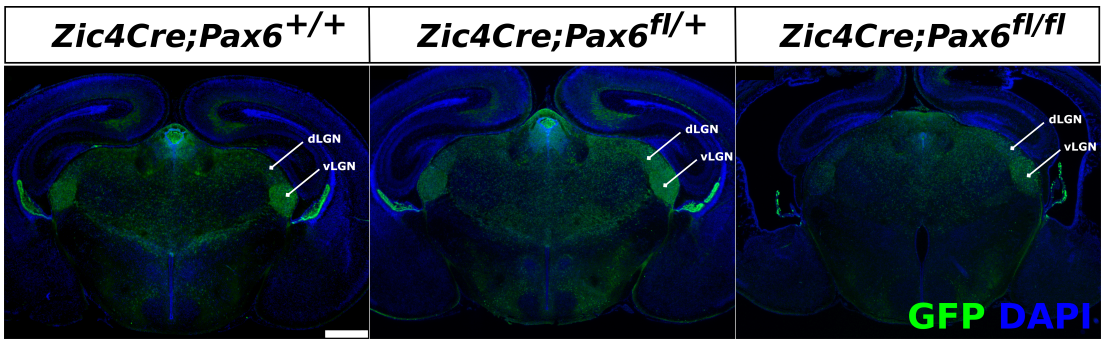


Figure 6.35: ***GFP staining of coronal brain sections from*** **Pax6$^{+/+}$**, ***the*** **Pax6$^{fl/+}$** ***and the*** **Pax6$^{fl/fl}$** ***brains.*** *Scale bar: 75 μm.*

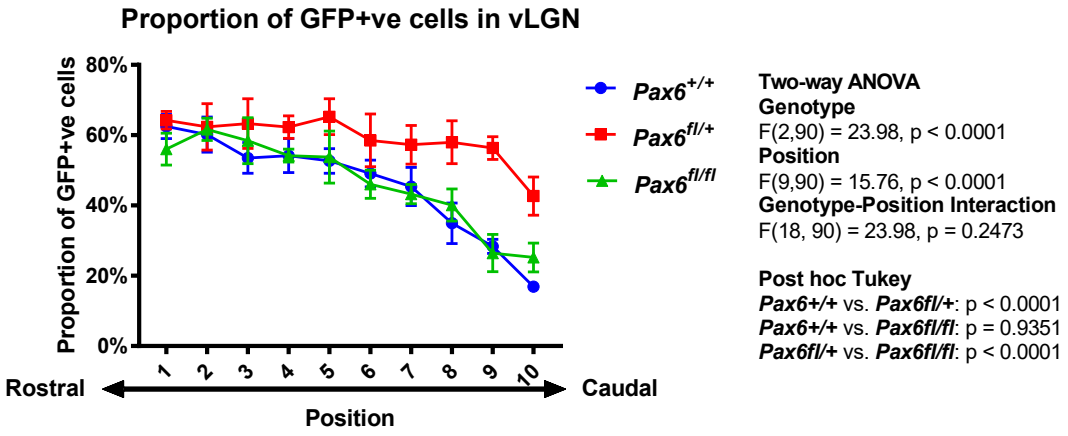


Figure 6.36: ***GFP+ve cell proportion change in vLGN in conditional Pax6 mutants.***

The proportion of GFP+ve cells in vLGN in the $Pax6^{fl/+}$ is significantly higher than in both the $Pax6^{+/+}$ ($P< 0.0001$) and the $Pax6^{fl/fl}$ ($P< 0.0001$) especially at the caudal levels (position 8, 9 and 10) whereas no significant difference is seen between the $Pax6^{+/+}$ and the $Pax6^{fl/fl}$ (Figure 6.36).

Thus, the cell composition in vLGN is changed in the $Pax6^{fl/+}$, with the proportion of GFP+ve cells increased, whereas the cell composition in the $Pax6^{fl/fl}$ is comparable to the $Pax6^{+/+}$.

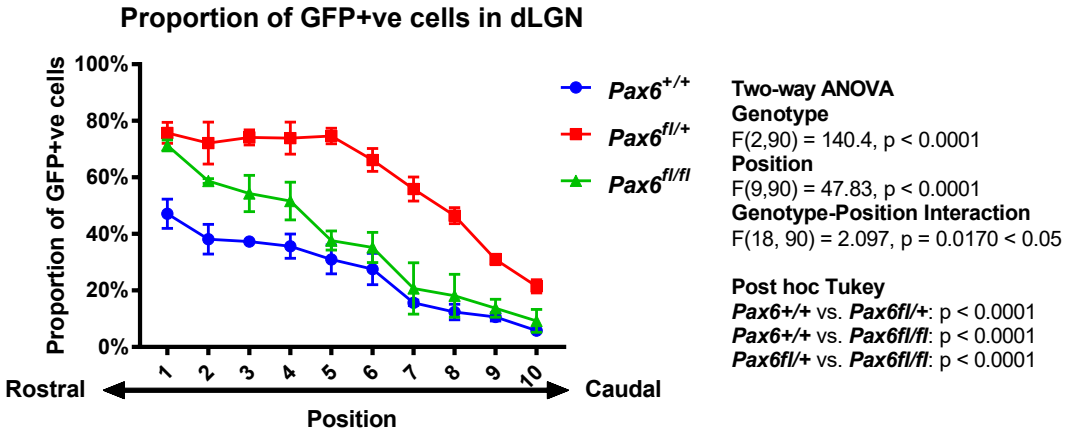


Figure 6.37: ***GFP+ve cell proportion change in dLGN in conditional Pax6 mutants.***

The proportions of GFP+ve cells in the $Pax6^{+/+}$, $Pax6^{fl/+}$ and $Pax6^{fl/fl}$ dLGN are significantly different from each other (Figure 6.37). The GFP+ve cell proportion in dLGN is highest in the $Pax6^{fl/+}$, then the $Pax6^{fl/fl}$, with the lowest seen in the $Pax6^{+/+}$. The difference between the

Pax6$^{+/+}$ and the *Pax6*$^{fl/fl}$ is mainly seen at the rostral levels (position 1, 2, 3 and 4) whereas the differece between the *Pax6*$^{+/+}$ and the *Pax6*$^{fl/+}$ is seen all the way through from rostral to caudal.

This result indicates that the increase in GFP+ve proportion is more prominent in the *Pax6*$^{fl/+}$ than in the *Pax6*$^{fl/fl}$.

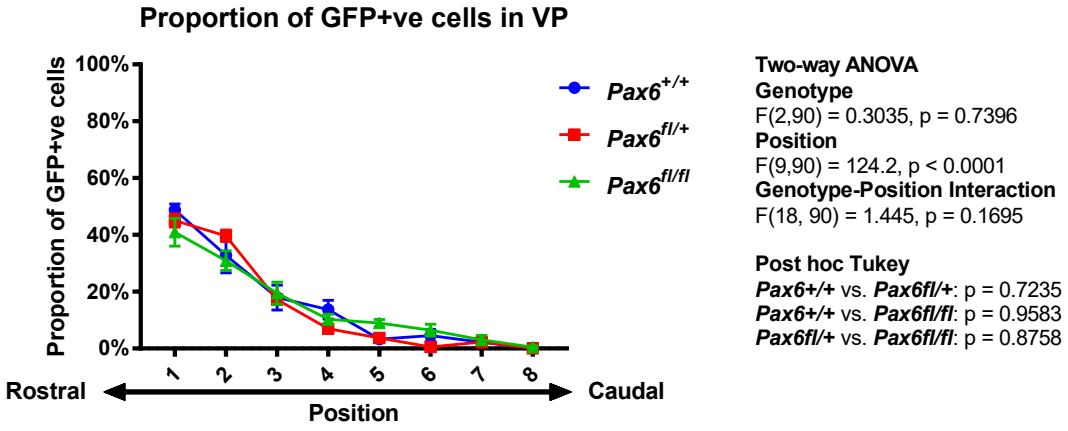


Figure 6.38: ***GFP+ve cell proportion change in VP in conditional Pax6 mutants.***

No significant differences are seen in the GFP+ve cell proportion in VP in the (*Pax6*$^{+/+}$, the *Pax6*$^{fl/+}$ and the *Pax6*$^{fl/fl}$ (Figure 6.38).

The cell composition of the VP was not affected by the deletion of *Pax6*.

6.3.3.3 Altered expression of Nkx2.2 and Lim1/2 in the vLGN in conditional *Pax6* mutants

The change in cell composition in the vLGN is likely to be accompanied by expression of other patterning markers. Thus I studied the expression of two markers for vLGN, Lim1/2 and Nkx2.2, in the three types of brains at P0 (Figure 6.39).

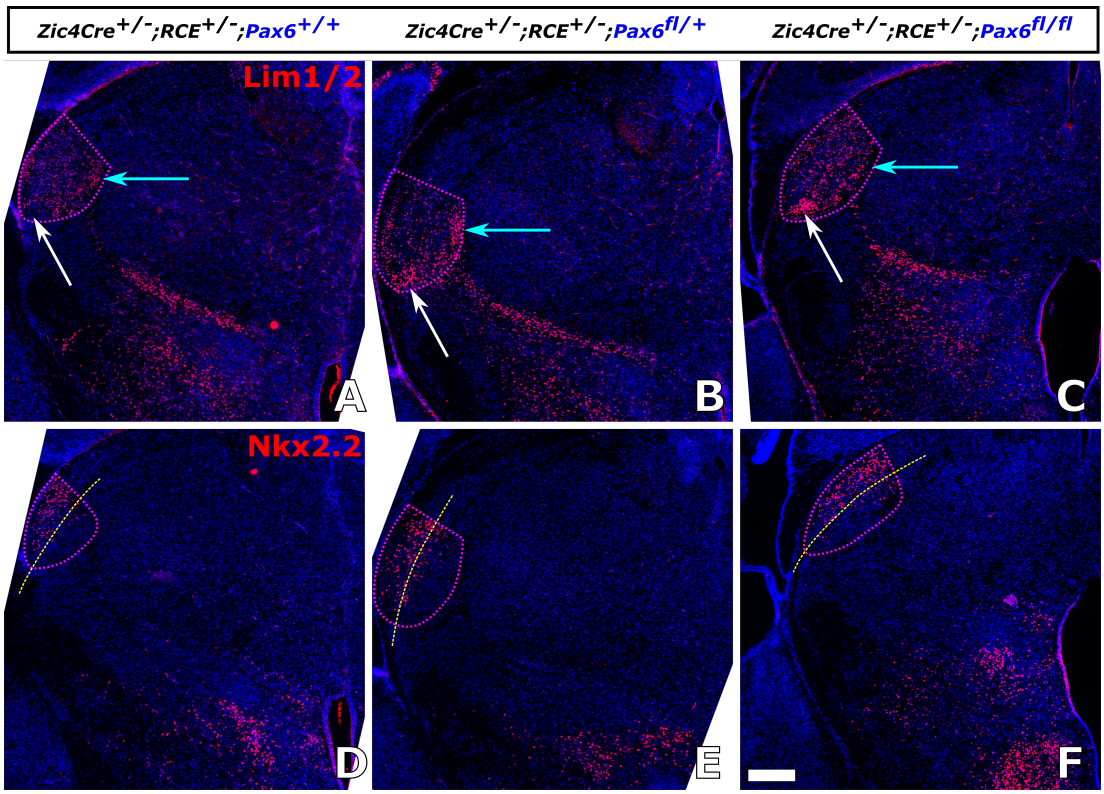


Figure 6.39: ***Expressions of Lim1/2 and Nkx2.2 are altered in vLGN in conditional Pax6 mutants.*** *Coronal brain sections from P0* $\text{Pax6}^{+/+}$, $\text{Pax6}^{fl/+}$ *and the* $\text{Pax6}^{fl/fl}$ *pups were stained for Lim1/2 (A-C) and Nkx2.2 (D-F). The vLGN is outlined using dashed magenta contour. (A-C) The alteration in Lim1/2 expression is indicated using white and cyan arrows. (B) The midline within the vLGN is indicated using dashed yellow curve. Scale bar: 250 μm.*

For the staining of Lim1/2, the positive cells are scattered fairly evenly across the $Pax6^{+/+}$ vLGN (Figure 6.39 A). In the $Pax6^{fl/+}$ vLGN (Figure 6.39 B), two areas, one at the ventral tip (white arrow) and the other is along the medial border (cyan arrow), have noticeably more Lim1/2 positive cells compared to adjacent areas within the vLGN. In the $Pax6^{fl/fl}$ (Figure 6.39 C), the positive cells aggregate at the ventral tip of the vLGN (white arrow), similar to what is seen in the $Pax6^{fl/+}$, but not along the medial border. Unlike the $Pax6^{fl/+}$ and the $Pax6^{fl/fl}$, Lim1/2 positive cells seem to be excluded from the corresponding vLGN region in the $Pax6^{+/+}$ (Figure 6.39 A, white arrow). For the staining of Nkx2.2, most of the positive cells populate the lateral half of the vLGN in all three types of brains (Figure 6.39 D-F). The dorsolateral tip of the vLGN in both the $Pax6^{+/+}$ and the $Pax6^{fl/fl}$ contains very high proportion of Nkx2.2 positive cells whereas the position of the corresponding area shifts toward the midline within the vLGN in the $Pax6^{fl/+}$.

6.4 Synopsis

Genotype	Nuclei name	Volume	Cell number	Cell density	GFP+ve cell proportion
Pax6$^{fl/+}$	vLGN	n.s.	n.s.	n.s.	⇑ (caudal)
	dLGN	n.s.	n.s.	n.s.	⇑⇑ (all)
	VP	n.s.	n.s.	n.s.	n.s.
Pax6$^{fl/fl}$	vLGN	⇑ (rostral)	n.s.	⇓ (all)	n.s.
	dLGN	n.s.	n.s.	n.s.	⇑ (rostral)
	VP	n.s.	n.s.	n.s.	n.s.

Table 6.1: ***Volume and cell composition change in the vLGN, dLGN and VP in the*** **Pax6$^{fl/+}$** ***and the*** **Pax6$^{fl/fl}$** ***mutants****. n.s., no significant change. ⇑, increase; ⇓, decrease. The positions of the difference seen are annotated using* ***rostral*** *(from rostral to middle),* ***caudal*** *(from middle to caudal) and* ***all*** *(from rostral to caudal).*

The main findings of this project (Table 6.1) can be summarised as: 1. the deletion of one or both copies of the functional *Pax6* gene in the *Zic4* lineage cells causes significant morphological change in the developing diencephalic nuclei vLGN and dLGN but not the VP at P0; 2. losing one copy of functional *Pax6* gene (*Pax6*$^{fl/+}$) causes increase in GFP+ve cell proportion in both the vLGN and the dLGN but has no effects on either the volume or the cell density of these two nuclei; 3. losing both copy of functional *Pax6* gene (*Pax6*$^{fl/fl}$) affects different aspects in different nuclei - volume and cell density in the vLGN and GFP+ve cell proportion in the dLGN; 4. the changes in the *Pax6*$^{fl/fl}$ are mainly seen at the rostral levels whereas in the *Pax6*$^{fl/+}$ the caudal levels show more defects; 5. though the total cell number remains similar between difference genotypes, the distributions of these cells along the rostral-caudal axis are significantly disturbed in the *Pax6*$^{fl/+}$ and the *Pax6*$^{fl/fl}$; 6. altered expression of regional markers such as Lim1/2 and Nkx2.2 is seen in the vLGN in the *Pax6*$^{fl/+}$ and the *Pax6*$^{fl/fl}$.

6.5 Discussion

There are several critical stages that could potentially affect the formation of diencephlic nuclei: 1. prepatterning of prosomeres involving the expression of Otx and Fez transcription factors which establishes the mid-diencephalic organiser, the ZLI [115]; 2. establishment of distinct progenitor populations within each prosomere involving the secretion of Shh from the ZLI and subsequent expression of transcription factors such as Ngn1/2 and Ascl1 [102];

3. postmitotic neuronal precursors are born after one or more rounds of cell divisions and committed to different fates depending on the expression of selector genes like Tal1/2, Gata2, Gbx2 and Dlx1/2/5 [17, 102, 116]; 4. neurons gain their electrophysiological identities and become either GABAergic or glutamatergic neurons and etc; 5. in the meantime, the newly born diencephalic neurons differentially migrate toward their destined position (newly born neurons at E12.5 in p2 already start migration at E13.5 whereas their counterparts in p3 remain close to the ventricular zone and later on migrate along the radial glial fibres) and become part of the newly formed nuclei [48]. It has been demonstrated in studies that: 1. Pax6 is involved in shaping the mid-diencephalic organiser as a broader expression of *Shh* is seen in the *pax6 null* mutants [36, 40]; 2. Pax6 regulates the progenitor cell cycle in the developing cortex [62], controls the formation of basal progenitor cells and basal-apical progenitor balance in the thalamus [38], establishes correct progenitor domain for neuron specification in the hindbrain and the spinal cord [117]; 3. Pax6 mediates the establishment of different adhesive properties between the dorsal and ventral telencephalon [49] and possibly controls the proneural gene Ngn2 expression in a subpopulation of cortical precursors [118]; 4. Pax6 controls the differentiation of the radial glia cells in the developing cortex [119]. Thus, Pax6 is potentially involved in multiple aspects during the development of diencephalic nuclei.

The loss of *Pax6*, either one or both copies, caused significant developmental defects in the vLGN and the dLGN but not the VP, suggesting that the deletion of *Pax6* driven by the *Zic4Cre* has nuclei specific effects. Both the VP and dLGN are derived from the ventricular zone of the thalamus, in which Pax6 is expressed in a low-rostroventral and high-caudodorsal gradient. The vLGN has three origins, the rostral progenitor zone of the thalamus (pTH-R), prethalamus and ZLI; and Pax6 is expressed at low levels in the pTH-R and high levels in both the ventricular zone and the mantle zone of the prethalamus and regulates the formation of the Shh-secreting ZLI. Thus, the deletion of *Pax6* could potentially affect the development of all three nuclei, mostly likely the vLGN. The neurons in vLGN and dLGN are mainly born between E11 and E12 during which Pax6 is highly expressed in the developing diencephalon and a fair amount of neurons in VP are born later in E13 when the Pax6 levels start to decrease rapidly [42]. Thus, it is possible that the neurogenesis of VP is not critically dependent on the presence of Pax6. Pax6's expression is seen at the prosomeric stage of diencephalic development as well as in mature vLGN neurons at P0 (Figure 6.40), suggesting that Pax6's presence is not only required during vLGN neurogenesis but critical in acquiring and potentially maintaining their electrophysiological properties as well. A recent study on dLGN origin also showed that dLGN recruits inhibitory interneurons from an Otx positive cell pool located in the adjacent vLGN, which suggests that Pax6 can indirectly affect the formation of dLGN by regulating the formation of vLGN [120]. Finally, Pax6 is a key player

in the development of the diencephalon and manages complex genetical regulatory network involving a great number of downstream factors. The differential expression of these factors in different nuclei could explain the distinct responses to the deletion of Pax6 as well.

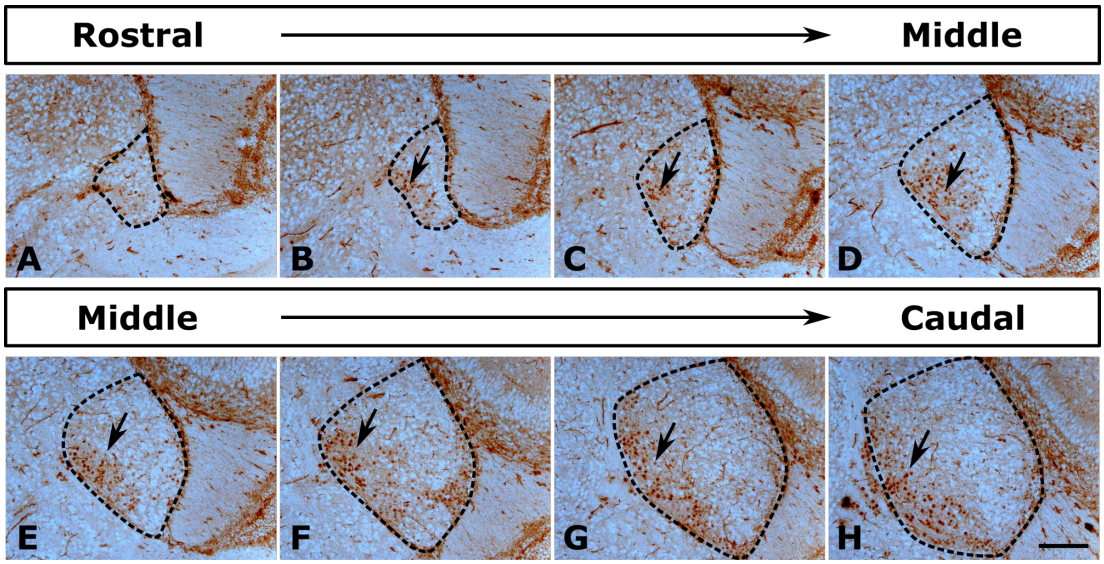


Figure 6.40: ***Pax6 immunohistochemistry of P0*** **Pax6$^{+/+}$** ***vLGN.*** *Black arrows, Pax6-expressing cells. Scale bar: 125 μm.*

The difference in phenotypes of the same nucleus between the *Pax6$^{fl/+}$* and the *Pax6$^{fl/fl}$* (Table 6.1) suggests dosage effects of Pax6 on the formation of the vLGN and dLGN. In the vLGN, the loss of one copy of functional *Pax6* causes an increase in the proportion of GFP+ve cells whereas losing both copies causes a significant increase in vLGN volume at the rostral part, a decrease in cell density and a potential increase in cell number (Figure 6.27). The proportion change in a subpopulation of vLGN cells could be due to defects in neurogenesis, alteration of cell fate and failure in cell sorting/migration. The change in vLGN volume and cell density could also be caused by neurogenetical defects and abnormal cell sorting/migration. In the dLGN, the loss of one copy of functional *Pax6* leads to an overall increase of GFP+ve cell proportion along the rostral-caudal axis whereas losing two copies, this increase is restricted to the rostral part of the dLGN. In a word, losing one copy of *Pax6* causes more severe phenotype in dLGN than losing both copies.

It is possible that the truncated polypeptide produced by the mutated *Pax6* allele acts as a poison peptide, which interferes with the function of the wild type one, and hinders the normal transcriptional regulatory functions of the Pax6 protein produced from the wild type allele. The Cre-mediated deletion of Pax6 exons 5, 5a and 6, the paired domain (PD), was predicted to cause a nonsense frame-shift. However, the remaining transcript contains

complete sequences encoding the second DNA binding domain, the Pax6 homeodomain (HD) and the PST-rich transactivation domain (PST), which could potentially be translated into truncated polypeptides that bind to target binding sites of HD and PST. Previous studies on CNS development in mice have demonstrated that the PD and HD recognize distinct DNA binding sites both cooperatively or separately and the loss of PD could affect the HD binding where the presence of PD is required in terms of both binding specificity and affinity [21]. However, it is difficult to predict whether the loss of PD will increase or decrease the transactivation property of the mutant protein, as it has been found that human PAX6 mutant protein R26G (with a mutation in the N-terminal half of the PD) lost DNA binding through its PD but gained greater DNA binding and transactivation than wild-type PAX6 on HD binding sites [121]. In an *in vitro* study carried out in Hela cells, the co-expression of the paired-less isoform of Pax6 and full-length Pax6 caused a 3 times increase in Pax6-mediated transactivation from paired domain binding sites than the full-length Pax6 itself, whereas paired-less Pax6 alone did not induce activation at all, which excluded the possibility that paired-less Pax6 activated the reporter itself. It was further discovered that the Pax6 HD alone without the C-terminal transactivation domain PST is not able to enhance Pax6 transactivation from paired domain-binding sites [122].

It is also possible that losing both copies of *Pax6* is critical enough to trigger the rescue mechanism within the developing diencephalon whereas losing only one copy of *Pax6* is not acute and thus tolerated by the system. The change of cell distribution within each of the nuclei in the $Pax6^{fl/+}$ and $Pax6^{fl/fl}$ could be due to abnormal neurogenetical gradient formed along the rostral-caudal axis and/or cell sorting defects caused by *Pax6* deletion. The alterations in regional marker expression suggests there could be changes in cell fate commitment and/or cell migration/sorting in the conditional *Pax6* mutants.

The mechanisms underlying the defects in the developing vLGN and dLGN caused by *Pax6* deletion could potentially include: 1. patterning factor expression change due to the loss of *Pax6*; 2. cell proliferation defects and abnormal apoptosis; 3. ocular developmental defects; 4. failure in cell sorting/migration; 5. cell fate change. These elements were investigated one by one except the last one and the results are summarised in the next few chapters.

Chapter 7

BrdU labelling identifies the birth dates of the GFP+ve cells in P0 vLGN, dLGN and VP in *Zic4Cre*$^{+/-}$;*RCE*$^{+/-}$;*Pax6*$^{+/+}$ mice

7.1 Introduction

Birthdating neurons with bromodeoxyuridine (BrdU) labelling has been widely used for cell proliferation study in embryonic, postnatal and adult brains. As a thymidine analogue, BrdU can be incorporated into newly synthesized DNA of proliferating cells during S phase of the cell cycle. Its detection is usually performed using immunohistochemistry with anti-BrdU antibodies. Similar to thymidine - H^3 labelling, two types of cells, heavily and lightly labelled, are observed in long-term survival BrdU labelling experiments. The heavily labelled cells are the cells born from the final division at the point of BrdU injection. The lightly labelled cells are either the cells born through several rounds of divisions after the injection or the ones going through the last division with only part of the S-phase exposed to the BrdU.

In the previous chapter, developmental defects in nucleic volume, cell density and GFP+ve cell proportion were found in the vLGN and dLGN in the *Zic4Cre* induced *Pax6* mutants *Pax6*$^{fl/+}$ and *Pax6*$^{fl/fl}$ (Table 6.1). These findings suggest a potential change in neurogenesis in these two nuclei. To investigate this possibility, I performed birthdating experiments for the vLGN and dLGN using long-term BrdU labelling to figure out the time origin of the neurons and the GFP+ve neurons that contribute to the two nuclei and the corresponding data for the

VP was collected as well.

7.2 Aim of the project

To study the time origin of the neurons and the GFP+ve *Zic4* lineage neurons that contribute to the vLGN, dLGN and VP and to narrow the time window of interest for further investigation on *Pax6*'s role in neurogenesis in the early developing thalamus and prethalamus.

7.3 Results

A single dose of bromodeoxyuridine (BrdU, 70 μg/g body weight, diluted in saline 10 μg/μl) was administrated via intraperitioneal injection to pregnant females that carry E10.5, E11.5, E12.5 and E13.5 embryos and four P0 $Zic4Cre^{+/-};RCE^{+/-};Pax6^{+/+}$ pups were collected for the brain tissues for each injection stage.

Images for cell counting were chosen by comparing with the standard series (Figure 6.3, Figure 6.4, Figure 6.5, Figure 6.6, Figure 6.9, Figure 6.10, Figure 6.7 and Figure 6.8) from the previous chapter. The vLGN, dLGN and VP regions were outlined and copied to a fixed-size (1500 pixel x 1500 pixel) black background for further processing in CellProfiler (Figure 7.1).

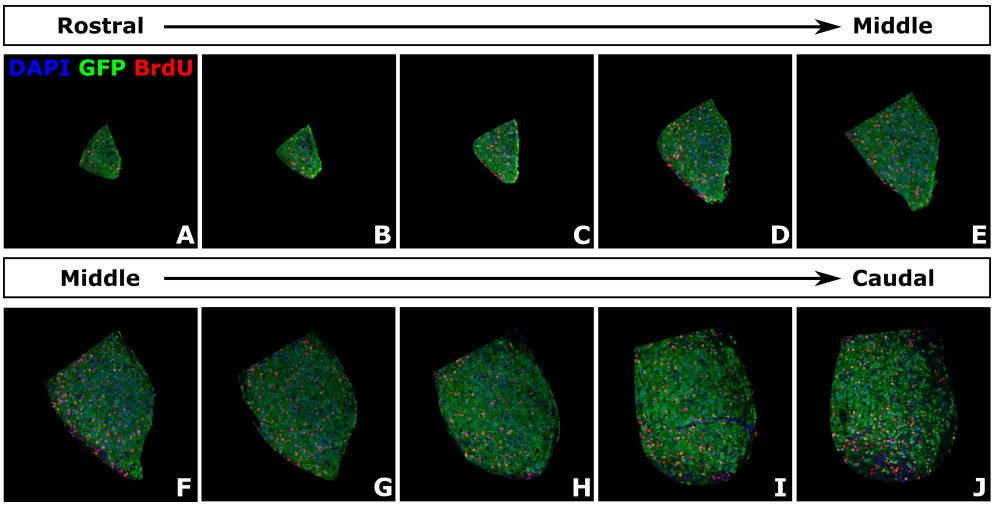


Figure 7.1: ***Preprocessed vLGN image series for CellProfiler analysis.***.

These images were imported into CellProfiler and processed with a custom protocol: 1. the RGB imags were split into three single-channel grayscale images, named OrigRed (for

BrdU), OrigGreen (for GFP) and OrigBlue (for DAPI); 2. global thresholding was performed to reduced the background noise for each of the three images to produce ThreshRed, ThreshGreen and ThreshBlue (Figure 7.2); 3. a feature suppress step was used on the ThreshRed image (for BrdU) to filter out the speckles with the diameter smaller than 4 pixel in order to reduce the residue BrdU signals from several rounds of divisions; 4. a similar feature suppress step was used on the ThreshGreen image (for GFP) to exclude false GFP+ve cells caused by being immediately adjacent to GFP+ve axons; 5. the cell nuclei were identified (Figure 7.3) using ThreshBlue (DAPI staining) image with custom setttings (Table 7.1); 6. fluorescence intensity of both the BrdU staining and the GFP staining were measured within each cell nuclei; 7. a cut-off intensity value of 5 was used to distinguish nuclei with positive or negtive stainings for both the BrdU and the GFP and all the cell nuclei are classified into four categories: GFP-veBrdU-ve, GFP-veBrdU+ve, GFP+veBrdU+ve and GFP+veBrdU-ve (Figure 7.4); 8. cell counting data was exported as *.csv files for further analysis.

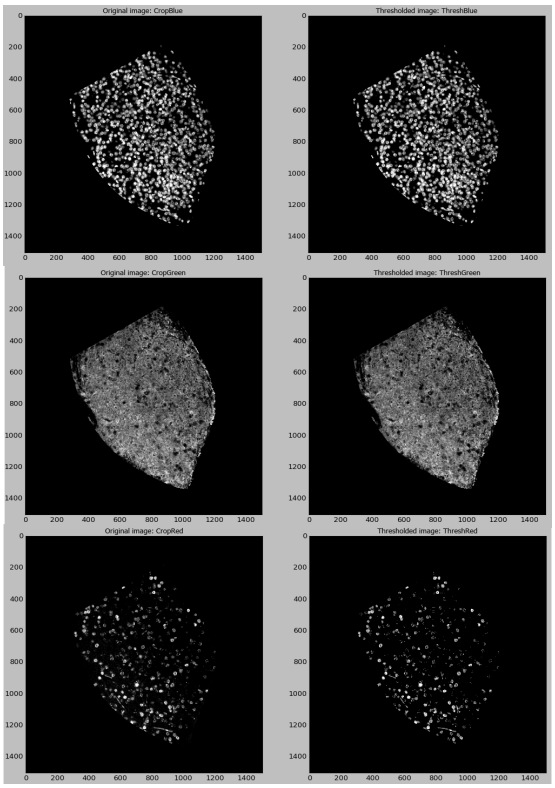


Figure 7.2: ***Thresholding three single-channel grayscale images of the vLGN.*** *Original and thresholded grayscale images for the blue channel (top row, DAPI), the green channel (middle row, GFP) and the red channel (bottom row, BrdU).*

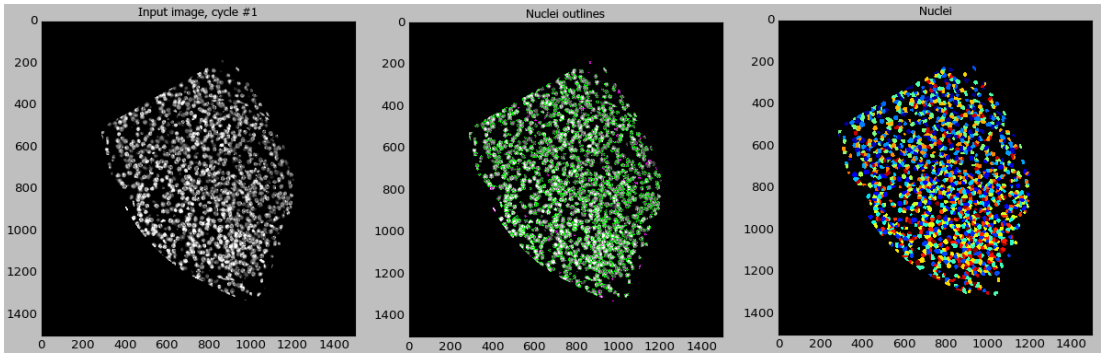


Figure 7.3: ***Cell nuclei identification in the vLGN based on DAPI staining.*** *Left, thresholded blue channel of nuclei staining; middle, outlined cell nuclei after image segmentation and object identification; right, pseudo-coloured cell nuclei.*

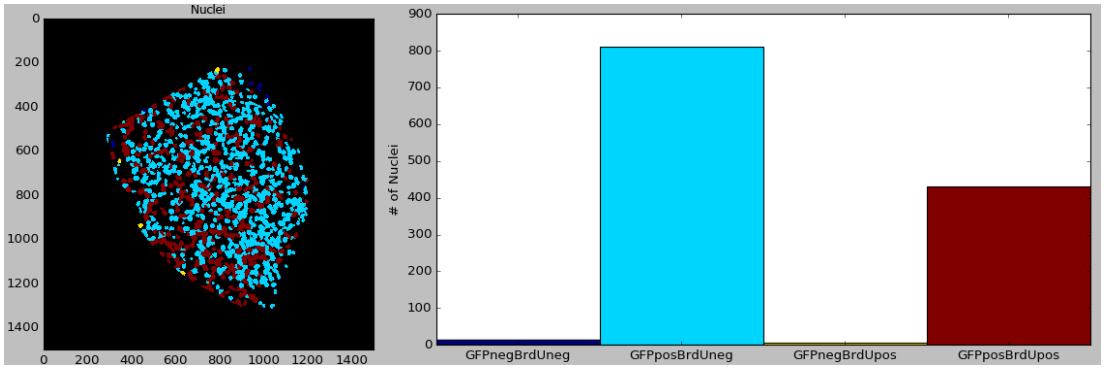


Figure 7.4: ***Cell categorisation based on GFP and BrdU staining.*** *Left, cells fallen into different categories according to the BrdU and the GFP fluorescence intensity are pseudo-colour coded; right, bar plot showing the number of cells in each category: GFP-veBrdU-ve, GFP+veBrdU-ve, GFP-veBrdU+ve and GFP+veBrdU+ve (from left to right).*

Parameters	Values
Typical diameter of objects, in pixel units (Min, Max)	12, 30
Discard objects outside the diameter range?	Yes
Discard objects touching the border of the image?	Yes
Threshold strategy	Adaptive
Threshold method	Otsu
Select the smoothing method for thresholding	Three classes
Minimize the weighted variance or the entropy?	Weighted variance
Assign pixels in the middle intensity class to the foreground or the background?	Foreground
Select the smoothing method for thresholding	Manual
Threshold smoothing scale	1
Threshold correction factor	0.9
Lower and upper bounds on the threshold	0.1, 1
Method to distinguish clumped objects	Intensity
Method to draw dividing lines between clumped objects	Propagate
Automatically calculate size of smoothing filter for declumping?	No
Size of smoothing filter	3
Automatically calculate minimum allowed distance between local maxima?	No
Suppress local maxima that are closer than this minimum allowed distance	8
Speed up by using lower-resolution image to find local maxima?	No
Fill holes in identified objects?	After declumping only

Table 7.1: ***Parameters used for DAPI based nuclei segmentation in vLGN using CellProfiler.*** *These parameters were chosen after trying out a spectrum of combinations of settings and were used for the segmentation in this chapter.*

The cell counting data was pre-processed and the proportion of cells and GFP+ve cells born at different ages were calculated and summarised using R. The summarised data was then imported into GraphPad Prism 7.01 for performing statistical tests and plotting graphs. Univariate statistics (means ± SEM) were performed for all studied variables. One-way ANOVA was performed to study the effect of age on the proportion of cells and GFP+ve cells born to contribute to the P0 vLGN, dLGN and VP. Two-way ANOVA was performed to examine the main effects of age and rostral-caudal position on the proportion of cells and GFP+ve cells born to contribute to the P0 vLGN and dLGN. The Tukey post hoc test was performed for all pair-wise comparisons subsequent to the ANOVAs. For two-way ANOVAs, the Tukey post hoc test results were only reported for the main effects of age. All experiments were repeated in four embryos for each genotype.

vLGN

This BrdU labelling experiment aims to identify the critical development stages when the majority of cells contributing the future vLGN are born. I first looked at the proportion of vLGN cells data are born at E10.5, E11.5, E12.5 and E14.5 as the main neurogenesis in the developing diencephalon occurs from E10.5 to E16.5. Then I focused on the GFP+ve population as the proportion of this population was seen changed in the conditional *Pax6* mutants.

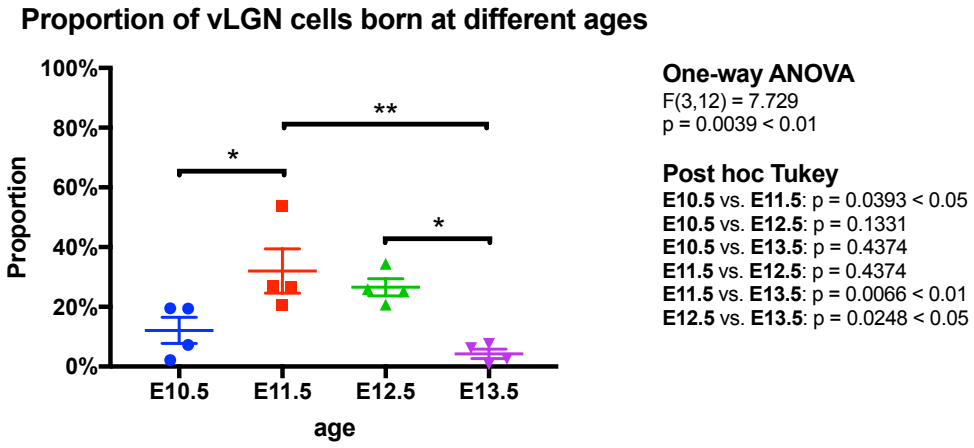


Figure 7.5: ***Proportion of vLGN cells born at E10.5, E11.5, E12.5 and E13.5.***

It was found that cells contributing to the vLGN are born from E10.5 to E13.5 especially at E11.5 (32.04% ± 7.401%) and E12.5 (26.59% ± 2.871%) (Figure 7.5).

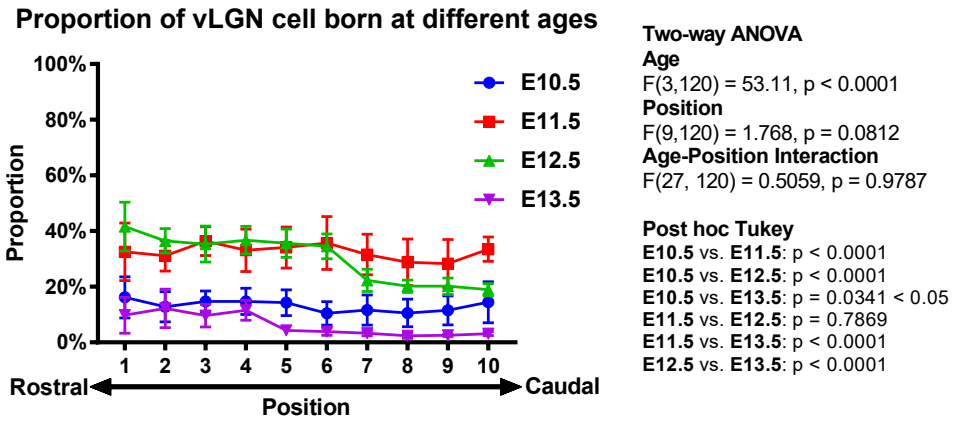


Figure 7.6: ***Proportion of vLGN cells born at each position at different ages.***

There is no significant difference ($F(9, 120) = 1.768$, $p = 0.0812 > 0.05$) along the rostral-caudal axis when looking at the data for each specific postion (Figure 7.6).

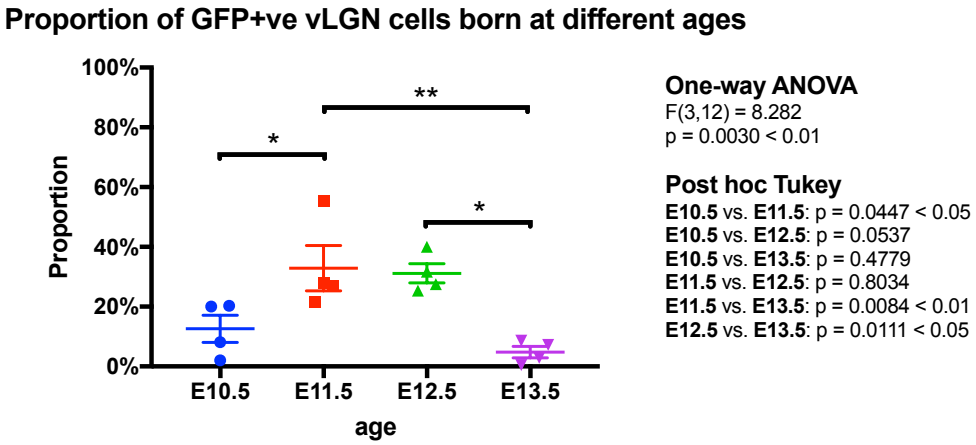


Figure 7.7: ***Proportion of GFP+ve vLGN cells born at E10.5, E11.5, E12.5 and E13.5***

As for the GFP+ve cells fated to be in the vLGN, they are mainly born between E11.5 (32.89% $\pm$ 7.595%) and E12.5 (31.16% $\pm$ 3.229%), similar to what we have seen in the general vLGN cells (Figure 7.7).

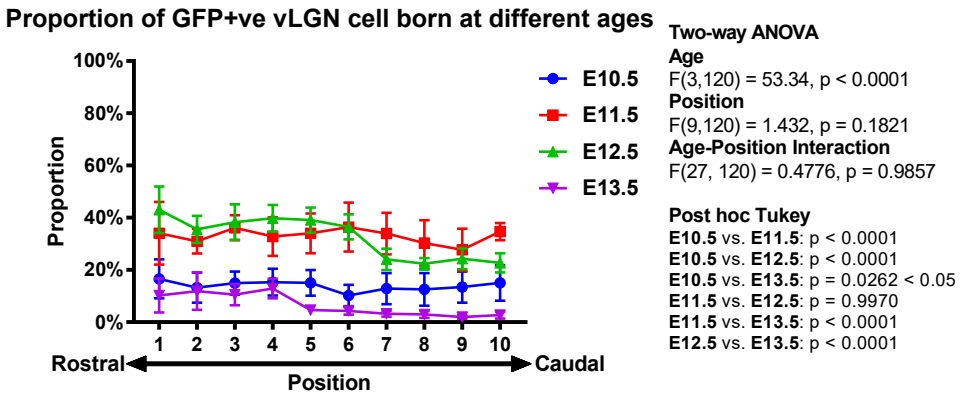


Figure 7.8: ***Proportion of GFP+ve vLGN cells born at each position at different ages.***

The rostral-caudal position has no significant effects ($F(9, 120) = 1.432$, $p = 0.1821 > 0.05$) on the GFP+ve neurogenesis (Figure 7.8).

These results showed that both GFP+ve population and non-GFP+ve population that contribute to the future vLGN are mainly born between E11.5 to E12.5 and there is no difference along the rostral-caudal axis.

dLGN

Then I lexamined both the whole population and the GFP+ve population in the dLGN since a change in the cell composition, the proportion of the GFP+ve cells, was observed in the mutant dLGN.

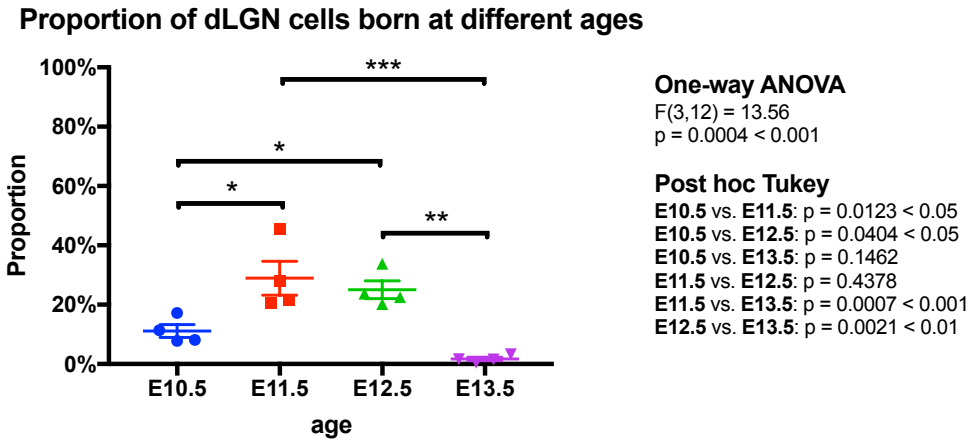


Figure 7.9: ***Proportion of dLGN cells born at E10.5, E11.5, E12.5 and E13.5.***

The cells contributing to the dLGN are mainly born from E10.5 to E12.5 especially at E11.5 (28.94% ± 5.715%) and E12.5 (25.06% ± 2.988%) (Figure 7.9).

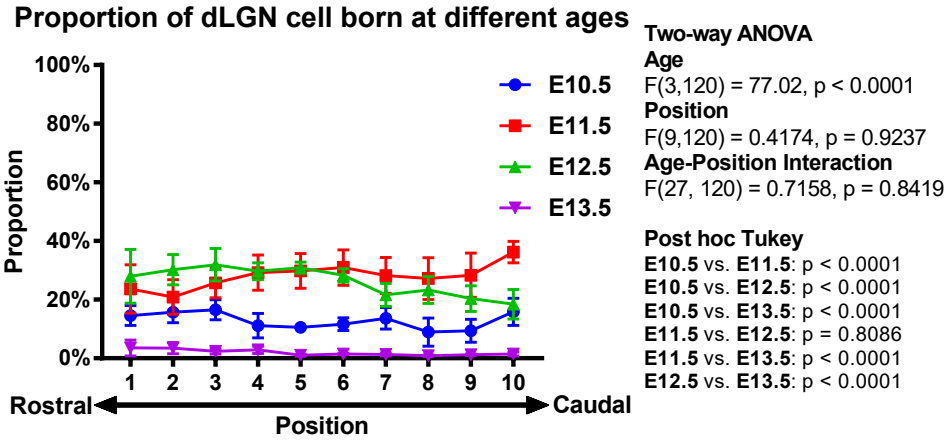


Figure 7.10: ***Proportion of dLGN cells born at each position at different ages.***

There is no significant difference ($F(9, 120) = 0.4174$, $p = 0.9237 > 0.05$) along the rostral-caudal axis when looking at the data for each specific postion (Figure 7.10).

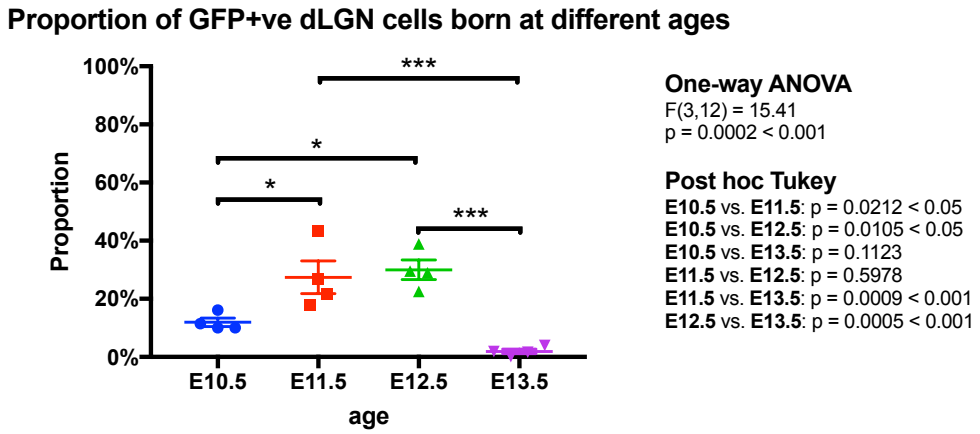


Figure 7.11: ***Proportion of GFP+ve dLGN cells born at E10.5, E11.5, E12.5 and E13.5.***

As for the GFP+ve cells destined to be in the dLGN, they are mainly born from E10.5 to E12.5 and the GFP+ve neurogenesis peaks at E11.5 (27.39% ± 5.619%) and E12.5 (29.98% ± 3.37%) (Figure 7.11), similar to what was seen in the general dLGN cells (Figure 7.9).

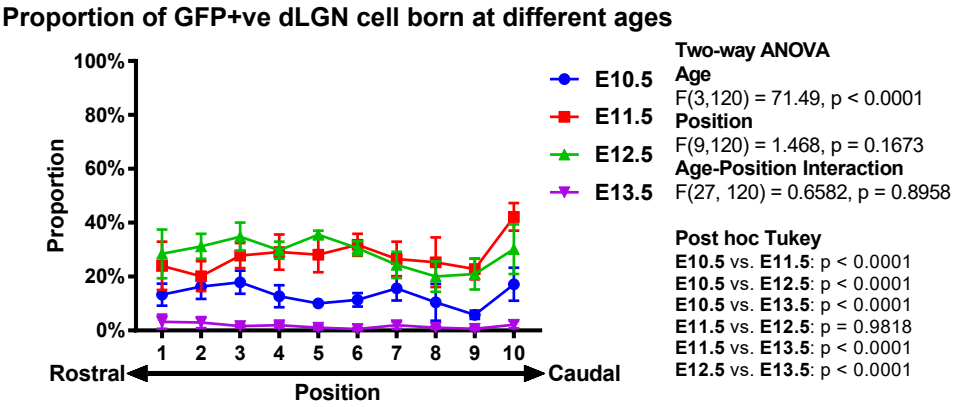


Figure 7.12: ***Proportion of GFP+ve dLGN cells born at each position at different ages.***

The rostral-caudal position has no effects ($F(9, 120) = 1.468$, $p = 0.1673 > 0.05$) on the GFP+ve neurogensis in dLGN either (Figure 7.12).

These results showed that both the whole population and the GFP+ve population that contribute to the future dLGN are born mainly at E11.5 and E12.5 and there is no difference along the rostral-caudal axis.

VP

Even though there were no significant changes in the volume or the cell composition in the VP, I still carried out the study of the birth date of these cells that contribute to the future VP for the sake of completeness.

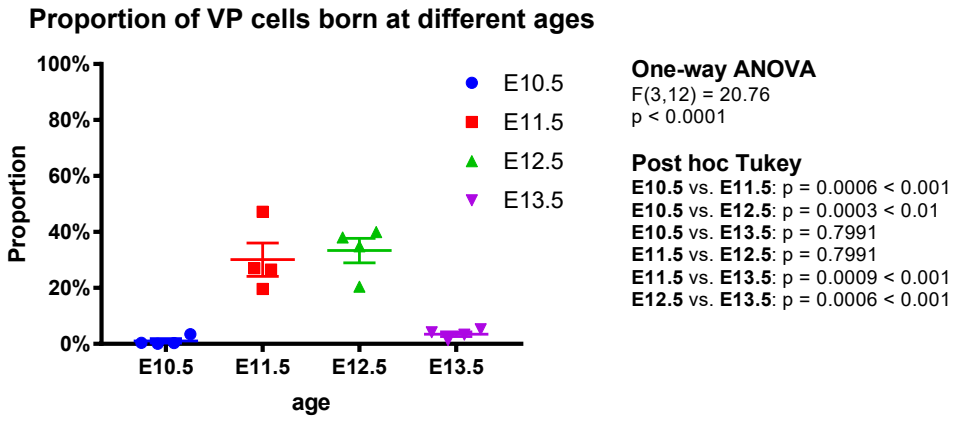


Figure 7.13: ***Proportion of VP cells born at E10.5, E11.5, E12.5 and E13.5.***

The cells contributing to the VP are mainly born from E11.5 (30.09% ± 5.951%) to E12.5 (33.34% ± 4.407%) among all the observed stages (Figure 7.13).

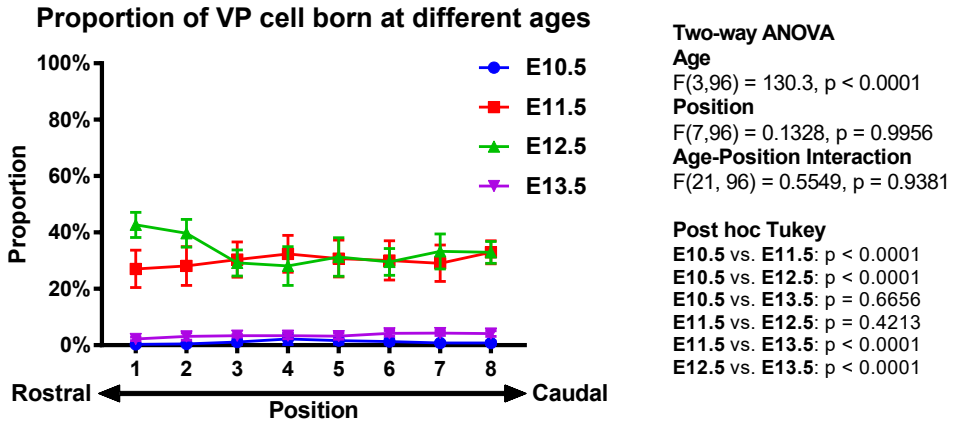


Figure 7.14: ***Proportion of VP cells born at each position at different ages.***

There is no significant difference ($F(7, 96) = 0.1328$, $p = 0.9956 > 0.05$) along the rostral-caudal axis when looking at the data for each specific postion (Figure 7.14).

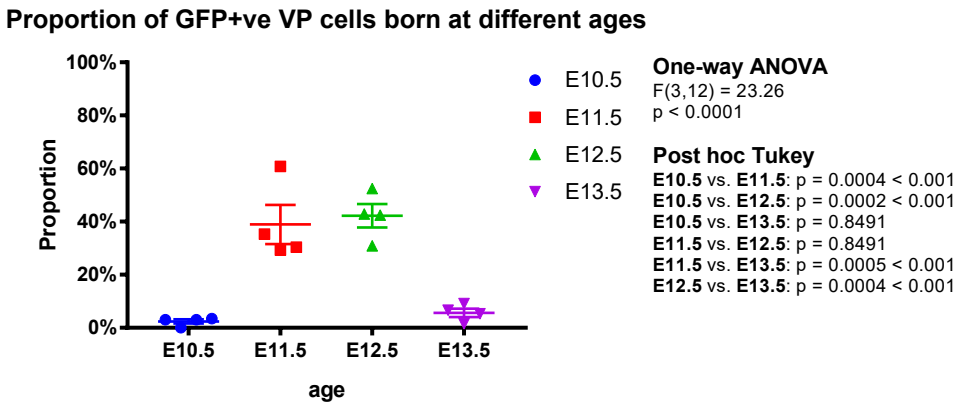


Figure 7.15: ***Proportion of GFP+ve VP cells born at E10.5, E11.5, E12.5 and E13.5.***

As for GFP+ve cells destined to be in the VP, they are mainly born from E11.5 (38.94% ± 7.39%) to E12.5 (42.17% ± 4.411%) (Figure 7.15), different from what was seen in vLGN and dLGN cells (Figure 7.13).

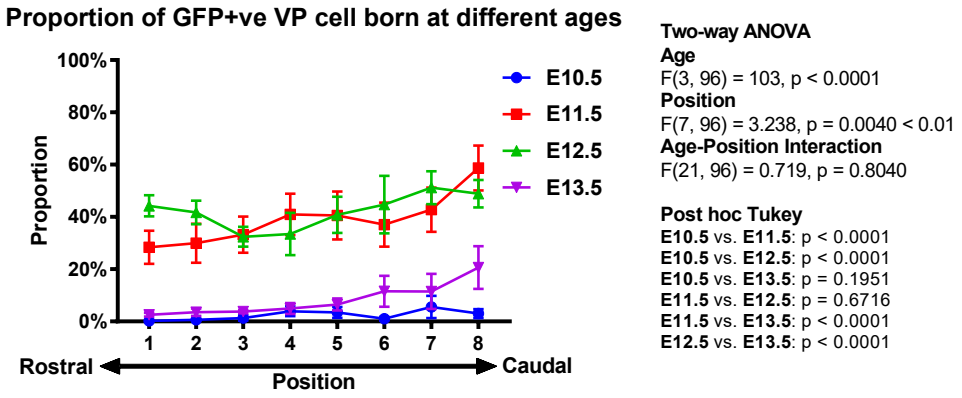


Figure 7.16: ***Proportion of GFP+ve VP cells born at each position at different ages.***

The rostral-caudal position does have significant effects ($F(7,96) = 3.238$, $p = 0.0040 < 0.01$) on the GFP+ve neurogensis in VP, with slightly more GFP+ve VP cells born at the caudal part than the rostral part of the VP at E11.5 and E13.5 (Figure 7.16).

7.4 Synopsis

The birthdating experiment using BrdU labelling revealed that the majority of vLGN and dLGN cells are born from E10.5 to E12.5, especially E11.5 and E12.5, which is in line with Angevine's study [42] and the GFP+ve *Zic4* lineage cells are mainly born during this time as

well, which suggests that **E11.5** and **E12.5** are critical ages to look at for any neurogenetical and early patterning defects. The proportions of cells and GFP+ve cells born to contribute to different parts of the vLGN and dLGN along the rostral-caudal axis are quite similar, which suggests newly born cells evenly populate the two nuclei from rostral to caudal. The data collected for VP revealed that the cells contribute to this nucleus are mainly born between E11.5 and E12.5, similar to the vLGN and dLGN, thus it is likely that the neurogenesis in all three nuclei are under the control of a similar spectrum of neurogenetical time-window associated factors/elements which potentially regulate cell proliferation, cell cycle exit and neuronal differentiation. In the subsequent chapter, I performed short-term BrdU labelling and stained for pHH3 and Caspase 3 to look into potential cell proliferation defects and abnormal apoptosis at E11.5, E12.5 and E13.5.

Chapter 8

Zic4Cre mediated deletion of *Pax6* causes cell proliferation defects and abnormal apoptosis at E11.5, E12.5 and E13.5

8.1 Introduction

In Chapter 6, a decrease in cell density was observed in the P0 $Pax6^{fl/fl}$ vLGN as well as an increase in the GFP+ve cell proportion in both the $Pax6^{fl/+}$ and $Pax6^{fl/fl}$ vLGN and dLGN with no total cell number change (Table 6.1). During thalamic development, cell birth and cell death overlap. A relatively stable cell number may be the result of changes in both factors thus it is possible that the deletion of *Pax6* causes defects in cell proliferation and cell death which subsequently leads to cell composition change in the vLGN and dLGN at P0. To investigate this possibility, I performed: 1. 2 hr BrdU labelling combined with immunohistochemistry for Ki67 (marker for all cycling cells), BrdU (S phase marker), pHH3 (G2/M phase marker) and Tuj1(newly differetiated neuron marker) to study potential changes in cell proliferation and differentiation in the thalamus from E11.5 to E13.5; 2. immunohistochemistry for cleaved caspase-3 to study early apoptosis from E11.5 to E14.5.

8.2 Aim of the project

To investigate whether the deletion of *Pax6* causes cell proliferation defects and abnormal apoptosis at early stages of development, which could potentially result in the vLGN and dLGN defects at P0 as described in chapter 6.

8.3 Results

8.3.1 Cell Proliferation

Fluorescent staining for BrdU, Ki67, pHH3 and Tuj1 plus GFP and DAPI was carried out in two separate series of sections due to the limited number of microscope filters and origins of the antibodies. The paraffin embedded brains were sectioned into three series, among which one series was used for the stainings of BrdU, pHH3, GFP and DAPI and another was used for the stainings of Ki67, Tuj1, GFP and DAPI, making the results comparable.

The .nd2 image files acquired on the confocal microscope were exported as stacks of 4 mono-channel grayscale tif files. The files were then imported into ImageJ to extract the region of interest (ROI). A box with a fixed height of 150 pixels was positioned and stretched to include the whole diencephalic wall for three structures of interest, the prethalamus (Pth) and the pTH-R and pTH-C in the thalamus (Figure 8.1). The cropped images were then processed using CellProfiler following a custom protocol in which the DAPI staining was used for nuclei segmentation (Table 8.1). The fluorescence intensities of other stainings were measured to distinguish positively stained cells from negative ones for BrdU, pHH3, Ki67, Tuj1 and GFP. Five anatomical positions along the front-back axis were studied for each of the three regions in all three genotypes from E11.5 to E13.5.

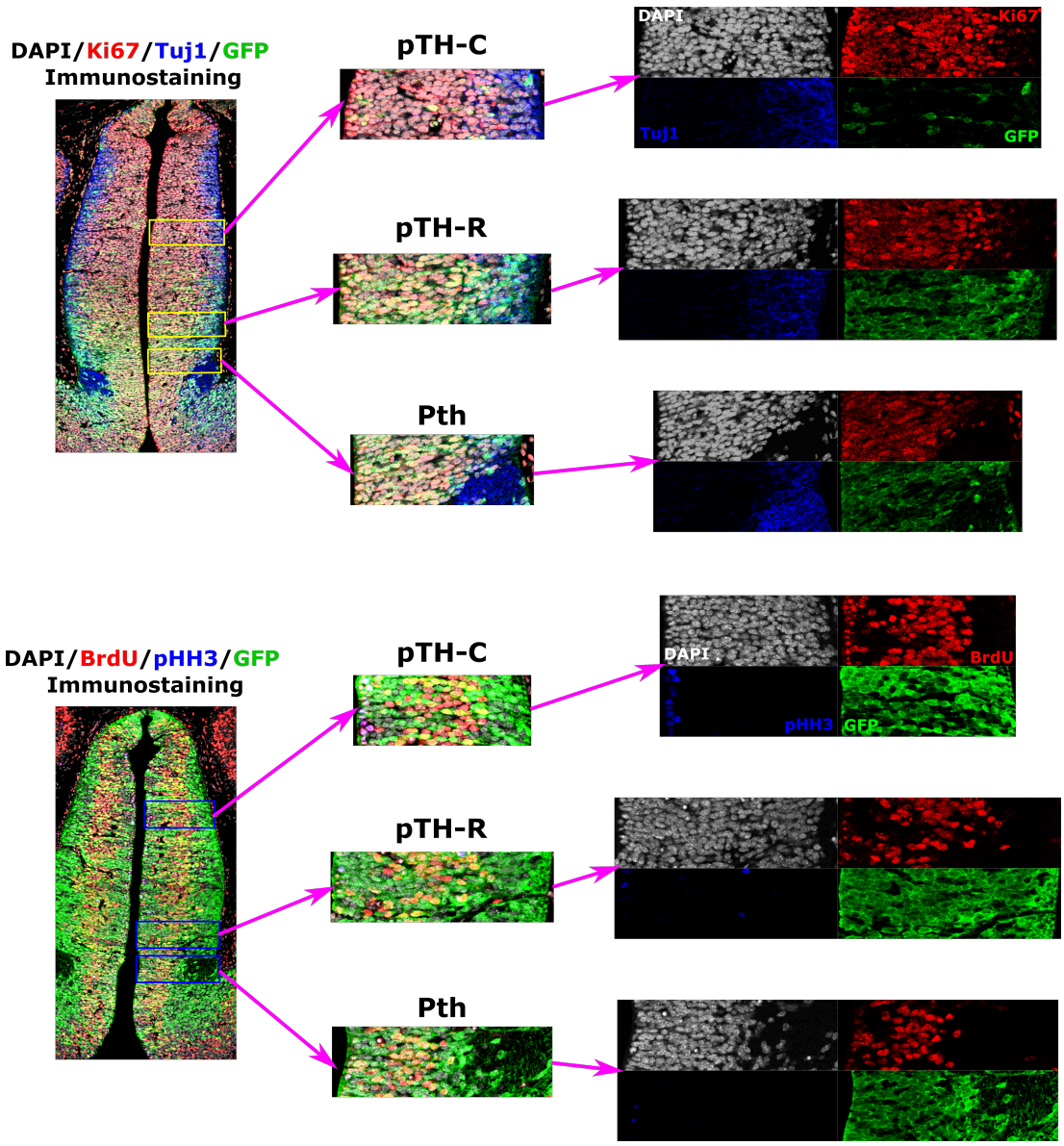


Figure 8.1: ***ROI selection for BrdU/pHH3/GFP/DAPI and Ki67/Tuj1/GFP/DAPI immunostainings.*** *Stretchable boxes with a fixed height of 150 pixels were positioned transverse the diencephalic wall in the prethalamus, the pTH-C and the pTH-R. Sample images of the three regions are presented for both sets of the experiments with mono-channelled images showing stainings for specific molecules.*

Parameters	Values
Typical diameter of objects, in pixel units (Min, Max)	9, 26
Discard objects outside the diameter range?	Yes
Discard objects touching the border of the image?	No
Threshold strategy	Global
Threshold method	Otsu
Select the smoothing method for thresholding	Three classes
Minimize the weighted variance or the entropy?	Weighted variance
Assign pixels in the middle intensity class to the foreground or the background?	Foreground
Select the smoothing method for thresholding	No smoothing
Threshold correction factor	0.8
Lower and upper bounds on the threshold	0.2, 1
Method to distinguish clumped objects	Intensity
Method to draw dividing lines between clumped objects	Intensity
Automatically calculate size of smoothing filter for declumping?	No
Size of smoothing filter	1
Automatically calculate minimum allowed distance between local maxima?	No
Suppress local maxima that are closer than this minimum allowed distance	5
Speed up by using lower-resolution image to find local maxima?	No
Fill holes in identified objects?	After declumping only

Table 8.1: ***Parameters used for DAPI based nuclei segmentation in cell cycle analysis using CellProfiler.*** *These parameters were chosen after trying out a spectrum of combinations of settings and were used for the segmentation in this chapter.*

Two cell proliferation related parametres were calculated for both the GFP+ve cell group and the whole cell population, including:

$$\textbf{Growth Fraction} = N^{Ki67+}/N^{DAPI} \times 100\%$$

$$\textbf{Proliferation rate} = N^{BrdU+}/N^{Ki67+} \times 100\% = (N^{BrdU+}/N^{DAPI})/(N^{Ki67+}/N^{DAPI'}) \times 100\%$$

As Ki67 and BrdU stainings were carried out in different sets of comparable sections, the proliferation rate was calculated by using the proportion of BrdU+ve cells (N^{BrdU+}/N^{DAPI}) in one set and the proportion of Ki67+ve cells ($N^{Ki67+}/N^{DAPI'}$) in another set.

Conventionally, cell cycle kinetics is studied using the sequential BrdU/IdU double incorporation especially in the developing cortex. The methodology is based on the assumptions that: 1. the progenitor cells progress through the cell cycle asynchronously (all of the cells have the same cell cycle times and they are evenly distributed across the cell cycle); 2. the population is growing at a steady-state (one-half of the daughter cells leave the proliferative population and the other half remains); 3. there are no non-proliferating cells to consider [97]. Since no previous studies have shown that the developing diencephalon fit all the criteria, the conventional method was not used in this study. Instead, I focused on the group of cells that were labelled by BrdU after 0.5 hr of the pulse and studied how this group of cells go through the cell cycle.

Assuming that cells progress through the cell cycle at a steady speed, then the speed measured at any time point within the cell cycle represents the cycling speed and in this case it is the S-G2/M transition speed, which is defined as:

$$\textbf{Cycling speed} = N^{BrdU+pHH3+}/N^{BrdU+}$$ Figure 8.2

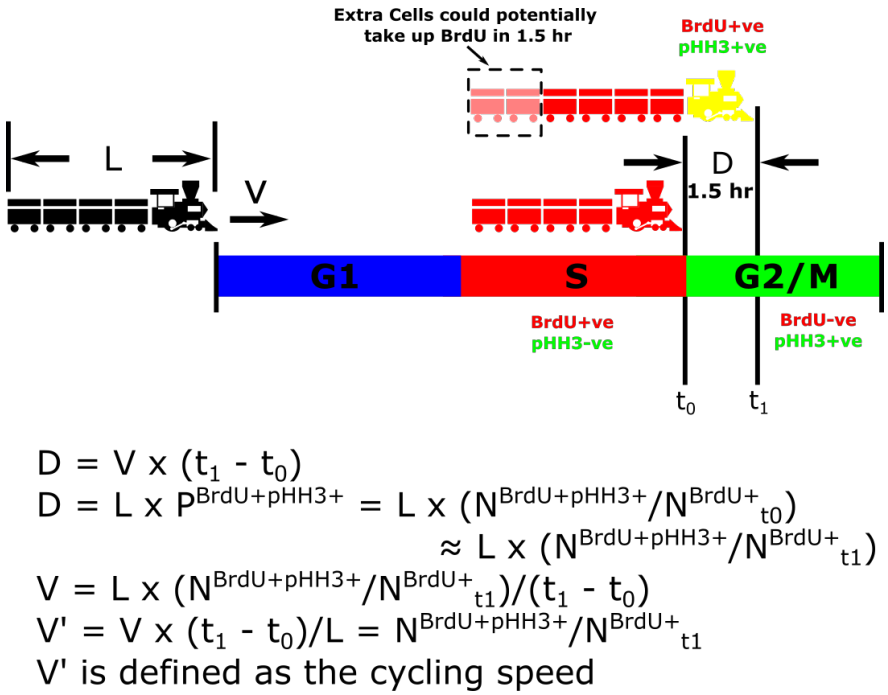


Figure 8.2: ***Schematic of cell cycling speed calculation.***

Imagine the cell group of interest as a train, the cells all travel at the same speed **V** through the cell cycle but at different positions of the cycle. This group of cells are labelled by BrdU in S phase after 0.5 hr of the injection and they keep advancing through the cycle for another 1.5 hr before the tissue is collected and fixed. During the 1.5 hr, this group of cells advance a distance of **D** and some of the cells transition into G2/M phase to become BrdU and pHH3 double positive. The distance **D** can be calculated by multiplying the speed **V** with 1.5 hr and it can also be calculated by multiplying the length of the train **L** by the proportion of BrdU and pHH3 double positive train at $\mathbf{t_0}$ (the locomotive in Figure 8.2). However, the number of BrdU+ve cells at time point $\mathbf{t_0}$ can not be obtained directly by counting BrdU+ve cells since extra cells could potentially take up BrdU during 1.5 hr. A way of circumventing this problem is to approximate the number of BrdU+ve cells at $\mathbf{t_0}$ by using BrdU+ve cells at $\mathbf{t_1}$ instead, which can be directly counted. Provided that the proportion of cells transitioning into G2/M phase is small, the number of extra cells that could potentially take up BrdU can be ignored. Since the length of the train **L** and the advancing time ($\mathbf{t_1}$ - $\mathbf{t_0}$ = 1.5 hr) are constants and **V** is proportional to $N^{BrdU+pHH3+}/N^{BrdU+}$, I simply defined the cycling speed **V′** as $N^{BrdU+pHH3+}/N^{BrdU+}$. Cell counting was carried out using the ROI already described and the cycling speed was calculated for three structures at different anatomical levels. The cycling speed data along different anatomical levels was combined by taking the mean of the values acquired at each position, which was treated as a single data point for each structure.

The dividing cells, especially the basal dividing population, were also studied by looking at the total number of pHH3+ve cells and the proportion of the basal pHH3+ve cells. The basal dividing cells are defined as the pHH3+ve cells that are not positioned along the ventricular surface. Cell counting was carried out using the ROI described previously, then the sum of the cell numbers across different levels was treated as a single data point for each structure.

For the growth fraction and the proliferation rate, four factors including **age** (E11.5, E12.5 and E13.5), **structure** (pTH-C, pTH-R and Pth), **genotype** ($Pax6^{+/+}$, $Pax6^{fl/+}$ and $Pax6^{fl/fl}$) and **anatomical position** along the front-back axis (4 levels for Pth and 5 levels for pTH-C and pTH-R) were explored. Two-way ANOVAs were performed to examine the main effects of genotype and position on different structures at different ages. The resulting graphs were organised into matrices. For the cycling speed, pHH3+ve cell number and basal pHH3+ve proportion, two sets of two-way ANOVAs were performed respectively to examind the main effects of genotype and structure, or genotype and age. Thus, two sets of different graphs were produced from the same data. For the average number of apoptosis cells/units per section, a two-way ANOVA was performed to examine the main effects of genotype and age. Tukey post hoc tests were performed for pair-wise comparisons subsequent to the ANOVAs. Since quite a few of two-way ANOVAs were performed in this section, the F values and p values were only reported in texts where the examined factor(s) significantly affect(s) the observed parametres.

8.3.2 Cell proliferation change in conditional *Pax6* mutants at E11.5, E12.5 and E13.5

Since most of the cells contributing to the future vLGN and dLGN are born mainly from E11.5 to E13.5, I decided to study the cell proliferatioin, including the growth fraction, proliferation rate, cell cycling speed and basal dividing cell population at these stages.

8.3.2.1 Growth fraction

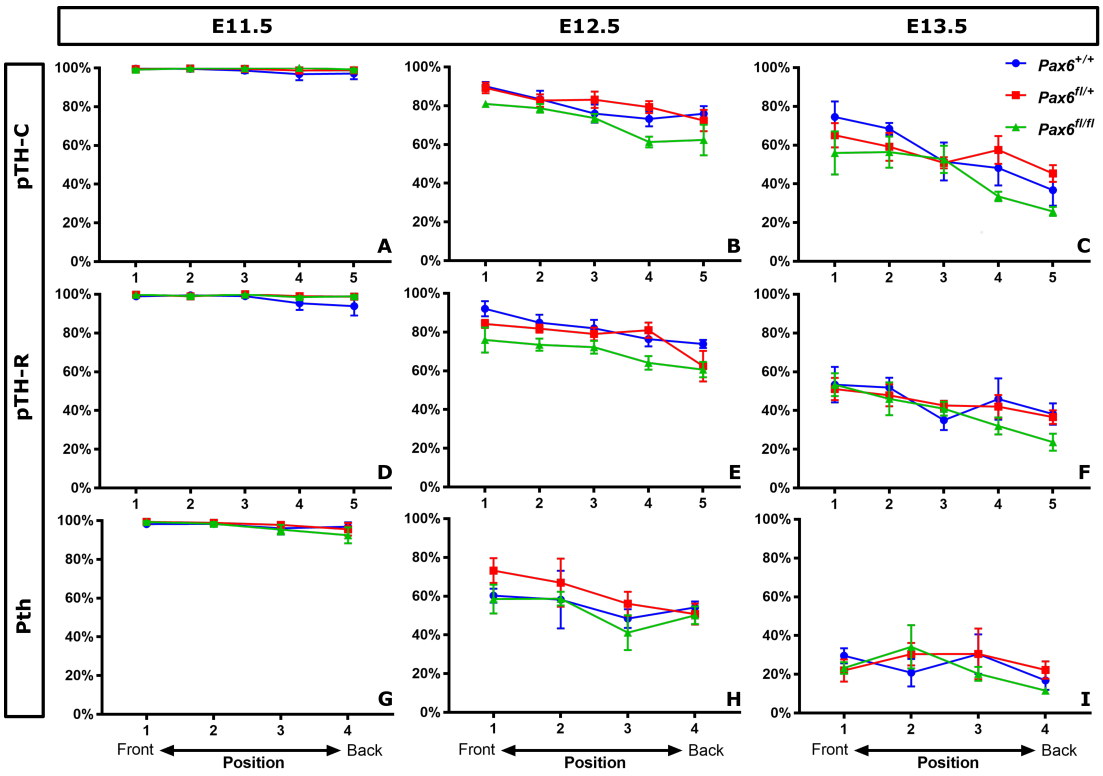


Figure 8.3: ***Growth fraction in pTH-C, pTH-R and Pth in E11.5, E12.5 and E13.5 Pax6$^{+/+}$, Pax6$^{fl/+}$ and Pax6$^{fl/fl}$ mice.***

In general, the growth fraction (GF) decreases from E11.5 to E13.5 in all three structures, the pTH-C, pTH-R and Pth (Figure 8.3). At E11.5, more than 95% of the cells in the observed structres were cycling in all three genotypes. A decrease of the GF at the back level was seen in the Pax6$^{+/+}$ pTH-R and Pth, however the change is not significant compared to the Pax6$^{fl/+}$ and Pax6$^{fl/fl}$ (Figure 8.3 A, D and G).

In the E12.5 Pth, no conspicuous difference in the GF was seen among the three genotypes at different positions, whereas in the pTH-R and pTH-C the analysis revealed a significant main effect for both the position ($F(4, 30) = 8.602$, $P < 0.0001$; $F(4, 30) = 9.304$, $P < 0.0001$) and the genotype ($F(2, 30) = 11.97$, $P = 0.0002 < 0.01$; $F(2, 30) = 9.109$, $P = 0.0008 < 0.01$). Post hoc Tukey tests showed that the significant difference between genotypes was found both between Pax6$^{+/+}$ & Pax6$^{fl/fl}$ and Pax6$^{fl/+}$ & Pax6$^{fl/fl}$ in the pTH-R (Pax6$^{+/+}$ vs. Pax6$^{fl/fl}$, $P = 0.0001$; Pax6$^{fl/+}$ vs. Pax6$^{fl/fl}$, $P = 0.0085 < 0.01$) and pTH-C (Pax6$^{+/+}$ vs. Pax6$^{fl/fl}$, $P = 0.0064 < 0.01$; Pax6$^{fl/+}$ vs. Pax6$^{fl/fl}$, $P = 0.0011$) respectively (Figure 8.3 B and E). Both the Pax6$^{+/+}$ and Pax6$^{fl/+}$ have a significantly higher GF in the pTH-R and pTH-C than the Pax6$^{fl/fl}$, at every observed position along the front-back axis.

At E13.5, a further decrease of the GF was seen in both the pTH-R and Pth. and the

analysis showed that the position significantly affects the former ($F(4, 30) = 5.028$, $P = 0.0032 < 0.01$), showing a front-high and back-low trend (Figure 8.3 F). The GF in the pTH-C at the same stage is affected by both the position ($F(4, 30) = 8.457$, $P = 0.0001$) and the genotype ($F(2, 30) = 4.049$, $P = 0.0278 < 0.01$). Post hoc Tukey tests revealed that the significant difference between genotypes is between the $Pax6^{+/+}$ and the $Pax6^{fl/fl}$ ($Pax6^{+/+}$ vs. $Pax6^{fl/fl}$, $P = 0.0456 < 0.05$) with the growth fraction higher at 4 out of the 5 observed positions in the $Pax6^{+/+}$ than in the $Pax6^{fl/fl}$ (Figure 8.3 C).

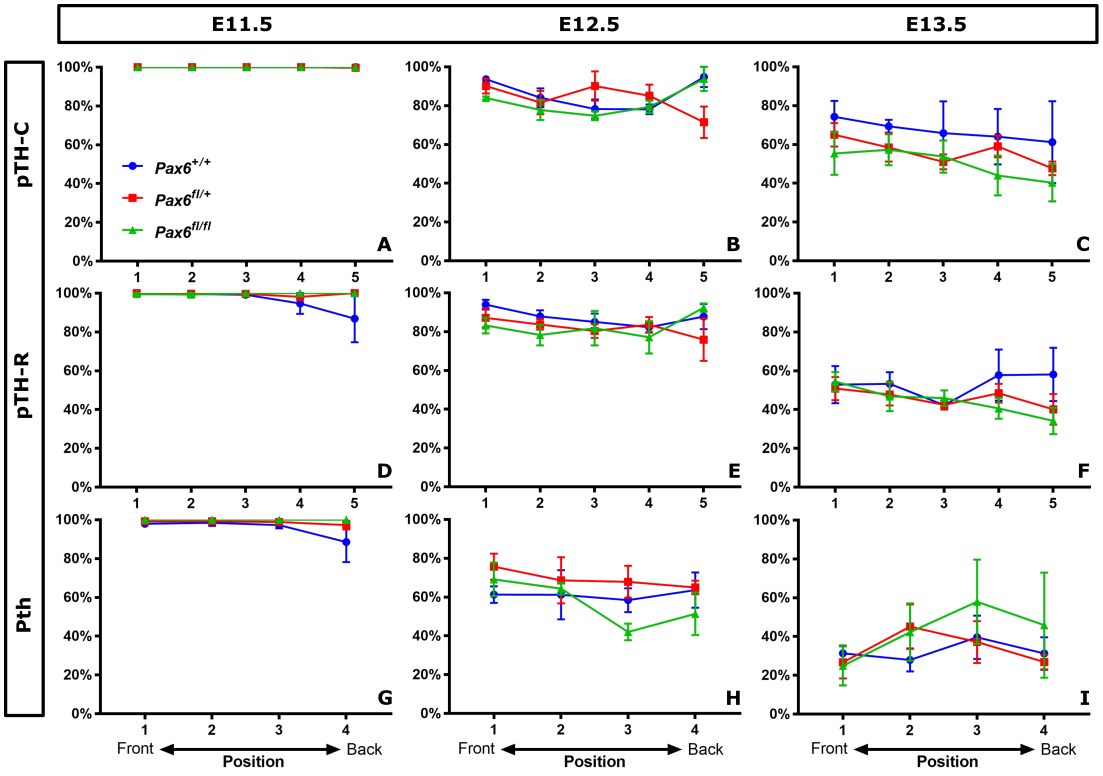


Figure 8.4: ***GFP+ve cell growth fraction in pTH-C, pTH-R and Pth in E11.5, E12.5 and E13.5 $Pax6^{+/+}$, $Pax6^{fl/+}$ and $Pax6^{fl/fl}$ mice.***

A similar decrease of GF through E11.5 to E13.5 was seen in the GFP+ve population in the pTH-C, pTH-R and Pth (Figure 8.4). Analyses of the GFP+ve population across different structures, ages, genotypes and positions revealed that the genotype significantly affects the GFP+ve GF in the E13.5 pTH-C ($F(2, 30) = 3.415$, $P = 0.0461 < 0.05$). Post hoc Tukey tests showed that the significant difference between genotypes is only between the $Pax6^{+/+}$ and the $Pax6^{fl/fl}$ ($Pax6^{+/+}$ vs. $Pax6^{fl/fl}$, $P = 0.0387 < 0.05$) with the GF higher at each position in the former than in the latter (Figure 8.4 C).

8.3.2.2 Proliferation rate

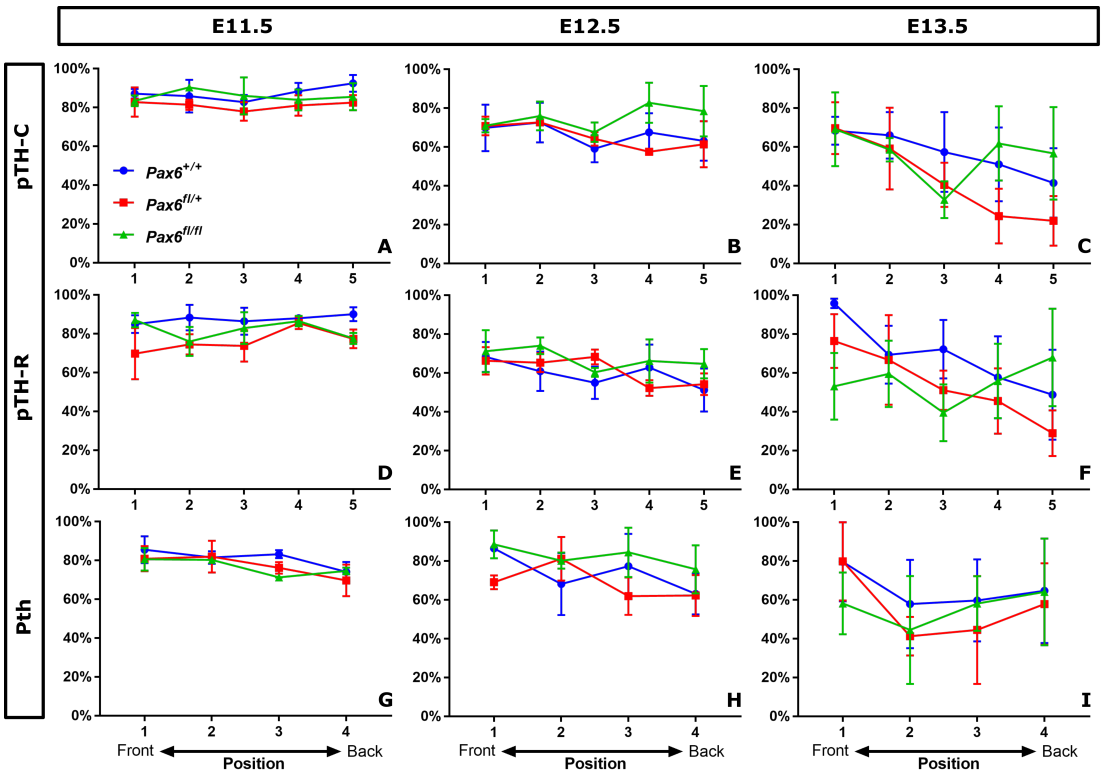


Figure 8.5: ***Proliferation rate in pTH-C, pTH-R and Pth in E11.5, E12.5 and E13.5 Pax6$^{+/+}$, Pax6$^{fl/+}$ and Pax6$^{fl/fl}$ mice.***

The proliferation rate (PR) of both the whole population (Figure 8.5) and the GFP+ve population (Figure 8.6) was also studied in the pTH-C, pTH-R and Pth at E11.5, E12.5 and E13.5.

There is a general decreasing trend in the PR toward E13.5, however it is not as obvious as what was seen in the GF (Figure 8.3 and Figure 8.4). The PR shows a great amount of variance especially at E13.5, for the whole population and the GFP+ve population at most of the stages. Since the PR was obtained and corrected by dividing the BrdU+ve proportions with the Ki67+ proportion, the variance at each position is expected to be great - especially at E13.5 when the cycling population is very small (Figure 8.5 and Figure 8.6 C, F and I). At the back level, only a few GFP+ve cells were present and the cycling proportion is even smaller, which leads to great variances especially in the pTH-C and pTH-R (Figure 8.6 A and D). The analyses revealed only that the genotype significantly affects the PR in the E11.5 pTH-R ($F(2, 30) = 4.206$, $P = 0.0245 < 0.05$). Post hoc Tukey tests showed that the significant difference between genotypes is between the Pax6$^{+/+}$ and the Pax6$^{fl/+}$ (Pax6$^{+/+}$ vs. Pax6$^{fl/+}$, $P = 0.0184 < 0.05$) with the proliferation highter at each position in the former than in the latter (Figure 8.5 D).

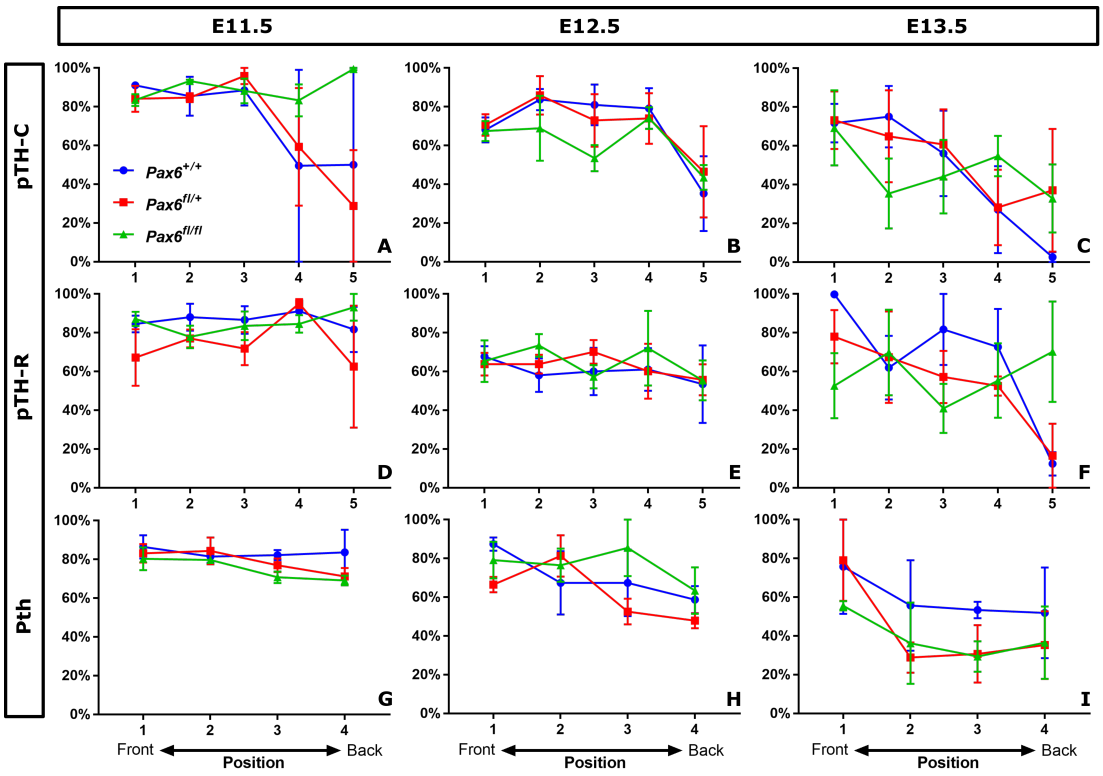


Figure 8.6: ***GFP+ve cell proliferation rate in pTH-C, pTH-R and Pth in E11.5, E12.5 and E13.5 $Pax6^{+/+}$, $Pax6^{fl/+}$ and $Pax6^{fl/fl}$ mice.***

8.3.2.3 Cycling speed

The effects of age, structure and genotype on the cell cycling speed were also studied. No significant difference was found among different genotypes and different structures within the diencephalon across all the observed stages (Figure 8.7 A, C and E). However, structure-specific analyses revealed that the age significantly affects the cycling speed in the pTH-C ($F(2, 18) = 4.444$, $P = 0.0270 < 0.05$) (Figure 8.7 B). Post hoc Tukey tests showed that the only difference among ages is between E11.5 and E13.5 (E11.5 vs. E13.5, $P = 0.0218 < 0.05$). The results suggests that the cells in the pTH-C cycle faster at E11.5 and gradually slow down toward E13.5. A similar trend was also seen in the Pth (Figure 8.7 F). The age was shown to significantly affect the cycling speed ($F(2, 18) = 11.02$, $P = 0.9927 < 0.05$) and post hoc Tukey tests revealed that the difference among ages was between both E11.5 & E12.5 (E11.5 vs. E12.5, $P = 0.0117 < 0.05$) and E11.5 & E13.5 (E11.5 vs. E13.5, $P = 0.0007 < 0.001$). The result suggests that unlike the gradual slowing-down of the cell cycle in the pTH-C, the cell cycling speed in the Pth drops more abruptly after E11.5 and then maintains a slow decline from E12.5 onwards.

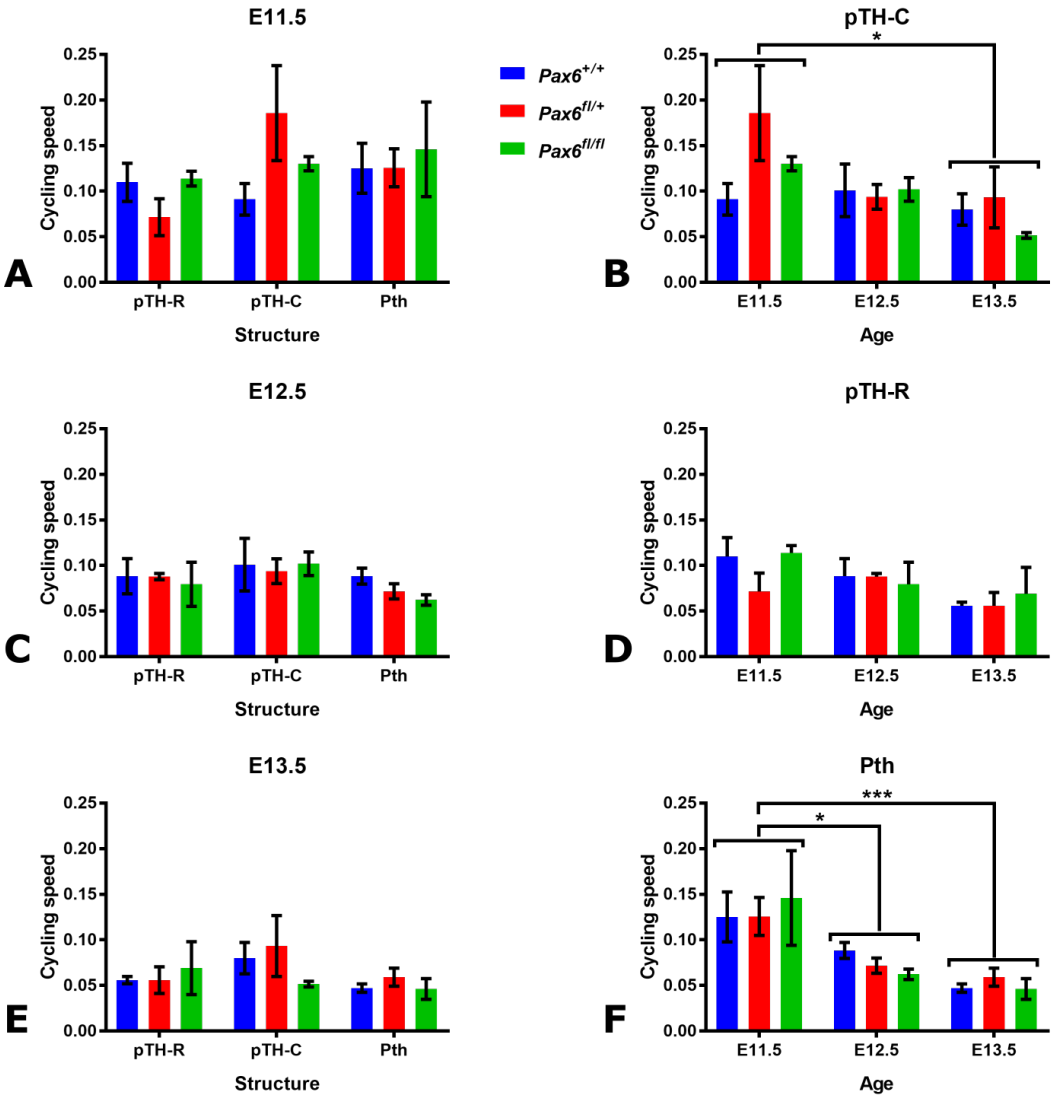


Figure 8.7: ***Cell cycling speed in pTH-C, pTH-R and Pth in E11.5, E12.5 and E13.5 $Pax6^{+/+}$, $Pax6^{fl/+}$ and $Pax6^{fl/fl}$ mice.***

8.3.2.4 Basal dividing population

The basal dividing population was first described by Nakagawa's group and it was shown that Pax6 plays a role in generating basal progenitors from apical progenitors and regulates the balance between the two [38]. In this part of the project, the total number of the pHH3+ dividing cells (Figure 8.8) and the proportion of the basally positioned ones (Figure 8.9) were studied with a main focus on the three factors - genotype, age and structure.

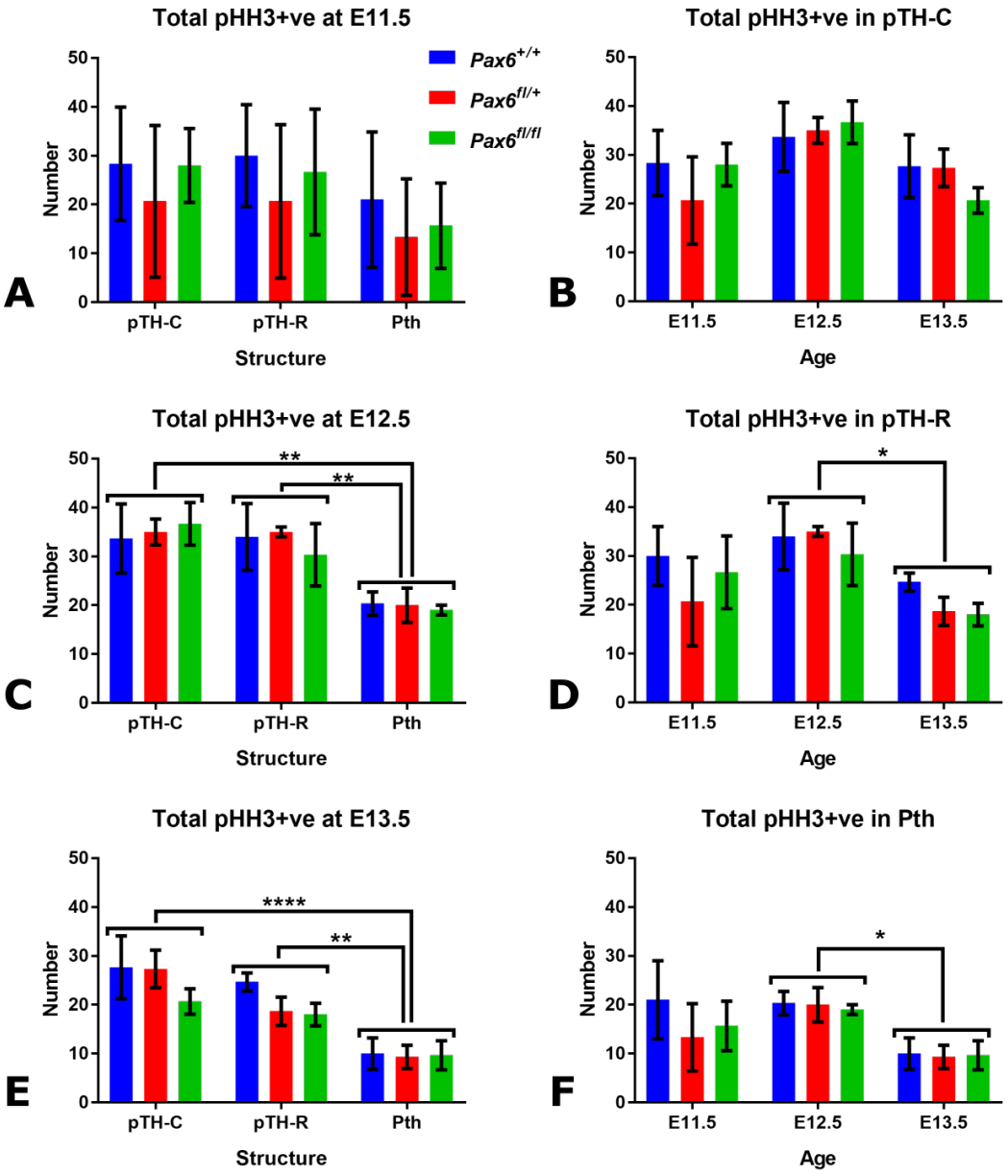


Figure 8.8: ***pHH3+ve cell number in pTH-C, pTH-R and Pth in E11.5, E12.5 and E13.5 Pax6$^{+/+}$, Pax6$^{fl/+}$ and Pax6$^{fl/fl}$ mice.***

At E11.5, a lot of variances were seen in the pHH3+ve cell number among difference genotypes in different structures and no significant effects were found (Figure 8.8 A).

At E12.5 (Figure 8.8 C), the analysis revealed that the structure significantly affects the number of the pHH3+ve cells ((F(2, 18) = 10.26, P = 0.0011 $<$ 0.01)) and the difference among structures was found both between the pTH-C & Pth (pTH-C vs. Pth, P = 0.0016 $<$ 0.01) and the pTH-R & Pth (pTH-R vs. Pth, P = 0.0052 $<$ 0.01).

A similar situation was seen at E13.5 (Figure 8.8 E) and the analysis showed that structure is the main factor affecting the pHH3+ve cell number ((F(2, 18) = 16.31, P $<$ 0.0001)) and the difference between structures was found both between the pTH-C & Pth (pTH-C vs. Pth, P $<$ 0.0001) and the pTH-R & Pth (pTH-R vs. Pth, P = 0.0031 $<$ 0.01).

The results from E12.5 and E13.5 suggest that the Pth is significantly different from the pTH-C and pTH-R in terms of the number of the pHH3+ve cells. When looking at specific structures, age was shown to be the main factor that affects the pHH3+ve cell number, in both the pTH-R ((F(2, 18) = 3.916, P = 0.0387 $<$ 0.05)) and Pth ((F(2, 18) = 4.003, P = 0.0327 $<$ 0.05)). The difference among ages was only shown between E12.5 and E13.5 in both the pTH-R (E12.5 vs. E13.5, P = 0.0311 $<$ 0.05) and Pth (E12.5 vs. E13.5, P = 0.0327 $<$ 0.05). The results suggest that the pTH-R and Pth are similar in terms of showing the decline in the pHH3+ve cell number from E12.5 to E13.5, a characteristic that is absent in the pTH-C.

The analyses of the basal dividing pHH3+ve cells (Figure 8.9 A, C and E) revealed that at E12.5, the structure significantly affects the proportion of this cell population ((F(2, 18) = 20.96, P $<$ 0.0001)) and the difference among structures was found both between pTH-C & Pth (pTH-C vs. Pth, P = 0.0004 $<$ 0.001) and pTH-R & Pth (pTH-R vs. Pth, P $<$ 0.0001). The proportion is smaller in the Pth (17.33%) than in both the pTH-C (36.24%) and pTH-R (41.51%) at E12.5. Structure-specific analyses showed that age is the critical factor that affects the proportion of the basal dividing population across all three structures, the pTH-C ((F(2, 18) = 59.56, P $<$ 0.0001)), pTH-R ((F(2, 18) = 5.402, P = 0.0145 $<$ 0.05)) and Pth ((F(2, 18) = 4.488, P = 0.0262 $<$ 0.05)) (Figure 8.9 B, D and F). In the pTH-C (Figure 8.9 B), significance was seen in all three pair-wise comparisons (E11.5 vs. E12.5, P = 0.0138 $<$ 0.05; E11.5 vs. E13.5, P $<$ 0.0001; E12.5 vs. E13.5, P $<$ 0.0001), suggesting that the proportion of the basal dividing cells increases conspicuously from E11.5 (23.34%) to E12.5 (36.24%) and from E12.5 (36.24%) to E13.5 (66.55%). In the pTH-R (Figure 8.9 D), the difference among ages was only shown between E11.5 (29.18%) and E13.5 (51.14%) (E11.5 vs. E13.5, P = 0.0111 $<$ 0.05). In the Pth, the difference was seen both between E11.5 & E13.5 (E11.5 vs. E13.5, P = 0.0460 $<$ 0.05) and E12.5

& E13.5 (E12.5 vs. E13.5, P = 0.0459 < 0.05), suggesting the proportions of the basal dividing cells at E11.5 (17.35%) and E12.5 (17.33%) are rather similar and it significantly increases at E13.5 (43.67%).

Neither the total pHH3+ve cell number nor the proportion of the basal dividing population analyses revealed any genotype related change.

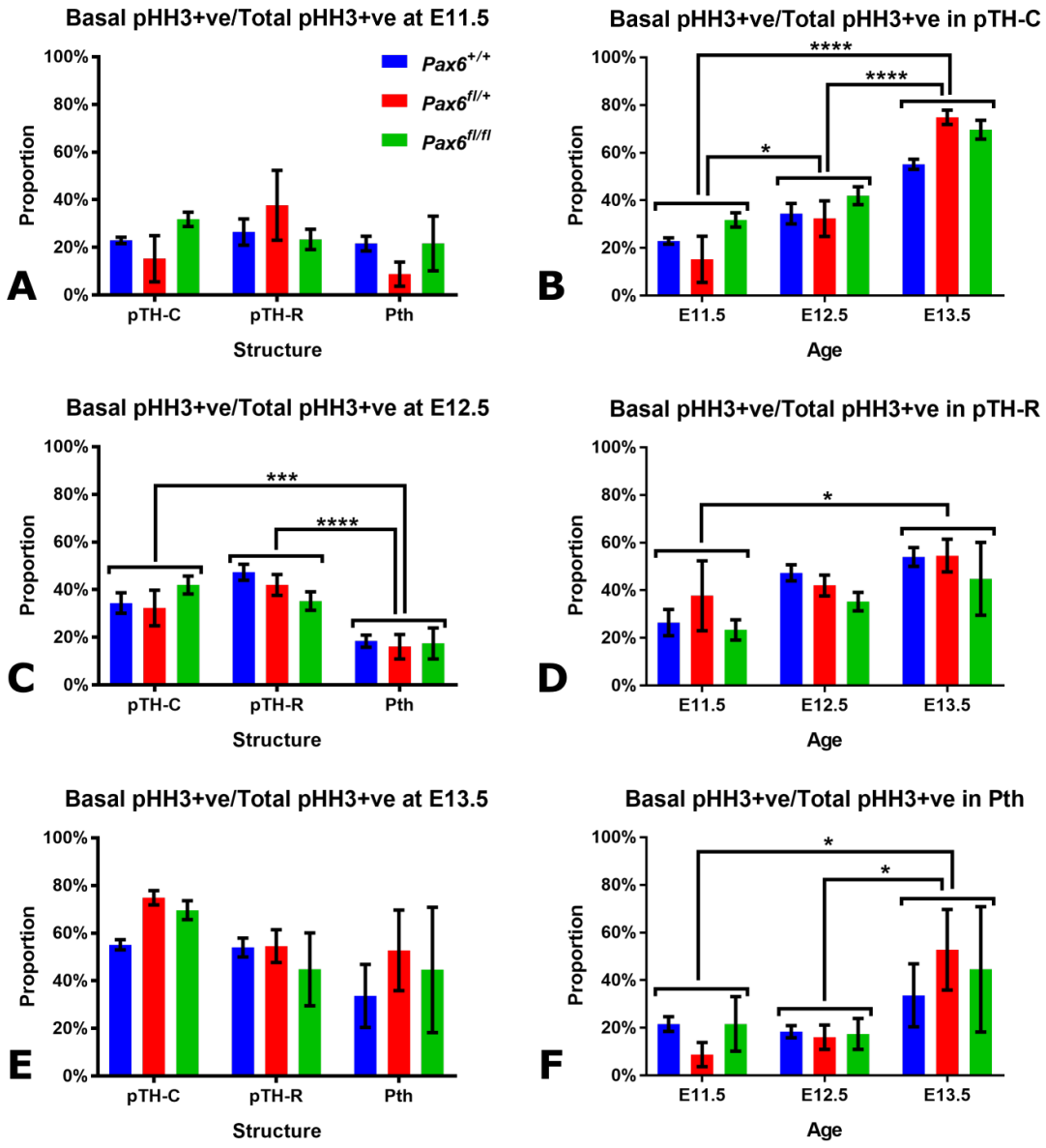


Figure 8.9: ***Basal pHH3+ve cell proportion in pTH-C, pTH-R and Pth in E11.5, E12.5 and E13.5 $Pax6^{+/+}$, $Pax6^{fl/+}$ and $Pax6^{fl/fl}$ mice.***

8.3.3 Cell apoptosis in conditional *Pax6* mutants induced by *Zic4Cre* at E11.5, E12.5, E13.5 and E14.5

The DAB histochemistry for the cleaved caspase-3 was performed on E11.5, E12.5, E13.5 and E14.5 coronal brain sections. The number of the caspase-3+ve apoptotic cells/units are manually counted on the observed sections and the mean value was calculated for each genotype. The experiment was repeated for three times from E11.5 to E13.5 but only performed once for E14.5. Staining of caspase-3 on E13.5 mouse paw section (Figure 8.10) was used as the positive control for the staining on the brain sectoins.

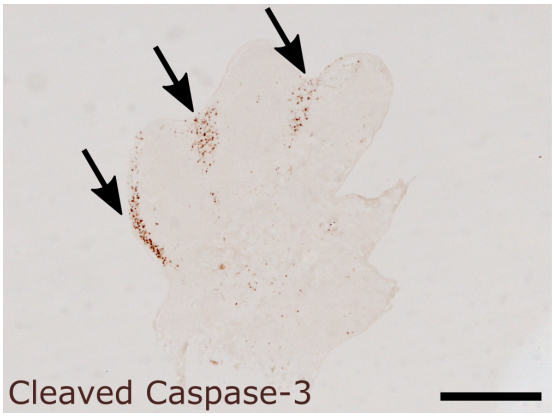


Figure 8.10: ***Cleaved caspase 3 immunohistochemistry on E13.5 coronal paw sections of Pax6$^{+/+}$ mice.*** *The interdigital cells that have undergone apoptosis were indicated with black arrows. Scale bar: 500 μm.*

The staining for cleaved caspase-3 was studied in the developing diencephalon at E11.5 (Figure 8.11), E12.5 (Figure 8.12), E13.5 (Figure 8.13) and E14.5 (Figure 8.14) in all three types of brains, Pax6$^{+/+}$, Pax6$^{fl/+}$ and Pax6$^{fl/fl}$.

At E11.5, the caspase-3+ve cells distribute across the diencephalon in a stochastic fashion except around the dorsal midline, where the aggregation of the caspase-3+ve cells was observed (Figure 8.11 B1, C1, C2, A3, B4, B5 and C5). Comparing to E11.5, fewer caspase-3+ve cells were observed at E12.5 in all three genotypes but the distribution pattern of these cells remains random (Figure 8.12). The aggreagtion of the caspase-3+ve cells can still be seen in the developing epithalamus in the Pax6$^{fl/fl}$ but not in the Pax6$^{+/+}$ or Pax6$^{fl/+}$ any more (Figure 8.12 A1-C1 and A2-C2). At E13.5, no caspase-3+ve cells are observed in the developing epithalamus in any of the three genotypes and the number and distribution of the caspase-3+ve cells in the diencephalon remain similar to E12.5 (Figure 8.13). At E14.5, it seems that most caspase-3+ve cells distribute around the ventricular and the subventricular regions of the diencephalon in all three genotypes and fewer caspase-3+ve cells are observed

in the Pax6$^{fl/fl}$ compared to the Pax6$^{+/+}$ and Pax6$^{fl/+}$.

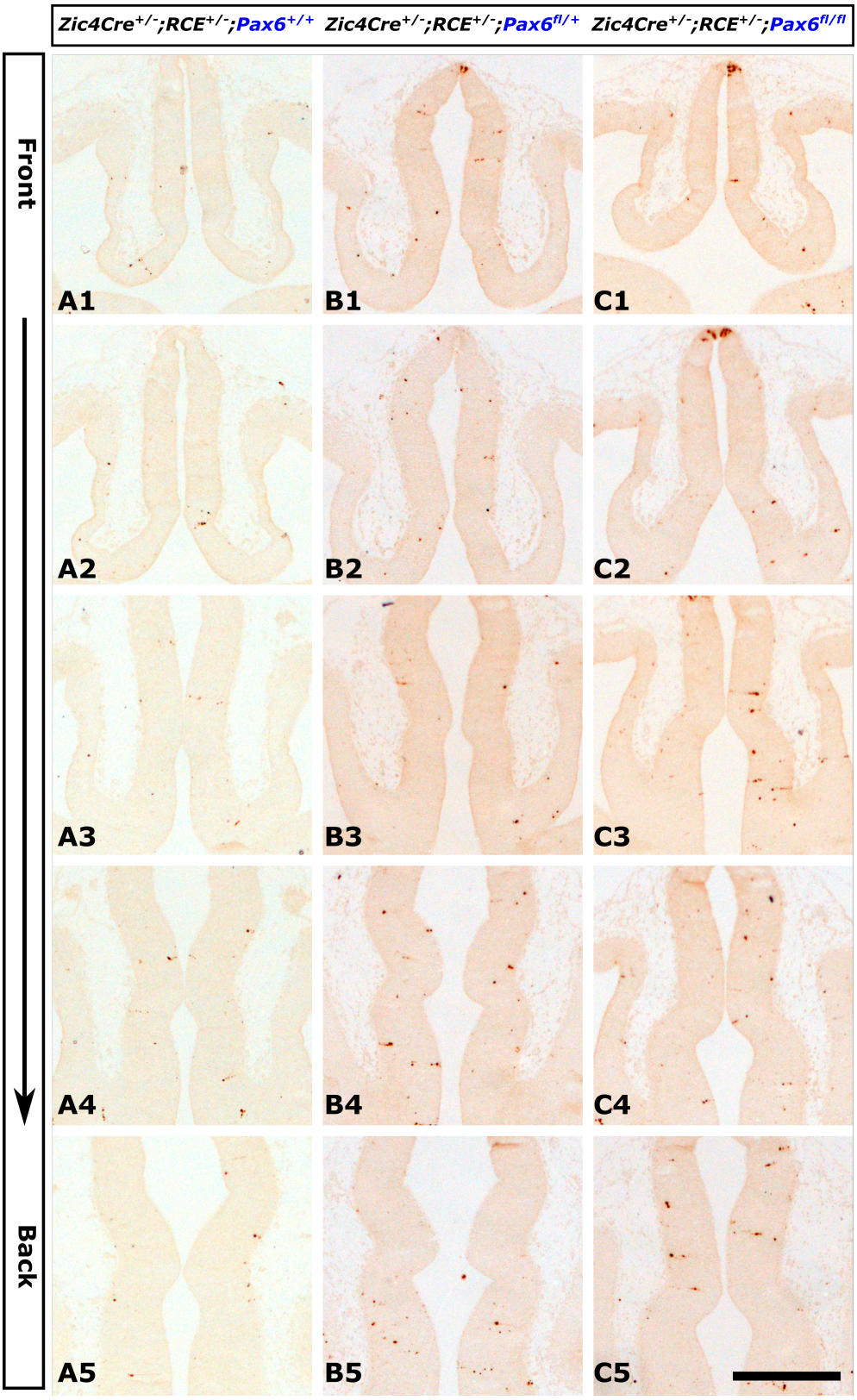


Figure 8.11: ***Cleaved caspase 3 immunohistochemistry on E11.5 coronal brain sections of Pax6$^{+/+}$, Pax6$^{fl/+}$ and Pax6$^{fl/fl}$ mice.*** *The apoptotic units were outlined using black circles. Scale bar: 300 μm.*

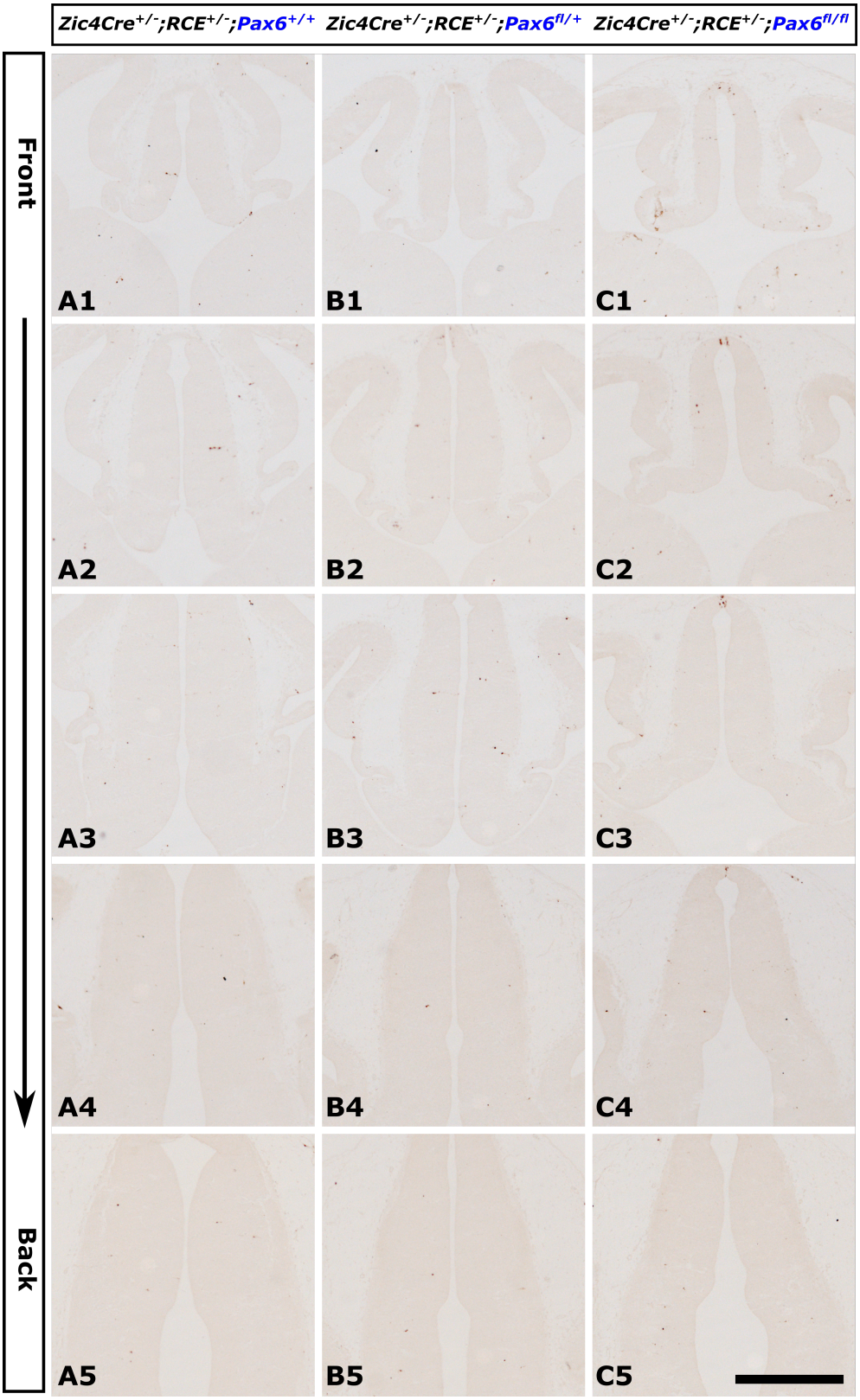


Figure 8.12: ***Cleaved caspase 3 immunohistochemistry on E12.5 coronal brain sections of $Pax6^{+/+}$, $Pax6^{fl/+}$ and $Pax6^{fl/fl}$ mice.*** *Scale bar: 500 μm.*

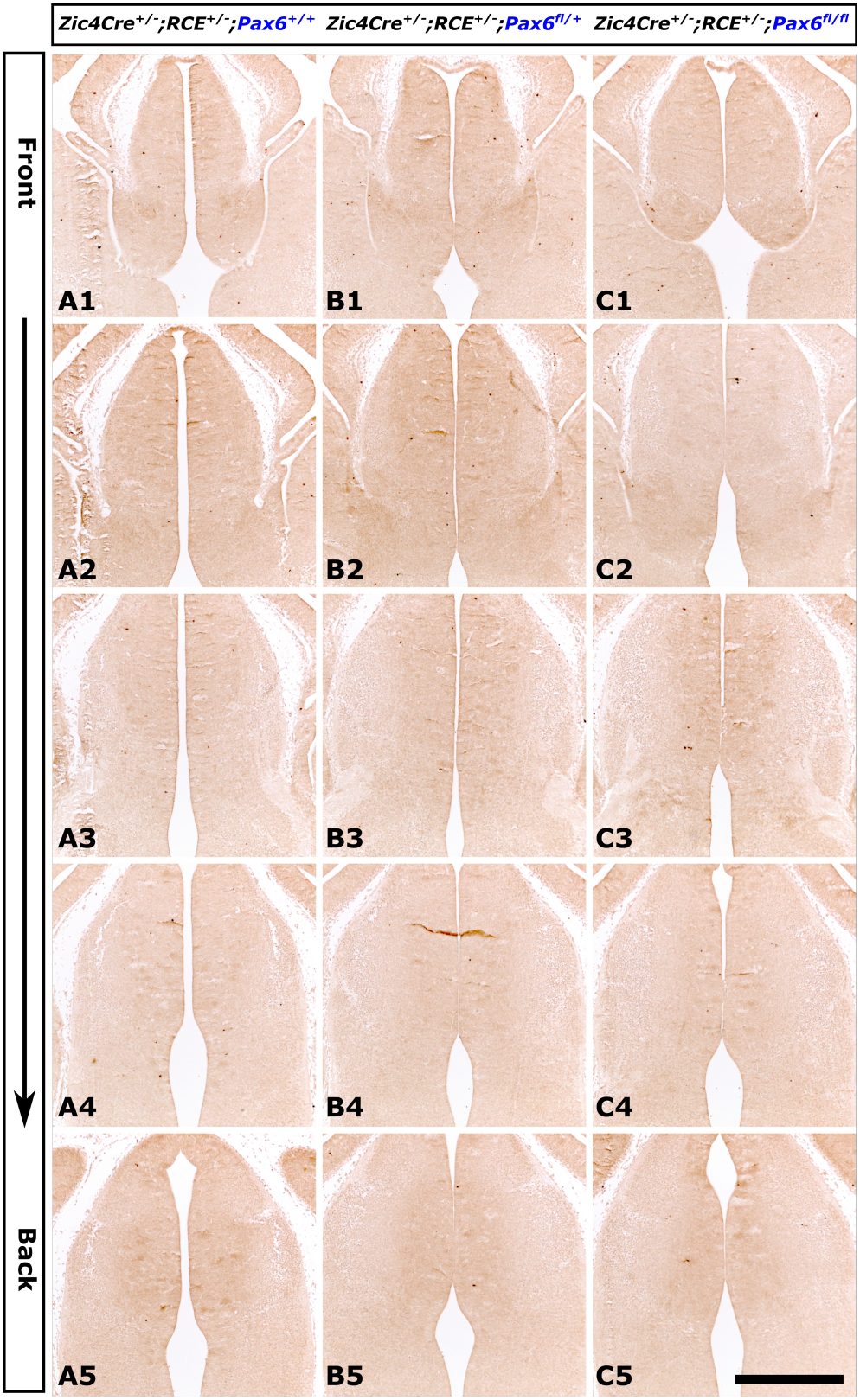


Figure 8.13: ***Cleaved caspase 3 immunohistochemistry on E13.5 coronal brain sections of $Pax6^{+/+}$, $Pax6^{fl/+}$ and $Pax6^{fl/fl}$ mice.*** *Scale bar: 450 μm.*

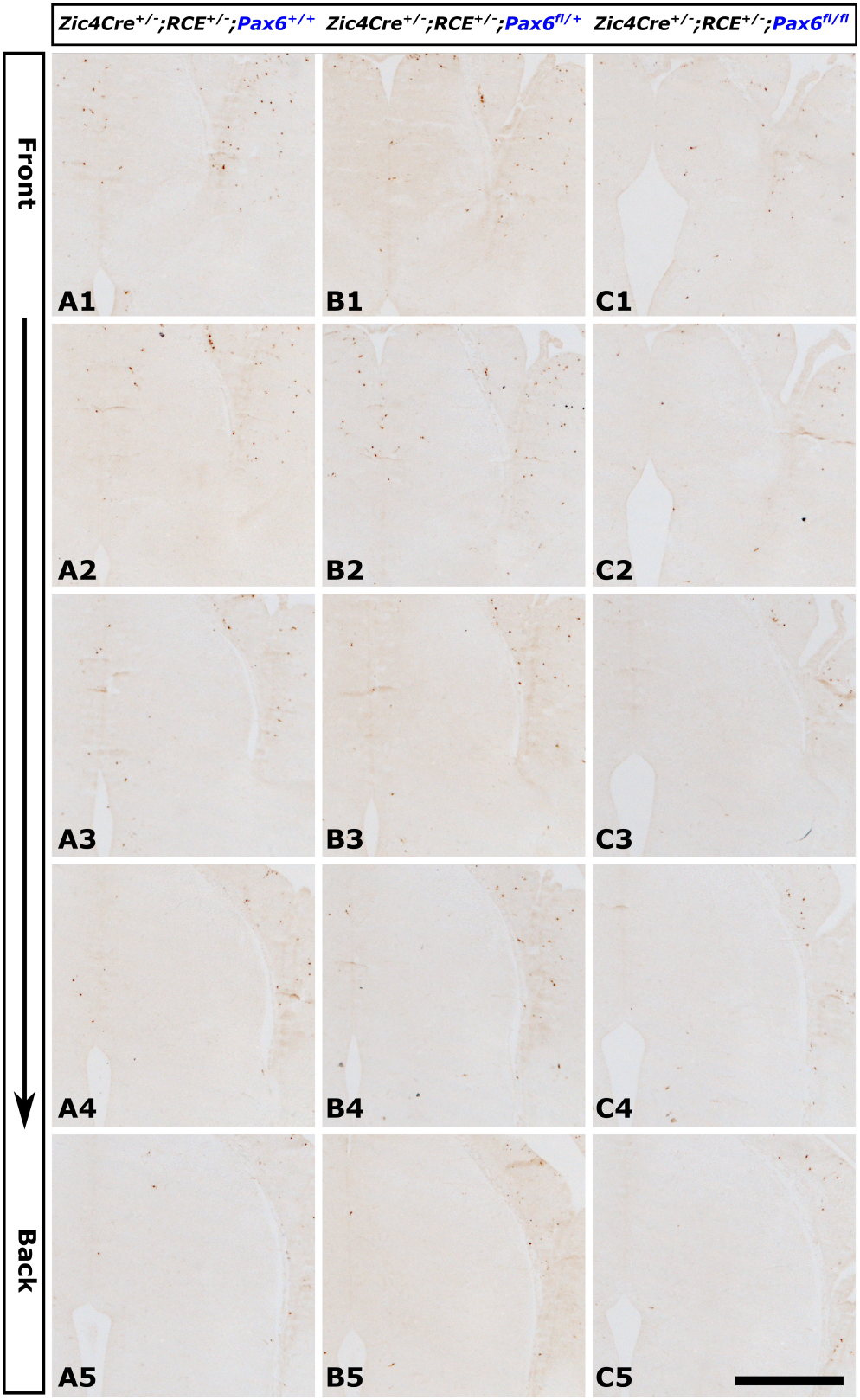


Figure 8.14: ***Cleaved caspase 3 immunohistochemistry on E14.5 coronal brain sections of $Pax6^{+/+}$, $Pax6^{fl/+}$ and $Pax6^{fl/fl}$ mice.*** *n = 1. Scale bar: 450 μm.*

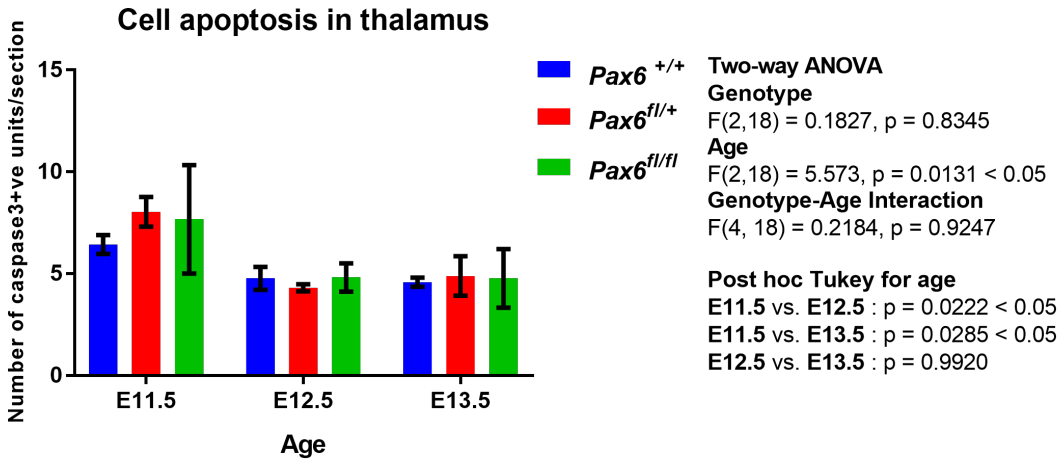


Figure 8.15: ***Cell apoptotic rate in E11.5 to E13.5 thalamus of Pax6$^{+/+}$, Pax6$^{fl/+}$ and Pax6$^{fl/fl}$ mice.*** *The analysis did not include the E14.5 data since the experiment was not repeated at this age.*

The average number of the caspase-3+ve cells/units per section was calculated for the data obtained at E11.5, E12.5 and E13.5 (Figure 8.15). It was found that there is no significant difference in cell apoptosis among different genotypes ($F(2, 18) = 0.1827$, $p = 0.8345$) but there is a difference between different ages ($F(2, 18) = 5.573$, $p = 0.0131$) - more caspase-3+ve cells were observed at E11.5 compared to E12.5 and E13.5.

8.4 Synopsis

The main findings of the cell proliferation related studies of this project are summarised into two categories, the general knowledge and the genotype (*Pax6* deletion) related knowledge. The general knowledge includes: 1. almost all the cells in the structures of interest, the pTH-C, pTH-R and Pth are cycling cells at E11.5 and the growth fraction decreases from E11.5 onwards, more rapidly in the Pth compared to the pTH-C and pTH-R; 2. the proliferation rate of the cycling cells in the above structures shows a similar attenuating trend from E11.5 to E13.5, only less obvious; 3. the cells in the pTH-C, pTH-R and Pth have similar cycling speed at each studied developmental stage and the cycle slows down towards E13.5, especially conspicuous in the Pth; 4. the pTH-C and pTH-R generally possess more pHH3+ve cells than the Pth at both E12.5 and E13.5, and a significant decline of the pHH3+ve cell number at E13.5 is a shared feature between the pTH-R and Pth; 5. as for the basal dividing cells, the pTH-C and pTH-R have a larger population than the Pth at E12.5 and the proportion of these basal dividing cells increases in all three structures as development proceeds.

Genotype-wise, the change in cell proliferation related characteristics caused by *Pax6* deletion is rather subtle (Table 8.2): 1. the cell proliferation rate in the pTH-R in $Pax6^{fl/+}$ showed a decrease at E11.5; 2. a decease of growth fraction in $Pax6^{fl/fl}$ was observed in both pTH-C and pTH-R at E12.5 and in the pTH-C at E13.5; 3. no GFP+ve population specific change was found in any of the studied parametres in the conditional mutants except a decrease of growth fraction in E13.5 $Pax6^{fl/fl}$ pTH-C; 4. no change in the Pth was observed in any of the structures of any genotypes at any single stage studied.

Genotype	Age	Structure name	Growth fraction	Proliferation rate	Cell cycling speed	Total pHH3+ number	Basal pHH3+ proportion
$Pax6^{fl/+}$	E11.5	pTH-C	n.s.	n.s.	n.s.	n.s.	n.s.
		pTH-R	n.s.	⇓	n.s.	n.s.	n.s.
		Pth	n.s.	n.s.	n.s.	n.s.	n.s.
	E12.5	pTH-C	n.s.	n.s.	n.s.	n.s.	n.s.
		pTH-R	n.s.	n.s.	n.s.	n.s.	n.s.
		Pth	n.s.	n.s.	n.s.	n.s.	n.s.
	E13.5	pTH-C	n.s.	n.s.	n.s.	n.s.	n.s.
		pTH-R	n.s.	n.s.	n.s.	n.s.	n.s.
		Pth	n.s.	n.s.	n.s.	n.s.	n.s.
$Pax6^{fl/fl}$	E11.5	pTH-C	n.s.	n.s.	n.s.	n.s.	n.s.
		pTH-R	n.s.	n.s.	n.s.	n.s.	n.s.
		Pth	n.s.	n.s.	n.s.	n.s.	n.s.
	E12.5	pTH-C	⇓	n.s.	n.s.	n.s.	n.s.
		pTH-R	⇓	n.s.	n.s.	n.s.	n.s.
		Pth	n.s.	n.s.	n.s.	n.s.	n.s.
	E13.5	pTH-C	⇓	n.s.	n.s.	n.s.	n.s.
		pTH-R	n.s.	n.s.	n.s.	n.s.	n.s.
		Pth	n.s.	n.s.	n.s.	n.s.	n.s.

Table 8.2: ***Cell proliferation related change in the pTH-C, pTH-R and Pth in*** $\mathbf{Pax6^{fl/+}}$ ***and the*** $\mathbf{Pax6^{fl/fl}}$ ***mutants at E11.5, E12.5 and E13.5****. n.s., no significant change. ⇑, increase; ⇓, decrease.*

The staining for the cleaved caspase-3 from E11.5 to E14.5 $Pax6^{+/+}$ reveals that: 1. the distribution of the apoptotic cells across the developing thalamus (including the thalamus and the prethalamus) is rather stochastic from E11.5 to E13.5, no obvious preference for progenitors or postmitotic neurons; 2. at E14.5, the apoptotic cells mostly reside in the ventricular and subventricular region in the thalamus; 3. the number of cells undergoing

apoptosis seems greater at E11.5 than the other three ages and the aggregation of the apoptotic cells in the epithalamic primodium is observed exclusively at this stage. The staining of the apoptotic cells in the $Pax6^{fl/+}$ and $Pax6^{fl/fl}$ diencephalon from E11.5 to E14.5 shows a similar pattern to the $Pax6^{+/+}$ and a prolonged apoptosis in the developing epithalamus is observed in the $Pax6^{fl/fl}$ at E12.5 but not in the $Pax6^{+/+}$ or the $Pax6^{fl/+}$.

8.5 Discussion

The examination of the cell proliferation characteristic change in the conditional *Pax6* mutants from E11.5 and E13.5 provided useful information for understanding the mechanisms underlying the phenotypes observed at P0 in the vLGN and dLGN (Table 6.1).

In Chapter 6, an increase in the GFP+ve cell proportion was observed in both the vLGN and dLGN in the $Pax6^{fl/+}$, which cannot be explained by the decrease in the proliferation rate at E11.5 in the pTH-R. In the P0 $Pax6^{fl/fl}$, an increase in the nuclei volume and a decrease in the cell density were seen in the vLGN as well as an increase of the GFP+ve cell proportion in the dLGN. The decrease in the growth fraction in the E12.5 pTH-R can potentially cause the cell density change in the P0 vLGN, but the change in the nuclei volume and the GFP+ve cell proportion remain unexplained.

Unlike the project carried out by Nakagawa's group [38], no basal dividing population change was seen in either the $Pax6^{fl/+}$ or the $Pax6^{fl/fl}$ in this study, which can be explained by the difference in animal models. Nakagawa's group used $Pax6^{LacZ/LacZ}$ mutants, which have more severe brain development phenotypes than the conditional mutants used in this study.

Very little change was found in the proliferation related properties in the GFP+ve population, which could be explained by the nature of the *Pax6* deletion induced by the *Zic4Cre*. The GFP+ve population are the *Zic4* lineage cells and not all of these cells require the presence of functional Pax6 during the development. Thus, the deletion of *Pax6* in these cells generates a stochastic severity pattern at cellular levels, which could explain why the tempts of studying the growth fraction and proliferation rate generated rather messy results. Though the change in the GFP+ve population in the *Pax6* mutants was little, cell proliferation phenotypes were still observed at the magnitude of the whole cell population especially in the $Pax6^{fl/fl}$, suggesting that *Pax6* is likely to affect cell proliferation in a non-antonomous manner. No change in any of the proliferation parametres was observed in the Pth, which indicates that the amount of Pax6 produced by the non-*Zic4* lineage cells is sufficient to

maintain normal cell proliferation in the Pth and a possible innate rescue initiated upon *Pax6* deletion could also help minimise the damage.

The study of the cell proliferation property in the pTH-C, pTH-R and Pth revealed some similarities and differences among the three diencephalic structures. The closely related pTH-R and pTH-C share a number of properties that are different from the Pth: 1. the grow fraction decreases relatively slowly; 2. the cell cycle slows down relatively slowly; 3. they both possess more pHH3+ve cells than the Pth; 4. they both have a larger basal dividing population. There is one property shared by the pTH-R and Pth, which is the significant decline of the pHH3+ve cell number at E13.5. Combining all this informtion, it is not difficult to understand why the volume of the thalamus is a lot bigger than the prethalamus.

Although Tuj1 staining was performed in this study, it was not quantitatively analysed. It is difficult to distinguish the positively stained cells from the negatively stained ones in the developing brain tissue, in which the cells are so densely packed. A better marker NeuN could have been used to label the newly differentiated neurons and Tuj1 would be better used in primary cell culture where neuronal morphology is the focus of the study.

The significance of cell apoptosis in the thalamus at early developmental stages such as E11.5 remains unknown. It can be speculated that it is an early wave of cell elimination to control the progenitor pool size at the beginning of the main neurogenesis in the thalamus, which is recalibrated at E14.5 by eliminating cells in the ventricular and subventricular zone, when the majority of neurogenesis has completed. This proposed two-step progenitor pool size control system stablises the number of postmitotic neurons to sufficiently assist the establishment of the reciprocal thalamus-cortex connection at this age. The elimination of a cell in thalamic primodia at E11.5 could potentially mean a complete removal of a whole population of cells derived from that very single cell. It will be interesting to study whether the apoptosis is associated with cells expressing a certain spectrum of genes/markers that are no longer required at later stages. The prolonged apoptosis at the dorsal midline, the epithalamic region, in the $Pax6^{fl/fl}$ mice indicated a more extensive cell death in the epithalamic progenitor pool, which could potentially explain the hypoplastic habenula present in the P0 $Pax6^{fl/fl}$ brain - the GFP+ve structure positioned at the dorsal midline of the diencephalon in the $Pax6^{+/+}$ and $Pax6^{fl/+}$ is not observed in the $Pax6^{fl/fl}$ (Figure 6.35).

8.6 Future work

The study of cell cycle kinetics in this project is lacking. The length of the total cell cycle and each phase were not studied. Since the traditional double labelling method was constructed upon certain assumptions that are either violated or cannot be confirmed in the developing thalamus, a study using the fluorescence ubiquitin cell cycle indicator (FUCCI) system should be carried out to look into it more closely [123]. Moreover, if we can combine the FUCCI system and the MADM technique [66], we can study the cell cycle dynamic through a few rounds of proliferation within a lineage of cells derived from a single radial glial cell, by introducing the Nestin-Cre to brain slice culture at a very low concentration via electroporation. It will undoubtedly provide crucial information of cell proliferation in the developing thalamus but finding the animal models that allow four-colour live imaging, animal breeding, slice culture and electroporation optimisation can be very challenging.

The staining for cleaved-caspase3 showed the rough position of the cells undergoing apoptosis during the development of the thalamus from E11.5 to E14.5, but is not able to tell whether these cells are progenitors or a postmitotic neurons. A double staining with cleaved-caspase3 and one of the markers for progenitors (Vimentin for RGCs) and postmitotic neurons (NeuN) will allow a further study of the cell identity and provide insights into population control in thalamic neurogenesis.

The examination of the changes in cell proliferation and apoptosis caused by the *Pax6* deletion in this project cannot fully explain the phenotype in the P0 vLGN and dLGN and potential early patterning defects were explored in the next chapter.

Chapter 9

Zic4Cre mediated deletion of *Pax6* causes early diencephalic patterning defects at E12.5 and E13.5

9.1 Introduction

In Chapter 7, the time of origin of the vLGN and dLGN cells, especially the GFP positive *Zic4* lineage cells, was studied and it was found that the cells populating these two nuclei are mainly born at E11.5 and E12.5. In Chapter 8, the changes in poliferation and apoptosis were studied in the conditional *Pax6* mutants at these two stages. The proliferation rate was shown to decrease in the $Pax6^{fl/+}$ pTH-R at E11.5. The growth fraction was shown to decrease in the E12.5 pTH-R and in the pTH-C at both E12.5 and E13.5 in the $Pax6^{fl/fl}$. The change could explain the low cell density in the $Pax6^{fl/fl}$ vLGN described in chapter 6, but cannot explain the increase in GFP+ve cell propotion in the vLGN and dLGN or the volume change of the vLGN. In this chapter, the possibility of early patterning defects contributing to the P0 phenotypes was explored.

During diencephalic patterning, the antero-posterior segmentation of the diencephalon into prosomere 1 (p1) - p3 starts at E9.5 and becomes morphologically recognisable at E10 to E11 by the formation of ZLI, which secretes diffusing morphogen such as Shh and functions as the mid-diencephalon organiser [5]. The ZLI-derived Shh signal has been proved to be essential for the molecular identity establishment for the prethalamus and thalamus [5] and the mutual repression between Shh and Pax6 around ZLI is crucial for diencephalic patterning [40]. The deletion of *Pax6* induced by *Zic4Cre* is highly likely to cause the expression of marker genes in the developing diencephalon including the expression of *Shh* and its downstream

factor *Nkx2.2*, which is examined and summarised in this chapter.

9.2 Aim of the project

This project aims to look at pivotal morphogens and transcription factors such as Shh and Nkx2.2, which help to shape the early developing diencephalon, to see if there are any changes in their expression patterns which could potentially cause the defects in the P0 vLGN and dLGN.

9.3 Results

Colourimetric *in situ* hybridisation for *Shh* and *Nkx2.2* was performed in the $Pax6^{+/+}$, $Pax6^{fl/+}$ and $Pax6^{fl/fl}$ diencephalon at E12.5 and E13.5. The experiment was repeated three times for each of the probes at both stages.

In situ hybridisation for *Shh* at E12.5 (Figure 9.1 A-C) shows a wedge shaped staining in the ventricular zone between the thalamus and prethalamus in the $Pax6^{+/+}$ and a slightly smaller and a slightly larger wedge shaped *Shh*+ve regions are seen in the $Pax6^{fl/+}$ and the $Pax6^{fl/fl}$ respectively. At E13.5 (Figure 9.1 D-F), the *Shh*+ve region is smaller compared to E12.5 in all three genotypes. In the $Pax6^{+/+}$, the *Shh*+ve region remains wedge shaped and in the $Pax6^{fl/+}$ the wedge shaped *Shh*+ve region is much smaller compared to the $Pax6^{+/+}$. In the $Pax6^{fl/fl}$ however, the *Shh*+ve region lost its wedge shape and expanded to a rectangle shaped band in the ventricular zone. Though the difference in *Shh* expression has been observed consistently between different genotypes, cautions are still required to examine these changes as the level of sectioning might influence the shape of *Shh* expression domain on each of the coronal sections - *Shh* expression domain appears as a spike shape extending from the basal plate toward the roof plate from sagittal views and a sectioning plane more parallel to the axis of the spike is likely to give a bigger *Shh* expression domain than one that is more perpendicular to the spike.

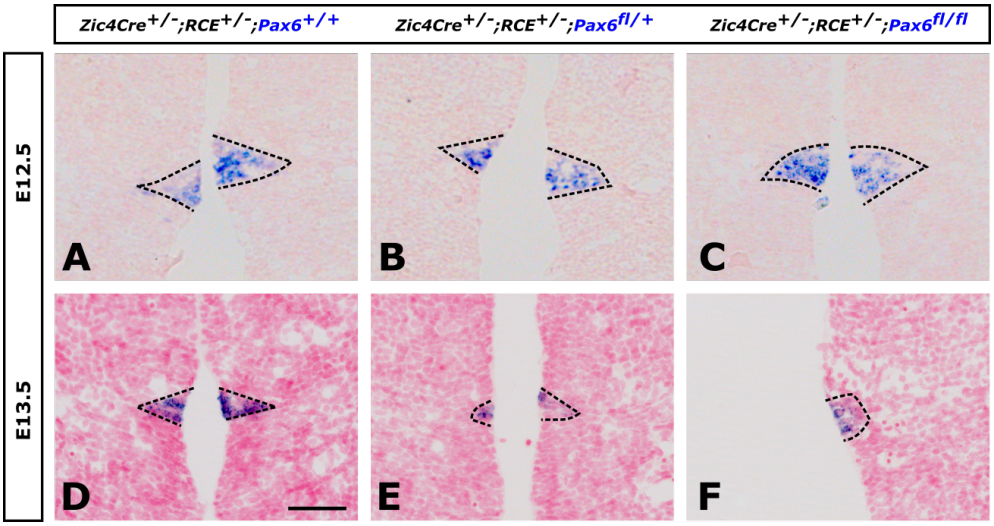


Figure 9.1: ***Shh in situ hybridisation in E12.5 and E13.5*** **Pax6$^{+/+}$, Pax6$^{fl/+}$** ***and*** **Pax6$^{fl/fl}$** ***diencephalon***. *Scale bar*: 62.5 μm.

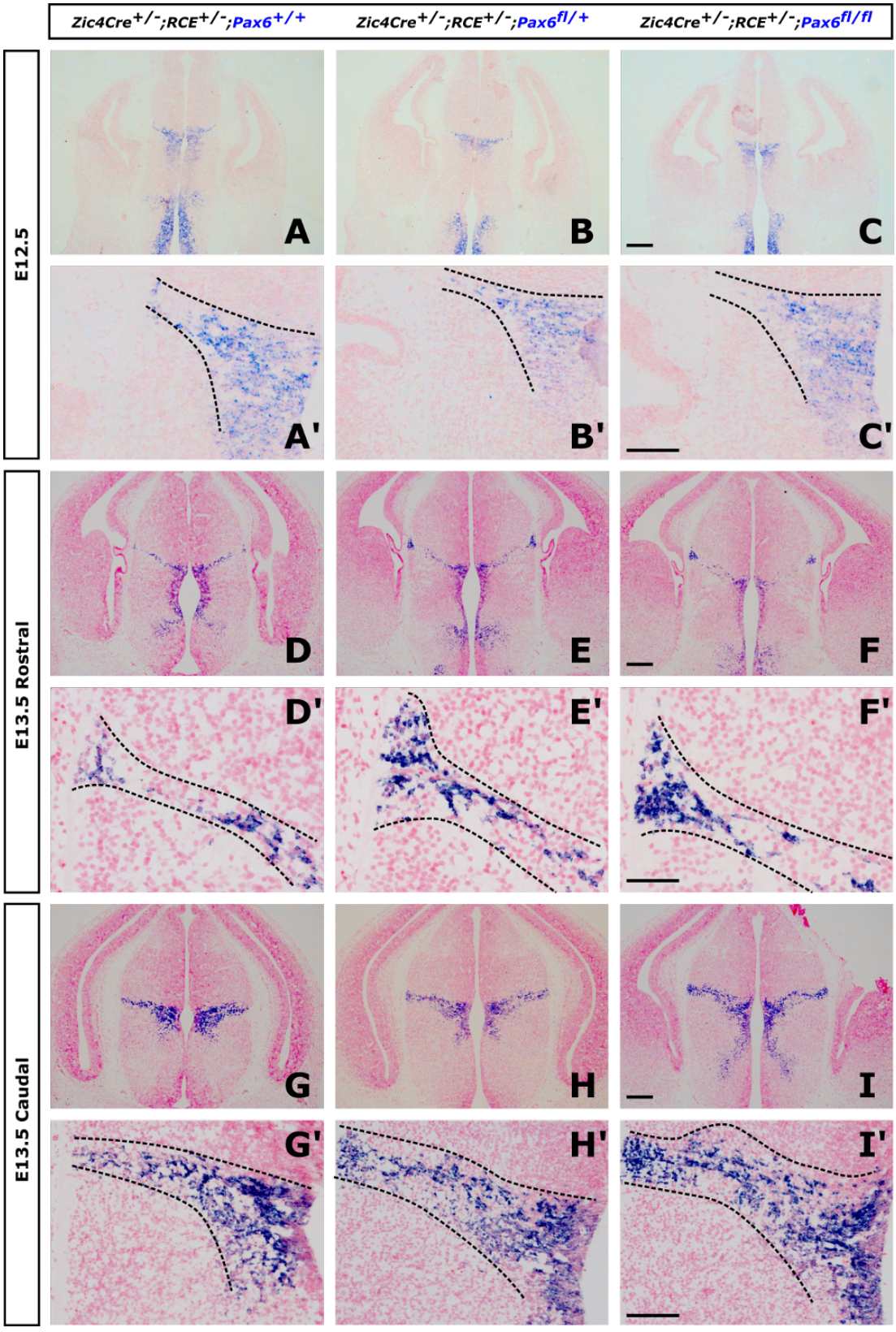


Figure 9.2: ***Nkx2.2 in situ hybridisation in E12.5 and E13.5*** **Pax6$^{+/+}$, Pax6$^{fl/+}$** ***and*** **Pax6$^{fl/fl}$** ***diencephalon****. Scale bar: 250 μm and 125 μm.*

The *in situ* hybridisation for *Nkx2.2* at E12.5 (Figure 9.2 A-C and A'-C') shows that it is expressed in the ventricular zone of the prethalamus and a stream of radially migrating cells toward the lateral surface of the diencephalic wall in the $Pax6^{+/+}$, $Pax6^{fl/+}$ and $Pax6^{fl/fl}$. The radial migrating cell stream seems broader in the $Pax6^{+/+}$ than the $Pax6^{fl/fl}$ and $Pax6^{fl/+}$. At E13.5 (Figure 9.2 D-I and D'-I') , the cells migrating along the boundary between the prethalamus and thalamus have reached and settled in the forming vLGN in all three genotypes. However, more *Nkx2.2* positive cells were seen in the forming vLGN area in the $Pax6^{fl/+}$ and $Pax6^{fl/fl}$ than in the $Pax6^{+/+}$ (Figure 9.2 D'-F'). When examining the more caudal levels, the migratory stream is much broader in the $Pax6^{fl/+}$ and $Pax6^{fl/fl}$ than in the $Pax6^{+/+}$ (Figure 9.2 G'-I'). Comparing the *Nkx2.2* expression in the forming vLGN area of the $Pax6^{fl/+}$ and $Pax6^{fl/fl}$, I found: 1. more *Nkx2.2*+ve cells have reached the vLGN area in the $Pax6^{fl/fl}$ (Figure 9.2 F' and I') than in the $Pax6^{fl/+}$ (Figure 9.2 E' and H') at E13.5; 2. the migratory stream in the $Pax6^{fl/fl}$ is slightly broader than in the $Pax6^{fl/+}$ with some seemingly off-route cells at the dorsal border of the stream (Figure 9.2 I').

9.4 Synopsis

Genotype	Age	Marker	Change	Structure
$Pax6^{fl/+}$	E12.5	*Shh*	⇓	ZLI
		Nkx2.2	⇓	pTH-R
	E13.5	*Shh*	⇓	ZLI
		Nkx2.2	⇑	pTH-R
$Pax6^{fl/fl}$	E12.5	*Shh*	⇑	ZLI
		Nkx2.2	⇓	pTH-R
	E13.5	*Shh*	⇑	ZLI
		Nkx2.2	⇑	pTH-R

Table 9.1: ***Early patterning change in the pTH-R and ZLI in*** $\mathbf{Pax6^{fl/+}}$ ***and the*** $\mathbf{Pax6^{fl/fl}}$ ***mutants at E12.5 and E13.5****. n.s., no significant change.* ⇑*, increase;* ⇓*, decrease.*

The stainings for markers such as *Shh* and *Nkx2.2* in the conditional *Pax6* mutants shows that: 1. at E12.5, the ZLI is slightly contracted in the $Pax6^{fl/+}$ and enlarged in the $Pax6^{fl/fl}$ compared to the $Pax6^{+/+}$; at E13.5, the ZLI is conspicuously smaller in the $Pax6^{fl/+}$ compared to the $Pax6^{+/+}$ on the corresponding sections and the shape of the *Shh*+ve area is greatly altered in the $Pax6^{fl/fl}$; 2. at E12.5, the radial migrating cell stream between the thalamus and prethalamus is narrower in the $Pax6^{fl/+}$ compared to the $Pax6^{fl/fl}$ and $Pax6^{+/+}$ whereas at E13.5, the stream is much broader in the $Pax6^{fl/+}$ and $Pax6^{fl/fl}$ compared to the $Pax6^{+/+}$.

9.5 Discussion

The mutual repression between *Shh* and *Pax6* around the ZLI and the subsequent patterning change of the ZLI and pTH-R in both the *Pax6* and *Shh* mutants have been described in quite a few studies [17, 40]. The expansion of the *Shh*-expressing ZLI and the *Nkx2.2*-expressing pTH-R in the $Pax6^{fl/fl}$ is expected. The deletion of *Pax6* led to the expansion of the *Shh* expression around the ZLI, which subsequently induces the expanded expression of a *Shh* downstream gene *Nkx2.2* and thus the pTH-R. Studies have shown that the ZLI derived cells [47, 48] and the pTH-R derived *Nkx2.2* lineage cells [50, 48] contribute to the forming vLGN, thus the increase in the volume of the P0 vLGN observed at the rostral to the middle levels in the $Pax6^{fl/fl}$ can be partially explained by the expansion of the *Shh* and *Nkx2.2* expression. In fact, an excessive number of Nkx2.2 positive cells were observed at the rostral part of the vLGN in the $Pax6^{fl/fl}$ at P0 but not in the $Pax6^{fl/+}$ or the $Pax6^{+/+}$ (Figure 9.3).

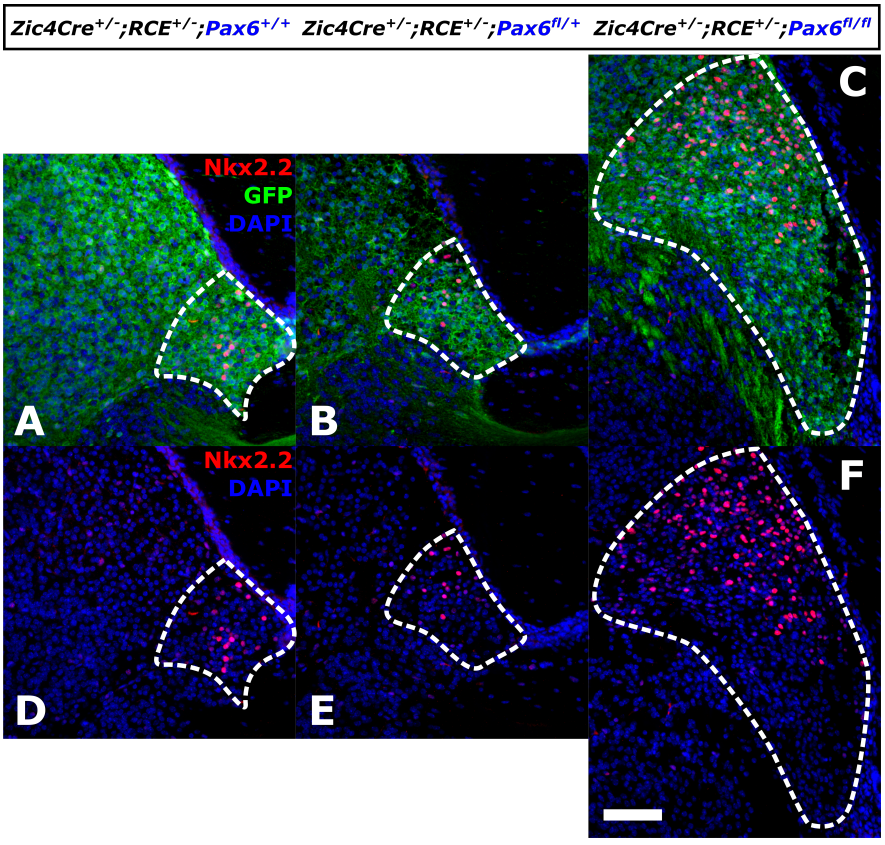


Figure 9.3: ***Nkx2.2 and GFP immunohistochemistry of coronal sections of vLGN at the rostral most postion in*** **Pax6$^{+/+}$, Pax6$^{fl/+}$,** ***and*** **Pax6$^{fl/fl}$** ***at P0.*** *Scale bar: 125 μm.*

The excessive number of Nkx2.2 positive cells can be explained by an early expansion of the *Nkx2.2* expressing migratory stream observed at E13.5 (Figure 9.2), however a conspicuous increase of the Nkx2.2 negative cells is also observed in the P0 $Pax6^{fl/fl}$ vLGN at the rostral most level (Figure 9.3), which can not be explained by Nkx2.2 expression change only. The vLGN cell composition study carried out by Kitamura and colleagues showed that the rostral part of the vLGN contains a great number of cells expressing *Dlx1* [50], which could be a good target to look at. However, the expression overlap between Nkx2.2 and *Dlx1* might make the situation more complicated. It is also possible that those Nkx2.2 negative cells are *Shh* lineage cells but this hypothesis can not be tested in the current model. Another possibility is that in the early developing $Pax6^{fl/fl}$ diencephalon, the newly born cells migrate along the boundary between the thalamus and prethalamus a lot faster toward the lateral surface than their counterparts in both the $Pax6^{fl/+}$ and the $Pax6^{+/+}$. This can lead to an excessive number of cells ending up in the vLGN, hence the increase in the volume. A recent study showed that the neuronal clones in the medial ventral and posterior region of the thalamus exposed to high levels of Shh activity were more radially organised, whereas the anterior and medial dorsal regions with low levels of Shh activity contains neuronal clones that are more tangentially organised [66]. Enhanced Shh activity promotes radial organisation of clones along media-lateral axis in the anterior and dorsal regions and suppressed tangential organisation [66], which supports the possibility that the the elevated Shh signals subsequent to the *Pax6* deletion causes the migratory defects, which eventually leads to the volume change in the $Pax6^{fl/fl}$ vLGN at P0.

The expression change of *Shh* and its downstream gene *Nkx2.2* at E12.5 and E13.5 can explain the volume change of P0 vLGN in the $Pax6^{fl/fl}$ (summarised in Figure 9.4). It also opened a possibility that migratory defects could contribute to the volume phenotype.

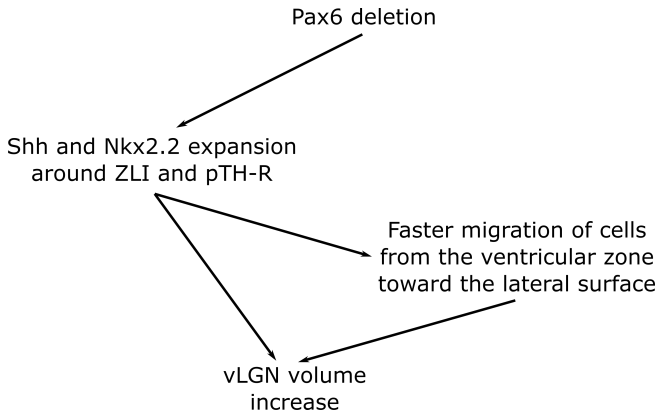


Figure 9.4: ***A model showing how the changes in the expression of Shh and Nkx2.2 at E12.5 and E13.5 can contribute to the volume change of vLGN.***

Chapter 10

Zic4Cre mediated deletion of Pax6 causes eye malformation but has no effects on the innervation of retinal ganglionic processes into vLGN or dLGN

10.1 Introduction

Pax6 is expressed in the developing eye. *Zic4* is weakly expressed in the retina and highly expressed in the optic stalk in the E11.5 $Pax6^{+/+}$ eyes, with GFP reporter showing the Cre activity in the same areas (Figure 10.1). It suggests that in the conditional mutants, *Pax6* will be deleted in the cells within the retina and optic stalk upon the Cre recombination.

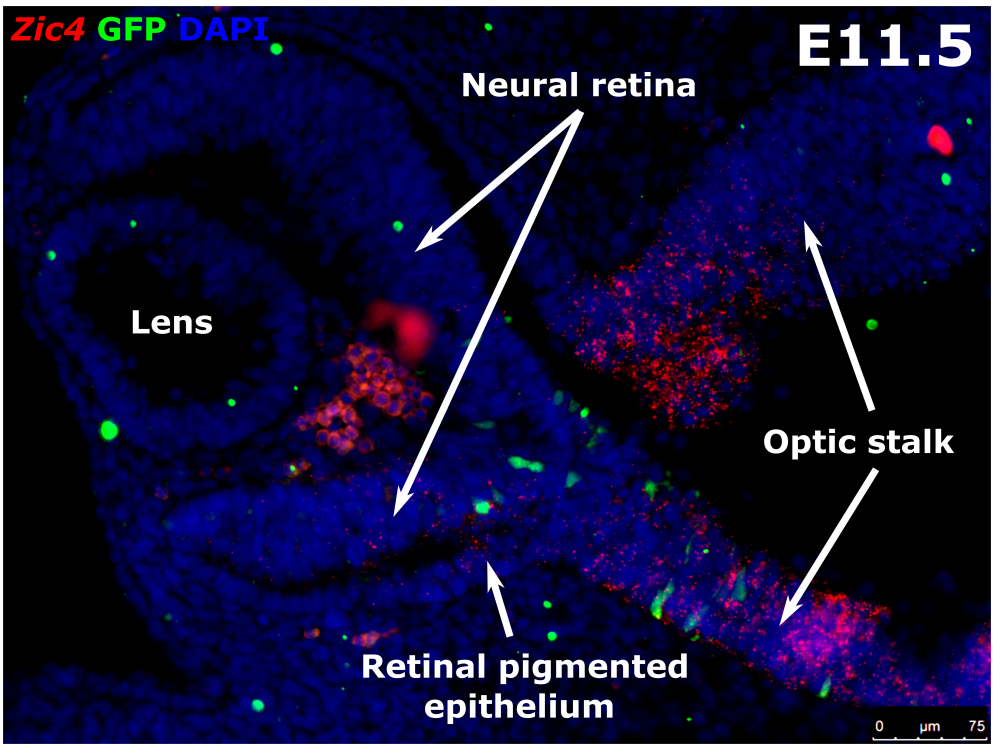


Figure 10.1: ***Zic4 in situ and GFP immunohistochemistry of E11.5 Pax6$^{+/+}$ eyes.*** *Scale bar: 75 µm.*

The vLGN and dLGN are two of the main innervation targets of retinal ganglionic cells. It is possible that the defects in the developing eyes of mice with *Zic4Cre* mediated deletion of *Pax6* could have secondary effects on LGN development. To explore this possibility, I performed immunohistochemistry stainings of cresyl violet and Pax6 on the developing eyes at E13.5, E14.5 and P0, as well as an axon tracing study following an ocular dye injection in the P0 pups.

10.2 Aim of the project

To explore the possibility that the vLGN and dLGN defects in the conditional mutants are due to the gross change in the innervation of retinal ganglionic cell processes subsequent to the deletion of Pax6.

10.3 Result

The morphology of eyes was checked by cresyl violet and Pax6 immunostainings for all three genotypes. It was observed that the lens in the *Pax6*$^{fl/fl}$ eyes is much smaller than in the *Pax6*$^{+/+}$ and the *Pax6*$^{fl/+}$ ones at E13.5 and E14.5. The temporal surface of the retinas of the *Pax6*$^{+/+}$ and *Pax6*$^{fl/+}$ eyes are smooth but not in the *Pax6*$^{fl/fl}$. The morphological change in the retina is more obvious at P0 when the retinal tissue in the *Pax6*$^{fl/fl}$ is severely folded and no lens can be recognised.

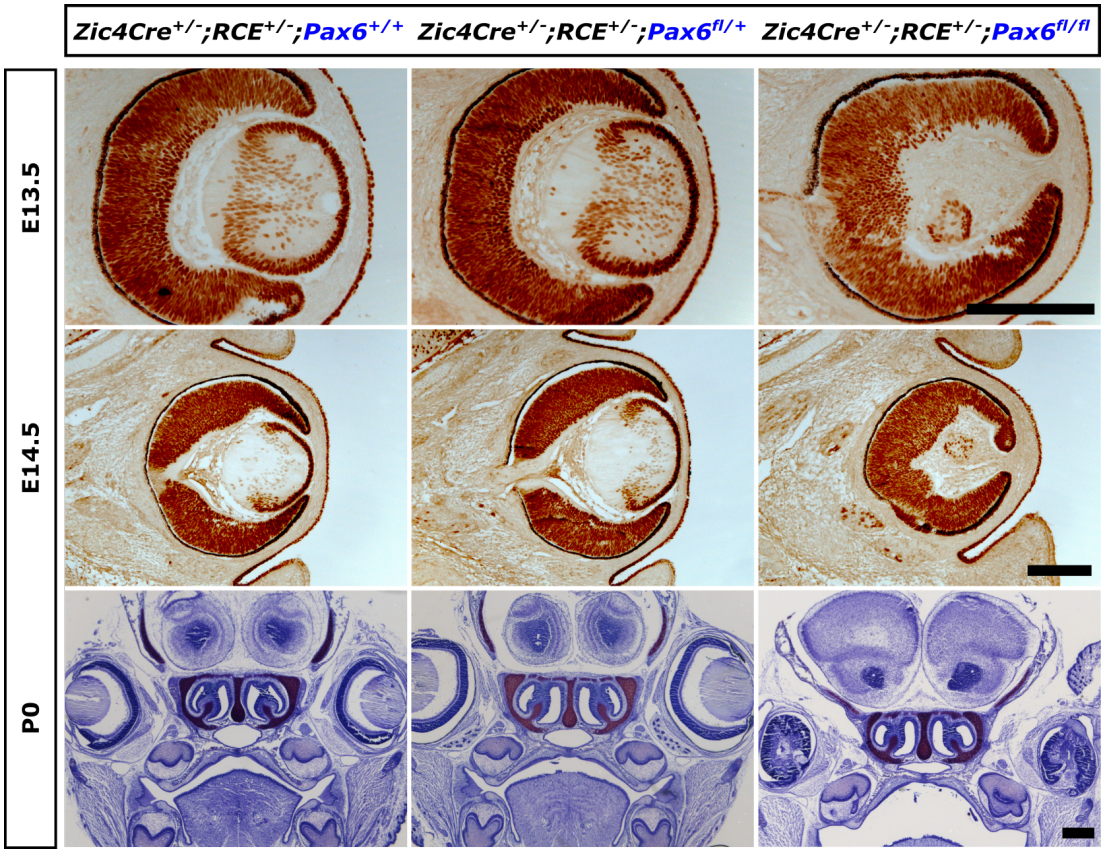


Figure 10.2: ***DAB-Pax6 and cresyl violet stainings of E13.5, E14.5 and P0*** **Pax6$^{+/+}$, Pax6$^{fl/+}$** ***and*** **Pax6$^{fl/fl}$** ***eyes****. Scale bar: 250 μm and 500 μm.*

Observing these eye defects caused by the deletion of *Pax6*, I went on to label the axons extended by the retinal ganglionic cells, using a lipophilic dye to check whehter the innervation of these axons in the vLGN and dLGN changed. First, I used P0 *Pax6*$^{+/+}$ brains to practise the technique and find the right amount of the dye to label the whole ascending visual pathway including the optic chiasm, the optic tract, the vLGN, the dLGN and the superior colliculus (Figure 10.3). The labelling results were compared to existing literatures to make sure the labelling is reliable and the technique is good.

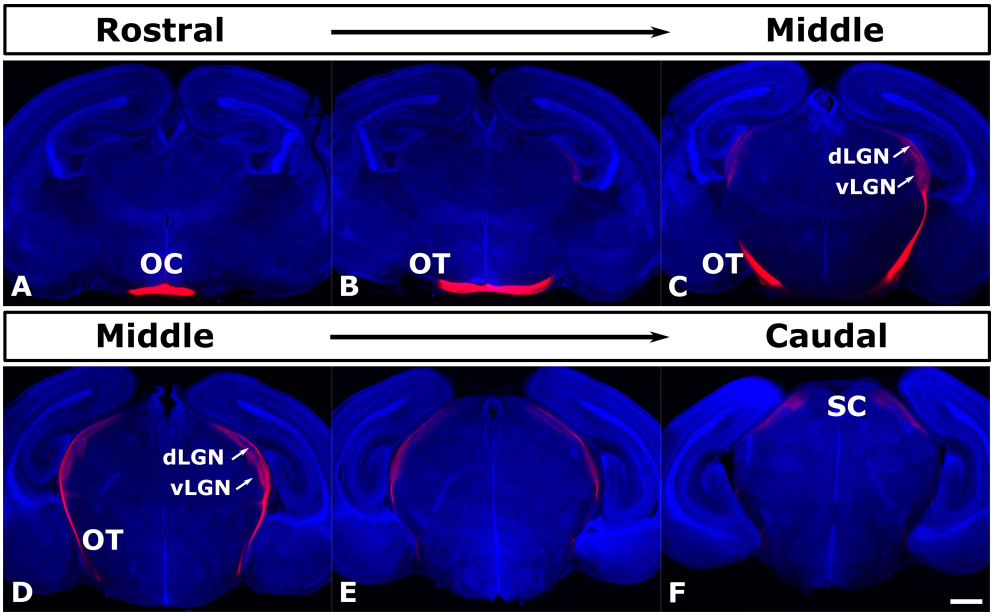


Figure 10.3: ***Axon tracing using lipophilic dye in the P0 Pax6$^{+/+}$ reveals the ascending visual pathway****. OC, optic chaism; OT, optic tract; SC, superior colliculous. Scale bar: 500 μm.*

Then I performed axon tracing in all three genotypes and found no gross difference between the *Pax6*$^{+/+}$, the *Pax6*$^{fl/+}$ and the *Pax6*$^{fl/fl}$ (Figure 10.4).

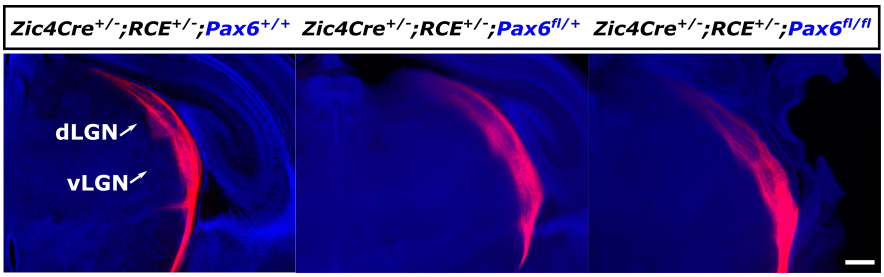


Figure 10.4: ***Axon tracing using lipophilic dye in the P0 Pax6$^{+/+}$, Pax6$^{fl/+}$ and Pax6$^{fl/fl}$ brains reveals no differences among different genotypes****. Scale bar: 250 μm.*

10.4 Synopsis

The development of the eye is severely affected in the *Pax6*$^{fl/fl}$, showing tiny lens and folded retinas. However, the innervation of retina ganglionic cell axons into the dLGN and vLGN is not significantly affected. Thus, the possibility that a abnormal innervation of retina ganglionic axons causes the vLGN and dLGN defects can be excluded.

Chapter 11

Discussion

In this study, I explored the role of Pax6 in the development of the vLGN, by deleting *Pax6* conditionally in the diencephalon-specific *Zic4* lineage cells. I found the morphological and compositional properties of the vLGN were changed in the absence of functional Pax6, including: 1. the nuclear volume and cell density decreased and the GFP+ve cell proportion increased in the P0 $Pax6^{fl/fl}$ vLGN; 2. the GFP+ve cell proportion increased in the P0 dLGN in both the $Pax6^{fl/+}$ and $Pax6^{fl/fl}$; 3. the expression pattern of Lim1/2 and Nkx2.2 in the P0 vLGN changed in both the $Pax6^{fl/+}$ and $Pax6^{fl/fl}$.

I performed BrdU birth dating experiment to study the time of origin of the vLGN and dLGN and found the cells contribute to these two nuclei are mainly born between E11.5 to E12.5. I went on to look at cell proliferation (including the growth fraction, proliferation rate and cell cycling speed), cell apoptosis, expression of patterning factors (*Shh* and *Nkx2.2*) in the early stage and the innervation of RGCs processes postnatally to unravel the mechanisms underlying the P0 vLGN and dLGN defects. The results suggest that: 1. the increase of the $Pax6^{fl/fl}$ vLGN volume is likely to be caused by the expansion of the ZLI and pTH-R; 2. the decrease in the $Pax6^{fl/fl}$ vLGN cell density is likely to be caused by a smaller growth fraction at E12.5; 3. the proliferation rate, cell cycling speed and cell apoptosis rate do not change when the deletion of *Pax6* is driven by the *Zic4Cre*; 4. no gross RGCs innervation change was found in the vLGN and dLGN despite the fact that the eyes are malformed.

My results suggest that Pax6 is involved in multiple aspects of the development of the diencephalic nucleus vLGN, mainly through its regulation of cell proliferation and early patterning, and perhaps cell migration and fate determination as well, in potentially both cell autonomous and cell non-autonomous manners.

11.1 Diencephalic developmental defects observed in *Pax6*$^{fl/+}$: haploinsufficiency or dominant negative effects?

Among the great number of genetically engineered mouse models with haploinsufficiency of certain transcription factors, most heterozygous knockouts have been reported showing no obvious phenotypes [124]. In conditional knockouts, the deletion of the given transcription factors is often restricted to specific time points, tissues and sometimes even cell lineages and the phenotype is expected to be milder compared to their null counterparts. Furthermore, multiple transcription factors can regulate common downstream targets, which renders the absence or shortage of one transcription factor much more tolerable and hence the lack of phenotypes. Thus, it is quite surprising that phenotypic change was observed in the developing diencephalon in the *Pax6*$^{fl/+}$ embryos.

Transcription factors such as PAX6 have been found to cause disease in human patients by haploinsufficiency [124]. In most PAX6-mediated aniridia cases, the mutant PAX6 alleles give rise to premature termination codons which lead to the haploinsufficent levels of wild type PAX6 proteins [125]. In *Pax6*$^{Sey/+}$ mice, Pax6 haploinsufficiency caused the *Small eye* phenotype, smaller eyes than the wild type [33]. The *Pax6*^{fl} allele used in this project was produced by inserting two *loxP* sites into the intron 4 and 6, flanking the exons 5, 5a and 6 which encode the paired domain. These exons are deleted upon Cre-recombination, which is expected to produce a non-sense frame-shift mutation giving rise to a functionally null allele [92]. Thus, it is likely that the defects in the *Pax6*$^{fl/+}$ are caused by Pax6 haploinsufficiency.

However, haploinsufficiency might not be the only cause. The fact that a more severe phenotype - a bigger increase in GFP+ve cell proportion in both the vLGN and dLGN - in the *Pax6*$^{fl/+}$ than in the *Pax6*$^{fl/fl}$, suggests that the mutant allele generated after the Cre-recombination may have a dominant negative effect.

Typical dominant negative effects can come from the factors that are part of a protein complex in which the mutant polypeptide affects the function of the whole protein complex [126]. For transcription factors (TF), dominant negative effects can be produced by: 1. removing the transactivation domain of a modular TF, which leaves the truncated TF to act as a strong competitor of the wild type factor; 2. removing the DNA binding domain, in the case of basic-helix-loop-helix (bHLH) TFs, which gives rise to a truncated protein with only the dimerisation domain, imposing regulation on other bHLH factors [126]. Pax6, as a transcription factor, has two DNA-binding domains, the paired domain (PD) and the homeodomain (HD), a linker region between the two, followed by a proline-, serine- and

threonine-rich (PST) domain at its C-terminus, which serves as a transactivation domain [21, 22]. Its PST domain has been shown to exert potent transactivation functions when fused to the DNA-binding domain of the yeast TF GAL4 independently of other regions of Pax6 [22]. Interestingly, GAL4 fused with full-length Pax6 did not show any transcriptional activation, whereas the depletion of the paired domain led to a very efficient transcriptional activation of the reporter gene [22]. The auther's hypothesis was that either the paired domain interferes with GAL4's binding to the target sequence or it conformationally interferes with the PST domains and its function in the general transcription [22]. The $Pax6^{fl}$ allele used in this project does have intact homeodomain and PST domain, though predicted to be non-functional, still has a chance to produce poison polypeptides, which can potentially interfere with the transcripational function of the wild type Pax6 protein. It has been found that human PAX6 mutant protein R26G (with a mutation in the N-terminal half of the PD) lost DNA binding through its PD but gained greater DNA binding and transactivation than wild-type PAX6 on HD binding sites [121]. In the *in vitro* study carried out in HeLa cells, the co-expression of the paired-less isoform of Pax6 and full-length Pax6 caused a 3 times increase in Pax6-mediated transactivation from paired domain binding sites than the full-length Pax6 itself, whereas paired-less Pax6 alone did not induce activation at all, which excluded the possibility that paired-less Pax6 activated the reporter itself [122]. This is similar to the situation in the $Pax6^{fl/+}$, in which both a wild type *Pax6* and a truncated $Pax6^{fl}$ alleles are present. It was speculated in the *in vitro* study that the PD-less protein could: (1) titrates a negative cofactor(s) that interact(s) with the HD and/or PST; (2) the PD-less protein can interact directly with the Pax6 protein, then recruiting an additional transactivation domain to the promoter; (3) a direct binding of PD-less protein to wild type Pax6 protein could induce a conformational change that relieves intramolecular repression [122].

For the time limit of my PhD, I was not able to pursue this possibility further. However, it is definitely a crucial point that needs to be checked before going on to interpret and understand the phenotypes seen in the $Pax6^{fl/+}$. Being a master regulator of the transcription of a plethora of other genes, Pax6 self-regulates the production of itself [127, 128]. The level of Pax6 protein also changes the ratio between Pax6's two isoforms, Pax6 and Pax6(5a) [129], which are involved in different aspects of eye and brain development [21]. The potentially existing domainant negative effects from the post-recombination $Pax6^{fl/+}$ allele could make the change of the Pax6 protein level and the ratio between two isoforms more complicated and generates phenotypes in a context-dependent manner. Works need to be done to check the existance of the potential dominant negative effects, which will certainly advance our understanding of Pax6's fine-tuning role during the development of the diencephalon and other brain regions.

A potential way of checking whether a dominant negative effect exists in our case is to carry out an *in vitro* study such as co-transfecting HeLa cells with plasmids that contain $Pax6^{+}$ allele, truncated $Pax6^{fl}$ allele and a luciferase reporter that contains consensus binding sites for the PD of Pax6 upstream of a minimal promoter, to test whether the polypeptides produced from the truncated $Pax6^{fl}$ allele interfere with the transactivation property of the wild type Pax6 proteins. If a conspicuous change in transactivation property of $Pax6^{+}$ allele is observed when the truncated $Pax6^{fl}$ allele is present, then it is likely there is a dominant negative effect. If the more severe phenotype observed in the $Pax6^{fl/+}$ - a bigger increase in GFP+ve cell proportion is due to cell fate change, it can be further tested *in vitro* by harvesting the thalamic and prethalamic cells from the $Pax6^{+/+}$ to set up primary cell cultures, then introducing PD-less *Pax6* expressing plasmids to see if the GFP+ve cell proportion increases along with the increase of PD-less Pax6 protein concentration.

11.2 Developmental defects observed in non-GFP+ve diencephalic cells suggests Pax6 plays a non-cell autonomous role in the developing diencephalon

During the analysis of early cell proliferation related defects in the pTH-C, pTH-R and Pth, I did not find any GFP+ve population specific change while the whole cell population for each of the structure show significant changes. This suggests that in the pTH-C and pTH-R, Pax6 has some cell non-autonomous influence on the cells which do not normally express Pax6.

Homeoprotein transcription factors such as Engrailed 1 and Otx2 can be passed between cells to exert important functions during development [130]. Being one of the homeoprotein transcription factors, Pax6 has been shown to regulate eye development in *Zebrafish* as a cell non-autonomous signaling molecule [131]. The intercellular Pax6 transfer originates from the presence of two small sequences within the homeodomain of Pax6, allowing the internalisation and secretion of the protein. The study showed that interfering with the cell non-autonomous activity of Pax6 resulted in reduction of eye size in *Zebrafish* though no further assessment on cell proliferation was carried out to see how exactly this activity plays out [131]. It is possible that the likely cell non-autonomous effect of Pax6 on cell proliferation in the developing diencephalon shares the same mechanism as the one underlying the eye phenotype in *Zebrafish*. It will be interesting to investigate this phenomenon further using a similar strategy mentioned in the above study, utilising specific extracellular Pax6 antibody to block Pax6 intercellular transfer in cultured disassociated thalamus and prethalamus cells. It

is also possible that Pax6 regulates some secreted molecules to indirectly affects the biological functions of the neighbouring cells.

11.3 Pax6 plays different roles in the development of the thalamus and the prethalamus

Revisiting the results obtained either from embryonic stages or postnatal days, it is clear that the thalamus and prethalamus responds significantly differently to the deletion of Pax6. Admittedly, Pax6 is expressed in different types of cells within these two tissues and the duration of its presence is quite different. It is still possible that Pax6's function is context dependent - the deletion of Pax6 affected the cell proliferation in the thalamus but not in the prethalamus and it affected diencephalic nuclei composition more in the prethalamus than in the thalamus. The preliminary data (see Appendix VI) obtained from an migration experiment I did at the end of my PhD, showed that the *Zic4* lineage GPF+ve cells in the prethalamus move at a higher speed in the conditional mutants lacking function Pax6. In the thalamus, instead of moving directly towards the lateral surface of the diencephalic wall, the GFP+ve cells wonder about in the mantle zone of the thalamus. This indicates that Pax6 may also regulate cell migration/sorting to ensure the normal morhpology is maintained in the developing diencephalon.

The analysis of RNA-seq experiment carried out in the lab showed that the mean Pax6 RPKM (Reads Per Kilobase of transcript per Million mapped reads) in the thalamus is similar to the average of all genes' RPKM whereas in the prethalamus it is 5 times higher (data not show). The latter fits the fact that haploinsufficiency genes normally express at a lot higher levels than the average of the whole genome [132]. The fact that Pax6 is highly expressed in the prethalamus but not the thalamus, suggesting it is required at a very high level in the prethalamus and the prethalamus is likely to be more sensitive to Pax6 dosage change caused by the mutation. It also opens the possibility that haploinsuficiency is also context dependent, true in some tissues but not in others.

In order to understand Pax6's differential roles in the development of these two tissues, it is important to study what makes these two tissues different from each other in the first place.

11.4 Pax6's role in vLGN formation - the big picture

Previous studies of diencephalic development have provided invaluable insights into the patterning, the establishment of diecephalic subdivisions and the origrins of the cells contribute to different nuclei. However, not so many studies have been looking into the formation of individual nuclei and the mechanisms underlying the process, which is the focus and aim of this particular study.

Pax6 has been rigorously studied during the last decades for its role in the development of the cortex, the eyes and the thalamus, however its main role that has been emphasized is its regulation of patterning, cell cycle and proliferation/differentiation balance. The deletion of Pax6 in the conditional mutants used in this study is driven by a diencephalon specific *Zic4Cre* and mosaic like, with a fair amount of cells still expressing Pax6 during the peak of thalamic neurogenesis. The proliferative properties of the mutant thalamus and prethalamus is mildly interrupted compared to the $Pax6^{+/+}$. With little disturbance in the proliferation of diencephalic cells which will later contribute to vLGN, I still saw the volume and cell composition change significantly in the mutant vLGN, indicating that there are other factors affecting the formation of this nucleus, including early patterning, cell migration/sorting, defects secondary to the gross change of visual input and cell fate change. The change of *shh* and *Nkx2.2* expression in the early diencephalon suggests that the lack of Pax6 disrupts the normal patterning of the thalamus and the prethalamus, which is not surprising since Pax6's involvement in diencephalic patterning has been studied in a number of models and the mutual repression between Pax6 and *shh* has been considered essential in diencephalic development. The volume change in vLGN opens the possibility that there is a cell migration/sorting defect in the conditional mutants in the absence of Pax6, which indicates that Pax6 may regulate cell migration/sorting during nuclei formation. There are several ways that Pax6 could potentially execute this function: 1. Pax6 may regulate the expression of adhesion molecules; 2. Pax6 may regulate the production of radial glial cells, whose processes may be essential for lateral migration of certain cells; 3. Pax6 may regulate the expression of chemoattractants and chemorepellents to guide cells to migrate through the diencephalon. The increase of the GFP+ve cells could be caused by an interruption in cell migration/sorting and could also be the result of cell fate change - the non-*Zic4* lineage cells that contribute to vLGN take on *Zic4* lineage fate in the absence of functional Pax6. By exploring and excluding potential mechanisms by which Pax6 could affect the formation of vLGN, I opened new areas that worth investigating further, especially the potential role of Pax6 in cell migration/sorting and cell fate determination in the diencpehalic development.

With the cell composition change in the vLGN and dLGN but not the VP in the conditional

mutants, it can be expected that large axon tracts such as the thalamo-cortical axons will not be severely affected but there might be some disruption in the projection between the dLGN and the visual cortex and the superior colliculus, eg. the increase in the GFP+ve axons subsequent to the increase of GFP+ve proportion in the dLGN. However, it is difficult to speculate potential change in the physiological function subsequent to the change of the projection.

Referring back to the aims of the study at the begining of the introduction, this study revealed the role of Pax6 in the formation of a specific diencephalic nucleus, the vLGN, which includes regulating cell proliferation and early patterning. My preliminary data on cell migration indicates that Pax6 may be involved in cell migration/sorting as well. Finally, the possibility that Pax6 may also control cell fate commitment remains to be investigated.

Chapter 12

Future directions

Rho signalling in diencephalic development

The Rho signalling pathway associated proteins have been shown to have distinct expression in human RGCs in the cortex [53], suggesting that they may play a role in human RGCs. Rnd3, a Rho family protein, has been shown to regulate the interkinetic nuclear migraition of RGCs and their adherens junctions [54]. It is likely that the Rho family proteins also play a role in the RGCs of the developing prethalamus. The RNA-seq analysis carried out in our lab showed that the expression of several Rho family proteins were changed in the prethalamus but not in the cortex or the thalamus in the conditional *Pax6* mutants, including Rnd1 (up-regulated), Rac2 (up-regulated), Rhob2b2 (up-regulated) and Rhof (up-regulated). It will be interesting to see whether there is a interaction between Pax6 and Rho family members in the prethalamic RGCs and if so, whether this interaction regulates the migration of the newly born postmitotic neurons along the RGC processes toward the lateral surface of the diencephalic wall.

microRNAs and their functions in diencephalic development

Heterochronic genes are defined by mutations that cause changes of timings of developmental events and the main members of these genes encode microRNAs and RNA binding proteins [58]. It has been reported that the mammalian heterochronic gene miRNA-23 regulates the timing of the expression of the basic-helix-loop-helix transcription repressor Hes1 through post-transcriptional regulation [58]. In the developing brain, groups of miRNAs regulate either RGC proliferation or neuronal differentiation, suggesting that miRNA play a critical role in neural determination. In the developing mouse cortex, miRNA-9-2 suppresses the transition of RGC into IPs by silencing the transcription factor Tbr2 that induces IP fate [133]. In the postnatal and adult mouse forebrain, it is shown that Pax6 is regulated

post-transcriptionally by miR-7a, which subsequently controls the generation of dopaminergic neurons in the olfactory bulb [**?**]. It will be interesting to do a micro-RNA profiling and study their roles and potential interactions with Pax6 in the developing diencephalon.

Epigenetics and chromatin-remodelling in diencephalic development

The degree of chromatin condensation changes through the cell cycle. In S-phase, the chromosomes lose their histones and loosen to replicate their DNA, and the the chromosomes recondense, sometimes with chromatin-remodelling incorporated [58]. Several studies showed that the chromatin-remodelling complex SWI/SNF plays an important role in neural development. Mice that are heterozygous for a mutant form of the Srg3 gene (also known as SMARCC1), which encodes a core subunit of the SWI/SNF complex, show severe defects in neural proliferation and differentiation associated with exencephaly (a cephalic disorder in which the brain is located outside of the skull) [134]. A study also showed that the chromatin-remodelling protein CBF-1 complex recruits the SWI/SNF complex to the promoters of Notch-regulated genes such as Hes1 and Hes5 [135]. During cortical development, Pax6 regulates the transcription of a broad spectrum of genes that are involved in patterning, neural progenitor cell proliferation and neurogenesis. It was shown that Pax6 interacts with BAF155 and BAF170, components of ATP-dependent multi-subunit mSWI/SNF nucleosome remodeling complexes. During early neurogenesis, these two subunits compete with each other to modify euchromatin structure [56]. It will be interesting to further explore how Pax6 is involved in chromatin remodelling in the context of diencephalic development.

Chapter 13

Conclusion

In this study, I explored the role of the transcription factor Pax6 in the development of the thalamus, especially the vLGN, by deleting *Pax6* conditionally in the diencephalon-specific *Zic4* lineage cells. I found: 1. the nuclear volume and cell density decreased and the GFP+ve cell proportion increased in the P0 $Pax6^{fl/fl}$ vLGN; 2. the GFP+ve cell proportion increased in the P0 dLGN in both the $Pax6^{fl/+}$ and $Pax6^{fl/fl}$; 3. the expression pattern of Lim1/2 and Nkx2.2 in the P0 vLGN changed in both the $Pax6^{fl/+}$ and $Pax6^{fl/fl}$.

A BrdU birth dating experiment was then performed to study the time of origin of the vLGN and dLGN, which was found to be mainly between E11.5 to E12.5. Based on this finding, I went on to look at cell proliferation (including the growth fraction, proliferation rate and cell cycling speed), cell apoptosis, expression of patterning factors (*Shh* and *Nkx2.2*) in the early stage and the innervation of RGCs processes postnatally to unravel the mechanisms underlying the P0 vLGN and dLGN defects. The results suggest that: 1. the increase of the $Pax6^{fl/fl}$ vLGN volume is likely to be caused by the expansion of the ZLI and pTH-R; 2. the decrease in the $Pax6^{fl/fl}$ vLGN cell density is likely to be caused by a smaller growth fraction at E12.5; 3. the proliferation rate, cell cycling speed and cell apoptosis rate do not change when the deletion of *Pax6* is driven by the *Zic4Cre*; 4. no gross RGCs innervation change was found in the vLGN and dLGN despite the fact that the eyes are malformed. The exploration of cell migration in the mutant toward the end of this PhD raised a possibility that Pax6 may also play a role in cell migration/sorting.

To summarise, Pax6 is involved in multiple aspects of the development of the diencephalic nucleus vLGN mainly through its regulation of cell proliferation and early patterning, and perhaps cell migration as well, in potentially both cell autonomous and cell non-autonomous manners.

In the near future, the completion of the cell migration study should be the priority as it represents of the last of the hypothesized mechanisms involved in diencephalic development. It would also be crucial to investigate further the possibility of the existence of a poisonous polypeptide potentially produced by the truncated *Pax6* allele upon recombination. It will be interesting to look at whether Pax6 acts as a signalling molecule that is passed between cells in the developing diencephalon. A close and systematic look at the cell cycle kinetics using a modified FUCCI system would be the next on the to-do list, as it is fundamental to the formation of the future nuclei. In the long run, involving microRNA and chromatin remodelling into the study of diencephalic development will offer valuable insights into how gene expression is regulated through multiple layers of fine tuning to ensure the formation of a perfectly functional diencephalon.

Bibliography

[1] A. J. Copp, N. D. E. Greene, and J. N. Murdoch, *The genetic basis of mammalian neurulation*, Nature Reviews Genetics **4** (2003) no. 10, 784–793. https://doi.org/10.1038%2Fnrg1181.

[2] D. Price, A. Jarman, J. Mason, and P. Kind, *Building Brains*. Wiley-Blackwell, 2011. https://doi.org/10.1002%2F9780470979624.

[3] N.-E. Szabo, T. Zhao, M. Cankaya, T. Theil, X. Zhou, and G. Alvarez-Bolado, *Role of Neuroepithelial Sonic hedgehog in Hypothalamic Patterning*, Journal of Neuroscience **29** (2009) no. 21, 6989–7002. https://doi.org/10.1523%2Fjneurosci.1089-09.2009.

[4] A. Martinez-Ferre and S. Martinez, *Molecular Regionalization of the Diencephalon*, Frontiers in Neuroscience **6** (2012) . https://doi.org/10.3389/fnins.2012.00073.

[5] L. Puelles and S. Martinez, *Patterning and Cell Type Specification in the Developing CNS and PNS - Patterning of the Diencephalon*. Elsevier BV, 2013. https://doi.org/10.1016%2Fb978-0-12-397265-1.00048-4.

[6] L. Puelles and J. L. Rubenstein, *Forebrain gene expression domains and the evolving prosomeric model*, Trends in Neurosciences **26** (2003) no. 9, 469–476. https://doi.org/10.1016/s0166-2236(03)00234-0.

[7] Y. Suda, Z. M. Hossain, C. Kobayashi, O. Hatano, M. Yoshida, I. Matsuo, and S. Aizawa, *Emx2 directs the development of diencephalon in cooperation with Otx2*, Development **128** (2001) no. 13, 2433–2450. http://dev.biologists.org/content/develop/128/13/2433.full.pdf.

[8] Y. Lim and J. A. Golden, *Patterning the developing diencephalon*, Brain Research Reviews **53** (2007) no. 1, 17–26. https://doi.org/10.1016/j.brainresrev.2006.06.004.

[9] Y. Nakagawa and T. Shimogori, *Diversity of thalamic progenitor cells and postmitotic neurons*, European Journal of Neuroscience **35** (2012) no. 10, 1554–1562. http://dx.doi.org/10.1111/j.1460-9568.2012.08089.x.

[10] D. J. Price, J. Clegg, X. O. Duocastella, D. Willshaw, and T. Pratt, *The Importance of Combinatorial Gene Expression in Early Mammalian Thalamic Patterning and Thalamocortical Axonal Guidance*, Frontiers in Neuroscience **6** (2012) . https://doi.org/10.3389/fnins.2012.00037.

[11] E. Jones, *The thalamus*. Cambridge University Press, 2007.

[12] T. Y. Vue, K. Bluske, A. Alishahi, L. L. Yang, N. Koyano-Nakagawa, B. Novitch, and Y. Nakagawa, *Sonic Hedgehog Signaling Controls Thalamic Progenitor Identity and Nuclei Specification in Mice*, Journal of Neuroscience **29** (2009) no. 14, 4484–4497. https://doi.org/10.1523/jneurosci.0656-09.2009.

[13] A. Kataoka and T. Shimogori, *Fgf8 controls regional identity in the developing thalamus*, Development **135** (2008) no. 17, 2873–2881. https://doi.org/10.1242/dev.021618.

[14] A. Martinez-Ferre and S. Martinez, *The Development of the Thalamic Motor Learning Area Is Regulated by Fgf8 Expression*, Journal of Neuroscience **29** (2009) no. 42, 13389–13400. https://doi.org/10.1523/jneurosci.2625-09.2009.

[15] C.-J. Zhou, *Severe Defects in Dorsal Thalamic Development in Low-Density Lipoprotein Receptor-Related Protein-6 Mutants*, Journal of Neuroscience **24** (2004) no. 35, 7632–7639. https://doi.org/10.1523/jneurosci.2123-04.2004.

[16] T. Hirata, *Zinc finger genes Fez and Fez-like function in the establishment of diencephalon subdivisions*, Development **133** (2006) no. 20, 3993–4004. https://doi.org/10.1242/dev.02585.

[17] E. Robertshaw, K. Matsumoto, A. Lumsden, and C. Kiecker, *Irx3 and Pax6 establish differential competence for Shh-mediated induction of GABAergic and glutamatergic neurons of the thalamus*, Proceedings of the National Academy of Sciences **110** (2013) no. 41, E3919–E3926. https://doi.org/10.1073%2Fpnas.1304311110.

[18] M. Chatterjee, Q. Guo, S. Weber, S. Scholpp, and J. Y. Li, *Pax6 regulates the formation of the habenular nuclei by controlling the temporospatial expression of Shh in the diencephalon in vertebrates*, BMC Biology **12** (2014) no. 1, 13. http://dx.doi.org/10.1186/1741-7007-12-13.

[19] C. Kiecker and A. Lumsden, *The Role of Organizers in Patterning the Nervous System*, Annual Review of Neuroscience **35** (2012) no. 1, 347–367. https://doi.org/10.1146/annurev-neuro-062111-150543.

[20] T. Y. Vue, J. Aaker, A. Taniguchi, C. Kazemzadeh, J. M. Skidmore, D. M. Martin, J. F. Martin, M. Treier, and Y. Nakagawa, *Characterization of progenitor domains in the developing mouse thalamus*, The Journal of Comparative Neurology **505** (2007) no. 1, 73–91. http://dx.doi.org/10.1002/cne.21467.

[21] N. Haubst, *Molecular dissection of Pax6 function: the specific roles of the paired domain and homeodomain in brain development*, Development **131** (2004) no. 24, 6131–6140. https://doi.org/10.1242/dev.01524.

[22] H. K. Tang, S. Singh, and G. F. Saunders, *Dissection of the Transactivation Function of the Transcription Factor Encoded by the Eye Developmental GenePAX6*, Journal of Biological Chemistry **273** (1998) no. 13, 7210–7221. https://doi.org/10.1074/jbc.273.13.7210.

[23] T. Jordan, I. Hanson, D. Zaletayev, S. Hodgson, J. Prosser, A. Seawright, N. Hastie, and V. van Heyningen, *The human PAX6 gene is mutated in two patients with aniridia*, Nature Genetics **1** (1992) no. 5, 328–332. https://doi.org/10.1038/ng0892-328.

[24] T. Glaser, D. S. Walton, and R. L. Maas, *Genomic structure, evolutionary conservation and aniridia mutations in the human PAX6 gene*, Nature Genetics **2** (1992) no. 3, 232–239. https://doi.org/10.1038/ng1192-232.

[25] T. Glaser, L. Jepeal, J. G. Edwards, S. R. Young, J. Favor, and R. L. Maas, *PAX6 gene dosage effect in a family with congenital cataracts, aniridia, anophthalmia and central nervous system defects*, Nature Genetics **7** (1994) no. 4, 463–471. https://doi.org/10.1038/ng0894-463.

[26] R. C. Roberts, *Small eyes—a new dominant eye mutant in the mouse*, Genetical Research **9** (1967) no. 01, 121. https://doi.org/10.1017/s0016672300010387.

[27] J. C. Quinn, J. D. West, and R. E. Hill, *Multiple functions for Pax6 in mouse eye and nasal development.*, Genes & Development **10** (1996) no. 4, 435–446. https://doi.org/10.1101/gad.10.4.435.

[28] P. A. Georgala, M. Manuel, and D. J. Price, *The Generation of Superficial Cortical Layers Is Regulated by Levels of the Transcription Factor Pax6*, Cerebral Cortex **21** (2010) no. 1, 81–94. https://doi.org/10.1093/cercor/bhq061.

[29] K. Yun, S. Potter, and J. Rubenstein, *Gsh2 and Pax6 play complementary roles in dorsoventral patterning of the mammalian telencephalon*, Development **128** (2001) no. 2,

193–205.
http://dev.biologists.org/content/develop/128/2/193.full.pdf.

[30] L. A. Cocas, P. A. Georgala, J.-M. Mangin, J. M. Clegg, N. Kessaris, T. F. Haydar, V. Gallo, D. J. Price, and J. G. Corbin, *Pax6 Is Required at the Telencephalic Pallial-Subpallial Boundary for the Generation of Neuronal Diversity in the Postnatal Limbic System*, Journal of Neuroscience **31** (2011) no. 14, 5313–5324.
https://doi.org/10.1523/jneurosci.3867-10.2011.

[31] M. Manuel, P. A. Georgala, C. B. Carr, S. Chanas, D. A. Kleinjan, B. Martynoga, J. O. Mason, M. Molinek, J. Pinson, T. Pratt, J. C. Quinn, T. I. Simpson, D. A. Tyas, V. van Heyningen, J. D. West, and D. J. Price, *Controlled overexpression of Pax6 in vivo negatively autoregulates the Pax6 locus, causing cell-autonomous defects of late cortical progenitor proliferation with little effect on cortical arealization*, Development **134** (2006) no. 3, 545–555. https://doi.org/10.1242/dev.02764.

[32] M. Manuel, T. Pratt, M. Liu, G. Jeffery, and D. J. Price, *Overexpression of Pax6 results in microphthalmia, retinal dysplasia and defective retinal ganglion cell axon guidance*, BMC Developmental Biology **8** (2008) no. 1, 59.
https://doi.org/10.1186/1471-213x-8-59.

[33] R. E. Hill, J. Favor, B. L. M. Hogan, C. C. T. Ton, G. F. Saunders, I. M. Hanson, J. Prosser, T. Jordan, N. D. Hastie, and V. van Heyningen, *Mouse Small eye results from mutations in a paired-like homeobox-containing gene*, Nature **354** (1991) no. 6354, 522–525.
http://dx.doi.org/10.1038/354522a0.

[34] N.Warren and D.J.Price, *Roles of Pax-6 in murine diencephalic developmnt*, Development **124** (1997) no. 8, 1573–1582.
http://dev.biologists.org/content/124/8/1573.

[35] J. C. Grindley, L. K. Hargett, R. E. Hill, A. Ross, and B. L. Hogan, *Disruption of PAX6 function in mice homozygous for the Pax6Sey-1Neu mutation produces abnormalities in the early development and regionalization of the diencephalon*, Mechanisms of Development **64** (1997) no. 1-2, 111–126.
http://dx.doi.org/10.1016/S0925-4773(97)00055-5.

[36] T.Pratt, T.Vitalis, N.Warren, J.M.Edgar, J.O.Mason, and D.J.Price, *A role for Pax6 in the normal development of dorsal thalamus and its cortical connections*, Development **127** (2000) no. 23, 5167–5178. http://dev.biologists.org/content/127/23/5167.

[37] G. S. Mastick and G. L. Andrews, *Pax6 Regulates the Identity of Embryonic Diencephalic Neurons*, Molecular and Cellular Neuroscience **17** (2001) no. 1, 190–207.
http://dx.doi.org/10.1006/mcne.2000.0924.

[38] L. Wang, K. K. Bluske, L. K. Dickel, and Y. Nakagawa, *Basal progenitor cells in the embryonic mouse thalamus - their molecular characterization and the role of neurogenins and Pax6*, Neural Development **6** (2011) no. 1, 35. http://dx.doi.org/10.1186/1749-8104-6-35.

[39] L. St-Onge, B. Sosa-Pineda, K. Chowdhury, A. Mansouri, and P. Gruss, *Pax6 is required for differentiation of glucagon-producing α-cells in mouse pancreas*, Nature **387** (1997) no. 6631, 406–409. http://dx.doi.org/10.1038/387406a0.

[40] I. M. Caballero, M. N. Manuel, M. Molinek, I. Quintana-Urzainqui, D. Mi, T. Shimogori, and D. J. Price, *Cell-Autonomous Repression of Shh by Transcription Factor Pax6 Regulates Diencephalic Patterning by Controlling the Central Diencephalic Organizer*, Cell Reports **8** (2014) no. 5, 1405–1418. http://dx.doi.org/10.1016/j.celrep.2014.07.051.

[41] J. M. Clegg, Z. Li, M. Molinek, I. M. Caballero, M. N. Manuel, and D. J. Price, *Pax6 is required intrinsically by thalamic progenitors for the normal molecular patterning of thalamic neurons but not the growth and guidance of their axons*, Neural Development **10** (2015) no. 1, . http://dx.doi.org/10.1186/s13064-015-0053-7.

[42] J. B. Angevine, *Time of neuron origin in the diencephalon of the mouse. An autoradiographic study*, The Journal of Comparative Neurology **139** (1970) no. 2, 129–187. https://doi.org/10.1002%2Fcne.901390202.

[43] S. C. Suzuki, T. Inoue, Y. Kimura, T. Tanaka, and M. Takeichi, *Neuronal Circuits Are Subdivided by Differential Expression of Type-II Classic Cadherins in Postnatal Mouse Brains*, Molecular and Cellular Neuroscience **9** (1997) no. 5-6, 433–447. https://doi.org/10.1006/mcne.1997.0626.

[44] M. E. HARRINGTON, *The Ventral Lateral Geniculate Nucleus and the Intergeniculate Leaflet: Interrelated Structures in the Visual and Circadian Systems*, Neuroscience & Biobehavioral Reviews **21** (1997) no. 5, 705–727. https://doi.org/10.1016%2Fs0149-7634%2896%2900019-x.

[45] R. L. Holmes, *Nuclear studies on the thalamus of the mouse*, The Journal of Comparative Neurology **99** (1953) no. 2, 377–413. https://doi.org/10.1002%2Fcne.900990209.

[46] Y. Jeong, D. K. Dolson, R. R. Waclaw, M. P. Matise, L. Sussel, K. Campbell, K. H. Kaestner, and D. J. Epstein, *Spatial and temporal requirements for sonic hedgehog in the regulation of thalamic interneuron identity*, Development **138** (2011) no. 3, 531–541. http://dx.doi.org/10.1242/dev.058917.

[47] D. Delaunay, K. Heydon, A. Miguez, M. Schwab, K.-A. Nave, J. L. Thomas, N. Spassky, S. Martinez, and B. Zalc, *Genetic tracing of subpopulation neurons in the prethalamus of mice (Mus musculus)*, The Journal of Comparative Neurology **512** (2009) no. 1, 74–83. https://doi.org/10.1002%2Fcne.21904.

[48] A. Suzuki-Hirano, M. Ogawa, A. Kataoka, A. C. Yoshida, D. Itoh, M. Ueno, S. Blackshaw, and T. Shimogori, *Dynamic spatiotemporal gene expression in embryonic mouse thalamus*, The Journal of Comparative Neurology **519** (2010) no. 3, 528–543. http://dx.doi.org/10.1002/cne.22531.

[49] C. A. Stoykova, R.Fritsch and P.Gruss, *Forebrain patterning defects in Small eye mutant mice*, Development **122** (1996) no. 11, 3453–3465. http://dev.biologists.org/content/122/11/3453.

[50] K. Kitamura, H. Miura, M. Yanazawa, T. Miyashita, and K. Kato, *Expression patterns of Brx1 (Rieg gene), Sonic hedgehog, Nkx2.2, Dlx1 and Arx during zona limitans intrathalamica and embryonic ventral lateral geniculate nuclear formation*, Mechanisms of Development **67** (1997) no. 1, 83–96. http://dx.doi.org/10.1016/S0925-4773(97)00110-X.

[51] M. Götz and W. B. Huttner, *The cell biology of neurogenesis*, Nature Reviews Molecular Cell Biology **6** (2005) no. 10, 777–788. https://doi.org/10.1038%2Fnrm1739.

[52] J. T. Paridaen and W. B. Huttner, *Neurogenesis during development of the vertebrate central nervous system*, EMBO reports **15** (2014) no. 4, 351–364. https://doi.org/10.1002%2Fembr.201438447.

[53] M. Florio, M. Albert, E. Taverna, T. Namba, H. Brandl, E. Lewitus, C. Haffner, A. Sykes, F. K. Wong, J. Peters, E. Guhr, S. Klemroth, K. Prufer, J. Kelso, R. Naumann, I. Nusslein, A. Dahl, R. Lachmann, S. Paabo, and W. B. Huttner, *Human-specific gene ARHGAP11B promotes basal progenitor amplification and neocortex expansion*, Science **347** (2015) no. 6229, 1465–1470. https://doi.org/10.1126%2Fscience.aaa1975.

[54] E. Pacary, R. Azzarelli, and F. Guillemot, *Rnd3 coordinates early steps of cortical neurogenesis through actin-dependent and -independent mechanisms*, Nature Communications **4** (2013) 1635. https://doi.org/10.1038%2Fncomms2614.

[55] T. Walcher, Q. Xie, J. Sun, M. Irmler, J. Beckers, T. Ozturk, D. Niessing, A. Stoykova, A. Cvekl, J. Ninkovic, and M. Gotz, *Functional dissection of the paired domain of Pax6 reveals molecular mechanisms of coordinating neurogenesis and proliferation*, Development **140** (2013) no. 5, 1123–1136. https://doi.org/10.1242%2Fdev.082875.

[56] T. C. Tuoc, S. Boretius, S. N. Sansom, M.-E. Pitulescu, J. Frahm, F. J. Livesey, and A. Stoykova, *Chromatin Regulation by BAF170 Controls Cerebral Cortical Size and*

Thickness, Developmental Cell **25** (2013) no. 3, 256–269. https://doi.org/10.1016%2Fj.devcel.2013.04.005.

[57] B. Alberts, A. Johnson, J. Lewis, M. Raff, K. Roberts, and P. Walter, *Molecular Biology of the Cell*. Garland Science, 2007.

[58] S. ichi Ohnuma and W. A. Harris, *Neurogenesis and the Cell Cycle*, Neuron **40** (2003) no. 2, 199–208. https://doi.org/10.1016%2Fs0896-6273%2803%2900632-9.

[59] C. Dehay and H. Kennedy, *Cell-cycle control and cortical development*, Nature Reviews Neuroscience **8** (2007) no. 6, 438–450. https://doi.org/10.1038%2Fnrn2097.

[60] Y. Arai, J. N. Pulvers, C. Haffner, B. Schilling, I. Nüsslein, F. Calegari, and W. B. Huttner, *Neural stem and progenitor cells shorten S-phase on commitment to neuron production*, Nature Communications **2** (2011) no. 1, 154. https://doi.org/10.1038%2Fncomms1155.

[61] P. Gao, M. P. Postiglione, T. G. Krieger, L. Hernandez, C. Wang, Z. Han, C. Streicher, E. Papusheva, R. Insolera, and K. Chugh, *Deterministic Progenitor Behavior and Unitary Production of Neurons in the Neocortex*, Cell **159** (2014) no. 4, 775–788. https://doi.org/10.1016%2Fj.cell.2014.10.027.

[62] D. Mi, C. B. Carr, P. A. Georgala, Y.-T. Huang, M. N. Manuel, E. Jeanes, E. Niisato, S. N. Sansom, F. J. Livesey, T. Theil, K. Hasenpusch-Theil, T. I. Simpson, J. O. Mason, and D. J. Price, *Pax6 Exerts Regional Control of Cortical Progenitor Proliferation via Direct Repression of Cdk6 and Hypophosphorylation of pRb*, Neuron **78** (2013) no. 2, 269–284. https://doi.org/10.1016%2Fj.neuron.2013.02.012.

[63] K. K. Bluske, T. Y. Vue, Y. Kawakami, M. M. Taketo, K. Yoshikawa, J. E. Johnson, and Y. Nakagawa, *-Catenin signaling specifies progenitor cell identity in parallel with Shh signaling in the developing mammalian thalamus*, Development **139** (2012) no. 15, 2692–2702. http://dx.doi.org/10.1242/dev.072314.

[64] C. Frassoni, A. Amadeo, B. Ortino, A. Jaranowska, and R. Spreafico, *Organization of radial and non-radial glia in the developing rat thalamus*, The Journal of Comparative Neurology **428** (2000) no. 3, 527–542. https://doi.org/10.1002%2F1096-9861%2820001218%29428%3A3%3C527%3A%3Aaid-cne9%3E3.0.co%3B2-x.

[65] H. Zong, J. S. Espinosa, H. H. Su, M. D. Muzumdar, and L. Luo, *Mosaic Analysis with Double Markers in Mice*, Cell **121** (2005) no. 3, 479–492. https://doi.org/10.1016%2Fj.cell.2005.02.012.

[66] W. Shi, A. Xianyu, Z. Han, X. Tang, Z. Li, H. Zhong, T. Mao, K. Huang, and S.-H. Shi, *Ontogenetic establishment of order-specific nuclear organization in the mammalian thalamus*,

Nature Neuroscience **20** (2017) no. 4, 516–528. https://doi.org/10.1038%2Fnn.4519.

[67] M. Kristiansen and J. Ham, *Programmed cell death during neuronal development: the sympathetic neuron model*, Cell Death and Differentiation **21** (2014) no. 7, 1025–1035. https://doi.org/10.1038%2Fcdd.2014.47.

[68] C.-Y. Kuan, K. A. Roth, R. A. Flavell, and P. Rakic, *Mechanisms of programmed cell death in the developing brain*, Trends in Neurosciences **23** (2000) no. 7, 291–297. https://doi.org/10.1016%2Fs0166-2236%2800%2901581-2.

[69] M. P. Dekkers, V. Nikoletopoulou, and Y.-A. Barde, *Death of developing neurons: New insights and implications for connectivity*, The Journal of Cell Biology **203** (2013) no. 3, 385–393. https://doi.org/10.1083%2Fjcb.201306136.

[70] A. G. Porter and R. U. Jänicke, *Emerging roles of caspase-3 in apoptosis*, Cell Death and Differentiation **6** no. 2, 99–104. https://doi.org/10.1038%2Fsj.cdd.4400476.

[71] J. Berger, S. Berger, T. C. Tuoc, M. D. Amelio, F. Cecconi, J. A. Gorski, K. R. Jones, P. Gruss, and A. Stoykova, *Conditional activation of Pax6 in the developing cortex of transgenic mice causes progenitor apoptosis*, Development **134** (2007) no. 7, 1311–1322. https://doi.org/10.1242%2Fdev.02809.

[72] J. Aruga, T. Nagai, T. Tokuyama, Y. Hayashizaki, Y. Okazaki, V. M. Chapman, and K. Mikoshiba, *The Mouse Zic Gene Family: HOMOLOGUES OF THE DROSOPHILA PAIR-RULE GENE odd-paired*, Journal of Biological Chemistry **271** (1996) no. 2, 1043–1047. http://dx.doi.org/10.1074/jbc.271.2.1043.

[73] J. Aruga, A. Yozu, Y. Hayashizaki, Y. Okazaki, V. M. Chapman, and K. Mikoshiba, *Identification and characterization of Zic4, a new member of the mouse Zic gene family*, Gene **172** (1996) no. 2, 291–294. http://dx.doi.org/10.1016/0378-1119(96)00111-4.

[74] D. M. Cimbora and S. Sakonju, *Drosophila Midgut Morphogenesis Requires the Function of the Segmentation Gene odd-paired*, Developmental Biology **169** (1995) no. 2, 580–595. http://dx.doi.org/10.1006/dbio.1995.1171.

[75] R. G. Ali, H. M. Bellchambers, and R. M. Arkell, *Zinc fingers of the cerebellum (Zic): Transcription factors and co-factors*, The International Journal of Biochemistry & Cell Biology **44** (2012) no. 11, 2065–2068. http://dx.doi.org/10.1016/j.biocel.2012.08.012.

[76] I. Grinberg, H. Northrup, H. Ardinger, C. Prasad, W. B. Dobyns, and K. J. Millen, *Heterozygous deletion of the linked genes ZIC1 and ZIC4 is involved in Dandy-Walker*

malformation, Nature Genetics **36** (2004) no. 10, 1053–1055. http://dx.doi.org/10.1038/ng1420.

[77] J. Aruga, O. Minowa, H. Yaginuma, J. Kuno, T. Nagai, T. Noda, and K. Mikoshiba, *Mouse Zic1 Is Involved in Cerebellar Development*, Journal of Neuroscience **18** (1998) no. 1, 284–293. http://www.jneurosci.org/content/18/1/284.full.pdf+html.

[78] M. C. Blank, I. Grinberg, E. Aryee, C. Laliberte, V. V. Chizhikov, R. M. Henkelman, and K. J. Millen, *Multiple developmental programs are altered by loss of Zic1 and Zic4 to cause Dandy-Walker malformation cerebellar pathogenesis*, Development **138** (2011) no. 6, 1207–1216. http://dx.doi.org/10.1242/dev.054114.

[79] J. D. Corrales, *Spatial pattern of sonic hedgehog signaling through Gli genes during cerebellum development*, Development **131** (2004) no. 22, 5581–5590. http://dx.doi.org/10.1242/dev.01438.

[80] C. Vaillant and D. Monard, *SHH Pathway and Cerebellar Development*, Cerebellum **8** (2009) no. 3, 291–301. http://dx.doi.org/10.1007/s12311-009-0094-8.

[81] J. J. White and R. V. Sillitoe, *Development of the cerebellum: from gene expression patterns to circuit maps*, WIREs Dev Biol **2** (2012) no. 1, 149–164. http://dx.doi.org/10.1002/wdev.65.

[82] C. Gaston-Massuet, D. J. Henderson, N. D. Greene, and A. J. Copp, *Zic4, a zinc-finger transcription factor, is expressed in the developing mouse nervous system*, Dev. Dyn. **233** (2005) no. 3, 1110–1115. http://dx.doi.org/10.1002/dvdy.20417.

[83] G. E. Elsen, L. Y. Choi, K. J. Millen, Y. Grinblat, and V. E. Prince, *Zic1 and Zic4 regulate zebrafish roof plate specification and hindbrain ventricle morphogenesis*, Developmental Biology **314** (2008) no. 2, 376–392. http://dx.doi.org/10.1016/j.ydbio.2007.12.006.

[84] T. J. Fujimi, K. Mikoshiba, and J. Aruga, *Xenopus Zic4 : Conservation and diversification of expression profiles and protein function among the Xenopus Zic family*, Dev. Dyn. **235** (2006) no. 12, 3379–3386. http://dx.doi.org/10.1002/dvdy.20906.

[85] S. Horng, G. Kreiman, C. Ellsworth, D. Page, M. Blank, K. Millen, and M. Sur, *Differential Gene Expression in the Developing Lateral Geniculate Nucleus and Medial Geniculate Nucleus Reveals Novel Roles for Zic4 and Foxp2 in Visual and Auditory Pathway Development*, Journal of Neuroscience **29** (2009) no. 43, 13672–13683. http://dx.doi.org/10.1523/JNEUROSCI.2127-09.2009.

[86] B. Murillo, N. Ruiz-Reig, M. Herrera, A. Fairen, and E. Herrera, *Zic2 Controls the Migration of Specific Neuronal Populations in the Developing Forebrain*, Journal of

Neuroscience **35** (2015) no. 32, 11266–11280. http://dx.doi.org/10.1523/JNEUROSCI.0779-15.2015.

[87] A. P. Chervenak, L. M. Bank, N. Thomsen, H. C. Glanville-Jones, S. Jonathan, K. J. Millen, R. M. Arkell, and K. F. Barald, *The role of Zic genes in inner ear development in the mouse: Exploring mutant mouse phenotypes*, Dev. Dyn. **243** (2014) no. 11, 1487–1498. http://dx.doi.org/10.1002/dvdy.24186.

[88] M. E. Buckingham and S. M. Meilhac, *Tracing Cells for Tracking Cell Lineage and Clonal Behavior*, Developmental Cell **21** (2011) no. 3, 394–409. http://dx.doi.org/10.1016/j.devcel.2011.07.019.

[89] K. Kretzschmar and F. M. Watt, *Lineage Tracing*, Cell **148** (2012) no. 1-2, 33–45. http://dx.doi.org/10.1016/j.cell.2012.01.002.

[90] W. L. Stanford, J. B. Cohn, and S. P. Cordes, *MOUSE GENOMIC TECHNOLOGIES: GENE-TRAP MUTAGENESIS: PAST, PRESENT AND BEYOND*, Nature Reviews Genetics **2** (2001) no. 10, 756–768. https://doi.org/10.1038%2F35093548.

[91] S. Hayashi and A. P. McMahon, *Efficient Recombination in Diverse Tissues by a Tamoxifen-Inducible Form of Cre: A Tool for Temporally Regulated Gene Activation/Inactivation in the Mouse*, Developmental Biology **244** (2002) no. 2, 305–318. http://dx.doi.org/10.1006/dbio.2002.0597.

[92] T. I. Simpson, T. Pratt, J. O. Mason, and D. J. Price, *Normal ventral telencephalic expression of Pax6 is required for normal development of thalamocortical axons in embryonic mice*, Neural Development **4** (2009) no. 1, 19. https://doi.org/10.1186/1749-8104-4-19.

[93] G. Miyoshi, J. Hjerling-Leffler, T. Karayannis, V. H. Sousa, S. J. B. Butt, J. Battiste, J. E. Johnson, R. P. Machold, and G. Fishell, *Genetic Fate Mapping Reveals That the Caudal Ganglionic Eminence Produces a Large and Diverse Population of Superficial Cortical Interneurons*, Journal of Neuroscience **30** (2010) no. 5, 1582–1594. http://dx.doi.org/10.1523/JNEUROSCI.4515-09.2010.

[94] T. R. Jones, I. Kang, D. B. Wheeler, R. A. Lindquist, A. Papallo, D. M. Sabatini, P. Golland, and A. E. Carpenter, *CellProfiler Analyst: data exploration and analysis software for complex image-based screens*, BMC Bioinformatics **9** (2008) no. 1, 482. https://doi.org/10.1186%2F1471-2105-9-482.

[95] *Multi ROI/Mask Editor Class*, https://uk.mathworks.com/matlabcentral/fileexchange/31388-multi-roi-mask-editor-class. Accessed: 2016-07-15.

[96] M. Merzin, *Applying stereological method in radiology. Volume measurement.*, . Bachelor's thesis. University of Tartu. 2008.

[97] R. S. Nowakowski, S. B. Lewin, and M. W. Miller, *Bromodeoxyuridine immunohistochemical determination of the lengths of the cell cycle and the DNA-synthetic phase for an anatomically defined population*, Journal of Neurocytology **18** (1989) no. 3, 311–318. https://doi.org/10.1007%2Fbf01190834.

[98] A. N. Rubin, F. Alfonsi, M. P. Humphreys, C. K. P. Choi, S. F. Rocha, and N. Kessaris, *The Germinal Zones of the Basal Ganglia But Not the Septum Generate GABAergic Interneurons for the Cortex*, Journal of Neuroscience **30** (2010) no. 36, 12050–12062. http://dx.doi.org/10.1523/JNEUROSCI.6178-09.2010.

[99] S. Srinivas, T. Watanabe, C.-S. Lin, C. M. William, Y. Tanabe, T. M. Jessell, and F. Costantini, *Cre reporter strains produced by targeted insertion of EYFP and ECFP into the ROSA26 locus*, BMC Developmental Biology **1** (2001) no. 1, 4. http://dx.doi.org/10.1186/1471-213X-1-4.

[100] U. Schambra, *Prenatal Mouse Brain Atlas*. Springer Nature, 2008. http://dx.doi.org/10.1007/978-0-387-47093-1.

[101] L. Chen, Q. Guo, and J. Y. H. Li, *Transcription factor Gbx2 acts cell-nonautonomously to regulate the formation of lineage-restriction boundaries of the thalamus*, Development **136** (2009) no. 8, 1317–1326. http://dx.doi.org/10.1242/dev.030510.

[102] S.-M. Virolainen, K. Achim, P. Peltopuro, M. Salminen, and J. Partanen, *Transcriptional regulatory mechanisms underlying the GABAergic neuron fate in different diencephalic prosomeres*, Development **139** (2012) no. 20, 3795–3805. http://dx.doi.org/10.1242/dev.075192.

[103] A. Roy, M. Gonzalez-Gomez, A. Pierani, G. Meyer, and S. Tole, *Lhx2 Regulates the Development of the Forebrain Hem System*, Cerebral Cortex **24** (2013) no. 5, 1361–1372. http://dx.doi.org/10.1093/cercor/bhs421.

[104] C. N. Sunnen, J. C. Simonet, E. D. Marsh, and J. A. Golden, *Arx Is Required for Specification of the Zona Incerta and Reticular Nucleus of the Thalamus*, Journal of Neuropathology & Experimental Neurology **73** (2014) no. 3, 253–261. http://dx.doi.org/10.1097/NEN.0000000000000048.

[105] A. Filippi, C. Jainok, and W. Driever, *Analysis of transcriptional codes for zebrafish dopaminergic neurons reveals essential functions of Arx and Isl1 in prethalamic dopaminergic neuron development*, Developmental Biology **369** (2012) no. 1, 133–149. http://dx.doi.org/10.1016/j.ydbio.2012.06.010.

[106] K. Ono, A. Clavairoly, T. Nomura, H. Gotoh, A. Uno, O. Armant, H. Takebayashi, Q. Zhang, K. Shimamura, S. Itohara, C. M. Parras, and K. Ikenaka, *Development of the*

prethalamus is crucial for thalamocortical projection formation and is regulated by Olig2, Development **141** (2014) no. 10, 2075–2084. http://dx.doi.org/10.1242/dev.097790.

[107] S. Garel, *The early topography of thalamocortical projections is shifted in Ebf1 and Dlx1/2 mutant mice*, Development **129** (2002) no. 24, 5621–5634. http://dx.doi.org/10.1242/dev.00166.

[108] S. Kwon, *Single-molecule fluorescence in situ hybridization: Quantitative imaging of single RNA molecules*, BMB reports **46** (2013) no. 2, 65–72. http://dx.doi.org/10.5483/BMBRep.2013.46.2.016.

[109] T. Trcek, J. A. Chao, D. R. Larson, H. Y. Park, D. Zenklusen, S. M. Shenoy, and R. H. Singer, *Single-mRNA counting using fluorescent in situ hybridization in budding yeast*, Nat Protoc **7** (2012) no. 2, 408–419. http://dx.doi.org/10.1038/nprot.2011.451.

[110] G. Danuser, *Computer Vision in Cell Biology*, Cell **147** (2011) no. 5, 973–978. http://dx.doi.org/10.1016/j.cell.2011.11.001.

[111] E. Meijering, *Cell Segmentation: 50 Years Down the Road [Life Sciences]*, IEEE Signal Process. Mag. **29** (2012) no. 5, 140–145. http://dx.doi.org/10.1109/MSP.2012.2204190.

[112] A. H. K. Roeder, A. Cunha, M. C. Burl, and E. M. Meyerowitz, *A computational image analysis glossary for biologists*, Development **139** (2012) no. 17, 3071–3080. http://dx.doi.org/10.1242/dev.076414.

[113] A. R. Buxbaum, G. Haimovich, and R. H. Singer, *In the right place at the right time: visualizing and understanding mRNA localization*, Nature Reviews Molecular Cell Biology **16** (2014) no. 2, 95–109. http://dx.doi.org/10.1038/nrm3918.

[114] J. Pinson, *The role of Pax6 isoforms in embryonic development.*, . PhD's thesis. University of Edinburgh. 2002.

[115] S. Scholpp and A. Lumsden, *Building a bridal chamber: development of the thalamus*, Trends in Neurosciences **33** (2010) no. 8, 373–380. https://doi.org/10.1016%2Fj.tins.2010.05.003.

[116] M. Chatterjee, K. Li, L. Chen, X. Maisano, Q. Guo, L. Gan, and J. Y. H. Li, *Gbx2 regulates thalamocortical axon guidance by modifying the LIM and Robo codes*, Development **139** (2012) no. 24, 4633–4643. https://doi.org/10.1242%2Fdev.086991.

[117] M. Takahashi and N. Osumi, *Pax6 regulates specification of ventral neurone subtypes in the hindbrain by establishing progenitor domains*, Development **129** (2002) no. 6, 1327–1338. http://dev.biologists.org/content/129/6/1327.

[118] A. Stoykova, D. Treichel, M. Hallonet, and P. Gruss, *Pax6 Modulates the Dorsoventral Patterning of the Mammalian Telencephalon*, Journal of Neuroscience **20** (2000) no. 21, 8042–8050. http://www.jneurosci.org/content/20/21/8042.

[119] M. Götz, A. Stoykova, and P. Gruss, *Pax6 Controls Radial Glia Differentiation in the Cerebral Cortex*, Neuron **21** (1998) no. 5, 1031–1044. https://doi.org/10.1016%2Fs0896-6273%2800%2980621-2.

[120] B. Golding, G. Pouchelon, C. Bellone, S. Murthy, A. A. D. Nardo, S. Govindan, M. Ogawa, T. Shimogori, C. Lüscher, A. Dayer, and D. Jabaudon, *Retinal Input Directs the Recruitment of Inhibitory Interneurons into Thalamic Visual Circuits*, Neuron **81** (2014) no. 5, 1057–1069. https://doi.org/10.1016%2Fj.neuron.2014.01.032.

[121] S. Singh, C. M. Stellrecht, H. K. Tang, and G. F. Saunders, *Modulation of PAX6 Homeodomain Function by the Paired Domain*, Journal of Biological Chemistry **275** (2000) no. 23, 17306–17313. https://doi.org/10.1074/jbc.m000359200.

[122] I. Mikkola, J.-A. Bruun, T. Holm, and T. Johansen, *Superactivation of Pax6-mediated Transactivation from Paired Domain-binding Sites by DNA-independent Recruitment of Different Homeodomain Proteins*, Journal of Biological Chemistry **276** (2000) no. 6, 4109–4118. https://doi.org/10.1074/jbc.m008882200.

[123] N. Zielke and B. A. Edgar, *FUCCI sensors: powerful new tools for analysis of cell proliferation*, Wiley Interdisciplinary Reviews: Developmental Biology **4** (2015) no. 5, 469–487. https://doi.org/10.1002%2Fwdev.189.

[124] J. Seidman and C. Seidman, *Transcription factor haploinsufficiency: when half a loaf is not enough*, Journal of Clinical Investigation **109** (2002) no. 4, 451–455. https://doi.org/10.1172/jci0215043.

[125] A. Bobilev, M. McDougal, W. Taylor, E. Geisert, P. Netland, and J. Lauderdale, *Assessment of PAX6 alleles in 66 families with aniridia*, Clinical Genetics **89** (2016) no. 6, 669–677. https://doi.org/10.1111/cge.12708.

[126] R. A. Veitia, *Exploring the Molecular Etiology of Dominant-Negative Mutations*, THE PLANT CELL ONLINE **19** (2007) no. 12, 3843–3851. https://doi.org/10.1105/tpc.107.055053.

[127] J. Pinson, T. I. Simpson, J. O. Mason, and D. J. Price BMC Developmental Biology **6** (2006) no. 1, 25. https://doi.org/10.1186/1471-213x-6-25.

[128] S. Bhatia, H. Bengani, M. Fish, A. Brown, M. T. Divizia, R. de Marco, G. Damante, R. Grainger, V. van Heyningen, and D. A. Kleinjan, *Disruption of Autoregulatory Feedback*

by a Mutation in a Remote, Ultraconserved PAX6 Enhancer Causes Aniridia, The American Journal of Human Genetics **93** (2013) no. 6, 1126–1134. https://doi.org/10.1016/j.ajhg.2013.10.028.

[129] J. Pinson, J. O. Mason, T. I. Simpson, and D. J. Price BMC Developmental Biology **5** (2005) no. 1, 13. https://doi.org/10.1186/1471-213x-5-13.

[130] R. L. Joshi, R. T. Ibad, J. Rheey, F. Castagner, A. Prochiantz, and K. L. Moya, *Cell non-autonomous functions of homeoproteins in neuroprotection in the brain*, FEBS Letters **585** (2011) no. 11, 1573–1578. https://doi.org/10.1016/j.febslet.2011.05.006.

[131] B. Lesaffre, A. Joliot, A. Prochiantz, and M. Volovitch Neural Development **2** (2007) no. 1, 2. https://doi.org/10.1186/1749-8104-2-2.

[132] A. M. Deutschbauer, *Mechanisms of Haploinsufficiency Revealed by Genome Wide Profiling in Yeast*, Genetics **169** (2005) no. 4, 1915–1925. https://doi.org/10.1534/genetics.104.036871.

[133] T. J. Nowakowski, V. Fotaki, A. Pollock, T. Sun, T. Pratt, and D. J. Price, *MicroRNA-92b regulates the development of intermediate cortical progenitors in embryonic mouse brain*, Proceedings of the National Academy of Sciences **110** (2013) no. 17, 7056–7061. https://doi.org/10.1073%2Fpnas.1219385110.

[134] J. K. Kim, S.-O. Huh, H. Choi, K.-S. Lee, D. Shin, C. Lee, J.-S. Nam, H. Kim, H. Chung, H. W. Lee, S. D. Park, and R. H. Seong, *Srg3, a Mouse Homolog of Yeast SWI3, Is Essential for Early Embryogenesis and Involved in Brain Development*, Molecular and Cellular Biology **21** (2001) no. 22, 7787–7795. https://doi.org/10.1128%2Fmcb.21.22.7787-7795.2001.

[135] S. Kadam and B. M. Emerson, *Transcriptional Specificity of Human SWI/SNF BRG1 and BRM Chromatin Remodeling Complexes*, Molecular Cell **11** (2003) no. 2, 377–389. https://doi.org/10.1016%2Fs1097-2765%2803%2900034-0.

[136] N. Warren, *The Transcription Factor, Pax6, is Required for Cell Proliferation and Differentiation in the Developing Cerebral Cortex*, Cerebral Cortex **9** (1999) no. 6, 627–635. https://doi.org/10.1093%2Fcercor%2F9.6.627.

[137] J. Luo, M. Ju, and C. Redies, *Regionalized cadherin-7 expression by radial glia is regulated by Shh and Pax7 during chicken spinal cord development*, Neuroscience **142** (2006) no. 4, 1133–1143. https://doi.org/10.1016/j.neuroscience.2006.07.038.

Appendix I

Abbreviation

vLGN	ventral lateral geniculate nucleus	dLGN	dorsal lateral geniculate nucleus
IGL	intergeniculate leaflet	ZI	zona incerta
MGN	medial geniculate nucleus	VP	ventral posterior complex
Cx	cortex	cp	choroid plexus
MGE	medial ganglionic eminence	LGE	lateral ganglionic eminence
th (Th)	thalamus	pth (Pth)	prethalamus
emt	eminentia thalami	epi	epithalamus
pTH-R	thalamic progenitor rostral	pTH-C	thalamic progenitor caudal
ZLI	zona limitans intrathalamica	MDO	mid-diencephalon organiser
NEC	neuroepithelial cell	RGC	radial glial cell
IP	intermediate progenitor	bRG	basal radial glial cell
hESC	human embryonic stem cell		
MADM	mosaic analysis with double markers		

Appendix II

Statistical tests results for Chapter 4

Stage	Cell type	Transformation	One-way ANOVA	Tukey
E11.5	Zic4-GFP-	logistic	F(3,8) = 118.9 p < 0.0001	Ctx vs. Epi: p < 0.0001 Ctx vs. Th: p < 0.0001 Ctx vs. Pth: p < 0.0001 Epi vs. Th: p = 0.0169 Epi vs. Pth: p = 0.9116 Th vs. Pth: p = 0.0072
E11.5	Zic4+GFP-	logistic	F(3,8) = 5.23 p = 0.0273	Ctx vs. Epi: p = 0.9664 Ctx vs. Th: p = 0.3300 Ctx vs. Pth: p = 0.0288 Epi vs. Th: p = 0.5508 Epi vs. Pth: p = 0.0544 Th vs. Pth: p = 0.3501
E11.5	Zic4+GFP+	arcsine square root	F(3,8) = 31.18 p < 0.0001	Ctx vs. Epi: p = 0.0002 Ctx vs. Th: p = 0.0031 Ctx vs. Pth: p = 0.0001 Epi vs. Th: p = 0.0772 Epi vs. Pth: p = 0.9903 Th vs. Pth: p = 0.0508
E11.5	Zic4-GFP+	logistic	F(3,8) = 16.98 p = 0.0008	Ctx vs. Epi: p = 0.0007 Ctx vs. Th: p = 0.0034 Ctx vs. Pth: p = 0.0061 Epi vs. Th: p = 0.4905 Epi vs. Pth: p = 0.2796 Th vs. Pth: p = 0.9624

Stage	Cell type	Transformation	One-way ANOVA	Tukey
E12.5	Zic4-GFP-	logistic	F(3,8) = 11.4 p = 0.0029	Ctx vs. Epi: p < 0.0052 Ctx vs. Th: p = 0.0045 Ctx vs. Pth: p = 0.0117 Epi vs. Th: p = 0.9995 Epi vs. Pth: p = 0.9158 Th vs. Pth: p = 0.8754
E12.5	Zic4+GFP-	logistic	F(3,8) = 3.6 p = 0.0655	Ctx vs. Epi: p = 0.0665 Ctx vs. Th: p = 0.5645 Ctx vs. Pth: p = 0.1285 Epi vs. Th: p = 0.4024 Epi vs. Pth: p = 0.9642 Th vs. Pth: p = 0.6490
E12.5	Zic4+GFP+	logistic	F(3,8) = 5.122 p = 0.0288	Ctx vs. Epi: p = 0.0259 Ctx vs. Th: p = 0.0659 Ctx vs. Pth: p = 0.2403 Epi vs. Th: p = 0.9061 Epi vs. Pth: p = 0.4285 Th vs. Pth: p = 0.7881
E12.5	Zic4-GFP+	arcsine square root	F(3,8) = 13.08 p = 0.0019	Ctx vs. Epi: p = 0.0067 Ctx vs. Th: p = 0.0024 Ctx vs. Pth: p = 0.0050 Epi vs. Th: p = 0.8312 Epi vs. Pth: p = 0.9947 Th vs. Pth: p = 0.9275
E13.5	Zic4-GFP-	logistic	F(3,8) = 19.16 p = 0.0005	Ctx vs. Epi: p = 0.0005 Ctx vs. Th: p = 0.0040 Ctx vs. Pth: p = 0.0023 Epi vs. Th: p = 0.2609 Epi vs. Pth: p = 0.4575 Th vs. Pth: p = 0.9647

Stage	Cell type	Transformation	One-way ANOVA	Tukey
E13.5	Zic4+GFP-	logistic	F(3,8) = 0.7805 p = 0.5373	Ctx vs. Epi: p = 0.5918 Ctx vs. Th: p = 0.6852 Ctx vs. Pth: p = 0.5884 Epi vs. Th: p = 0.9982 Epi vs. Pth: p > 0.9999 Th vs. Pth: p = 0.9980
E13.5	Zic4+GFP+	logistic	F(3,8) = 20.5 p = 0.0004	Ctx vs. Epi: p = 0.0005 Ctx vs. Th: p = 0.0012 Ctx vs. Pth: p = 0.0017 Epi vs. Th: p = 0.8575 Epi vs. Pth: p = 0.7120 Th vs. Pth: p = 0.9910
E13.5	Zic4-GFP+	logistic	F(3,8) = 0.5895 p = 0.6389	Ctx vs. Epi: p = 0.5899 Ctx vs. Th: p = 0.8212 Ctx vs. Pth: p = 0.8302 Epi vs. Th: p = 0.9719 Epi vs. Pth: p = 0.9683 Th vs. Pth: p > 0.9999
E14.5	Zic4-GFP-	logistic	F(3,8) = 82.31 p < 0.0001	Ctx vs. Epi: p < 0.0001 Ctx vs. Th: p = 0.0003 Ctx vs. Pth: p = 0.0001 Epi vs. Th: p = 0.0002 Epi vs. Pth: p = 0.0004 Th vs. Pth: p = 0.8822
E14.5	Zic4+GFP-	logistic	F(3,8) = 34.77 p < 0.0001	Ctx vs. Epi: p = 0.0003 Ctx vs. Th: p < 0.0001 Ctx vs. Pth: p = 0.0012 Epi vs. Th: p = 0.2069 Epi vs. Pth: p = 0.5692 Th vs. Pth: p = 0.0321

Stage	Cell type	Transformation	One-way ANOVA	Tukey
E14.5	Zic4+GFP+	logistic	F(3,8) = 29.13 p = 0.0001	Ctx vs. Epi: p < 0.0001 Ctx vs. Th: p = 0.0136 Ctx vs. Pth: p = 0.0017 Epi vs. Th: p = 0.0045 Epi vs. Pth: p = 0.0410 Th vs. Pth: p = 0.3913
E14.5	Zic4-GFP+	logistic	F(3,8) = 3.104 p = 0.0889	Ctx vs. Epi: p = 0.7848 Ctx vs. Th: p = 0.9264 Ctx vs. Pth: p = 0.2539 Epi vs. Th: p = 0.4547 Epi vs. Pth: p = 0.0693 Th vs. Pth: p = 0.5215
E15.5	Zic4-GFP-	logistic	F(3,8) = 197.1 p < 0.0001	Ctx vs. Epi: p < 0.0001 Ctx vs. Th: p < 0.0001 Ctx vs. Pth: p = < 0.0001 Epi vs. Th: p = 0.0299 Epi vs. Pth: p = 0.9994 Th vs. Pth: p = 0.0255
E15.5	Zic4+GFP-	logistic	F(3,8) = 22.11 p = 0.0003	Ctx vs. Epi: p = 0.1965 Ctx vs. Th: p = 0.0006 Ctx vs. Pth: p = 0.0008 Epi vs. Th: p = 0.0082 Epi vs. Pth: p = 0.0110 Th vs. Pth: p = 0.9953
E15.5	Zic4+GFP+	arcsine square root	F(3,8) = 22.29 p = 0.0006	Ctx vs. Epi: p = 0.0030 Ctx vs. Th: p = 0.0005 Ctx vs. Pth: p = 0.0012 Epi vs. Th: p = 0.2040 Epi vs. Pth: p = 0.6803 Th vs. Pth: p = 0.7035
E15.5	Zic4-GFP+	logistic	F(3,8) = 9.437 p = 0.0053	Ctx vs. Epi: p = 0.0032 Ctx vs. Th: p = 0.0840 Ctx vs. Pth: p = 0.0730 Epi vs. Th: p = 0.1391 Epi vs. Pth: p = 0.1596 Th vs. Pth: p = 0.9996

Cell type	Transformation	Two-way ANOVA
Zic4-GFP-	logistic	Interaction F(9,32) = 2.403, p = 0.0329 Structure F(3,32) = 97.69, p < 0.0001 Stage F(3,32) = 6.34, p = 0.0017
Zic4+GFP-	logistic	Interaction F(9,32) = 1.479, p = 0.1978 Structure F(3,32) = 4.374, p = 0.0109 Stage F(3,32) = 2.223, p = 0.1045
Zic4+GFP+	arcsine square root	Interaction F(9,32) = 2.893, p = 0.0128 Structure F(3,32) = 56.22, p < 0.0001 Stage F(3,32) = 14.18, p < 0.0001
Zic4-GFP+	logistic	Interaction F(9,32) = 3.25, p = 0.0065 Structure F(3,32) = 14.08, p < 0.0001 Stage F(3,32) = 3.898, p = 0.0176

Appendix III

Codes

Matlab code for processing raw images in Chapter 4

```
%% This code aims to solve the segmentation of the objects that overlap in images.
%% The method used for segmentation is watershed transformation.
%% clear command windows
clc
clear all
close all
tic
%% main body
files = dir('G:\Matlab␣Image␣Analysis\trial_image\');
for k = 3 : length(files)
    % read in files and split channels
    filename = strcat ('G:\Matlab␣Image␣Analysis\trial_image\', files (k).name);
    %% channel split
    bmat = imread (filename, 1); % read blue channel
    % figure, imshow (bmat), title ('DAPI original');
    gmat = imread (filename, 2); % read green channel
    % figure, imshow (gmat), title ('GFP original');
    rmat = imread (filename, 3); % read red channel
    % figure, imshow (rmat), title ('Zic4 original');
    %% extract information from the filename
    % this piece of code need to be adjusted for every batch of images
    [pathstr,name,ext] = fileparts(filename);
    tidyname = strrep(name, '_', ''); % find and replace substring
    tidyname = strrep(tidyname, '␣', '');
    tidyname = strrep(tidyname, '.', '');
    age_pattern = 'e\d\d\d'; % recognise age
    age = regexp(tidyname,age_pattern,'match'); % extract age

    section_pattern = '\db\d'; % recognise section and the letter need to be changed
    section = regexp(tidyname,section_pattern,'match'); % extract section

    name1 = strrep (tidyname, age, ''); % shorten by removing age
```

```
name2 = strrep (name1, section, ''); % shorten by removine section

experiment_pattern = 'zic4gfp40x';
experiment = regexp(name2{1}, experiment_pattern, 'match');
name3 = strrep (name2, experiment, '');
stack_pattern = 'z\d';
stack = regexp(name2{1}, stack_pattern, 'match');
structure = strrep (name3, stack, '');

age = age{1}; % extract character
section = section{1}; % extract character
structure = structure{1};
stack = stack{1};
%% step 2 obtain and subtract background noise for each channel
% background noise subtraction for blue channel
bbg = imcrop (bmat); % crop a part of image to get the background
bbgv = mean(mean(bbg)); % bbgv stands for mean value of blue channel background region
b0 = bmat - bbgv; % remove background
% background noise substraction for red channel
rbg = imcrop (rmat); % crop a part of image to get the background
rbgv = mean(mean(rbg)); % rbgv stands for mean value of red channel background region
r0 = rmat - rbgv; % get rid of background
% figure, imshow (r0), title('background subtracted Zic4');
% background noise substraction for green channel
gbg = imcrop (gmat); % crop a part of image to get the background
gbgv = mean(mean(gbg)); % gbgv stands for mean value of green channel background
% region and mass cells
g0 = gmat - gbgv; % get rid of background
% figure, imshow (g0), title('background subtracted GFP');
close;
%% blue channel process
% Perform WATERSHED TRANSFORMATION on the DAPI channel to seggregate individual cells
% [level,Ib] = thresh_tool(b0); % change grayscale image into binary image
% figure, imshow (Ib);
% close;
roiwindow = CROIEditor(b0); % get multiple rois to remove mass cells
m = input('Do␣you␣want␣to␣continue,␣Y/N␣[Y]:','s'); % The roi is required for proceeding
if m == 'N'
break
end
% Use the roi to remove the unwanted regions
rgbImage = cat(3, r0, g0, b0);
Ib = rgbImage .* (1 - roiwindow.roi);
close; % the window should be closed after the Ib1 is calculated

imwrite(Ib, strcat(, age, section, structure, stack, '.tif'));
close all force;
```

```
end
%clear
```

R code for generating the summary graph in the synopsis of Chapter 4

```
# This code aims to summarise the proportion change of the four type of cells
# across time and structure based on the Zic4 and GFP expression levels.

library(ggplot2)
library(stringr)
library(plyr)
library(grid)
library(scales)
list.files() # look at all the file names
files = list.files ( pattern = "*.csv" )

# extract information according to the file name and the content of the files
df <- data.frame()

for ( i in 1 : length(files) ) {
        string = tolower(files[i])
        string = gsub("_", "", string)
        age <- str_extract(string, "e[0-9][0-9][0-9]") # extract age info
        df1 <- read.csv (files[i], header = TRUE, row.names = NULL)
        df1$age = age
        df <- rbind (df, df1)
}

newdf <- df[, (-1)] # remove row name column
newdf[newdf$structure == "prethalamus",]$structure <- "pth" # check structure names
newdf[newdf$structure == "thalamus",]$structure <- "th"

# calculate the standard error of mean

finaldf <- ddply(newdf, c("age", "type", "structure"), summarise
        , mean = mean(Proportion), sd = sd(Proportion)
        , sem = sd(Proportion)/sqrt(length(Proportion)))
levels(finaldf$type) <- c("Zic4-GFP-", "Zic4+GFP-", "Zic4+GFP+", "Zic4-GFP+")
levels(finaldf$structure) <- c("Cortex", "Epithalamus", "Prethalamus", "Thalamus")

# plot the data

ggsave(filename="phasesummary.png", height = 30, width = 24, units = "cm"
                , bg = "transparent", dpi = 300)
require(grid)
ggplot(finaldf, aes(age, mean)) +
        geom_point(size = 4) +
        geom_errorbar(aes(ymin = mean - sem, ymax = mean + sem), size = 2
```

```
        , width = .3, position=position_dodge(.9)) +
        facet_grid (type ~ structure, scales = "free") +
        scale_y_continuous (labels = percent_format(), limits = c(0, 1)) +
        scale_x_discrete (labels = c("E11.5", "E12.5", "E13.5", "E14.5")) +
        geom_smooth (stat = "identity", aes(group = 1), colour = "darkgrey", size = 1, lty = 5) +
        theme_bw() +
        theme(plot.margin =  unit(c(1.5, 1.5, 1.5, 1.5), "cm")) +
        theme(plot.background = element_blank(), panel.grid.minor = element_blank(),
        panel.background = element_rect(fill = "transparent", colour = NULL)) +
        theme(axis.line = element_line(color = "black", size = 1)) +
        theme(axis.ticks = element_line(colour = "black", size = 1)) +
        theme(axis.text.x = element_text(face = "bold", angle = -45, hjust = 0,
        size = 14, color = "black")) +
        theme(axis.text.y = element_text(face = "bold", angle = 00, hjust = 0.5,
        size = 14, color = "black")) +
        xlab("Age") +
        ylab("Proportion") +
        ggtitle("Summary␣of␣cell␣distribution␣into␣four␣types␣in␣the␣structures␣of␣interest") +
        theme(plot.title = element_text(face="bold", color="black", size= 16, vjust = 2)) +
        theme(axis.title.y = element_text(vjust = 2,face = "bold", size = rel(1.5), angle = 90)) +
        theme(axis.title.x = element_text(vjust = - 0.5,face = "bold", size = rel(1.5),
                angle = 00)) +
        theme(strip.text.x = element_text(size = 14, face="bold", vjust = .8),
              strip.text.y = element_text(size = 14, face="bold", vjust = .8),
              strip.background = element_rect(colour="black"))
dev.off()
```

Java code for random sampling in Chapter 6

```
import ij.*; // import class IJ
import ij.process.*; // import Package ij.process
import ij.gui.*; // import Package ij.gui
import java.awt.*; // import Package java.awt
// (Contains all of the classes for creating user interfaces and for painting graphics and images.)
import java.awt.geom.*; // import Package java.awt.geom
//(Provides the Java 2D classes for defining and performing operations on objects
// related to two-dimensional geometry.)
import java.util.*; // import Package java.util
// (Contains the collections framework, legacy collection classes, event model, date
// and time facilities, internationalization, and miscellaneous utility classes
// (a string tokenizer, a random-number generator, and a bit array))
import ij.plugin.*; // import Package ij.plugin
// (Plugins that acquire images or display windows should implement this interface.)
import ij.measure.*; // import Package ij.measure
// (A plugin should implement this interface for minimizing a single-valued
// function or fitting a curve with a custom fit function.)

public class Get_sampleBoxes100 implements PlugIn, DialogListener {
```

```
private static ImagePlus imp;
private static Roi impRoi;
private static Rectangle impRoiBounds;
private static double areaPerPoint;
private double boxWidth, boxHeight;
private double width, height;
private double xstart, ystart;
private int linesV, linesH;
private double pixelWidth = 1.0, pixelHeight = 1.0;
private String units = "pixels";

public void run(String arg) {
        if (IJ.versionLessThan("1.43u"))
                return;
        imp = IJ.getImage();
        impRoi = imp.getRoi();  // Get the region of interest that users have selected.

        // If the user has not selected the region of interest, make an error.
        if (impRoi == null) {
                IJ.error ("You need to select the region of interest.");
        } else {
                // If the region of interest has been selected,
                // run the main part of the plugin.
                impRoiBounds = impRoi.getBounds();
                createBoxes();
                showDialog();
        }
}

// Display the boxes on top of the image.
void showBoxes(Shape shape) {
        if (shape == null)
                imp.setOverlay(null);
        else
                imp.setOverlay(shape, Color.blue, null);
}

// Randomly sample boxes fully contained in the region of interest.
void createBoxes() {
        GeneralPath path = new GeneralPath();
        // The created boxes will be stored in the path.

        // Get the Width and Height of the bounding rectangle of the region of interest.
        double width = impRoiBounds.getWidth();
        double height = impRoiBounds.getHeight();
        double xstart = impRoiBounds.getX();
        double ystart = impRoiBounds.getY();
```

```
// Get a list of the positions of the boxes of interest.
java.util.ArrayList<Point2D> Positions = new java.util.ArrayList<Point2D>();
// Test the x coordinates within the bounding rectangle
// at intervals of the box width.
for (int i = 0; i < linesV; i++) {
        double x = (double) (xstart + i * boxWidth);
        // The contains method only accepts integers
        // so all the parameters are converted to integers.
        int xInt = (int) x;
        int xBox = (int) (x + boxWidth);
        // Test the y coordinates within the bounding rectangle
        // at intervals of the box height.
        for (int j = 0; j < linesH; j++) {
                double y = (double) (ystart + j * boxHeight);
                int yInt = (int) y;
                int yBox = (int) (y + boxHeight);
                // Check if the four corners are in the region of interest.
                // If so, store the position of the box.
                Point2D p =  new Point2D.Double(x, y);
                if (impRoi.contains (xInt, yInt) &&
                        impRoi.contains (xBox, yInt) &&
                        impRoi.contains (xBox, yBox) &&
                        impRoi.contains (xInt, yBox)) {
                        Positions.add (p);
                }
        }
}

// Get the number of the boxes that need to be sampled.
int boxesToCount = Positions.size();
// Store all the boxes that need to be sampled in the list.
java.util.ArrayList<Point2D> boxes = new java.util.ArrayList<Point2D>();
Random randomGenerator = new Random();
// Non-repeatedly move the boxes that need to be sampled from
// the list of all the boxes in the region of interest.
for (int i = 0; i < boxesToCount; i++) {
        // Randomly choose boxes that need to be sampled.
        int randomInt = randomGenerator.nextInt(Positions.size());
        Point2D p = Positions.get(randomInt);
        Positions.remove(randomInt);
        boxes.add(p);
}

// Draw the boxes of interest.
for (int i = 0; i < boxes.size(); i++) {
        double x = boxes.get(i).getX();
```

```
                double y = boxes.get(i).getY();
                path.moveTo(x, y);
                path.lineTo(x + boxWidth, y);
                path.lineTo(x + boxWidth, y + boxHeight);
                path.lineTo(x, y + boxHeight);
                path.lineTo(x, y);
        }
        showBoxes(path);
}

// Get the size of the boxes from users' input.
void showDialog() {
        double width = impRoiBounds.getWidth();
        double height = impRoiBounds.getHeight();

        // Different image formats can have different units for size.
        // Get that information from the image, and save it for later.
        Calibration cal = imp.getCalibration();
        int places;
        if (cal.scaled()) {
                pixelWidth = cal.pixelWidth;
                pixelHeight = cal.pixelHeight;
                units = cal.getUnits();
                places = 2;
        } else {
                // The default setting.
                pixelWidth = 1.0;
                pixelHeight = 1.0;
                units = "pixels";
                places = 0;
        }


        if (areaPerPoint == 0.0)
                areaPerPoint = (width * cal.pixelWidth * height * cal.pixelHeight) / 81.0;
        //default to 9 * 9
        //ImageWindow win = imp.getWindow();

        // Create a dialog to get the input of the box size from users.
        GenericDialog gd = new GenericDialog("Boxes");
        gd.addNumericField("Area␣per␣Point:", areaPerPoint, places, 6, units + "^2");
        gd.addDialogListener(this);
        gd.showDialog();

        // If the user presses "cancel" button, any boxes that have been drawn
        // will be removed.
        if (gd.wasCanceled())
```

```
                showBoxes(null);
        }

        // Change the size of the boxes according to users' input.
        public boolean dialogItemChanged(GenericDialog gd, AWTEvent e) {
                double width = impRoiBounds.getWidth();
                double height = impRoiBounds.getHeight();
                // Get the user's input.
                areaPerPoint = gd.getNextNumber();

                // Set a minimum size of the boxes.
                double minArea = (width * height) / 50000.0;
                if (areaPerPoint/(pixelWidth * pixelHeight) < minArea) {
                        String err = "\" Area per Point\" too small";
                        if (gd.wasOKed())
                                IJ.error("Boxes", err);
                        else
                                IJ.showStatus(err);
                        return true;
                }

                // Calculate the size of the box and the number of the boxes that can be
                // fit inside the bounding rectangle of the region of interest.
                double boxSize = Math.sqrt(areaPerPoint);
                boxWidth = boxSize/pixelWidth;
                boxHeight = boxSize/pixelHeight;
                linesV = (int) ((width - xstart)/boxWidth) + 1;
                linesH = (int) ((height - ystart)/boxHeight) + 1;
                if (gd.invalidNumber ())
                        return true;
                else {
                        createBoxes();
                        return true;
                }

        }

}
```

Appendix IV

Pax6 may regulate cell migration in the developing diencephalon

In vitro experiments have indicated that Pax6 binds to specific sequences in the neural cell adhesion molecule and L1 adhesion molecule promoters [136]. *In vivo* studies demonstrated that loss of Pax6 causes pallium-subpallium boundary disruption, which is thought to be maintained by differential adhesion between the pallium and subpallium [136]. The study of the ontogenetic establishment of the thalamic nuclear organisation showed that the enhanced Shh signalling promotes radial migration of the thalamic cells toward pial surface along the medial-lateral axis [66]. Shh has also been shown regulating the expression of adhesion molecules such as cadherin-7 in the developing spinal cord [137]. Thus, Pax6 can regulate cell migration/sorting by either directly regulating the expression of cell adhesion molecules or by interacting with Shh, which could indirectly cause adhesion property change in thalamic cells.

Towards the end of my PhD, I explored the possibility that migratory defects cause the volume change in the P0 vLGN by two pilot studies - a short-term BrdU survival experiment and a time-lapse imaging and cell tracking experiment.

A single dose of BrdU was given to the pregnant females that carry E13.5 embryos and the embryos were collected for the brain tissue a day later at E14.5. The progress of cell migration in the pTH-C, pTH-R and Pth regions were quantified by profiling the immuno staining of BrdU. I found that the cells born in the $Pax6^{+/+}$ and $Pax6^{fl/+}$ pTH-C progress towards the lateral surface of the diencephalic wall much faster than the ones born in the $Pax6^{fl/fl}$ (Figure 13.1 top-left). A similar trend was seen in the pTH-R but the difference betwen the $Pax6^{fl/fl}$ and the $Pax6^{+/+}$ and $Pax6^{fl/+}$ was not as big as in the pTH-C (Figure 13.1 top-right). In the Pth, the newly born cells show similar migration progresses between the $Pax6^{+/+}$, the $Pax6^{fl/+}$ and the $Pax6^{fl/fl}$ (Figure 13.1 bottom).

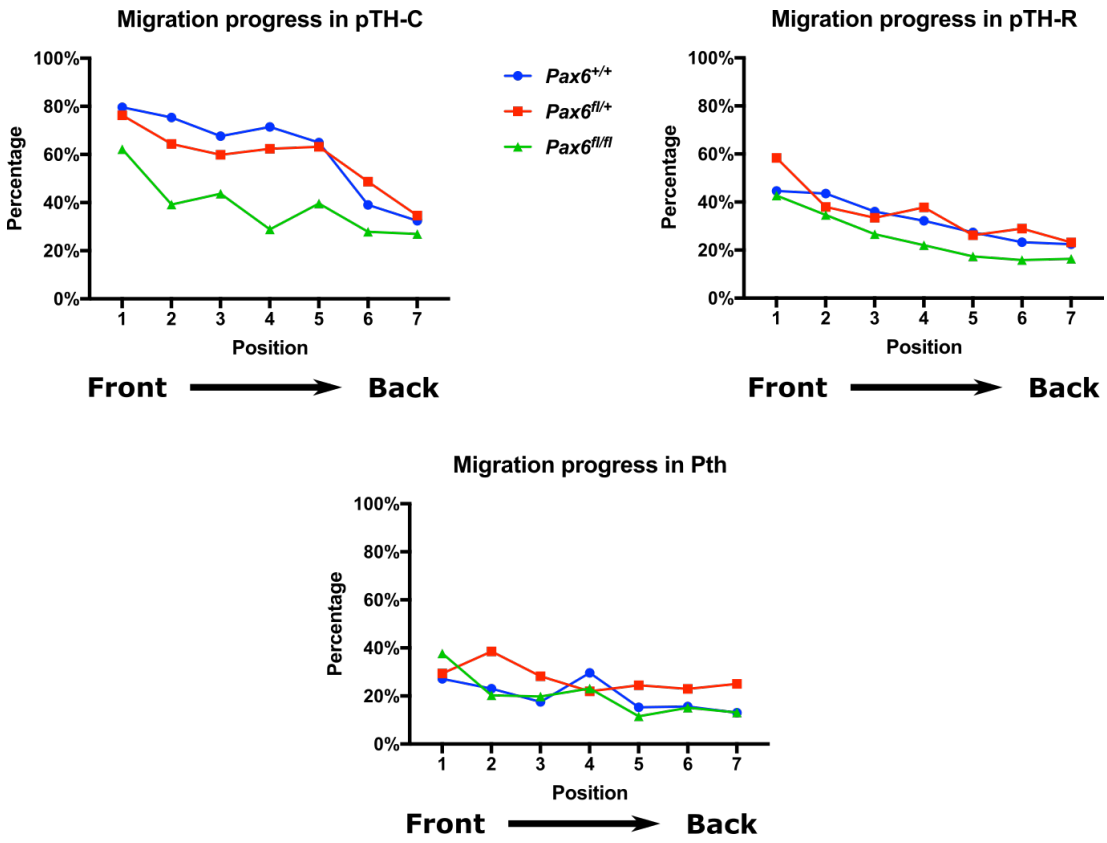


Figure 13.1: ***Migration progress of cells born from E13.5 to E14.5 in the pTH-C, pTH-R and Pth in*** **Pax6$^{+/+}$, Pax6$^{fl/+}$** ***and*** **Pax6$^{fl/fl}$**. *n = 1 embryo for each genotype.*

I also performed brain slice culture and time-lapse imaging using E13.5 *Pax6$^{fl/+}$* and *Pax6$^{fl/fl}$* embryos to track the movement of the GFP+ve cells that are already half way through their journey toward the vLGN. The mean movement speed of the GFP+ve cells was calculated using Imaris. The result shows clearly that the GFP+ve cells in the *Pax6$^{fl/fl}$* have a much higher movement speed on average compared to their counterparts in the *Pax6$^{fl/+}$* (Figure 13.2). This result seems contradictory to the one from the BrdU experiment but it is possible that the cells in the *Pax6$^{fl/fl}$* move at very high speed, but instead of moving directly toward the vLGN, they take a detour, which explains the slow progress shown in the BrdU experiment. In the mean time, it cannot be excluded that a potential 'tissue drift' could result in the difference observed between the *Pax6$^{fl/+}$* and the *Pax6$^{fl/fl}$*. The 'tissue drift' refers to the change of the positioning of the cultured slice due to machanical force change of the microscope setup during the imaging, as the tissue slice is not fixed to the bottom of the culture chamber but rather floating on the surface of the culture media.

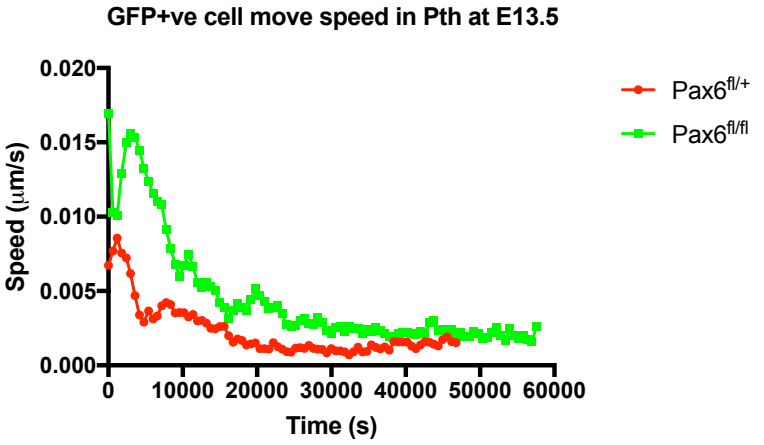


Figure 13.2: ***GFP+ve cell movement speed comparison in E13.5 Pth.*** *n = 1 embryo for each genotype.*

The results of these two experiments opened the possibility of Pax6 regulating cell migration in the developing diencephalon, which could further be explained the defects observed in the vLGN and dLGN.

The BrdU short-term survival experiment did show the newly-born cells in the pTH-C in the *Pax6*$^{fl/fl}$ made less progress migrating radially towards the pial surface than their counterparts in the *Pax6*$^{+/+}$ and the *Pax6*$^{fl/+}$, but the experiment did not consider the possibility that the widths of the proliferating ventricular zone could affect the results. In fact the growth fraction of the pTH-C at both E12.5 and E13.5 were smaller in the *Pax6*$^{fl/fl}$ compared to the *Pax6*$^{+/+}$ and *Pax6*$^{fl/+}$ based on my study in chapter 8. Thus, further experiments should take this into consideration and extra stainings for appreciating the ventricular zone should be performed.

The live imaging result provided invaluable insights into how the GFP+ve cells migrate within the living tissue towards the region where vLGN is to form, and showed that the GFP+ve cells in the Pth moved at a higher speed in the *Pax6*$^{fl/fl}$ lacking functional Pax6. There are several things that should be done for any further experiments: 1. the tissues from different genotypes should be cultured and imaged in the same petri dish to ensure that they are under exactly the same environment and so results are comparable; 2. the staining of the tissue with membrane dye should be performed to provide reference for cell relative movement analysis within the tissue; 3. the tissue drift should be monitored probably by marking the petri dish with ultra violet UV mark pen, whose markings could be used to correct the drift and calculate the movement of the GFP+ve cells relative to the tissue; 4. the movement of the cells in the coronally sectioned tissue along the Z-axis should be considered

and horizontally sectioned slices should be studied as well; 5. thinner sections should be obtained to increase the chance of collecting anatomically matched sections between different genotypes.

It is definitely worthwhile to persue this direction further to look carefully into Pax6's role in the cell sorting/migration in the developing diencephalon. Completing the tissue culture experiments with high qualities and a good number of repeats would be the most straightforward thing to do. Then Pax6's regulation on cell adhesion molecules such as L1, Ncam1 and Ncam1 (all three genes are shown upregulated in the *Pax6* mutant Pth in the E13.5 RNA-seq data analysis performed by Zrinko Kozic in the lab), and the proper function of radial glial cells would be the next to look into.